ECHINODOME RESPONSE TO DYNAMIC LOADING

by

Khaled Mohamed Mahmoud El-Deeb

B. Sc.

Thesis submitted for the degree of

Doctor of Philosophy

Department of Civil Engineering and Building Science

University of Edinburgh

September 1990

PREFACE

It is declared that this thesis has been composed by the author himself. The work embodied is the result of original research work which has been carried out and achieved solely by himself unless otherwise stated, and has not been submitted for a higher degree to any other university or institute.

During the course of the research the following papers have been published and are included as Appendix H of this thesis :

1. "Response of Echinodomes to Asymmetric Loading", Co-authors R. ROYLES and J. M. LLAMBIAS, *Proceedings of the International Conference on Non*–Conventional Structures, ed. B. H. V. TOPPING, vol. 1, pp. 167–183, Civil–Comp Press, Edinburgh, (1987).
2. "Deformation Measurements on an Underwater Structure Relating to Buckling", Co-authors R. ROYLES and J. M. LLAMBIAS, *Proceedings of the International Conference on Stress Determination and Strain Measurement in Aeronautics*, pp. 11.1–11.16, Royal Aeronautical Society, London, (1988).

Edinburgh, September 1990

K. M. El-Deeb

ABSTRACT

The response of an Echinodome to static and dynamic point loads, and explosive type loadings was examined both theoretically and experimentally. The finite element method of analysis was employed in the theoretical investigation. Semi–loof thin shell elements were used to model a GRP prototype on which the experiments were performed.

The stress distribution of the Echinodome under a static symmetric point load was investigated both experimentally and theoretically. Then the Southwell technique was employed in estimating the critical buckling load from deflection measurements. Experimental estimates were then compared with the numerical predictions in the form of non–linear collapse and non–linear bifurcation buckling loads.

A free vibration analysis was performed to determine the structural natural frequencies and typify the mode shapes. The shock response spectra of several pulse shapes were determined using the finite element method. The most severe loading function was established to be a step loading with infinite duration and zero ramping time and was then employed as the load–time history in an axisymmetric and symmetric non–linear dynamic buckling analysis. The dynamic collapse buckling loads were found to be smaller in magnitude than their static correspondents.

A modal testing was then carried out on the Echinodome prototype to determine the experimental modal parameters (natural frequencies, damping values and mode shapes). Newly developed correlation techniques were adopted in the comparison of the experimentally derived parameters with those predicted and poorly modelled regions were identified. Great improvement was achieved by correcting the experimental data and updating the finite element model's boundary conditions.

A set of underwater free field experiments was performed to determine the pulse characteristics for a specific explosive charge, followed by another set while the prototype was in a floating submerged state and acting as the target for the same explosive charge. A theoretical simulation was accomplished by employing a finite element–boundary element approximation for the modelling of the structure and infinite fluid media respectively. Measured responses were compared with the numerical predictions and means of acquiring better theoretical approximations are mentioned.

The loading conditions to be experienced by an underwater LNG Echinodome vessel are reviewed with emphasis on accidental dynamic loads (impact and explosion). A state of the art storing configuration is proposed for the Echinodome in order to limit the extent of damage and hence minimise risk during upset conditions. Finally, appropriate design, construction and prestressing procedures were recommended.

ACKNOWLEDGEMENTS

The author wishes to express his gratitude to the following people :

i. Professor A. W. Hendry, the former Head of Department of Civil Engineering and Building Science, for his encouragement during the initial and intermediate stages of the research project;

ii. Professor J. M. Rotter, the current Head of Department of Civil Engineering and Building Science, for showing his interest in the undertaken research topic;

iii. Dr Rodney Royles, the author's supervisor, for his continuous support, firm guidance, fruitful discussions and friendliness;

iv. Professor M. Forde for putting his laboratory's equipment at the author's disposal;

v. Dr S. R. Davies for answering some of the technical questions;

vi. Members of staff at A.R.E. for permitting the use of the facilities in their vibration laboratory and underwater explosive testing unit, and for their invaluable advice during the experimental set–ups;

vii. Mr A. C. Gibson, from Brüel & Kjær, for supplying most of the modal testing literature from which the author's background in that particular subject was formed;

viii. Mr I. D. Ramage, from Techni Measure, for lending the miniature tourmaline pressure gauge used in the explosive tests;

ix. Mr S. Coe and Mr P. Bell, from Scientific Atlanta, for loaning the Modal 3.0 software which was employed in the analysis of the modal testing measurements;

x. Dr P. Macey and Mr J. King, from PAFEC Ltd, Mr D. Barry and Mr D. Bigwood, from FEA Ltd for their technical support;

xi. Mr F. Mill, Mr S. Warrington and Mr C. Spencer, from the Department of Mechanical Engineering at the University of Edinburgh, for authorising the use of their departmental computing facilities;

xii. Every member of the computing services Science User Support Group at the University of Edinburgh and in particular Mr M. Robinson for his readiness at all times to sort any arising computing problem;

xiii. Mr B. Murdoch and Dr J. Bartlett of the ERCVAX System's Team for providing whenever required the necessary environment for running particularly large finite element modelling problems;

xiv. All colleagues especially Nabeel and June for their warm companionship;

xv. Special friends Mr G. Hall and Dr W.F.K. Timpo for their moral support;

xvi. Nana for her love, caring and advice; and,

xvii. Mrs C. Corsie for her patience and promptness during the typing of the thesis.

The author is most grateful to his beloved parents, Hanem and Mohamed for their caring, understanding, encouragement, and both moral and financial support, and who have patiently awaited the date for his finishing the undertaken work.

"GOD I do thank You for where I am standing today, without You nothing could have been possible."

To my parents

TABLE OF CONTENTS

LIST OF SYMBOLS

b_o	Intercept of fitted line with the Y—axis in a linear regression analysis
b_1	Slope of fitted line with the X—axis in a linear regression analysis
c	Shock wave speed underwater
c_r	Modal damping of the r^{th} mode shape
$e^{i\omega t}$	$\cos(\omega t) + i \sin(\omega t)$
e^x	Exponential of x
$\{e\}$	Unit vector containing zero elements throughout except for one element having a value of +1
f	Frequency in Hz
f_c	Cut off frequency in Hz
f_i	Natural frequency of the i^{th} mode of vibration in Hz
f_m	Highest natural frequency of interest in Hz
f_s	Sampling frequency in Hz
f_N	Nyquist frequency in Hz
$h(t)$	Impulse response function
i	$\sqrt{-1}$
k_r	Modal stiffness of the r^{th} mode shape
l	Incremental displacement length in a geometrically non–linear analysis
m_r	Modal mass of the r^{th} mode shape
$p(t)$	Pressure as a function of time
p_a	Atmospheric pressure
p_i	Incident pressure
p_m	Peak pressure
p_r	Radiated pressure
p_s	Scattered pressure

p_w	Hydrostatic pressure
p_R	Reflected pressure
r	Correlation coefficient between observed and fitted Y values in a linear regression analysis
s	Reading of transducer's scale
s_o	True reading of transducer's scale at $\delta = 0$
s_r	Complex eigenvalue of the r^{th} mode of vibration (r^{th} pole location of an FRF on the frequency axis)
s_y	Standard error of estimate in a linear regression analysis
t	Time in secs
t_d	Pulse time duration in secs
t_r	Step load ramping time in secs
t_1	Rise time of triangular pulse in secs
t_2	Decay time of triangular pulse in secs
t_w	Shell wall thickness
w	Normal deflection
$\bar{x}(t)$	Hilbert transform of the time domain signal x(t)
$x_r \equiv x(t_r)$	r^{th} element of a time domain sequence
z_o	Pressure head at the apex of the Echinodome
$A(\omega)$	Accelerance frequency response function
[B]	Strain–displacement matrix
[C]	Damping matrix
[D]	Stress–strain modulus matrix
E	Young's modulus
E_f	Energy flux density
F	Average of the force spectrum
F(t)	Force magnitude as a function of time
F_o	Peak magnitude of a transient pulse
$F(\omega)$	Force frequency spectrum

$G_{FF}(\omega)$	Auto–spectrum of excitation signal
$G_{FR}(\omega)$	Cross spectrum between excitation and response signals
$G_{RR}(\omega)$	Auto–spectrum of response signal
$H(\omega)$	Frequency response function
I	Impulse per unit area
$\{I\}_x$	Vector containing unit values for each row of the mass matrix that is associated with the X direction and the remaining elements are zeros
$[I]$	Identity matrix
$[K]$	Linear stiffness matrix
$[K_t]$	Theoretical linear stiffness matrix
$[K_o]$	Small displacements stiffness matrix
$[K_L]$	Large displacements stiffness matrix
$[K_T]$	Total tangential stiffness matrix
$[K_\sigma]$	Initial stresses or geometric stiffness matrix
$[M]$	Mass matrix
$[M_t]$	Theoretical mass matrix
$[M_d]$	Mass matrix of a deformed structure
P	Point load
P_{cr}	Critical buckling point load
P_{dc}	Non–linear dynamic collapse buckling point load
P_{lb}	Linear bifurcation buckling point load
P_{nb}	Non–linear bifurcation buckling point load
P_{nc}	Non–linear static collapse buckling point load
P^*, s^*	Pivot point load–deflection pair
$\{P\}$	External loads vector
$\{P_{ref}\}$	Normalised external load vector
R	Stand off distance from an explosive charge
${}_rR_{jk}$	Complex modal residue of the r^{th} mode of vibration for excitation at point j and measured response at k

$\{R\}$	Residual load vector
$R(\omega)$	Response frequency spectrum
S_o	Overall sensitivity of an accelerometer and force cell combination in kg^{-1} units
S_p	Current stiffness parameter
T	Natural period of a periodic signal in secs
T_c	Natural period of f_c
T_m	Natural period of f_m
T_r	Natural period of the r^{th} mode of vibration
T_N	Natural period of f_N
$V_{\ddot{\delta}}$	Voltage across the electronics of an accelerometer
V_F	Voltage across the electronics of a force cell.
W	Mass of explosive charge
X	Predictor in a linear regression analysis
$X_k \equiv X(\omega_k)$	k^{th} element of a discrete Fourier transform
Y	Response in a linear regression analysis (observed Y values)
Y_f	Fitted Y values obtained from a linear regression analysis
$\{0\}$	Null vector
$[0]$	Null matrix
$\alpha(\omega)$	Receptance frequency response function
δ	Displacement
$\ddot{\bar{\delta}}$	Average of the acceleration spectrum
δ_d	Dynamic displacement
δ_o	Initial deflection or initial geometrical imperfection
δ_s	Static displacement
$\delta(\omega)$	Displacement frequency spectrum
$\dot{\delta}(\omega)$	Velocity frequency spectrum
$\ddot{\delta}(\omega)$	Acceleration frequency spectrum
$\{\delta\}$	Nodal displacement vector

$\{\dot{\delta}\}$	Nodal velocity vector
$\{\ddot{\delta}\}$	Nodal acceleration vector
$\{\delta_m\}$	Nodal displacements vector for master degrees of freedom
$\{\delta_s\}$	Nodal displacements vector for slave degrees of freedom
ε	Strain
$\{\varepsilon\}$	Generalised strain vector
$\{\varepsilon_o\}$	Generalised initial strain vector
η_r	Structural damping constant of the r^{th} mode for a hysteretic damping model
γ_i	i^{th} eigenvalue of a modified bifurcation buckling analysis
$\overline{\gamma}_i$	i^{th} shifted eigenvalue of a modified bifurcation buckling analysis
γ_{xz}, γ_{yz}	Shear strain in the local xz and yz planes respectively
$\gamma(\omega)$	Mobility frequency response function
$[\gamma]$	Eigenvalue diagonal matrix of a modified bifurcation buckling analysis
$[\overline{\gamma}]$	Shifted eigenvalue diagonal matrix of a modified bifurcation buckling analysis
κ	Skewness factor
λ_a	Acoustic wavelength
λ_s	Structural wavelength
λ_i	i^{th} load multiplier of a bifurcation buckling analysis
μ_r^x, μ_r^y, μ_r^z	Effective modal mass of the r^{th} mode of vibration in the **X**, **Y** and **Z** direction respectively
$[\mu]$	Diagonal shift matrix with the constant μ on its leading diagonal
ν	Poisson's ratio
ω	Frequency in rad/sec
ω_c	Cut off frequency in rad/sec
ω_N	Nyquist frequency in rad/sec
ω_r	Natural frequency of the r^{th} mode of vibration in rad/sec
ω_s	Sampling frequency in rad/sec
ϕ	Meridional angle

$\{\phi\}_r$	r^{th} mass normalised vibrating mode shape vector
$\{\phi_i\}_r$	i^{th} element of the r^{th} mass normalised vibrating mode shape vector
$\{\psi\}_r$	r^{th} vibrating mode shape vector
$\{\psi_i\}_r$	i^{th} element of the r^{th} vibrating mode shape vector
$\{_t\psi\}_r$	r^{th} theoretical vibrating mode shape vector
$\{_t\psi_i\}_r$	i^{th} element of the r^{th} theoretical vibrating mode shape vector
$\{_x\psi\}_r$	r^{th} experimental vibrating mode shape vector
$\{_x\psi_i\}_r$	i^{th} element of the r^{th} experimental vibrating mode shape vector
ρ	Mass density
σ_d	Design stress
σ_e	Equivalent stress
σ_1	Maximum principal stress (most positive)
σ_2	Minimum principal stress (most negative)
$\{\sigma\}$	Generalised stress vector
$\{\sigma_o\}$	Generalised initial stress vector
τ	Time normalised by T_1
τ_d	Pulse duration normalised by T_1
τ_r	Step load ramping time normalised by T_1
τ_w	Time constant of an exponential weighting function
τ_1	Rise time of triangular pulse normalised by T_1
τ_2	Decay time of triangular pulse normalised by T_1
θ	Azimuth angle
θ_p	Principal stress angle
ζ_r	Critical damping constant of the r^{th} mode of vibration for a viscous damping model
Δf	Frequency spacing (resolution) of a spectrum in Hz
Δp	Load parameter increment
Δt	Time step used in numerical integration in secs

Δt_{cr}	Critical time step in secs
$[\Delta K]$	Stiffness error matrix
$[\Delta K_{ii}]$	i^{th} diagonal element of stiffness error matrix
$[\Delta K_m]$	Modified stiffness error matrix
$[\Delta K_{m\ ii}]$	i^{th} diagonal element of modified stiffness error matrix
$[\Delta M]$	Mass error matrix
$\{\Delta\delta\}$	Incremental nodal displacement vector
$\Delta\omega$	Frequency spacing (resolution) of a spectrum in rad/sec
$[\Lambda]$	Load multipliers diagonal matrix
$[\Omega^2]$	Eigenvalue diagonal matrix of a free vibration analysis
$[\Omega_t^{\ 2}]$	Diagonal matrix formed of the square of the theoretical natural frequency estimates in rad/sec^2 squared
$[\Omega_x^{\ 2}]$	Diagonal matrix formed of the square of the experimental natural frequency estimates in rad/sec^2 squared
$[\Phi]$	Mass normalised vibrating mode shapes matrix
$[\Psi_t]$	Theoretical mass normalised vibrating mode shape vector
$[\Psi_x]$	Experimental mass normalised vibrating mode shape vector
$[\Psi]$	Vibrating mode shapes matrix
$[\Theta]$	Bifurcation buckling mode shapes matrix
*	Denotes a complex conjugate
$\|\ \|$	Denotes the modulus of a real number or the magnitude of a complex number
$\|\ \|_2$	Denotes an Euclidean vector norm
Σ	Denotes ''the summation of''
•	Denotes vector multiplication

ABBREVIATIONS

CALM	Catenary anchor leg moored
COMAC	Coordinate modal assurance criterion
C.O.V.	Coefficient of variation
CMPN	Correlated mode pair number
CPU	Central processor unit
DAA	Doubly asymptotic approximation
DFT	Discrete Fourier transform
DLF	Dynamic load factor
DLNORM	Limit for the sum of the squares of the iterative displacements as a percentage of the sum of squares of the total displacements
ESD	Energy spectral density
FFT	Fast Fourier transform
FIR	Finite impulse response
FRF	Frequency response function
GRP	Glass reinforced plastic
IDFT	Inverse discrete Fourier transform
K.E.	Kinetic energy
MAC	Modal assurance criterion
MDOF	Multi–degree of freedom
MDM	Modulus difference matrix
PSD	Power spectral density
PWR	Power
PUF	Polyurethane foam
RLNORM	Limit for the sum of squares of all residual forces as a percentage of the sum of the squares of all reactions

RMS	Root mean square
RPT	Rapid phase transition
SBM	Single buoy mooring
SDOF	Single degree of freedom
S.E.	Strain energy
3-D	Three dimensional
VMA	Virtual mass approximation
WLNORM	Limit for the work done by the residuals acting through the iterative displacements as a percentage of the work done by the loads on iteration zero of the increment

LIST OF FIGURES

CHAPTER THREE

CHAPTER FOUR

CHAPTER FIVE

CHAPTER SIX

LIST OF TABLES

CHAPTER TWO

CHAPTER THREE

CHAPTER FOUR

CHAPTER FIVE

CHAPTER 1

INTRODUCTION

1.1 VARIOUS NEEDS FOR STORAGE TANKS

For many years shell structures have been utilised for industrial as well as domestic purposes.

Today, containers are being used widely in different application fields such as agriculture, sewage, oil industry, ... , etc., to name but a few.

Their structural form, wall strength and composition are primarily dependent on the amount and type of contained material. Storage vessels may retain anything from granular materials to cryogenic liquids. Another parameter affecting the shape of such structures and their construction material is the media in which they are to operate, e.g. air, sea or underground.

In the following subsections some applications for storage tanks are presented.

1.1.1 Agriculture

Over the years cylindrical storage bins have been used for storage of grains. Recently however, research was conducted at the University of Illinois at Urbana–Champaign (UIUC) [1] on dome type shell structures to investigate their potential for storage of grains or fertilisers.

1.1.2 Water Desalination

In water desalination plants sea water is brought to onshore intake houses with the aid of suction pumps. It is then processed to produce desalinated water which is eventually stored in large reservoirs for distribution.

1.1.3 Chemical Industry

Containment structures are very common in the chemical industry. Storage of hazardous substances (e.g. high explosives) is one of their uses. Another is the retaining of industrial chemical waste materials for long periods of time or treating it to produce less harmful substances having minimum impact on the environment.

Cylindrical, cubical and spherical containments are typical structural forms used in the chemical industry.

1.1.4 Oil Industry

Oil is a major source of energy. Over the years considerable research has been carried out on storage structures for such a material before, during and after purification.

With the dramatic fluctuation in oil prices substantial efforts were made towards oil exploration offshore. New problems appeared : is it more economic, efficient and safe to operate on crude oil offshore or onshore? If offshore, where is it best to store the crude oil and its extracts? In caissons under the drilling rig or in separate containments? How to export material to onshore; expensive piping systems or ferrying tankers?

All of the above questions were new challenging engineering problems and in the current research an attempt is made towards finding answers to some of the above questions.

1.2 VARIOUS STRUCTURAL FORMS

Storage tanks may vary in shape, e.g. spherical, cylindrical with flat, toroidal or spherical ends, etc. . . . . , with choice depending on their economy, efficiency and safety.

During the last two decades intensive research was undertaken at the UNIVERSITY OF EDINBURGH / CIVIL ENGINEERING DEPARTMENT to assess the potential of the drop shaped tank [2-4] which will be described in the following subsection.

1.2.1 The Drop Shaped Tank

The drop shaped tank is a shell of revolution having constant wall thickness and strength under a specific uniform pressure (see Fig. 1.1). Such a structure would utilise uniform material throughout the meridional profile and consequently the design principle can be considered as an optimum one.

For each pressure head there is a new shape. The differential equations governing the shape of the meridional profile and methods for solving such equations (graphical and numerical) have been described elsewhere [2,3,5-7] . It was observed that as the value of pressure at the apex increased the reservoir approached the form of a sphere.

The drop shaped tank is exactly similar to a drop of liquid resting on a flat horizontal plane. The liquid would be under constant tension due to capillarity while the inside hydrostatic varies linearly.

By 1980, a shape prediction program in Fortran IV was developed by Royles *et al.* [2] and refined by Sofoluwe [3] . This was later transformed by the current author to Fortran 77 and employed in the current research. The program used an explicit modified Euler method to solve the non–linear differential equations governing the profile of the shell. Sofoluwe then investigated the response of the drop shaped tank to hydrostatic pressure both experimentally and theoretically (using the membrane theory and linear elastic finite element analysis).

Later, by 1985, Llambias [4] investigated the stability of the shell of constant strength under hydrostatic pressure load, studied the shell response to axisymmetric and symmetric point loads and carried out a free vibration analysis. The above investigation was conducted experimentally and theoretically utilising the finite element method.

From a library of finite elements Llambias recommended a particular element for each specific load case and used each accordingly to design a full size shell based on a linear elastic static analysis except for structural stability under hydrostatic pressure where geometric non–linearity was considered.

Earlier [2] the drop shaped tank or shell of constant strength was observed to be similar to a Sea Urchin of the phylum Echinodermata and hence the generic name — The Echinodome. Throughout the current research the terms drop shaped tank, shell of constant strength and Echinodome are used interchangeably to refer to the same shell structure.

1.3 APPLICATIONS OF ECHINODOMES

Echinodomes have a great potential serving as storage tanks in air or water media. Application fields vary from agricultural, sewage, chemical, water or oil industry. Employing Echinodomes on board LNG and LPG carriers instead of spherical tanks is just another attractive application as buckling is the main mode of failure for large self–supporting cargo tanks [8] , which was proven earlier [4] not to be the case for the drop shaped shell.

Underwater, the shell of optimum shape is applicable to storage of hazardous and other liquids or for use as a one atmosphere enclosure for human habitation or industrial type activities.

In 1984 [9] a proposal was made for the storage of LNG in an Echinodome (or a series of them) tethered underwater in a floating submerged state with the aid of tension legs. It was suggested that the tank would be proximate to an oil production platform and that the LNG would then be ferried onshore using tankers. The feasibility of storing LNG underwater safely in such a container is assessed later in Chapter 6.

1.4 SCOPE AND SUMMARY OF THE THESIS

With recent developments in fixed and compliant offshore structures dynamic loads are gaining ever increasing attention by design engineers because of their apparent detrimental effects on structures when compared with their static counterparts.

Therefore the main objective of the thesis is to determine the Echinodome response to dynamic loadings (impact and explosion) and to establish a design procedure for such a structure when operating underwater to sustain operational and accidental dynamic loads.

The work carried out during the course of the current research (relating to the Echinodome shell structure), described in the following chapters, is summarised as follows :

1. Examination of the principal stresses distribution under axisymmetric and non–axisymmetric static point loads, and studying the structural stability under such loadings (Chapter 2).
2. Determination of the shock response spectra for various transient loadings. Establishing the dynamic response to step functions and examining the structural stability under the preceding dynamic load (Chapter 3).
3. Identifying and updating poorly modelled regions in a finite element mesh by performing a modal test on a test structure and hence achieving a better simulation (Chapter 4).
4. Assessment of the performance of a numerical technique used in predicting structural response of underwater structures to shock waves (Chapter 5).
5. Examination of the dynamic response of a full size Echinodome underwater storage vessel to impact loads induced by accidentally dropped slender or bulky objects (Chapter 6).
6. Establishing a design and construction procedure for Echinodomes operating underwater and subject to accidental dynamic loadings (Chapter 6).

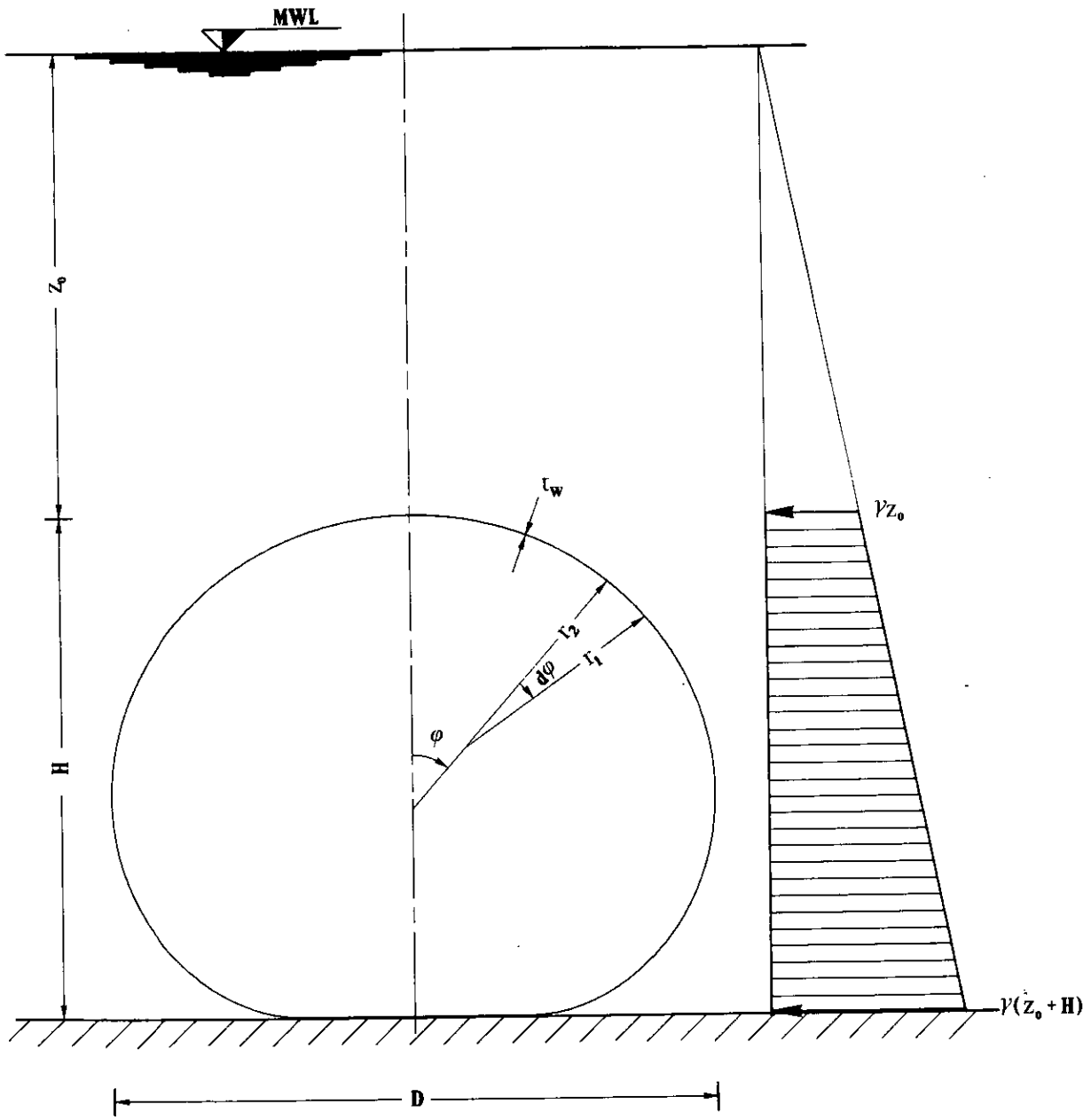

FIG. 1.1–THE DROP SHAPED TANK

CHAPTER 2

THE ECHINODOME UNDER A STATIC POINT LOAD

2.1 SUMMARY

This chapter reviews the Echinodome response to a static symmetric concentrated load. An experiment was carried out using a glass reinforced plastic(GRP) prototype (see Fig. 2.1). Theoretical simulation was achieved by means of the finite element method. Subsequently experimental and theoretical results are compared.

Two non-destructive methods for determining the critical buckling load are presented and one was applied to the prototype. Numerical buckling analyses for various types of instability, to a symmetric point load, are reported and compared with the experimental value.

2.2 INTRODUCTION

The emphasis in the previous chapter was on the increasing requirement of shell structures for storage. One of the most optimum shapes to be used for such a purpose, is the Echinodome. Habitation of the Echinodome shell structure can take place in air or underwater, being subjected to a wide variety of load cases ranging from static (e.g. hydrostatic pressure) to dynamic (e.g. impact, explosion). In order to assess the severity of dynamic loadings comprehension of the Echinodome behaviour under static loadings must be achieved.

2.3 SYMMETRIC POINT LOAD EXAMINATION

There are three possible point loadings on the Echinodome namely axisymmetric, symmetric and asymmetric (see Fig. 2.2). The first and last load cases have been discussed elsewhere [4,10]. The following sections relate to symmetric point loadings.

2.3.1 Experimental Approach

No numerical procedure is declared viable without experimental proof and in order to assess the performance of the finite element method applied to thin shells, an experiment on the Echinodome prototype was undertaken. A point load of 300 N was applied via a wooden strut. The load was normal to the surface and 60^{o} away from apex.

2.3.1.1 Test structure— The test shell meridional profile (see Fig. 2.3) was determined by a shape prediction program. It was designed for an apex pressure head, z_0 = 1.525 m of water, with a uniform design stress, σ_d = 0.446 MPa, and a mean shell wall thickness, t_w = 3.8 mm (average thickness values along the meridian and circumference are given in Ref. (11)). The material used was GRP having an epoxy matrix and 0.26 glass fraction, the fibres being in the form of layers of randomly arranged chopped strand mat fabric. The shell was constructed in two halves each from the same mould and then bonded together along a meridional seam using a slow curing araldite. The shell was later fixed to a tufnol square base of dimensions 200 × 200 × 20 mm. Variations in the wall thickness were determined utilising an ultrasonic thickness tester [12] . The material properties were determined from material control tests [3] and were as follows :

Young's modulus (E)	= 8800 MPa	(extrapolated)
Poisson's ratio (ν)	= 0.36	
Ultimate tensile strength	= 55.4 MPa	
Mass density (ρ)	= 1100 kg/m^3	

2.3.1.2 Loading set–up— Fig. 2.4 shows the prototype in the loading rig under a normal point load acting at an angle, $\phi = 60^\circ$ away from apex. The shell was fixed to a rotating table which in turn allowed it to rotate between 0° and 90° in a vertical plane. Static point loading normal to the surface was applied to the shell via a vertical stiff wooden strut using a dead load lever system.

2.3.1.3 Disposition of displacement transducers— In the current research 12 meridians were marked on the prototype each 30° apart. The meridians were named starting from the loaded meridian onwards as M1, M2, M3,. . . . . , M12. In symmetric loading the first seven meridians were necessary only as the shell is axisymmetric (ignoring imperfections) (see Fig. 2.5).

For the present load case nine rectilinear potentiometric displacement transducers model S30FLP100A were arranged around M1 and M7 normal to the surface as seen in Fig. 2.6. Due to the obstruction from the lever arm it was impossible to mount two extra displacement transducers between transducers 6 and 7 and between 7 and 8. Each transducer was characterised by a full scale resistance of 2 kΩ and a full scale output of 5 V d.c. for a maximum mechanical stroke of 100 mm with a linearity of 0.25 percent and a resolution of ±1 micron. Energisation of 5 V d.c. for the displacement transducers was supplied from a power supply TECHNI MEASURE

model TPU–30.

2.3.1.4 Data acquisition system— A multi–channel system [13] was used to scan the output of the displacement transducers, a block diagram of which is shown in Fig. 2.7. The system consisted of a microcomputer CBM model 8032 to which an 80 column tractor printer CBM model 4022 and a 1–MBYTE dual floppy disk drive CBM model 8052 for backup storage were attached. The microcomputer controlled a multi–channel scanner via its user port. The scanner accepted signals from up to 32 channels either electrical resistance strain gauge half bridges or other low frequency voltage sources in the range $0 \rightarrow 10$ Hz, or any combination of the two. A KEITHLY programmable digital multimeter model 192 was used to measure the voltage incoming from the scanned channels which was in turn connected to the microcomputer through the general purpose interface bus (GPIB).

The whole operation was managed by a computer program of two parts, the first of which controlled the scanning while the second processed the results (transformed voltage values into displacement or strain values). The program also instructed the microcomputer to store the datum readings and subtract them from the results of subsequent scans as an experiment progressed.

2.3.1.5 Test procedure— After securing the test structure in its position, a maximum point load of 300 N was applied via a stiff wooden strut normal to the surface at an angle $\phi = 60^{\circ}$ away from the apex. The load was incremented by 50 N from 0 to 300 N. Three initial runs were performed in order to put the system into a cyclic state. Following this, 10 runs were carried out to scan the 9 displacement transducers from 0 to 300 N and the results were listed to the line printer. A 5 min. duration was allowed between each of the 13 runs to allow for creep recovery, a characteristic of GRP [14] . The scanning was done using the computer program on the ascending part of each run and the loading rate was kept constant for the series of runs.

2.3.1.6 Test results— The average displacement values are listed in Table 2.1(a) for the individual transducers at each load increment. Corresponding coefficients of variation [§] follow in Table 2.1(b). Values not listed were erratic because of the small displacement magnitudes associated with the low load levels.

---

§ **The Coefficient of Variation** [15] is the ratio of the standard deviation to the mean. This statistic quantifies the spread of data as it provides a normalised measure of the spread.

DISPLACEMENT TRANSDUCER NUMBER (EQUIVALENT NODE NUMBER IN FINITE ELEMENT SIMULATION)	AVERAGE NORMAL DISPLACEMENTS AT DIFFERENT LOAD INCREMENTS (mm)					
	50 N	100 N	150 N	200 N	250 N	300 N
1 (501)	0.050	0.107	0.164	0.220	0.284	0.336
2 (421)	0.060	0.134	0.207	0.272	0.356	0.433
3 (321)	0.078	0.157	0.239	0.319	0.399	0.482
4 (221)	0.073	0.169	0.263	0.337	0.412	0.480
5 (121)	____	____	0.023	0.052	0.093	0.116
6 (1)	0.025	0.048	0.062	0.074	0.086	0.101
7 (215)	0.076	0.182	0.280	0.391	0.499	0.601
8 (415)	0.063	0.138	0.217	0.301	0.383	0.466
9 (495)	0.043	0.099	0.156	0.217	0.275	0.338

TABLE 2.1(a) — *AVERAGE NORMAL DISPLACEMENT VALUES FOR A NORMAL POINT LOAD ACTING 60° AWAY FROM APEX*

DISPLACEMENT TRANSDUCER NUMBER (EQUIVALENT NODE NUMBER IN FINITE ELEMENT SIMULATION)	COEFFICIENT OF VARIATION FOR DISPLACEMENT VALUES AT DIFFERENT LOAD INCREMENTS (%)					
	50 N	100 N	150 N	200 N	250 N	300 N
1 (501)	9.2	5.5	4.4	1.9	2.2	2.0
2 (421)	5.0	2.5	2.4	9.2	1.3	1.2
3 (321)	5.1	2.6	2.2	1.2	1.1	1.0
4 (221)	4.1	2.1	2.5	5.0	1.1	5.4
5 (121)	____	____	27.5	17.3	20.3	9.5
6 (1)	18.6	8.2	10.0	8.5	7.6	4.9
7 (215)	12.8	6.1	9.8	2.7	3.3	2.2
8 (415)	7.3	4.2	2.8	2.3	2.5	2.2
9 (495)	6.7	5.3	3.0	2.5	3.0	2.4

TABLE 2.1(b) — *COEFFICIENT OF VARIATION FOR EXPERIMENTAL DISPLACEMENT VALUES*

2.3.1.7 Discussion— Table 2.1(a) shows that the shell was slightly following a non–linear behaviour in the loading range from 0 to 300 N with a maximum deformation under the point load and a minimum at the apex.

It is also noted that the following pairs of transducers had equal displacement values : 1, 9 and 2, 8 while 7 had a higher value than 4 and this may indicate that the general profile of the Echinodome prototype was not distorted except under the point load, meaning that the shell deformed both locally and globally.

2.3.2 Theoretical Approach

Theoretical analysis of shell structures can be approached in two different ways : either analytically or numerically. Analytical methods are limited to a certain class of problems and those include problems which can be approximated with linear models and those that have simple geometry. As a result analytical methods are of limited practicality in studying the response of Echinodomes to complex loadings (e.g. static and dynamic point loadings, explosions, etc.), and recourse must be made to numerical procedures, one of which is the finite element method.

2.3.2.1 Brief introduction to the finite element method— The finite element approach is a growing technique for structural analysis. It is based on a discretisation method [16,17] by which a continuum is replaced by a computational mesh. Since a number of authoritative texts are available no detailed explanation of the finite element method is attempted. A typical analysis can be summarised as follows [16] :

1. **Continuum Discretisation :** imaginary lines are utilised in dividing a continuum structure into a number of finite elements assumed to interact only at a discrete number of points known as nodes.
2. **Element Equilibrium :** a system of forces concentrated at the nodes that equilibrate external loads is determined. The result is a stiffness relationship involving internal loads, external loads, and nodal displacements for each element.
3. **Element Assemblage :** individual element data are assembled into overall matrices and solutions for nodal displacement are obtained after imposing the prescribed boundary conditions.
4. **Displacements :** the nodal displacements are used to describe the state of displacement over the individual elements.

5. **Strains and Stresses :** the state of strain within an element is defined in terms of nodal displacements. These, together with the constitutive properties of material will define the state of stress.

Two finite element codes LUSAS (London University Stress Analysis System) and PAFEC (Program for Automatic Finite Element Calculations) each with its graphics partner MYSTRO and PIGS respectively were implemented on a VAX 8550 at the University of Edinburgh Computing Centre.

LUSAS [18,19] incorporates facilities for linear and non–linear static stress analysis, step by step linear and non–linear dynamic analysis, eigenvalue extraction, linear buckling, steady and transient field analysis and spectral response analysis.

The PAFEC [20,21] finite element system consists of a general program, carrying the name PAFEC, together with a number of optional subsystems, two of which are SNAKES and DOLPHIN. SNAKES is the non–linear subsystem used for performing a more accurate non–linear analysis. DOLPHIN is an acoustics subsystem used for calculating the natural frequencies, sinusoidal response and transient response of systems in which the inertia and flexibility of a surrounding or a contained fluid play an important role in determining the behaviour of a structure.

2.3.2.2 **The semi–loof shell element—** Each of the above mentioned systems included the semi–loof shell element (see Fig. 2.8) as a member of its elements library. The following paragraphs state briefly the theoretical development of the semi–loof element which is due to Irons [22].

The family consists of two elements : eight noded quadrilateral and six noded triangular generally curved thin shell elements with eight and six loof points respectively located at $1/\sqrt{3}$ of the distance from a midside node to a corner node. Most of the following discussion applies to both the quadrilateral and triangular elements and for this reason the theoretical basis for the former only will be presented.

The semi–loof element is assumed to consist of a stack of membranes with equal surface area to that of the midplane. Prior to the application of any constraints there are forty three degrees of freedom which are itemised as follows :

1. **Translation :** there are three translational degrees of freedom (**u, v, w**) at each of the eight nodes corner–midside family accounting for twenty four of the total.

2. **Rotation :** at each of the loof points and the central node (at the centre of the element) there are two rotational degrees of freedom (rotation to introduce difference in displacement between upper and lower surface) loof family adding an extra eighteen.

3. **Bubble function :** this extra degree of freedom is introduced at the centre of the element to warrant its success in the quadrilateral patch test.

The forty three degrees of freedom are reduced to thirty two by applying the following shear constraints [§]:

1. **Loof point rotations :** the shear strain γ_{yz} is equal to zero at each of the loof points giving eight constraints.

2. **Central node rotations :** the integral of the components of shear strain in the curvilinear directions ξ and η at the central node is equal to zero giving two constraints.

3. **Bubble function :** the integral of the shear strain γ_{xz} around the boundary is equal to zero giving one constraint.

For the programming logic the loof rotations on each side were grouped along with the midside variables in five degrees of freedom at midside nodes and three degrees of freedom at corner nodes. The semi–loof shell element can be used to simulate generally curved shell geometries with multiple junctions and/or variable thicknesses. As discussed earlier the formulation takes account of both membrane (in plane) and flexural (out of plane) deformations while transverse shearing deformations are not catered for which is a basic assumption for the thin shell theory.

2.3.2.3 Idealisation of the test structure— The complete structure was idealised using 336 semi–loof shell elements twelve of which were six noded triangular elements comprising the apical cap while the rest were eight noded quadrilateral elements. The theoretical model was formed of twelve axisymmetric segments each extending an angle (θ) of 30^{o} in the horizontal plane as shown in Fig. 2.9. Nodal coordinates were determined using a shape prediction program [3] and shell thickness was assumed to vary along the meridional direction only.

---

§ x, y, z form a set of local cartesian axes with x always outwards normal to the element boundary, y parallel to the element boundary and z normal to the element surface and ξ, η are the natural coordinate system lying in the shell midsurface.

Table 2.2 contains a summary of data for different forms of the finite element mesh.

DATA TYPE	COMPLETE MODEL	HALF MODEL	QUARTER MODEL
Total number of elements	336	168	84
Total number of nodes	1009	561	309
Maximum bandwidth of stiffness matrix	125	72	48
Total number of degrees of freedom	4371	2411	1319

TABLE 2.2 — *DATA SUMMARY FOR VARIOUS FORMS OF THE FINITE ELEMENT MESH*

2.3.2.4 Symmetric point load simulation— Linear static stress analysis using the finite element method assumes that structural displacements are infinitesimally small, the material is linearly elastic and the state of the boundary conditions remains unaltered. For real structures the previous assumptions are in doubt and as a result a non–linear analysis is necessary. Non–linearity is classified into the following three categories :

1. **Materially non–linear only :** the stress–strain relationship is non–linear, at the same time displacements and strains are infinitesimally small.
2. **Large displacements and small strains :** displacements are large while strains are infinitesimally small, the stress–strain relationship can be linear or non–linear.
3. **Large displacements and large strains :** both displacements and strains are large, the stress–strain relationship can be linear or non–linear.

The term "**Geometrical Non–linearity**" is often used to cover the last two divisions. The response of the experimental structure to a symmetric point load acting at $\phi = 60^{\circ}$ away from the apex was studied using a linear and geometrically non–linear (large displacements and small strains) finite element analysis. Due to symmetry, half of the finite element model was considered.

The mesh was restrained along the plane of symmetry from translation normal to plane and rotation out of plane.

Initially, perfect rigidity was assumed for the base fixity by specifying a ring of restrained nodal supports for the lowest parallel circle, but displacement results under the point load were almost 60 percent of their experimental correspondents. As a result a new material test was performed on small specimens cut from the shell base which resulted in the following set of material properties :

$E = 8800$ MPa

$\nu = 0.36$

Then the stiffness at the base of the finite element model was varied until the predicted and the measured displacements were almost equal and this was performed by declaring a ring of spring supports instead of the normal supports. The stiffness of the springs was established to be 4×10^5 N/m for the translational degrees of freedom and 4×10^5 N/m/rad for the rotational degrees of freedom. The updated finite element model was used throughout the remaining part of the current chapter.

2.3.2.4.1 **Linear analysis**— The linear approach is based on the following equation :

$$[K]\{\delta\} = \{P\} \quad \text{.....} \quad (2.1)$$

where $[K]$ represents the assembled stiffness matrix;

$\{\delta\}$ represents the vector of unknown nodal displacements; and,

$\{P\}$ represents the vector of applied loads.

Evaluating the stiffness matrix and inverting it the nodal displacements can be calculated. Displacements are then used to compute the strains within each element using

$$\{\varepsilon\} = [B]\{\delta\} \quad \text{.....} \quad (2.2)$$

where $\{\varepsilon\}$ represents the generalised strain vector; and,

[B] represents the strain–displacement matrix.

Stresses are obtained employing the following relationship :

$$\{\sigma\} = [D](\{\varepsilon\} - \{\varepsilon_0\}) + \{\sigma_0\} \quad \text{.....} \quad (2.3)$$

where $\{\sigma\}$ represents the generalised stress vector;

[D] represents the stress–strain modulus matrix;

$\{\varepsilon_0\}$ represents the generalised initial strain vector; and,

$\{\sigma_0\}$ represents the generalised initial stress vector.

The word "generalised" is used only to include curvatures and moments in strains and stresses, respectively.

2.3.2.4.2 Geometrically non–linear analysis— Control tests carried out earlier on the prototype material (GRP) indicated that the stress–strain relationship was linear until failure and as a result the theoretical model was assumed to be materially linear. Therefore the appearance of non–linearity in the experimental results was due to the changes in the geometrical stiffness of the deformed prototype. A geometrically non–linear analysis was undertaken using LUSAS to be compared with the linear analysis and experimental results. This type of analysis implies a non–linear load–displacement relationship making a direct solution to the resulting non–linear equations unviable.

Appendix A contains the mathematical formulation of the non–linear equations and an optimum solution procedure for such equations.

For the 300 N point loading the load was incremented in steps of 50 N and convergence was achieved when all of the following conditions were satisfied :

$$\text{DLNORM} < 10^{-3}$$

$$\text{RLNORM} < 10^{-3}$$

$$\text{WLNORM} < 10^{-6}$$

where **DLNORM** represents the limit for the sum of the squares of all the iterative displacements as a percentage of the sum of squares of the total displacements (only translational degrees of freedom are considered);

RLNORM represents the limit for the sum of the squares of all the residual forces as a percentage of the sum of the squares of all the external forces (only translational degrees of freedom are considered); and,

WLNORM represents the limit for the work done by all the residuals acting through the iterative displacements as a percentage of the work done by the loads on the initial iteration of the increment (both translational and rotational degrees of freedom are considered).

2.3.2.5 Finite element results— Principal stresses, magnitude and direction, are illustrated for the various meridians in Figs 2.10(a → d) and 2.11(a, b) while the equivalent stresses are shown in Figs 2.12(a and b). Throughout this work tensile and compressive stresses are considered positive and negative respectively. In these figures the stresses are plotted for pairs of meridians (a meridian and its complement) and the distance is measured along the meridian from the apex as the origin to the base at the extremities with the load on the negative side. The preceding graphs contain both linear and geometrically non–linear results for a 300 N symmetric point load acting 60^{o} away from apex normal to the surface of the updated mesh.

A typical deformed shape for the preceding load case is depicted in Fig. 2.14 (plots were prepared using SWANS a surface modelling graphic software [25,26])and the corresponding displacement results are listed in Tables 2.3 and 2.4.

NODE NUMBER	NORMAL DISPLACEMENTS AT 300 N (mm)
501	0.393
421	0.533
321	0.523
221	0.371
121	0.169
1	0.054
215	0.604
415	0.476
495	0.300

TABLE 2.3 — *DISPLACEMENT RESULTS FROM A STATIC LINEAR ANALYSIS FOR A NORMAL POINT LOAD ACTING 60° AWAY FROM APEX (UPDATED MESH)*

NODE NUMBER	NORMAL DISPLACEMENTS AT DIFFERENT LOAD INCREMENTS (mm)					
	50 N	100 N	150 N	200 N	250 N	300 N
501	0.066	0.131	0.197	0.263	0.330	0.396
421	0.089	0.178	0.267	0.357	0.447	0.537
321	0.087	0.174	0.262	0.350	0.438	0.526
221	0.062	0.124	0.185	0.247	0.310	0.372
121	0.028	0.056	0.084	0.112	0.140	0.168
1	0.009	0.018	0.028	0.037	0.047	0.057
215	0.101	0.202	0.304	0.406	0.509	0.612
415	0.079	0.159	0.239	0.319	0.399	0.480
495	0.050	0.100	0.150	0.201	0.251	0.302

TABLE 2.4 — *DISPLACEMENT RESULTS FROM A GEOMETRICALLY NON–LINEAR ANALYSIS (LARGE DISPLACEMENTS AND SMALL STRAINS) FOR A NORMAL POINT LOAD ACTING 60° AWAY FROM APEX (UPDATED MESH)*

2.3.2.6 Discussion— It was clear from Fig. 2.15 and Table 2.4 that the 300 N symmetric point load was too low to invoke any geometrical non–linearity of the Echinodome prototype, a conclusion which was confirmed by the coincidence of the linear and geometrically non–linear stress results.

When viewing Figs 2.10(a → d) discontinuities were observed in the principal stresses distribution in two regions, near the base (covering the region 80 → 100 percent of the meridional length) and in the vicinity of the point load (covering the region 20 → 60 percent of the meridional length on M1 in a band about the loaded parallel circle and to a diminishing extent with other meridians up to M7). The figures indicated as well that the rest of the structure was under negligible stresses.

Limiting attention to the region around the point load it was noticed that the principal stresses were at their maximum positive or maximum negative on the loaded meridian and the further along the meridian from the point load the lower the principal stresses became.

However, when examining the base zone the stresses were found to be decreasing from the loaded meridian M1 ($\theta = 0^{\circ}$) up to M4 ($\theta = 90^{\circ}$) and then increasing until M7 ($\theta = 180^{\circ}$) was reached. Such a behaviour was consistent with the overturning effect on the structure consequent upon the application of the symmetric point load.

On the whole, although the principal stresses were larger in magnitude on both surfaces of the structure in the base region they did not even exceed one quarter of the ultimate strength of the material. If by increasing the load level the structure was to collapse by buckling, failure would initiate in the local regions of destabilising bending and high compressive stresses which are evident in the stress distribution diagrams. The principal angle (θ_p) distribution along any pair of meridians was measured with reference to the meridional direction, anticlockwise positive, e.g. if $\theta_p = 90^{\circ}$ it meant that σ_1 and σ_2 were in the circumferential and meridional directions respectively.

In Figs 2.11(a and b), directly under the point load the principal angles were approximately 90° and 0° for the outer and inner surfaces respectively. Indicating that σ_2 for the outer surface and σ_1 for the inner surface, which were shown in Figs 2.10(b and c) to be the most critical principal stresses under the point load for both surfaces, were in the meridional direction. The previous remark suggested that the meridional stresses were more critical than the circumferential in the vicinity of the point load.

In general the principal angle tended towards either 0° or 90° in the critical zones with some fluctuations, while it varied between 0° and 180° for the remaining parts. Yet it can be concluded that reinforcement would generally be in the meridional and circumferential directions because regions of the loaded structure with a principal angle other than 0° or 90° were suffering from

minimal stresses.

The equivalent stress distribution disclosed in Figs 12(a and b) indicated that the stresses were at their peak near the base for the meridian complementing the loaded one for both surfaces. The equivalent stresses in the base zone decreased from M7 to M4 where it increased again up to M1.

While around the loaded area, the peak equivalent stresses became more accentuated the closer the meridional section approached the loaded meridian.

The stress distributions (σ_1, σ_2 and σ_e) described above were suitable for the behaviour of the shell prototype under a symmetric point and as a result of the destabilising stresses induced under the point load and at the base a buckling investigation was carried out as described in later subsections.

2.3.3 Comparison Between Experimental and Theoretical Results

When comparing the measured displacements with their theoretical correspondents (excluding results for the point load) it was clear that both sets of results had a similar trend except for measurements of displacement transducer number 5 which indicated deformation in an opposite direction to that predicted by the finite element method (see Fig. 2.16). Earlier readings for the same transducer at lower load levels were erratic which cast doubts on its general behaviour.

Some discrepancies existed between the experimental and theoretical results and this was attributed to the geometrical imperfections inherent in the test structure in the form of thickness variations along the parallel circles as well as the existence of the bonding seam and neither were simulated in the finite element model.

2.4 BUCKLING STUDIES

Thin walled structures under compressive loads may fail to remain safe due to material failure or buckling (the term buckling will refer only to static buckling through this chapter). Thin shell structures have to be designed to avoid overstressing the material used in their construction under general types of loadings. Equally important, critical buckling loads must be predicted accurately to avoid reaching such loads.

2.4.1 Introduction to Buckling

The following subsections explain the buckling phenomenon of thin shells and the reasoning for it, as well as its various forms. Numerous examples of shell buckling are given in Ref. (27).

2.4.1.1 Buckling of thin shells— The buckling phenomenon is said to have taken place when structures undergo large deformations leading to a catastrophic failure. Thin shells are characterised by having a large membrane stiffness several times the bending stiffness. When subjected to membrane compression loads such structures absorb high membrane strain energy while experiencing small deformations and if that energy is transformed into bending strain energy the structure suffers large deformations accompanied by a sudden failure.

2.4.1.2 Various types of buckling— Theoretically there exists two types of instabilities for thin shells : "**Non–linear Collapse**" (often termed "**Snap Through**" or "**Limit Load**") and "**Bifurcation Buckling**" . The non–linear collapse buckling load is defined as the load at which the load–deflection curve from a non–linear analysis has zero slope and when using the finite element method this means that the total tangential stiffness matrix $[K_T]$ is non–positive definite (zero or negative values on the leading diagonal of the matrix). The bifurcation buckling load is predicted using an eigenvalue analysis and in the finite element method this involves solving the following equation :

$$([K_o] + [\Lambda][K_\sigma])[\Theta] = [0] \quad \text{.....} \quad (2.4)$$

where $[K_o]$ represents the small displacements stiffness matrix;

$[\Lambda]$ is a matrix containing the load multipliers λ on its leading diagonal and zero elsewhere;

$[K_\sigma]$ represents the initial stresses or geometric stiffness matrix;

$[\Theta]$ is a matrix containing the buckling mode shapes (eigenvectors) associated with each load multiplier (eigenvalue); and,

$[0]$ represents a null matrix.

This is often termed linearised buckling analysis. The estimated bifurcation buckling load can be considered accurate only if the elastic solution using $[K_o]$ gives deformations such that the terms contained in the large displacements stiffness matrix, $[K_L]$, are almost or equal to zero. Bifurcation buckling analysis can be combined with a non–linear analysis by performing an

eigenvalue analysis after each load increment on the deformed structure.

Modal displacements due to bifurcation buckling are orthogonal to the prebuckling deformations of a perfect structure and as a result their amplitudes are equal to zero until bifurcation takes place. The post–buckling behaviour can be typified as follows :

1. **Unstable :** if the load carrying capability decreases with the increase in the amplitude of modal displacement (e.g. cylindrical shells).
2. **Neutral :** if the load carrying capability remains constant with the increase in the amplitude of modal displacements (e.g. centrally loaded columns).
3. **Stable :** if the load carrying capability increases with the increase in the amplitude of modal displacements (e.g. plates).

Though bifurcation buckling is imaginary and does not take place in real structures which contain initial imperfections it often offers a good approximation to the true critical buckling load and its corresponding mode. Buckling behaviour of structures with geometric imperfections is similar to non–linear collapse buckling analysis in that it follows a non–linear load–deflection path with its post–buckling behaviour classified as for bifurcation buckling.

2.4.2 Experimental Investigation

An accurate estimate of critical buckling loads experimentally can only be achieved by a destructive test on a real structure or a model of it and such a method is expensive. In addition, precise buckling loads are not always attainable because structural failure can occur as a result of material overstressing not due to buckling. Various non–destructive experimental and theoretical buckling determination techniques have been evolving during the last few years some of which are explained in the following paragraphs.

2.4.2.1 The Souza method [28] — The concept of this technique is based on making use of the relationship between the natural frequency of a statically loaded elastic structure and the magnitude of the applied load to predict the critical static buckling load. Earlier reports [29] suggested the use of other dynamic characteristics (dynamic mass) as well. The technique was nominated the "**Souza Method**" because a similar procedure will be adopted in the current investigations as to that suggested by the former researcher.

Souza assumed that the graph of ω^2 versus $\mathbf{P}$ is of hyperbolic shape for structures characterised by unstable post–buckling behaviour with zero frequency at the buckling load. Therefore when plotting the experimental results in a parametric (normalised) form of $(1 - \overline{P})^2$ versus $(1 - \overline{f})$ (where $\overline{P}$ is the applied load normalised by the load corresponding to zero

frequency P_o coinciding with the centre of the above hyberbola and $\bar{f}$ is the natural frequency of the loaded structure normalised by the natural frequency of the unloaded structure f_o), a straight line should be obtained.

The Souza method has been applied to cylindrical shells with success [30] and will be adopted in this theoretical investigation to check the validity of applying such an approach to Echinodomes.

2.4.2.2 **The Southwell method**— Southwell proposed a simple method for predicting the theoretical buckling load P_{cr} of perfect columns from experiments on real columns with small initial imperfections. Basing the technique on the small deflection theory the deflection parameter was expanded using Fourier series and assumed equal to the first component of the series as the load level approached P_{cr}. This produced the following formula :

$$\delta = \frac{\delta_o}{\frac{P_{cr}}{P} - 1} \qquad \text{.....} \qquad (2.5)$$

where δ_o represents the initial deflection of the neutral axis of a column or initial geometrical imperfections; and,

δ represents the additional deflection.

This is an equation of a rectangular hyperbola in a P versus δ plane with the P—axis and the horizontal line passing through P_{cr} as its asymptotes, indicating that the method is applicable to columns characterised by a neutral post–buckling path. Rewriting Eqn (2.5) after arranging terms

$$\frac{\delta}{P} = \frac{\delta}{P_{cr}} + \frac{\delta_o}{P_{cr}} \qquad \text{.....} \qquad (2.6)$$

The above formula represents an equation of a straight line with slope $1/P_{cr}$ when plotted in a δ/P versus δ plane and is known as the "**Southwell Plot**".

Roorda [31] investigated the Southwell plot for post–buckling cases other than neutral and found that the relationship between δ/P and δ becomes non–linear resulting in an underestimation or overestimation of P_{cr} depending on the post–buckling buckling path type. After mathematical manipulation Roorda proved that the slope of the tangent to the initial part of the non–linear curve

of δ/P versus δ lent itself to the value of $1/P_{cr}$ for small imperfection cases.

In 1975 Spencer and Walker [32] argued that non–linearities in the Southwell plot may arise at low load levels due to any inherent zero error in the deflection and proposed the use of the "**Pivot Point**" concept from which the following equation was obtained :

$$\left[\frac{P^*P}{P-P^*}(s-s^*)\right] = P_{cr}\left[\frac{P^*s - Ps^*}{P-P^*}\right] + P_{cr}s_o \quad \text{.....} \quad (2.7)$$

where s represents the deflection transducer scale reading;

s_o represents the true (but unknown) transducer scale reading at $\delta = 0$; and,

P^*, s^* represents the load–displacement pair known as the Pivot Point [§].

Detailed derivation of Eqn (2.7), due to Spencer and Walker, is given in Appendix B.

The above named non–destructive buckling load determination technique can be summarised as follows :

1. Make displacement (or strain) measurements at a number of observation points (on the structure for which the buckling load is to be determined) for several load increments.
2. Plot δ/P (or ε/P) versus δ (or ε) and obtain the equation of the best fitted line, with the reciprocal of its slope as P_{cr}.
3. If non–linearities exist at low load levels make use of a pivot point to plot $[P^*P(P-P^*)^{-1}(s-s^*)]$ versus $[(P^*s - Ps^*)(P-P^*)^{-1}]$. Fit the best straight line through the points to obtain P_{cr} which is the slope of that line.

2.4.2.3 Linear regression— Least square regression is one of the techniques used to fit a curve through data points and when the fitted curve is a straight line the process is known as "**Linear Regression**". The method is based on minimising the discrepancy between the data points and the fitted curve.

Minitab [33] is a general purpose statistical system designed to analyse data. Regression analysis is one of the numerous facilities it offers. The program was utilised to analyse and fit curves to the experimental displacement results listed in Table 2.1(a).

§ The **Pivot Point** constitutes a load–displacement pair (P^*, s^*) which, in the judgement of the experimenter, is sufficiently accurate to be used in analysis.

For each displacement transducer data was submitted in the form of 5 columns : P, w, w/P, $[P^*P(P - P^*)^{-1}(s - s^*)]$ and $[(P^*s - Ps^*)(P - P^*)^{-1}]$, where w represents the normal deflection. Then the regression operation was carried out to acquire the linear equations for the following relationships :

$$P—w,\ w/P—w \text{ and } [P^*P(P - P^*)^{-1}(s - s^*)]—[(P^*s - Ps^*)(P - P^*)^{-1}]$$

where the pivot point (P^*, s^*) was assumed to be the maximum load level data (P^* = 300 N).

A linear equation will have the following form :

$$Y = b_o + b_1X \quad \text{.....} \quad (2.8)$$

where **X** is known as the predictor;

Y is known as the response;

b_o represents the intercept of the fitted line with the Y—axis; and,

b_1 represents the slope of the fitted line measured from the X—axis.

Thus when performing linear regression between P and w the coefficient b_o was specified as zero to force the fitted line to pass through the origin.

Minitab outputs statistical characteristics of the data and the fitted curve which can be used in assessing the quality of the regression equation [34] some of which are :

1. **Standard error of estimate** (s_y) : often called "the **Standard Deviation**" of Y about the regression line. The value of s_y can be used as a measure of the difference between the observed and the fitted Y values (Y_i and Y_{fi}), and it is calculated using the following formula :

$$s_y = \left[\frac{\sum_{i=1}^{n} (Y_i - Y_{fi})^2}{n - 2} \right]^{0.5} \quad \text{.....} \quad (2.9)$$

where **n** is the number of data points.

2. **Coefficient of determination** (r^2) : which is the square of the correlation coefficient (r) between Y_i and Y_{fi} values. The quantity r is always in the range of –1 to +1. If the correlation coefficient is evaluated between two columns of data C1 and C2, then r will have a positive value if C2 data increases with the increase of C1 data and a

negative value if C2 data decreases with the increase of C1 data. The correlation coefficient is a measure of how closely the points lie on a straight line thus r will be equal to +1 or −1 if all the data points lie on a straight line with a positive slope or a negative slope respectively while it will be equal to zero if there is no linear association between C1 and C2.

2.4.2.4 Non–destructive buckling estimates— The Southwell technique was used to predict the critical buckling point load when applied normal to the surface and 60^{o} away from apex. Graphs of **P** versus **w** and **w/P** versus **w** under the point load are shown in Figs 2.17(a and b). While graphs of load versus displacement and the Southwell plot, for displacement transducers numbers 6 and 5, can be seen in Figs 2.18(a, b) and 2.19(a, b) respectively. Tables 2.5 and 2.6 contain the results of the regression analysis where load is in Newtons and displacement in millimetres.

DISPLACEMENT TRANSDUCER NUMBER	LINEAR REGRESSION MODEL	s_y (mm)	r
1	Y= 829.9 × X	0.0070	0.998
2	Y= 709.2 × X	0.0131	0.996
3	Y= 625.0 × X	0.0046	1.000
4	Y= 606.1 × X	0.0160	0.994
5	Y= 3225.8 × X	0.0207	0.957
6	Y= 2754.8 × X	0.0091	0.975
7	Y= 510.2 × X	0.0202	0.996
8	Y= 657.9 × X	0.0124	0.999
9	Y= 909.1 × X	0.0103	0.998

TABLE 2.5 — *REGRESSION ANALYSIS RESULTS FOR THE P-w PLANE (X ≡ w and Y ≡ P)*

DISPLACEMENT TRANSDUCER NUMBER	LINEAR REGRESSION MODEL	S_y (mm/N)	r	P_{cr} (N)
1	Y= 0.001000 + 0.000443 × X	0.0000506	0.661	2257.3
2	Y= 0.001210 + 0.000598 × X	0.0000617	0.783	1672.2
3	Y= 0.001550 + 0.000125 × X	0.0000385	0.409	8000.0
4	Y= 0.001560 + 0.000275 × X	0.0001081	0.342	3636.4
5	Y= 0.000053 + 0.003210 × X	0.0000376	0.972	311.5
6	Y= 0.000564 − 0.002260 × X	0.0000570	0.724	stiffening
7	Y= 0.001580 + 0.000837 × X	0.0001343	0.738	1194.7
8	Y= 0.001260 + 0.000721 × X	0.0000587	0.866	1387.0
9	Y= 0.000875 + 0.000848 × X	0.0000488	0.871	1179.2

TABLE 2.6 — *REGRESSION ANALYSIS RESULTS FOR THE SOUTHWELL PLOT USING UNAVERAGED EXPERIMENTAL DATA (X ≡ w and Y ≡ w/P)*

2.4.2.5 Analysis of results— In an earlier section it was concluded from the theoretical analysis that the 300 N point load was relatively low to invoke any inherent geometrical non–linearity of the Echinodome prototype. At the same time, the experimental load–displacement relationship exhibited some non–linearity as is apparent in Fig. 2.17(a) (correlation coefficients ≠ 1.0 — see Table 2.5) for the various displacement transducers. This could be attributed to either random errors, (electrical noise, ..., etc.), initial structural imperfections or both. Initially, the Southwell technique was applied to the unaveraged displacement measurements and results are listed in Table 2.6 together with the buckling load estimates.

When viewing Figs 2.19 (a and b) it is clearly seen that the experimental data was erratic although the correlation coefficient indicated otherwise and therefore it is always very important to inspect the plot of the data points along with the regression line even for high correlation coefficient values. Attempts were made to improve the quality of the fits using the pivot point concept but this resulted in more scattered data points and consequently a worse fit was the outcome.

On examining the Southwell plot for each transducer it was noticed that the experimental results corresponding to the first load increment (50 N) were more widely dispersed than those for the higher load increments. As a result, the regression analysis was repeated excluding

measurements for the first load increment. In addition, the best fitted line was determined for the measurements average of each load increment rather than individual unaveraged measurements (in order to minimise any random errors) and averages possessing a coefficient of variation greater than 6 percent were omitted with the purpose of enhancing the quality of the fit. The new buckling load estimates are listed in Table 2.7 with the correlation coefficients of the fitted lines.

DISPLACEMENT TRANSDUCER NUMBER	LINEAR REGRESSION MODEL	S_y (mm/N)	r	P_{cr} (N)
1	$Y = 0.001050 + 0.000250 \times X$	0.0000127	0.902	3997.1
2	$Y = 0.001290 + 0.000339 \times X$	0.0000185	0.928	2947.3
3	$Y = 0.001560 + 0.000095 \times X$	0.0000068	0.910	10499.8
4	stiffening	———	———	———
5	erratic data	———	———	———
6	stiffening	———	———	———
7	$Y = 0.001870 + 0.000230 \times X$	0.0001332	0.932	4346.9
8	$Y = 0.001330 + 0.000514 \times X$	0.0000192	0.971	1946.4
9	$Y = 0.000947 + 0.000557 \times X$	0.0000136	0.976	1794.1

TABLE 2.7 — *REGRESSION ANALYSIS RESULTS FOR THE SOUTHWELL PLOT USING AVERAGED EXPERIMENTAL DATA* ($X \equiv w$ *and* $Y \equiv w/P$)

In general, the Southwell technique predicted different buckling loads for different points on the structure and it was observed from Table 2.7 that some parts of the structure were stiffening rather than softening.

When inspecting the preceding table it was noticed that parallel circles near the base predicted lower buckling loads than under the point load, suggesting that the former was more critical than the latter. The minimum estimated buckling load (P_{cr}) was found to be equal to 1794 N and corresponded to a point on the lowest parallel circle under consideration ($\phi = 150^{o}$).

2.4.3 Theoretical Investigation

The two theoretical buckling load types, collapse and bifurcation, were estimated using the finite element package LUSAS.

2.4.3.1 Collapse buckling estimate— A geometrically non–linear analysis was performed on the updated mesh to predict the collapse buckling load. In order to avoid singularity in the incremental stiffness matrix, at the extremum points of the load–deflection curve, an incremental displacement was prescribed normal to the shell surface and the reaction evaluated at a point 60^{o} away from apex. The solution procedure crossed the snap–through point by enabling the load level to vary between iterations and the change was computed to satisfy the following constraint :

$$\{\delta_i^{j+1}\}^T \bullet \{\delta_i^{j+1}\} = l^2 \qquad \text{(2.10)}$$

where $\{\delta_i^{j+1}\}$ represents the i^{th} incremental displacement vector for the $j+1^{th}$ iteration;

l represents the incremental displacement length; and,

$\bullet$ indicates vector product.

The derived load–deflection curve is depicted in Fig. 2.20.

In Refs (35) and (36) a quantity known as the current stiffness parameter (S_p) was proposed to provide a global measure for the stiffness of the structure. It is defined by the following formula :

$$S_{p_i} = \left[\frac{\Delta p_i}{\Delta p_1}\right]^2 \frac{\{\Delta\delta_1\}^T [K_{o\,1}]\{\Delta\delta_1\}}{\{\Delta\delta_i\}^T [K_{T\,i}]\{\Delta\delta_i\}} \qquad \text{(2.11)}$$

$$\{\Delta P\} = \Delta p \{P_{ref}\} \qquad \text{(2.12)}$$

where $\{P_{ref}\}$ represents the normalised external load vector;

Δp represents the load parameter increment (when the external load is incremented the load parameter changes by Δp while $\{P_{ref}\}$ remains constant);

$\{\Delta\delta_i\}$ represents the i^{th} incremental displacement vector corresponding to Δp_i ;

$\{\Delta\delta_1\}$ represents the linear displacement vector corresponding to Δp_1 ;

$[K_{o\,1}]$ represents the small displacement (linear) stiffness matrix corresponding to the first load increment; and,

$[K_{T\,i}]$ represents the i^{th} tangential stiffness matrix.

The current stiffness parameter which has an initial value of 1.0, increases and decreases with the stiffening and the softening of the structure respectively. For stable post–buckling behaviour S_p is positive, for unstable behaviour S_p is negative and at limit point (collapse) S_p is zero.

Figs 2.21(a and b) show the current stiffness plotted against load and displacement respectively. From these graphs an accurate estimate of the non–linear collapse buckling load for the updated mesh was established, P_{nc} = 7.64 kN. A typical deformed shape is illustrated in Fig. 2.22.

In order to assess the validity of using the Souza method to predict buckling loads for the Echinodome, a similar concept was applied to the theoretical results.

Natural frequencies of the updated mesh were determined after each prescribed displacement increment (simulating a point load acting normal to the surface, 60° away from apex) using the following eigenvalue formulation :

$$\left([K_T] - [\Omega^2][M_d]\right)[\Psi] = [0] \qquad \text{(2.13)}$$

where $[\Omega^2]$ is a matrix with diagonal elements equal to the natural frequencies squared (ω^2) and zero elements elsewhere;

$[M_d]$ represents the mass matrix of the deformed structure; and,

$[\Psi]$ is a matrix containing the mode shapes (eigenvectors) associated with each natural frequency (eigenvalue).

For zero load the tangential stiffness matrix is equal to the small displacement (linear) stiffness matrix $[K_o]$ while $[M_d]$ becomes the mass matrix of the original (underformed) structure [M].

Horton *et al.* [29] found that the frequency mode to be considered when plotting the frequency squared against the applied load was the one similar to the collapse shape. For the Echinodome this meant :

- axisymmetric mode → axisymmetric loading
- symmetric mode → symmetric loading
- torsional mode → torsional loading

One of the symmetric vibrational mode shapes (see Chapter 3) was related to the current load case by having motion in the direction of the applied load. The ω^2 versus **P** indicated that the relationship between both parameters is of hyperbolic form with $\mathbf{P}_{nc}$ corresponding to the vertex of the hyperbola. Unlike what has been suggested by Souza [28] for cylindrical shells the Echinodome under a load equal to $\mathbf{P}_{cr}$ did not have a zero natural frequency but rather a minimum value for the natural frequency was reached.

Consequently, the direct application of the Souza method to the Echinodome is not suitable (because of the dependency of the technique on the premise that the vertex of the hyperbola lies on the applied load axis). Instead, if a vibration test was carried out to determine the structural natural frequencies under various load increments it is possible to estimate the buckling load $\mathbf{P}_{cr}$ by carrying out a non–linear regression analysis on the assumption that ω^2 versus **P** is hyperbolic.

2.4.3.2 Bifurcation buckling estimate— When undertaking an eigenvalue analysis (employing the subspace iteration method described in Chapter 3) using Eqn (2.4) to predict the linear bifurcation buckling load the LUSAS finite element system indicated that the initial stress matrix $[\mathbf{K}_\sigma]$ was non–positive definite. Consequently Eqn (2.4) had to be reformulated as follows :

$$(([\mathbf{K}_o] + [\mathbf{K}_\sigma]) - [\gamma][\mathbf{K}_o])[\Theta] = [0] \quad \text{..... (2.14)}$$

where $[\gamma]$ is a matrix with the values $(1 - 1/\lambda)$ on its leading diagonal and zero elsewhere.

The resulting eigenvectors are similar to those of Eqn (2.4) and as a result the load multipliers were computed using the following formula :

$$\lambda_i = \frac{1}{1 - \gamma_i} \quad \text{..... (2.15)}$$

where i is a subscript denoting the eigenvalue and eigenvector number.

From the previous equation it can be noticed that when λ_i is large, γ_i will be close to 1.0 and any small error in the estimation of γ_i results in a large error in λ_i. Consequently the bifurcation buckling load was specified to be multiples of 20000 but this caused failure in the solution of Eqn (2.14) because the computed eigenvalues were negative (LUSAS is unable to carry a convergence check on negative eigenvalues). To overcome this problem a shift μ was applied to form a modified eigensystem, which had the same eigenvectors, as follows :

$$(([K_o] + [K_\sigma] + [\mu][K_o]) - [\bar{\gamma}][K_o])[\Theta] = [0] \quad \text{..... (2.16)}$$

where $[\mu]$ is a diagonal matrix and the actual eigenvalues were calculated as follows :

$$\gamma_i = \bar{\gamma}_i - \mu \quad \text{..... (2.17)}$$

The minimum bifurcation buckling load P_{lb} for the updated mesh was 10.75 kN (c.f. P_{nc} = 7.64 kN) which indicated the significance of the structure's geometrical changes and hence the large displacements stiffness matrix $[K_L]$ might have a great influence on the buckling load estimate.

Consequently a non–linear bifurcation buckling analysis was undertaken by performing an eigenvalue extraction using Eqn (2.16) after each application of the prescribed incremental displacement described in the previous subsection. The estimated bifurcation buckling load P_{nb} was equal to 9.90 kN and the accompanying mode shape can be seen in Fig. 2.23. It can be concluded that the non–linearity of the prebuckling state was important for the bifurcation buckling model.

Although P_{nb} was almost 90 percent of P_{lb} it was still of a less engineering significance than P_{nc}.

2.4.4 Comparison Between Experimental and Theoretical Estimates

For the current case a direct comparison between experimental and theoretical buckling load estimates is inappropriate. The reason is that the values determined using the Southwell technique were dependent on local points on the test structure and therefore local geometrical imperfections

in the form of local thinning or thickening of the shell wall can greatly affect the buckling load estimates. Each position on the test structure had its own imperfection and stiffness hence the variation in the determined P_{cr}.

Nevertheless, it was interesting to notice that both the Southwell technique and the collapse buckling analysis predicted the region near to the base as the most critical zone for buckling failure. The preceding remark was made on the basis that experimentally the minimum P_{cr} was for a position lying on the nearest parallel circle to the base and theoretically at P_{nc} a few elements comprising the last ring of semi–loof elements towards the base collapsed.

Both approaches (experimental and theoretical) predicted that the Echinodome prototype would fail by buckling after exceeding the maximum strength of the material. Thus, indicating that buckling of this specific shell under the given loading was not to be considered as a design criterion.

2.5 CONCLUSIONS

Limiting attention to the current Echinodome test structure, the following observations could be made :

1. For a symmetric point loading the critical zones were identified to be in the vicinity of the applied load and near the base of the structure because of the induced bending stresses which could initiate a buckling failure.
2. Away from the critical regions the structure suffered from minimal stresses and a membrane action dominated.
3. The principal angle distribution on both outer and inner surfaces indicated that at peak principal stresses $\theta_p = 0^\circ$ or 90° . Thus, any reinforcement for the structure should be generally in the meridional and circumferential directions.
4. When performing a bifurcation buckling analysis the non–linearity of the prebuckling state is important because the prebuckled shape of the structure is more likely to lose its stability.
5. The non–linear collapse buckling load is less than the bifurcation buckling load and hence it is more critical.
6. The material strength is expected to be exceeded before a static buckling failure takes place.

7. The Southwell technique employed in the non–destructive buckling tests produced consistent results by predicting the minimum $\mathbf{P_{cr}}$ from a point near to the base which was one of the critical regions.

8. The Souza method for buckling load determination might be an expensive test to perform because of the high costs of hardware and software involved. Unlike the former technique which is dependent on the degree of local imperfections inherent in a structure the Souza model is based on measuring a global property of the structure (natural frequency) under various load increments. A prerequisite step before applying the Souza concept is to carry out a modal test (see Chapter 4) in order to typify the vibrational mode shapes of the unloaded structure under consideration. Extreme care is necessary when applying the static load to ensure that any loading arrangement used does not introduce extra modes.

For full size Echinodome shell structures it is important to take account of the following points during the design, launching and operating stages :

1. The last 10 percent of the meridional profile is to be stiffened by the gradual thickening of the shell wall or extra reinforcement bars in that zone to avoid any premature failure due to buckling.

2. Extra reinforcement is required around openings and towing points to resist any local buckling.

3. In real structures sensitivity to construction or manufacturing imperfections is much less important and therefore the finite element method evolves as the most appropriate numerical method to be used in predicting the general behaviour of the Echinodome under static concentrated loads.

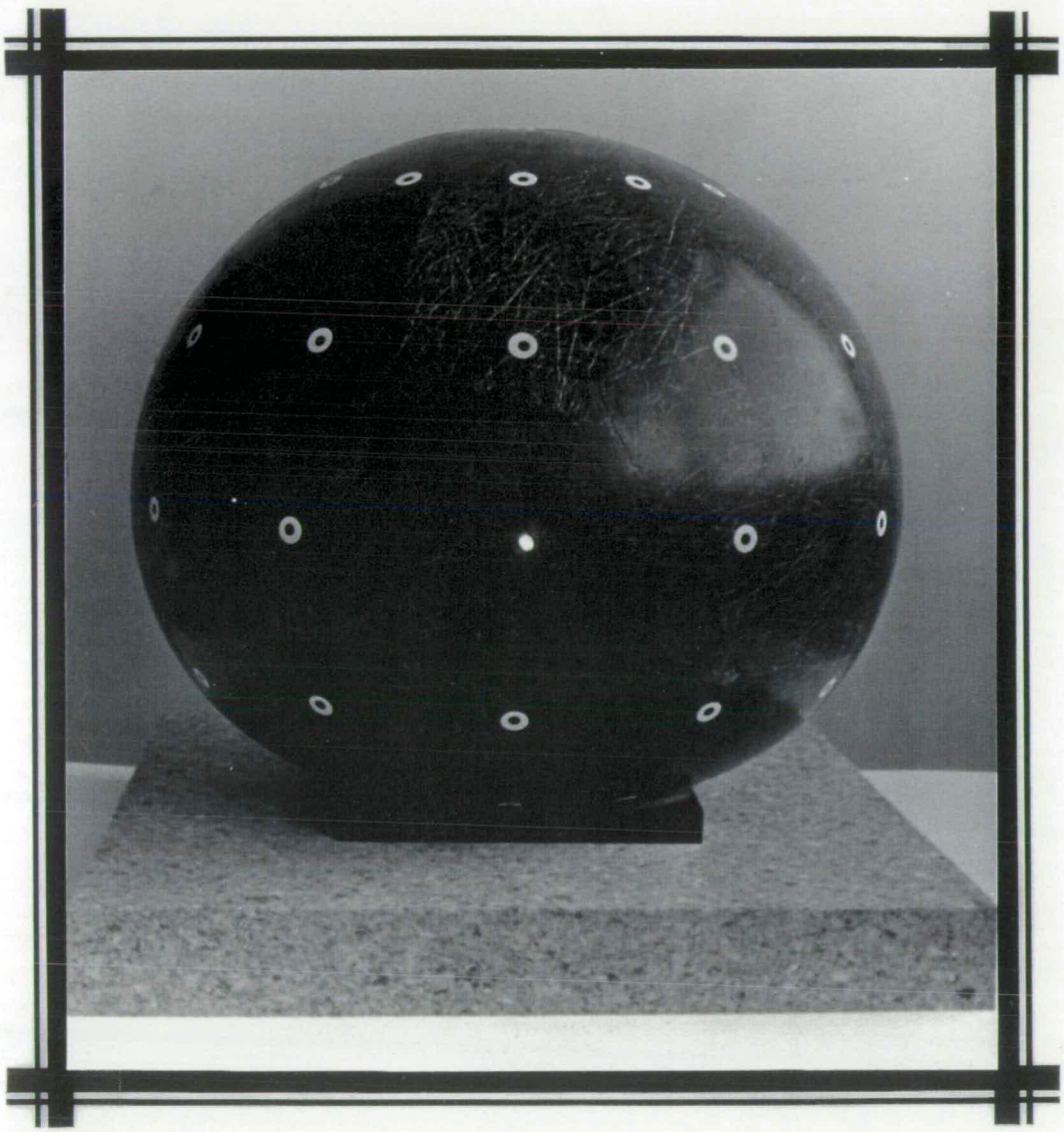

FIG. 2.1–GLASS REINFORCED PLASTIC ECHINODOME STRUCTURE

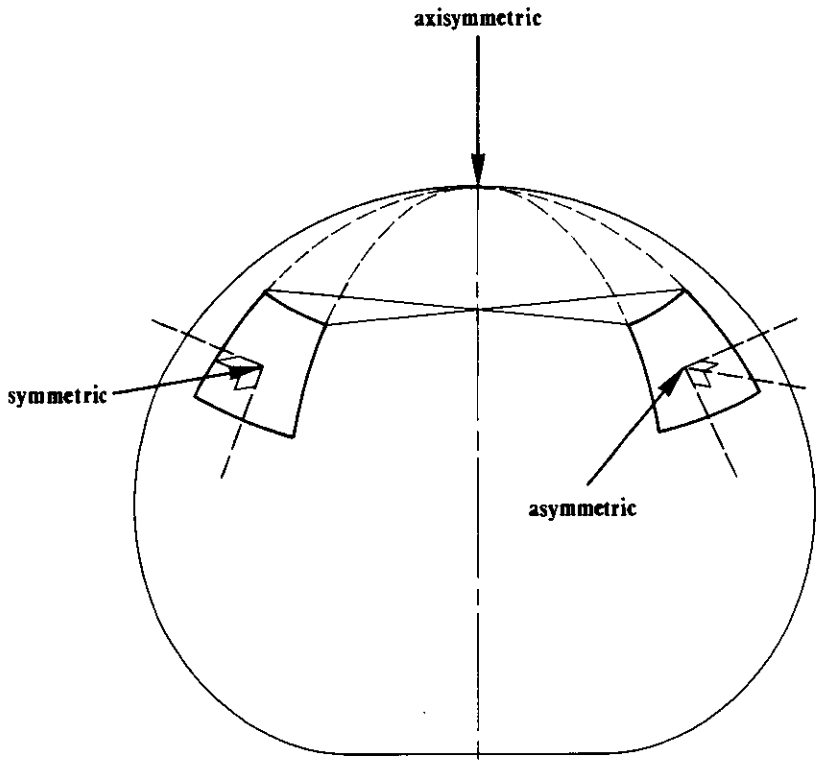

FIG. 2.2–SHELL UNDER VARIOUS POINT LOADINGS

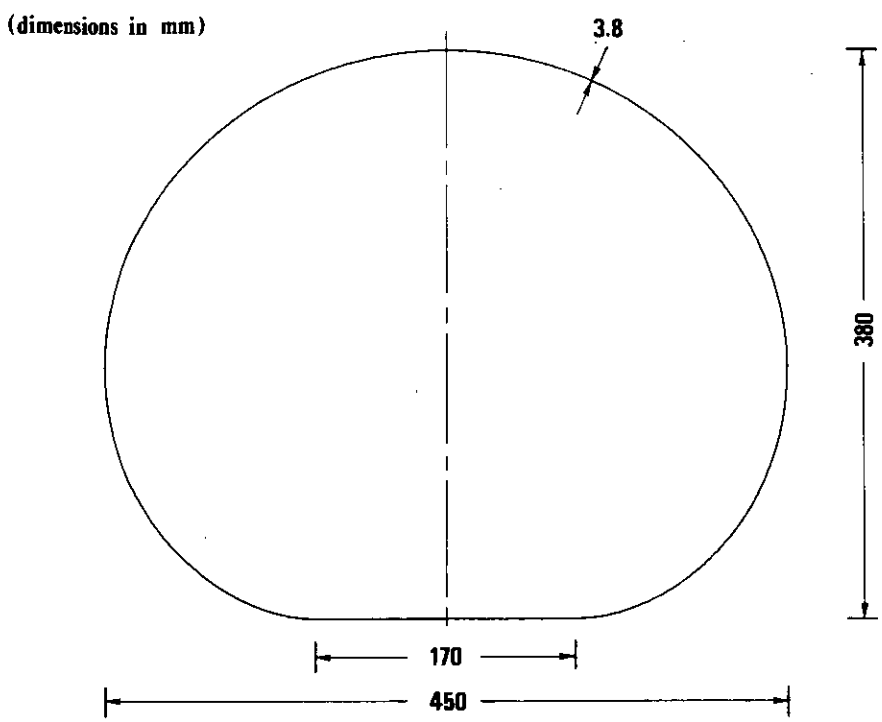

FIG. 2.3–TEST STRUCTURE DIMENSIONS

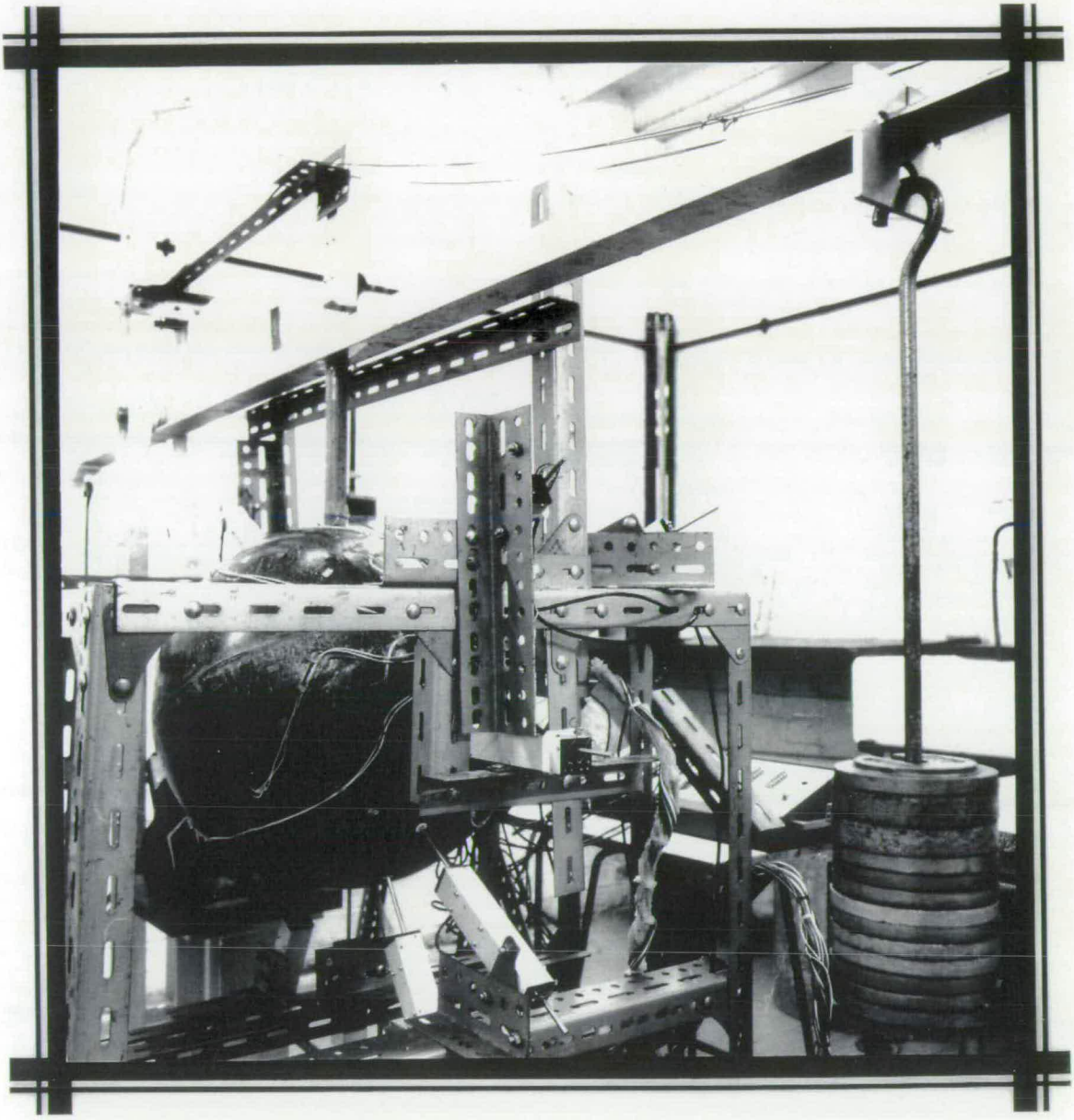

FIG. 2.4–PROTOTYPE UNDER A SYMMETRIC POINT LOAD

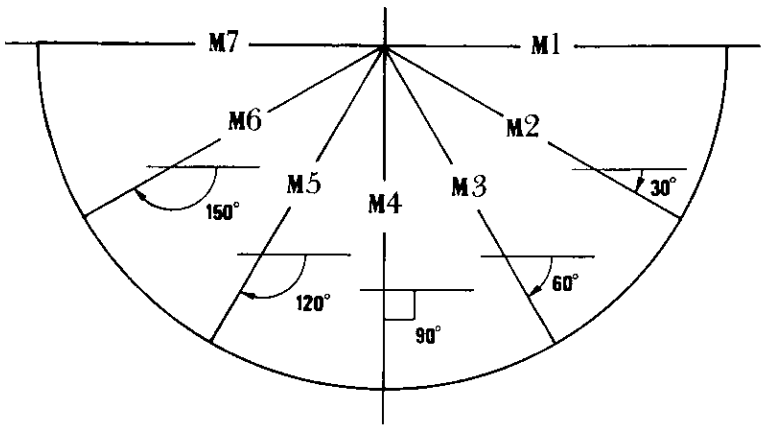

FIG. 2.5–NOMENCLATURE OF MERIDIANS ADOPTED IN CURRENT ANALYSIS

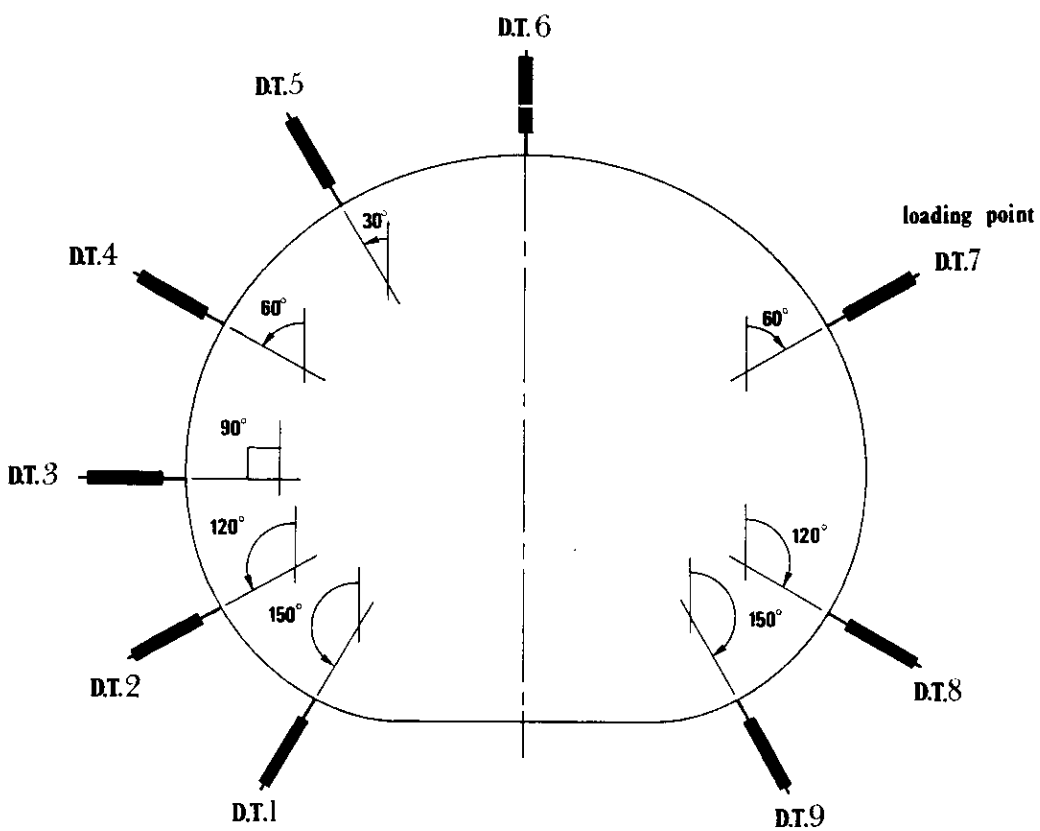

FIG. 2.6–DISPOSITION OF DISPLACEMENT TRANSDUCERS

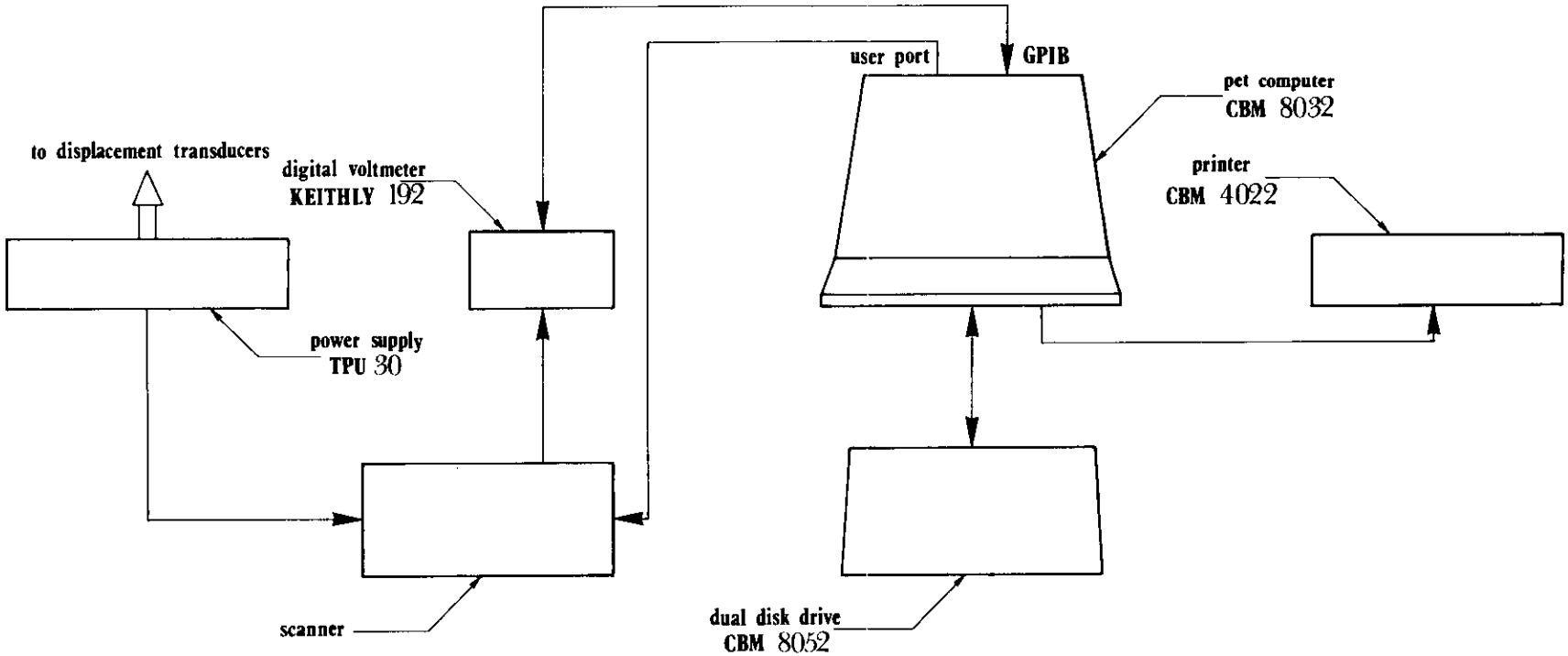

FIG. 2.7–INSTRUMENTATION USED IN STATIC POINT LOAD EXPERIMENT

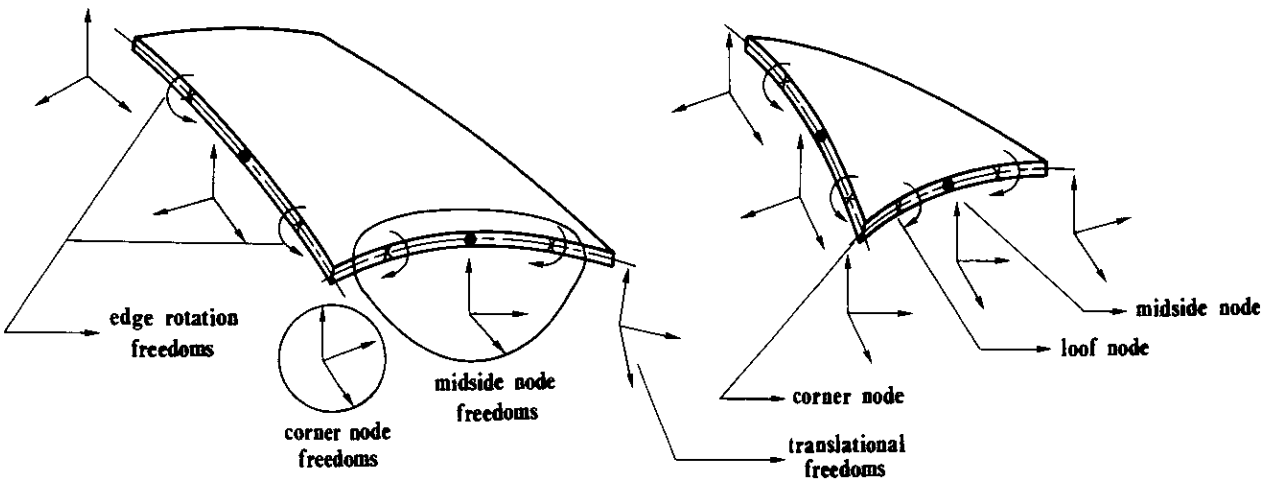

FIG. 2.8–NODAL VARIABLES FOR DOUBLY CURVED SEMI–LOOF QUADRILATERAL AND TRIANGULAR SHELL ELEMENTS

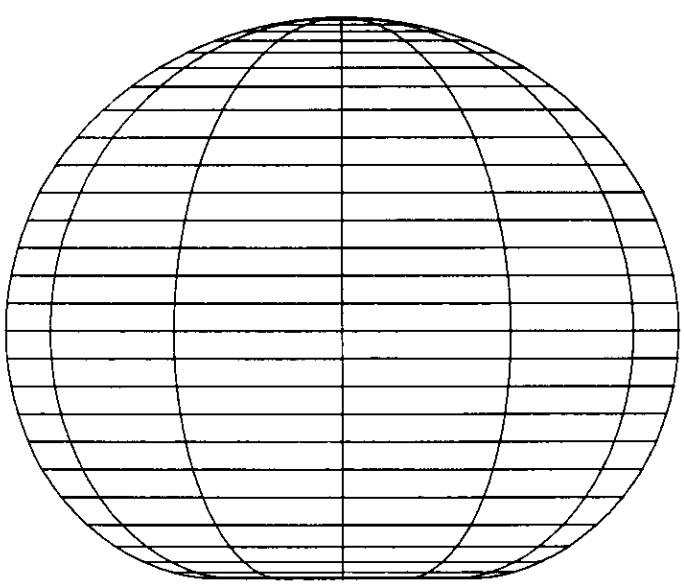

FIG. 2.9–MESH USED IN THE FINITE ELEMENT ANALYSIS

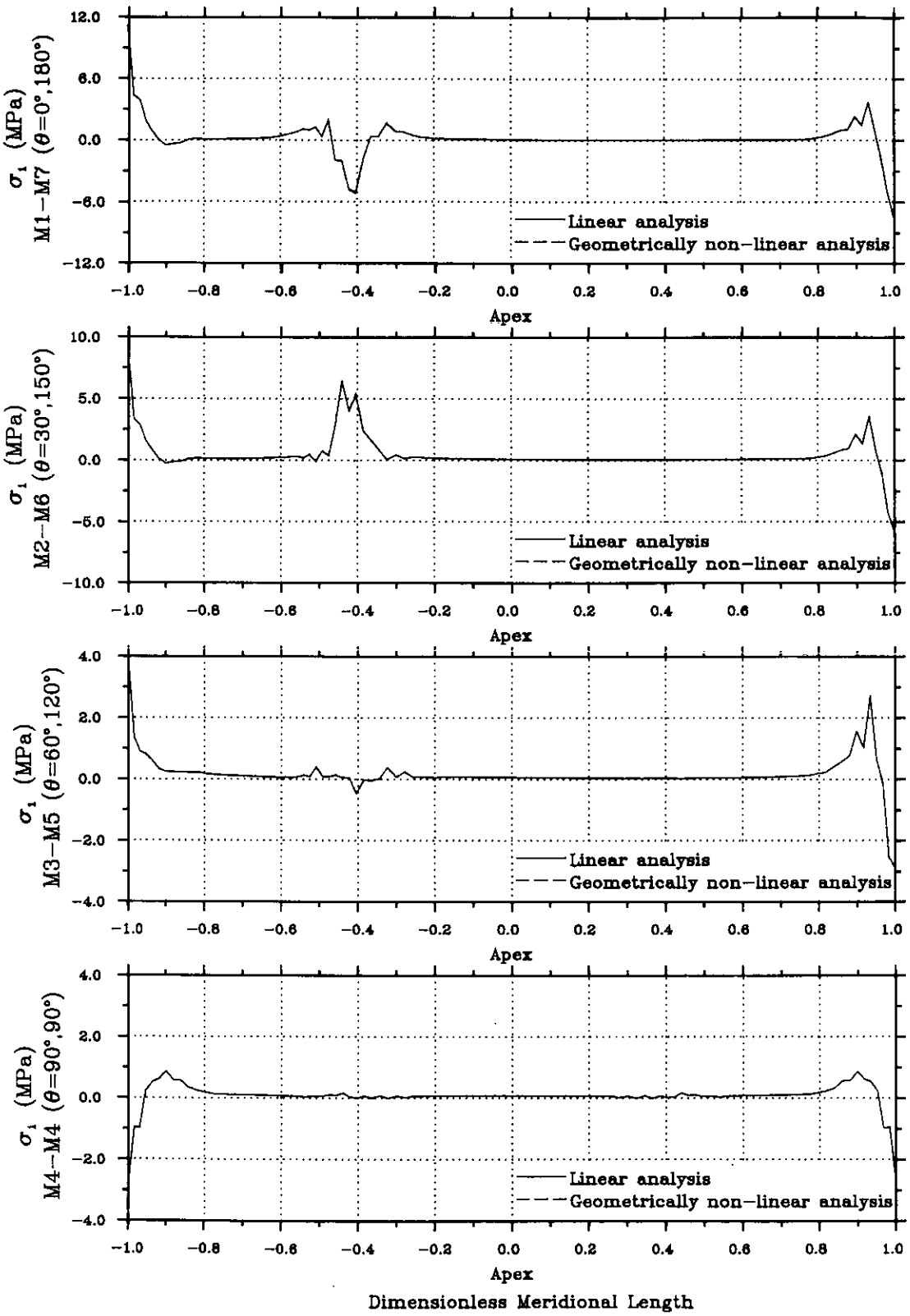

FIG. 2.10(a)–MAXIMUM PRINCIPAL STRESS DISTRIBUTION FOR OUTER SURFACE UNDER A NORMAL POINT LOAD OF 300 N ACTING 60° AWAY FROM APEX

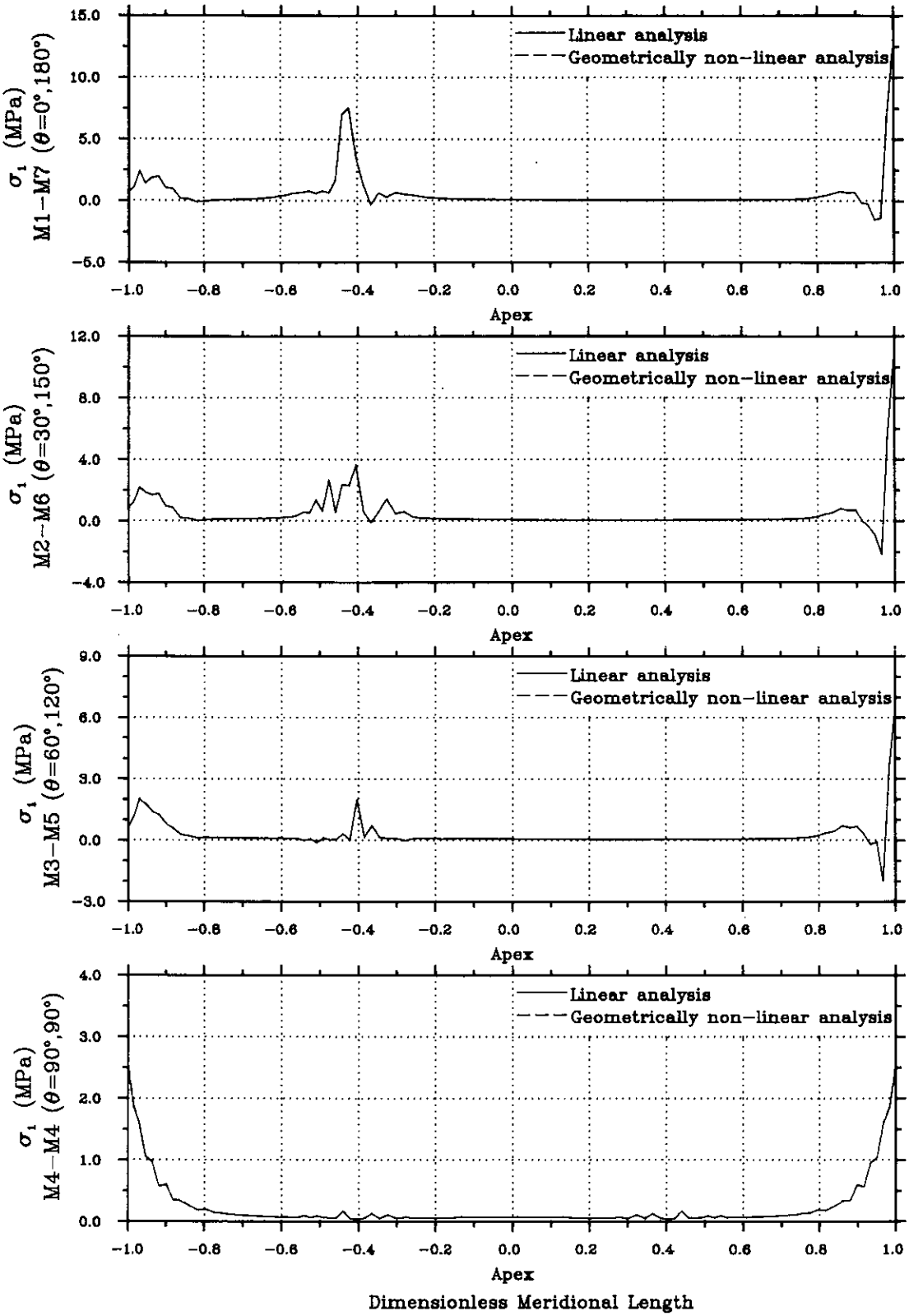

FIG. 2.10(b)–MAXIMUM PRINCIPAL STRESS DISTRIBUTION FOR INNER SURFACE UNDER A NORMAL POINT LOAD OF 300 N ACTING 60° AWAY FROM APEX

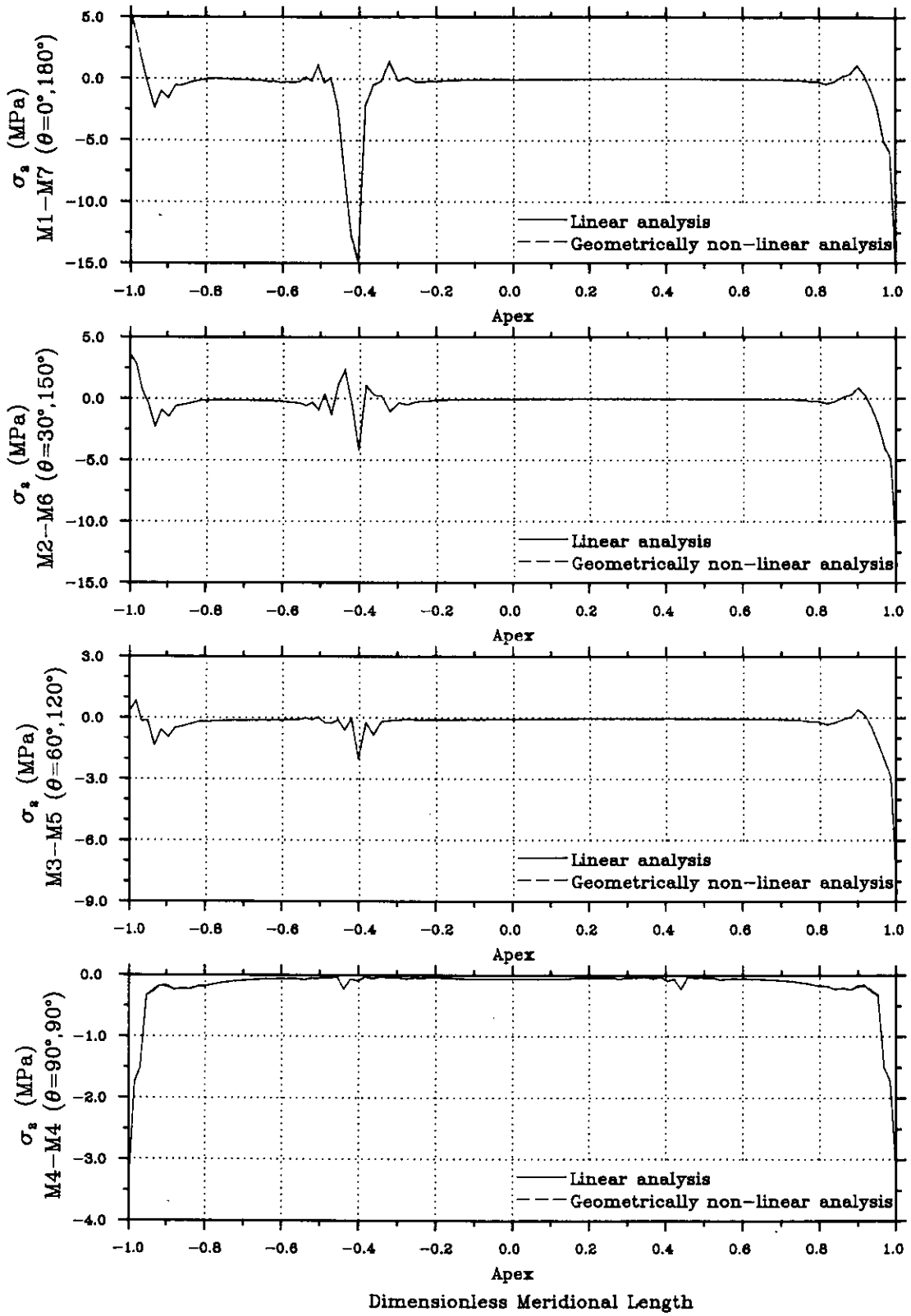

FIG. 2.10(c)–MINIMUM PRINCIPAL STRESS DISTRIBUTION FOR OUTER SURFACE UNDER A NORMAL POINT LOAD OF 300 N ACTING 60° AWAY FROM APEX

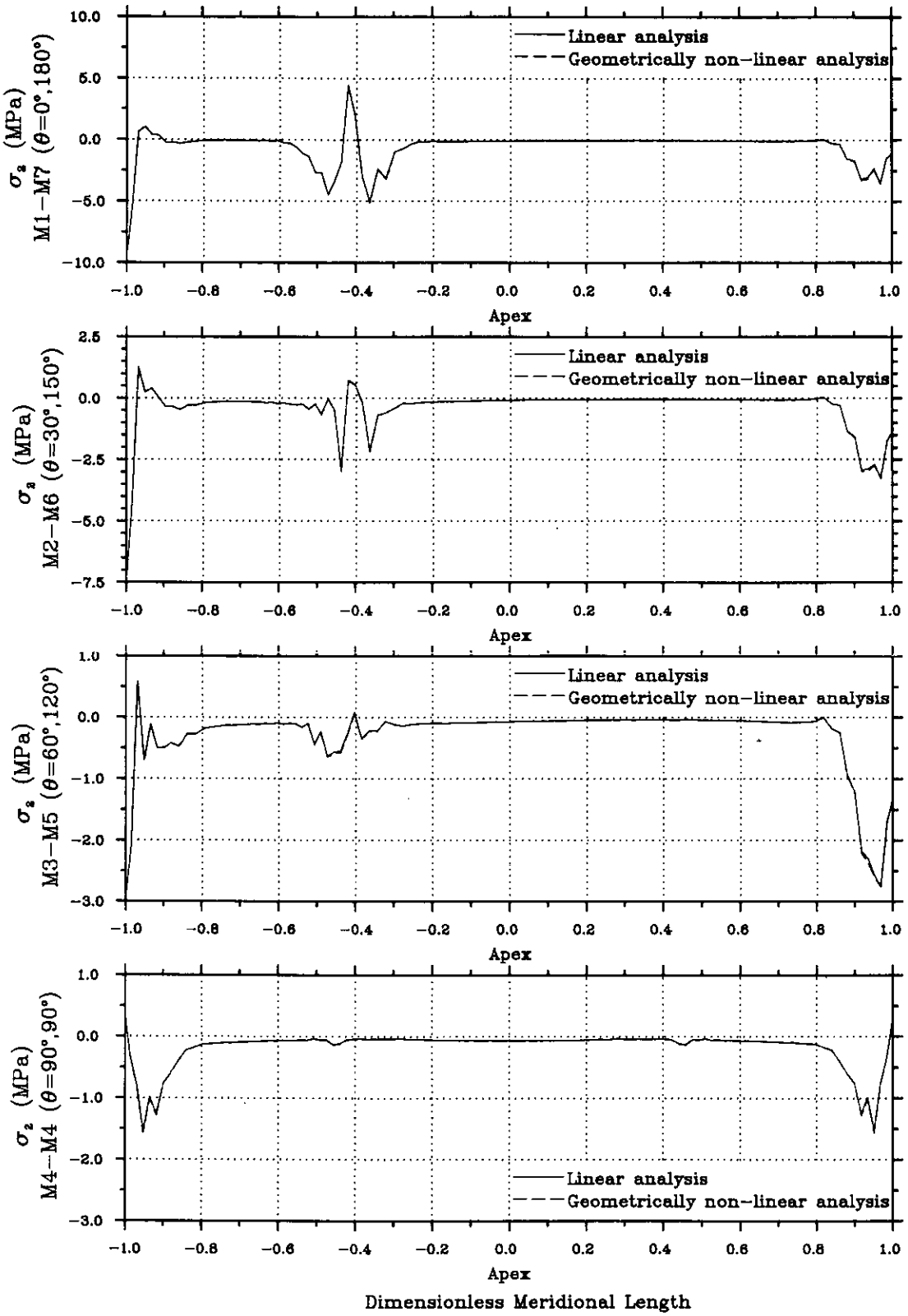

FIG. 2.10(d)–MINIMUM PRINCIPAL STRESS DISTRIBUTION FOR INNER SURFACE UNDER A NORMAL POINT LOAD OF 300 N ACTING 60° AWAY FROM APEX

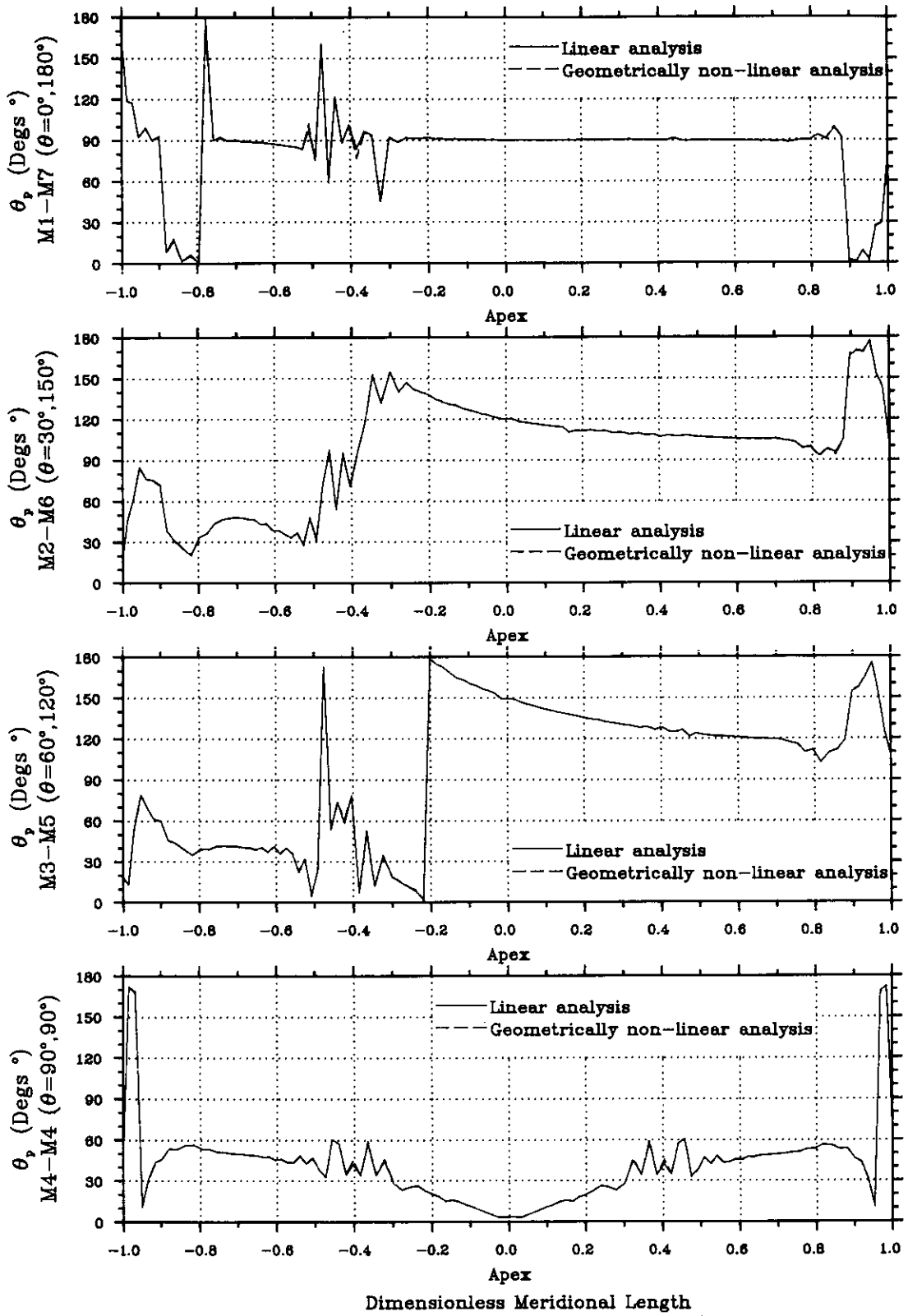

FIG. 2.11(a)–PRINCIPAL ANGLE DISTRIBUTION FOR OUTER SURFACE UNDER A NORMAL POINT LOAD OF 300 N ACTING 60° AWAY FROM APEX

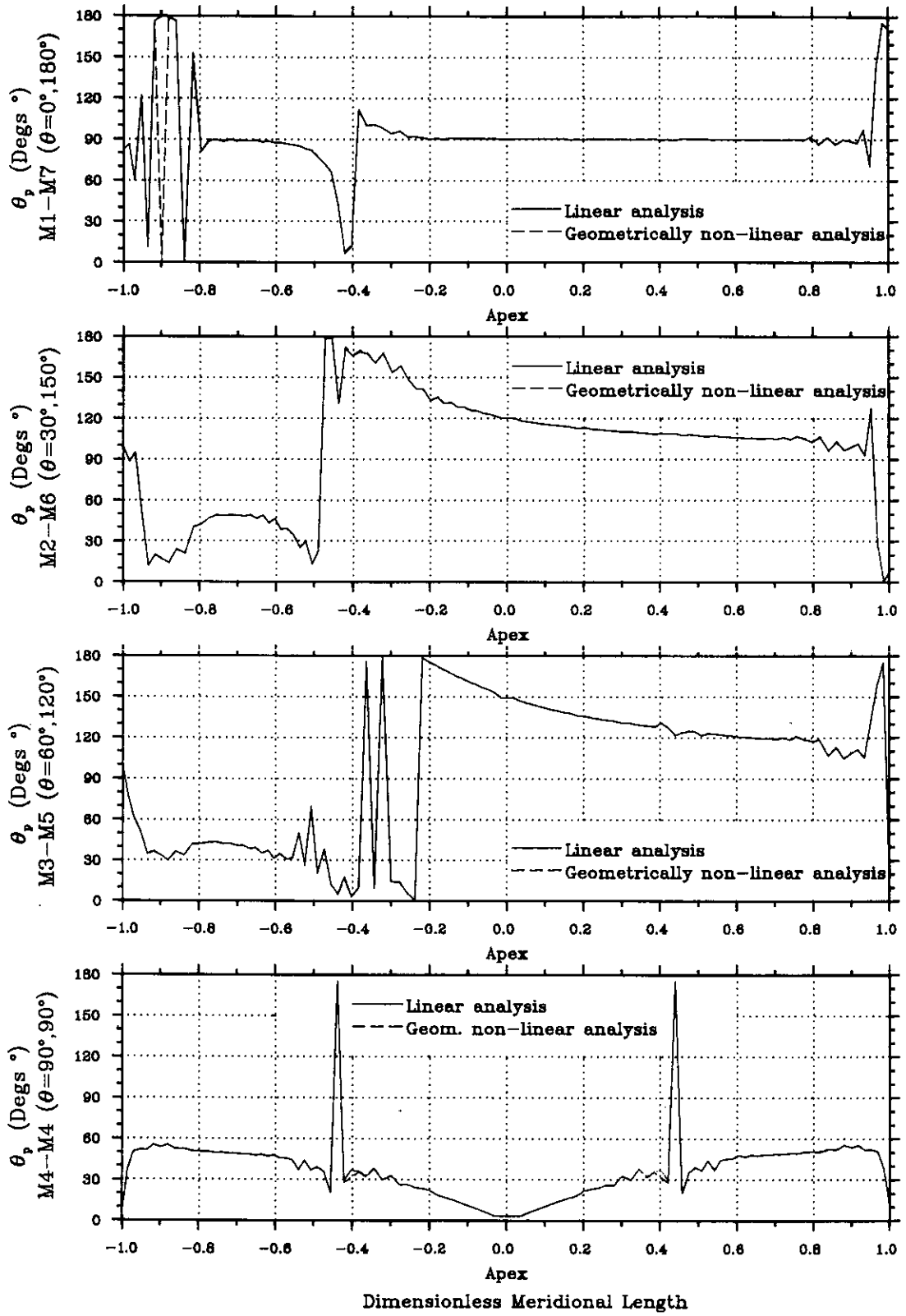

FIG. 2.11(b)–PRINCIPAL ANGLE DISTRIBUTION FOR INNER SURFACE UNDER A NORMAL POINT LOAD OF 300 N ACTING 60° AWAY FROM APEX

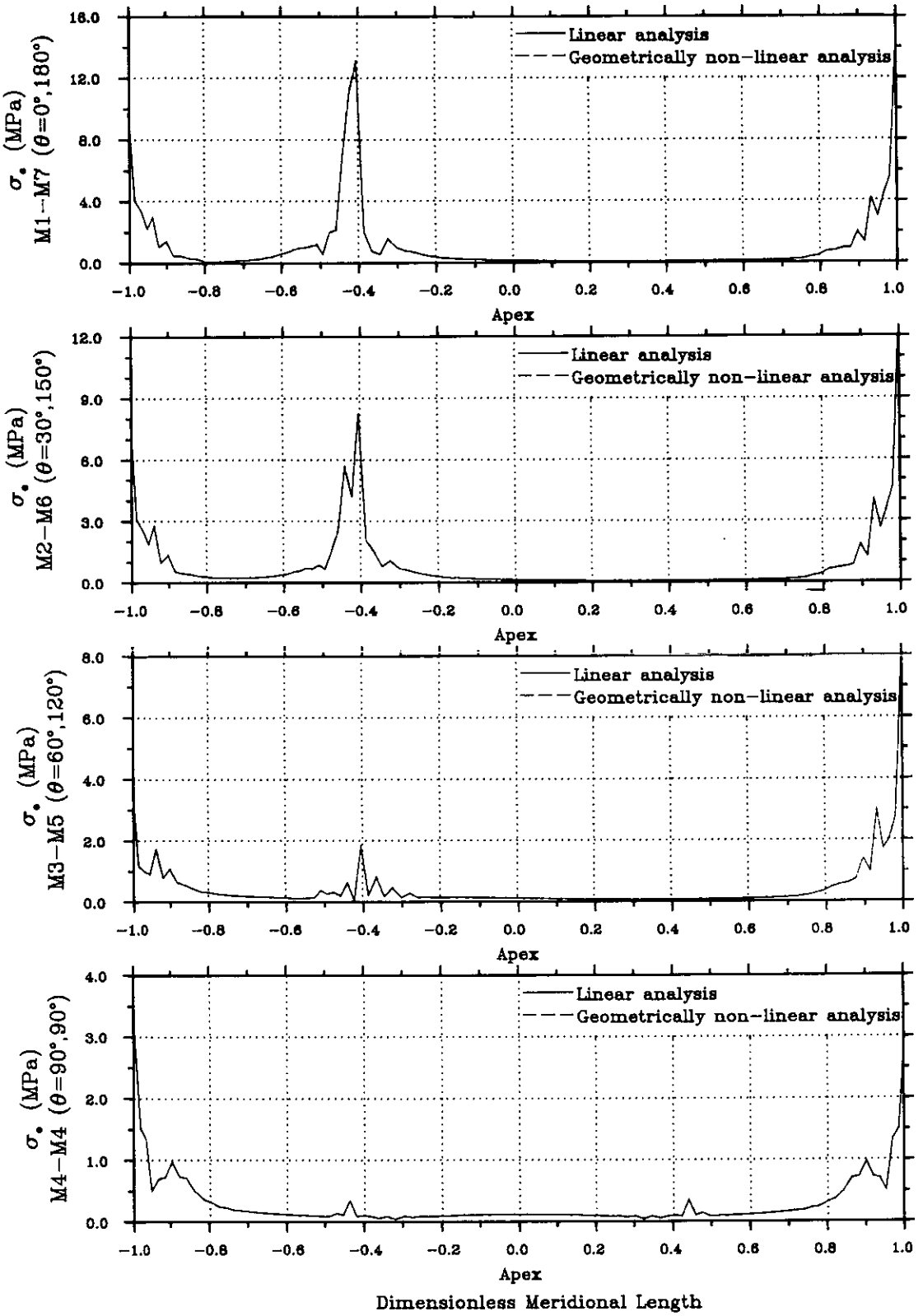

FIG. 2.12(a)–EQUIVALENT STRESS DISTRIBUTION FOR OUTER SURFACE UNDER A NORMAL POINT LOAD OF 300 N ACTING 60° AWAY FROM APEX

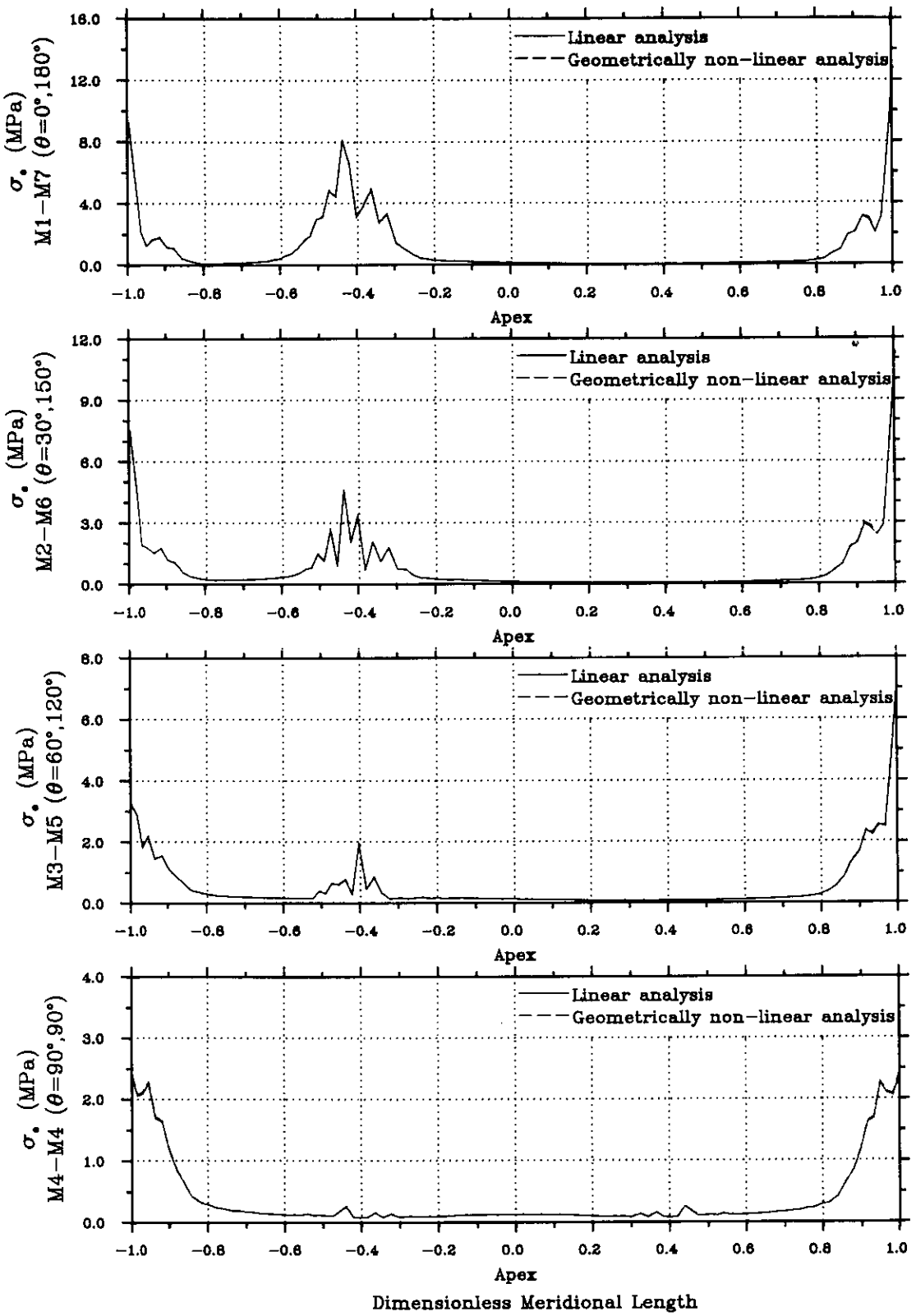

FIG. 2.12(b)–EQUIVALENT STRESS DISTRIBUTION FOR INNER SURFACE UNDER A NORMAL POINT LOAD OF 300 N ACTING 60° AWAY FROM APEX

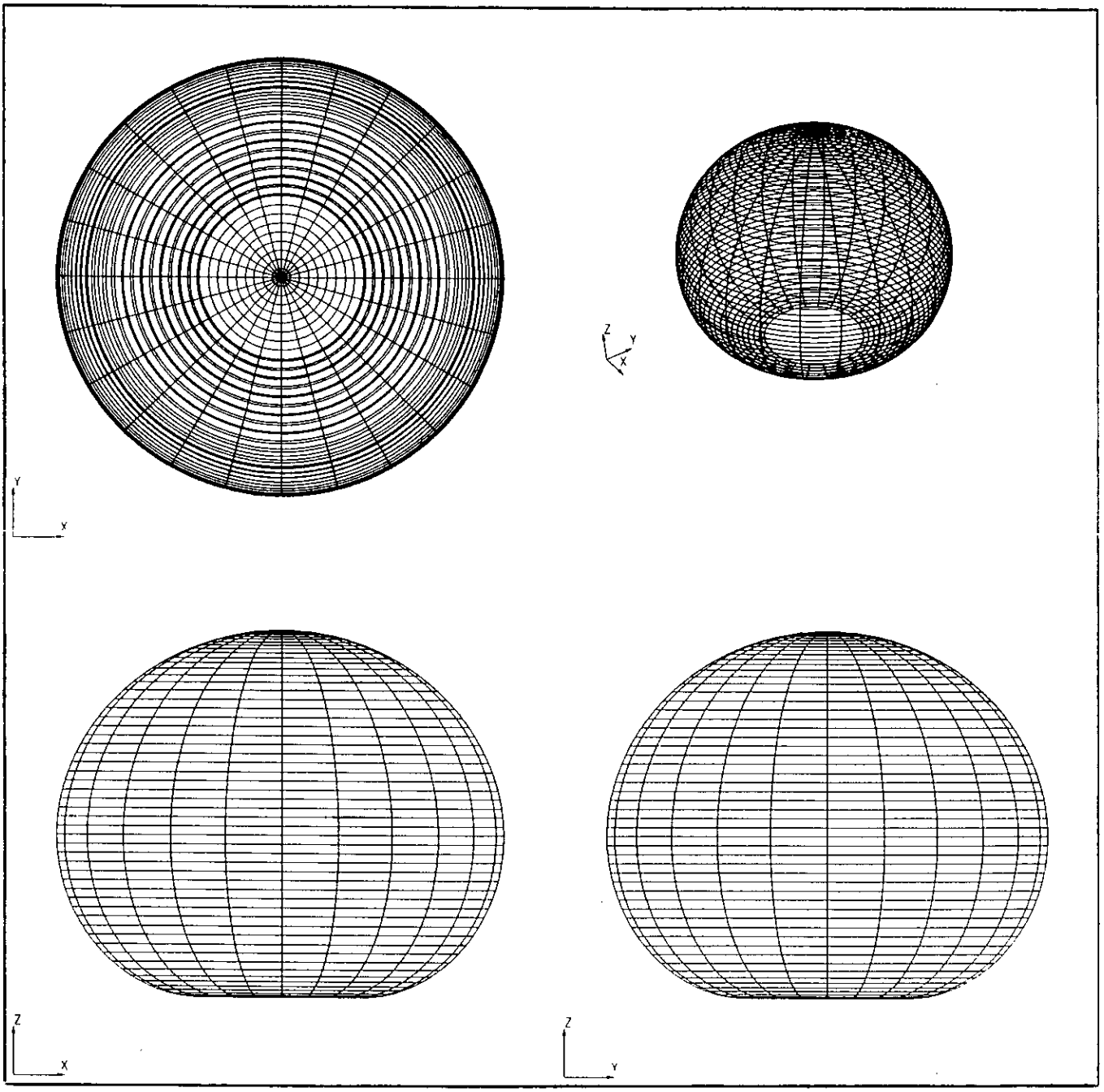

FIG. 2.13–ORIGINAL STRUCTURE BEFORE DEFORMATION

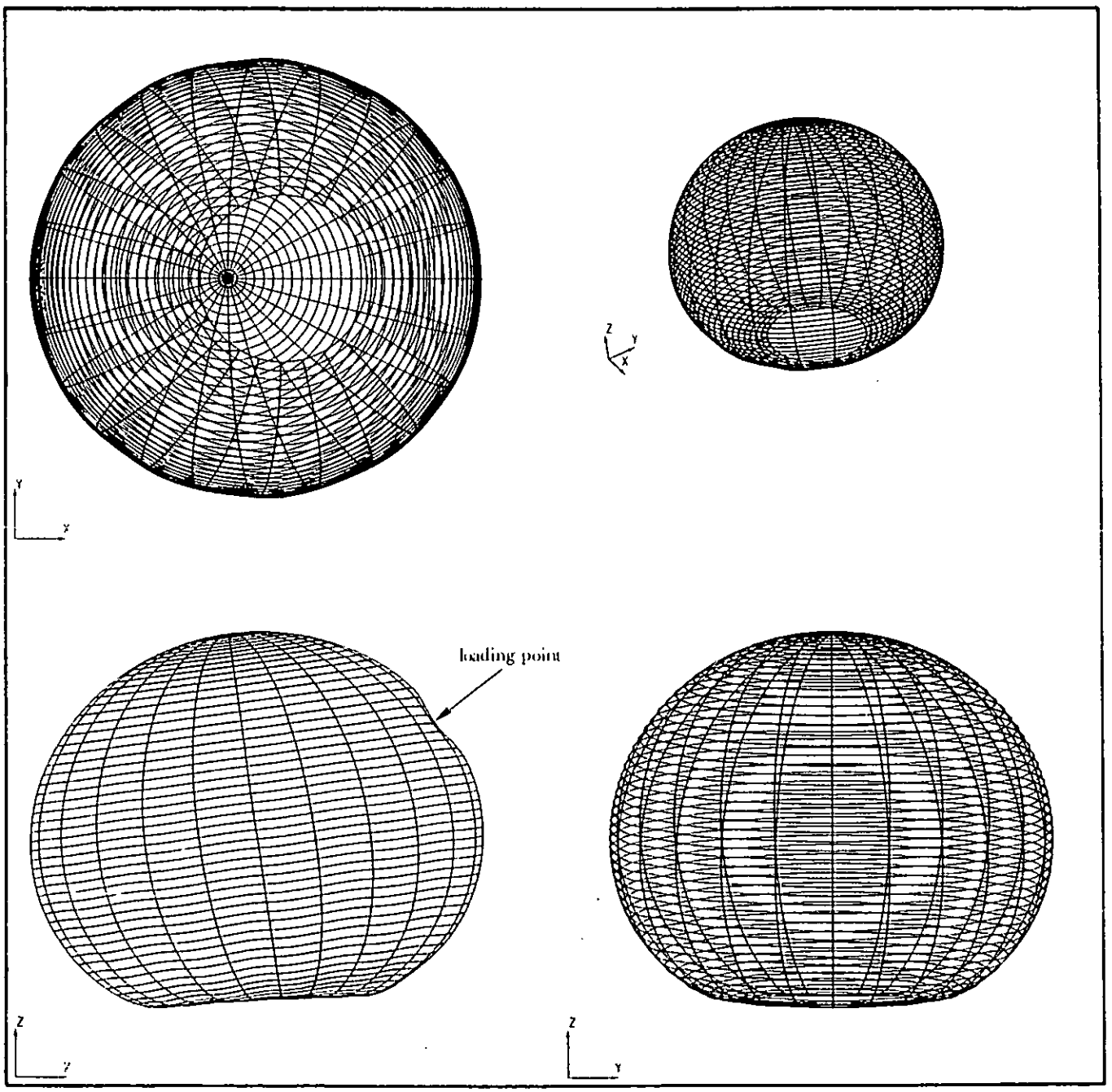

FIG. 2.14—DEFORMED STRUCTURE UNDER A NORMAL POINT LOAD OF 300 N ACTING 60° AWAY FROM APEX (DISPLACEMENTS ×50)

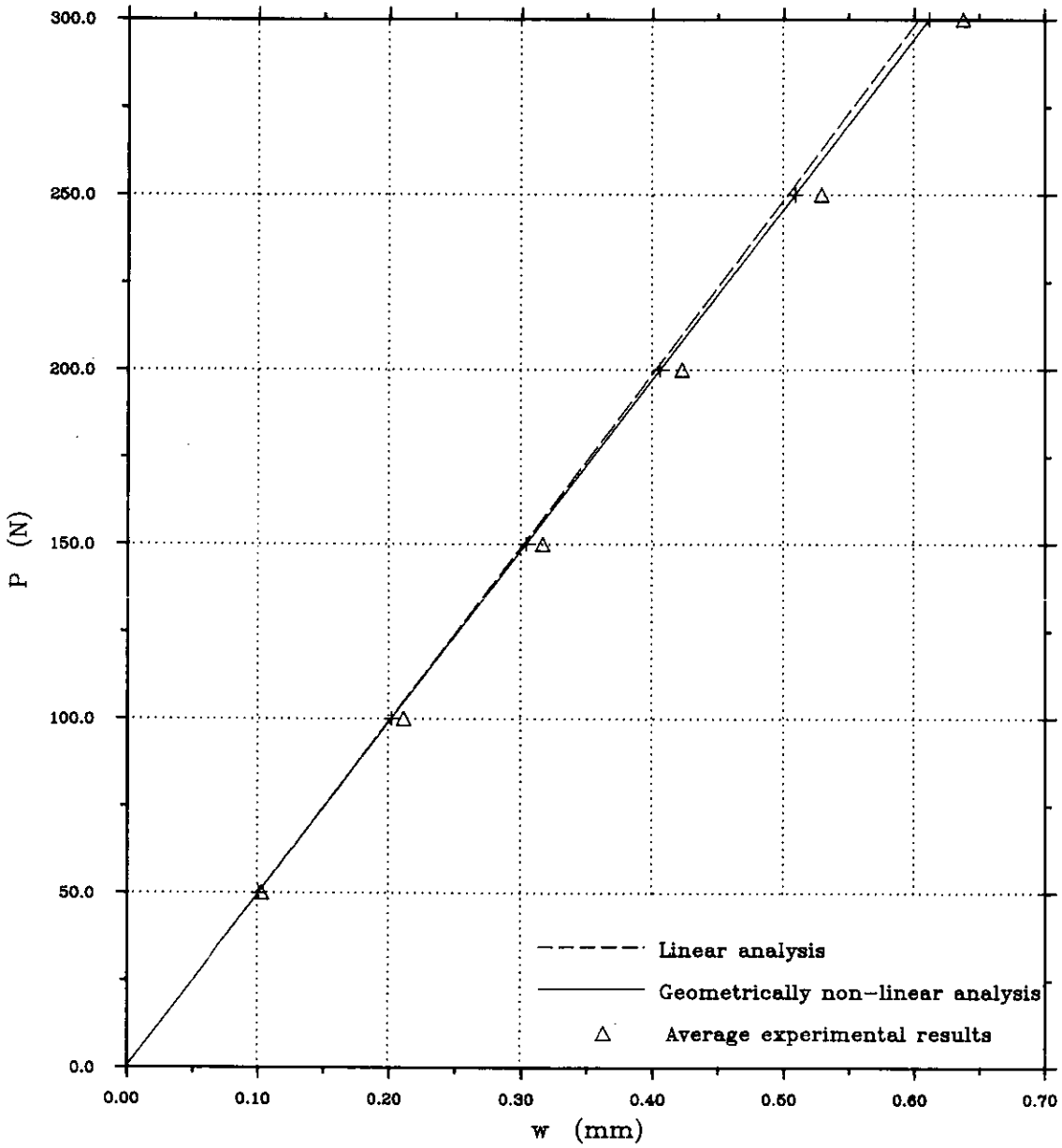

FIG. 2.15–LOAD VERSUS NORMAL DISPLACEMENT AT THE POINT OF APPLICATION OF A NORMAL CONCENTRATED LOAD ACTING 60° AWAY FROM APEX

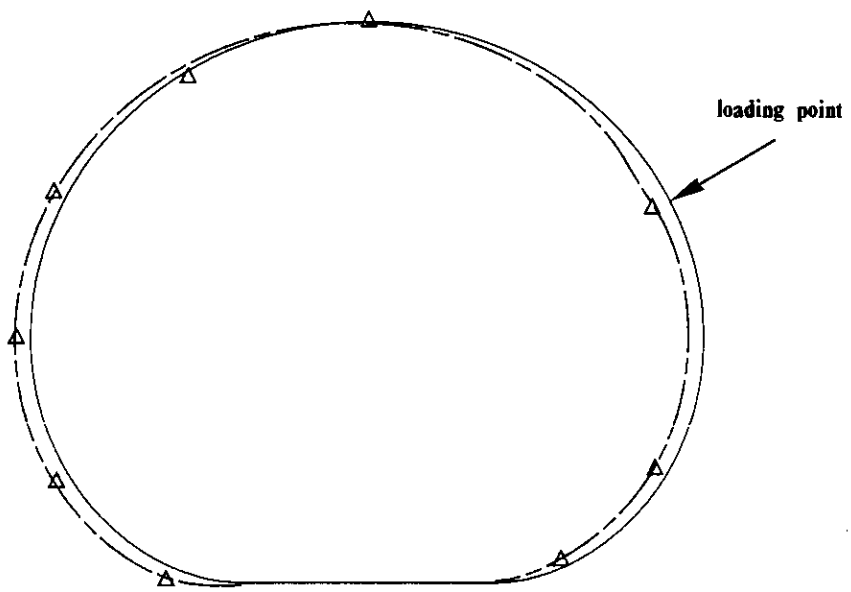

——————— Original profile
– – – – – – – – – – – Deformed profile (linear analysis)
——— – – ——— Deformed profile (geometrically non–linear analysis)
△ Experimental results

FIG. 2.16–*DEFORMED PROFILE OF MERIDIANS M1 AND M7* (θ=0°,180°) *UNDER A NORMAL POINT LOAD OF* 300 *N ACTING* 60° *AWAY FROM APEX* (*DISPLACEMENTS* ×20)

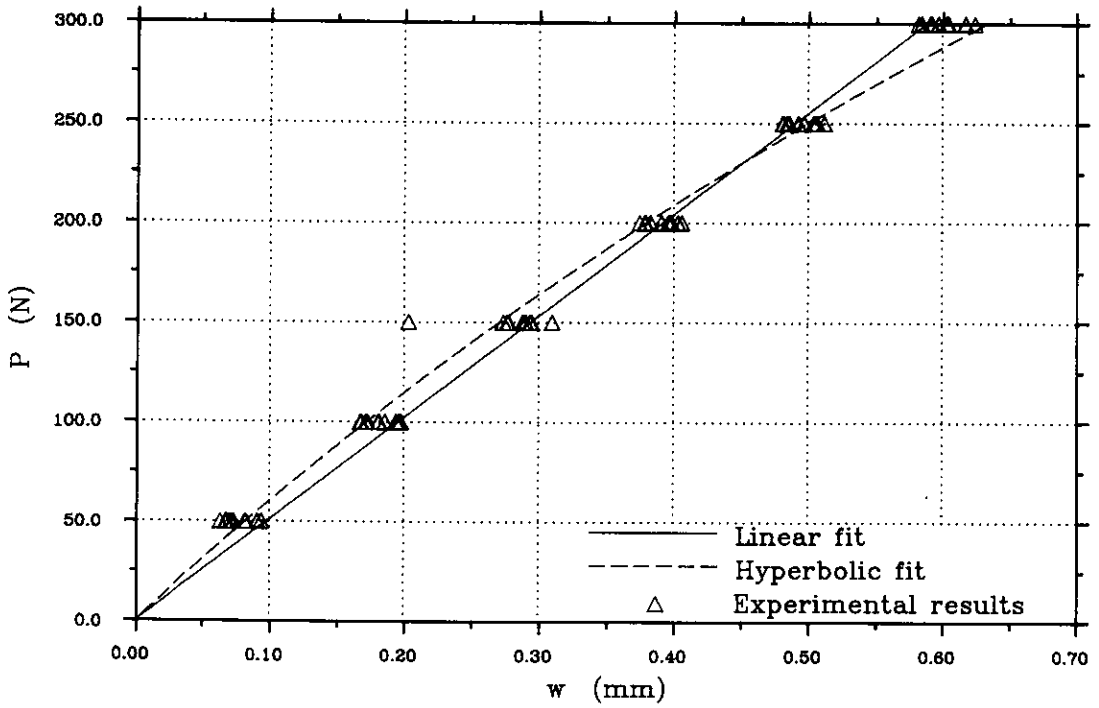

FIG. 2.17(a)–DIFFERENT FITTED MODELS FOR LOAD–DISPLACEMENT RELATIONSHIP AT A POINT 60° AWAY FROM APEX (POINT OF APPLICATION OF LOAD)

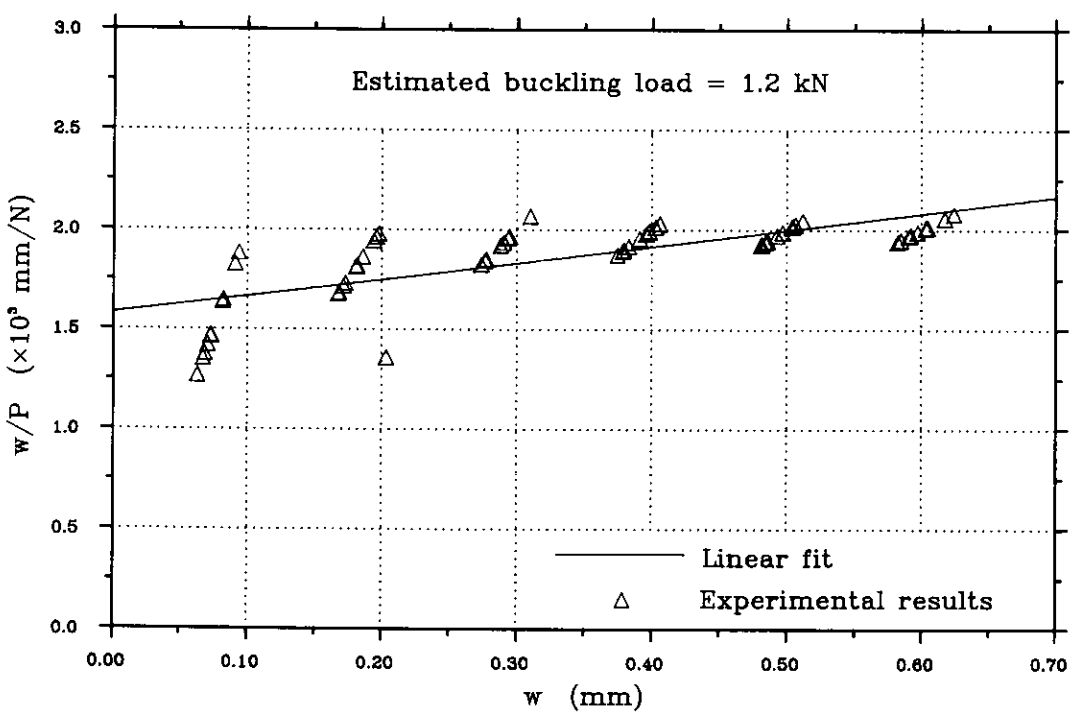

FIG. 2.17(b)–SOUTHWELL PLOT FOR A POINT 60° AWAY FROM APEX

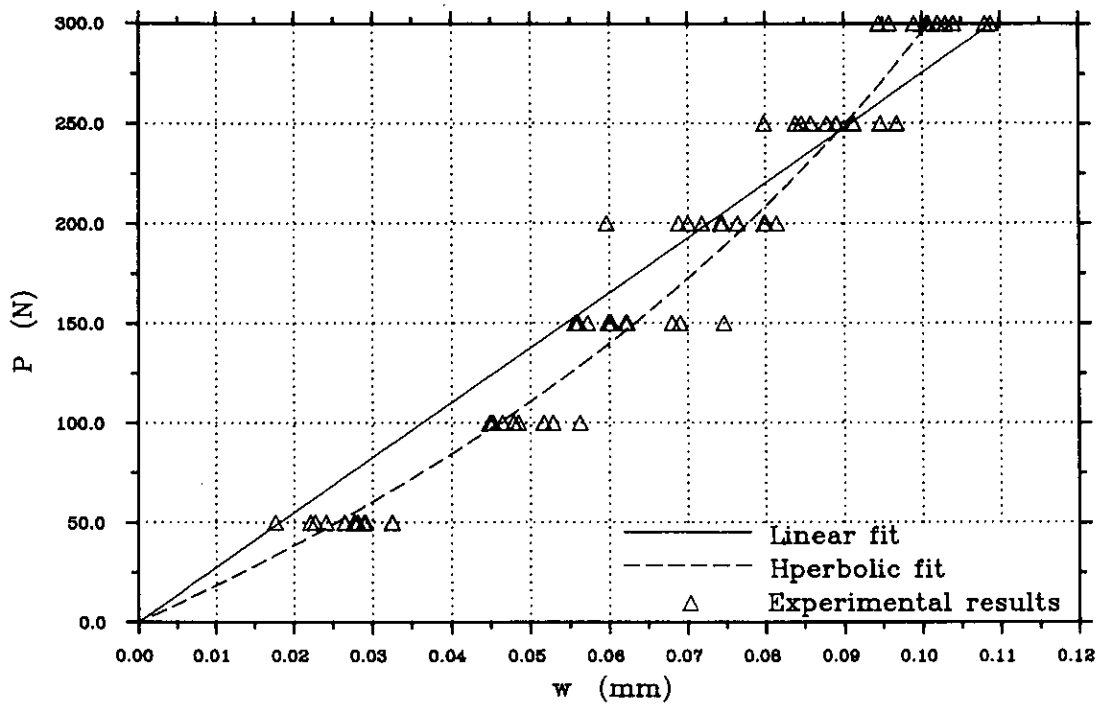

FIG. 2.18(a)–DIFFERENT FITTED MODELS FOR LOAD–DISPLACEMENT RELATIONSHIP AT APEX (LOADED POINT 60° AWAY FROM APEX)

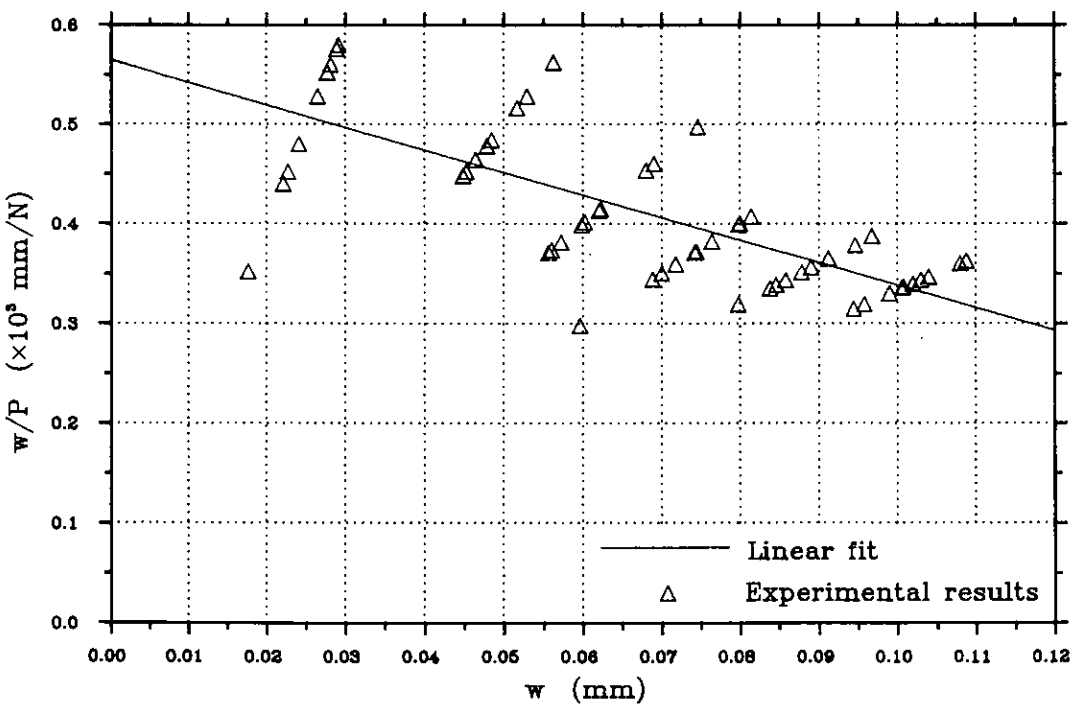

FIG. 2.18(b)–SOUTHWELL PLOT FOR APEX

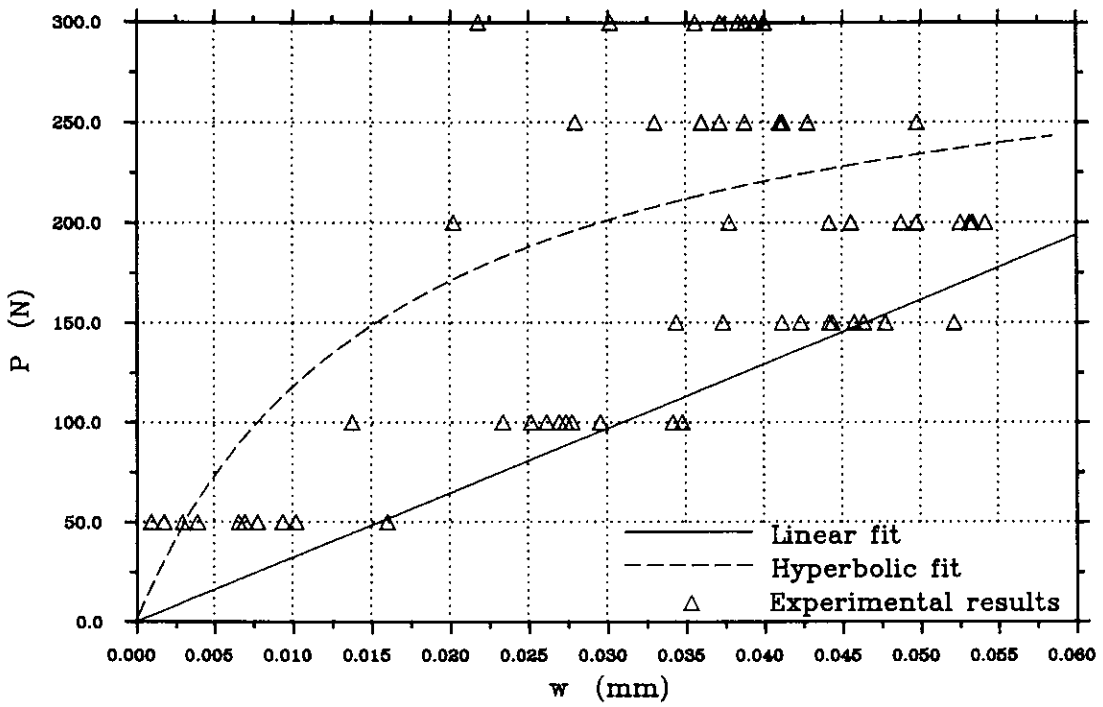

FIG. 2.19(a)–DIFFERENT FITTED MODELS FOR LOAD–DISPLACEMENT RELATIONSHIP FOR DISPLACEMENT TRANSDUCER 5

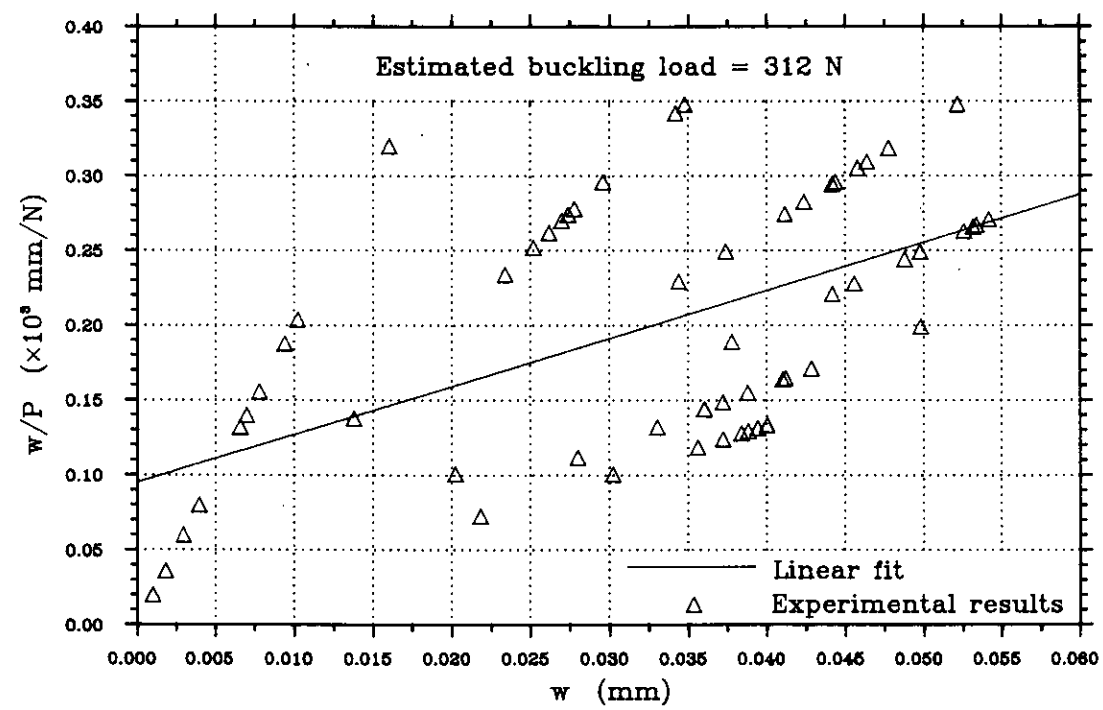

FIG. 2.19(b)–SOUTHWELL PLOT FOR DISPALCEMENT TRANSDUCER 5

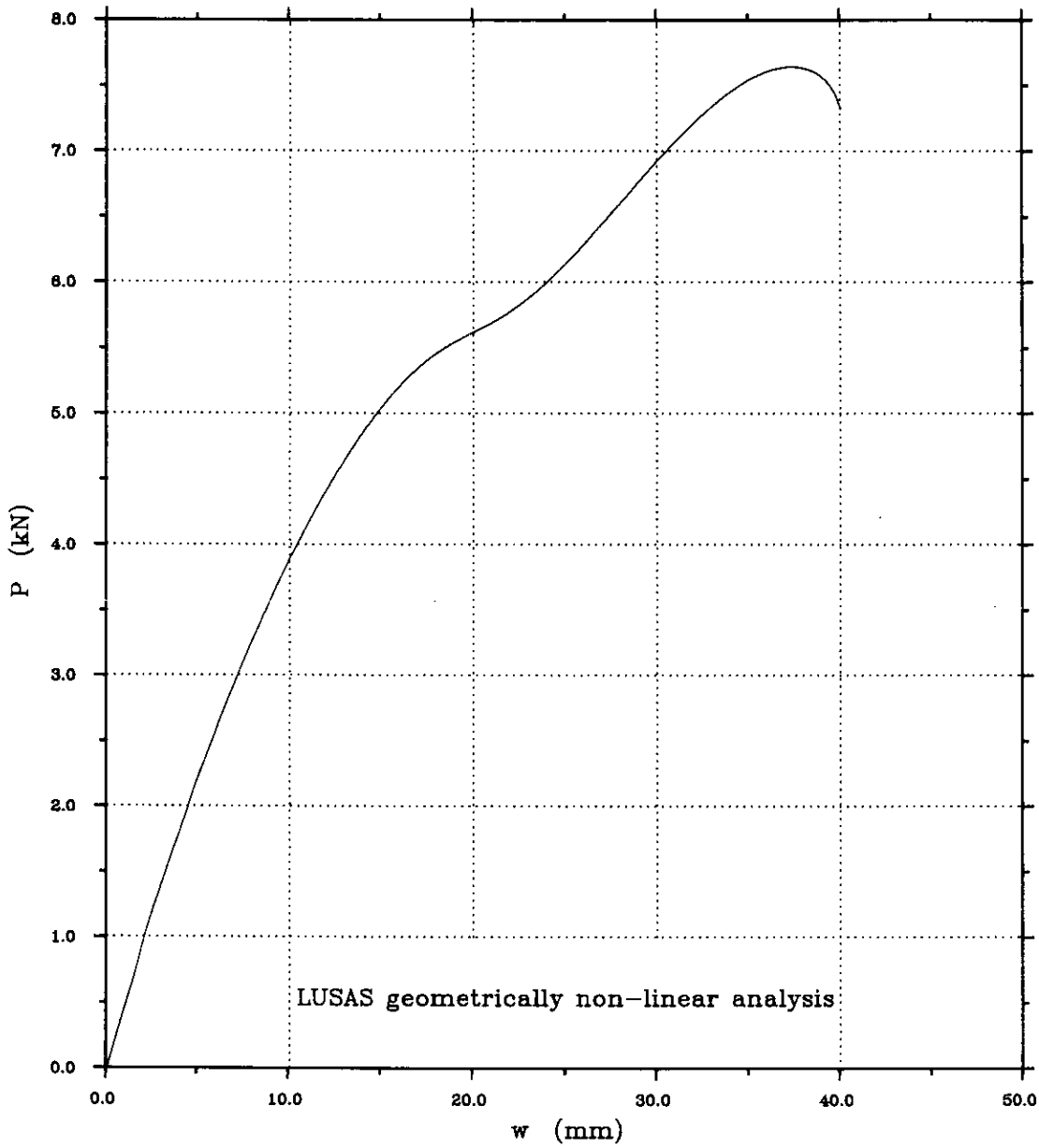

FIG. 2.20–LOAD VERSUS NORMAL DISPLACEMENT AT THE POINT OF APPLICATION OF A NORMAL POINT LOAD ACTING 60° AWAY FROM APEX

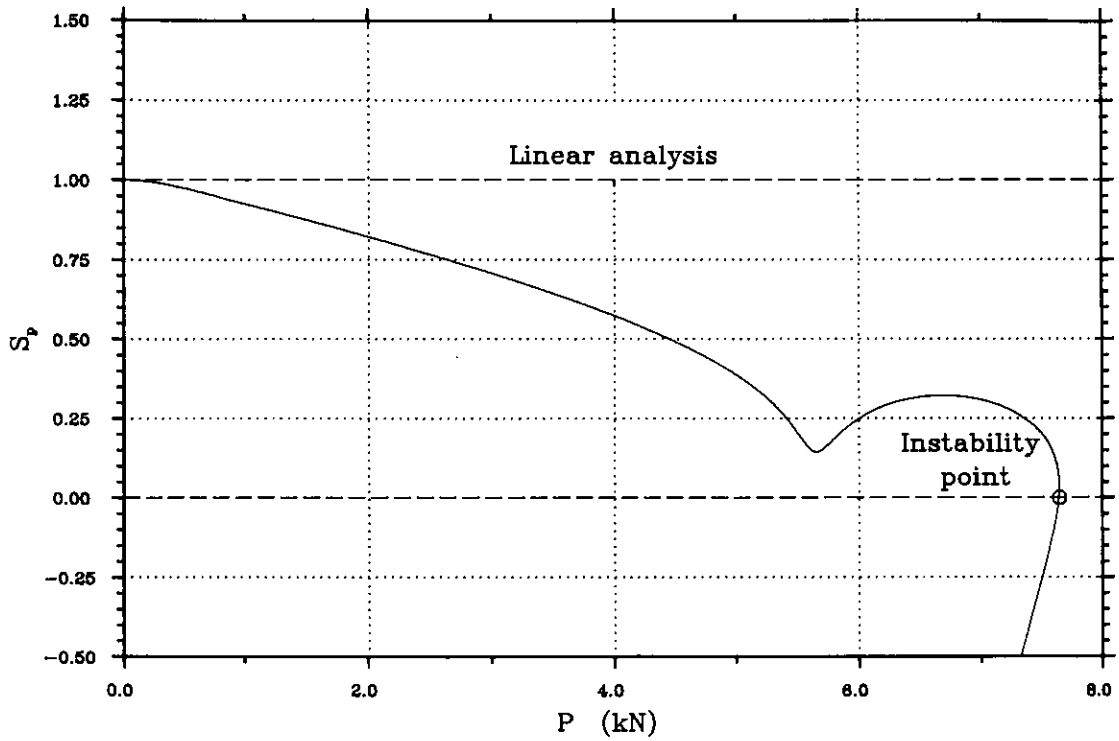

FIG. 2.21(a)–CURRENT STIFFNESS PARAMETER VERSUS LOAD FOR A NORMAL POINT LOAD ACTING 60° AWAY FROM APEX

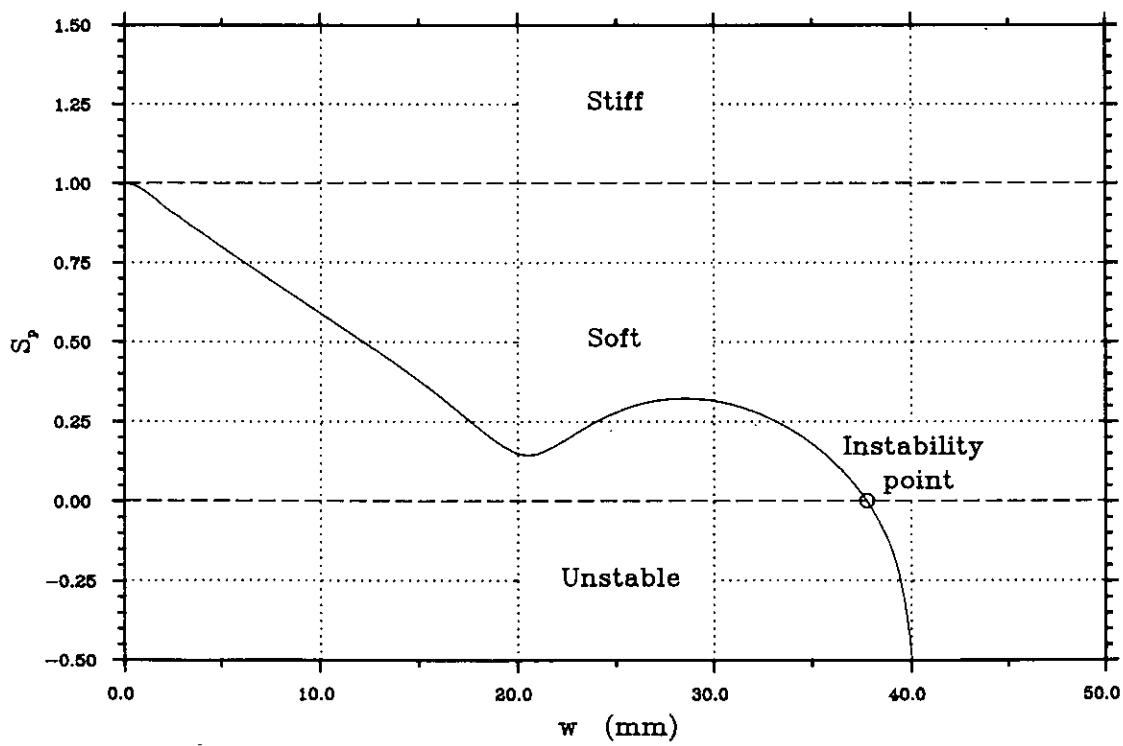

FIG. 2.21(b)–CURRENT STIFFNESS PARAMETER VERSUS NORMAL DISPLACEMENT FOR A NORMAL POINT LOAD ACTING 60° AWAY FROM APEX

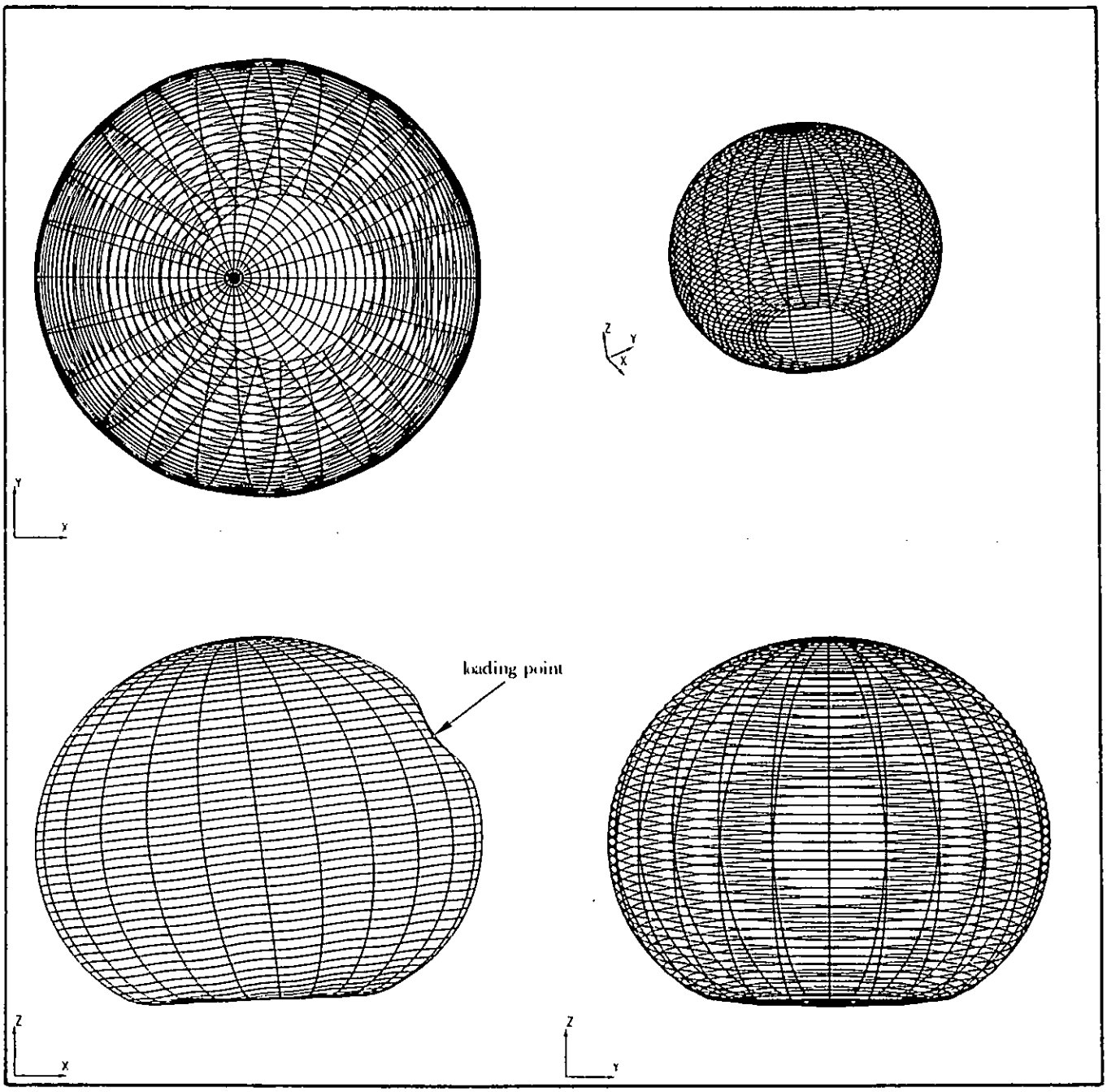

FIG. 2.22–DEFORMED STRUCTURE UNDER STATIC COLLAPSE BUCKLING FOR A NORMAL POINT LOAD ACTING 60° AWAY FROM APEX
––COLLAPSE LOAD = 7.64 kN––
(DISPLACEMENTS ×1)

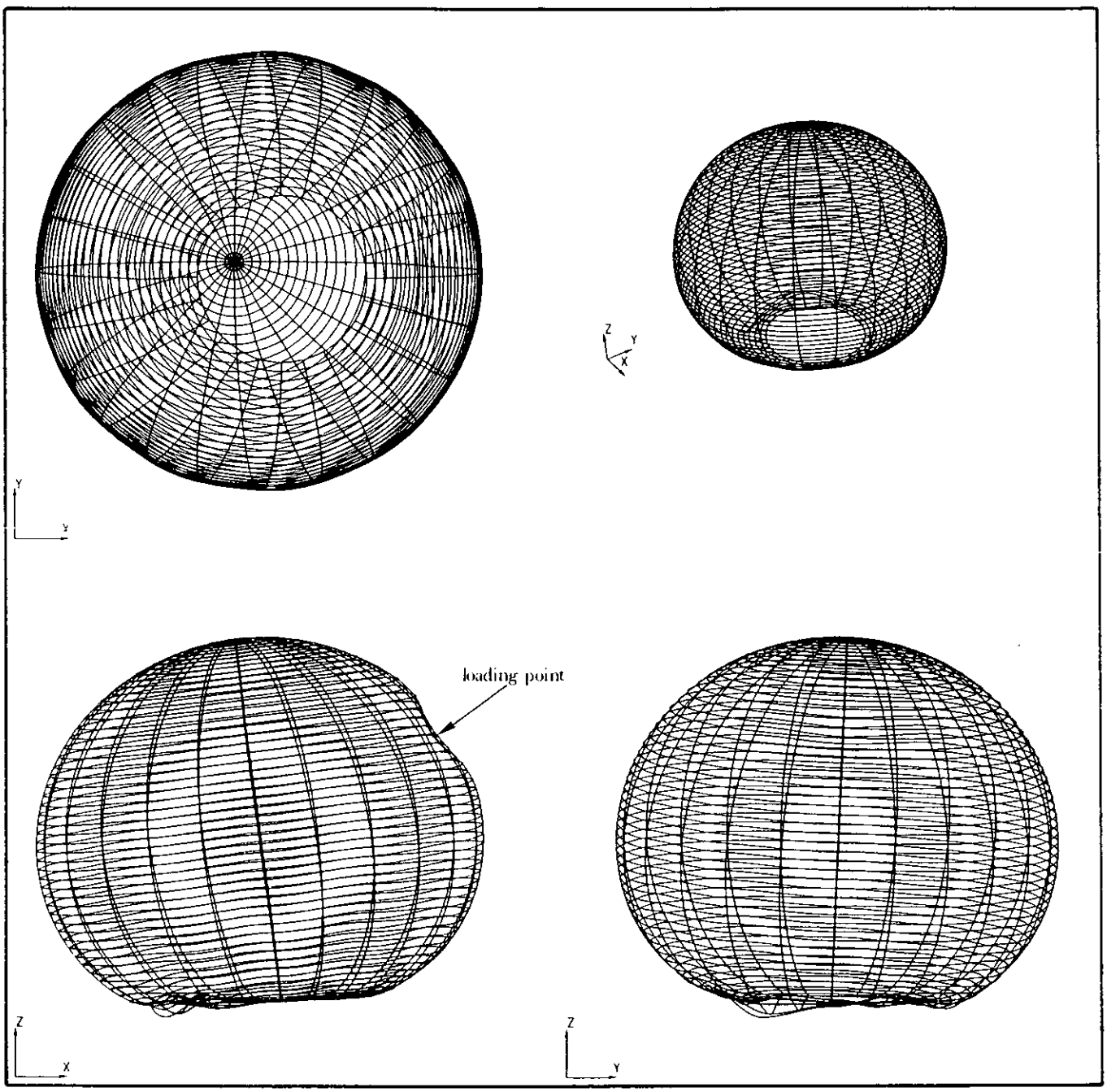

FIG. 2.23–BUCKLING MODE SHAPE UNDER A STATIC NORMAL POINT LOAD ACTING 60° AWAY FROM APEX
––BIFURCATION LOAD = 9.90 kN––
(GEOMETRICALLY NON–LINEAR ANALYSIS)

CHAPTER 3

THEORETICAL STUDIES ON THE ECHINODOME RESPONSE TO DYNAMIC POINT LOADS

3.1 SUMMARY

Theoretical dynamic analysis of the Echinodome was carried out employing two finite element systems, LUSAS and PAFEC.

Natural frequencies and mode shapes of the finite element mesh described earlier were computed using two different techniques.

Shock spectra for symmetrical pulse shapes, triangular pulses and response to step functions were determined disregarding damping and assuming linear relationships.

Non–linear dynamic analysis was performed for an axisymmetric and a symmetric point loading to determine the dynamic collapse buckling load.

3.2 INTRODUCTION

In their operational life, underwater storage vessels can be subjected to transient concentrated loads, e.g. as a result of dropped objects or sudden release of pressure.

Dynamic loads excite a frequency range dependent on the time duration of the loading pulse. If one or more of the structure's natural frequencies falls within that range then the structural response will be magnified when compared with its static correspondent, depending on the pulse duration. In order to study the general behaviour of the magnification factor a dynamic analysis must be carried out to determine the shock spectra for a wide variety of pulse shapes.

3.3 FREE VIBRATION ANALYSIS

The linear equation of motion for forced excitation may be written in matrix form as follows :

$$[M]\{\ddot{\delta}\} + [C]\{\dot{\delta}\} + [K]\{\delta\} = \{P\} \quad \text{.....} \quad (3.1)$$

where $[M]$ represents the mass matrix;

$[C]$ represents the damping matrix;

$[K]$ represents the stiffness matrix;

$\{\ddot{\delta}\}$ represents the acceleration vector (time dependent);

$\{\dot{\delta}\}$ represents the velocity vector (time dependent);

$\{\delta\}$ represents the displacement vector (time dependent); and,

$\{P\}$ represents the external load vector (time dependent).

For free vibration analysis the external load vector is equal to a null vector and the damping can be disregarded to give

$$[M]\{\ddot{\delta}\} + [K]\{\delta\} = \{0\} \quad \text{.....} \quad (3.2)$$

The solution of the previous equation can be assumed to be of the following form :

$$\{\delta\} = \{\psi\}e^{i\omega t} \quad \text{.....} \quad (3.3)$$

where $\{\psi\}$ is a vector of order n, and n represents the number of degrees of freedom (time dependent);

$e^{i\omega t}$ represents a complex function $\equiv \cos(\omega t) + i \sin(\omega t)$;

i is equal to the square root of -1 ; and,

ω represents the vibration frequency of vector $\{\psi\}$.

Substituting Eqn (3.3) into Eqn (3.2) it follows that

$$[K]\{\psi\} = \omega^2[M]\{\psi\} \quad \text{.....} \quad (3.4)$$

The eigenproblem in Eqn (3.4) yields n eigenvalues and n eigenvectors which are assembled in two matrices

$$[\Omega^2] = \begin{bmatrix} \omega_1^2 & & & 0 \\ & \omega_2^2 & & \\ & & \omega_3^2 & \\ & & & \ddots \\ 0 & & & \omega_n^2 \end{bmatrix}$$

$$[\Psi] = [\ \{\psi\}_1\ \{\psi\}_2\ \{\psi\}_3 \cdots \{\psi\}_n\ ]$$

Eqn (3.4) can be written for n solutions as

$$([K] - [\Omega^2][M])[\Psi] = [0] \qquad \text{.....} \qquad (3.5)$$

The eigenvectors are characterised by being orthogonal, which may be stated as follows :

$$[\Psi]^T[K][\Psi] = \begin{bmatrix} \ddots & & 0 \\ & k_r & \\ 0 & & \ddots \end{bmatrix} \qquad \text{.....} \qquad (3.6)$$

$$[\Psi]^T[M][\Psi] = \begin{bmatrix} \ddots & & 0 \\ & m_r & \\ 0 & & \ddots \end{bmatrix} \qquad \text{.....} \qquad (3.7)$$

where k_r, m_r represent the modal stiffness and mass for the r^{th} mode respectively.

Since the eigenvector matrix may be scaled by any factor, the values of k_r and m_r are not unique. Mass–normalisation is used to obtain a set of unique eigenvectors. This process is carried out by normalising each eigenvector with the square root of its corresponding modal mass.

$$\{\phi\}_r = \frac{1}{\sqrt{m_r}}\{\psi\}_r \qquad \text{.....} \qquad (3.8)$$

The mass–normalised eigenvectors have the following properties :

$$[\Phi]^T[K][\Phi] = [\Omega^2] \qquad \text{.....} \qquad (3.9)$$

$$[\Phi]^T[M][\Phi] = [I] \quad \text{.....} \quad (3.10)$$

where [I] represents the identity matrix.

If damping is taken into consideration then the eigenvalues and eigenvectors would in general be complex.

3.3.1 Natural Frequencies and Mode Shapes Extraction

There are several techniques to solve the eigenproblem of Eqn (3.5) a variety of which are reported in Ref. (17). The following subsections present a brief description of two methods for the solution of eigensystems, one is accurate and another is approximate. For a complex structure such as the Echinodome shell, the accurate technique requires an enormous amount of computer resources (memory and time), while the approximate technique if used effectively can produce relatively accurate results for the lowest eigenmodes using much lower computer resources.

3.3.1.1 The subspace iteration method— The main aim of the subspace iteration method is to extract the lowest **p** eigenvalues and corresponding eigenvectors satisfying the following equations :

$$([K] - [\Omega^2][M])[\Phi] = [0] \quad \text{.....} \quad (3.11)$$

Meaning that this technique extracts mass–normalised eigenvectors satisfying Eqns (3.9) and (3.10).

The method was developed by Bathe [17] and can be summarised in the following three steps :

1. **Starting procedure :** a set of q starting iteration vectors are established where q > p and p is the number of required eigenvalues and eigenvectors to be computed.
2. **Iteration :** an iteration procedure is followed to extract the best eigenvalue and eigenvector approximations.
3. **Sturm sequence check :** when convergence is achieved a sturm sequence check is carried out to verify that none of the intermediate eigenvalues have been missed.

The mathematical representation of the subspace iteration technique is given in Appendix C.

LUSAS adopts the subspace iteration method for solving eigenproblems and was utilised in extracting the eigenvalues and eigenvectors, for the initial mesh (perfect fixity at the base), by specifying

$$p = 8$$

$$q = 16$$

$$\text{Convergence tolerance} = 10^{-12}$$

Numerical results of the analysis are listed in Table 3.1 for the first eight vibrating modes with graphic presentation of the lowest six mode shapes in Figs 3.1(a → f), which are the most significant.

MODE NUMBER	NATURAL FREQUENCY (Hz)	ERROR NORM
1	73.40	0.1547×10^{-10}
2	73.40	0.1412×10^{-10}
3	273.20	0.1826×10^{-11}
4	577.97	0.2091×10^{-12}
5	1036.76	0.5671×10^{-12}
6	1036.76	0.2277×10^{-12}
7	1533.42	0.1184×10^{-05}
8	1545.45	0.3584×10^{-06}

TABLE 3.1 — *NATURAL FREQUENCY EXTRACTION RESULTS USING THE SUBSPACE ITERATION METHOD (AFTER 41 ITERATIONS)*

A sturm sequence check was performed after convergence was achieved and LUSAS stated that it had found the lowest eight eigenvalues. The results of the error norm associated with each eigenvalue indicate that the estimates of the natural frequencies were accurate.

3.3.1.2 The static condensation method— The whole finite element assemblage representing the Echinodome possessed 4371 degrees of freedom and to undertake a direct eigenvalue extraction process on such a mesh would be impractical.

Static condensation can be encountered in the solution of static equilibrium equations or in the calculation of natural frequencies and mode shapes. When utilised for an eigenproblem its main purpose is to lump the structural mass at specific degrees of freedom while leaving the stiffness intact causing small inaccuracies in the natural frequency and mode shape estimates.

One of the methods used to perform static condensation in a dynamic analysis is the Guyan reduction technique [37] . The reduction is carried out by neglecting the inertia effects of certain degrees of freedom characterised by the highest frequencies and modes thus retaining the lowest in the analysis. The Guyan reduction technique is summarised in Appendix D.

The standard technique used in PAFEC for the solution of eigenproblems is the static condensation method. The structural degrees of freedom are subdivided into masters and slaves. Master degrees of freedom are chosen to describe the deformations of the lowest modes of vibration. The eigensystem in Eqn (3.5) is rewritten as follows :

$$([K_m] - [\Omega_m^2][M_m])[\Phi] = [0] \quad \text{.....} \quad (3.12)$$

PAFEC transforms the generalised form of Eqn (3.12) into a standard eigenproblem form represented by

$$([\overline{K_m}] - [\Omega_m^2][I])[\overline{\Phi}] = [0] \quad \text{.....} \quad (3.13)$$

Then a most efficient technique known as the Householder tridiagonalisation method, [21] is used in the solution of the preceding equation. Once $[\overline{\Phi}]$ is computed it is back substituted to obtain $[\Phi]$ the required matrix of eigenvectors.

For the Echinodome the number of master degrees of freedom was 144 specified at four parallel circles and three translational at the apex giving a total of 147. Each parallel circle possessed 36 translational degrees of freedom located at 12 nodes lying on 12 meridians 30° apart.

The results of the analysis are listed in Table 3.2 and a comparison between the subspace iteration method and the static condensation method is presented in Table 3.3.

MODE NUMBER	NATURAL FREQUENCY (Hz)
1	73.47
2	73.47
3	274.37
4	582.41
5	1098.19
6	1098.99
7	1806.00
8	1806.60

TABLE 3.2 — *NATURAL FREQUENCY EXTRACTION RESULTS USING THE STATIC CONDENSATION METHOD*

METHOD OF EXTRACTION	USED DISK SPACE (MBYTE)	NUMBER OF EXTRACTED EIGENVALUES	NUMBER OF COMPUTED EIGENVECTORS	CPU TIME (min)	NUMBER OF ACCURATE NATURAL FREQUENCY ESTIMATES
Subspace iteration	54	8	8	73	8
Static condensation	17	147	8	27	32

TABLE 3.3 — *COMPARISON BETWEEN THE SUBSPACE ITERATION METHOD AND THE STATIC CONDENSATION METHOD*

3.4 TRANSIENT RESPONSE ANALYSIS

Structural response to dynamic loadings can be classified into [38,39] :

1. **Early time response :** highly localised deformations take place in structures subjected to severe impact or shock loadings. Stress waves are generated and interact with structural boundaries sometimes causing structural failure. Typical loading and response times are in microseconds.

2. **Transient response :** transient loads containing low frequency components excite the lowest vibrational modes of the overall structure, in which case loading and response times are of the order of milliseconds. Under such transient loading, structures respond globally and highly stressed points may not be in the vicinity of the loaded position.

In the current analysis only transient response will be considered.

3.4.1 Definitions

Prior to any discussion in the field of transient response analysis it is necessary to define the following list of terms :

- **Shock response spectrum** — is a plot of the maximum structural response at a specific point for a particular pulse shape against the ratio, τ_d, of the time duration of the pulse (t_d) to the longest structural natural period (T_1). From such a plot the effect of the pulse duration (relative to T_1) on the structural response can be observed.
- **Initial shock spectrum** — is a shock response spectrum of the maximum structural response while the shock pulse is acting, i.e. during the forced vibration state of the structure.
- **Residual shock spectrum** — is a shock response spectrum of the maximum structural response after the shock pulse is over, i.e. during the free vibration state of the structure.
- **Maximax shock spectrum** — is a shock response spectrum representing the overall maximum between the initial and residual shock spectra, i.e. during the motion of the structure.
- **Rise time** (t_1) — is the time for a triangular shock pulse to increase from zero to its maximum value (see Fig. 3.2(a)).
- **Decay time** (t_2) — is the time for a triangular shock pulse to decrease from its maximum value to zero (see Fig. 3.2(a)).
- **Skewness factor** (κ) — is a characteristic of triangular pulses and can be defined as the ratio of the rise time (t_1) to the total duration time of the triangular shock pulse ($t_d = t_1 + t_2$).
- **Ramp time** (t_r) — is the time taken by a step loading to reach its maximum value (see Fig. 3.2(b)).

- **Dynamic Load Factor (DLF)** — is defined as the ratio of the maximum displacement resulting from a dynamic load to the displacement which ensued from the same load applied statically.

3.4.2 Various Pulse Shapes

Structural response to a transient shock pulse depends primarily on the pulse shape and its duration. In general standard pulse shapes have been used to represent impact and blast loads. A half sine or a symmetrical triangle pulse shape would simulate an impact load while a pulse with a vertical rise ($\kappa = 0$) and constant or exponential decay would be an example of a blast loading.

Transient loads when applied to structures excite a frequency range $0 \rightarrow f_c$ where f_c is the cut off frequency above which there is not enough energy to cause vibration. The frequency spectra of such loads are periodic with a maximum amplitude at 0 Hz and decaying amplitude with almost zero load at equal frequency intervals the size of which depends on the pulse shape (c.f. Fig. 3.3 for a symmetric triangular pulse shape). Table 3.4 contains the zero load frequency interval of the frequency spectra for some of the standard pulse shapes.

PULSE SHAPE	ZERO-LOAD FREQUENCY INTERVAL
Symmetric triangular	$2/t_d$
Half sine	$1.5/t_d$
Rectangular	$1/t_d$

TABLE 3.4 — *ZERO LOAD FREQUENCY INTERVALS OF THE FREQUENCY SPECTRA FOR A SAMPLE OF STANDARD PULSE SHAPES*

From the above table it can be concluded that the cut off frequency depends on both the pulse shape and its overall duration time (t_d).

Step functions with a constant front are often used to represent dynamic loads with the ramping time as the factor controlling the width of the excited frequency range. A wide variety of pulse shapes together with their shock spectra for a SDOF oscillator can be found in Ref. (40).

3.4.3 The Discrete Fourier Transform (DFT)

Fourier transform is used in moving an independent variable of a signal **x(t)** from the time domain to the frequency domain. As a result of the transform no data is lost or added.

For a discrete periodic time signal with N samples, equally spaced in a period T, its DFT can be computed by

$$X_k = \frac{1}{N}\sum_{r=0}^{N-1}\left[x_r\, e^{-i(2\pi kr/N)}\right] \quad ; k = 0, 1, 2, \ldots\ldots, (N-1) \quad \ldots\ldots\ldots\ldots \quad (3.14)$$

It is possible to reconstruct the original time signal by an inverse discrete Fourier transform (IDFT) as follows :

$$x_r = \sum_{r=0}^{N-1}\left[X_k\, e^{i(2\pi kr/N)}\right] \quad ; r = 0, 1, 2, \ldots\ldots, (N-1) \quad \ldots\ldots\ldots\ldots\ldots\ldots \quad (3.15)$$

The fast Fourier transform (FFT) is an efficient algorithm used to compute the DFT of a block of sampled data. The technique takes advantage of the periodicity of the weighting function $e^{i(2\pi kr/N)}$ thus reducing the number of multiplication operations, required for an FFT algorithm with radix 2, from N^2 to $N \times \mathrm{Log}_2 N$. Consequently higher accuracy is achieved because of the lower round off errors due to fewer computer operations.

According to Shanon's sampling theorem [41] for a band limited signal with the highest frequency ω_N, the sampling frequency ω_s should be at least twice the highest signal frequency of interest which is represented mathematically as follows :

$$\omega_s = 2\alpha\omega_N \quad \ldots\ldots\ldots\ldots\ldots\ldots\ldots\ldots\ldots\ldots\ldots\ldots\ldots\ldots\ldots\ldots\ldots\ldots \quad (3.16)$$

where $\alpha \geq 1$;

ω_N represents the Nyquist frequency (maximum frequency of interest); and,

ω_s represents the sampling frequency.

The resulting frequency spectrum $X(\omega)$ (DFT of a time signal **x(t)**) would have a frequency range $0 \rightarrow \omega_N$ and a resolution $\Delta\omega$ where

$$\Delta\omega = 2\pi/T \qquad \text{(3.17)}$$

Pitfalls of the DFT (e.g. aliasing, leakage, wrap round error, picket fence effect) together with ways of minimising their effect or avoiding such errors, are discussed elsewhere [41,42] .

A modified version of the DFT subprogram listed in Ref. (43) (in FORTRAN 77 programming language) was mounted on the main frame. The program took in a block of real data representing a time domain signal and yielded the DFT in magnitude and phase format. Other formats such as root mean square (RMS), power (PWR), power spectral density (PSD) or energy spectral density (ESD) were also possible to produce. The second half of the output data was discarded because of aliasing defects and only the first half was considered as being valid.

3.4.4 Stability Examination of Numerical Integration Schemes

Transient response analysis is carried out by solving the set of second order differential Eqns in (3.1) taking damping and inertia forces into consideration.

In LUSAS the transient response analysis is performed by numerically integrating the time domain and with the assumption of some variation of displacements and velocities during small time intervals the set of second order differential equations are transformed into a set of simultaneous equations. Knowing the initial conditions at a time t the simultaneous equations are solved to obtain the displacements after a small time interval Δt. Two different recurrence schemes are implemented in LUSAS [19] as follows :

1. The three–point recurrence scheme

$$\begin{aligned}
&\left([M] + \gamma\Delta t[C]\right)\{\delta_{t+\Delta t}\} \\
&+ \left(-2[M] + (1 - 2\gamma)\Delta t[C] + \left(\tfrac{1}{2} - 2\beta + \gamma\right)\Delta t^2[K]\right)\{\delta_t\} \\
&+ \left([M] - (1 - \gamma)\Delta t[C] + \left(\tfrac{1}{2} + \beta - \gamma\right)\Delta t^2[K]\right)\{\delta_{t-\Delta t}\} \\
&= \Delta t^2\left(\beta\{P_{t+\Delta t}\} + \left(\tfrac{1}{2} - 2\beta + \gamma\right)\{P_t\} + \left(\tfrac{1}{2} + \beta - \gamma\right)\{P_{t-\Delta t}\}\right) \qquad \text{(3.18)}
\end{aligned}$$

where $\{\delta_t\}$ represents the displacement vector at time t ;

$\{P_t\}$ represents the external load vector at time t ; and,

β, γ represent the time integration constants.

2. The four–point recurrence scheme

$$\begin{aligned}
&\left([M](\gamma-1) + (\tfrac{1}{2}\beta - \gamma + \tfrac{1}{3})\Delta t[C] + (\tfrac{1}{6}\alpha - \tfrac{1}{2}\beta + \tfrac{1}{3}\gamma)\Delta t^2[K]\right)\{\delta_{t+\Delta t}\} \\
&+ \left((-3\gamma+4)[M] + (-\tfrac{3}{2}\beta + 4\gamma - \tfrac{3}{2})\Delta t[C] + (-\tfrac{1}{2}\alpha + 2\beta - \tfrac{3}{2}\gamma)\Delta t^2[K]\right)\{\delta_t\} \\
&+ \left((3\gamma-5)[M] + (\tfrac{3}{2}\beta - 5\gamma + 3)\Delta t[C] + (\tfrac{1}{2}\alpha - \tfrac{5}{2}\beta + 3\gamma)\Delta t^2[K]\right)\{\delta_{t-\Delta t}\} \\
&+ \left((-\gamma+2)[M] + (-\tfrac{1}{2}\beta + 2\gamma - \tfrac{11}{6})\Delta t[C] + (-\tfrac{1}{6}\alpha + \beta - \tfrac{11}{6}\gamma + 1)\Delta t^2[K]\right)\{\delta_{t-2\Delta t}\} \\
&= \left((\tfrac{1}{6}\alpha - \tfrac{1}{2}\beta - \tfrac{1}{3}\gamma)\{P_{t+\Delta t}\} + (-\tfrac{1}{2}\alpha + 2\beta - \tfrac{3}{2}\gamma)\{P_t\} + (\tfrac{1}{2}\alpha - \tfrac{5}{2}\beta + 3\gamma)\{P_{t-\Delta t}\}\right. \\
&\left. + (-\tfrac{1}{6}\alpha + \beta - \tfrac{11}{6} + 1)\{P_{t-2\Delta t}\}\right)\Delta t^2 \qquad \text{(3.19)}
\end{aligned}$$

where α, β, γ represent the time integration constants.

To start the three–point integration scheme the following equation would be used :

$$\begin{aligned}
&\left([M] + \beta\Delta t^2[K]\right)\{\delta_{\Delta t}\} = \left([M] - (\tfrac{1}{2} - \beta)\Delta t^2[K]\right)\{\delta_o\} \\
&+ \left(\Delta t[M] - (\tfrac{1}{2} - \beta)\Delta t^2[C]\right)\{\dot{\delta}_o\} \\
&+ \left((\tfrac{1}{2} - \beta)\Delta t^2\right)\{P_o\} + \left(\beta\Delta t^2\right)\{P_{\Delta t}\} \qquad \text{(3.20)}
\end{aligned}$$

where $\{\delta_o\}$ represents the vector of initial displacements computed from an initial linear analysis using [K] and $\{P_o\}$; and,

$\{\dot{\delta}_o\}$ represents the vector of initial velocities supplied by the analyst.

To initialise the four–point integration scheme the same equation is employed succeeded by a three–point integration scheme to calculate the displacements $\{\delta_{2\Delta t}\}$.

An explicit integration method is a numerical integration procedure which solves for $\{\delta_{t+\Delta t}\}$ by using the equilibrium conditions at a time t while an implicit integration method uses the equilibrium conditions at time $t+\Delta t$.

A temporal operator can be described as unconditionally stable if the solution for any initial conditions does not grow without bound for any $\Delta t/T_m$ ratio (where T_m represents the natural period of the highest natural frequency of interest f_m) but if there exists a certain limiting value for $\Delta t/T_m$ below which the solution does not grow without bound then the numerical integration procedure can be characterised by being conditionally stable.

Unconditionally stable implicit temporal operators suffer from two main errors,

i. period elongation causing frequency distortions; and,

ii. amplitude decay causing an increase in damping.

Amplitude decay is sometimes favourable to damp out any spurious participation of higher modes.

Earlier studies were carried out to investigate the stability and accuracy of numerical integration procedures for linear and non–linear dynamic response problems [17,44-48] . Various temporal operators are obtained when assuming different time integration constants for Eqns (3.18) and (3.19). Table 3.5 summarises the characteristics of such temporal operators.

TEMPORAL OPERATOR	INTEGRATION SCHEME	TIME INTEGRATION CONSTANTS			INTEGRATION METHOD	STABILITY §	PERIOD ELONGATION	AMPLITUDE DECAY	Δt_{cr}
		α	β	γ					
Central difference	Three—point	_____	0	1/2	Explicit	conditionally stable	—	—	$2/\omega_{max}$
Newmark	Three—point	_____	1/4	1/2	Implicit	unconditionally stable	yes	no	_____
Houbolt	Four—point	27	9	3	Implicit	unconditionally stable	yes	yes	_____
Wilson—θ	Four—point	2028/125	457/75	12/5	Implicit	unconditionally stable	yes	yes	_____
Galerkin higher order	Four—point	702/35	36/5	13/5	Implicit	conditionally stable	yes	yes	$(\pi/50)\omega_{max}$
Hilber—Hughes—Taylor	Four—point	22777/2000	917/200	2	Implicit	unconditionally stable	yes	yes	_____

TABLE 3.5 — *CHARACTERISTICS OF DIFFERENT TEMPORAL OPERATORS*

It is apparent that for the central difference numerical integration procedure to achieve stability the time step (Δt) should be less than a critical value Δt_{cr}. Another observation is that if damping is neglected ([C] = [0]) and the [M] is diagonal the central difference procedure becomes more economical as it requires less matrices manipulation but a small time step would still be necessary for a solution stability.

§ The general stability conditions for three and four—point integration schemes are stated in Appendix E together with their application on the tabulated temporal operators.

The choice of a temporal operator is guided by accuracy and economy, and because of the availability of a large number of conditionally and unconditionally stable numerical integration procedures in LUSAS tests were performed on some procedures to check their characteristics. Choice was made of unconditionally stable procedures (as described in the user manual [18]) only because of their economy, and time steps used for each solution procedure are listed in Table 3.6.

TEMPORAL OPERATOR	Δt_1 (ms)	$T_m/\Delta t_1$	$T_c/\Delta t_1$	Δt_2 (ms)	$T_m/\Delta t_2$	$T_c/\Delta t_2$
Newmark	0.6250	5.8	2	1.250	2.9	1
Houbolt	0.3125	11.5	4	0.625	5.8	2
Wilson–θ	0.3125	11.5	4	0.625	5.8	2
Galerkin higher order	0.3125	11.5	4	0.625	5.8	2
Hilber–Hughes–Taylor	0.6250	5.8	2	1.250	2.9	1

TABLE 3.6 — *TIME STEPS USED FOR DIFFERENT TEMPORAL OPERATORS*

Different ratios of $\Delta t/T_m$ and $\Delta t/T_c$ were used in the investigations where T_m is the periodic time of the highest natural frequency of interest, f_m, and T_c is the periodic time of the cut off frequency, f_c, above which there is not enough energy to cause structural vibration.

A dynamic force was applied at a point 60° away from apex normal to the surface, having a symmetrical triangle pulse shape with a maximum magnitude of 30 N and a duration time (t_d) of 2.5 ms. Graphic representation of the force–time history and the initial part of its energy spectral density (ESD) are shown in Fig. 3.3. The ESD was computed using the DFT program mentioned earlier, taking in 8192 samples (N) representing a time domain data block of 2.56 s length (T) and yielding 4096 frequency elements (N/2), approximately 0.4 Hz (Δf) apart.

The four point integration schemes (Houbolt, Wilson–θ, Galerkin and Hilber–Hughes–Taylor) were started up using a Newmark temporal for the first three time steps ($t = 0, \Delta t, 2\Delta t$).

The investigation results are presented in Figs 3.4 → 3.8. Dynamic displacements were normalised by their static correspondents resulting from a static force with a magnitude equal to the maximum value of the force–time pulse, while time was divided by the largest natural period of the mesh (T_1 = 1/73.4 s). For the current investigation T_m = 1/278 s and T_c = 1/800 s.

Fig. 3.4 shows that doubling the size of the time step for the Newmark procedure does not seriously affect the shape of the structural response or the peak to peak magnitudes. There is no amplitude decay but an increase in the period length when using Δt_2 can be noticed towards the

end of the signal due to the accumulation of the period elongation error. Therefore it can be assumed that decreasing the time step size will not change the general shape of the structural response or the peak to peak magnitudes and that the Newmark results are exact.

Observing Figs 3.5 → 3.8 for the Houbolt, Wilson–θ, Galerkin higher and Hilber–Hughes–Taylor numerical integration procedures respectively, it is noted that the peak to peak magnitudes decrease as the time step size decreased. Nevertheless agreement between both results (Δt_1 and Δt_2) was possible for some procedures (Houbolt) as the time record increased since the solution with Δt_2 suffered from a higher amplitude decay error than that when using Δt_1.

The Galerkin solution presented in Fig. 3.7 was unstable because the required stability conditions were not satisfied (vide Appendix E) and this meant that in order to achieve solution stability Δt would have had to be decreased enormously, thus making the solution very expensive.

Only the Hilber–Hughes–Taylor procedure produced results, when using Δt_2, which were in good agreement with the Newmark procedure. In conclusion, the Newmark solution scheme was found to be the most accurate and economic of all the five procedures.

The dynamic response of a MDOF system is a combination of the response of single mode shapes excited by the transient load. In Figs 3.4 → 3.8 a discontinuity is apparent in the normal direction of the response and not in the meridional direction. This is an indication of the predominant influence of the axisymmetric mode which is characterised by motion normal to the surface of the structure.

To summarise, if a transient dynamic analysis is to be carried out on a finite element mesh adopt the following steps :

1. Compute the natural frequencies of the structure.
2. Determine the highest frequency component (f_c) of the dynamic load applied to the structure.
3. Establish the highest excited structural frequency (f_m).
4. Estimate the size of the time step to be used by the most accurate and economic numerical integration procedure, e.g. when adopting the Newmark procedure $\Delta t = 1/(10 f_m)$ is recommended.

3.4.5 The Frequency Response Function (FRF)

The dynamic characteristics of a linear system can be described by its FRF which is defined as follows :

$$H(\omega) = \frac{R(\omega)}{F(\omega)} \quad \text{..... (3.21)}$$

where $F(\omega)$ represents the complex frequency spectrum of the excitation;

$R(\omega)$ represents the complex frequency spectrum of the response; and,

$H(\omega)$ represents the complex FRF.

In general the FRF is the structural response to a standard excitation which is a unit amplitude sinusoidal force.

3.4.5.1 Various forms of the FRF— The structural response to an applied dynamic force may be displacement, velocity or acceleration and for a MDOF linear system the FRF may take one of the following forms :

$$\alpha_{jk}(\omega) = \frac{\delta_j(\omega)}{F_k(\omega)} \quad \text{..... (3.22)}$$

$$\gamma_{jk}(\omega) = \frac{\dot{\delta}_j(\omega)}{F_k(\omega)} \quad \text{..... (3.23)}$$

$$A_{jk}(\omega) = \frac{\ddot{\delta}_j(\omega)}{F_k(\omega)} \quad \text{..... (3.24)}$$

where $\alpha_{jk}(\omega)$ represents the receptance FRF;

$\gamma_{jk}(\omega)$ represents the mobility FRF;

$A_{jk}(\omega)$ represents the accelerance or inertance FRF; and,

j, k are subscripts denoting the response and excitation locations respectively.

Eqns (3.22), (3.23) and (3.24) are inter–related as follows :

$$\alpha_{jk}(\omega) = i\omega\, \gamma_{jk}(\omega) = -\omega^2 A_{jk}(\omega) \quad \text{..... (3.25)}$$

A **point receptance** (mobility or accelerance) [49] is an FRF obtained by exciting and measuring response at the same location and in the same direction (j = k).

A **cross point receptance** is an FRF obtained by exciting and measuring response at the same location but in different directions (j = k).

A **transfer receptance** is an FRF obtained by exciting and measuring response at different locations ($j \neq k$).

3.4.5.2 Graphic representation of the FRF— The FRF is complex and can be presented graphically in three different formats ,

i. the magnitude and phase values versus frequency (Bode plot);

ii. the real and imaginary parts versus frequency (Co–quad plot); or,

iii. the imaginary part versus the real part (Nyquist plot).

3.4.5.3 Theoretical estimation of the FRF— A dynamic force with a symmetric triangular pulse shape was applied at a point 60° away from apex having three components in the global X, Y and Z directions each with a maximum amplitude of 30 N (see Fig. 3.9). In order to obtain a convenient value for the frequency spacing the pulse duration was chosen as $16 \times 0.12208 = 1.95328$ ms and the time step Δt used in the analysis was 0.12208 ms. Graphic representation of the resultant pulse shape accompanied by its ESD can be seen in Fig. 3.10. The resulting transform had 8192 frequency elements (N/2), 0.5 Hz (Δf) apart giving a frequency base band up to 4096 Hz.

The three force components constituted an asymmetric resultant thus enabling the excitation of all structural frequencies within the considered frequency band $0.0 \rightarrow 1024$ Hz.

The structural response was computed using the Newmark numerical integration scheme for the first 1896 time steps (consuming over 300 hours of CPU time). Dynamic response in the form of translation and rotation under the dynamic point load are plotted in Fig. 3.11. The response of only one loof point rotation (see Fig. 2.8) was presented because the results for both loof points were almost equal.

It is observed that there is no decay in the amplitude of the structural response when the structure is in a free vibration state since damping was neglected. An exponential weighting function with a time constant τ_w of 30 ms was applied to the time history signals in order to decrease its amplitude gradually to zero (see Fig. 3.12) to avoid leakage errors when discrete Fourier transformed.

As the earlier mentioned DFT subprogram was based on a radix two FFT a block of time domain data containing 16384 (2^{14}) elements was formed by zero filling the rest of the sequence (the first part containing one element for the initial conditions and 1896 elements computed by LUSAS). The zero elements had no contribution in the DFT summation and the transform had the following characteristics :

$$T = (16384 - 1) \times 0.12208 \times 10^{-3} \approx 2 \text{ s}$$

$$f_N = 0.5 \times (16384/2) = 4096 \text{ Hz}$$

$$\Delta f \approx 1/2 \approx 0.5 \text{ Hz}$$

Though the DFT permitted the analysis of a frequency band $0 \rightarrow 4096$ Hz the dynamic force applied excited a frequency range $0 \rightarrow 1024$ Hz and the time step Δt used for numerical integration was sufficient only for such a span.

A different version of the DFT subprogram was prepared to take in the force and response data sequences and generate the FRF. Cross point receptances were computed and are depicted in Fig. 3.13.

Taking a frequency response peak as the criterion for the occurrence of a natural mode, the period elongation error was calculated for the excited modes relative to the free vibration results determined using the subspace iteration method (see Table 3.1). The results are listed in Table 3.7.

MODE NUMBER	PERIOD ELONGATION ERROR (%)
1	3.3
2	3.3
3	1.0
4	0.9

TABLE 3.7 — *PERIOD ELONGATION ERROR FOR THE FIRST FOUR MODES*

It can be concluded that the size of the time step Δt employed in the current analysis was acceptable as it caused very small period elongation errors.

3.4.5.4 Applications— Recalling Eqn (3.21) it is obvious that with the knowledge of any two parameters the third can be computed , e.g.

i. if $F(\omega)$ and $R(\omega)$ are known, $H(\omega)$ can be derived;

ii. if $F(\omega)$ and $H(\omega)$ are known, $R(\omega)$ can be derived; and,

iii. if $H(\omega)$ and $R(\omega)$ are known, $F(\omega)$ can be derived.

In the previous subsection the first case has been presented by the calculation of the cross point receptances and in the following two subsections the second case will be applied to calculate the shock spectra for the Echinodome with the knowledge of the FRF and force spectrum.

3.4.6 Shock Response Spectra

Different forms of the maximum shock response spectrum have been defined earlier and there are two approaches to calculate such a spectrum :

1. A direct method is to apply a dynamic pulse with a known shape and duration, compute its corresponding transient response and then estimate the maximum initial, maximum residual and maximax response values. The process will need to be repeated several times until a specific range of pulse durations has been investigated.

2. An alternative method is to apply a dynamic pulse of any shape with a very short duration in order to excite a wide frequency band. With the knowledge of the dynamic force and transient response histories the FRF can be computed from the corresponding spectra through Eqn (3.21). The FRF is then used to calculate the transient response to any dynamic pulse with any duration on the condition that the excited frequency band does not exceed that used in the calculation of the FRF.

Though the first procedure is simple it is inefficient and uneconomic and as a result the second approach was used in the following analysis. A program called SRSTRA was prepared to calculate the shock response spectra of a number of dynamic pulses, e.g. full versed sine, half sine, rectangular, triangular symmetric and asymmetric shapes. A flow chart of the program is depicted in Fig. 3.14. The program takes in force ($F(t)$) and response ($\delta(t)$) histories as well as an indicator for the pulse shape. The transient response is weighted by an exponential window (e^{-t/τ_w}) to dampen the signal's amplitude to zero before the end of the time period (T) considered. The FRF is computed after the calculation of the DFT of both the force ($F(\omega)$) and transient response

($\delta(\omega)$). In the next stage the program enters a loop to perform the following steps for pulses with different durations :

1. Generate a dynamic pulse $F_g(t)$ with a certain duration (t_d) and discrete Fourier transform it ($F_g(\omega)$).
2. Calculate the transient dynamic response ($\delta_g(\omega)$) and inverse discrete Fourier transform it ($\delta_g(t)$).
3. Estimate the maximum initial (MAXI), maximum residual (MAXR) and maximax response (MAXM).
4. Normalise each of the above peak dynamic responses by a static response value δ_s resulting from a static force with a magnitude equal to the maximum value of the dynamic force–time pulse to obtain MXIN, MXRN and MXMN.

The number of times the loop is entered depends on the range of pulse durations of interest.

It is worth noting that by not compensating in the results for the exponential weighting function assisted in simulating damping which has been neglected throughout the current analysis and would exist for real structures.

3.4.6.1 Comparison of shock response spectra for a sample of symmetrical pulses— The shock response spectra for a set of five symmetrical dynamic pulses were computed using the above mentioned program. The pulses were selected on the basis of equal pulse area (or equal impulse) resulting in different maximum amplitudes for the various pulse shapes (see Fig. 3.15). The previously derived cross point receptances were utilised in the calculation of the maximum initial, maximum residual and maximax shock response spectra for each of the transient forces.

In Figs 3.16 → 3.20 the maximum dynamic response was normalised by the displacement which ensued from the application of a static load with a magnitude equal to the maximum amplitude of the corresponding force–time pulse. While response in Figs 3.21(a → d) and 3.22(a → d) was normalised by the displacement resulting from the application of a static force having a magnitude equal to the maximum amplitude of the FVS, RCT2 and TRG pulses. In Figs 3.16 → 3.20, due to the normalisation carried out, the Y—axis represented the DLF and from those figures the following deductions were made :

1. For all five pulses considered the meridional and normal dynamic load factors were the maximum and minimum of a DLF range respectively whilst circumferential and edge rotation dynamic load factors were approximately equal and in between both extremes of the range.

2. Any of the five transient forces possessing a time duration (τ_d) greater than 0.5 resulted in a maximum response equal to the maximum initial response.
3. As the time duration (τ_d) for FVS, HSN and TRG pulses approached the value of 4.0 the DLF tended towards the value of 1.0 leading to the following interpretation : as the time duration of the three preceding pulses increased the dynamic displacements (translation and rotation) inclined towards their static correspondents.
4. Each directional dynamic response for rectangular pulses tended towards its own DLF, e.g. normal DLF $\rightarrow$ 1.25, meridional DLF $\rightarrow$ 2.15, circumferential DLF $\rightarrow$ 1.75 and edge rotation DLF $\rightarrow$ 1.8.

The next set of observations were made by noticing Figs 3.21(a $\rightarrow$ d) :

1. Dynamic pulses with a time duration less than 0.25 produced similar response–time histories leading to the conclusion that for such transient forces the pulse shape does not influence the dynamic structural response.
2. As the pulse durations increased the maximum response varied in magnitude and time of occurrence for different pulse shapes.
3. High frequency components of small amplitudes were evident in the dynamic response resulting from the application of RCT1 and RCT2 pulses because of the sharp rise and decay of such pulses. The preceding effect was a result of the high sampling rate and was more pronounced in the normal response–time histories than in circumferential or edge rotation responses, while in the meridional direction it was almost non–existent.

The succeeding remarks were acquired by observing Figs 3.22(a $\rightarrow$ d) :

1. The dynamic pulse RCT2 produced the maximum shock response spectra though the transient force had a time duration half that of any of the other forces.
2. Although the FVS and TRG pulses had equal time duration, maximum amplitude and impulse, their shock response spectra varied, in essence meaning that altering the pulse shape influences the dynamic structural response.
3. The maximum amplitude of a dynamic transient force is one of the parameters affecting any structural response–time history.
4. The maximum dynamic response occurs for pulses with a time duration τ_d ranging from 0.5 to 1.0 , except for RCT2 which occurs during $\tau_d = 0.25 \rightarrow 0.5$.

3.4.6.2 Comparison of shock response spectra for triangular pulses with various skewness factors— The earlier mentioned program was used again to compute the shock response spectra for a set of triangular pulses with different skewness factors. The force–time pulses had equal maximum amplitude, time duration and pulse area, the only varying parameter was the skewness factor (see Fig. 3.23).

Dynamic response in Figs 3.20, and 3.24 → 3.27 was normalised by displacement caused by the static application of F_o and as a result the Y—axis represented the DLF in the latter set of figures. The undernoted remarks were drawn from Figs 3.20, 3.24 and 3.25 :

1. Circumferential and edge rotation dynamic load factors were almost equal and lay within a DLF range defined by a maximum and minimum represented by the meridional and normal dynamic load factors respectively.
2. For a TS0 pulse type as the time duration (τ_d) of the transient force increased the maximum initial response increased suggesting that as τ_d tended towards infinity the DLF would approach the value of 2.0 and might overtake it.

The following conclusions were made from Figs 3.26(a → d) :

1. Pulse shape of transient forces with time durations less than 0.25 has little influence on the dynamic peak response.
2. For larger time durations ($\tau_d > 0.25$) variation in the skewness factor resulted in an alteration of the magnitude and occurrence time of the maximum dynamic response, e.g. when considering the free vibration state for $\tau_d = 1.0$ the TS0 and TS1 transient forces generated dynamic responses which are opposite in phase and the TRG pulse produced dynamic response with a maximum occurring at the minimum dynamic responses of the TS0 and TS1 pulses. While for $\tau_d = 1.5$ the TRG pulse resulted in dynamic response opposite in phase with that of TS0 and TS1.
3. High frequency components were apparent in the response–time histories of the TS0 and TS1 pulses because of their sharp rise and decay respectively.

More remarks were possible to be drawn by noticing Figs 3.27(a → d) :

1. Except for TS0 all other triangular pulses with different skewness factors generated a DLF tending towards the value of 1.0 as τ_d approached higher values ($\tau_d \rightarrow 4.0$).
2. The maximum shock response spectrum for TSP2 was the maximum spectrum when compared with the spectra of other triangular pulses of different skewness factors, for $\tau_d > 2.0$ when considering the normal direction response and $\tau_d > 1.0$ for other directional dynamic responses.

3. In general for triangular pulses with different skewness factors the maximum dynamic response occurs for pulses having a time duration τ_d ranging from 0.5 to 1.5.

3.4.7 Step Loads

A forcing function starting instantaneously with a maximum value and staying constant is generally known as a step loading. In such a case the ramping time is considered very small when compared with the structure's natural period. In some cases dynamic step loadings take a considerable amount of time to reach a maximum constant value and as a result their effect on structures become similar to that of a static load.

The Echinodome response to step loading was studied with LUSAS using two different ramping times, $\tau_r = 0.0$ and $\tau_r = 1.5$. Three mutually perpendicular components (normal, meridional and circumferential) were applied at a point 60^o away from apex for each of the latter cases. Displacement–time histories under the point load are depicted in Fig. 3.28.

It was noticed that structural response to a step load with $\tau_r = 0.0$ was more critical than that for $\tau_r = 1.5$ and as the ramping time of the forcing function increased the structural response tended towards static response (DLF $\rightarrow$ 1.0).

When comparing the structural response of $\tau_r = 0.0$ with that of response to TS0 pulse with duration $\tau_d = 4.0$ it was found that the DLF for the former exceeded that of the latter and subsequently, it can be concluded that a step loading which reaches its maximum in a very short duration is the most severe dynamic load to be applied to the Echinodome.

3.5 DYNAMIC BUCKLING ANALYSIS

If a thin walled structure is to be subjected to a dynamic loading in real life then it is extremely important to investigate the dynamic stability of the whole structure under such loads.

In the previous section it was established that the step load was the most critical dynamic loading to be applied to the Echinodome and consequently it will be used in the current investigation.

LUSAS was used to predict the dynamic collapse buckling load of the Echinodome prototype. A dynamic buckling state was said to have been reached when LUSAS gave a warning stating that one or more of the leading diagonal terms in the stiffness matrix had become zero or negative. Although other investigators [50] employed different definitions for the dynamic buckling of a thin shell, based on describing changes in the enclosed geometrical volume, the pivot elements criterion was considered as the most representative of the structural stiffness.

The non–linearities of the problem entered the equilibrium equations through the tangential stiffness matrix and the equivalent nodal forces which were re–evaluated for each iteration within each time step. The finite element program computed the dynamic displacements for each time step by performing several iterations to achieve dynamic equilibrium, details of the solution technique can be found elsewhere [19,51] . LUSAS incorporates formulations for both geometry and material non–linearities.

For the current study the previously described finite element mesh was used assuming perfect base fixity and adopting total Langrangian formulations for geometrical non–linearity while the material properties were defined as being linear.

Two load cases were investigated, the first was for a concentrated step force acting at the apex, normal to the surface simulating an axisymmetric dynamic loading. The second was for a concentrated step force acting 60^{o} away from apex, normal to the surface representing a symmetric load case. An analysis was performed using a different time step Δt for each case, 0.375 ms for the former and 1.25 ms for the latter.

In previous work [52] it was found that artificial damping encountered when solving the equations of motion resulted in an overestimate of the dynamic buckling load and consequently a choice was made of the Newmark time integration procedure to be adopted in the current investigation as it suffers from no amplitude decay even by varying the size of time step. In addition, structural damping was ignored ([C]=0) in order to generate a conservative estimate of the dynamic collapse buckling load.

It was necessary to restrain the whole finite element model against any translation or rotation at time t = 0 in order to obtain zero response for the initial conditions because of the non–zero force at t = 0.

To establish the dynamic collapse buckling load (P_{dc}) several computer runs were performed using the trial and error concept until it was determined to the nearest 250 N according to the above mentioned criterion. Typical responses for both load cases are depicted in Fig. 3.29. The results indicate that for an axisymmetric case the ratio P_{dc}/P_{nc} was equal to 0.378 and for the symmetric case 0.833. The accompanying mode shapes are shown in Figs 3.30 and 3.31 It is worth mentioning that at such high load levels the induced stresses exceeded the ultimate strength of the material.

From the above results it was clearly indicated that the dynamic collapse buckling load was smaller in value than its static correspondent and hence more critical. Thus, if dynamic loads are to be exerted on thin walled structures in their operational life then it is a prerequisite to carry out a dynamic stability analysis preceded by a static stability analysis to determine if the designed structure can sustain such loads without experiencing serious damage or any form of instability.

The dynamic bifurcation phenomenon [53] is another form of dynamic buckling which could occur for the Echinodome shell structures and would require investigation. Due to the complexity of the Echinodome shape no attempt was made to establish such a parameter analytically and currently available software did not possess the facility for solving the involved equations numerically.

3.6 CONCLUSIONS

After studying the behaviour of the Echinodome under dynamic point loadings of various pulse shapes and time durations the following conclusions were drawn :

1. Structural response to transient loadings, with a time duration $\tau_d \geq 0.5$, reaches its maximum during the initial response phase (forced vibration state).
2. Pulse shapes, peak magnitudes and duration are all parameters which control the maximum structural response to transient loads.
3. The pulse shape effect on the peak structural response would be lost if the time duration (τ_d) decreased less than 0.25.
4. As the rise time of a dynamic load increases towards large values, when compared with the structure's periodic time, structural response tends towards static response (DLF $\rightarrow$ 1.0).
5. For triangular pulse shapes characterised by zero skewness factor, as the time duration τ_d increases the DLF tends towards a value of 2.0 (double the static response).
6. If the structure is to be subjected to dynamic point loads during its operation then it becomes necessary to carry out a dynamic buckling analysis.
7. Step loading with infinite duration and zero ramping time is the most severe dynamic load–time history to be applied to a structure and consequently, it is that type of load which is to be considered when studying structural dynamic stability.
8. The dynamic collapse buckling load is more critical than its static correspondent for the Echinodome. It is beneficial to perform a static non–linear analysis to determine if the load–deflection relationship was characterised by having a limit point (i.e. point of zero stiffness), because if such a point was non–existent, material fracture would be the most likely mode of failure.

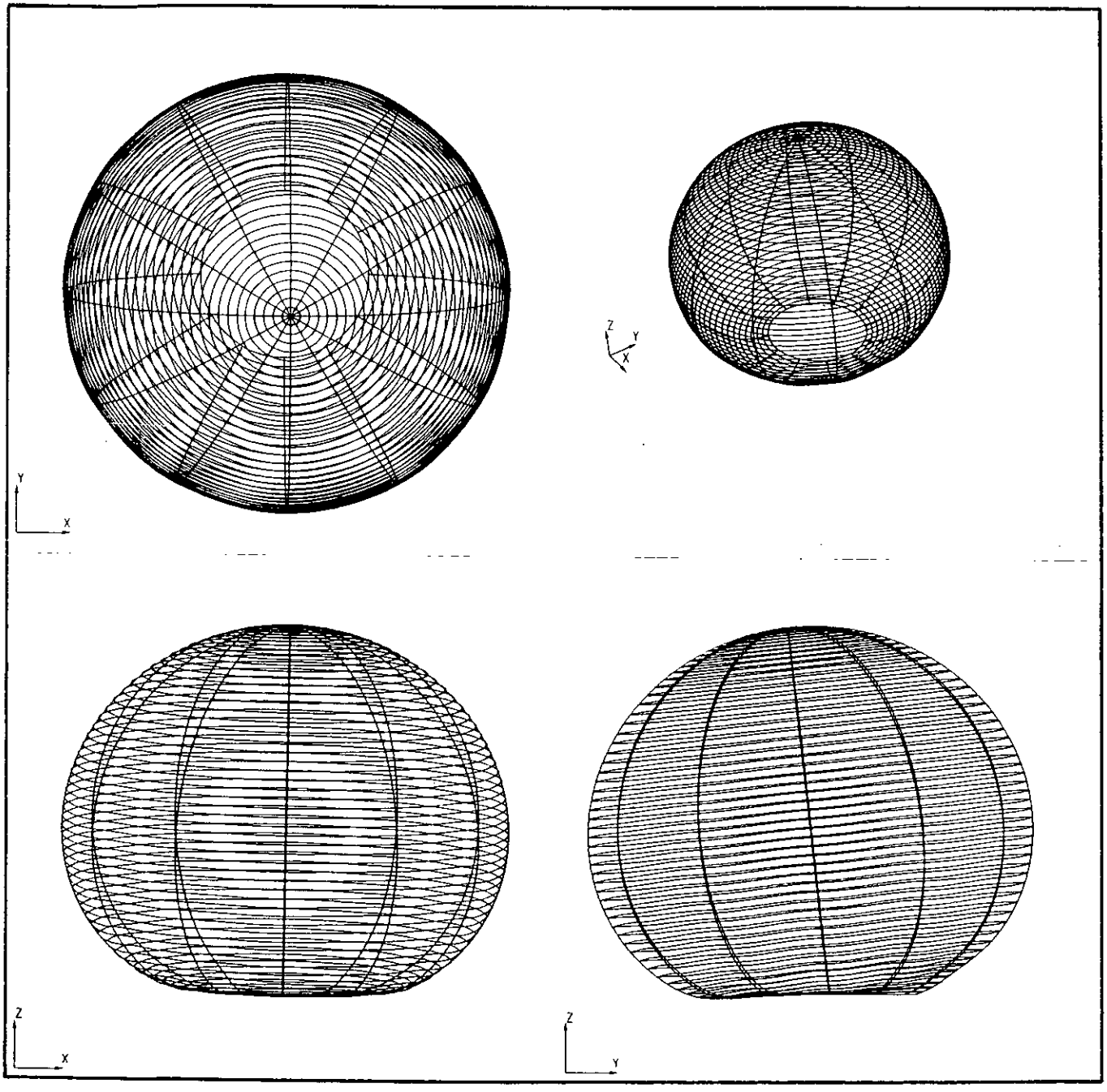

FIG. 3.1(*a*)–*VIBRATING MODE SHAPE* 1
––*FREQUENCY*=73.4 *Hz*––
FIRST SYMMETRIC MODE

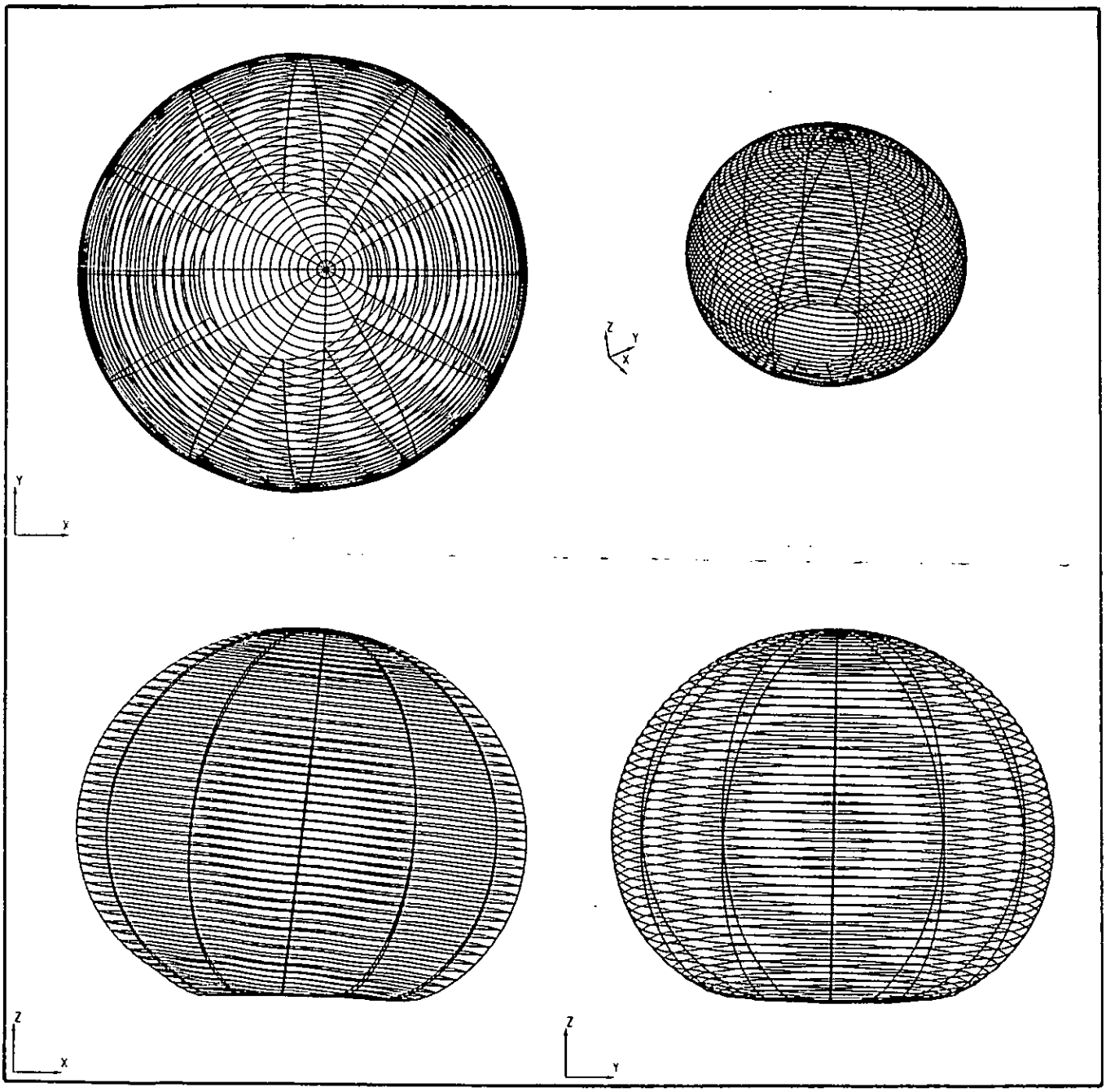

FIG. 3.1(b)–*VIBRATING MODE SHAPE 2*
––FREQUENCY=73.4 Hz––
SECOND SYMMETRIC MODE

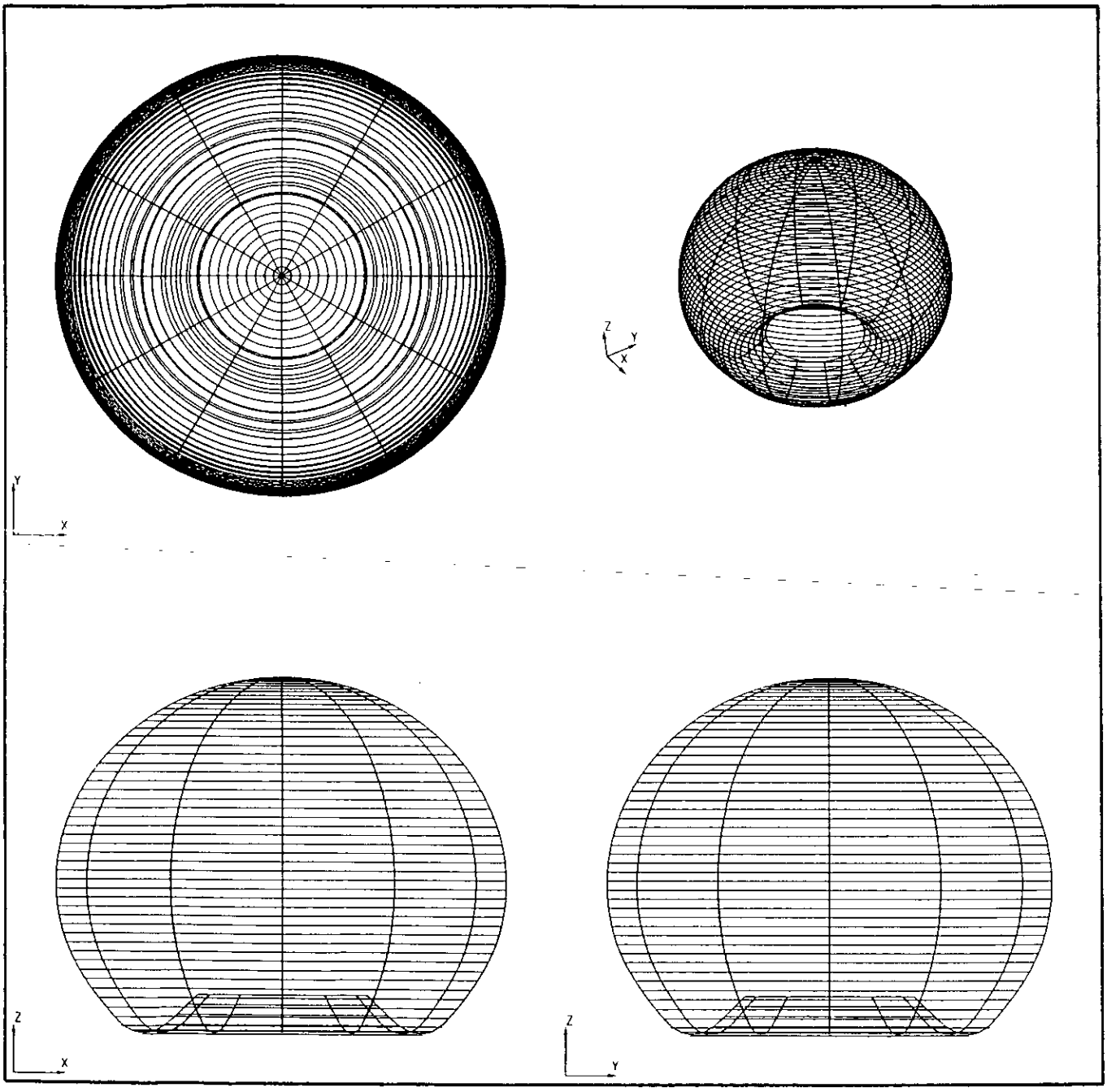

FIG. 3.1(c)–*VIBRATING MODE SHAPE* 3
––*FREQUENCY*=273.2 *Hz*––
FIRST AXISYMMETRIC MODE

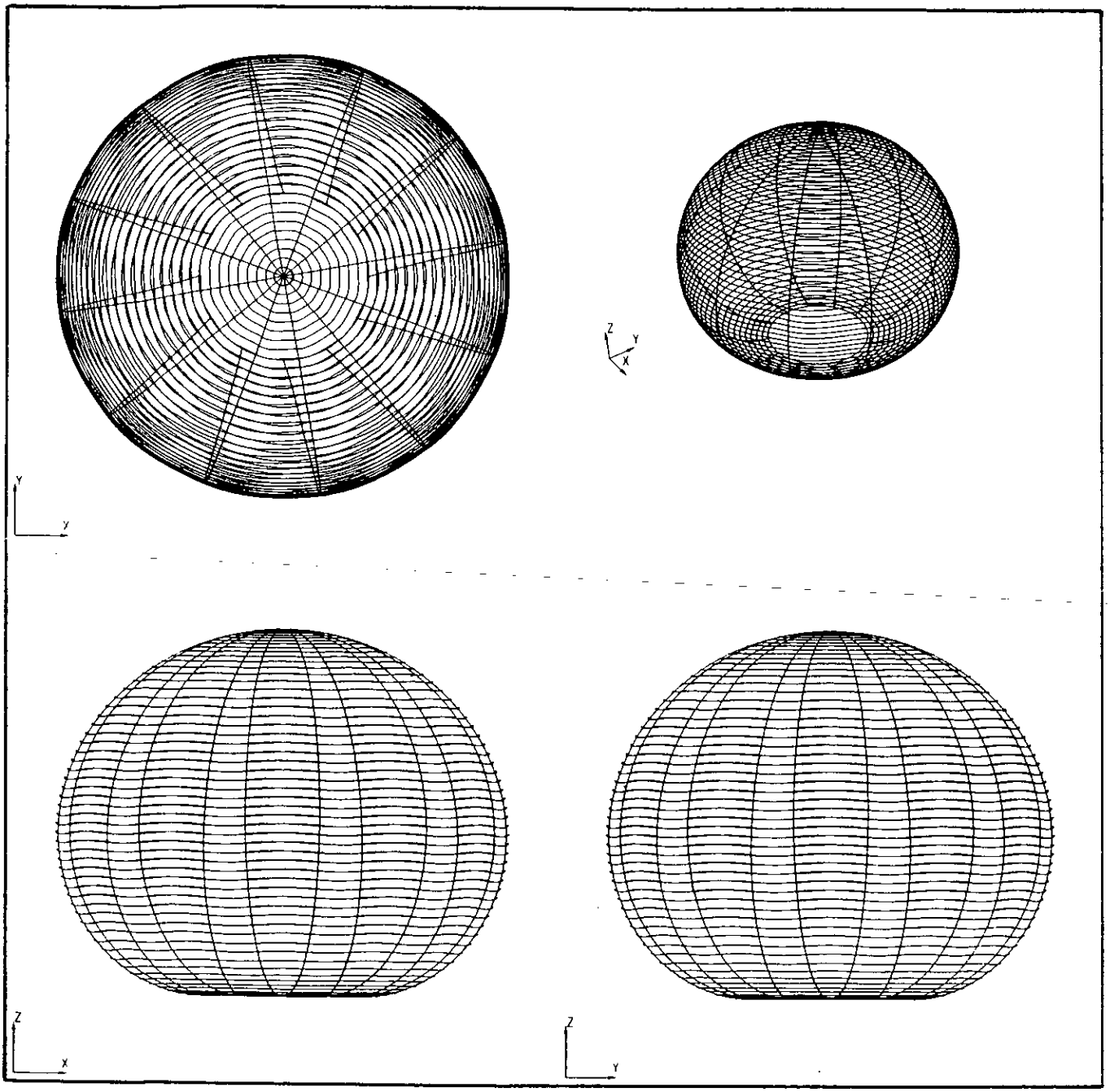

FIG. 3.1(*d*)*—VIBRATING MODE SHAPE* 4
——FREQUENCY=578.0 *Hz——*
FIRST TORSIONAL MODE

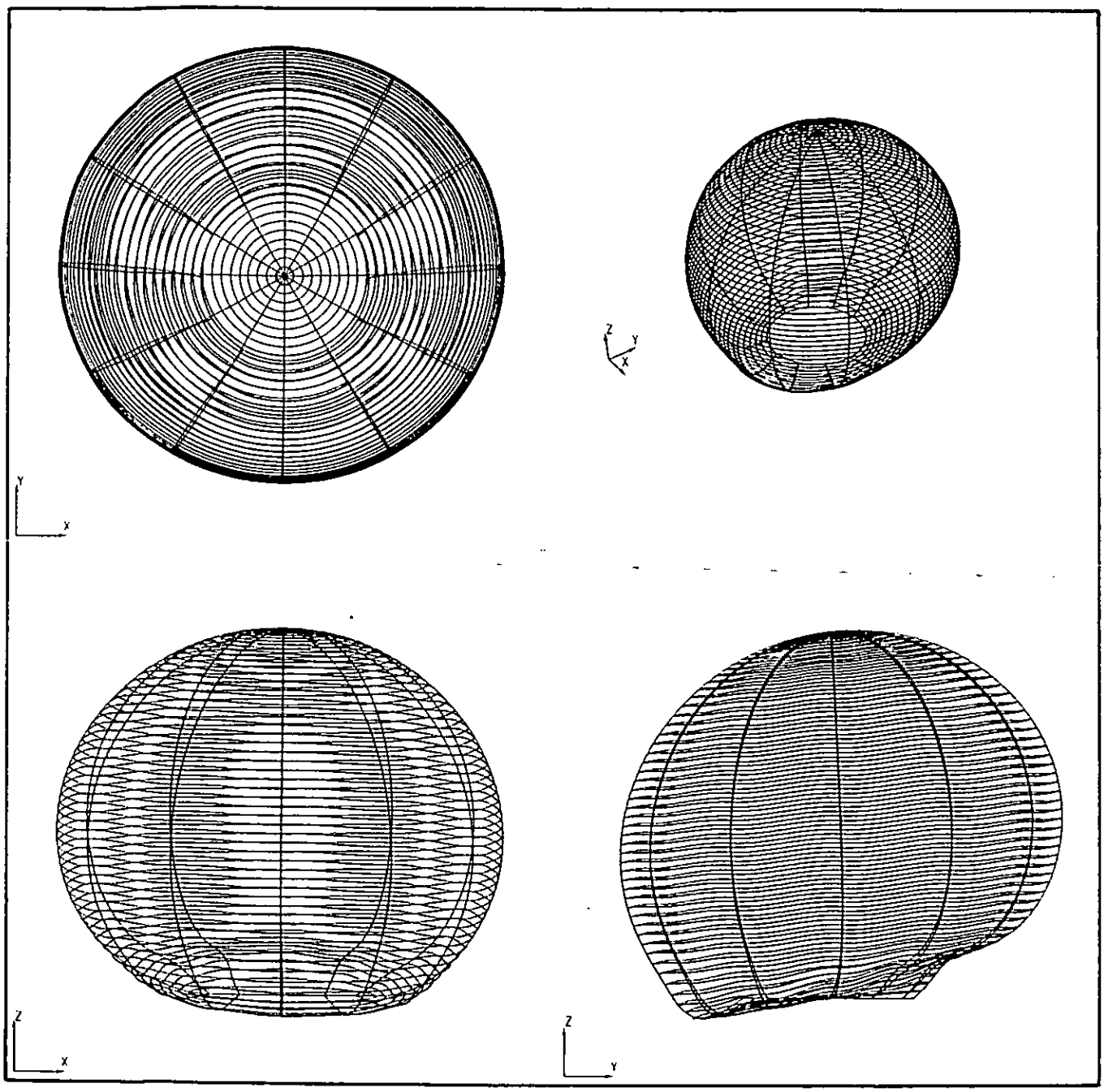

FIG. 3.1(e)–*VIBRATING MODE SHAPE* 5
––*FREQUENCY*=1036.7 *Hz*––
THIRD SYMMETRIC MODE

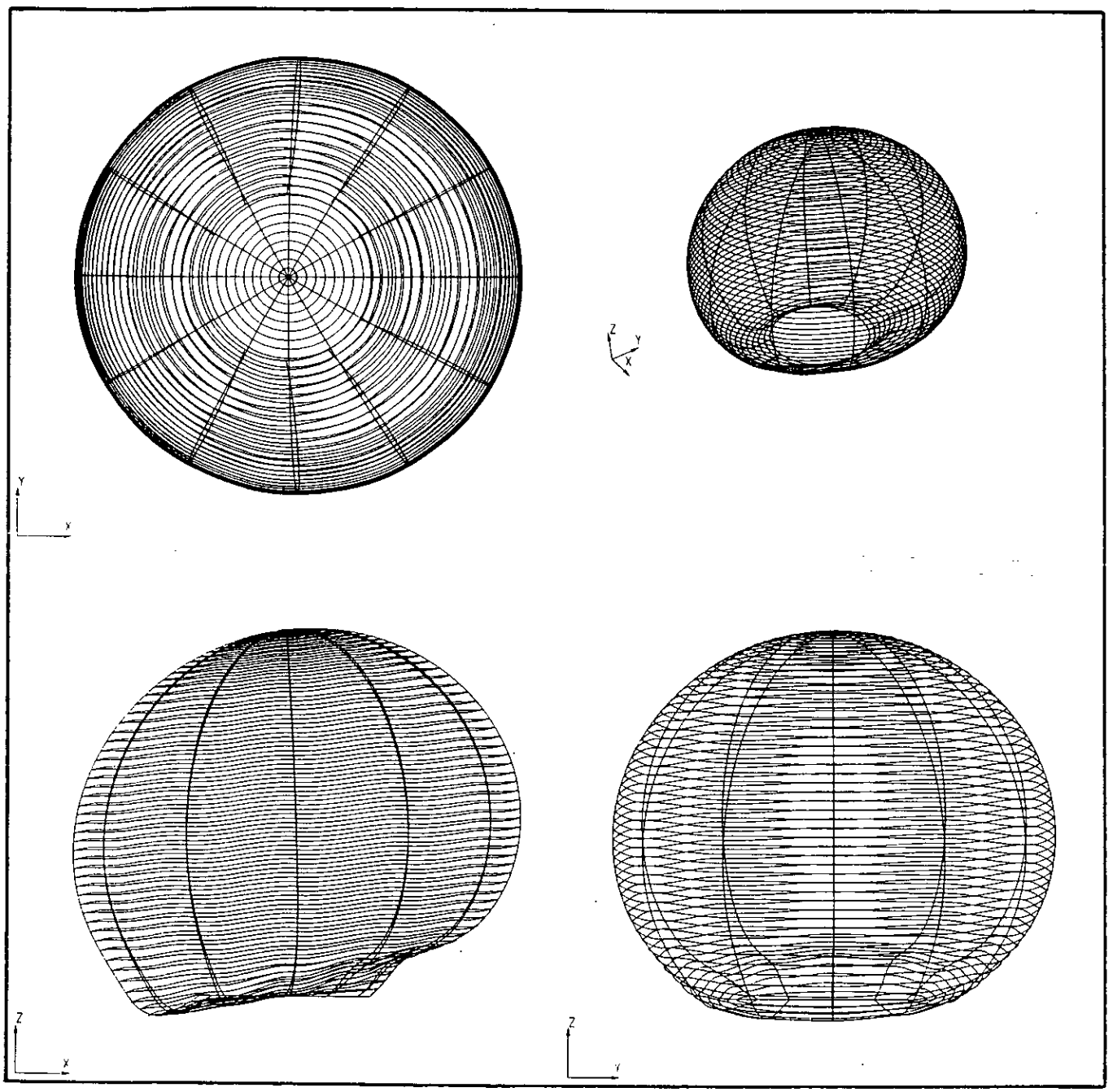

FIG. 3.1(*f*)*–VIBRATING MODE SHAPE* 6
––FREQUENCY=1036.7 *Hz––*
FOURTH SYMMETRIC MODE

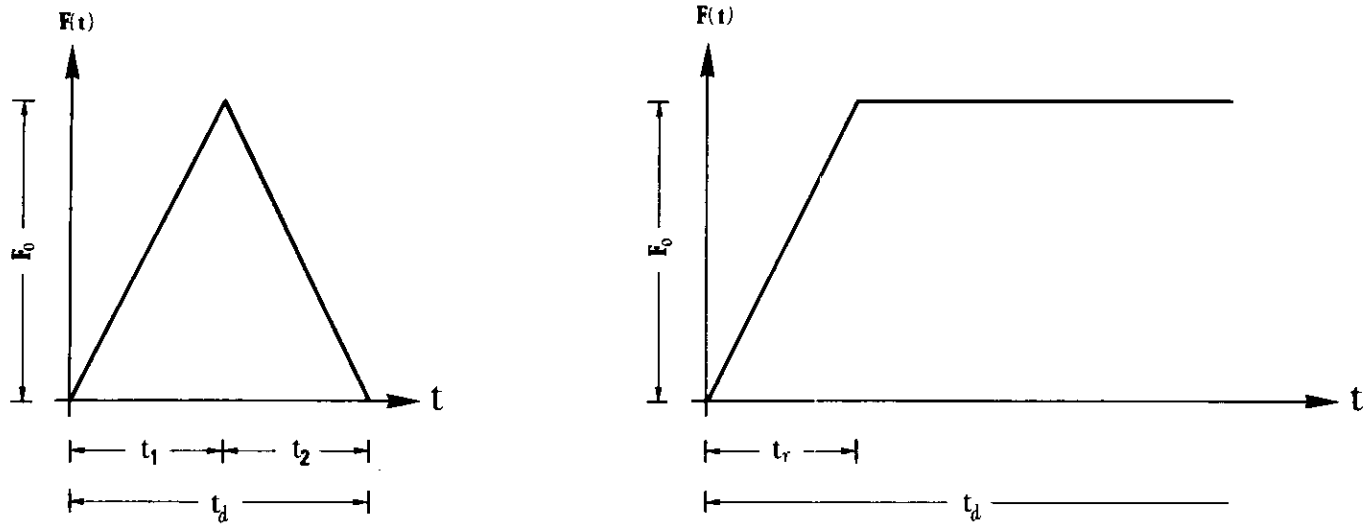

FIG. 3.2–CHARACTERISTICS OF DYNAMIC PULSE SHAPES

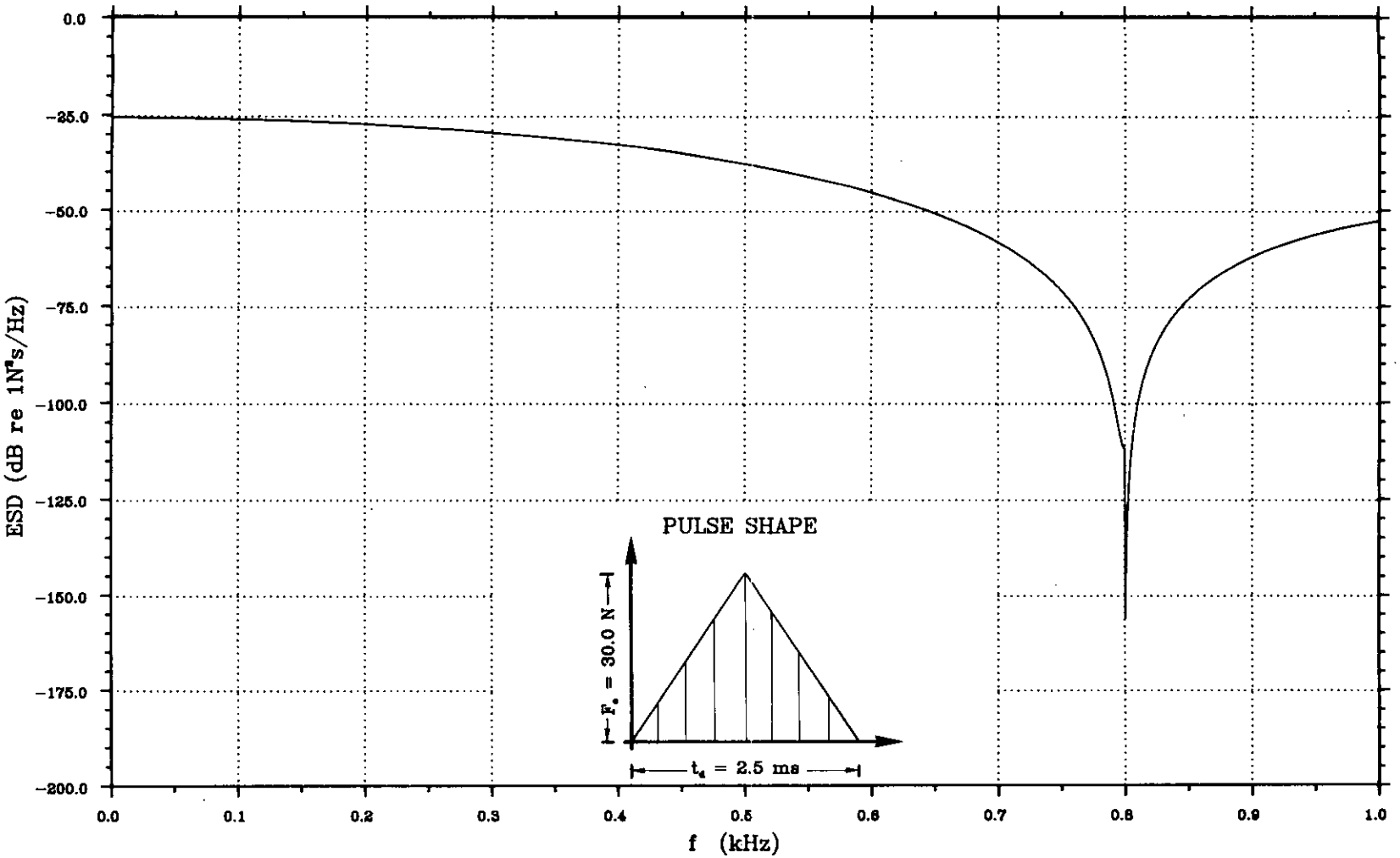

FIG. 3.3–ENERGY SPECTRAL DENSITY OF TRIANGULAR PULSE USED IN INVESTIGATING THE STABILITY OF NUMERICAL INTEGRATION SCHEMES FOR PROBLEMS OF STRUCTURAL DYNAMICS

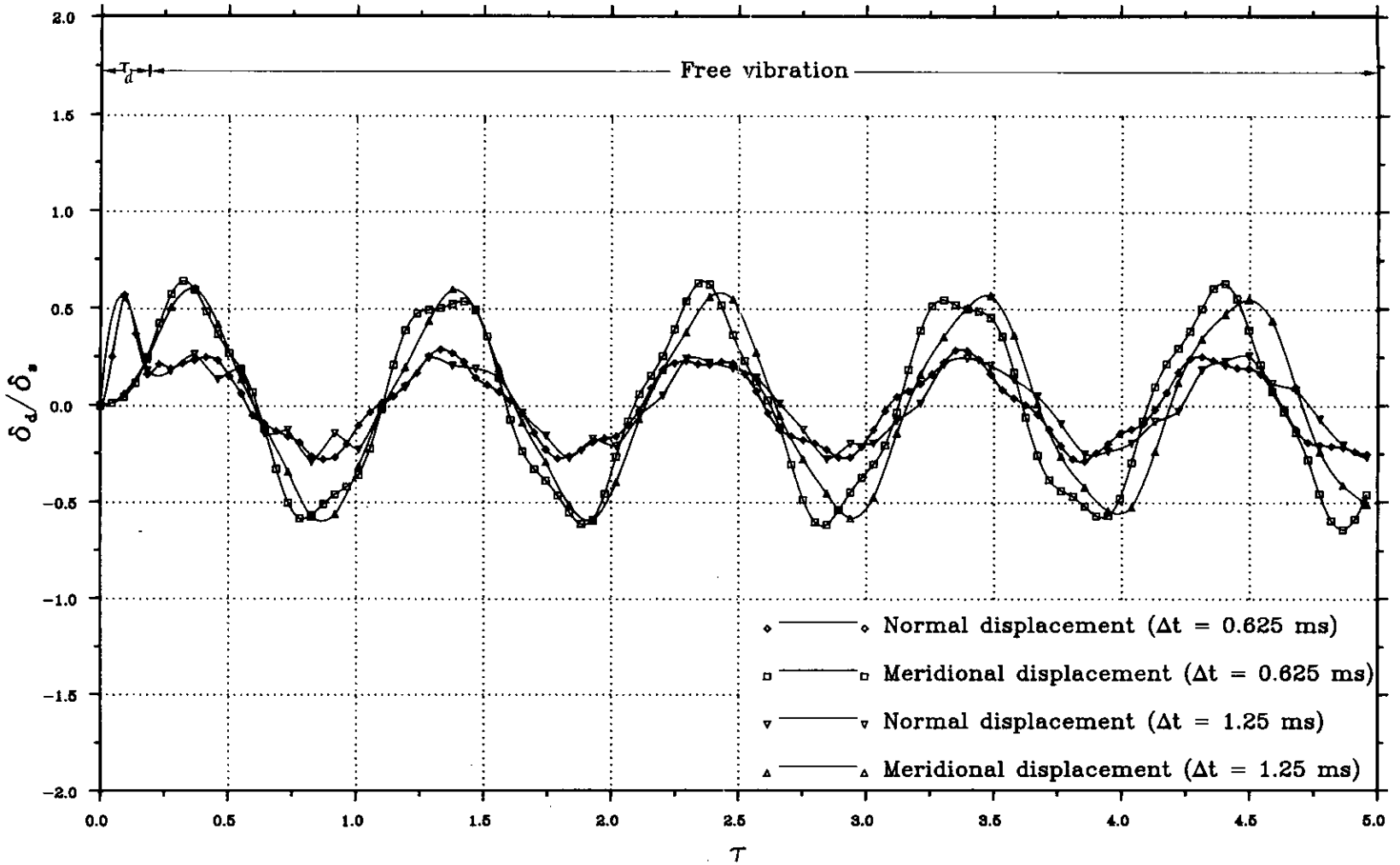

FIG. 3.4–EFFECT OF TIME INCREMENT SIZE UPON DYNAMIC RESPONSE USING THE NEWMARK INTEGRATION SCHEME

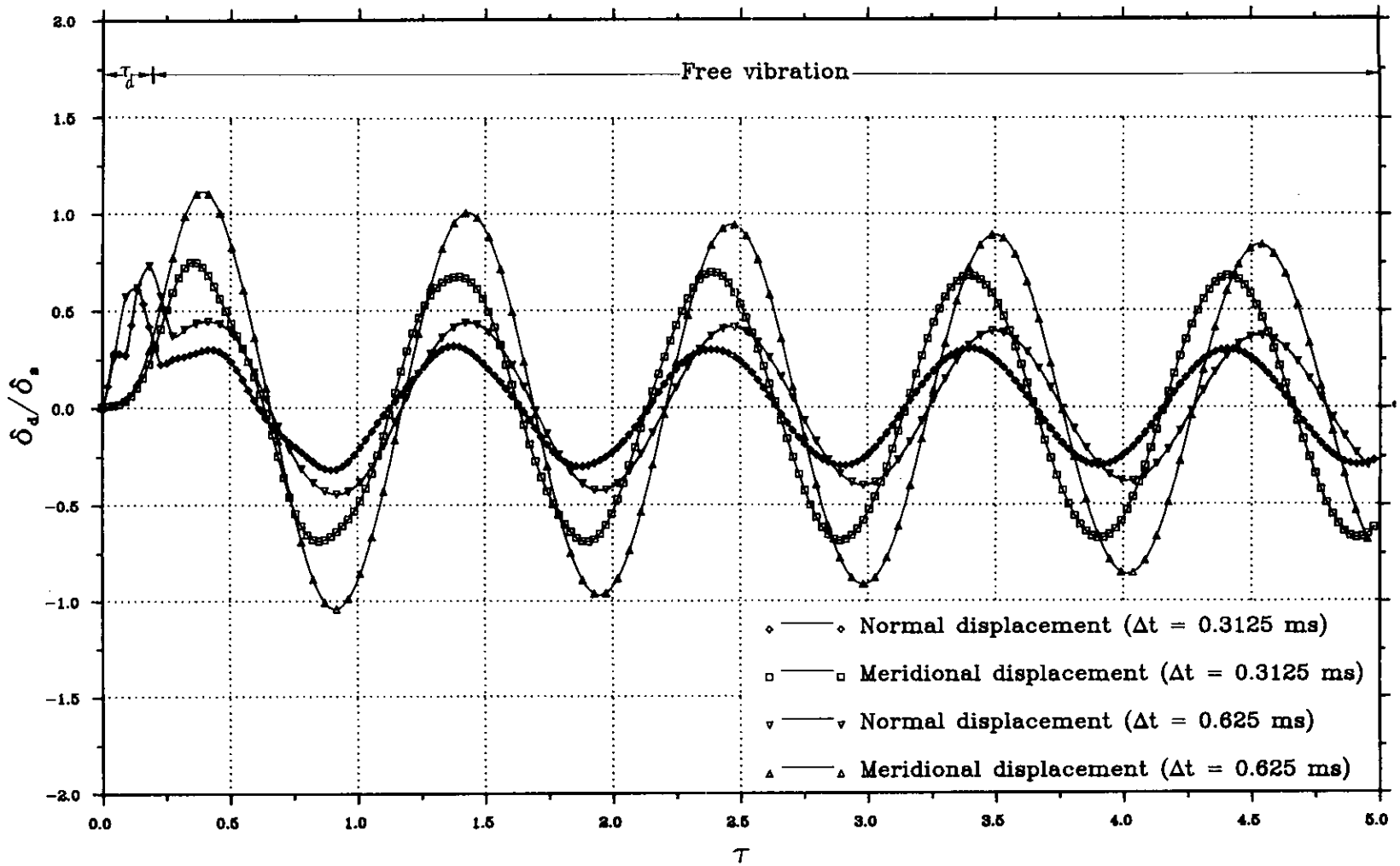

FIG. 3.5–EFFECT OF TIME INCREMENT SIZE UPON DYNAMIC RESPONSE USING THE HOUBOLT INTEGRATION SCHEME

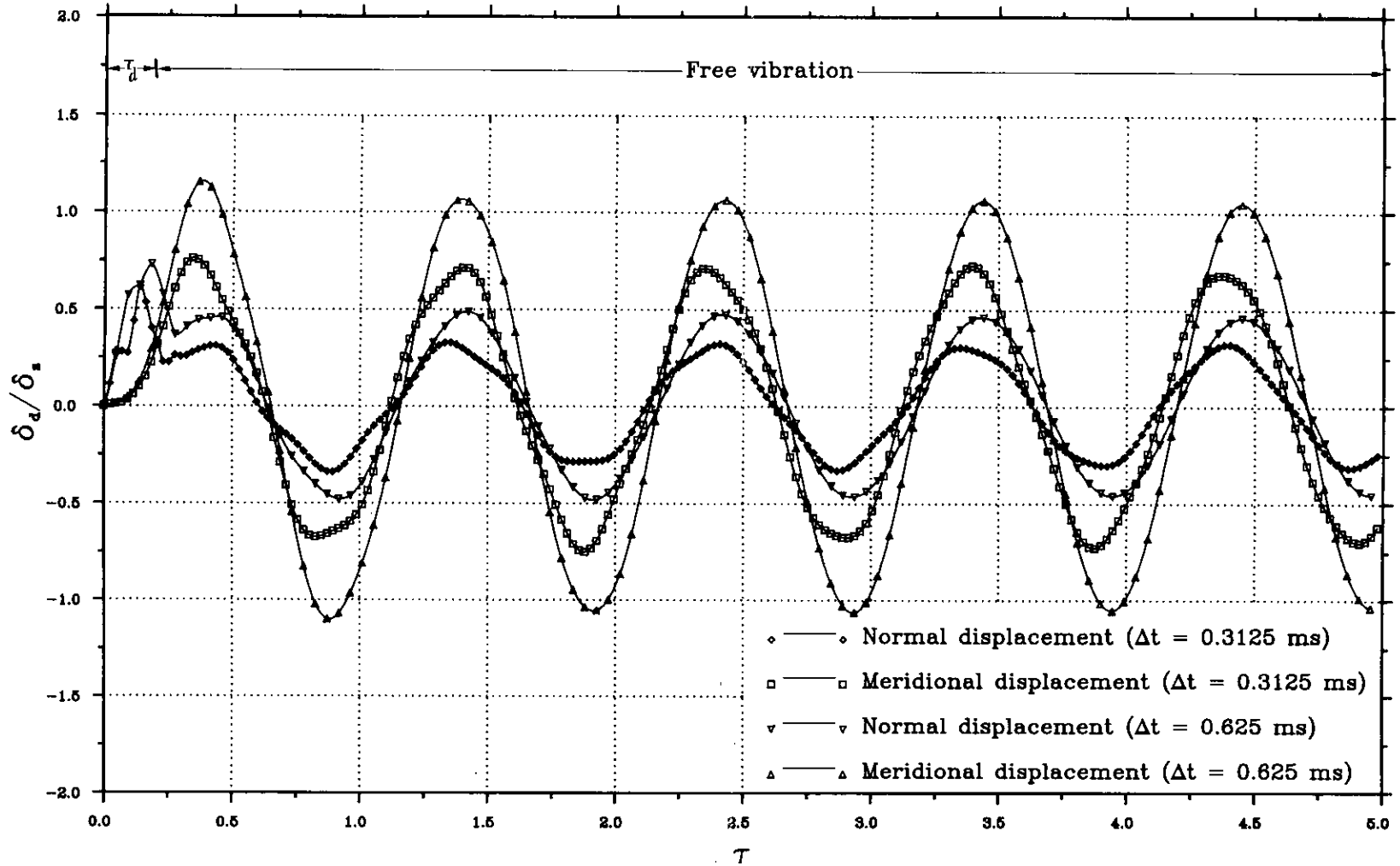

FIG. 3.6–EFFECT OF TIME INCREMENT SIZE UPON DYNAMIC RESPONSE USING THE WILSON–θ INTEGRATION SCHEME

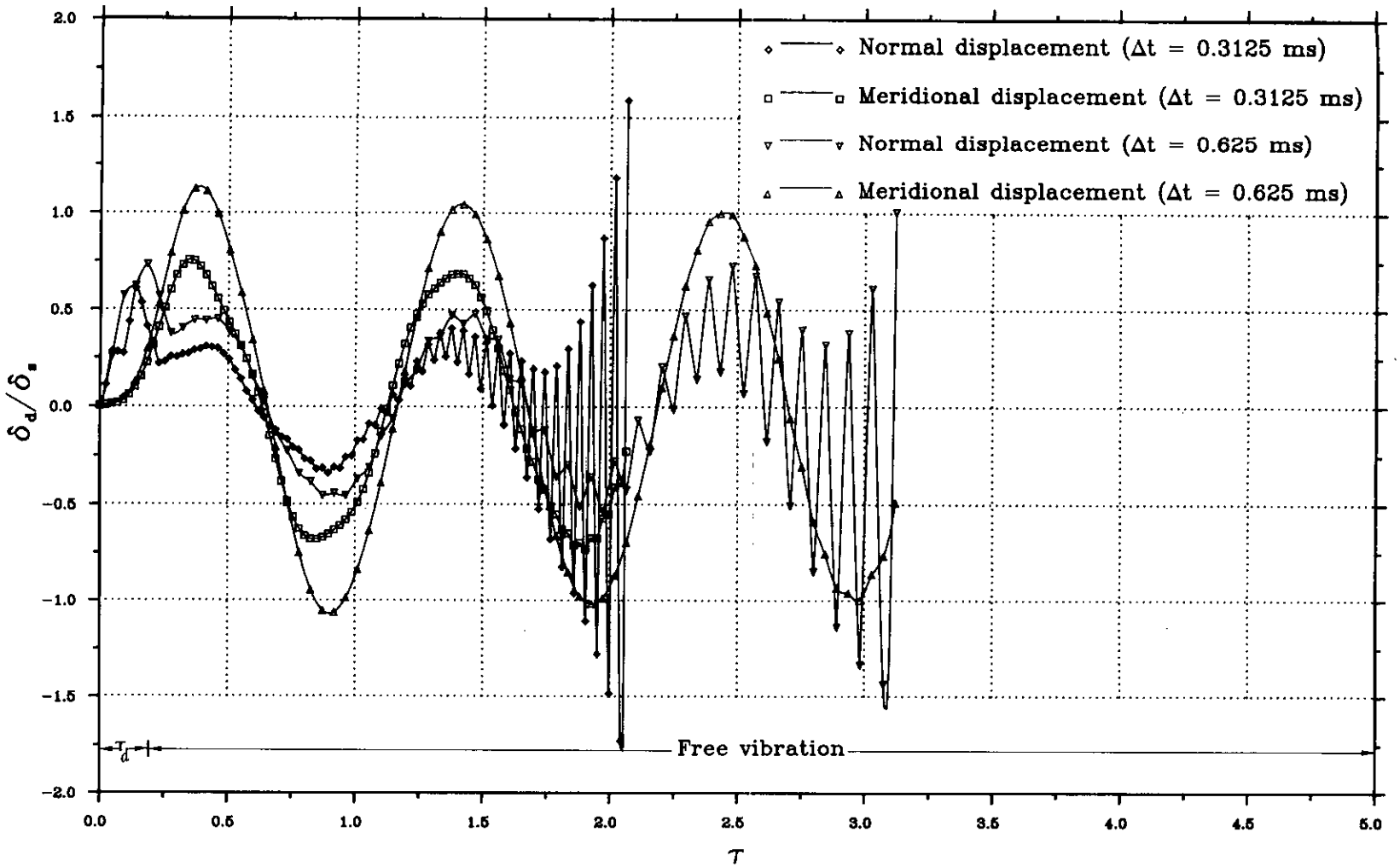

FIG. 3.7–EFFECT OF TIME INCREMENT SIZE UPON DYNAMIC RESPONSE USING THE GALERKIN HIGHER INTEGRATION SCHEME

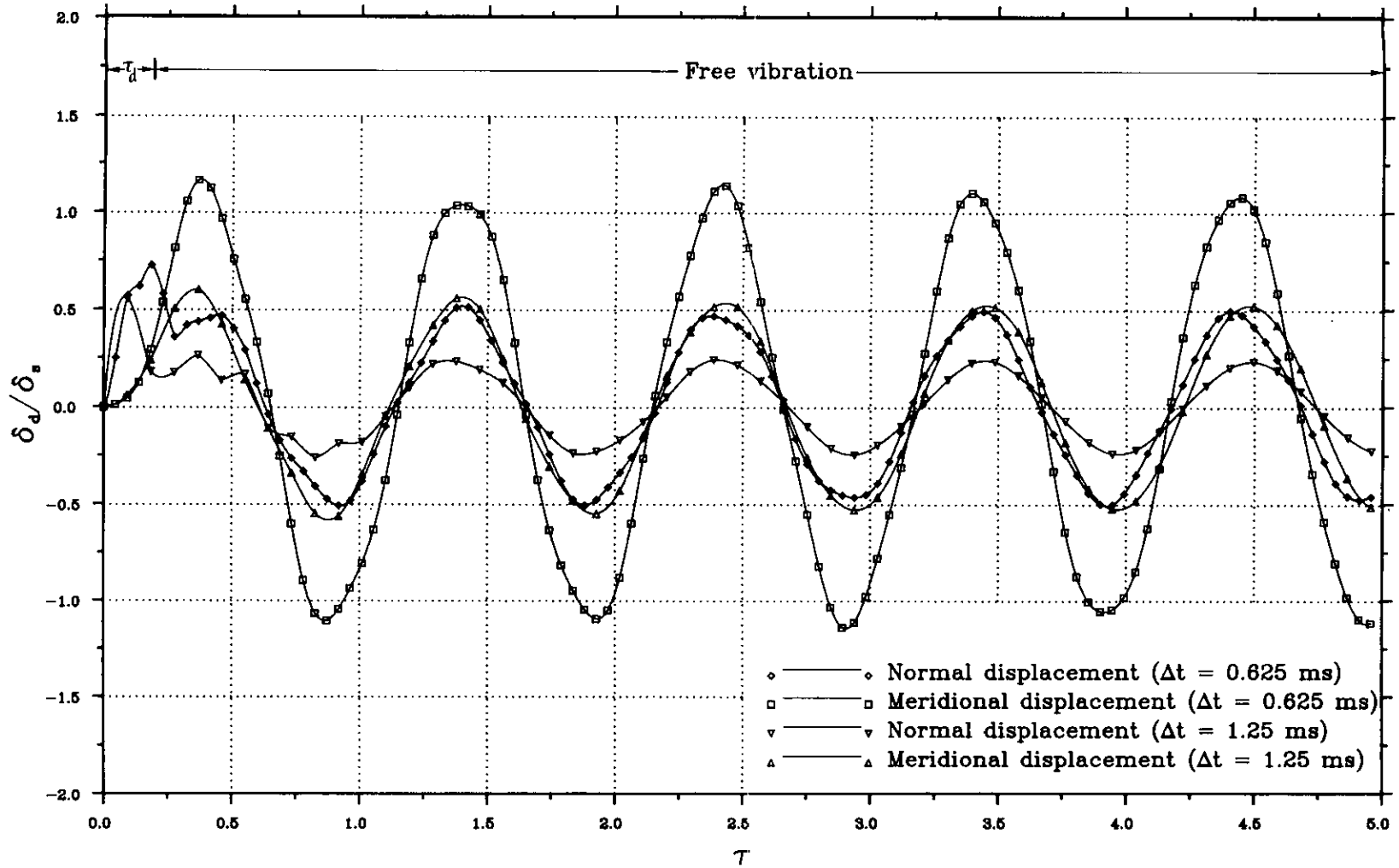

FIG. 3.8–EFFECT OF TIME INCREMENT SIZE UPON DYNAMIC RESPONSE USING THE HILBER–HUGHES–TAYLOR INTEGRATION SCHEME

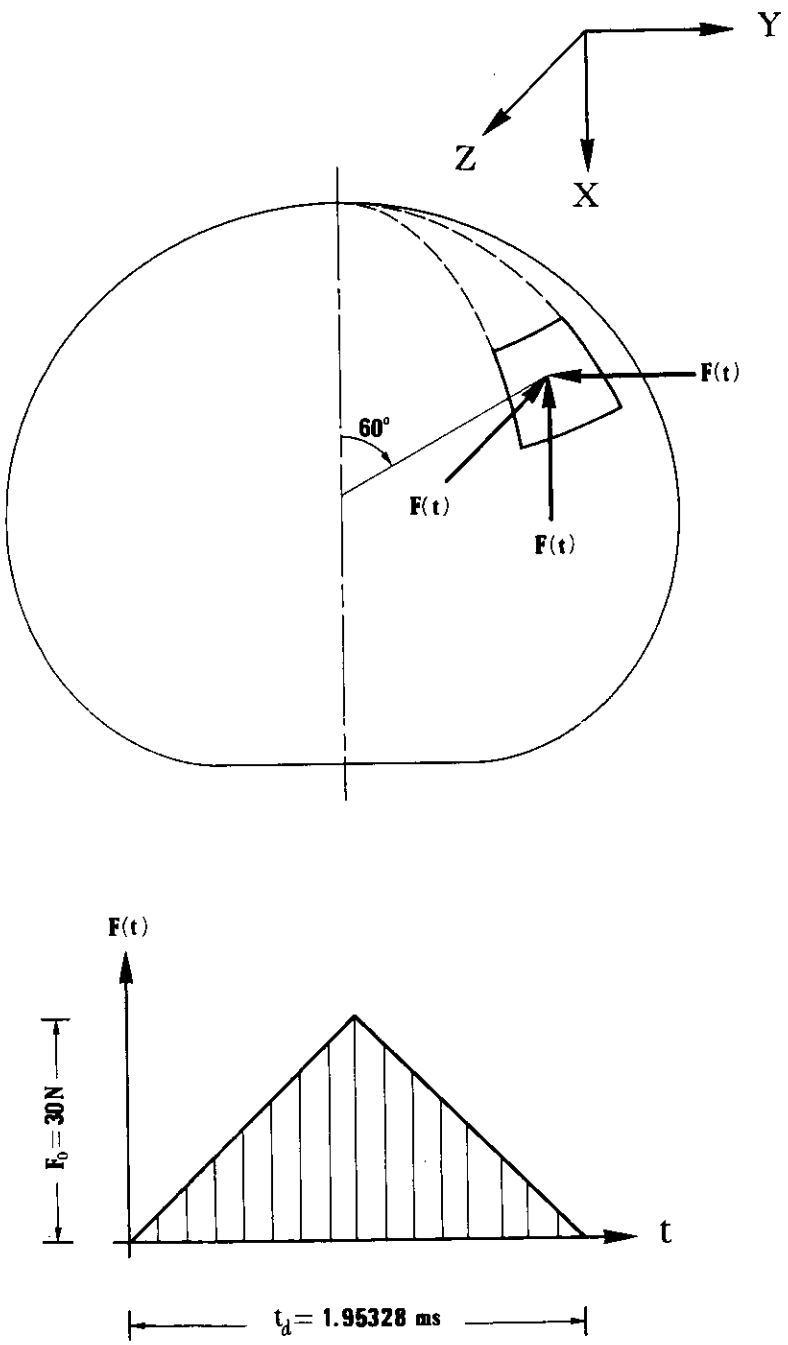

FIG. 3.9–ORIENTATION AND TIME HISTORY OF ASYMMETRIC DYNAMIC FORCE USED IN THE EXCITATION OF THE STRUCTURE

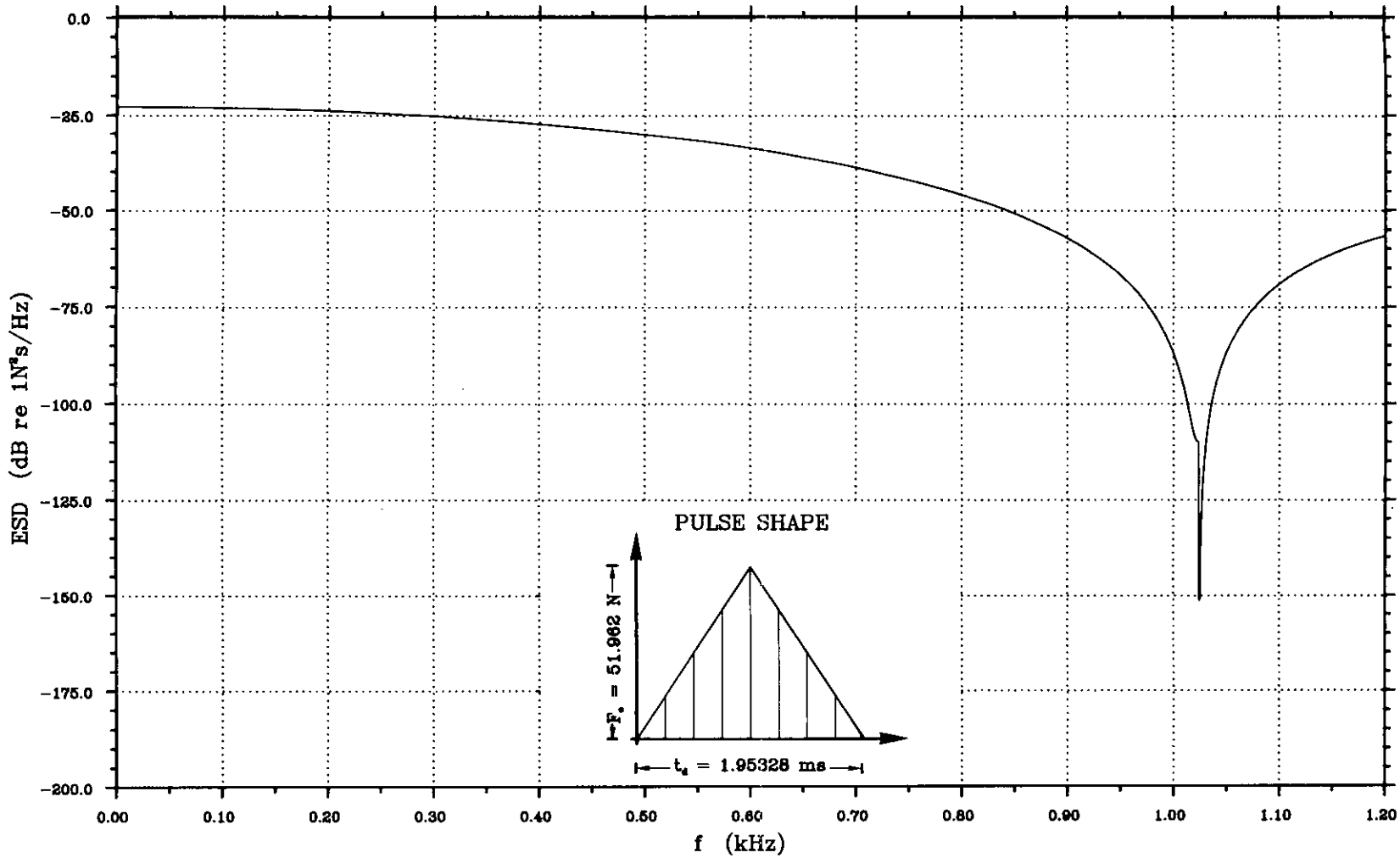

FIG. 3.10–ENERGY SPECTRAL DENSITY OF RESULTANT DYNAMIC FORCE USED IN CALCULATING THE FREQUENCY RESPONSE FUNCTION

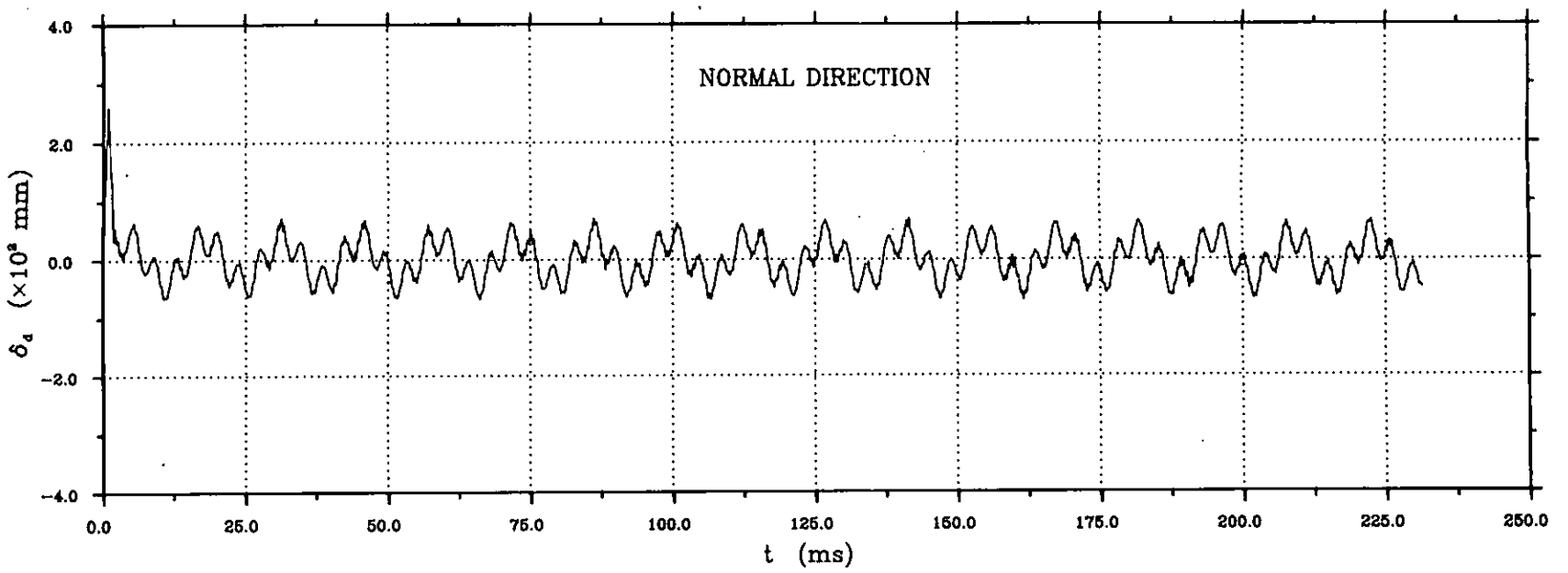

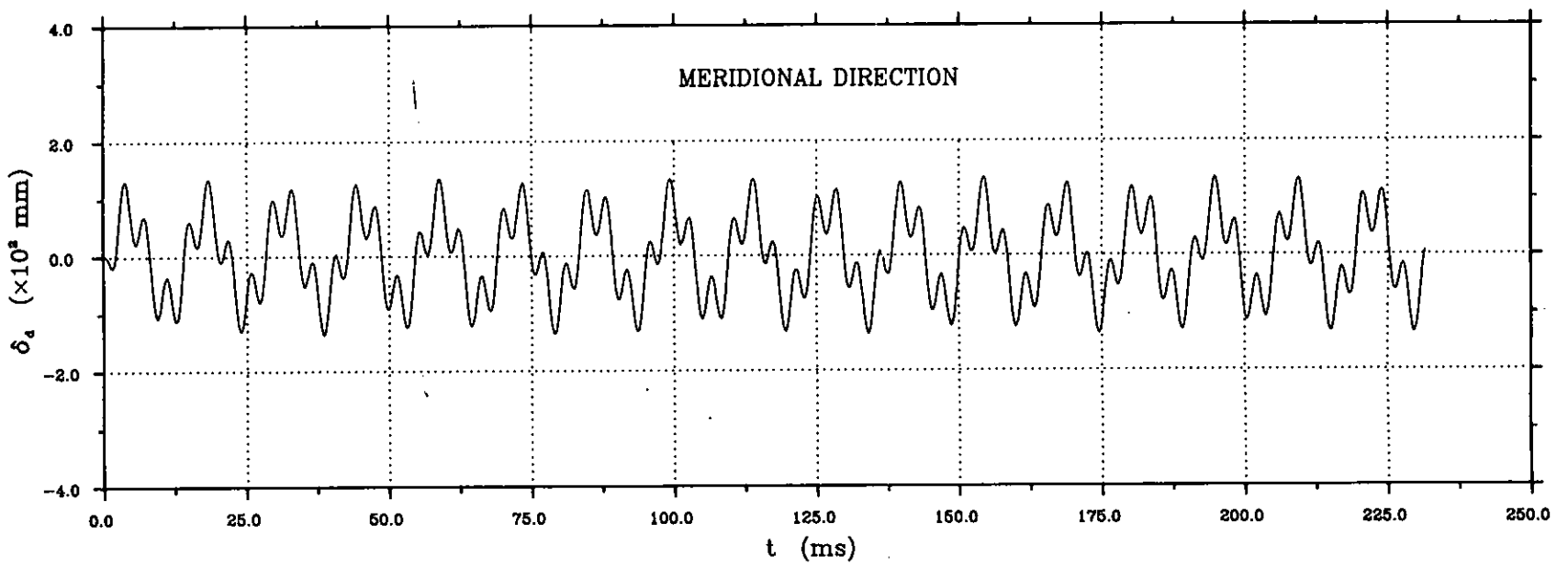

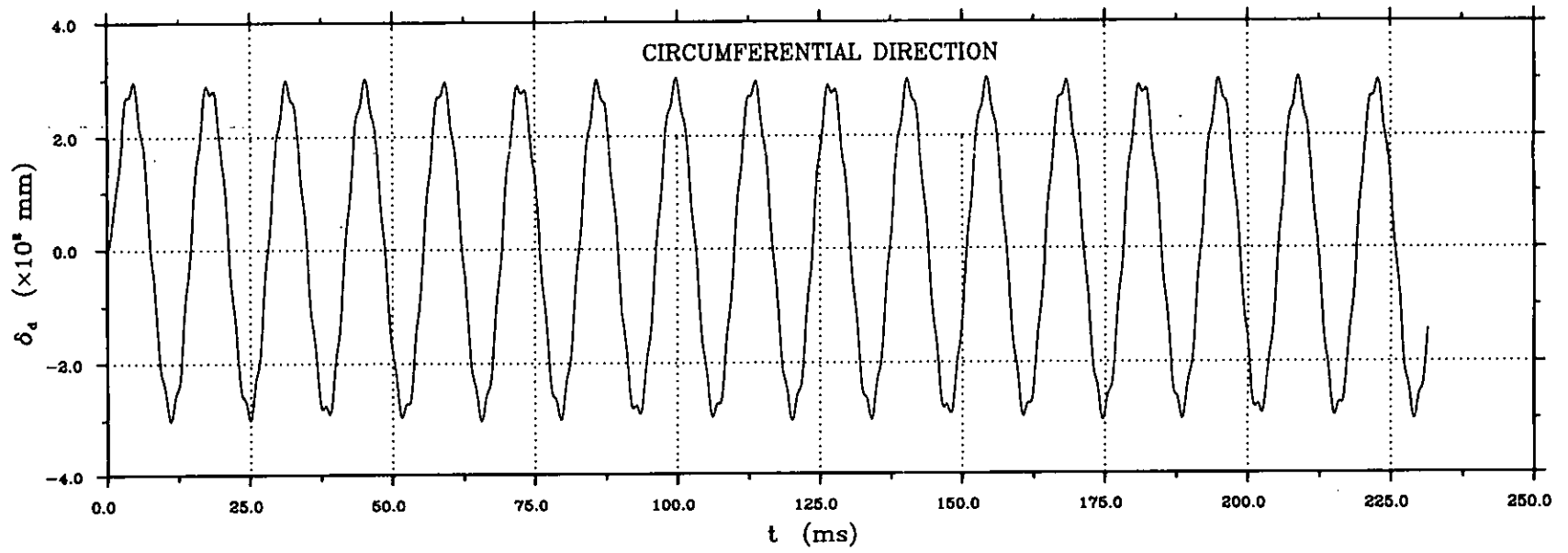

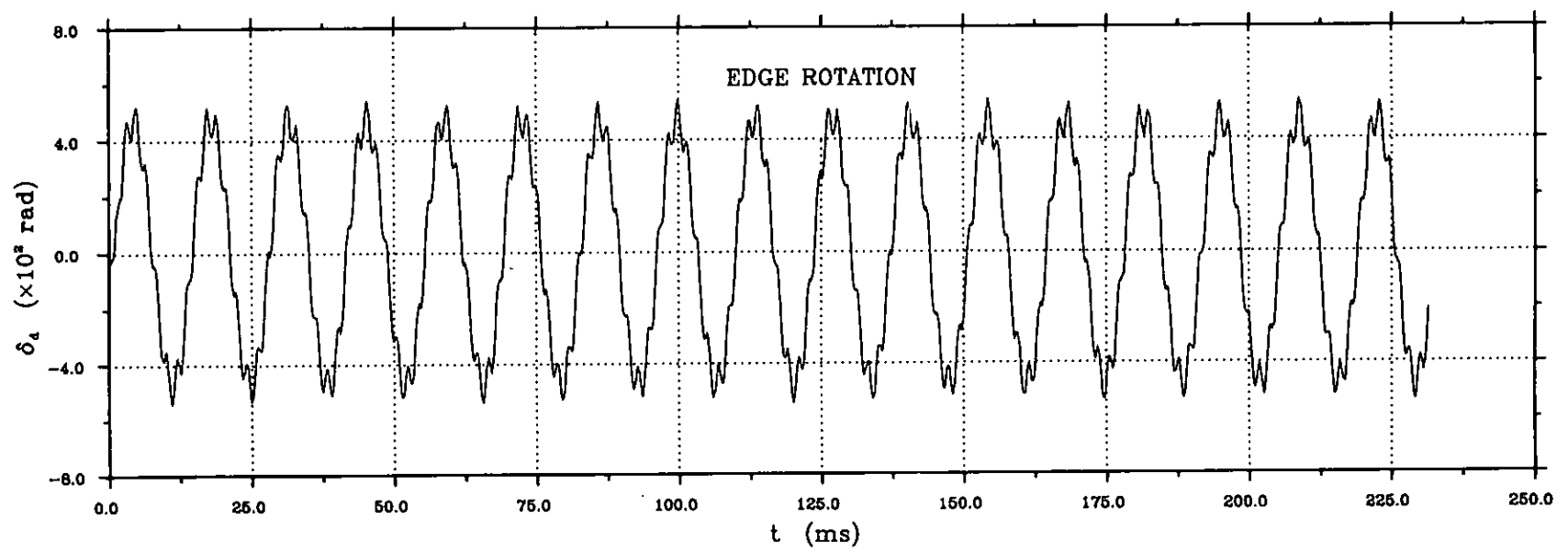

FIG. 3.11–TRANSIENT RESPONSE–TIME HISTORY

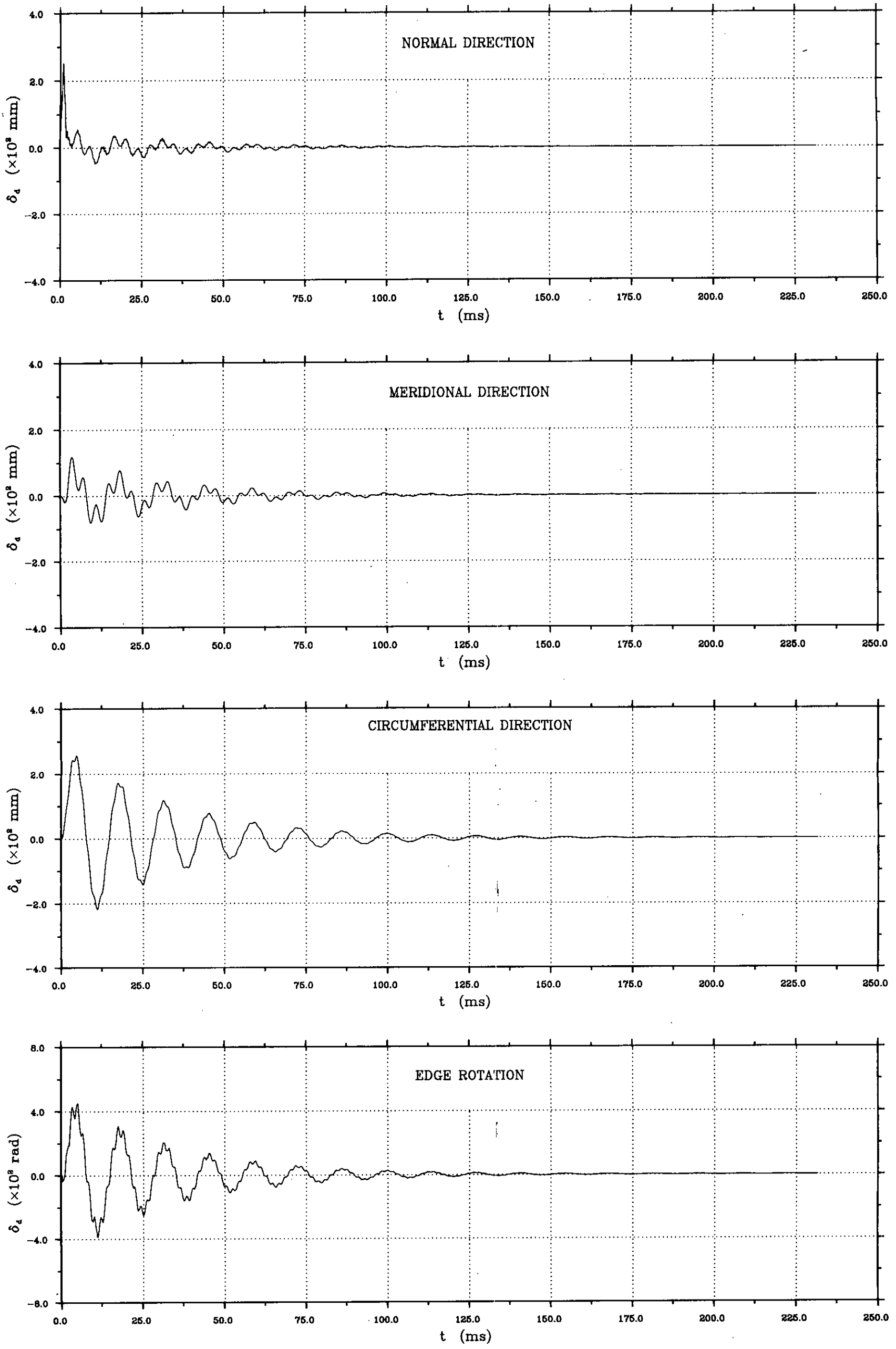

FIG. 3.12–WEIGHTED TRANSIENT RESPONSE–TIME HISTORY

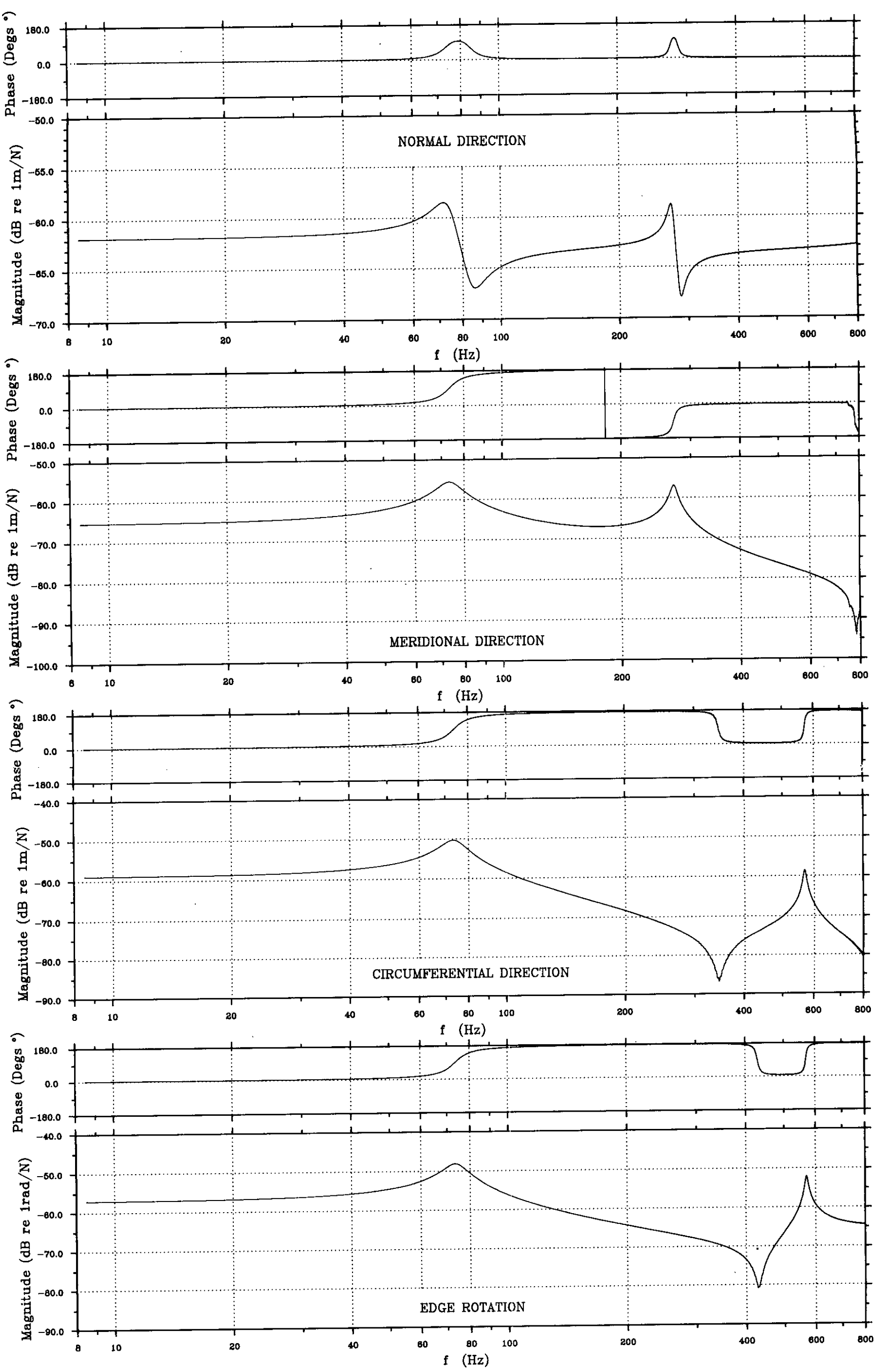

FIG. 3.13–VARIOUS CROSS POINT RECEPTANCES

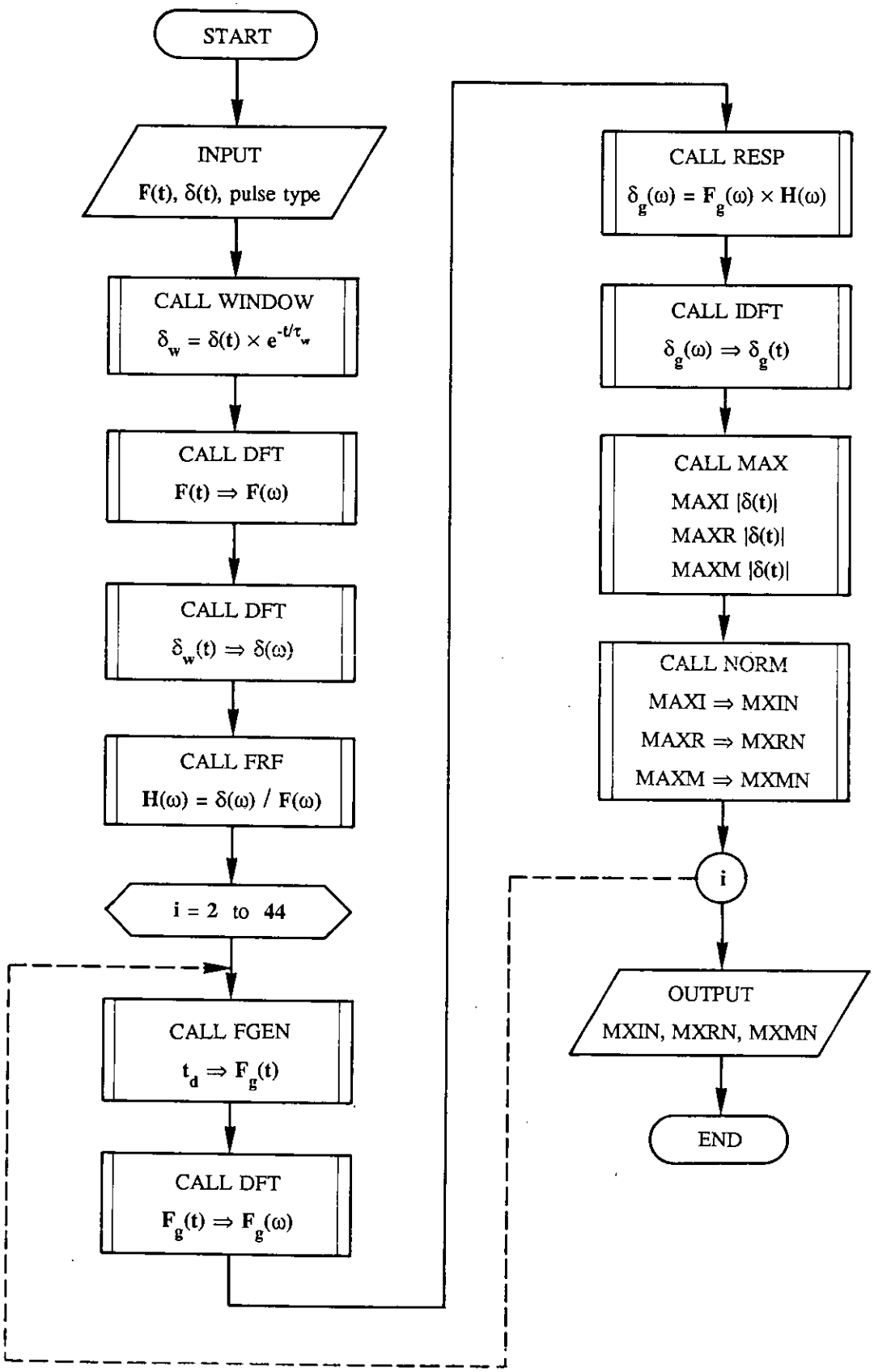

FIG. 3.14–FLOW CHART OF THE SRSTRA MAIN PROGRAM

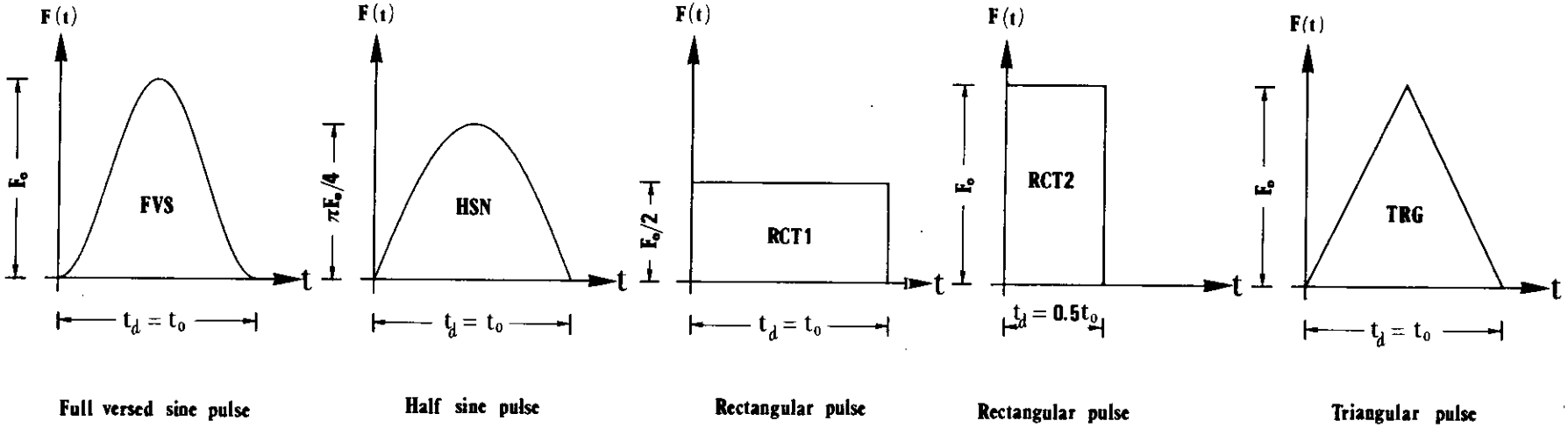

FIG. 3.15–DETAILS OF SYMMETRIC PULSES OF EQUAL IMPULSE AREA USED IN SHOCK RESPONSE ANALYSIS

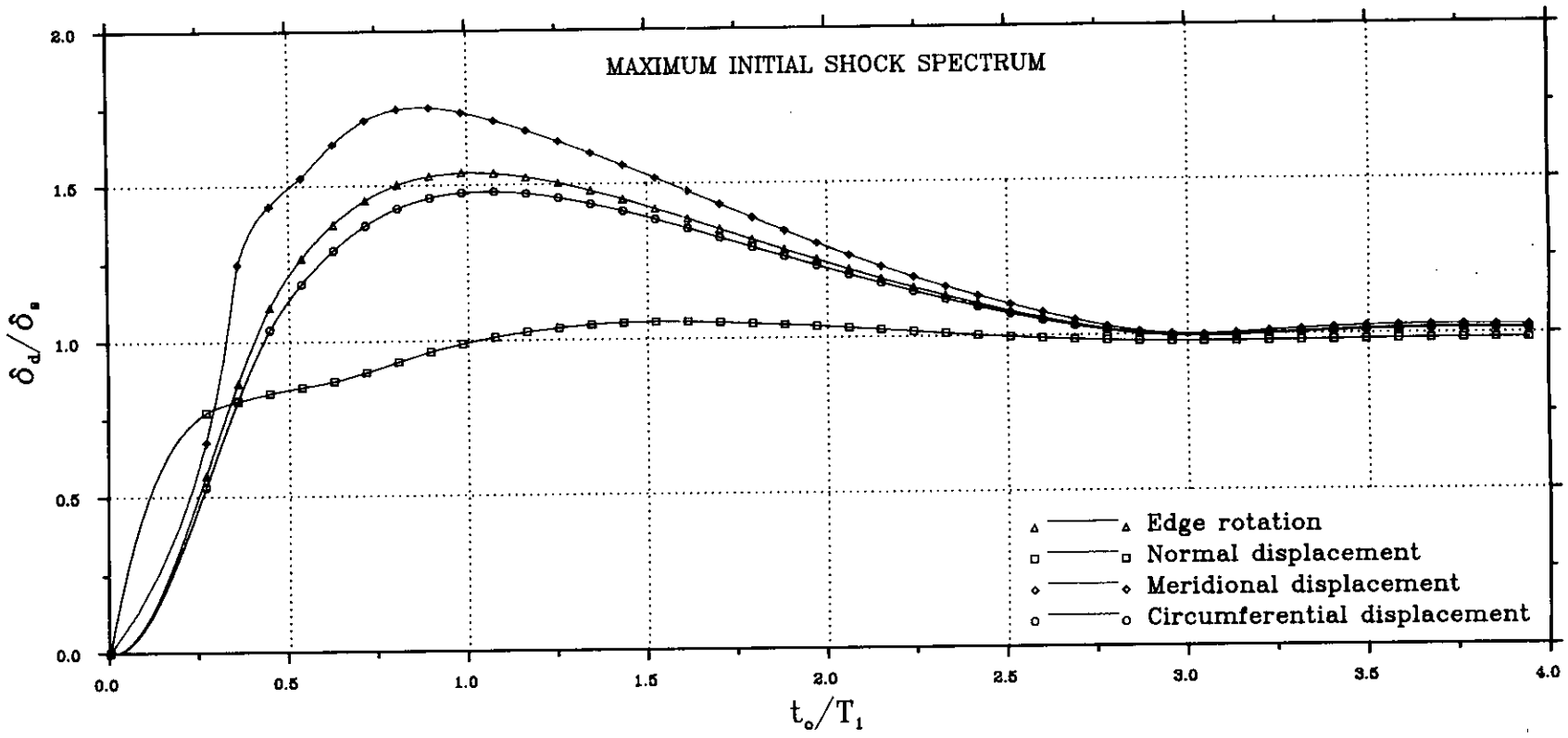

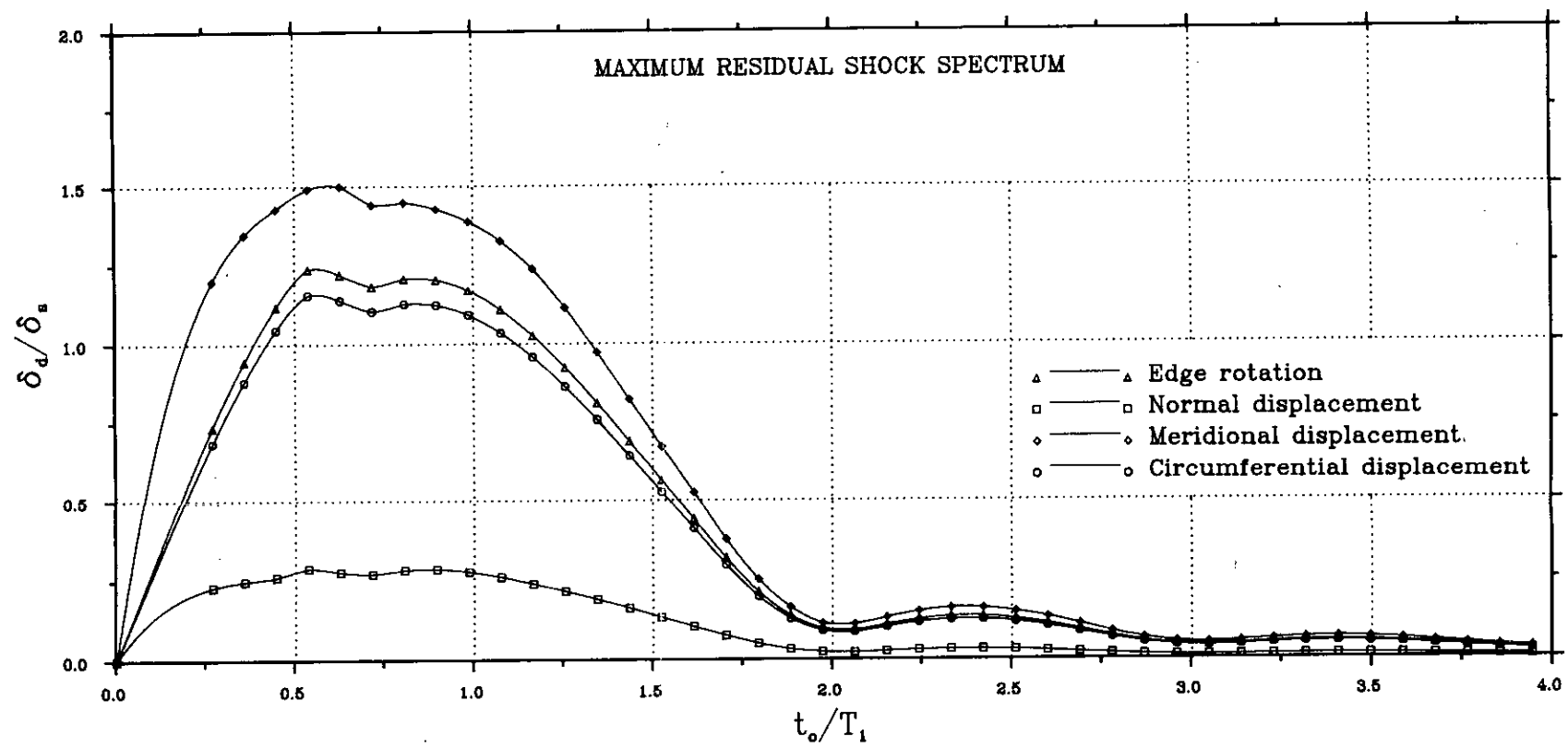

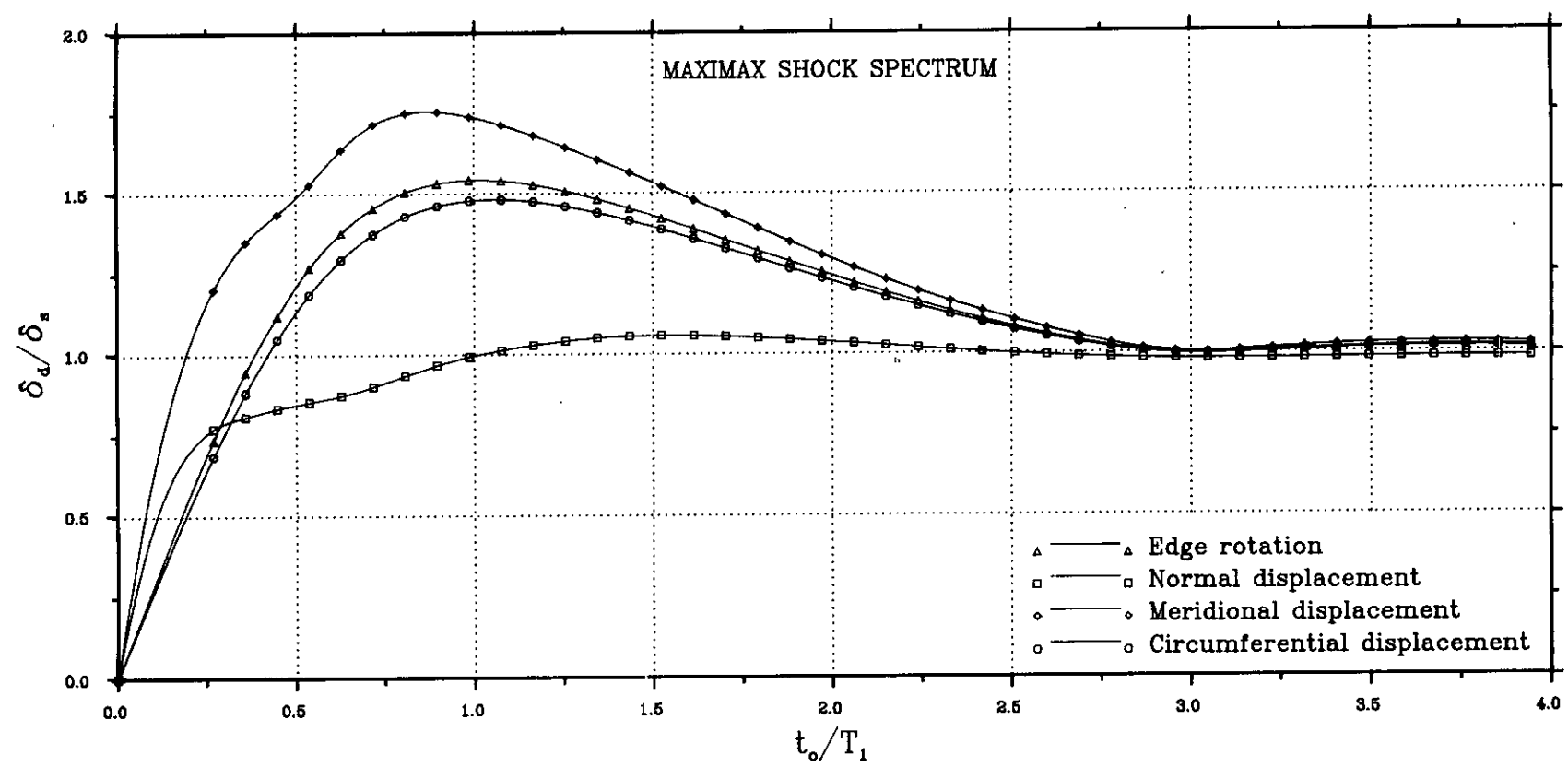

FIG. 3.16–EFFECT OF PULSE DURATION ON MAXIMUM RESPONSE SPECTRA (DLF) TO A FULL VERSED SINE PULSE

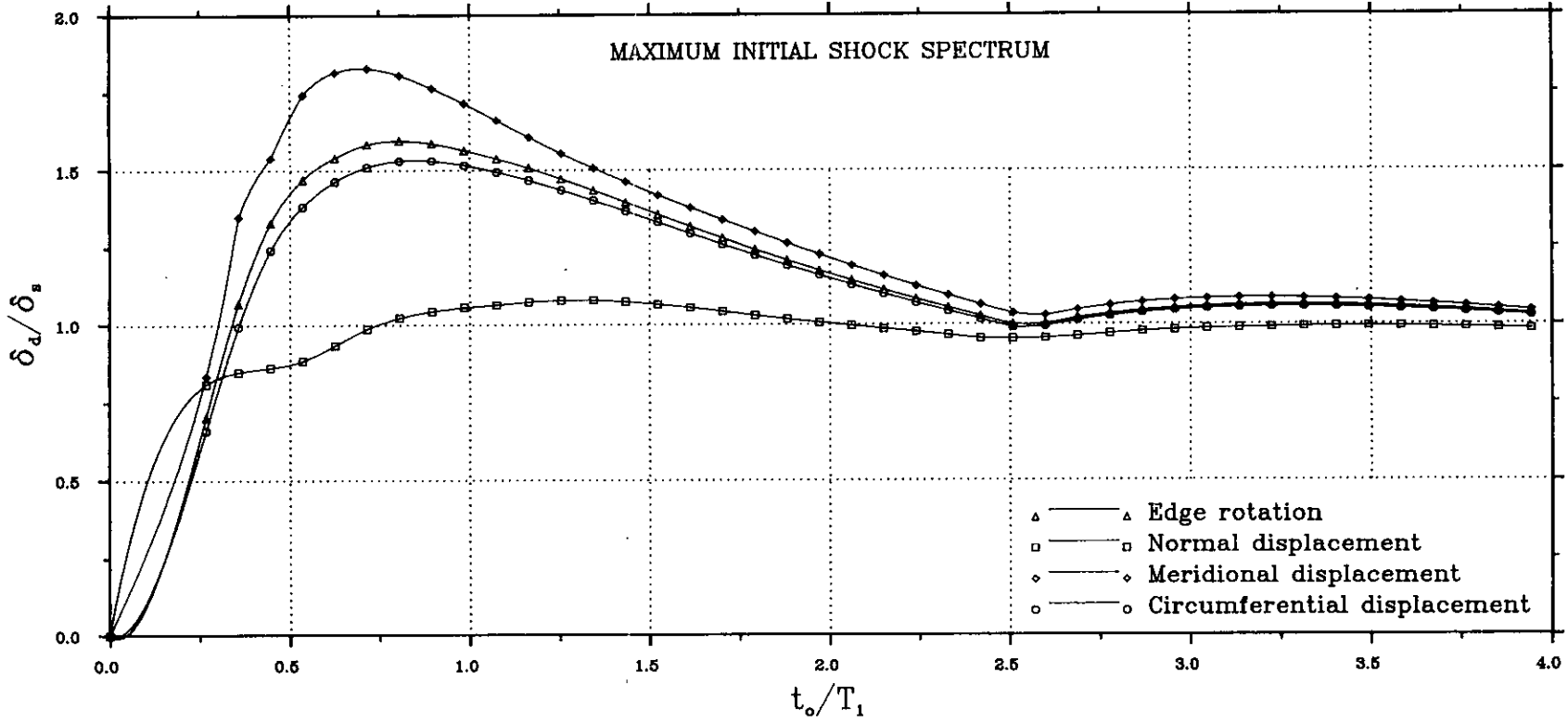

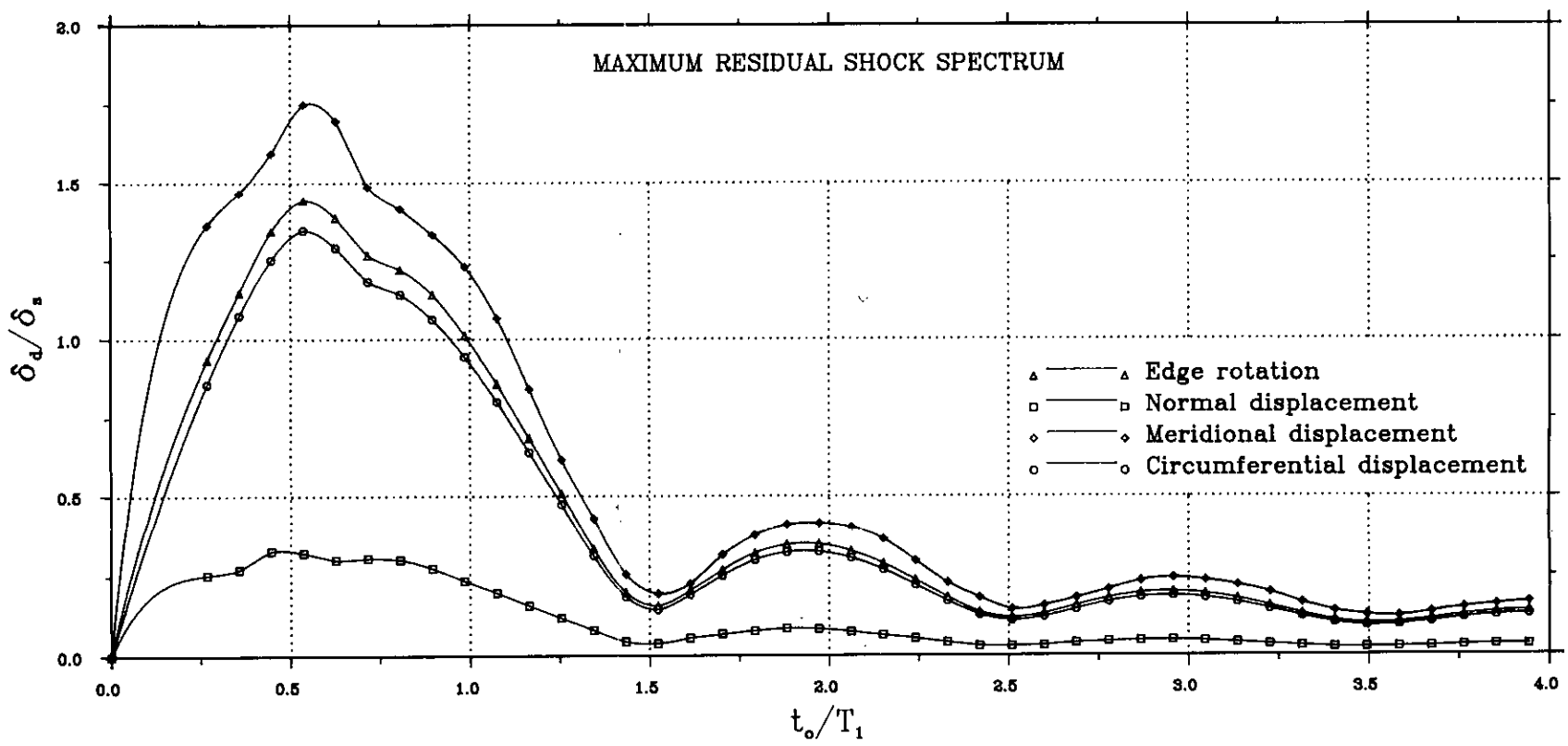

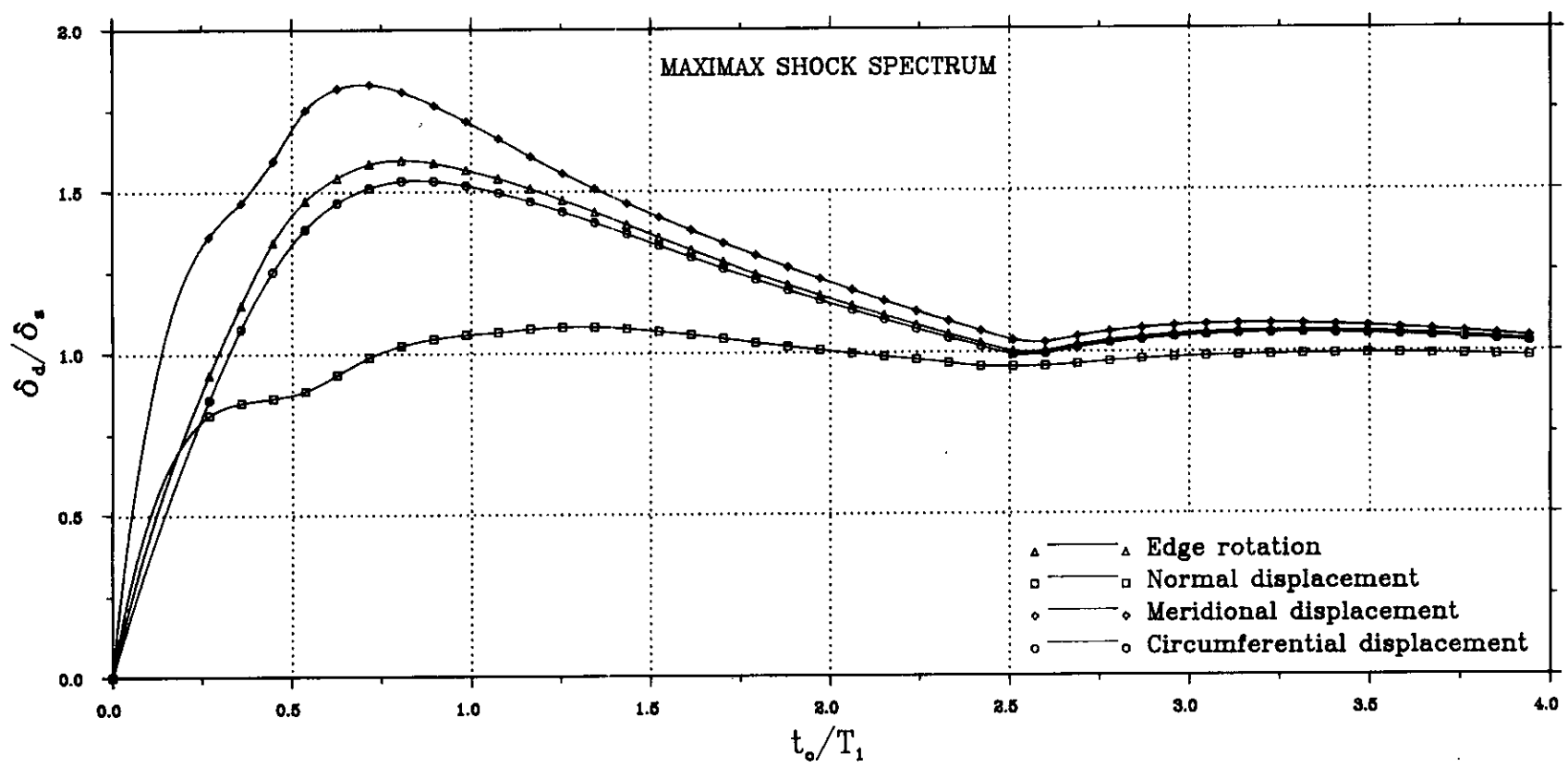

FIG. 3.17–EFFECT OF PULSE DURATION ON MAXIMUM RESPONSE SPECTRA (DLF) TO A HALF SINE PULSE

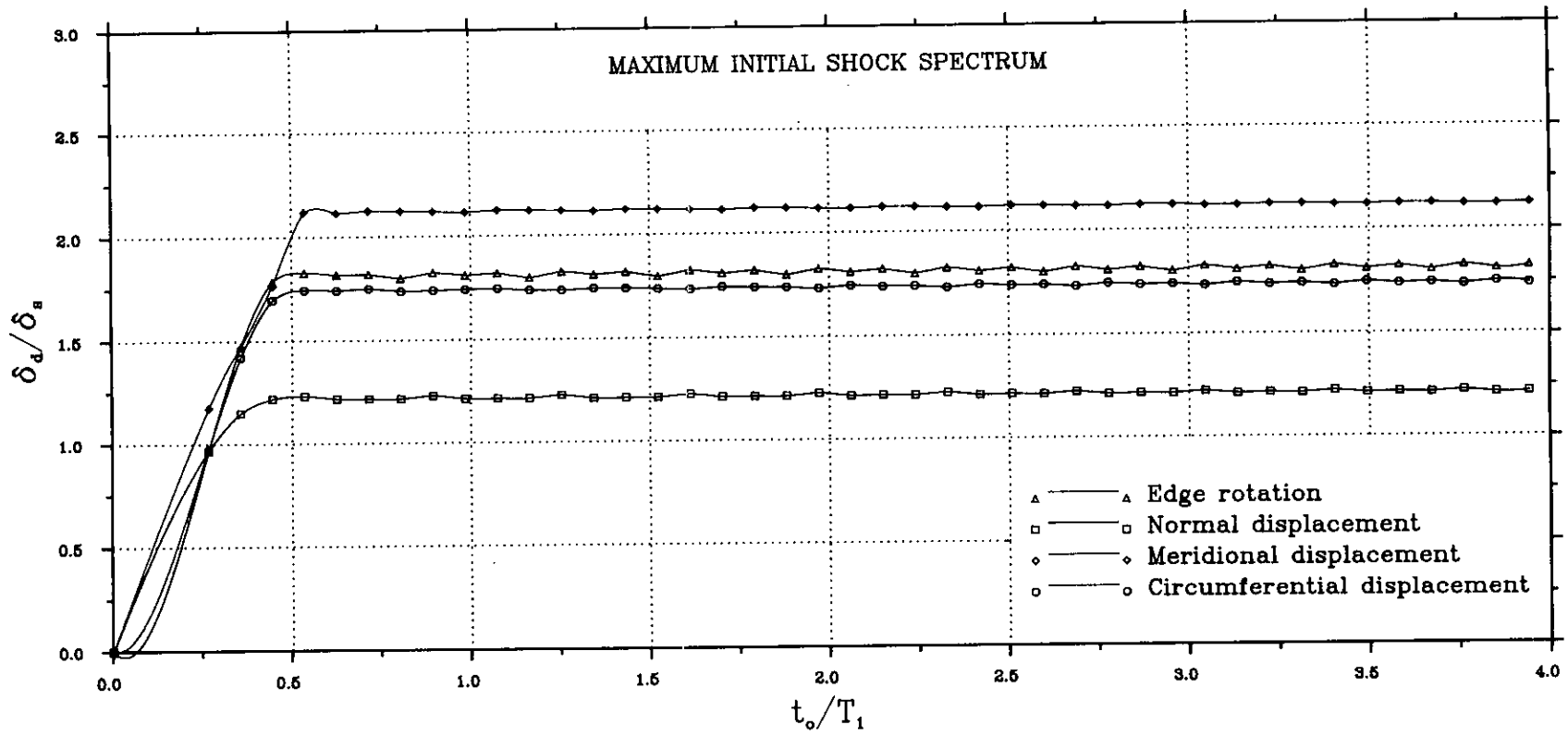

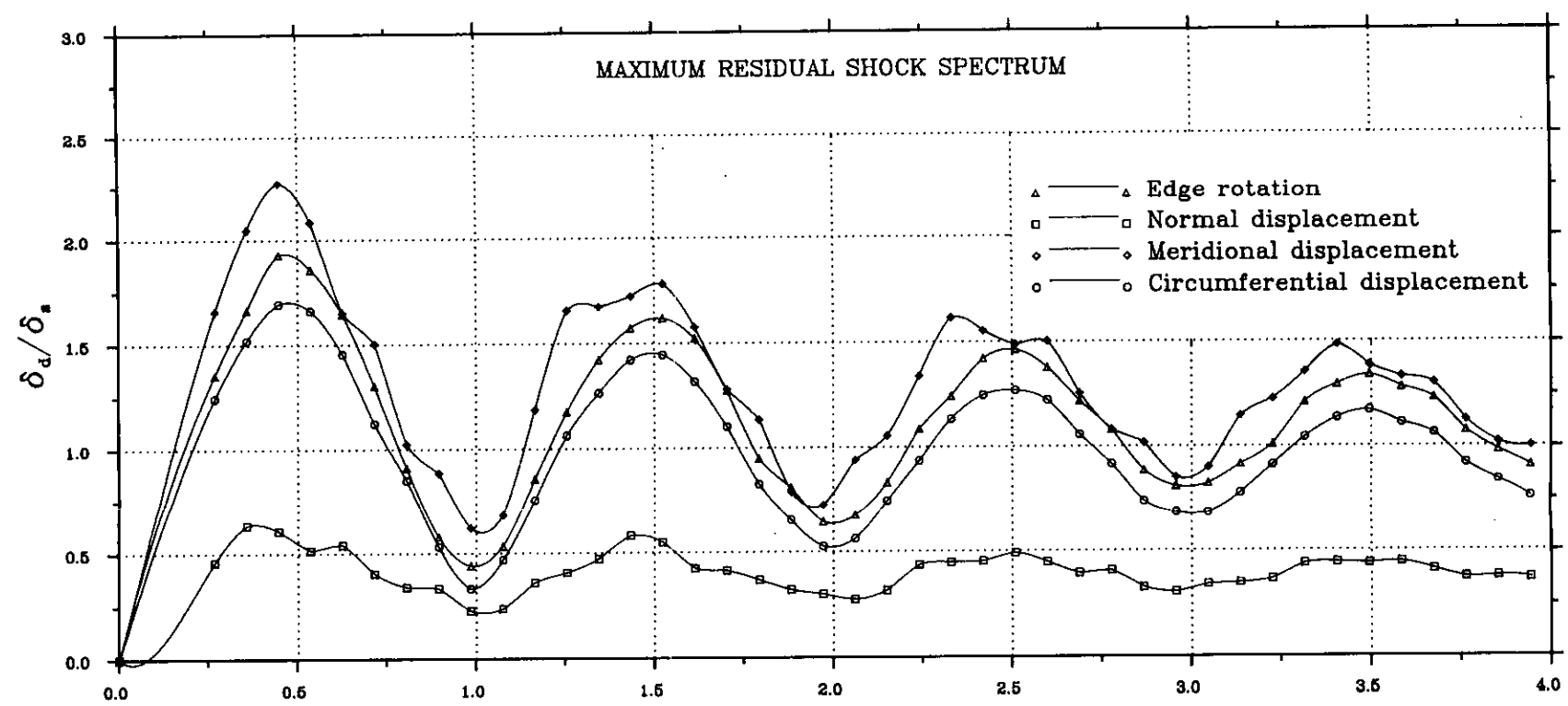

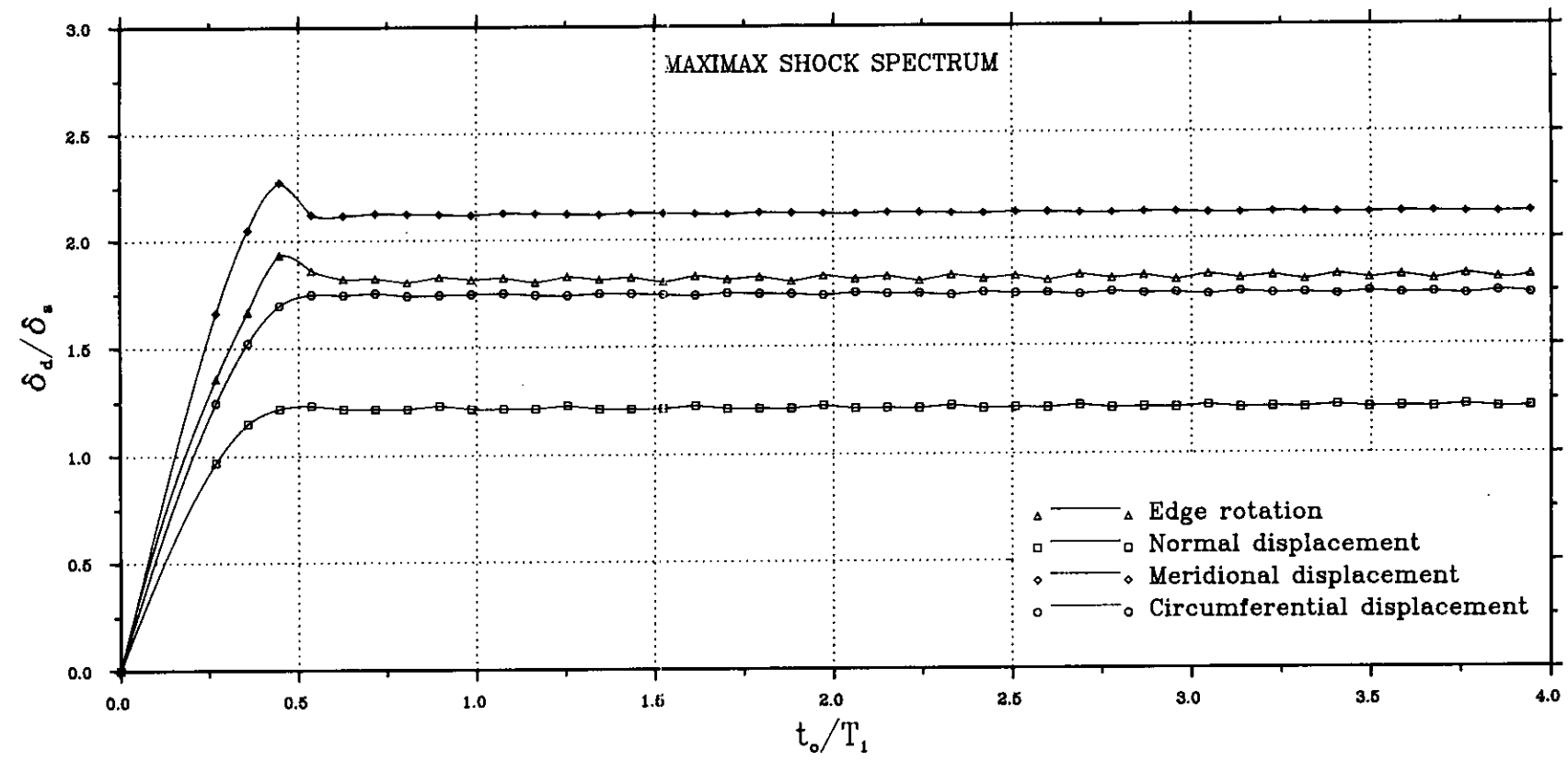

FIG. 3.18–EFFECT OF PULSE DURATION ON MAXIMUM RESPONSE SPECTRA (DLF) TO A RECTANGULAR PULSE --RCT1--

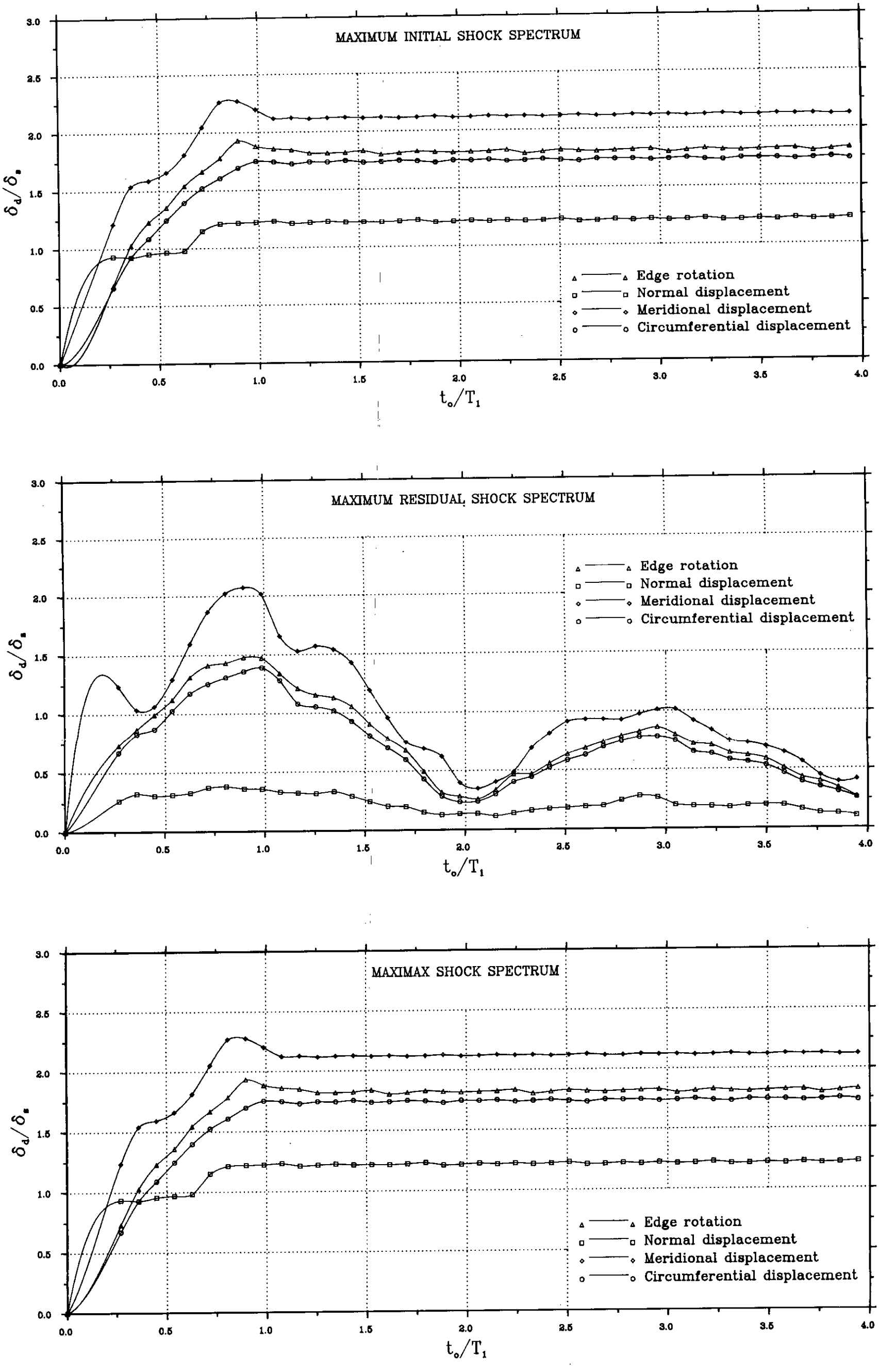

FIG. 3.19–EFFECT OF PULSE DURATION ON MAXIMUM RESPONSE SPECTRA (DLF) TO A RECTANGULAR PULSE --RCT2--

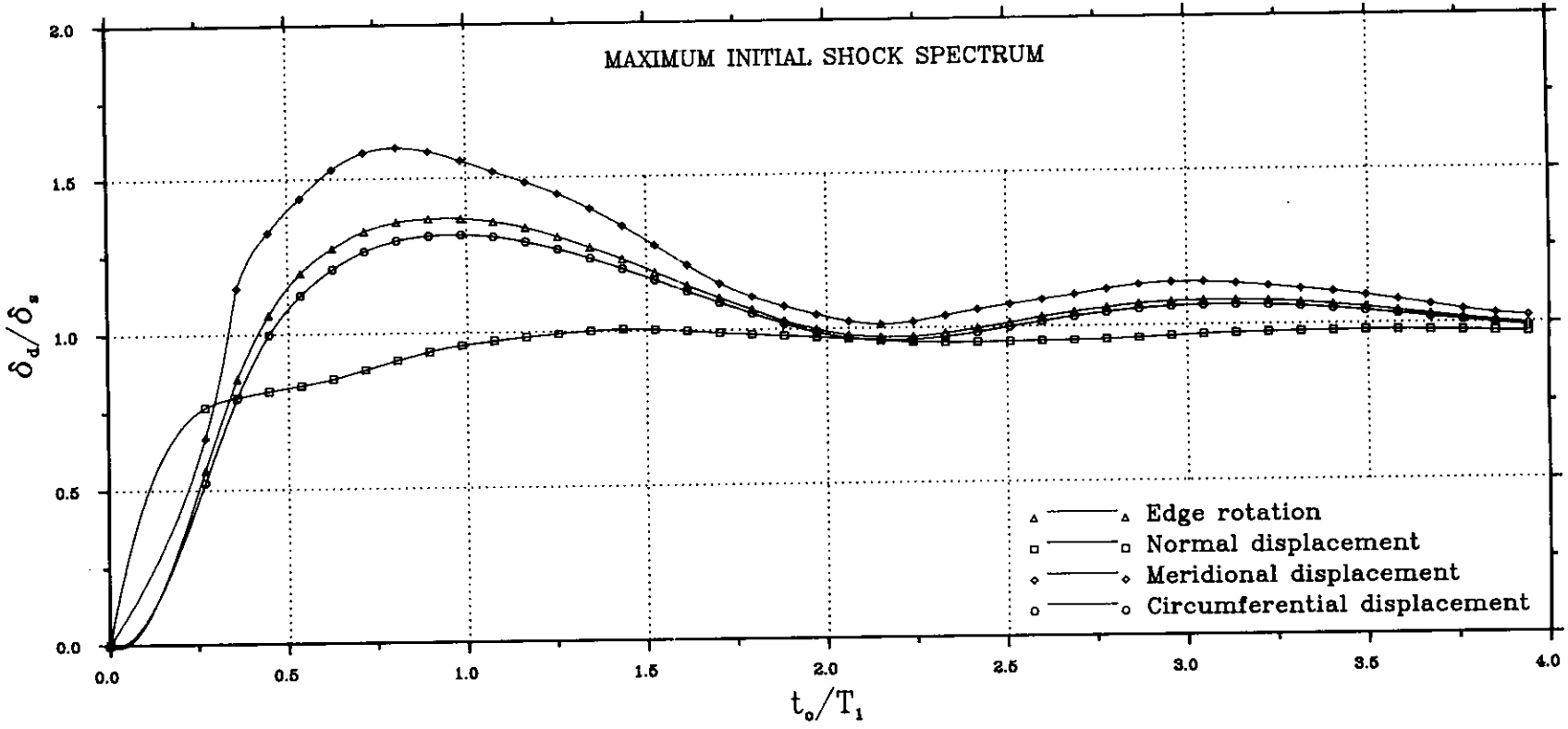

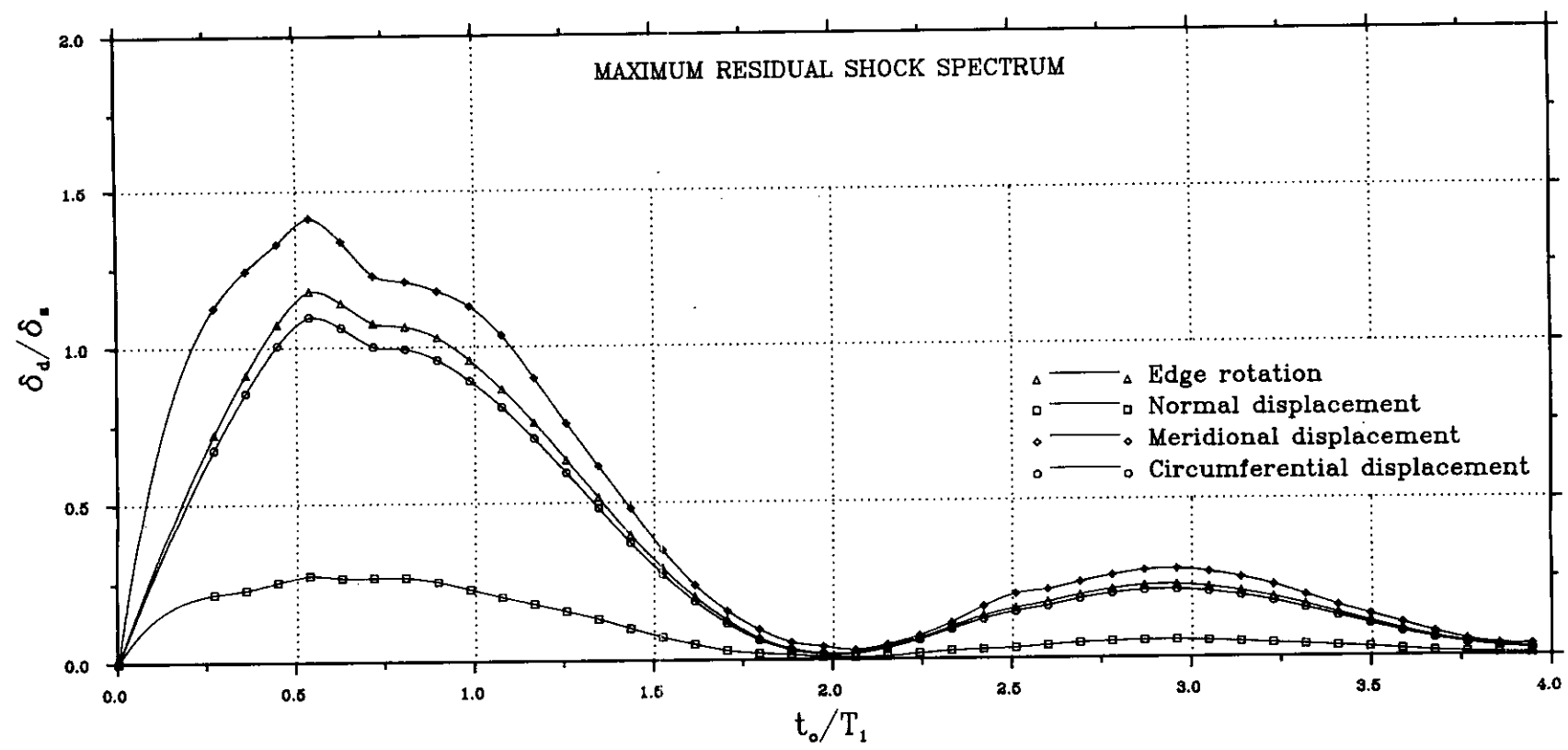

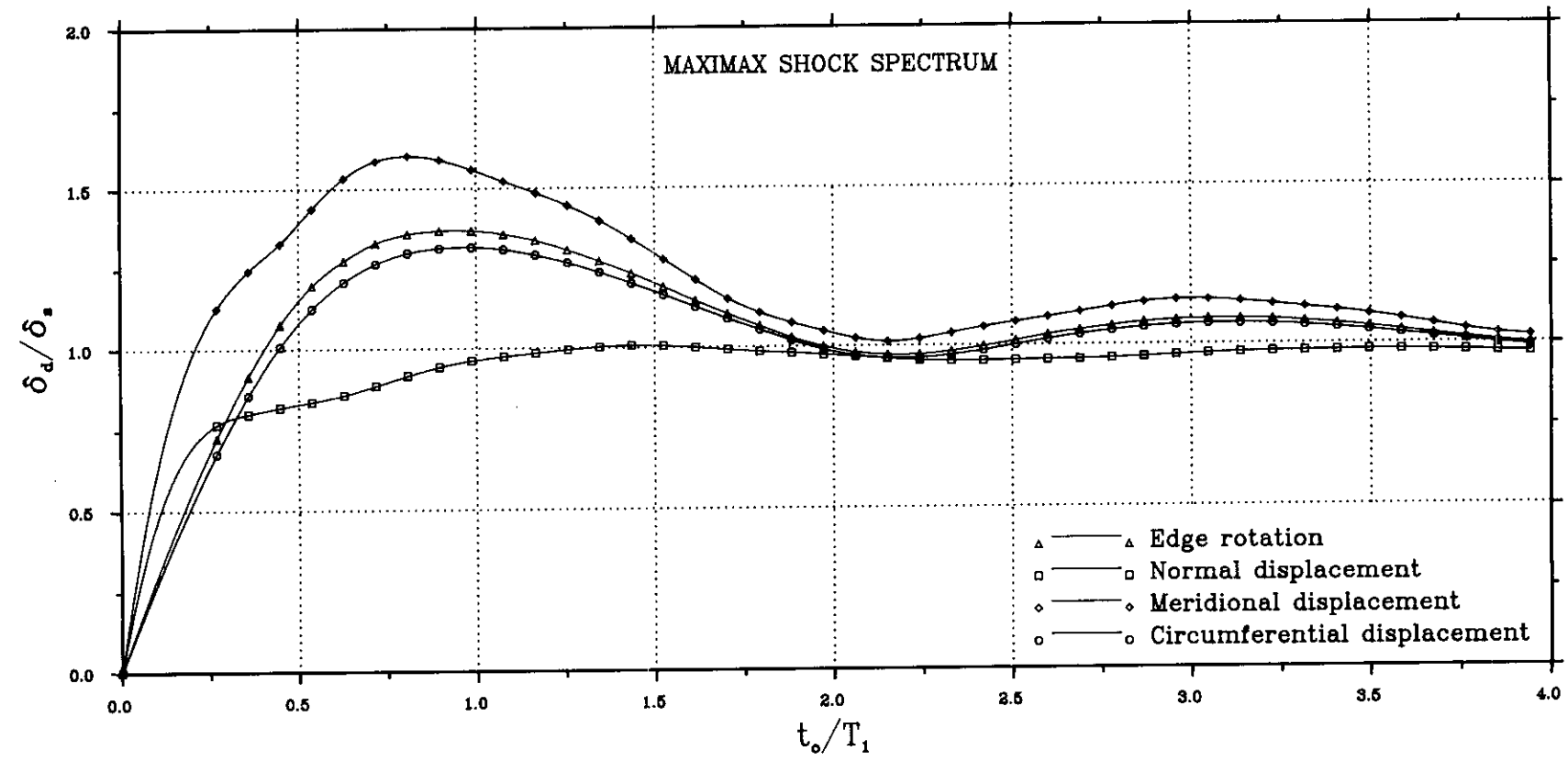

FIG. 3.20–EFFECT OF PULSE DURATION ON MAXIMUM RESPONSE SPECTRA (DLF) TO A TRIANGULAR PULSE --κ = 0.5--

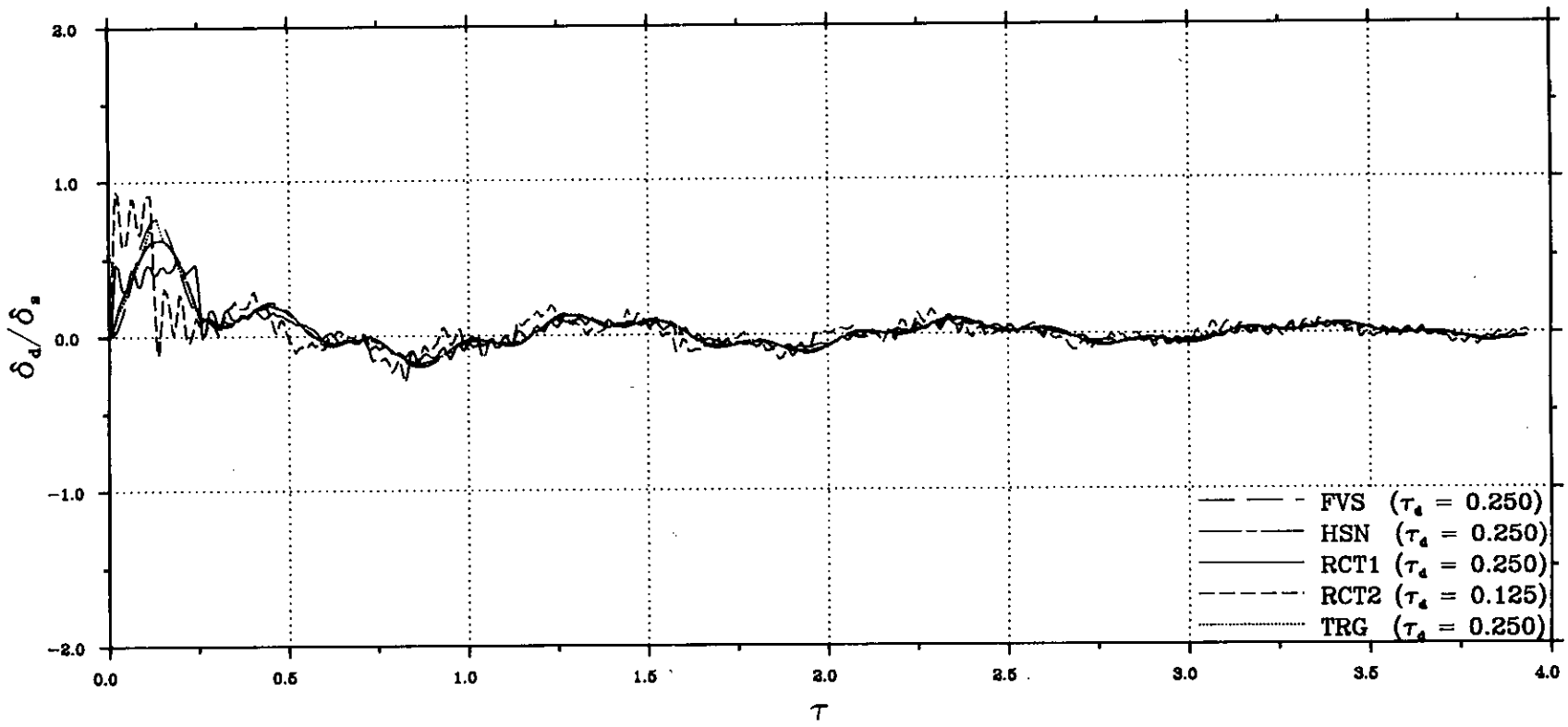

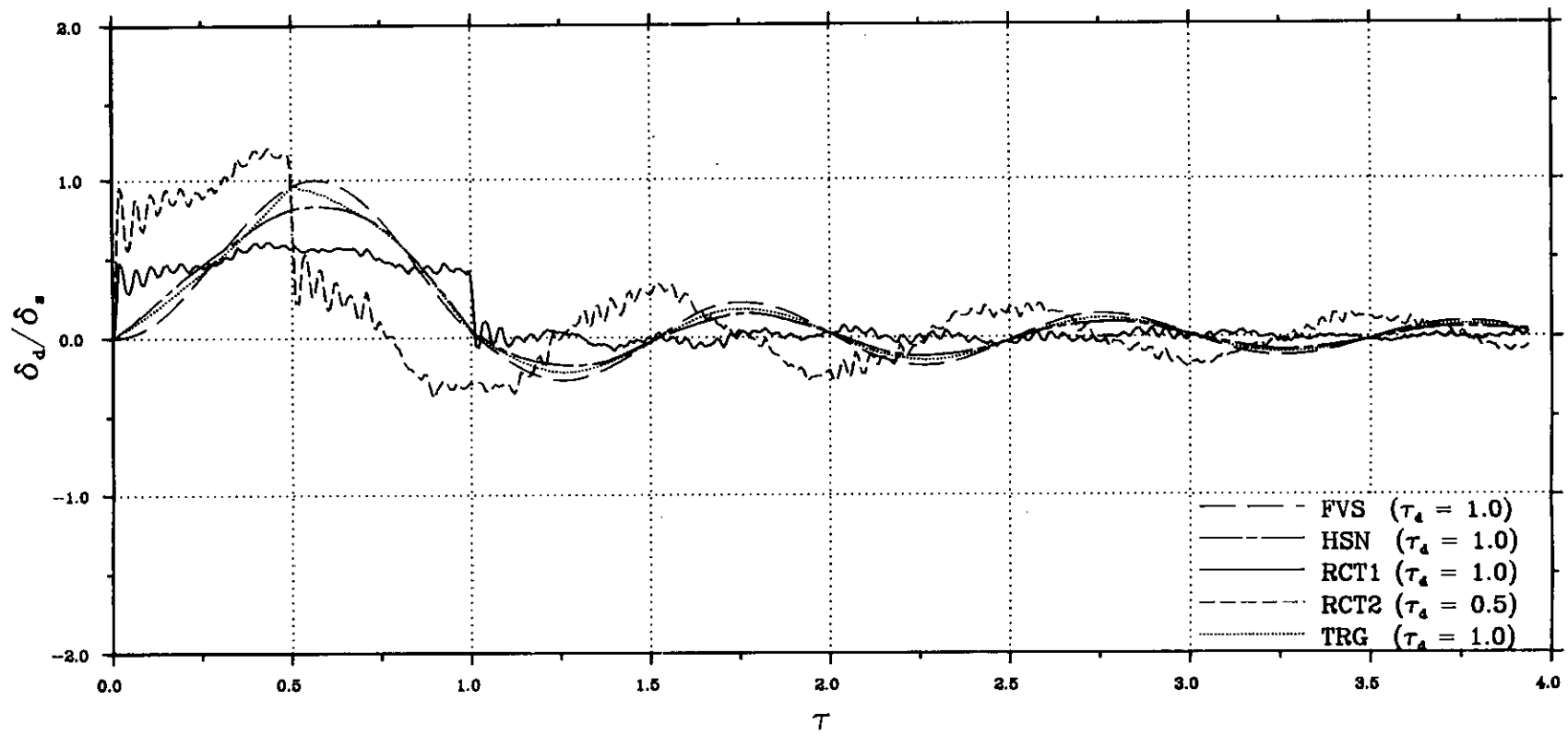

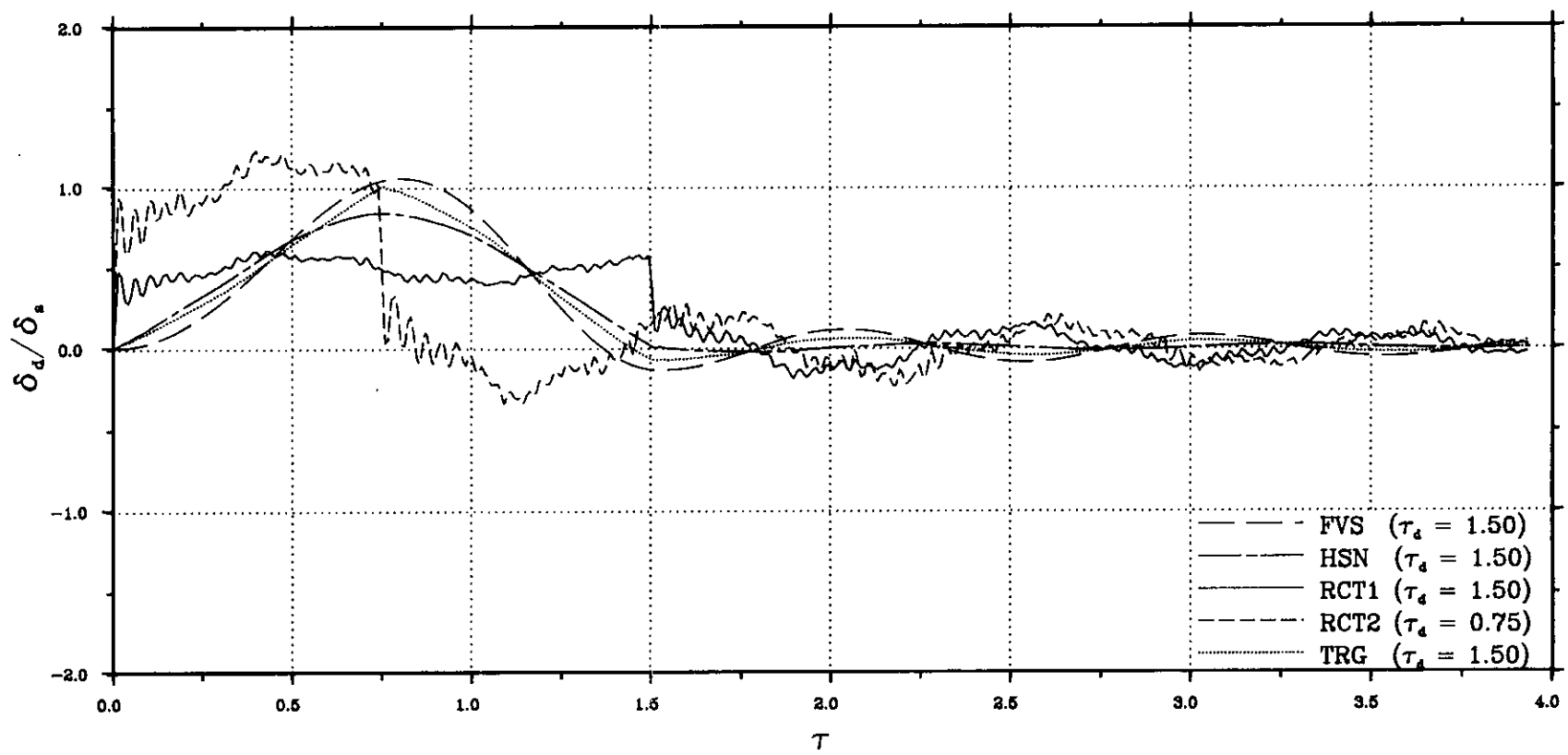

FIG. 3.21(a)–RESPONSE–TIME HISTORY TO VARIOUS SYMMETRICAL PULSES OF EQUAL IMPULSE AREA, FOR DIFFERENT VALUES OF PULSE DURATION
––NORMAL DIRECTION––

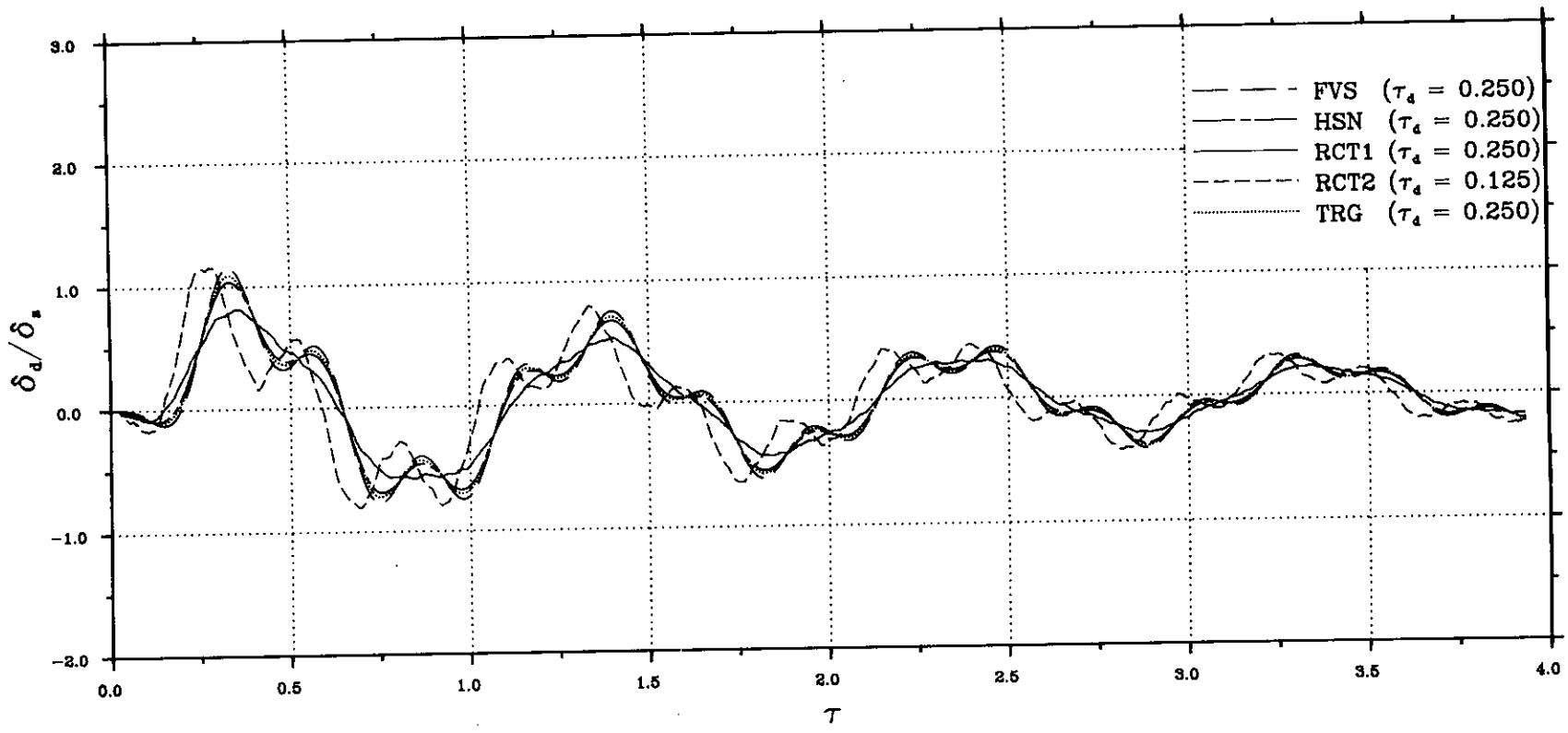

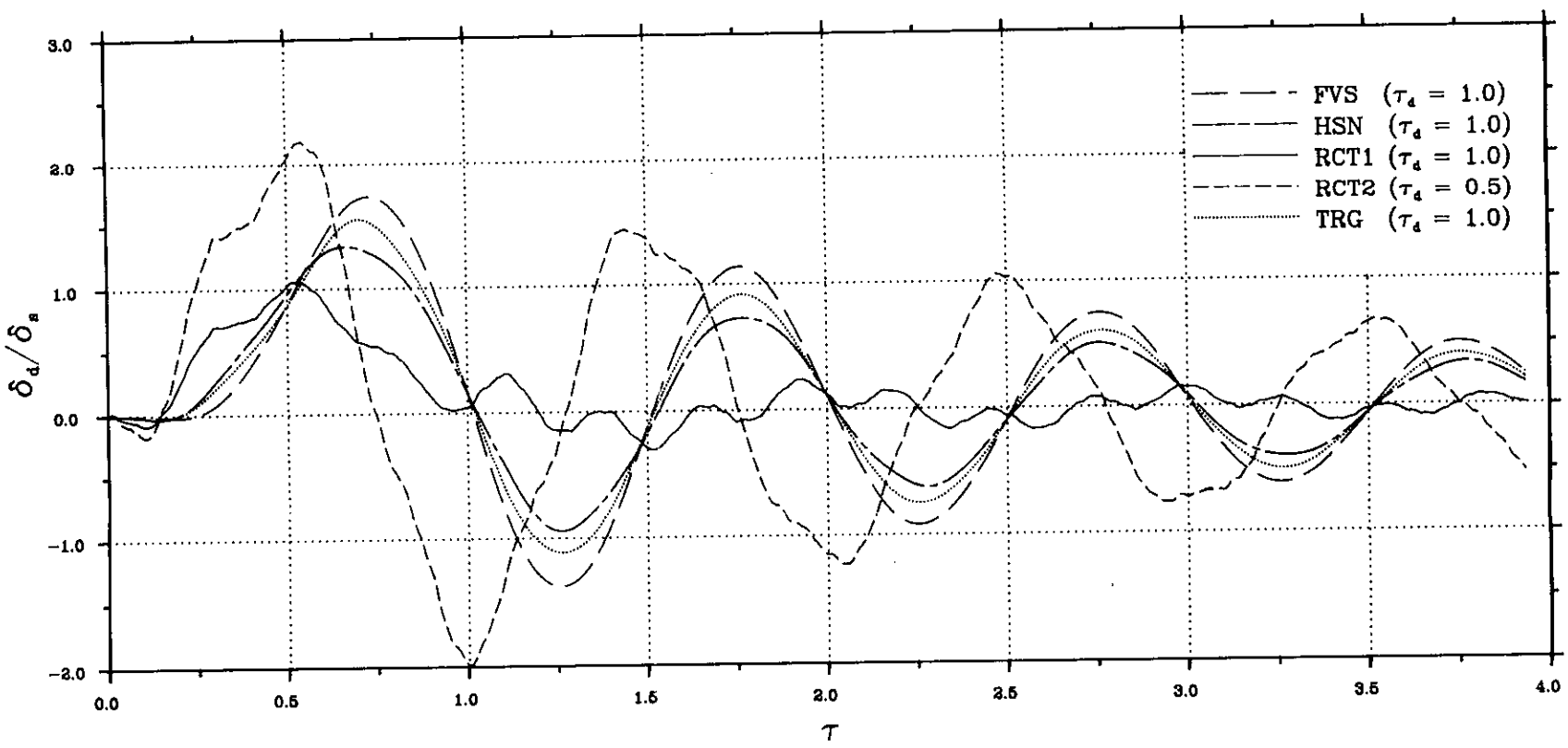

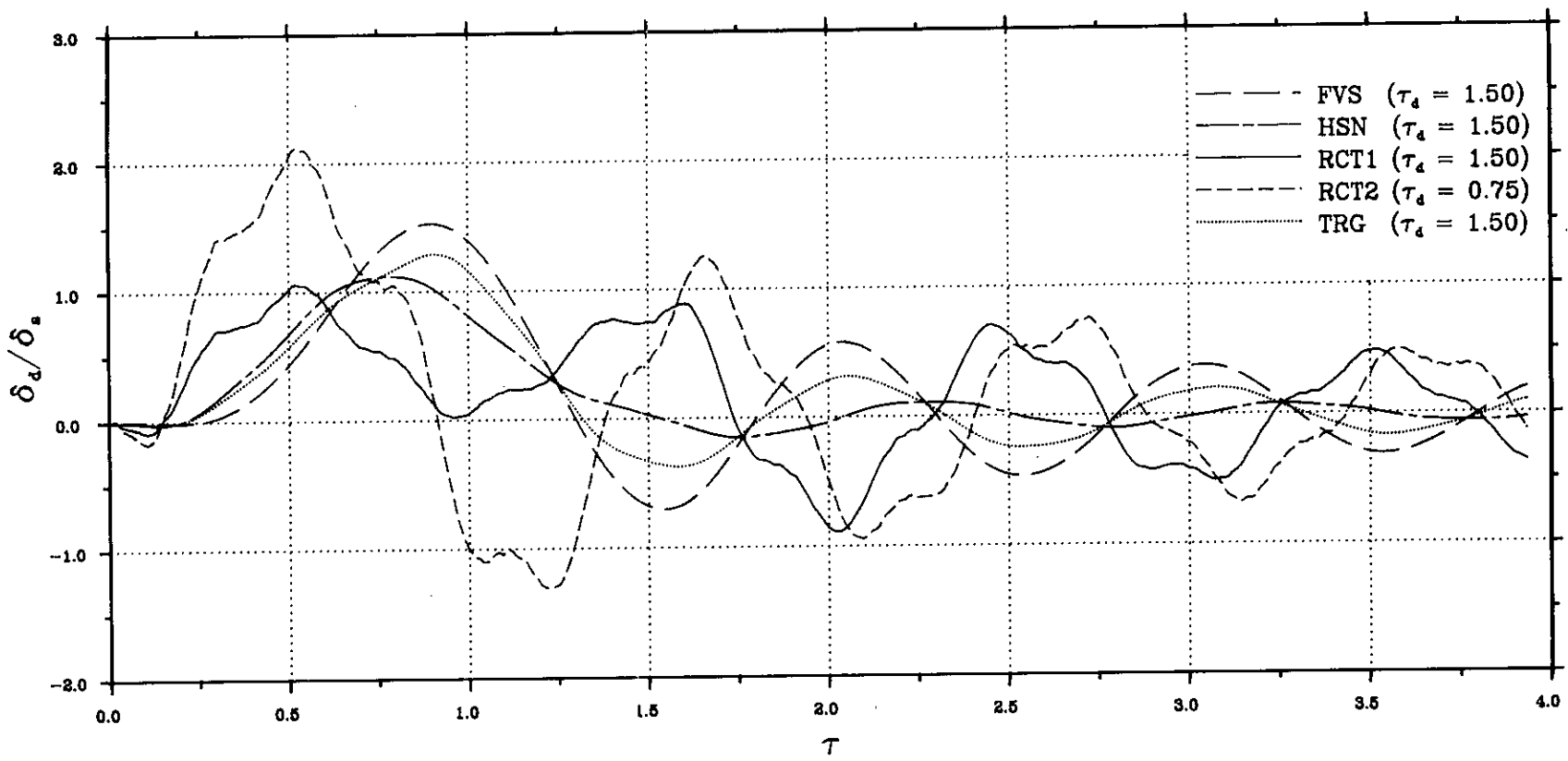

FIG. 3.21(b)–RESPONSE–TIME HISTORY TO VARIOUS SYMMETRICAL PULSES OF EQUAL IMPULSE AREA, FOR DIFFERENT VALUES OF PULSE DURATION
––MERIDIONAL DIRECTION––

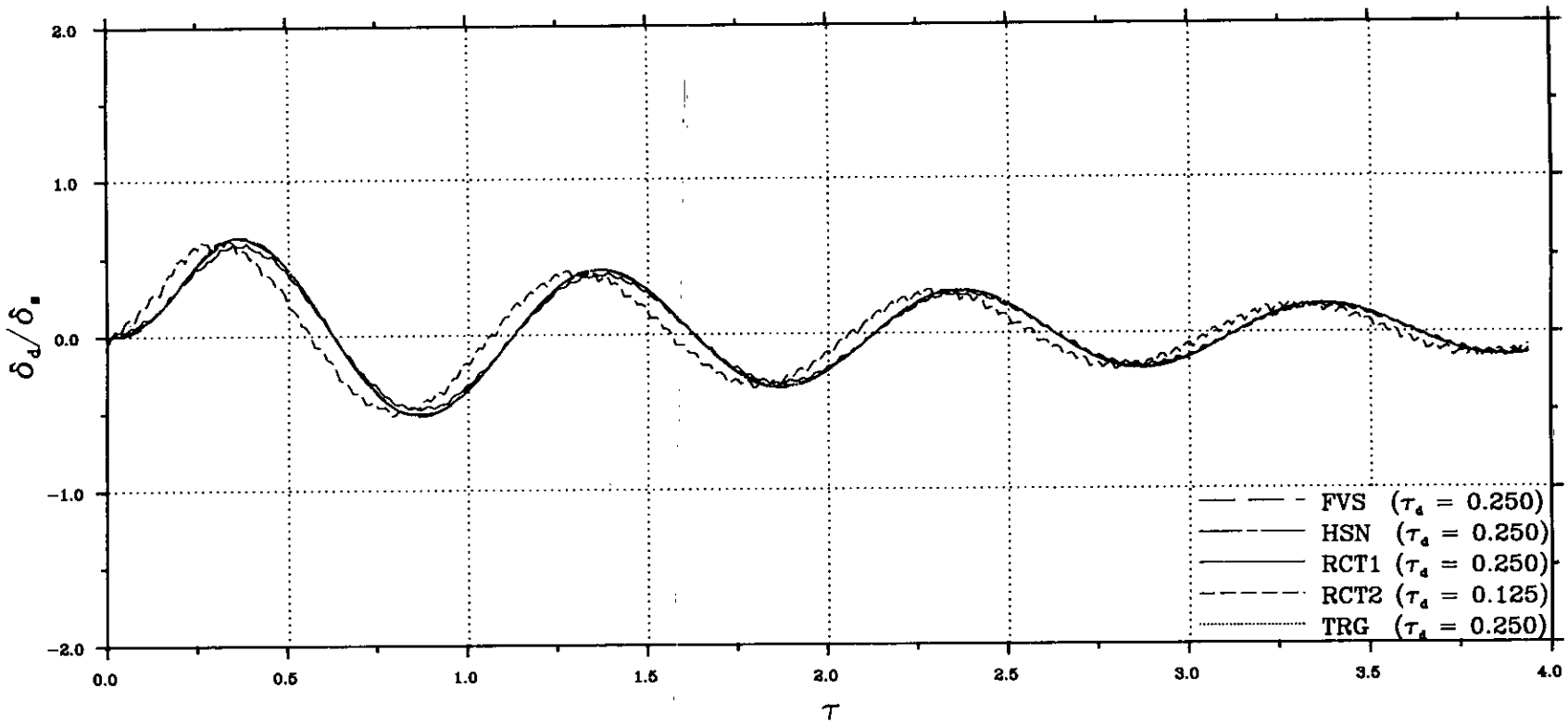

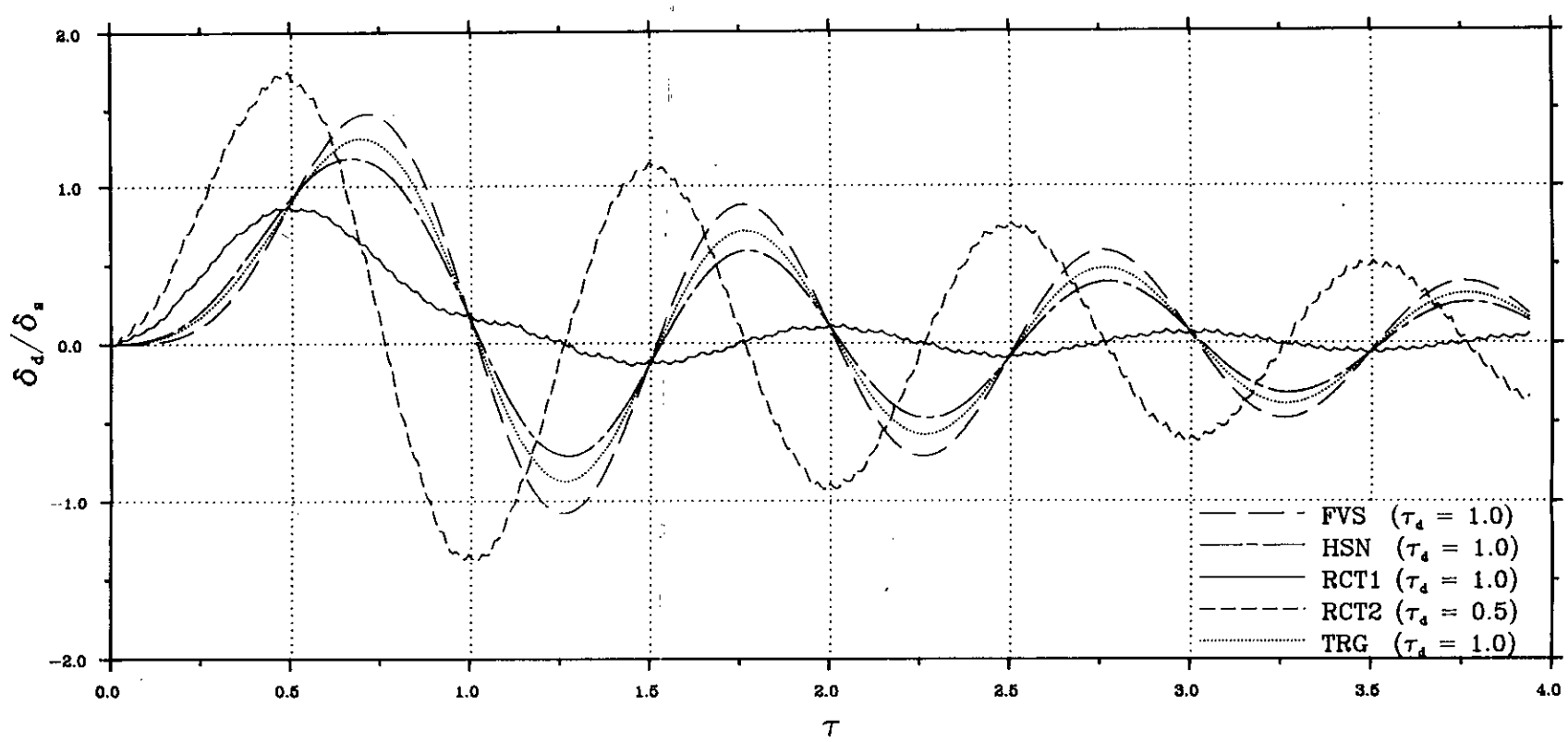

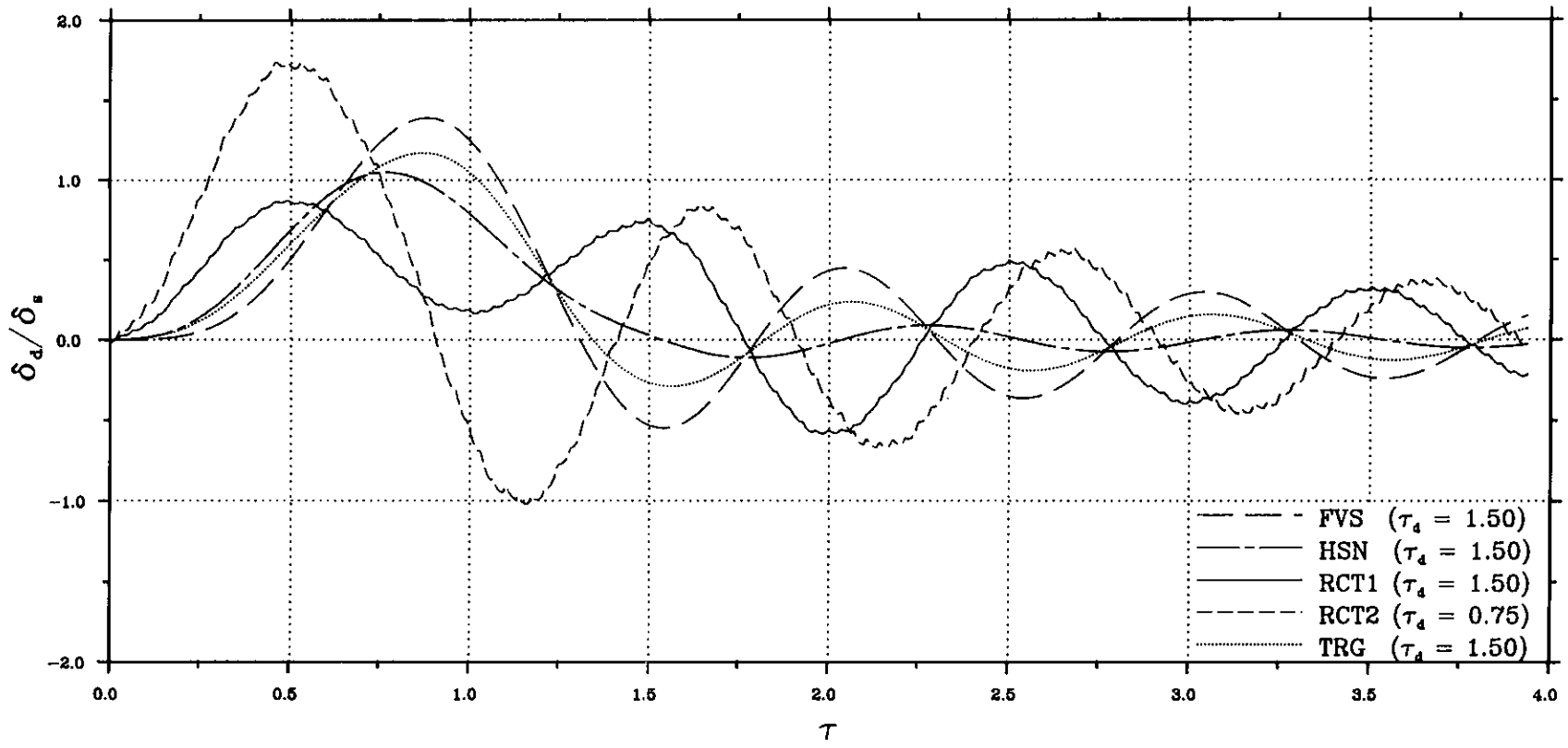

FIG. 3.21(c)–RESPONSE–TIME HISTORY TO VARIOUS SYMMETRICAL PULSES OF EQUAL IMPULSE AREA, FOR DIFFERENT VALUES OF PULSE DURATION --CIRCUMFERENTIAL DIRECTION--

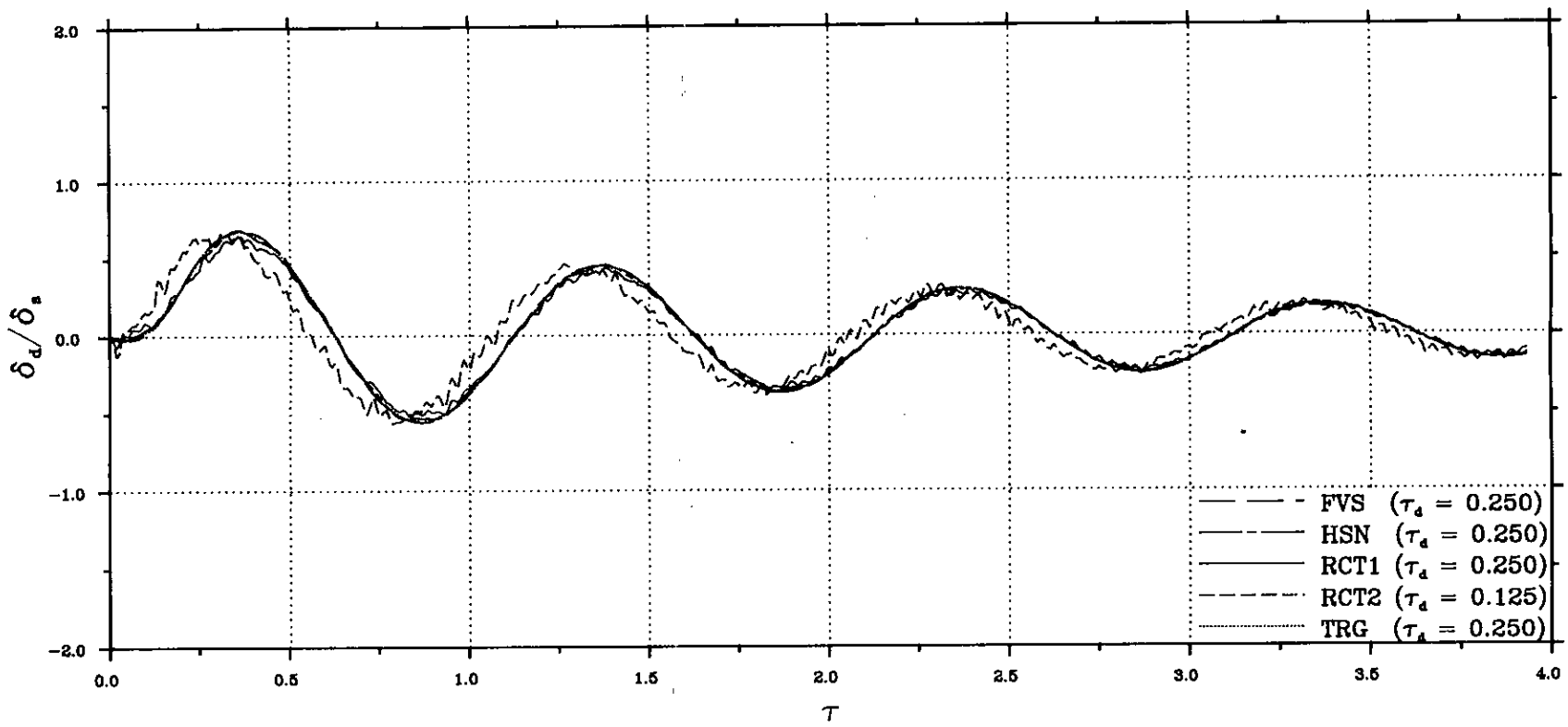

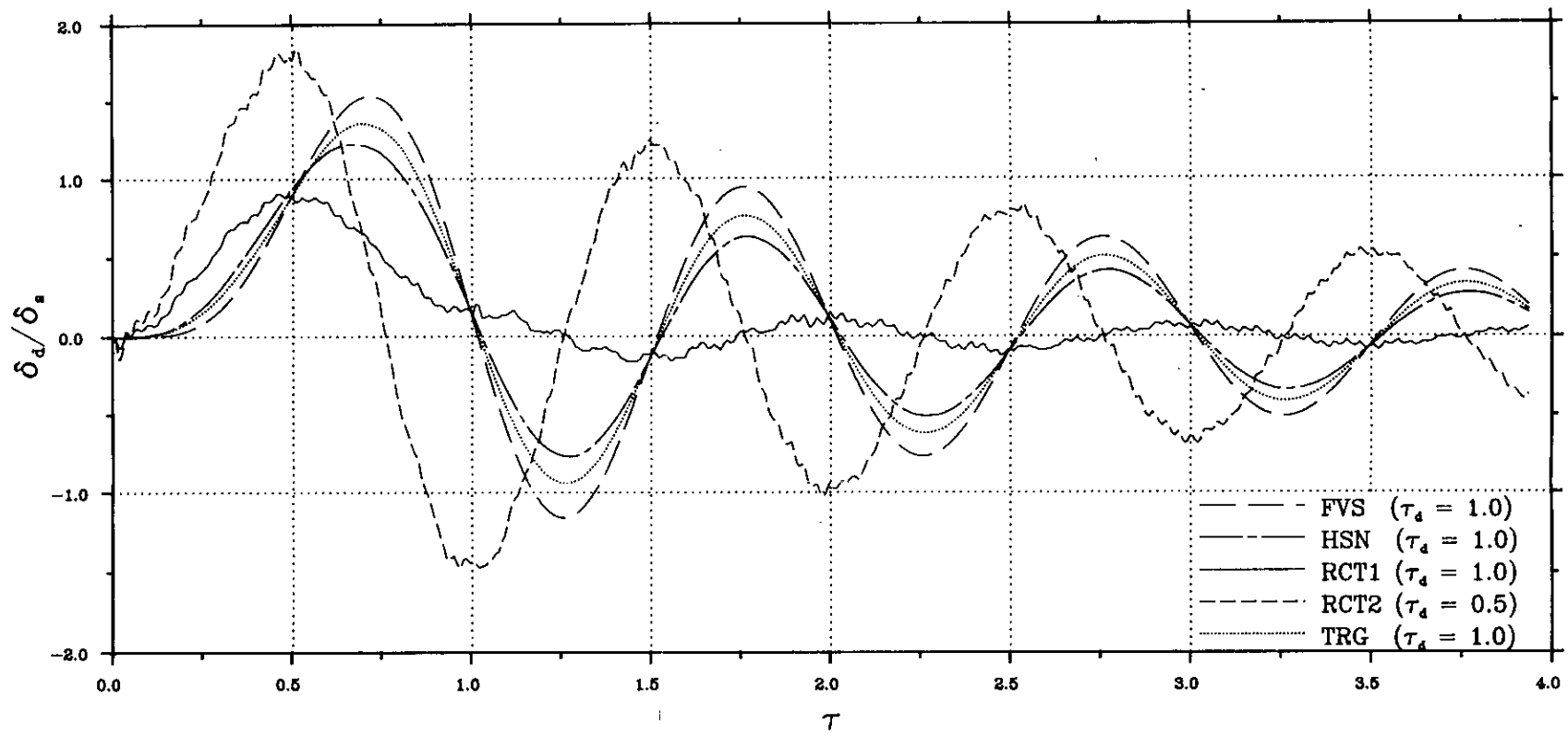

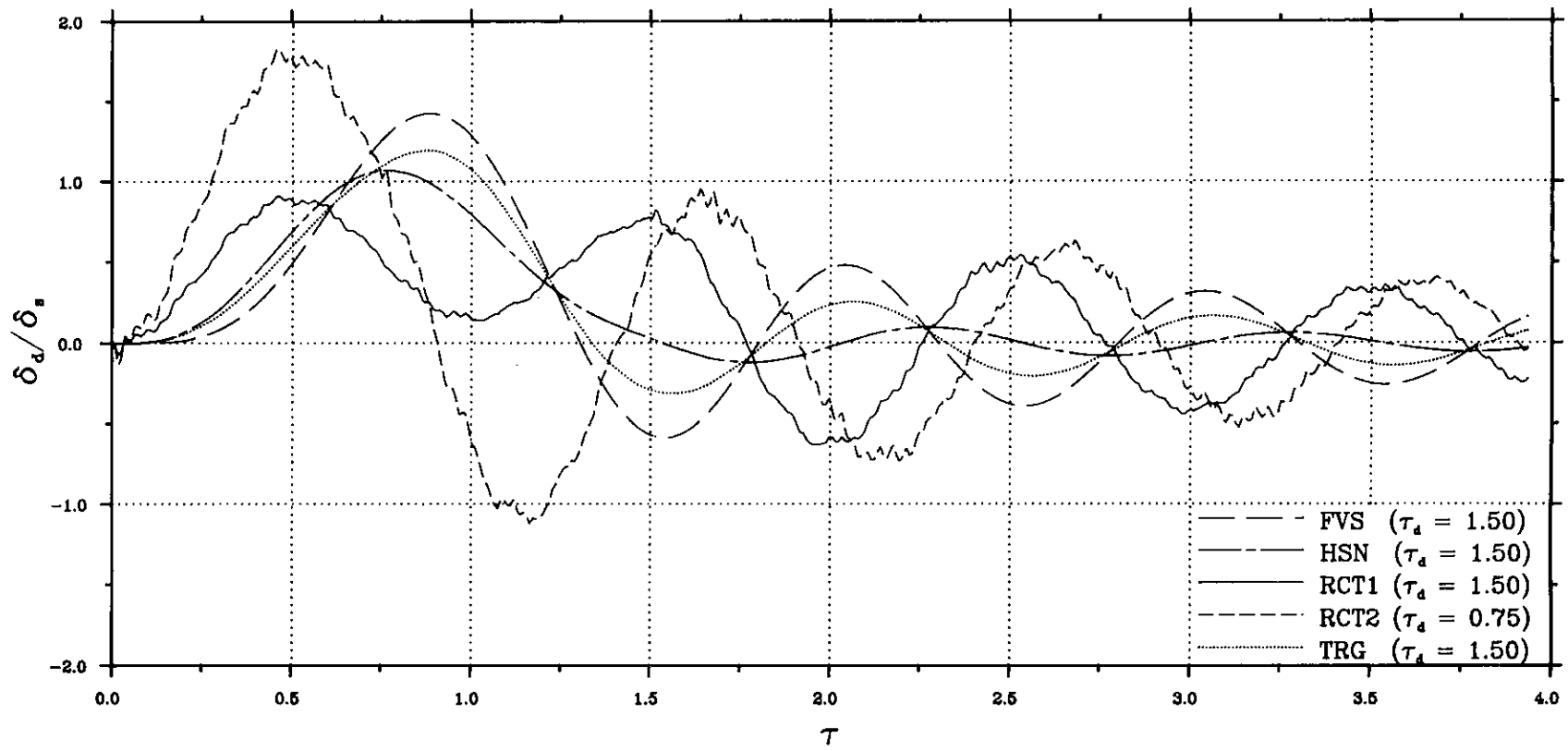

FIG. 3.21(d)–RESPONSE–TIME HISTORY TO VARIOUS SYMMETRICAL PULSES OF EQUAL IMPULSE AREA, FOR DIFFERENT VALUES OF PULSE DURATION --EDGE ROTATION--

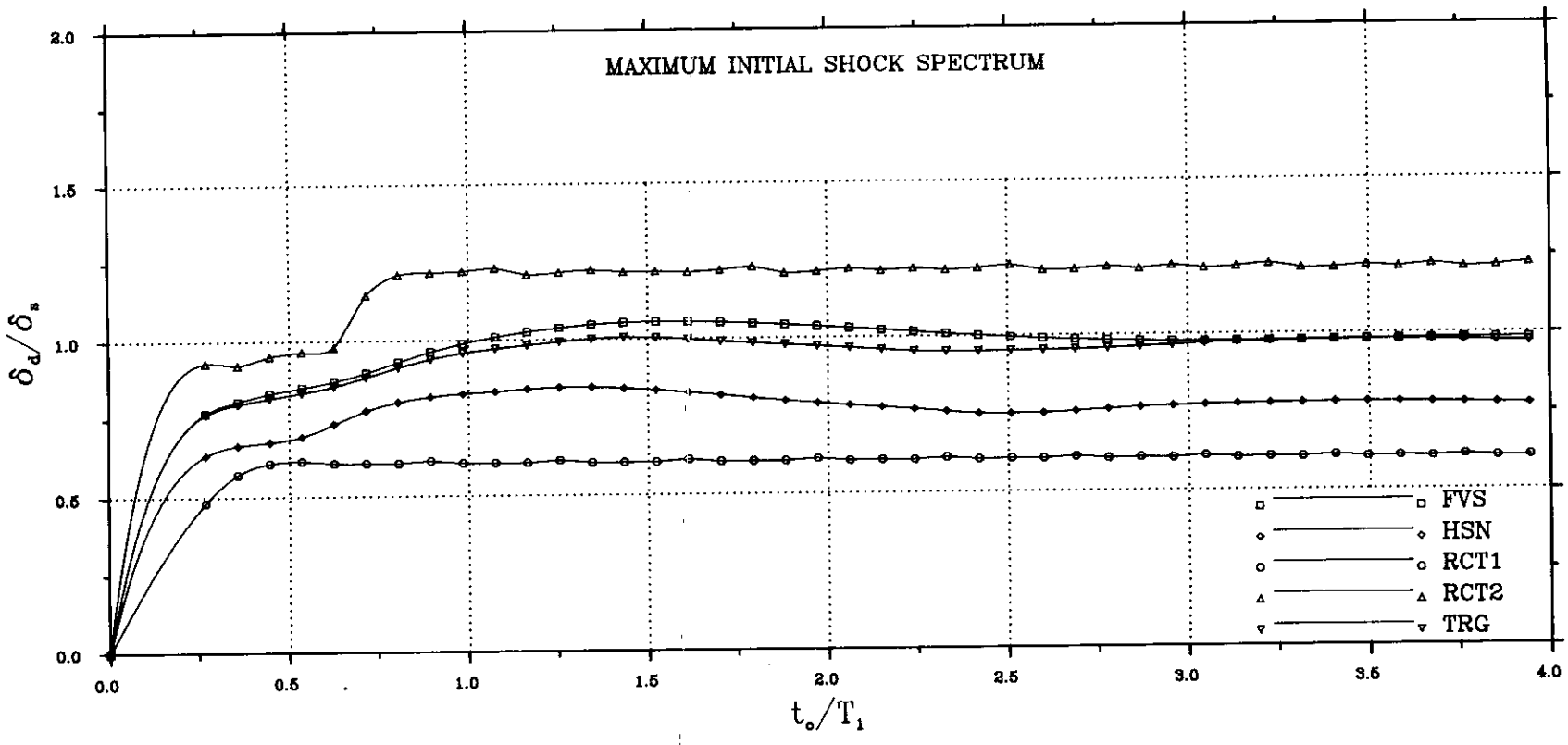

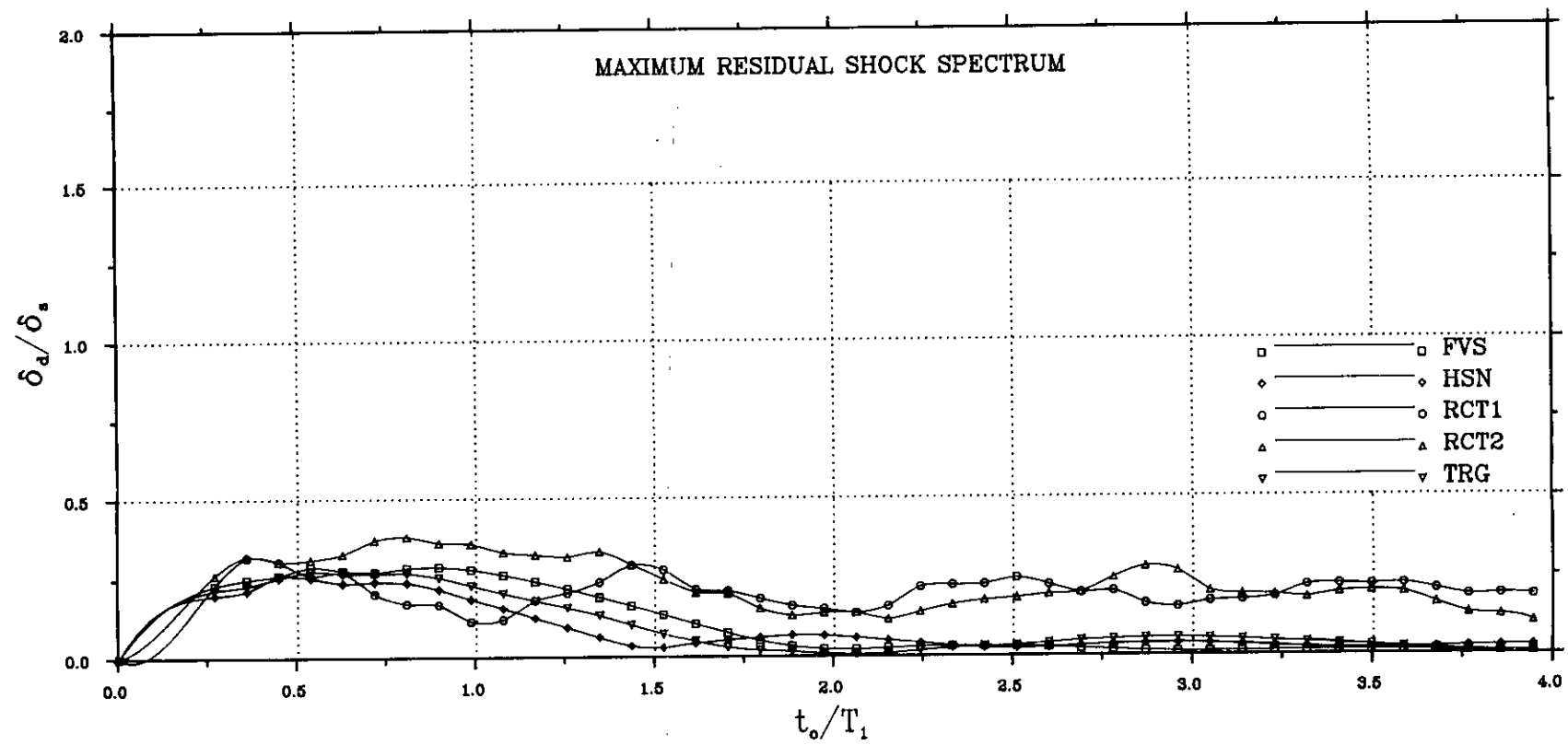

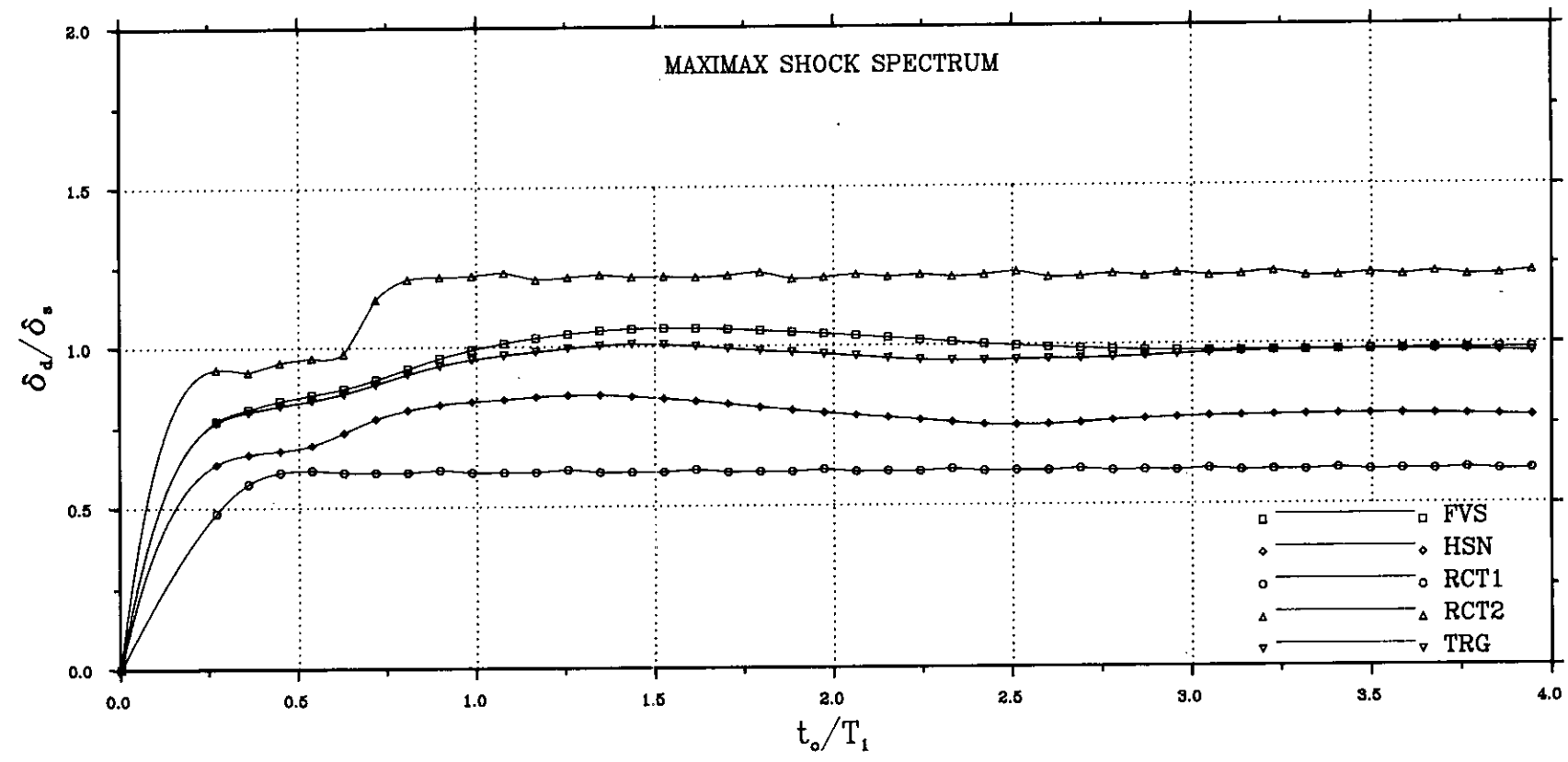

FIG. 3.22(a)–RESPONSE SPECTRA FOR VARIOUS SYMMETRICAL PULSES OF EQUAL IMPULSE AREA --NORMAL DIRECTION--

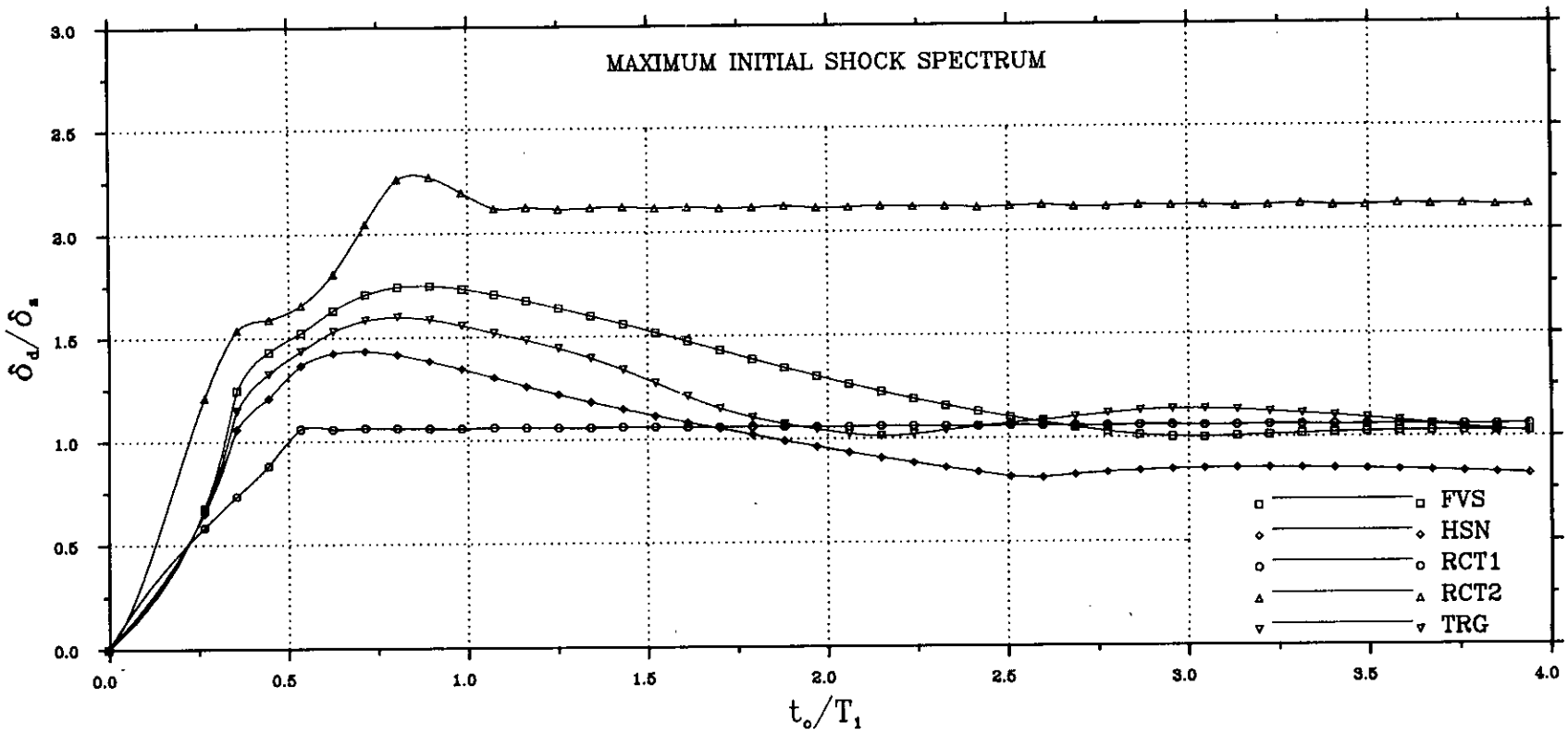

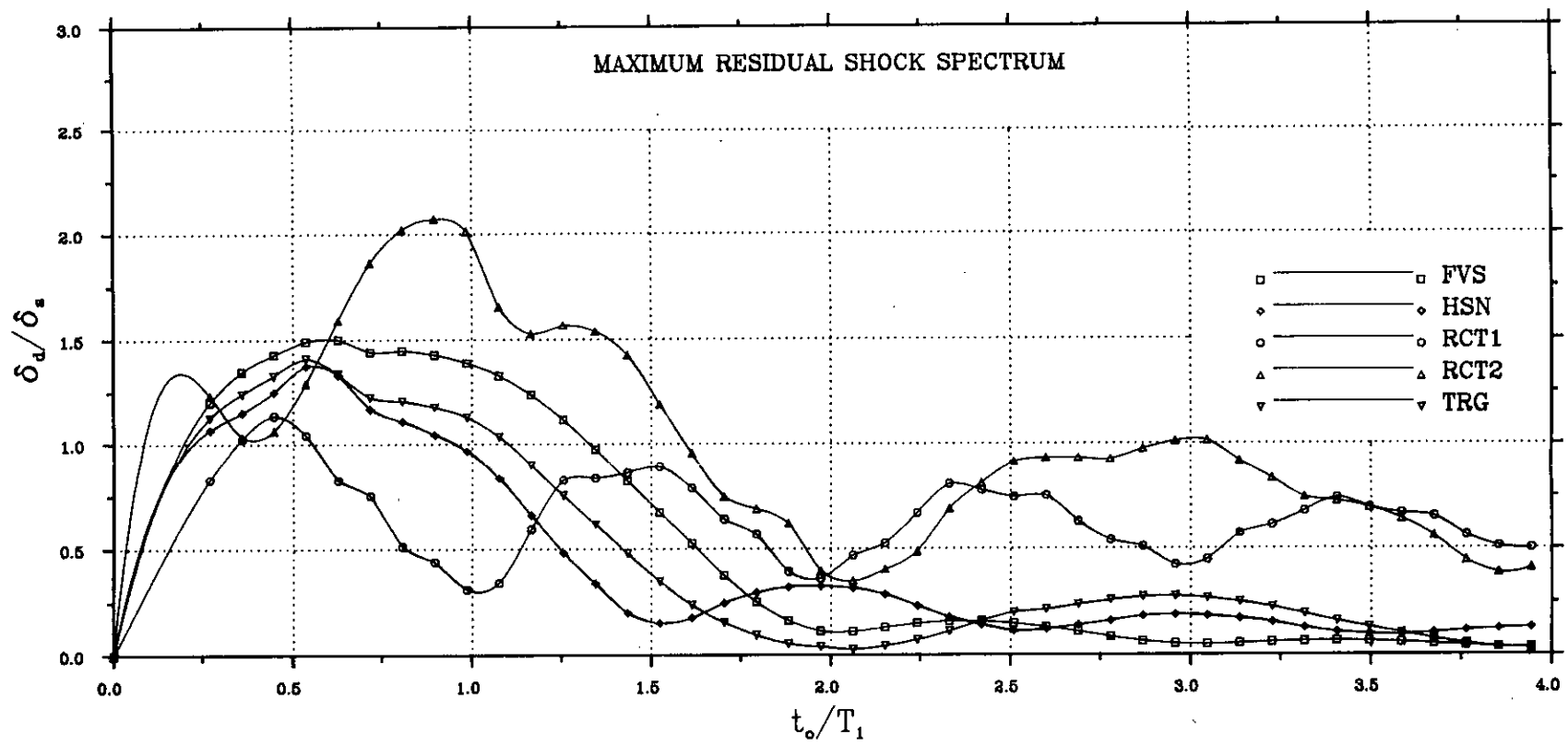

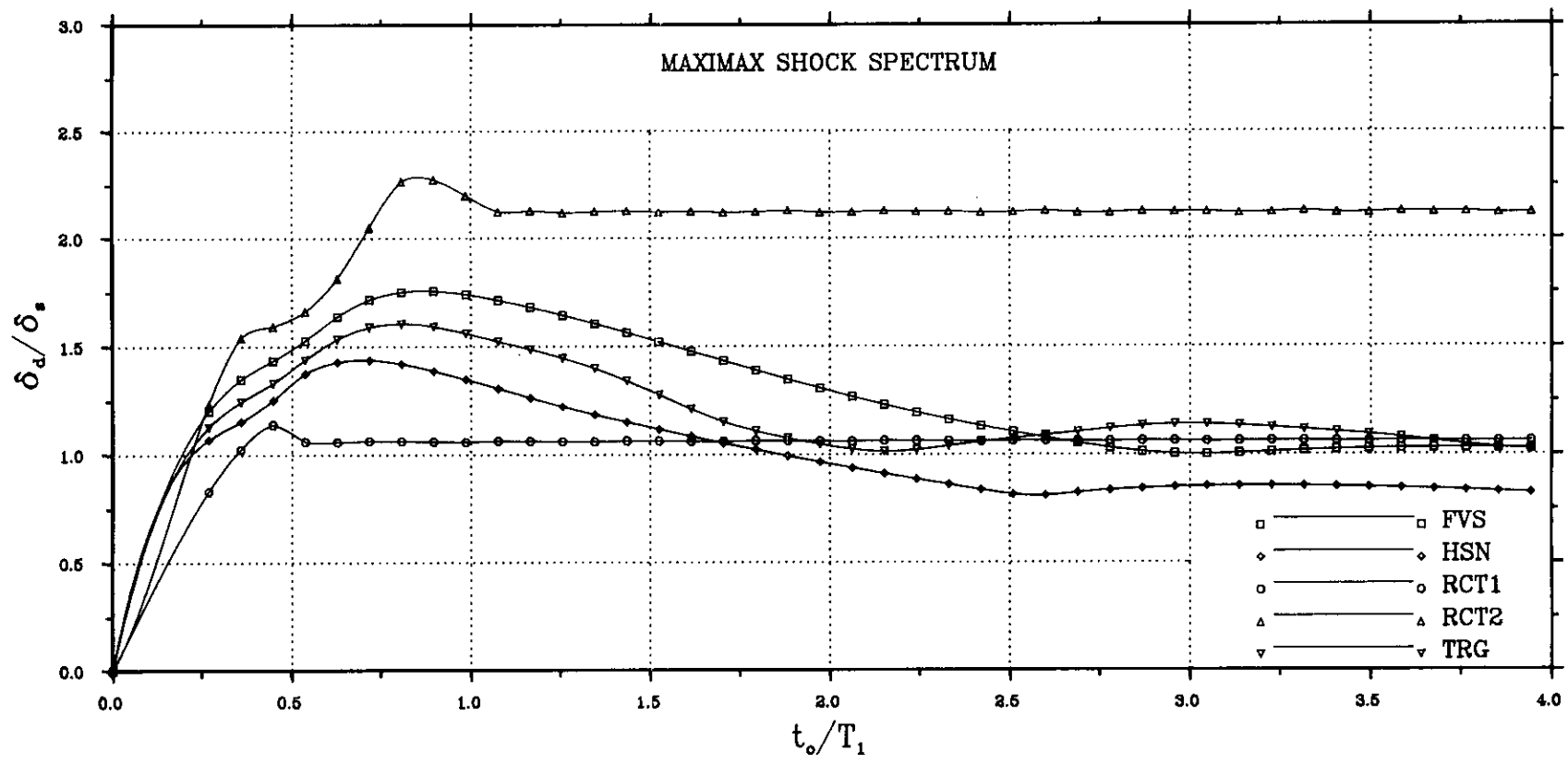

FIG. 3.22(b)–RESPONSE SPECTRA FOR VARIOUS SYMMETRICAL PULSES OF EQUAL IMPULSE AREA --MERIDIONAL DIRECTION--

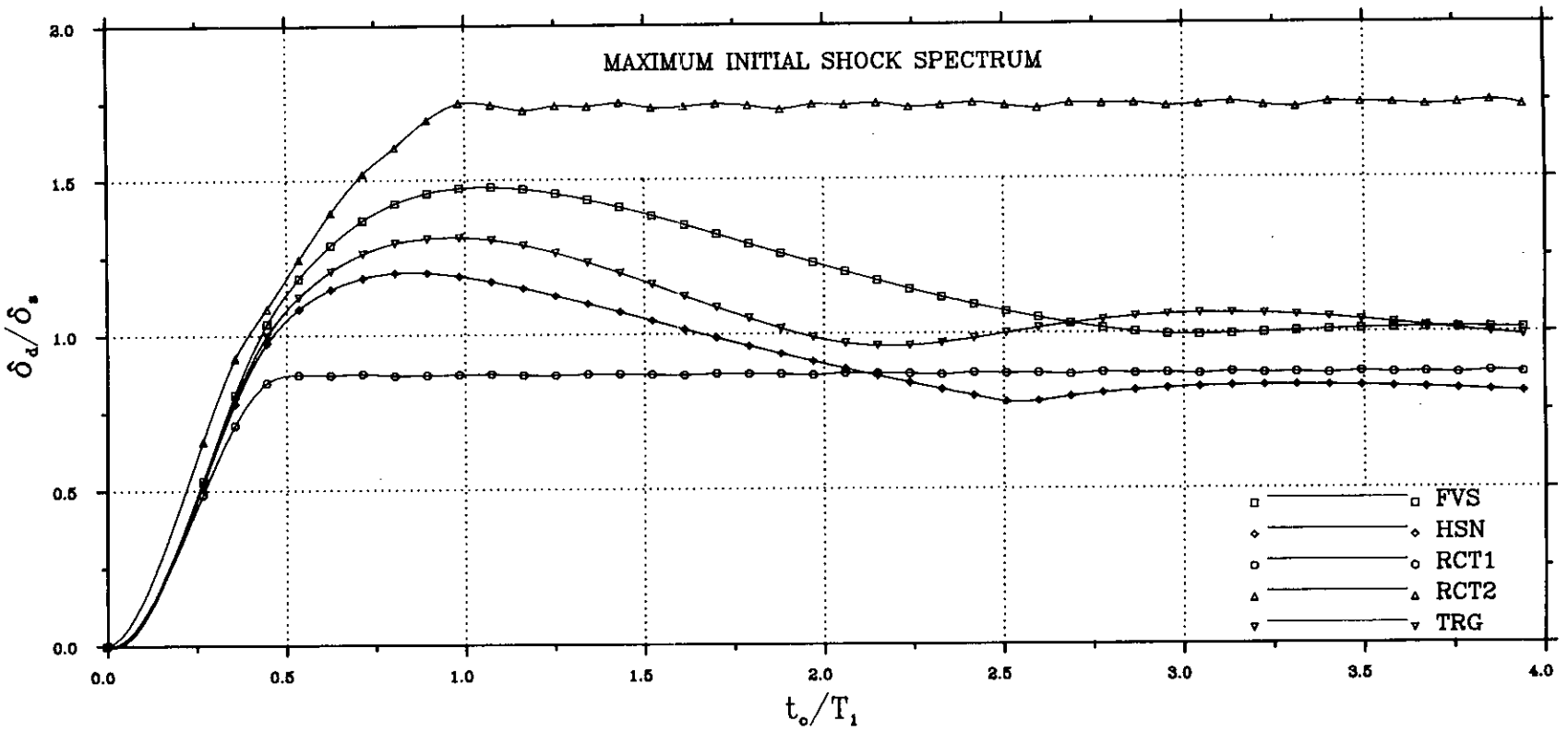

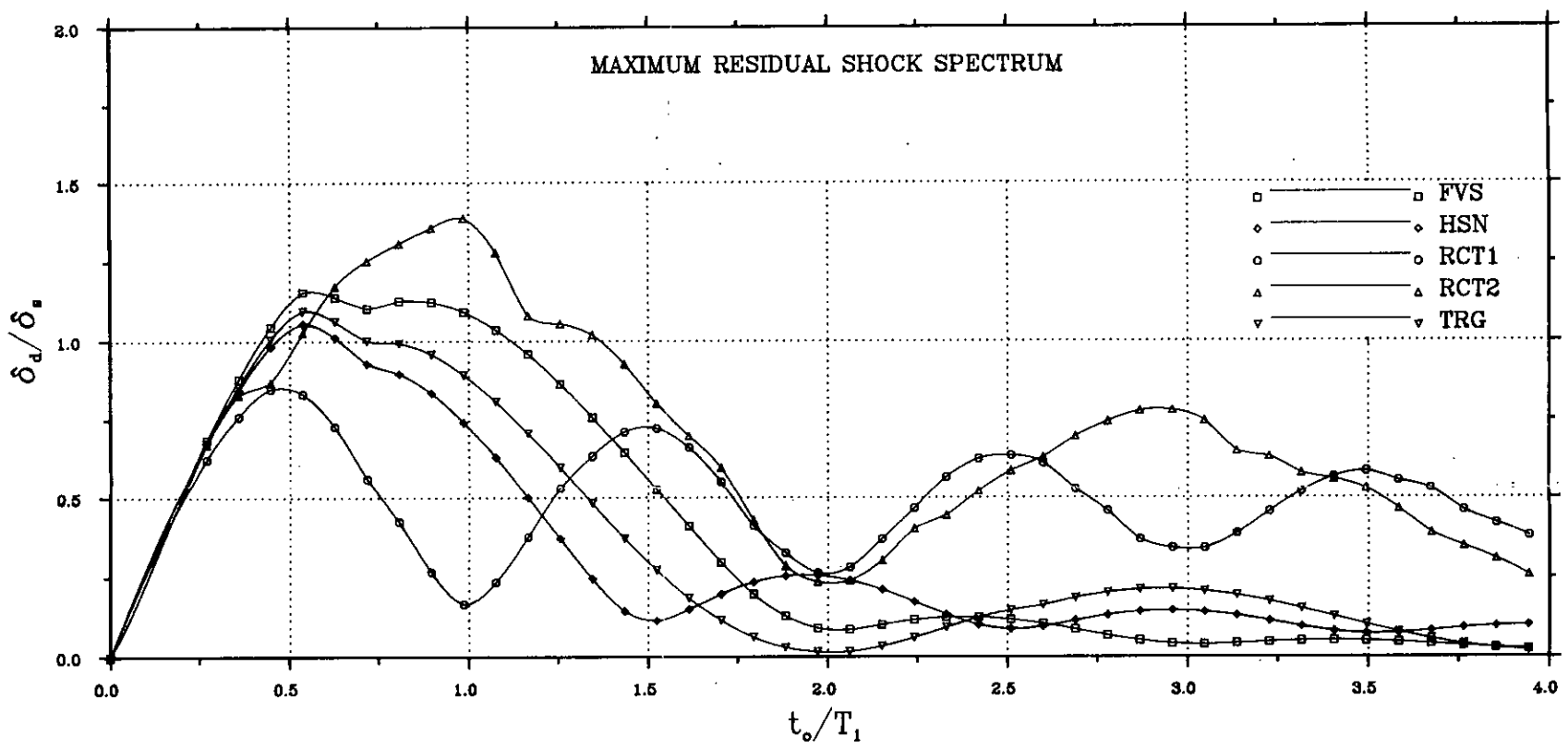

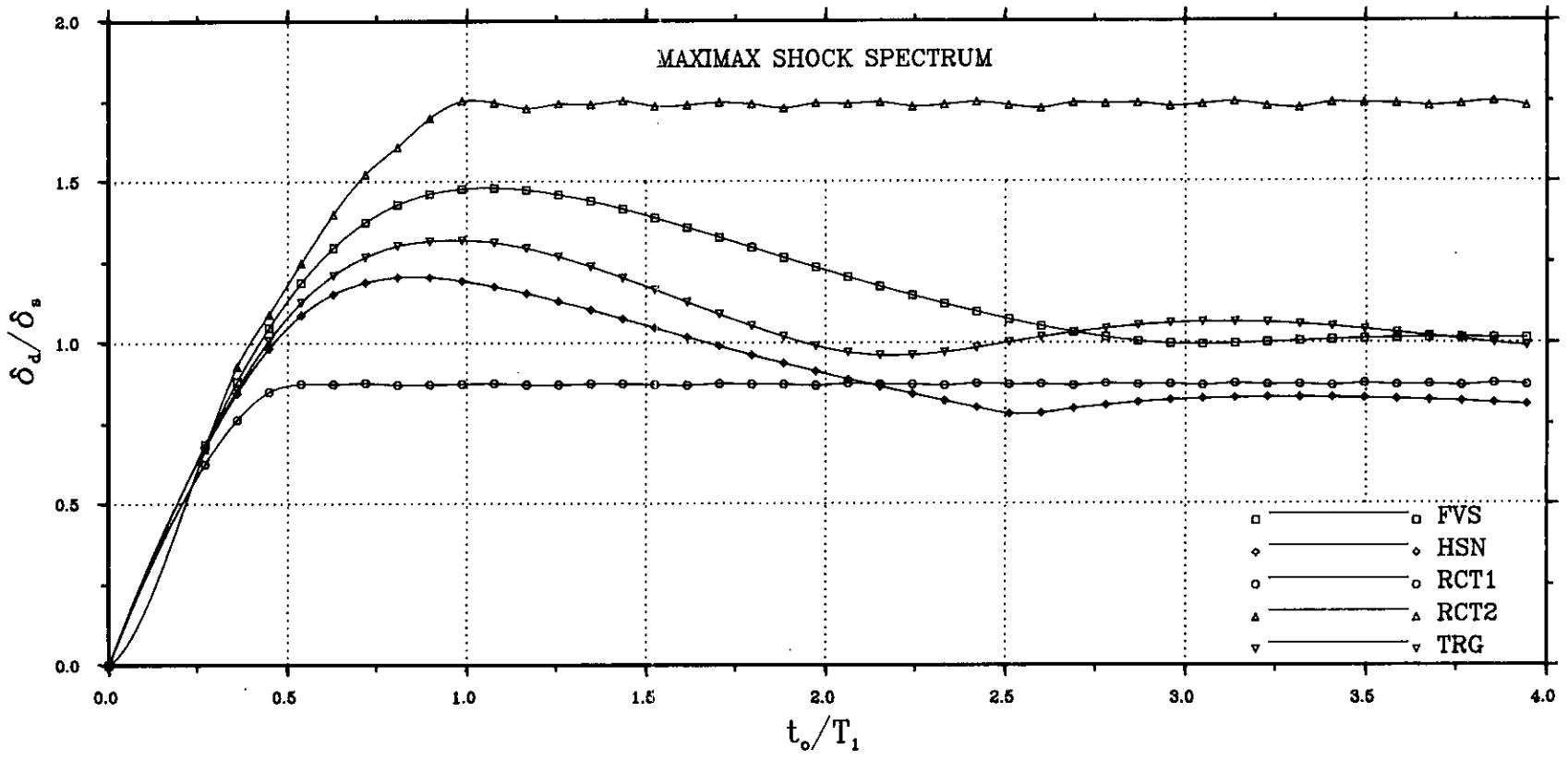

FIG. 3.22(c)–RESPONSE SPECTRA FOR VARIOUS SYMMETRICAL PULSES OF EQUAL IMPULSE AREA --CIRCUMFERENTIAL DIRECTION--

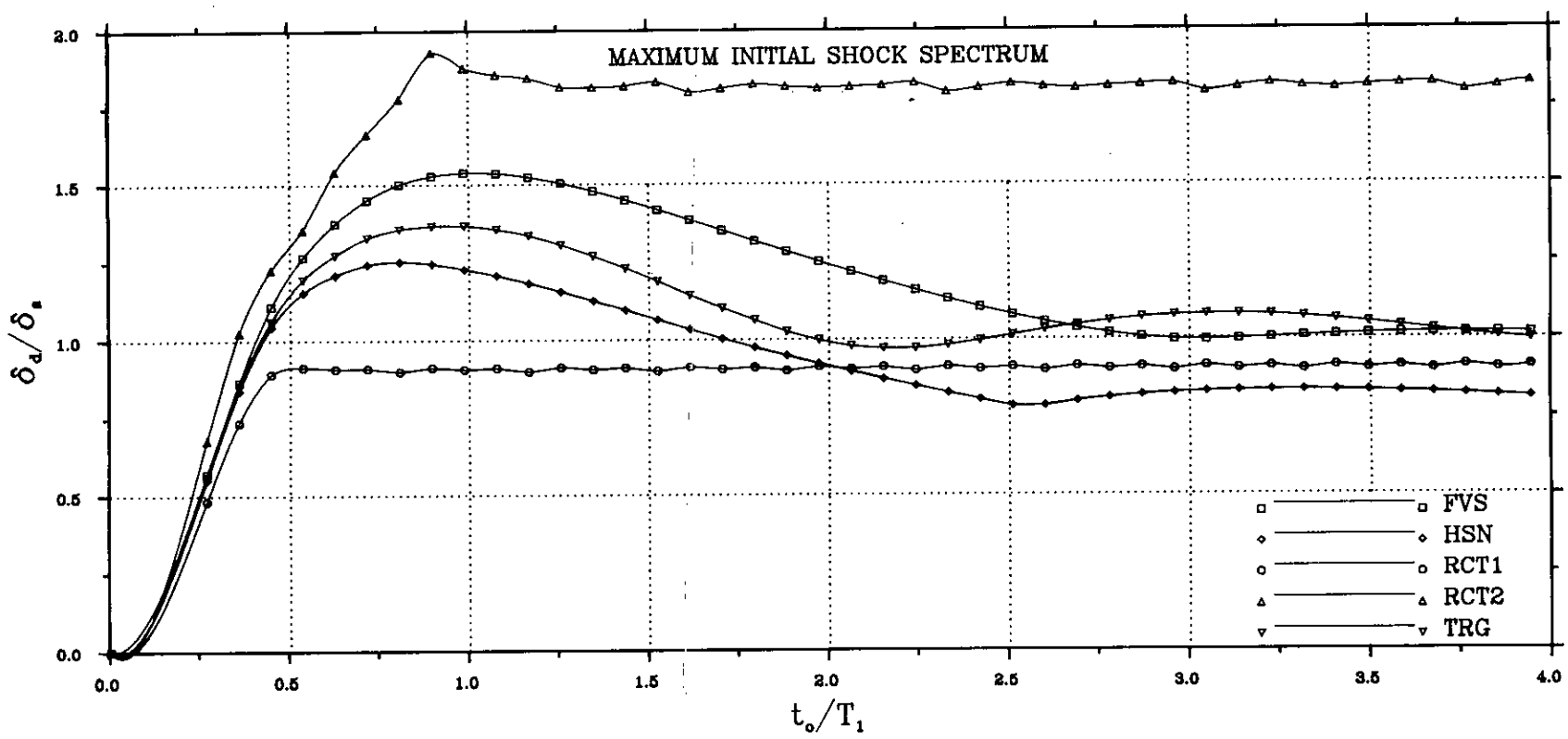

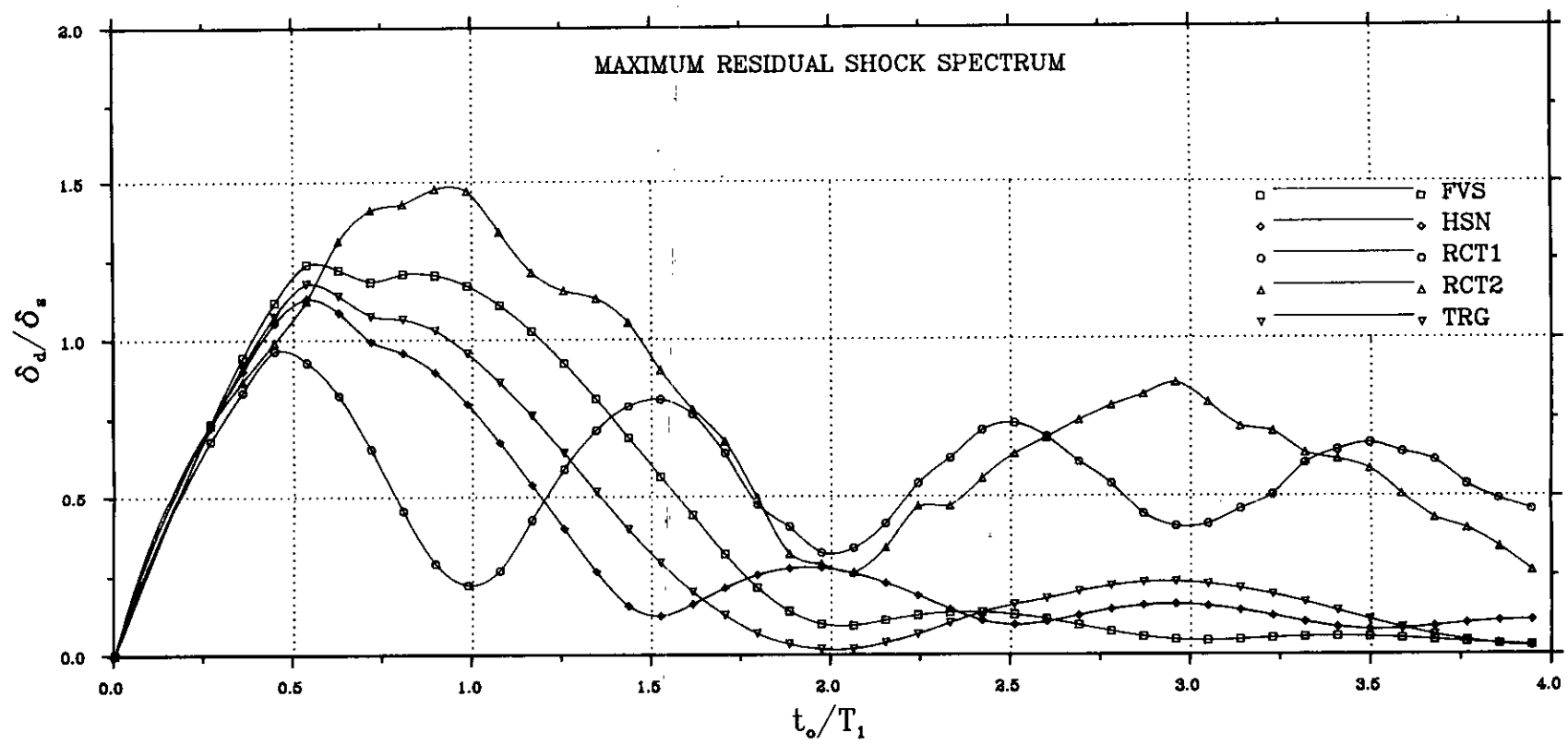

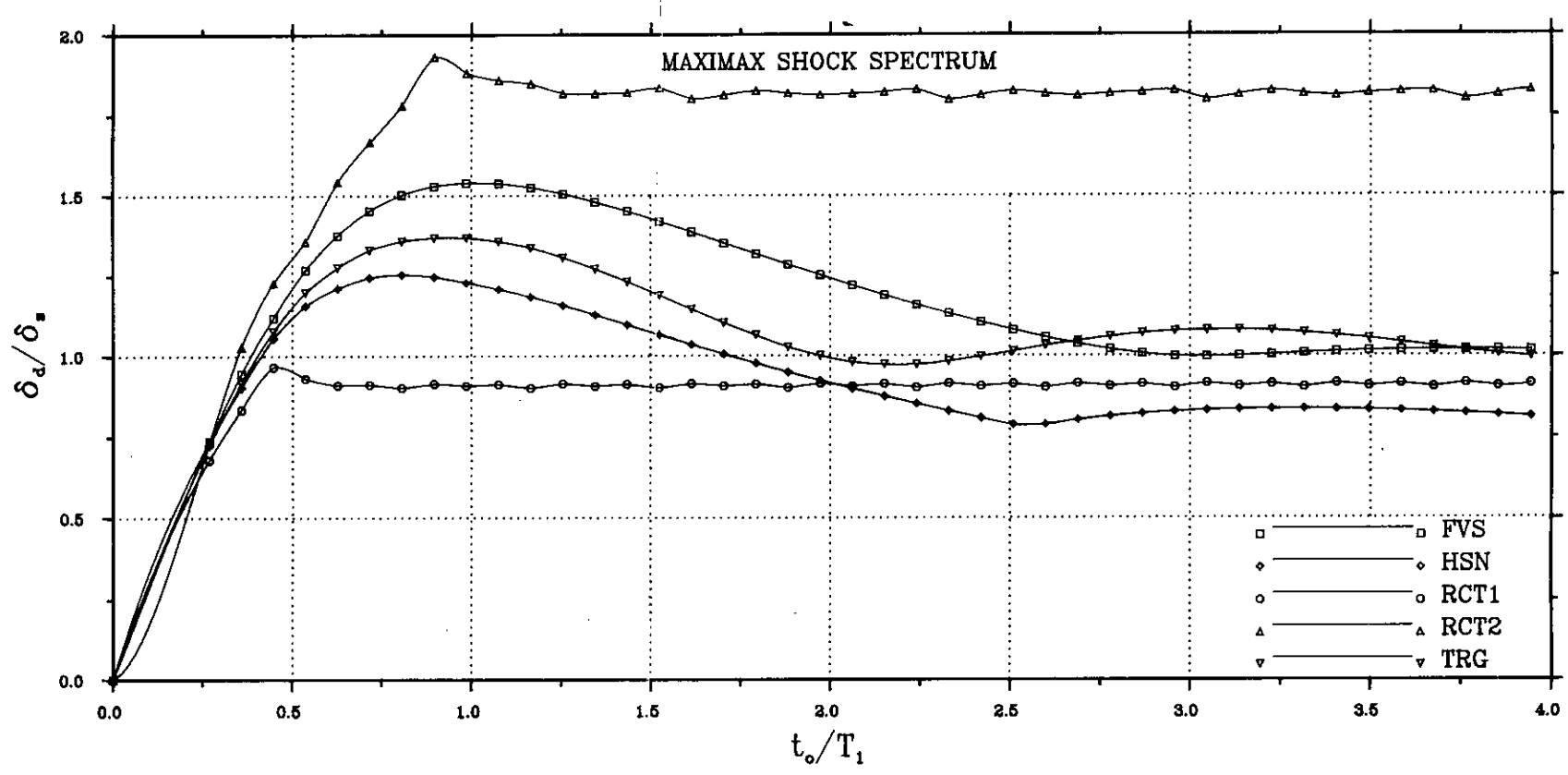

FIG. 3.22(d)–RESPONSE SPECTRA FOR VARIOUS SYMMETRICAL PULSES OF EQUAL IMPULSE AREA --EDGE ROTATION--

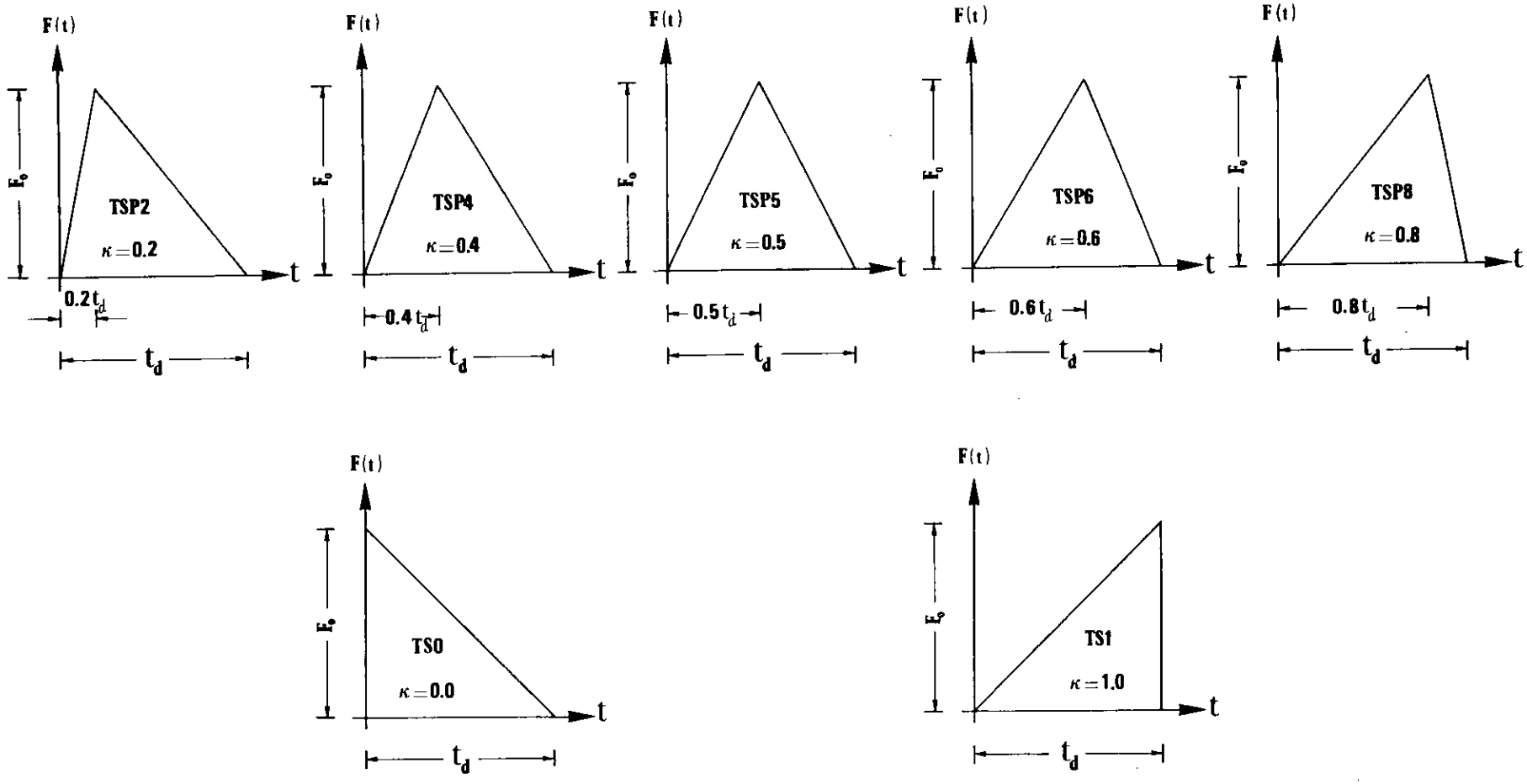

FIG. 3.23–DETAILS OF TRIANGULAR PULSES WITH DIFFERENT SKEWNESS FACTORS, κ, USED IN SHOCK RESPONSE ANALYSIS

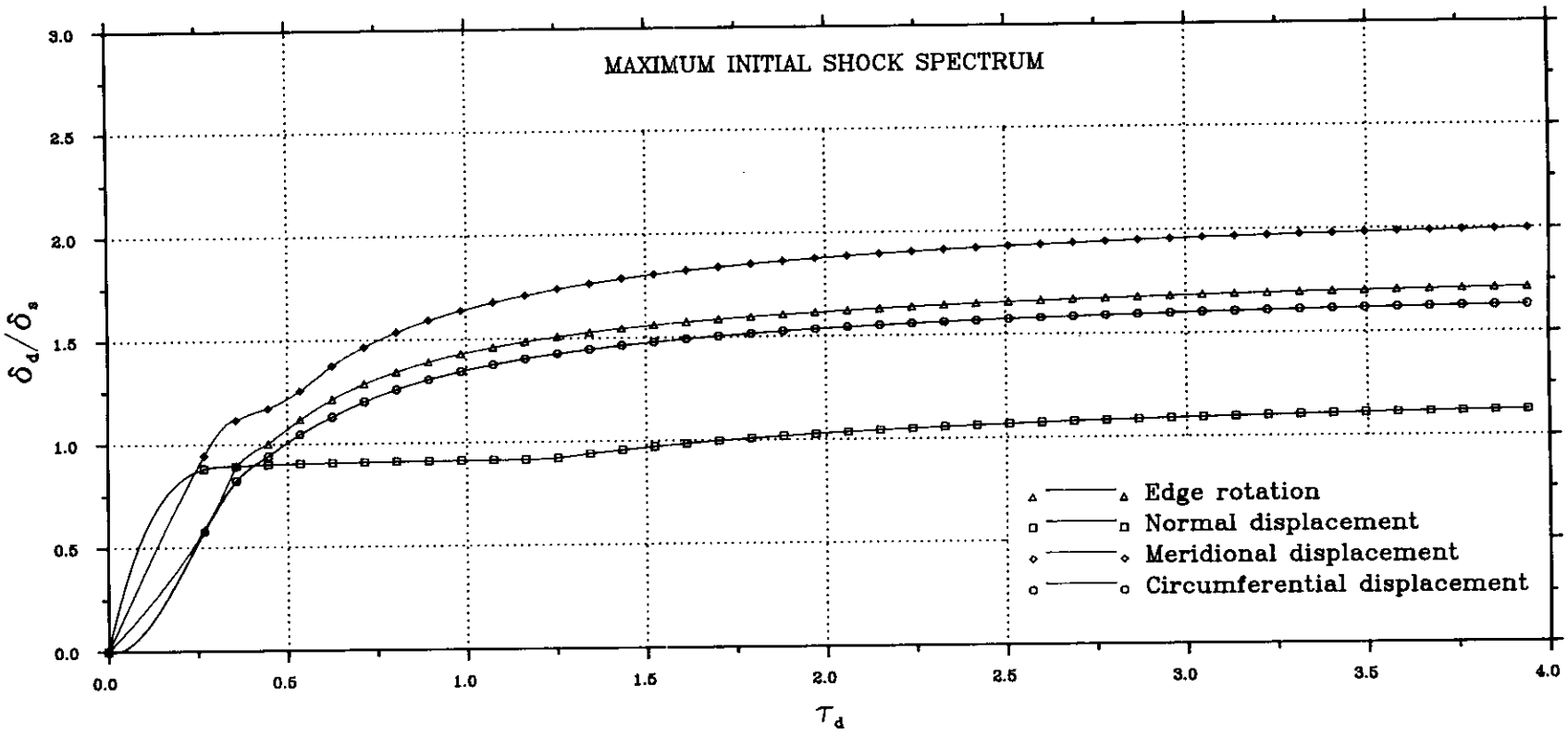

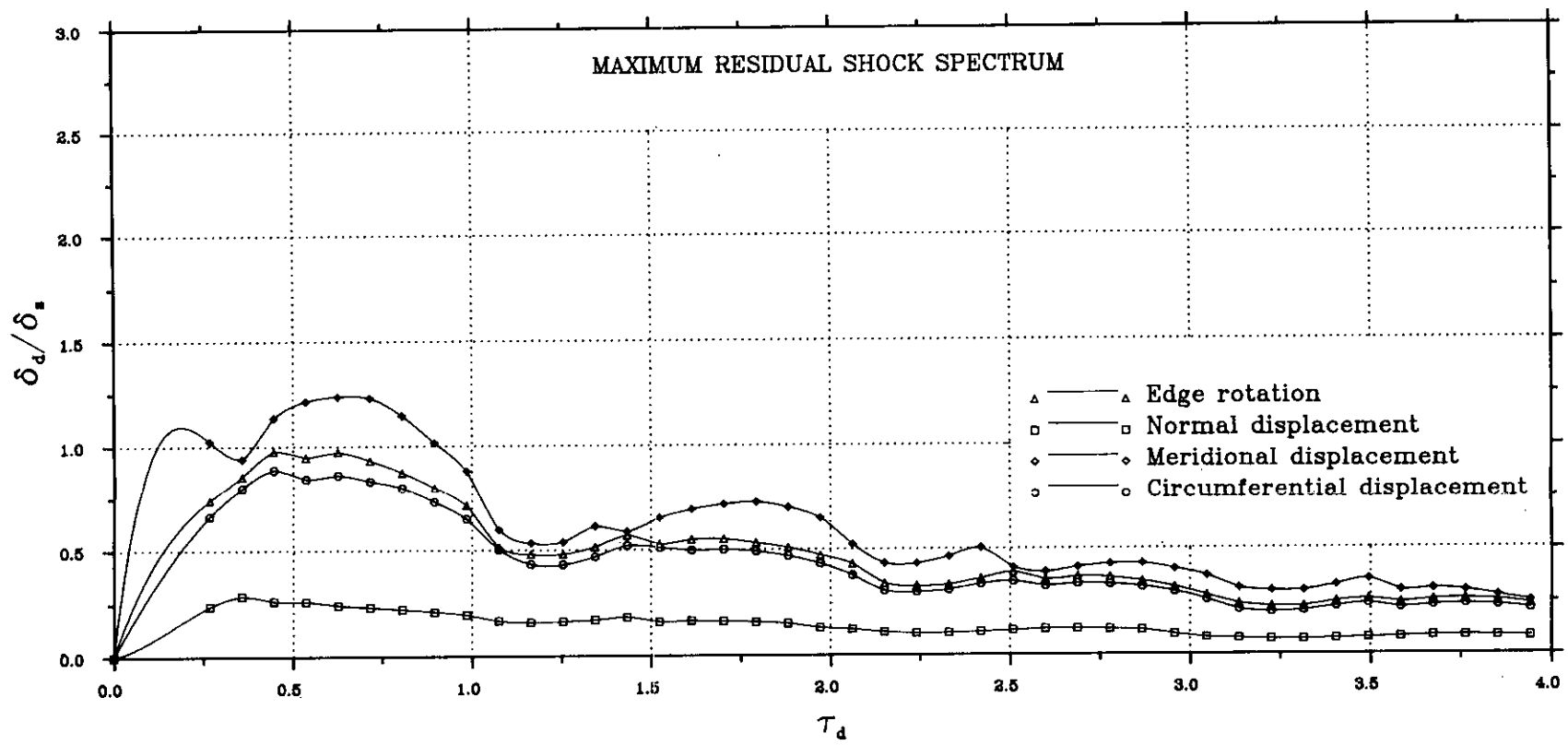

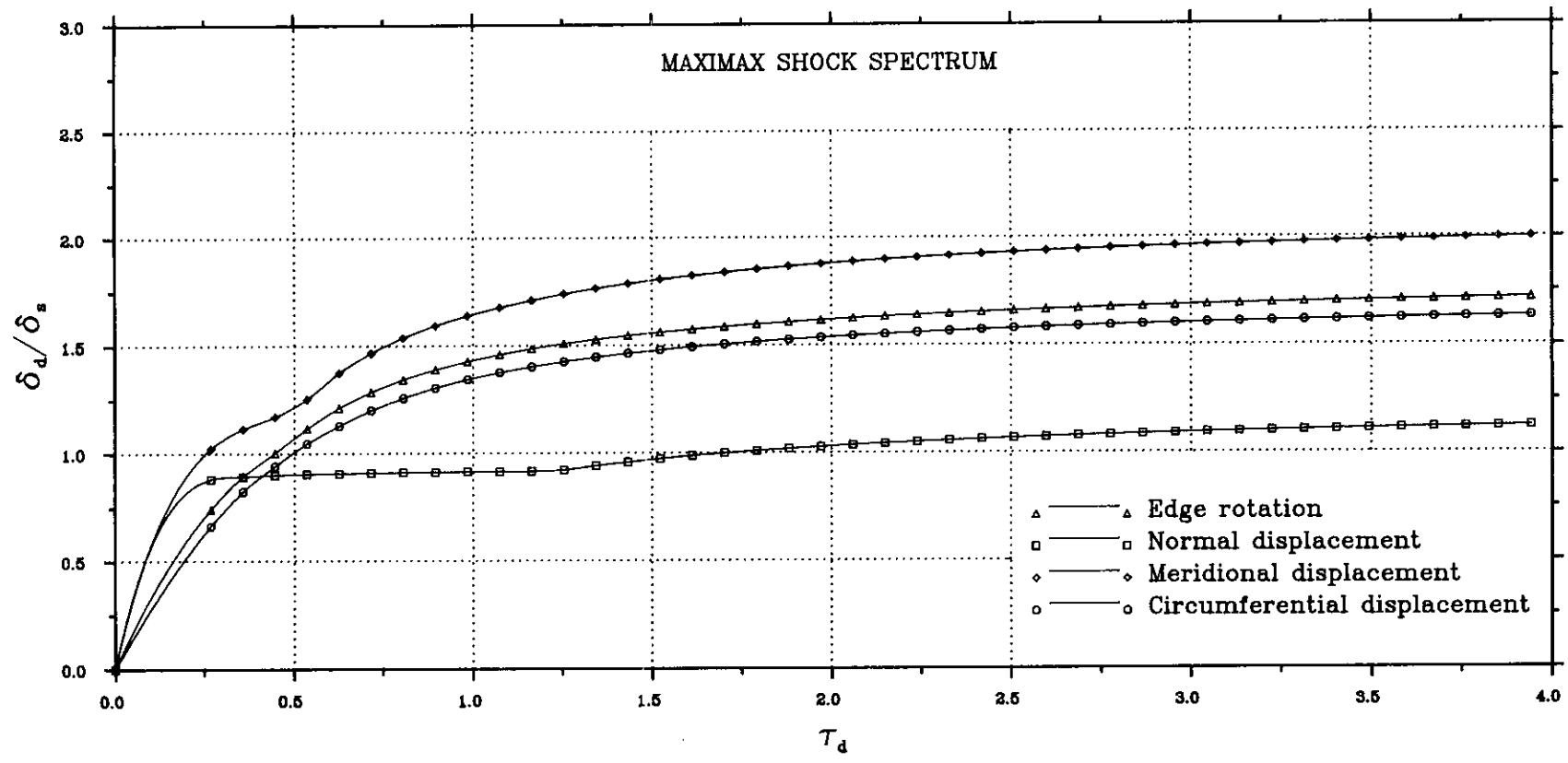

FIG. 3.24–EFFECT OF PULSE DURATION ON MAXIMUM RESPONSE SPECTRA (DLF) TO A TRIANGULAR PULSE --κ = 0.0--

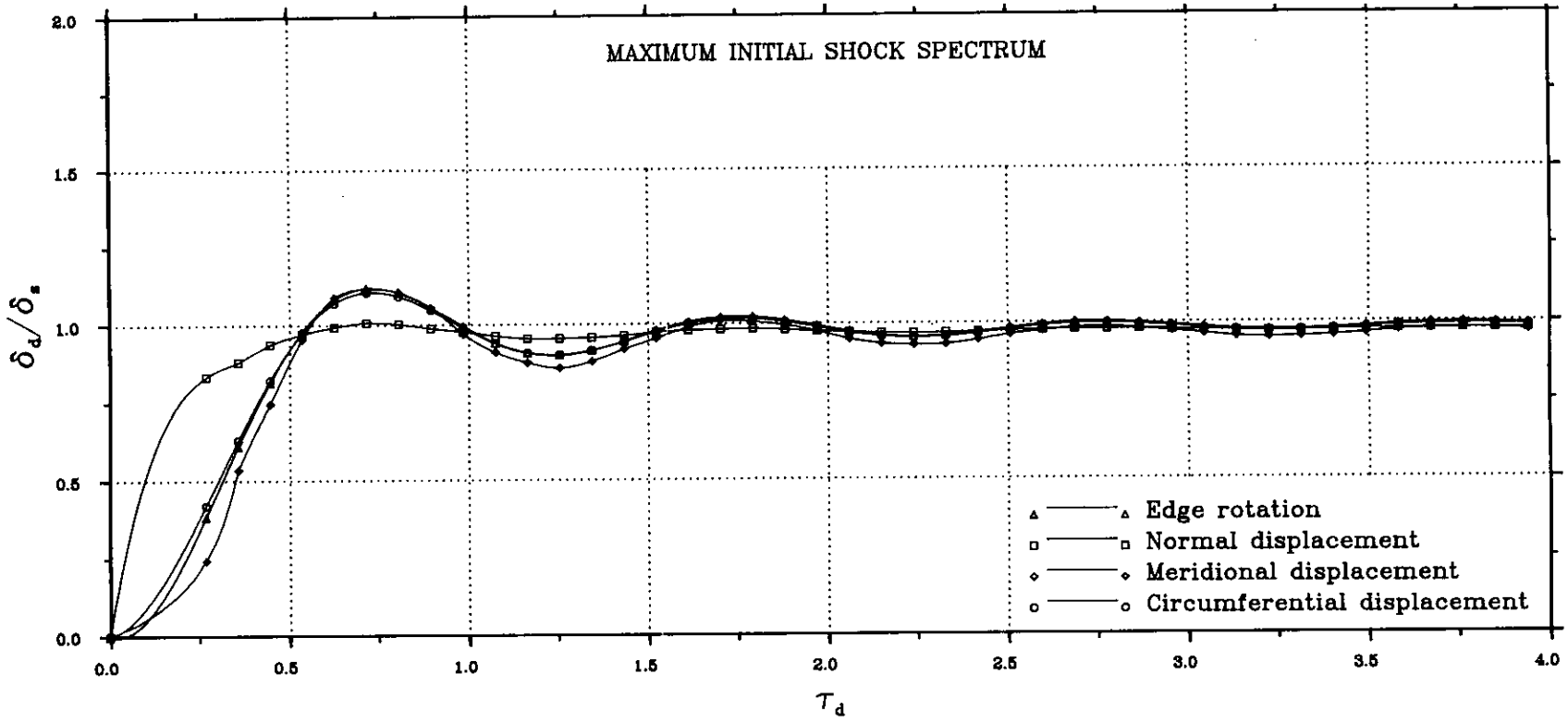

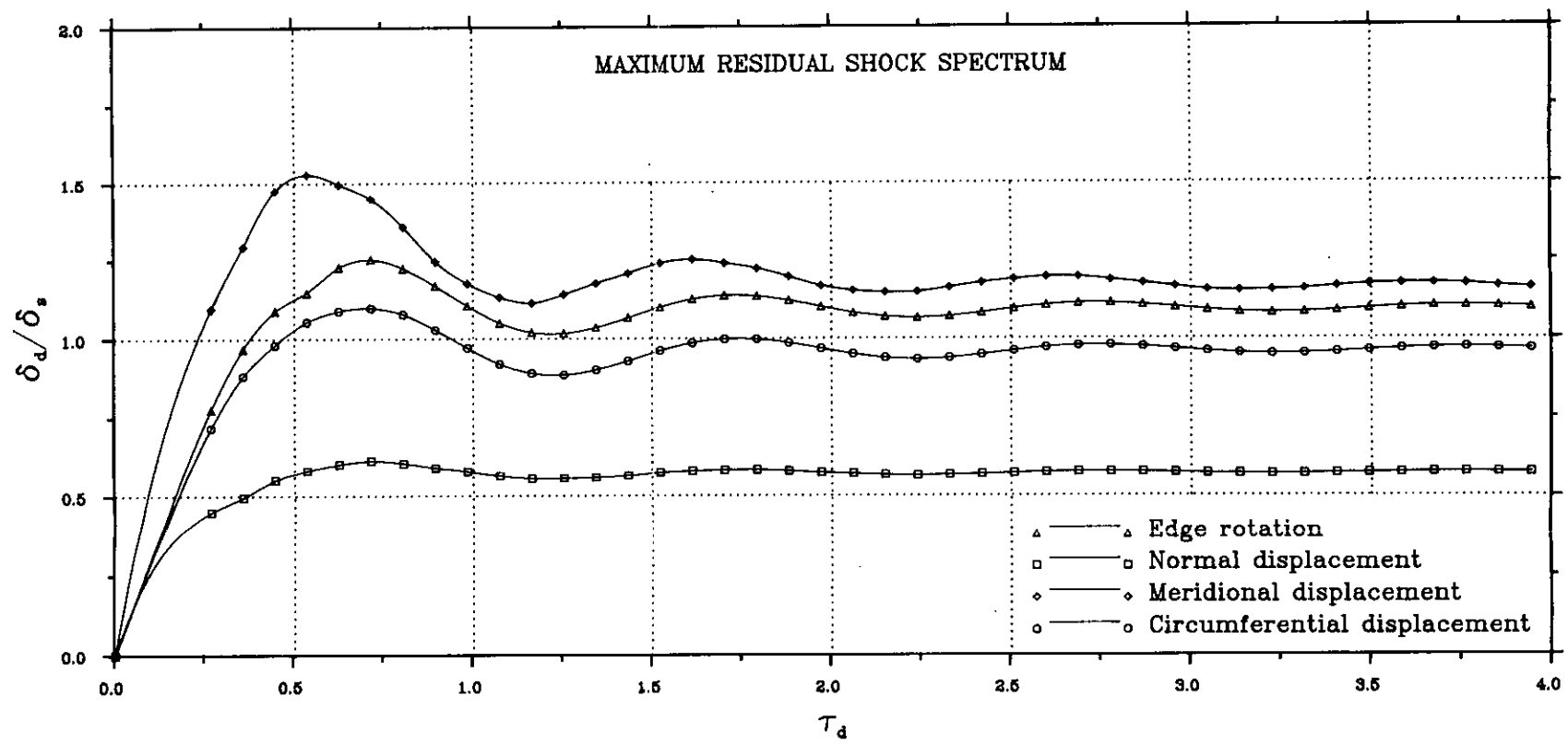

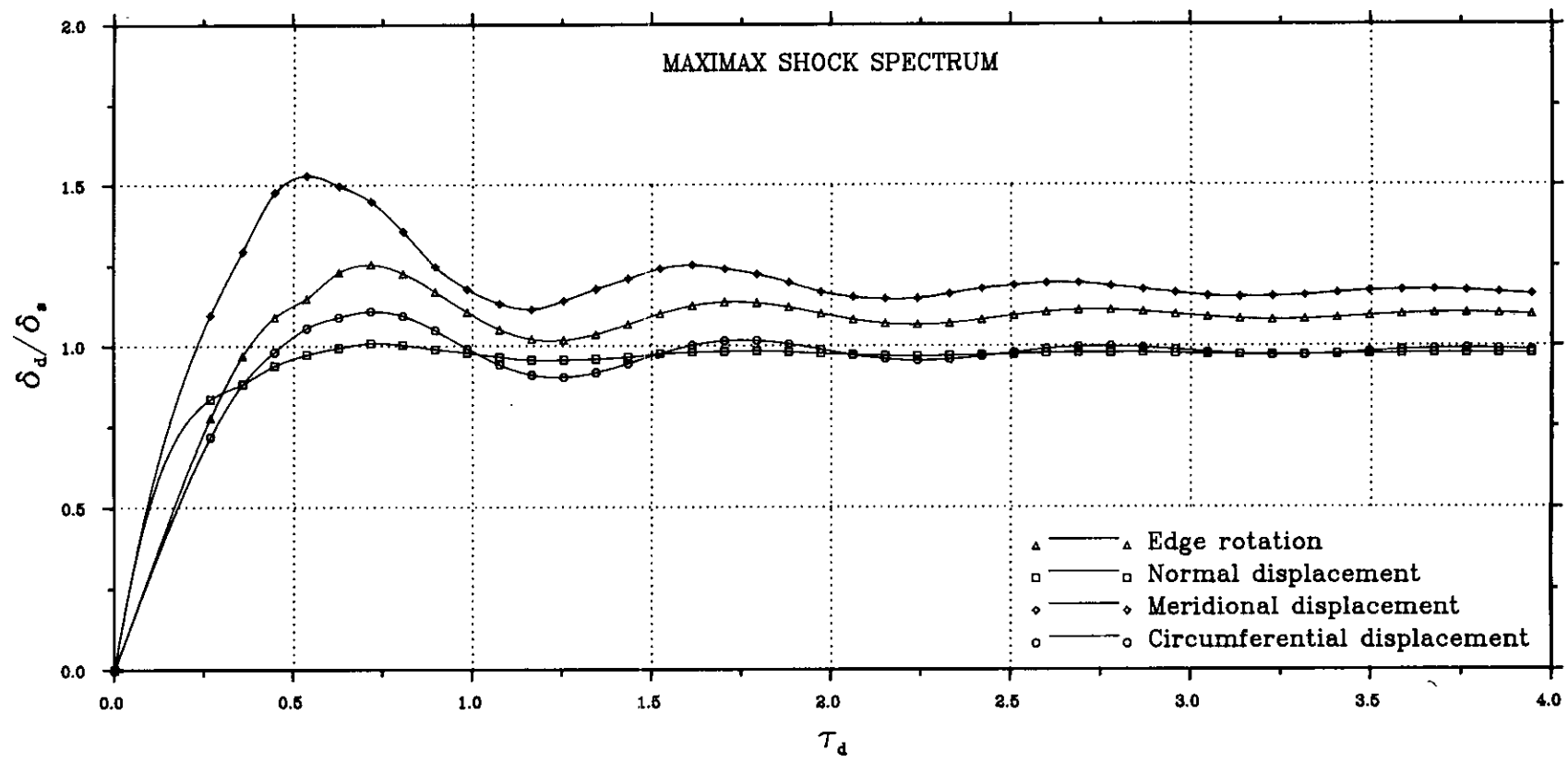

FIG. 3.25–EFFECT OF PULSE DURATION ON MAXIMUM RESPONSE SPECTRA (DLF) TO A TRIANGULAR PULSE --κ = 1.0--

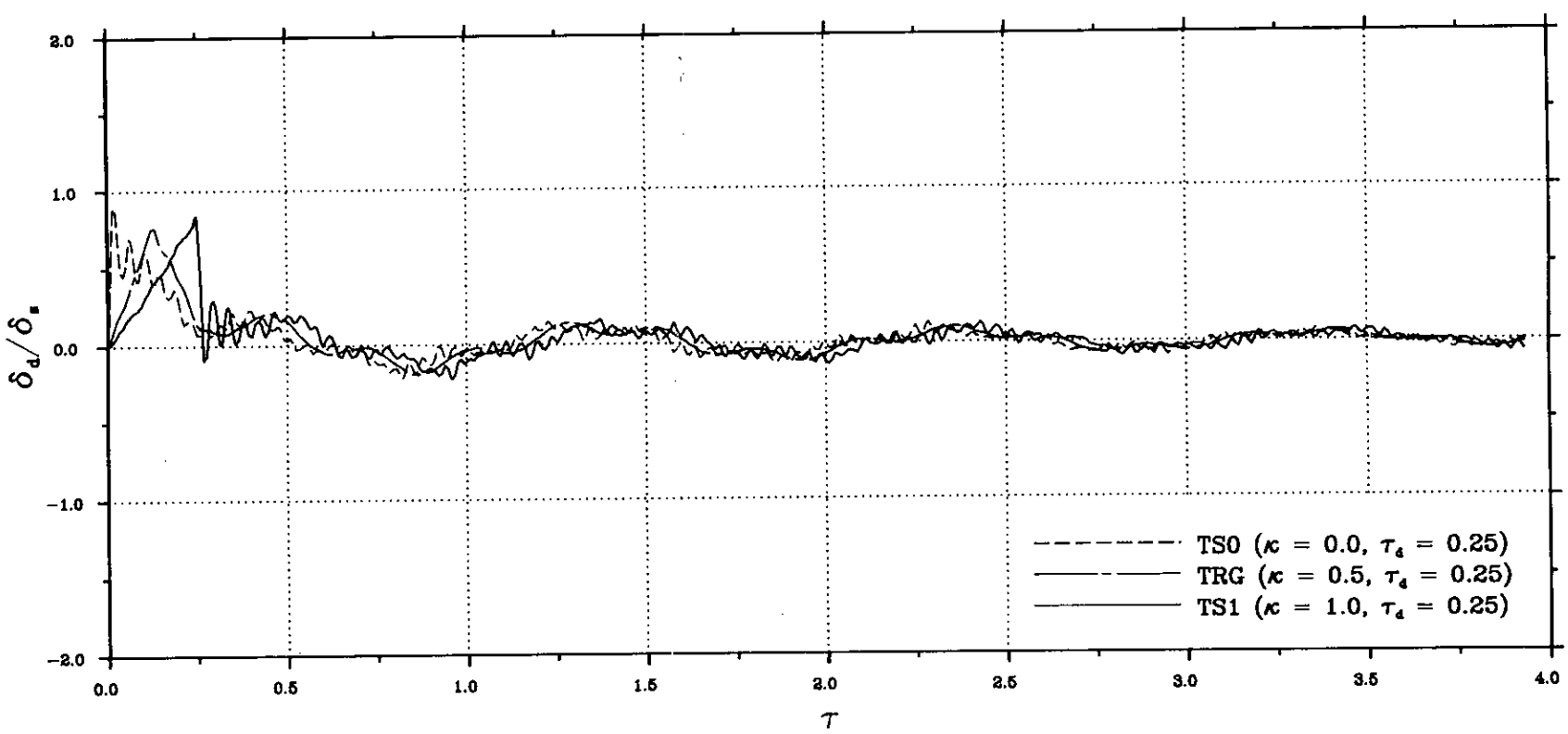

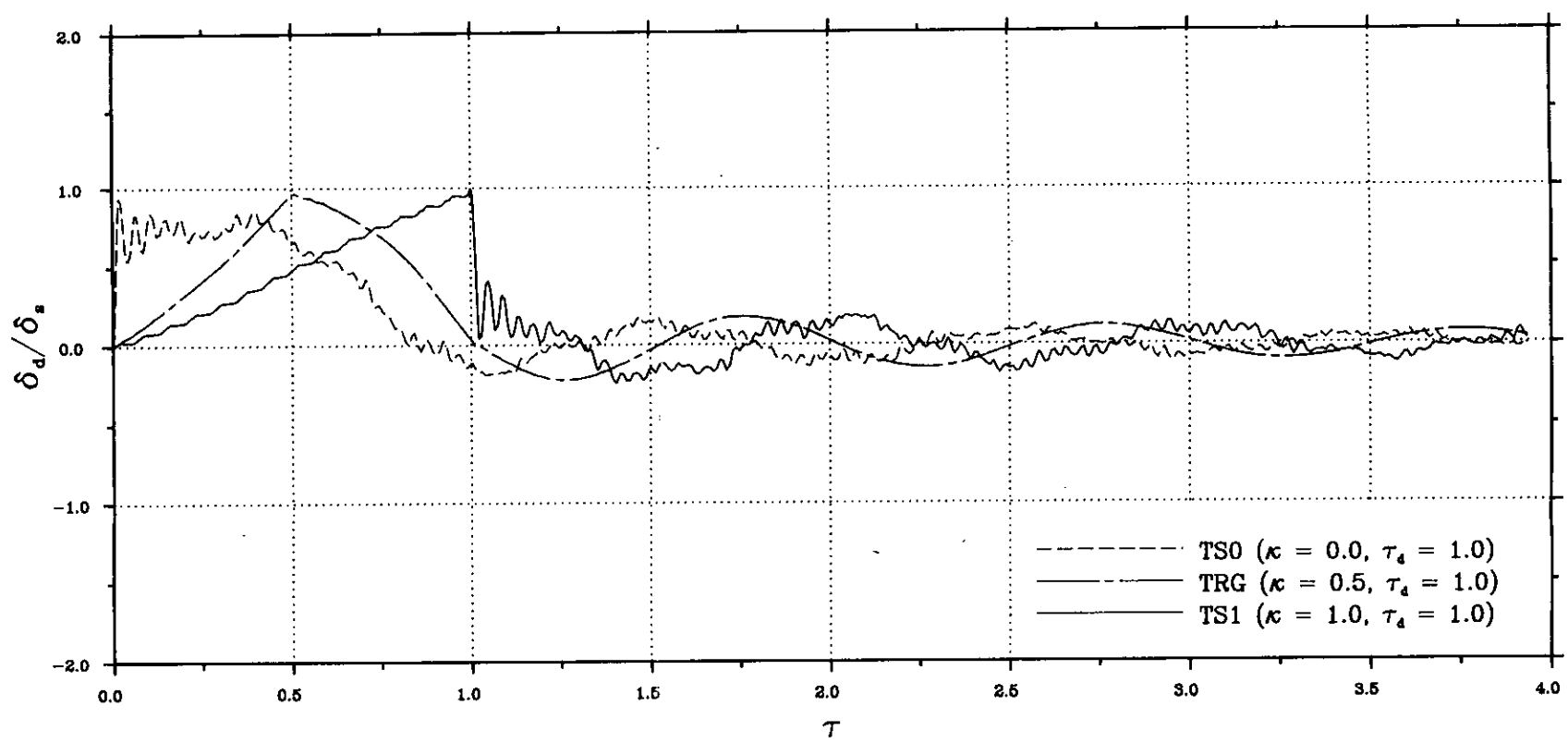

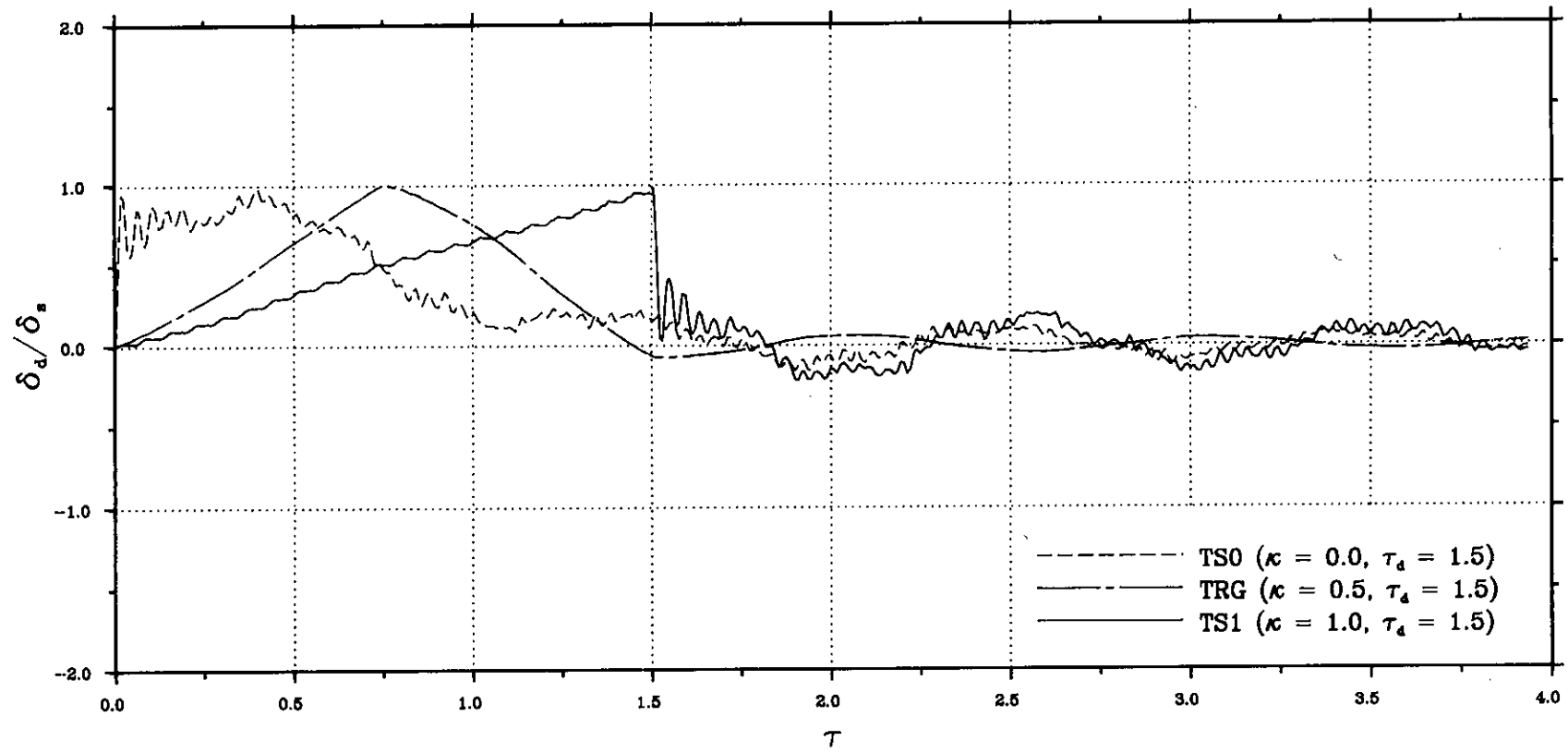

FIG. 3.26(a)–RESPONSE–TIME HISTORY TO VARIOUS TRIANGULAR PULSES OF EQUAL IMPULSE AREA, FOR DIFFERENT VALUES OF PULSE DURATION
––NORMAL DIRECTION––

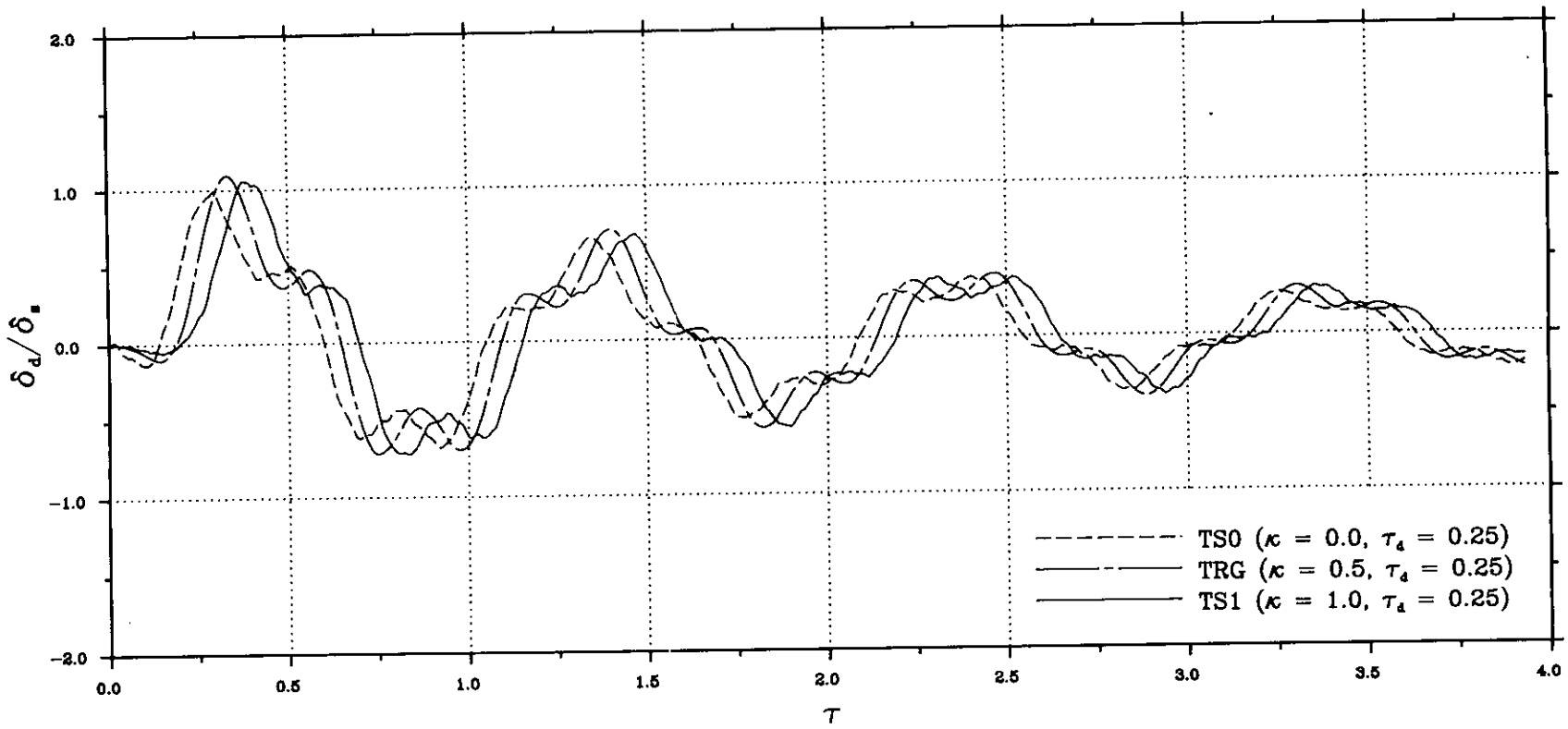

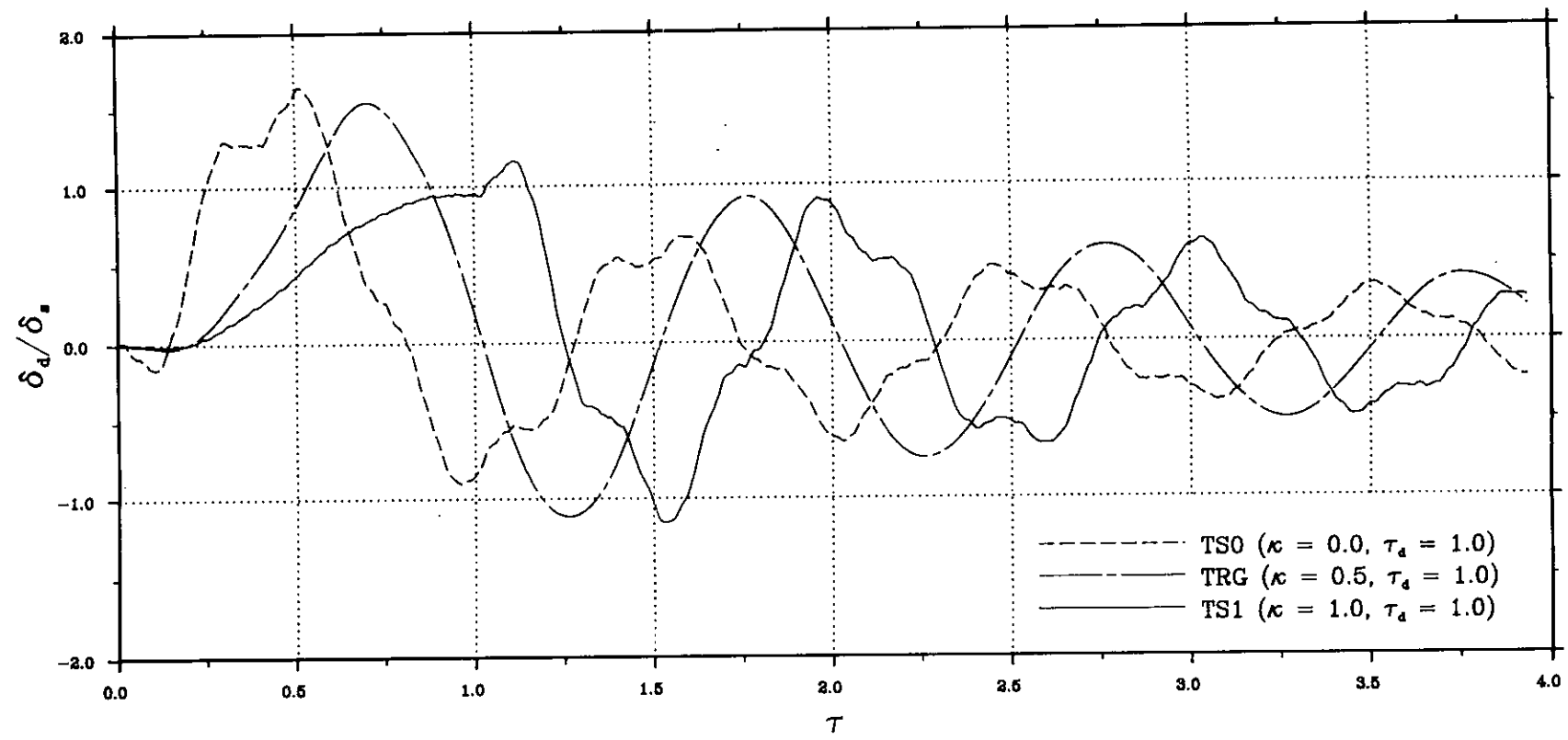

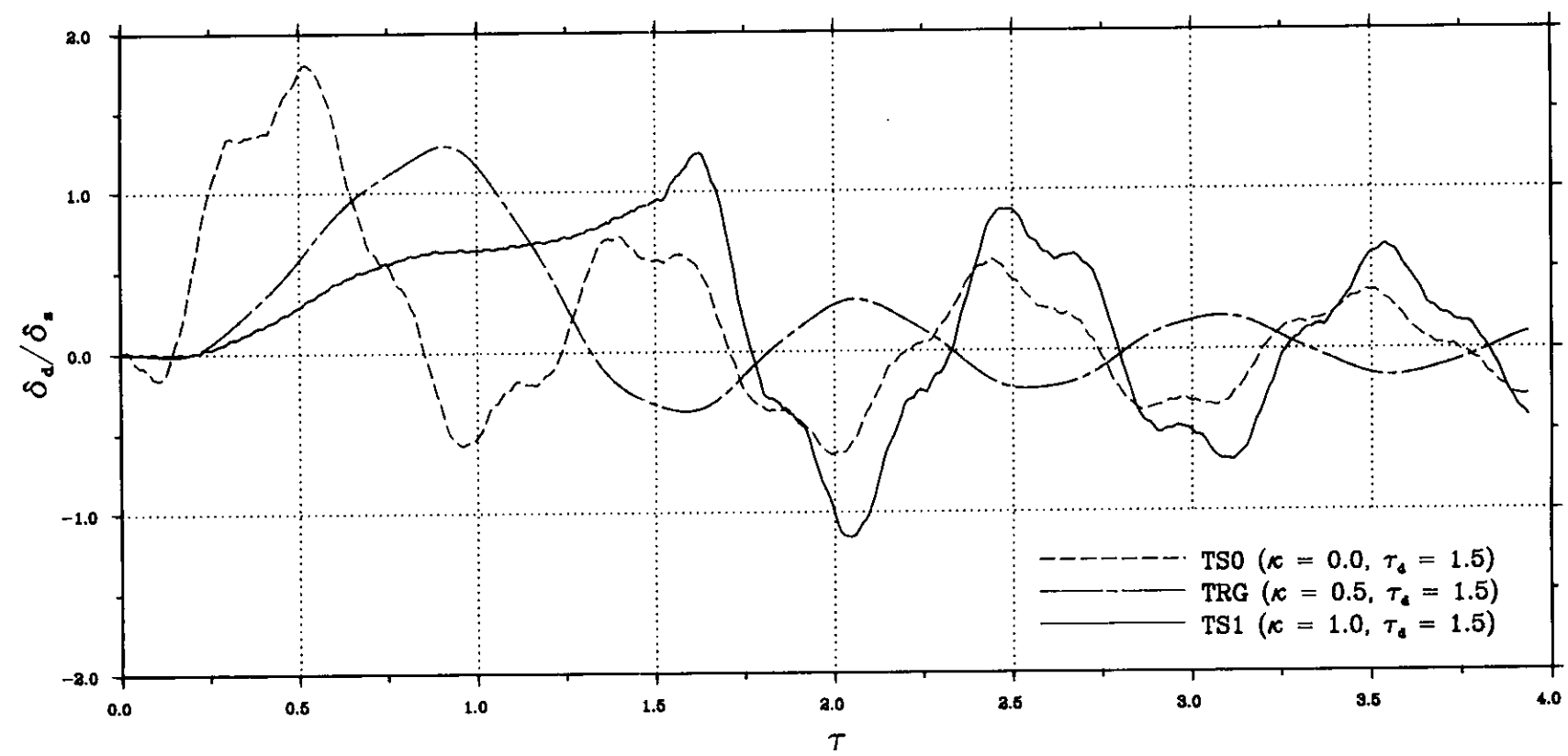

FIG. 3.26(b)–RESPONSE–TIME HISTORY TO VARIOUS TRIANGULAR PULSES OF EQUAL IMPULSE AREA, FOR DIFFERENT VALUES OF PULSE DURATION --MERIDIONAL DIRECTION--

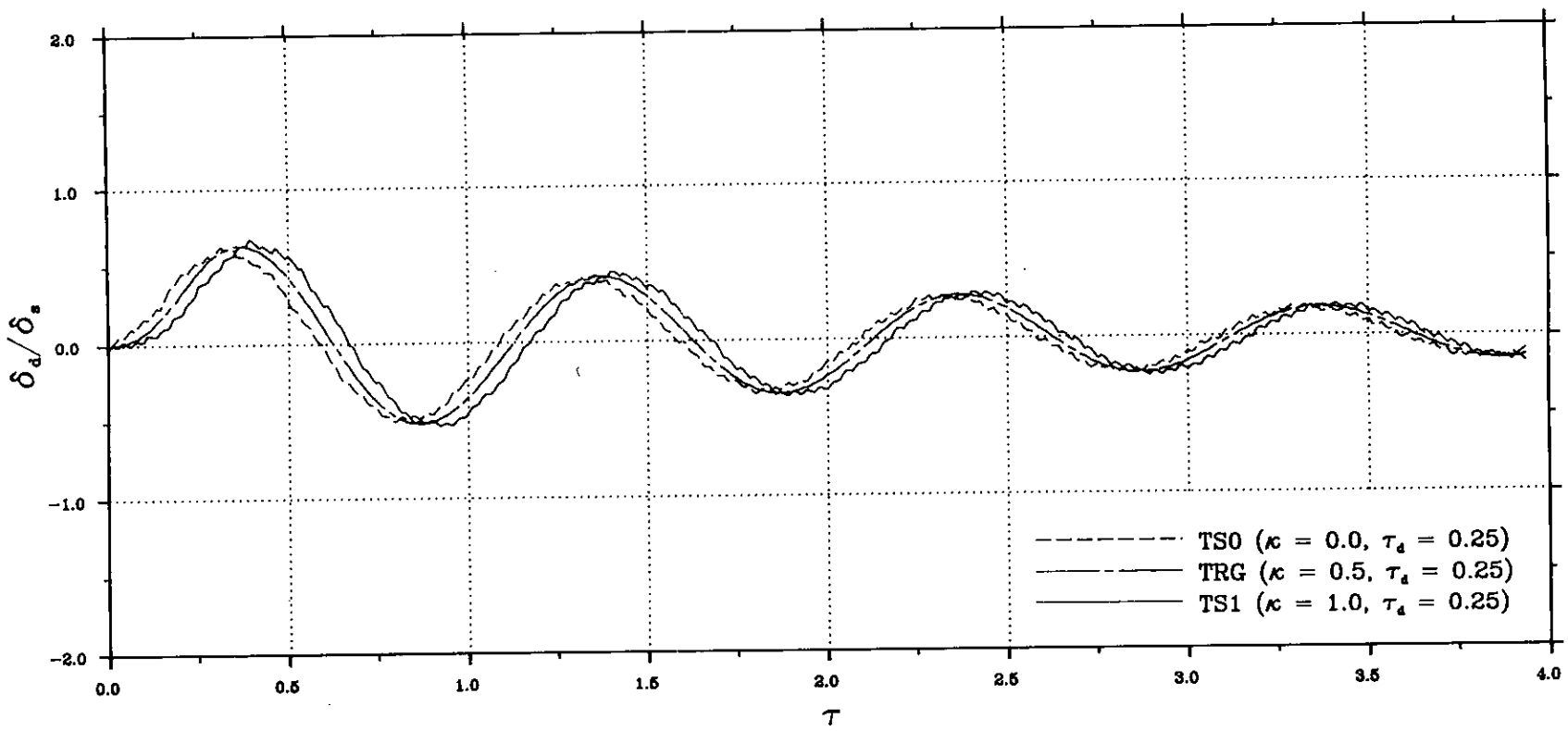

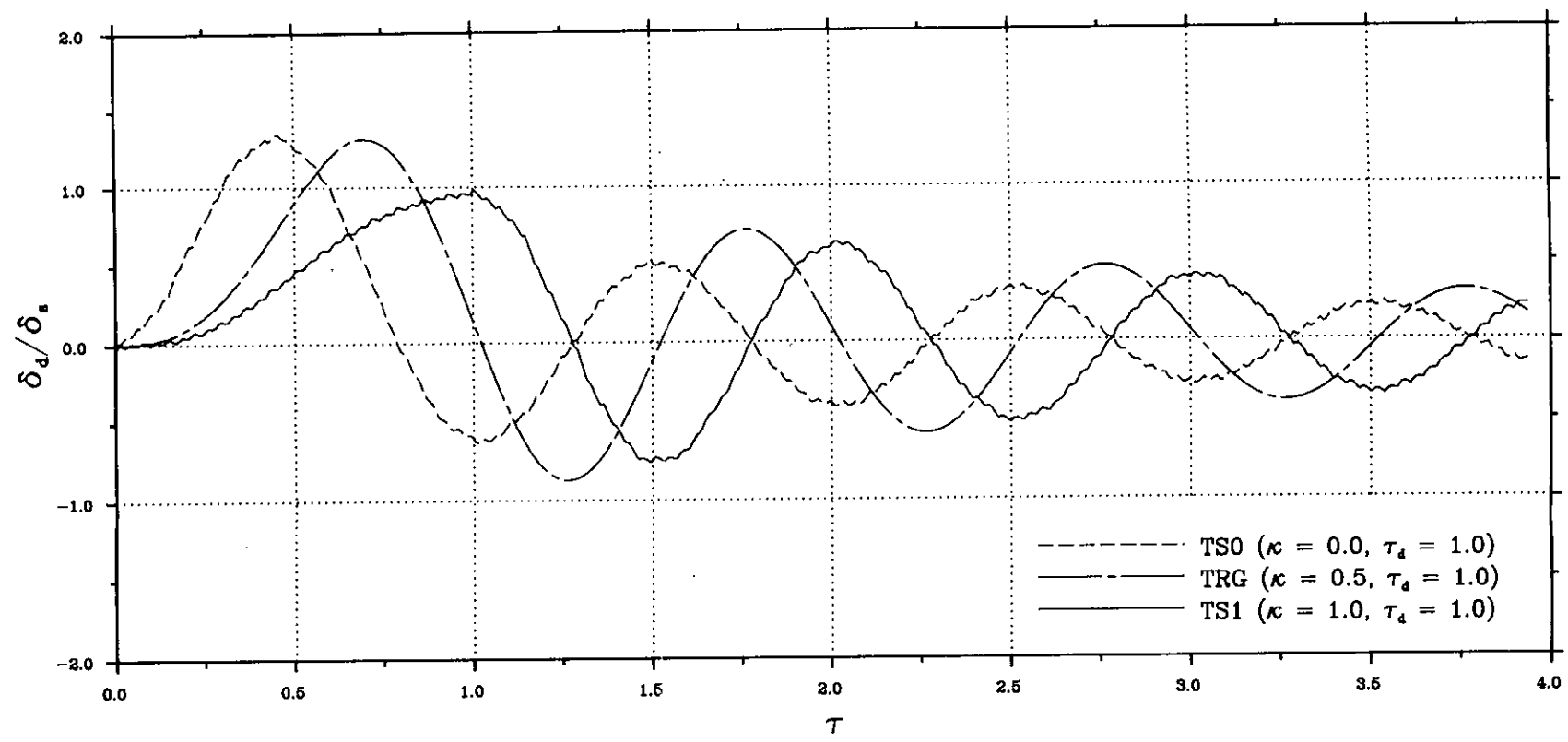

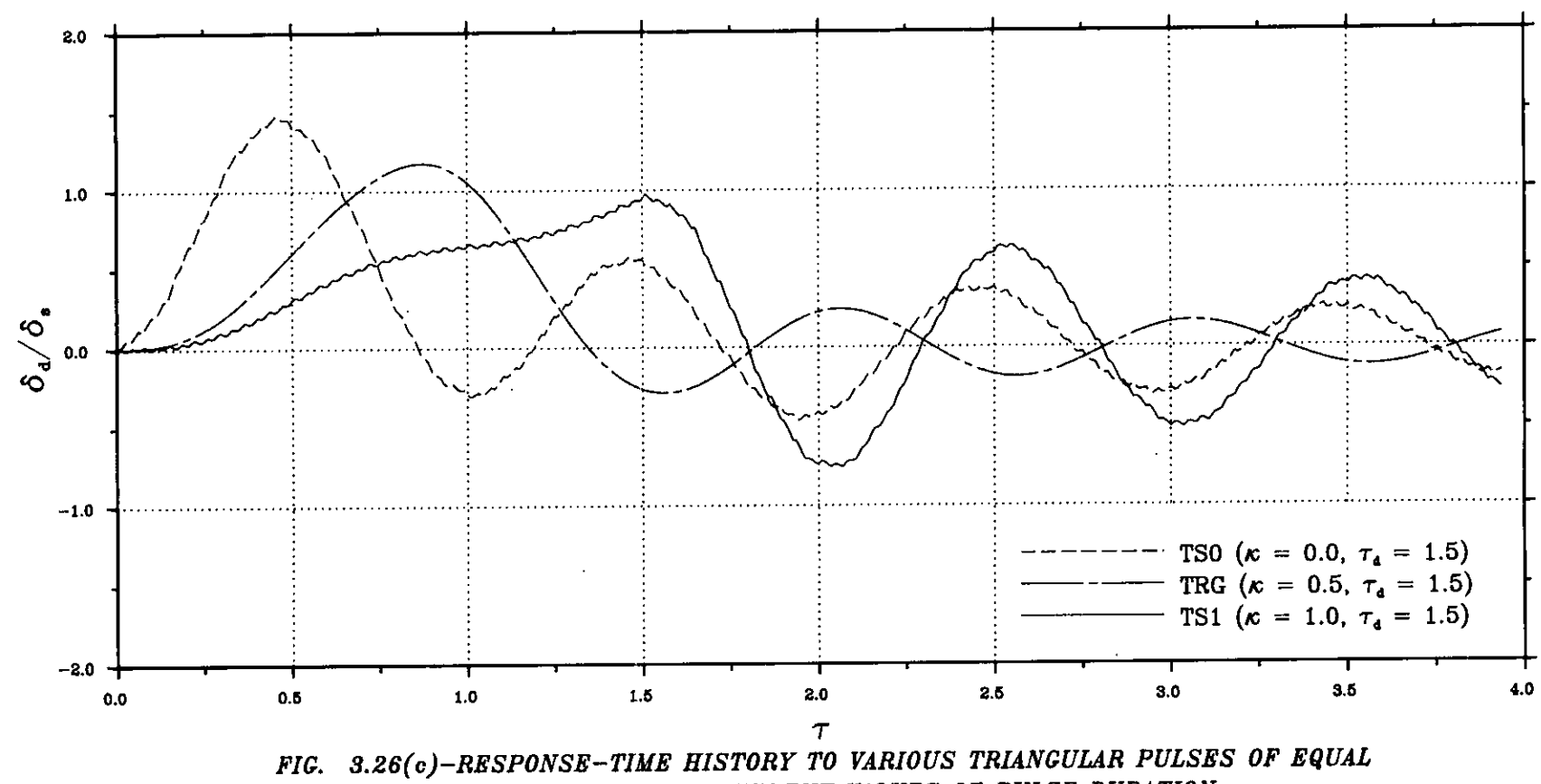

FIG. 3.26(c)–RESPONSE–TIME HISTORY TO VARIOUS TRIANGULAR PULSES OF EQUAL IMPULSE AREA, FOR DIFFERENT VALUES OF PULSE DURATION --CIRCUMFERENTIAL DIRECTION--

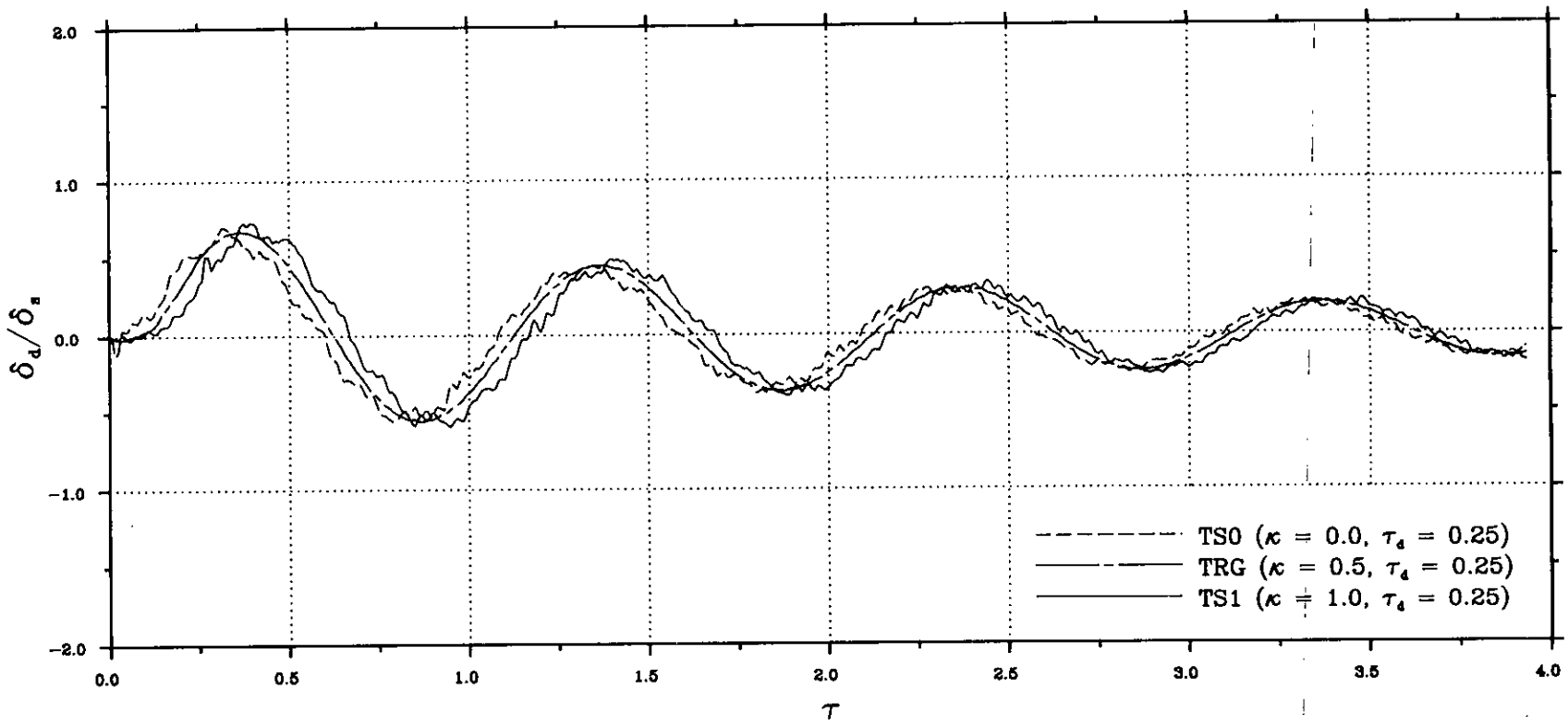

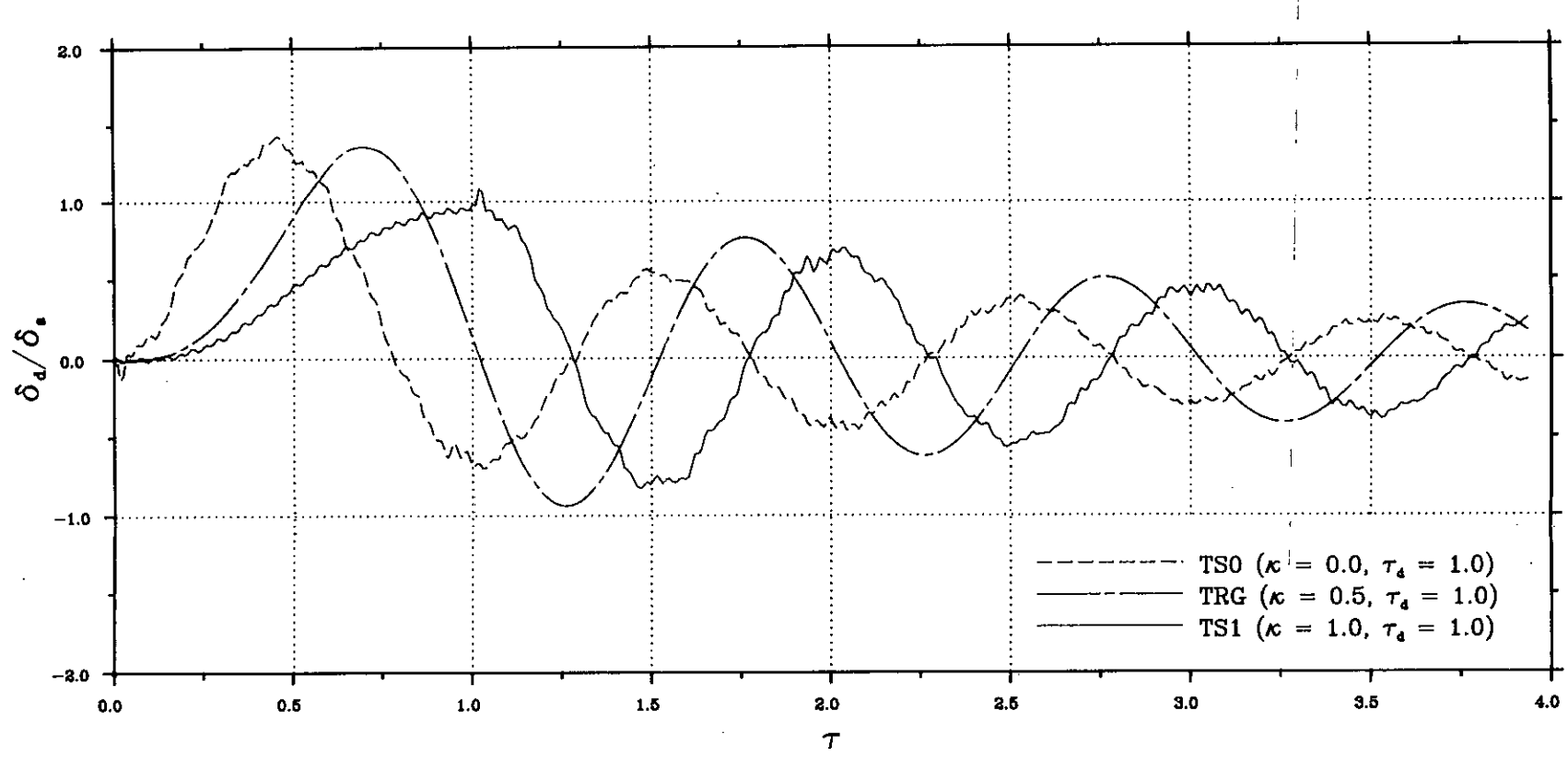

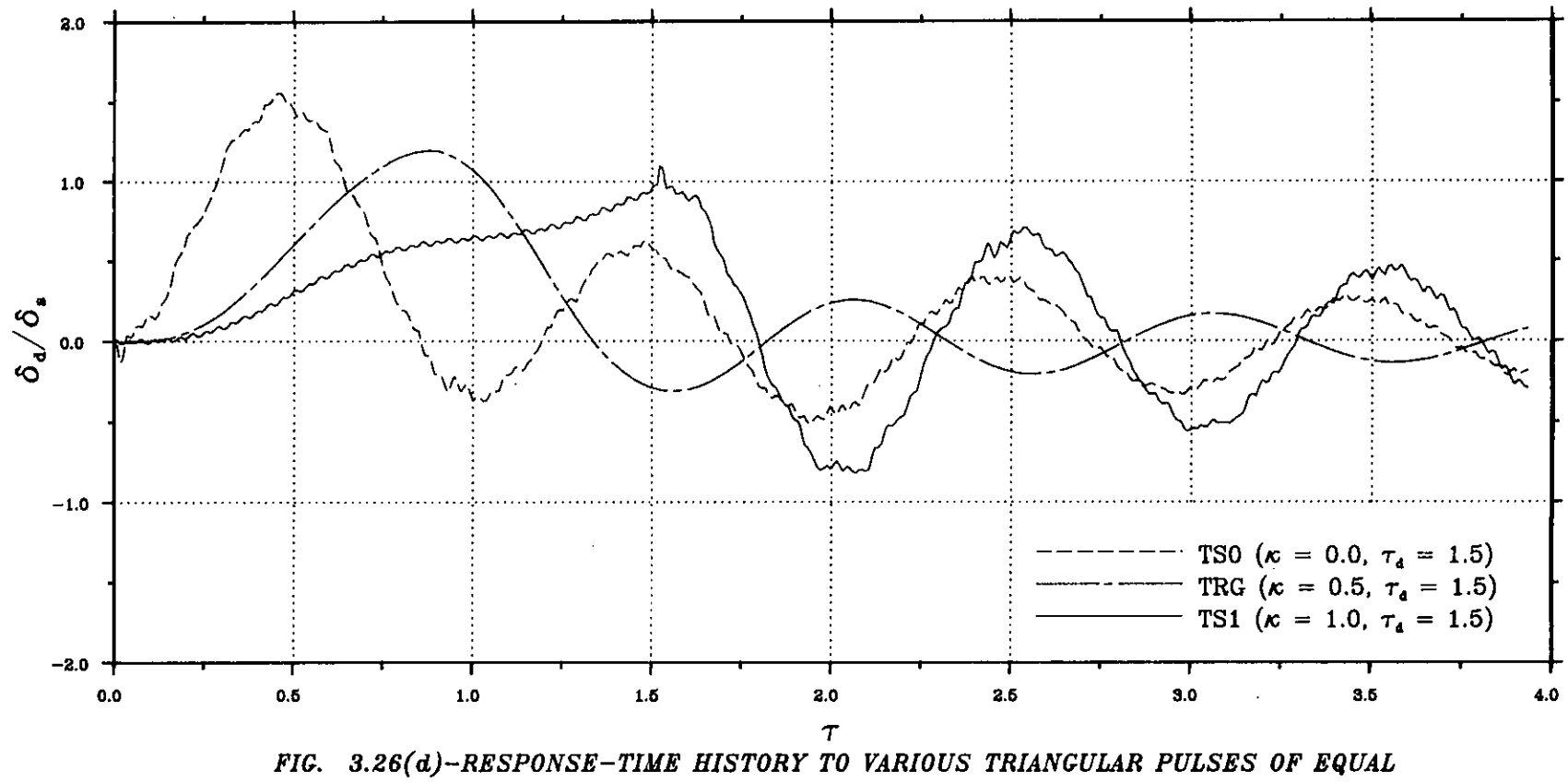

FIG. 3.26(d)–RESPONSE–TIME HISTORY TO VARIOUS TRIANGULAR PULSES OF EQUAL IMPULSE AREA, FOR DIFFERENT VALUES OF PULSE DURATION
––EDGE ROTATION––

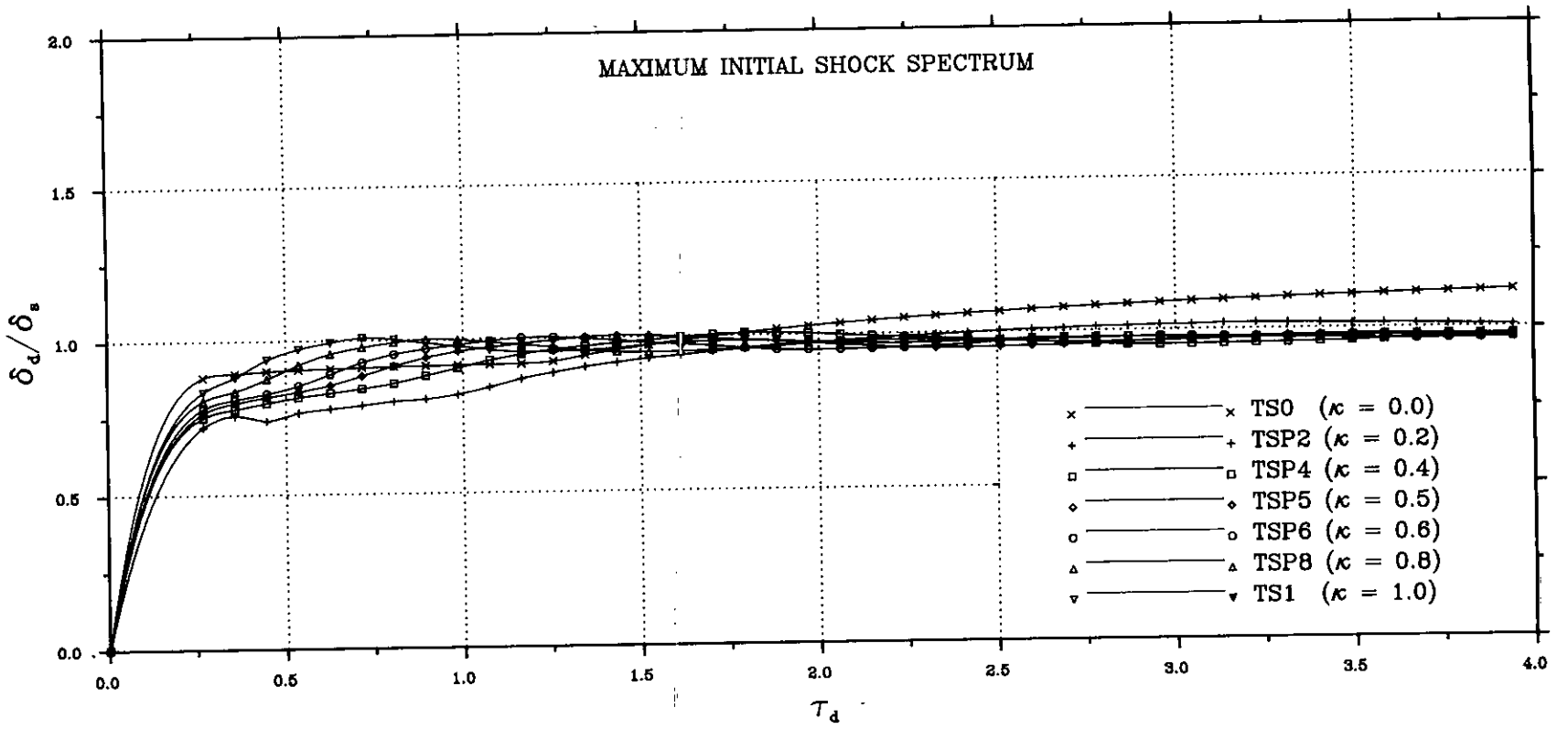

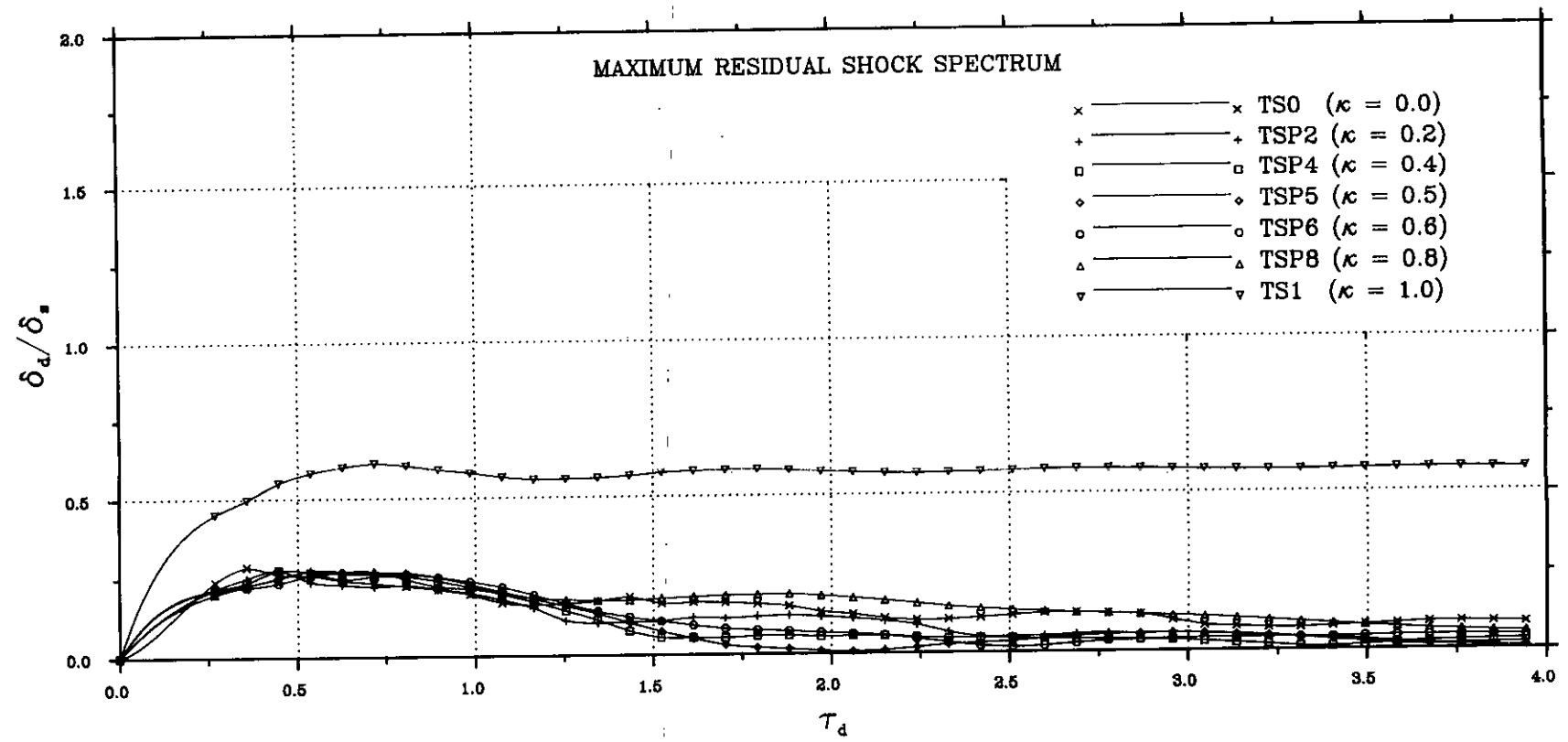

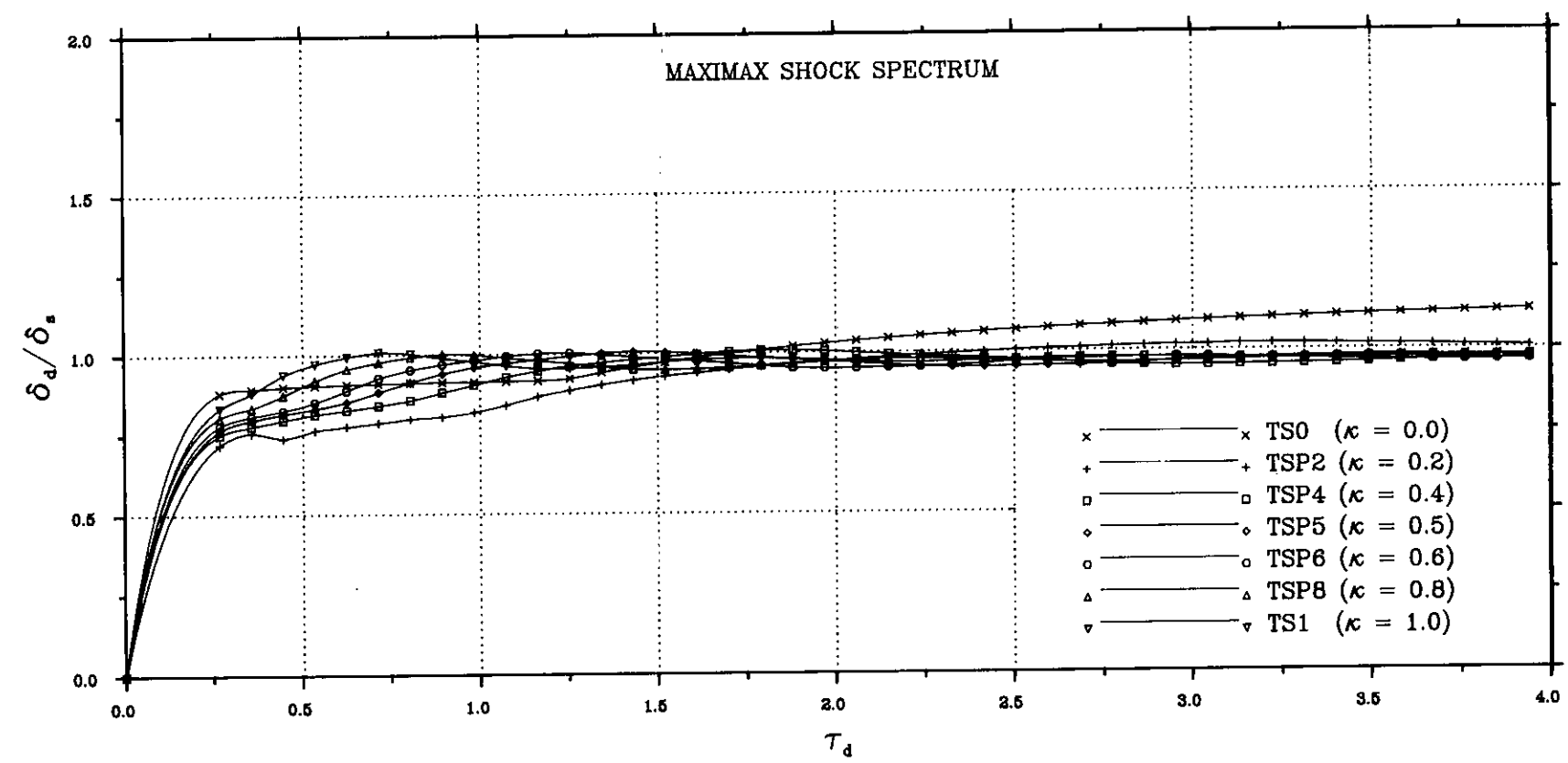

FIG. 3.27(a)–RESPONSE SPECTRA (DLF) FOR VARIOUS TRIANGULAR PULSES OF EQUAL IMPULSE AREA --NORMAL DIRECTION--

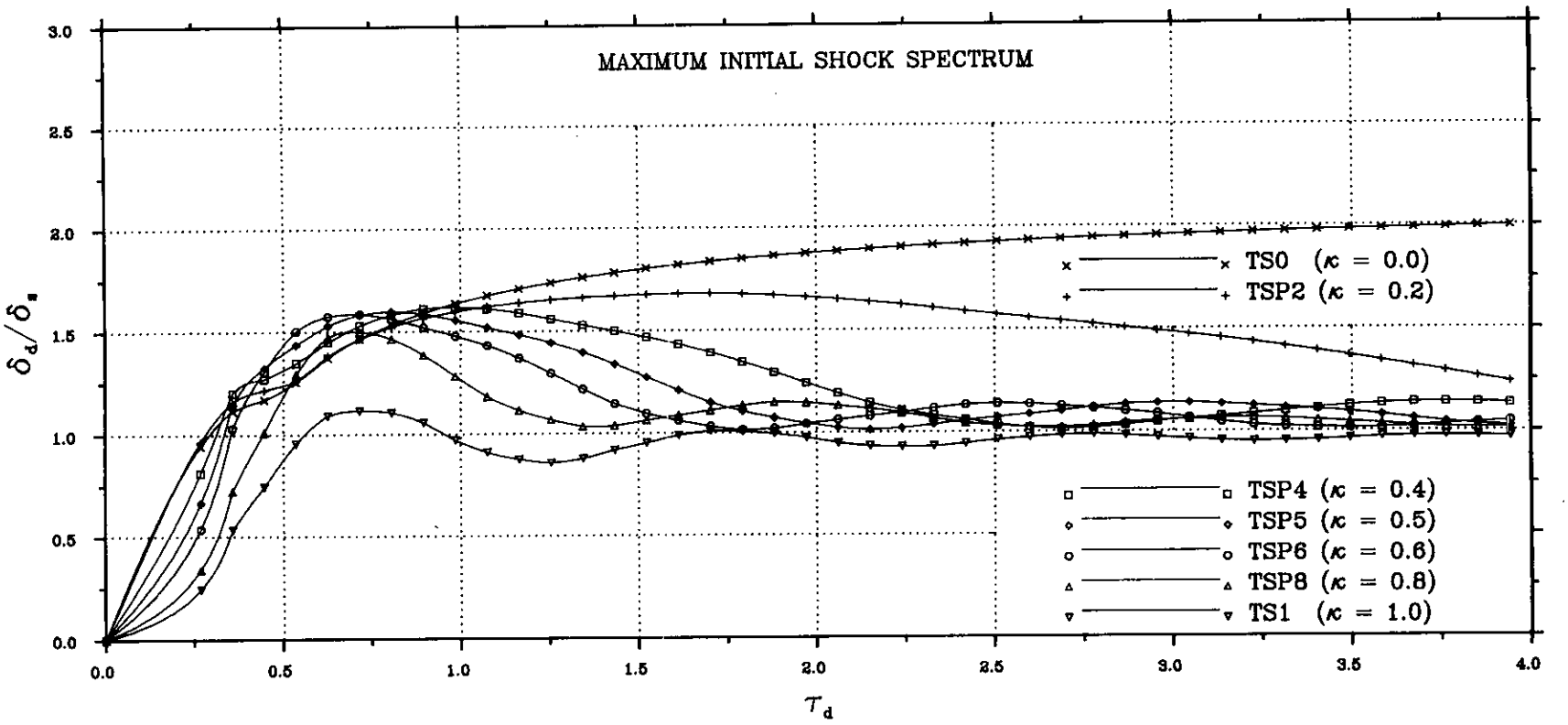

FIG. 3.27(b)–RESPONSE SPECTRA (DLF) FOR VARIOUS TRIANGULAR PULSES OF EQUAL IMPULSE AREA --MERIDIONAL DIRECTION--

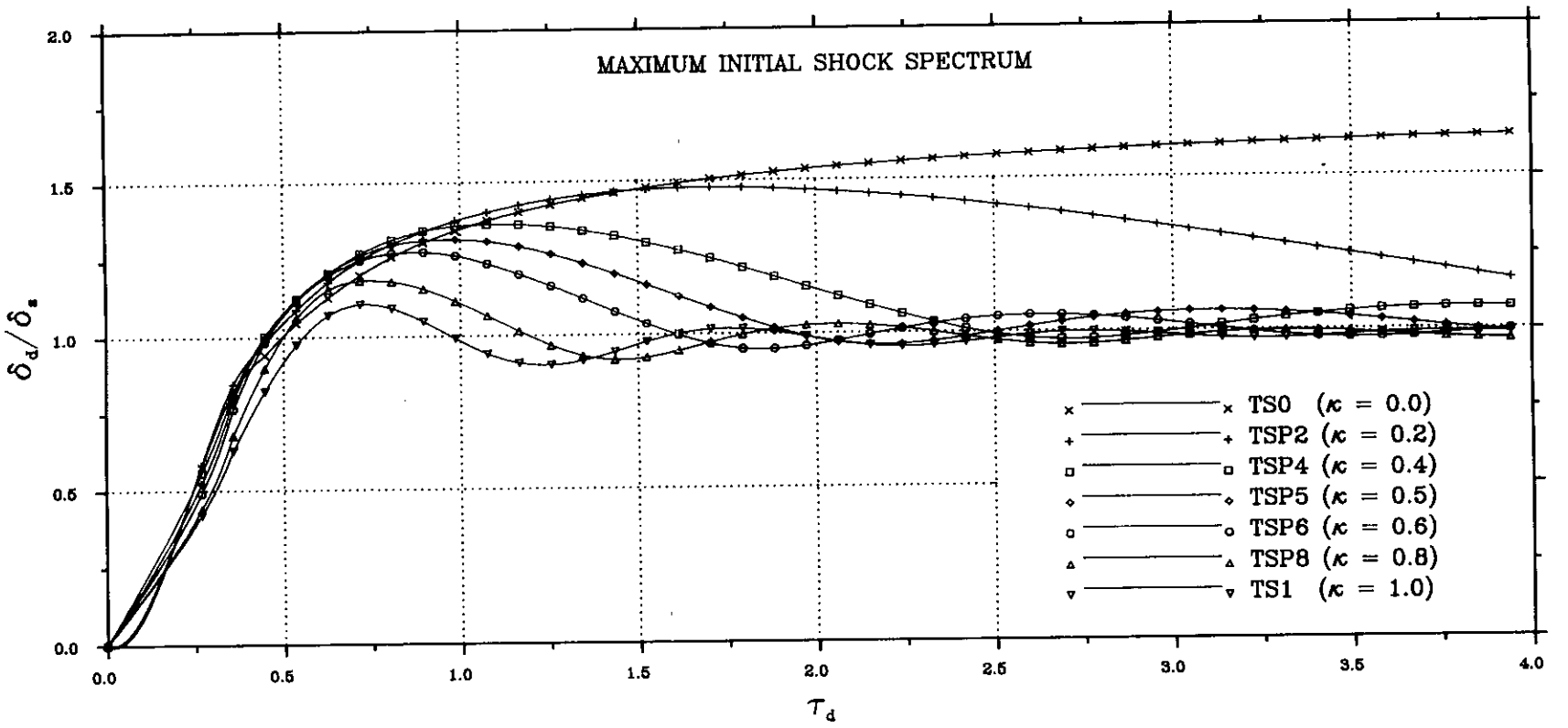

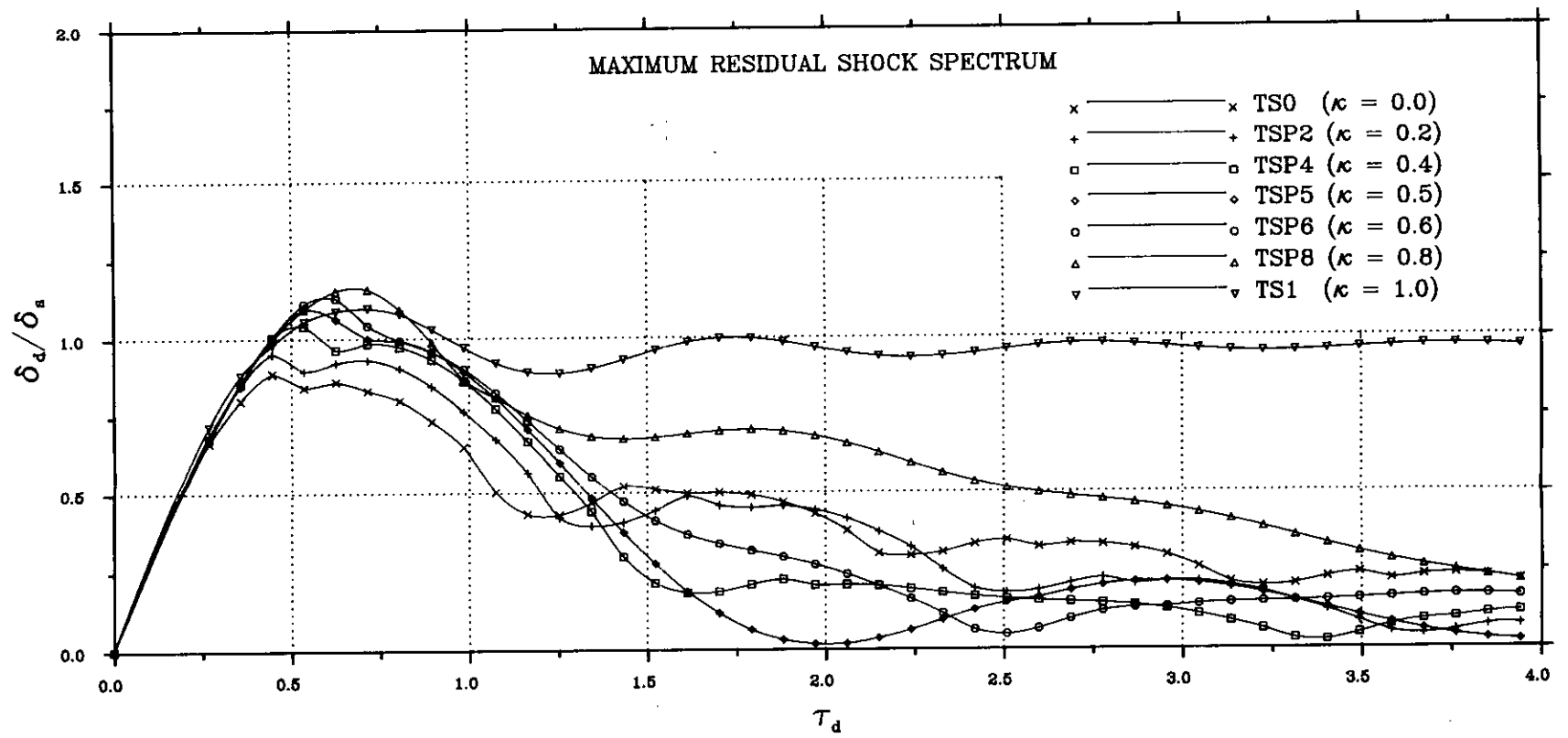

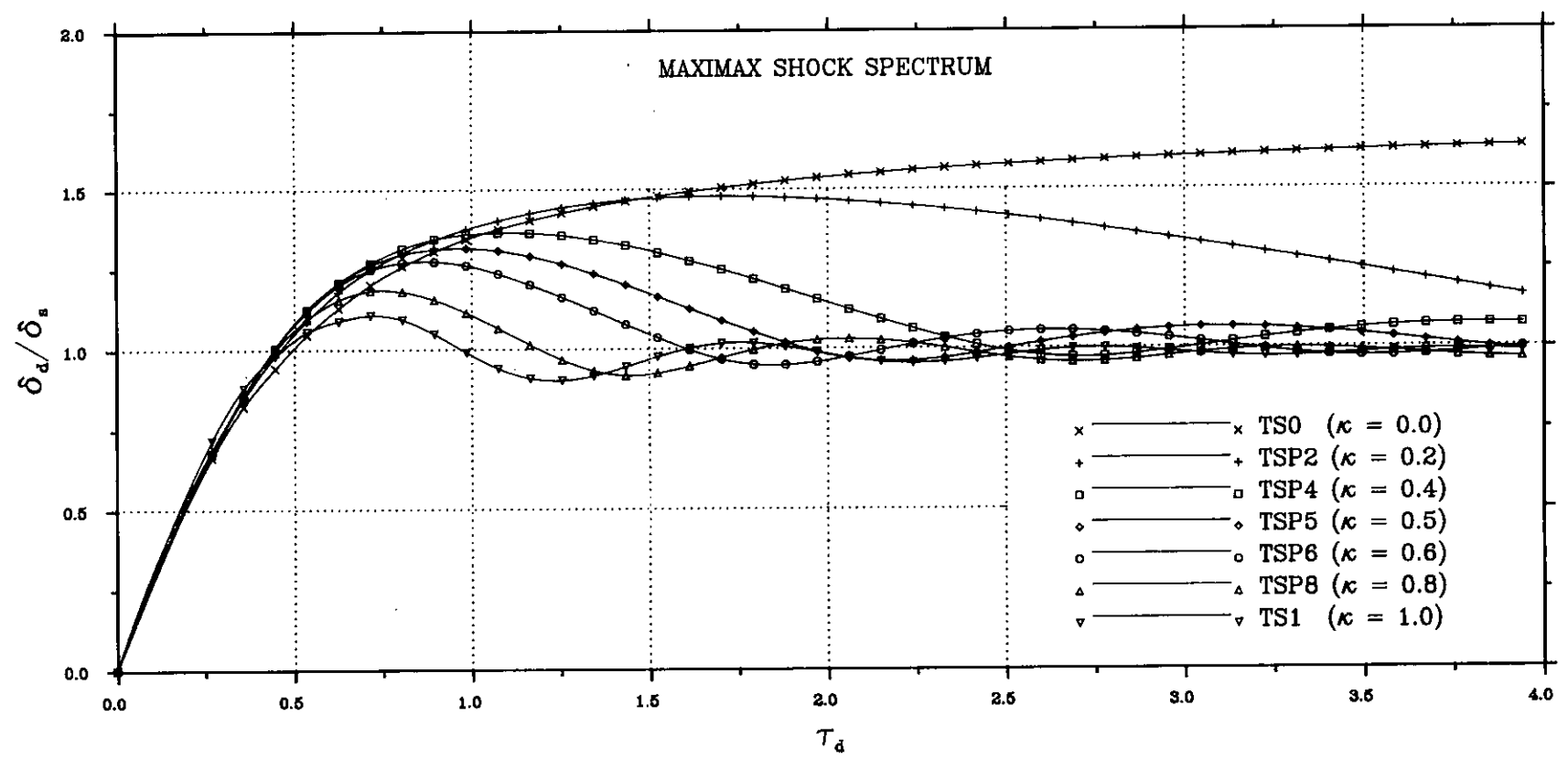

FIG. 3.27(c)–RESPONSE SPECTRA (DLF) FOR VARIOUS TRIANGULAR PULSES OF EQUAL IMPULSE AREA --CIRCUMFERENTIAL DIRECTION--

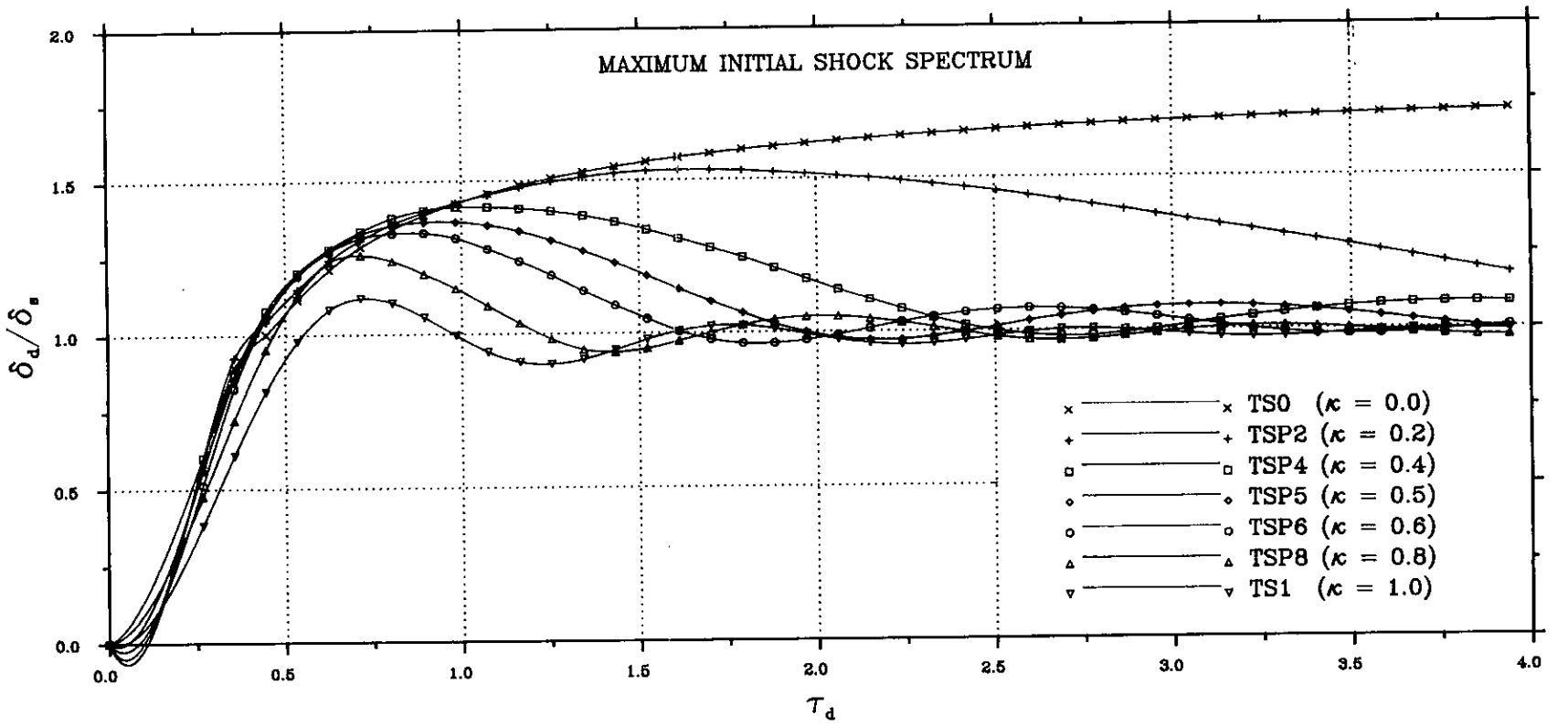

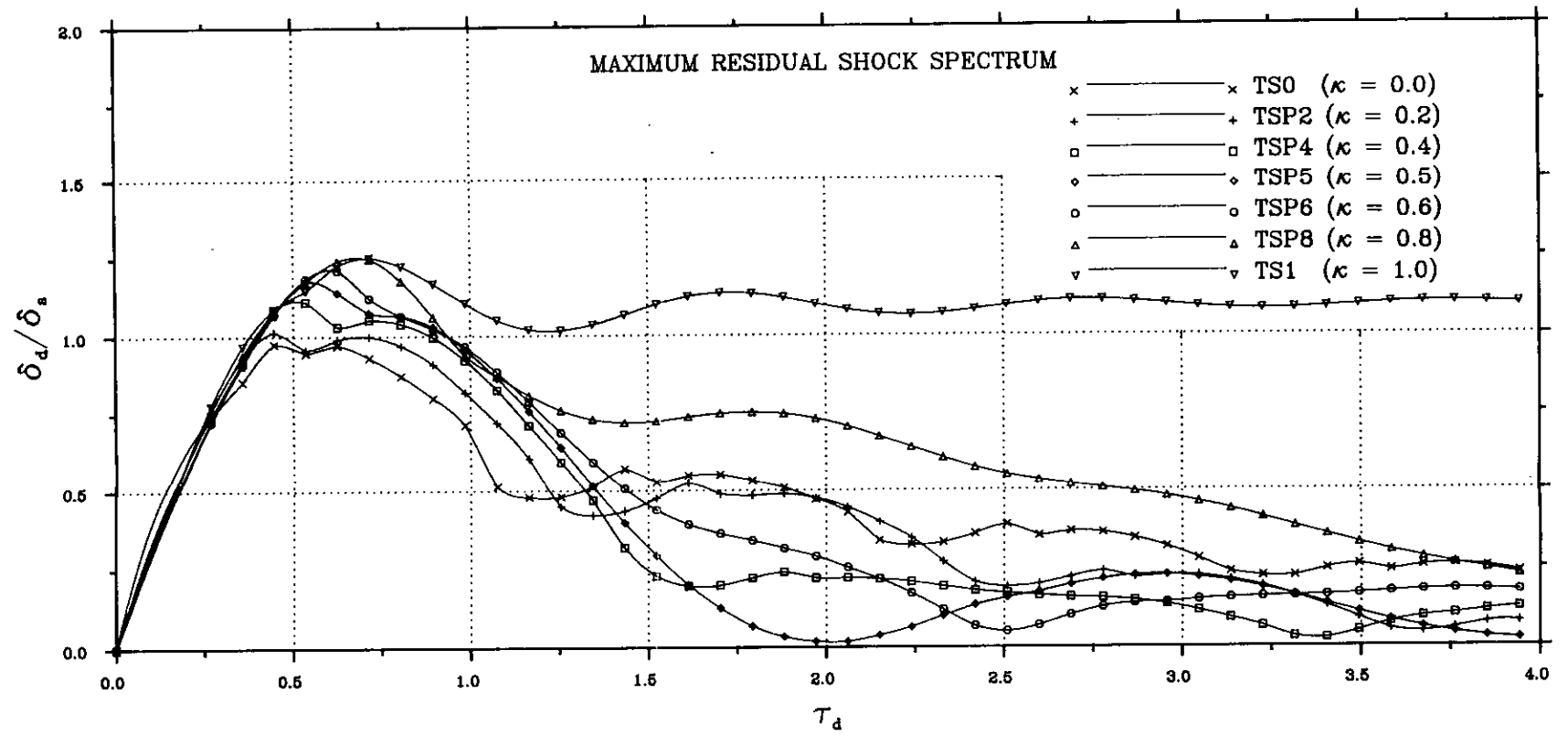

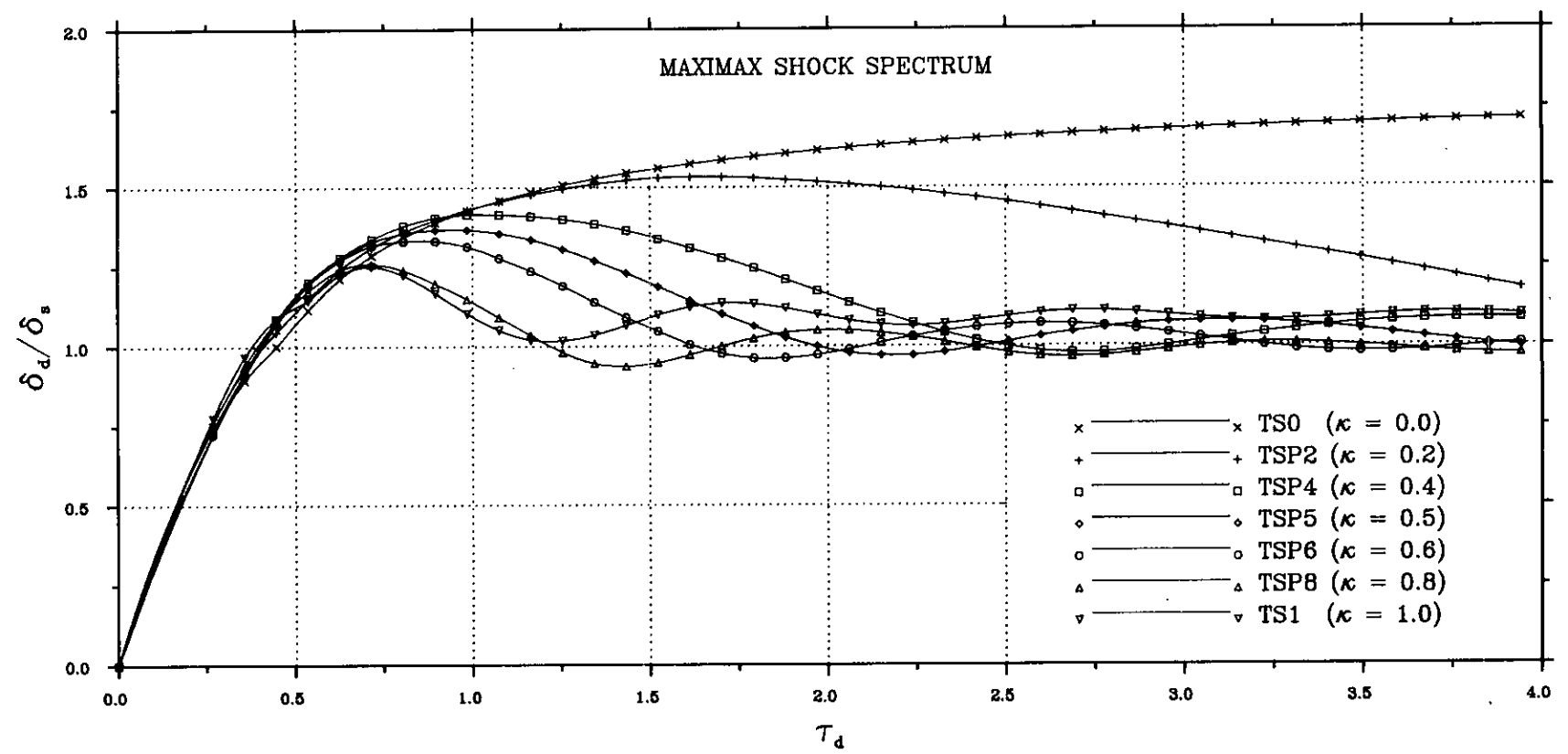

FIG. 3.27(d)–RESPONSE SPECTRA (DLF) FOR VARIOUS TRIANGULAR PULSES OF EQUAL IMPULSE AREA --EDGE ROTATION--

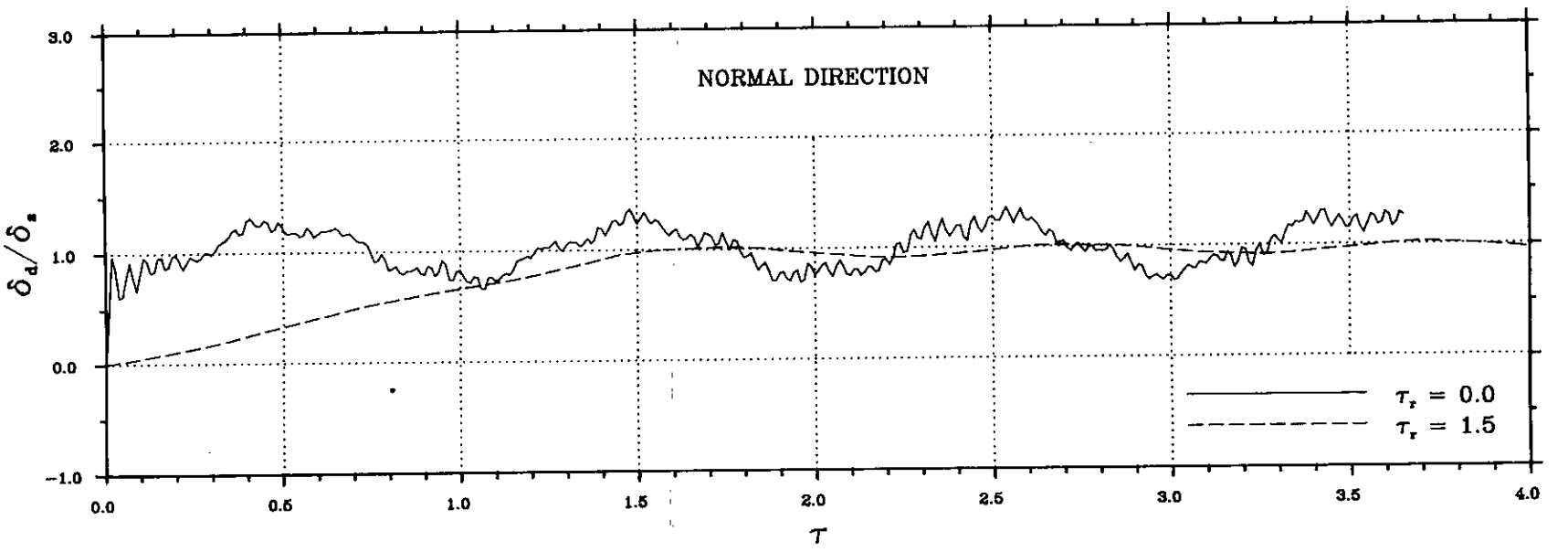

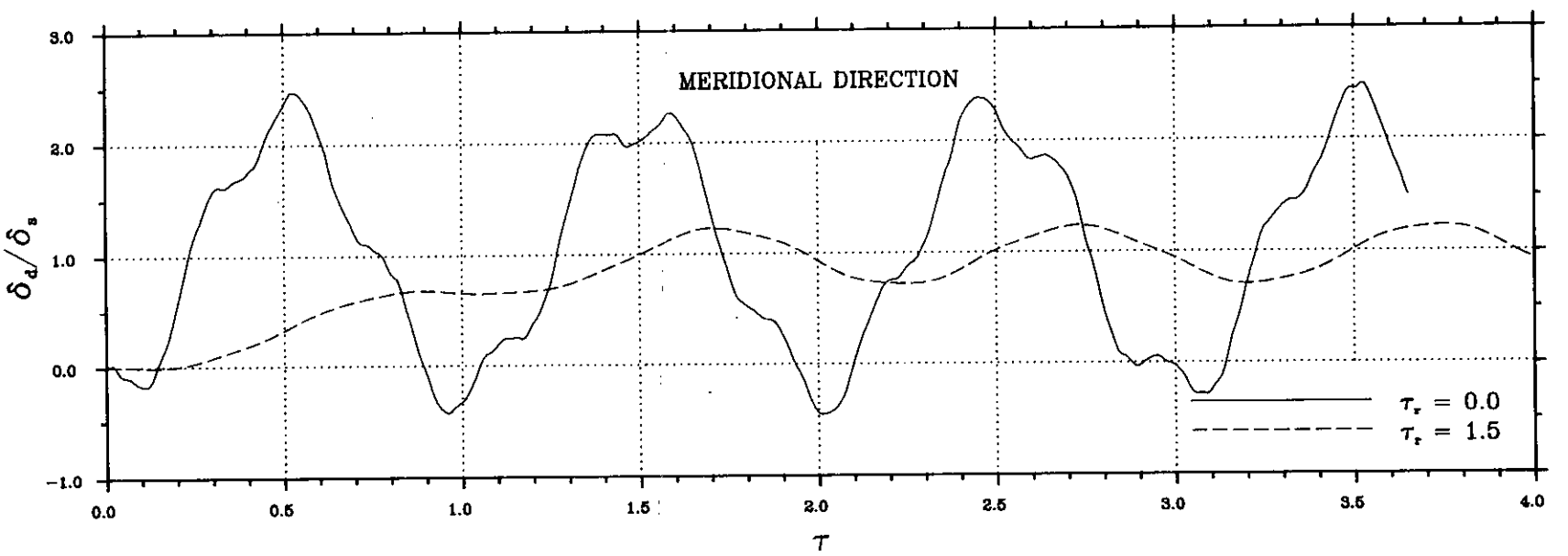

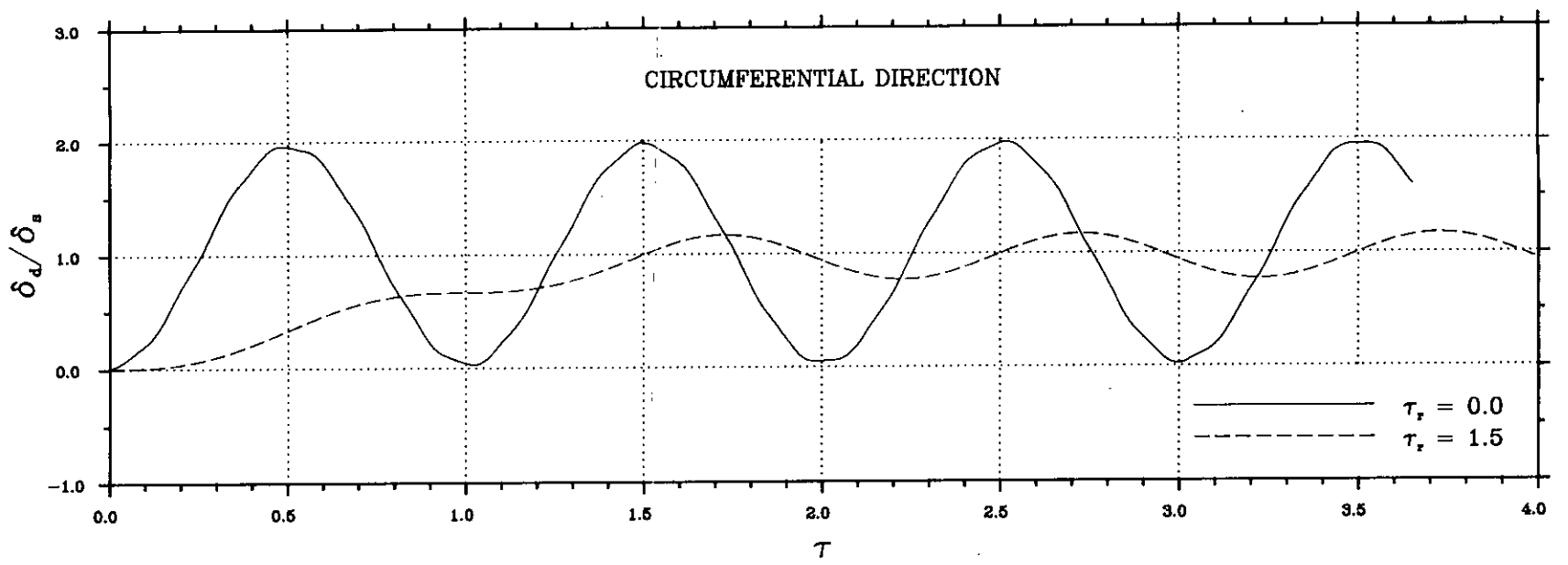

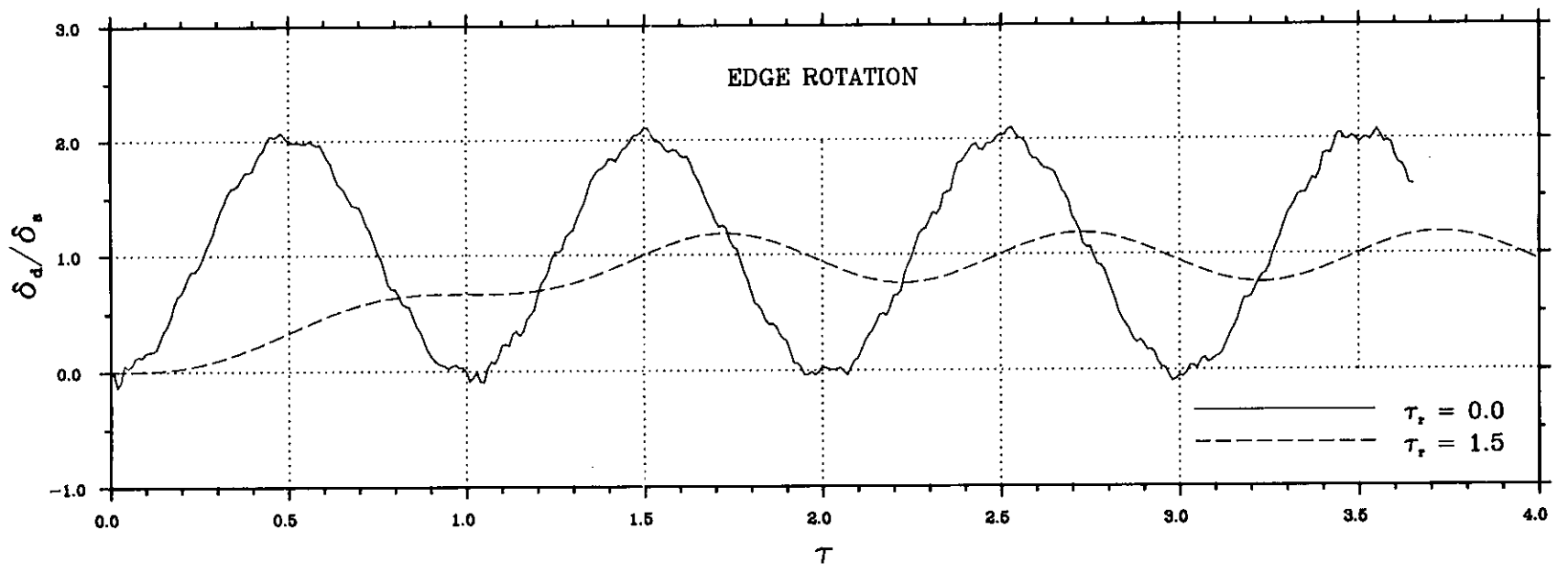

FIG. 3.28–RESPONSE–TIME HISTORY TO STEP LOADS WITH DIFFERENT RAMP DURATIONS

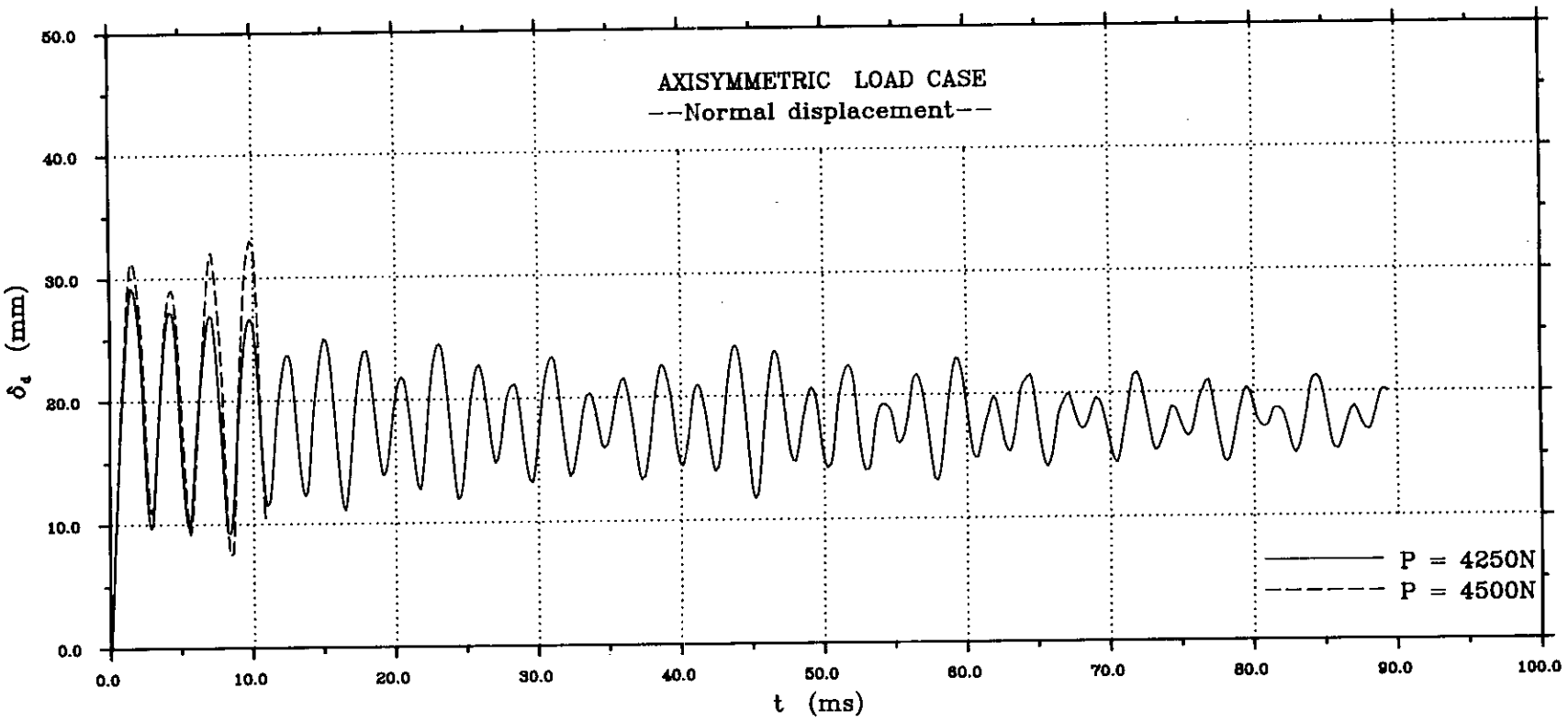

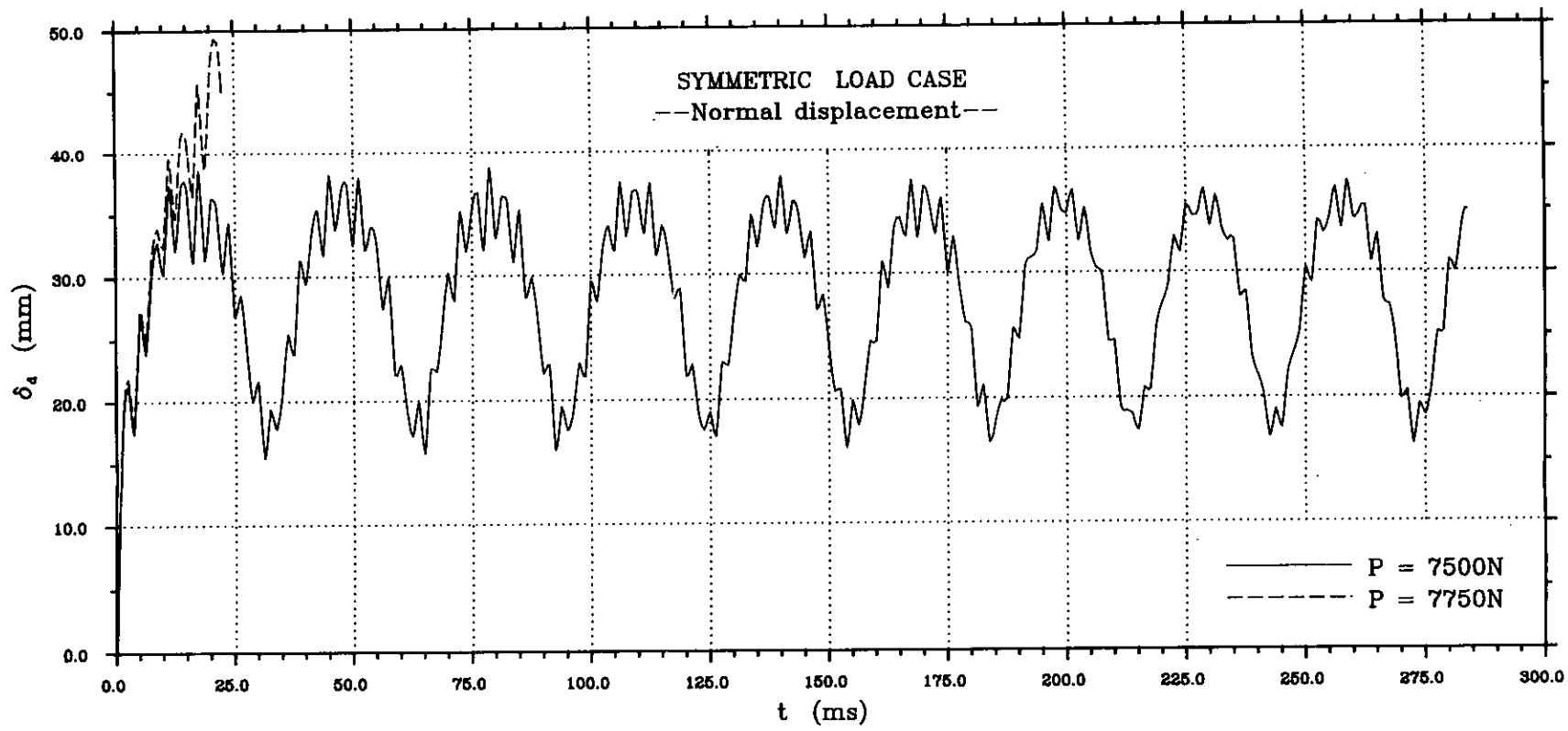

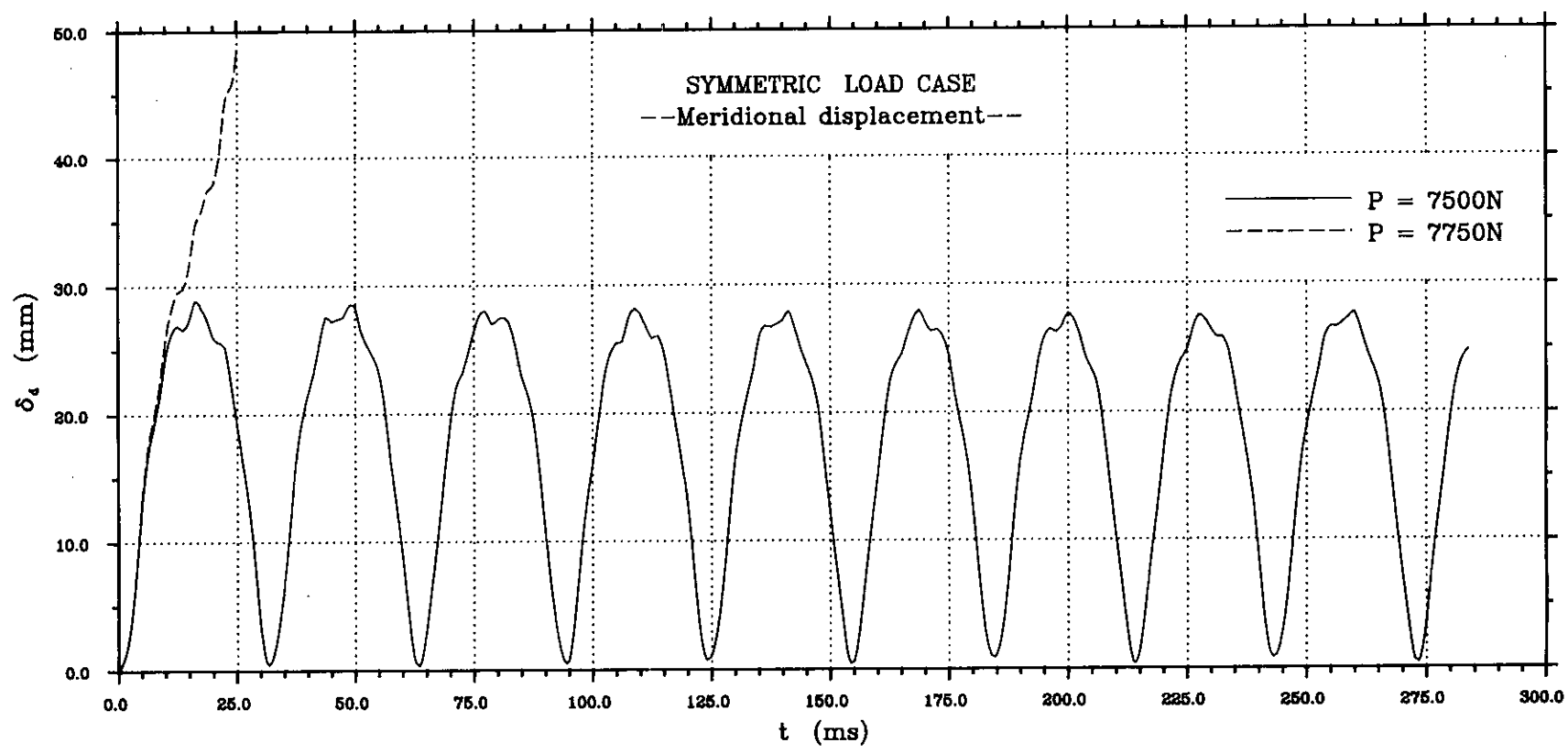

FIG. 3.29–NON–LINEAR DYNAMIC RESPONSE TO A STEP LOADING

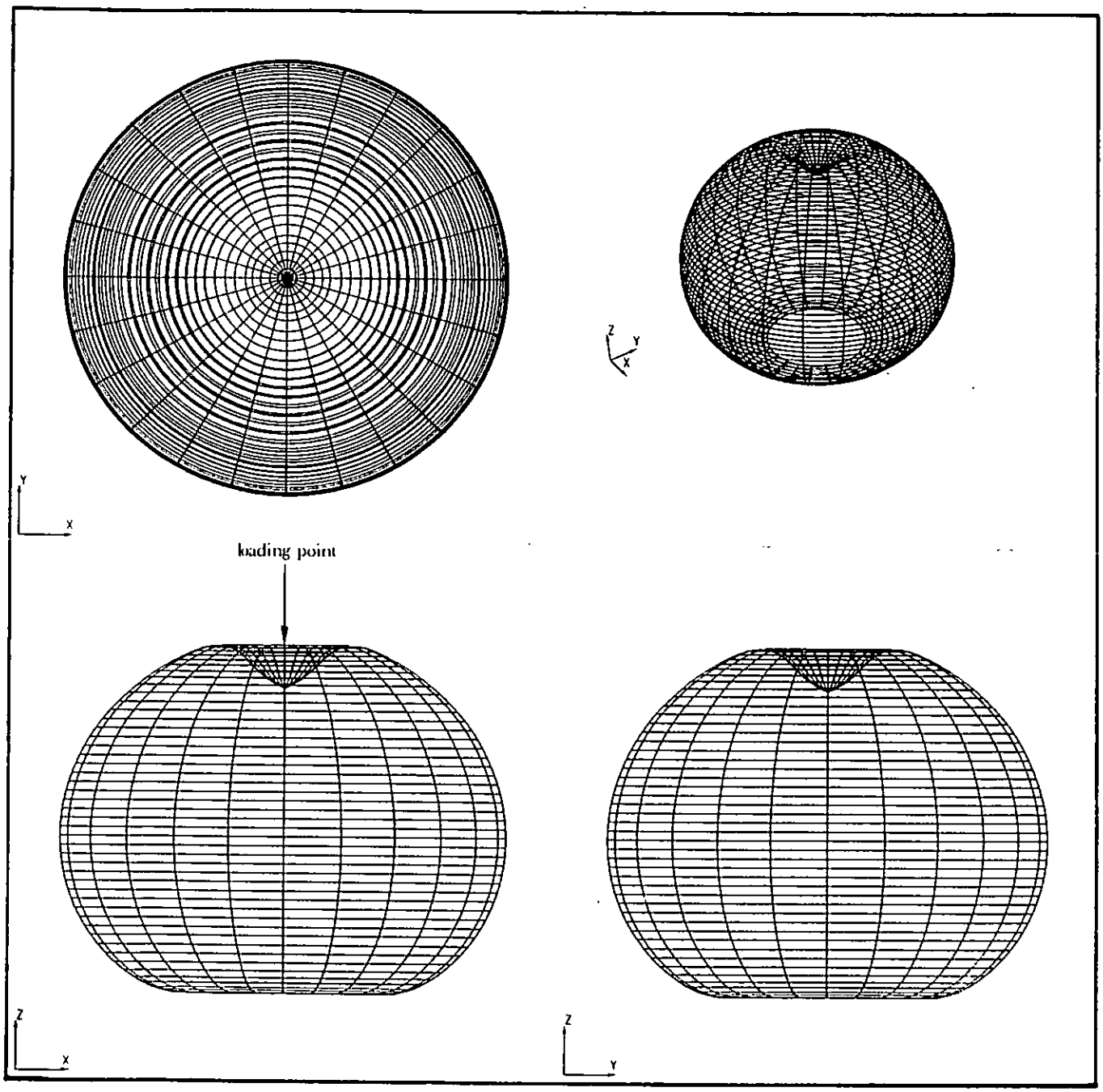

FIG. 3.30–*DEFORMED STRUCTURE UNDER DYNAMIC COLLAPSE BUCKLING FOR A NORMAL POINT LOAD ACTING AT APEX*
––COLLAPSE LOAD = 4.50 *kN––*
(*DISPLACEMENTS* ×2)

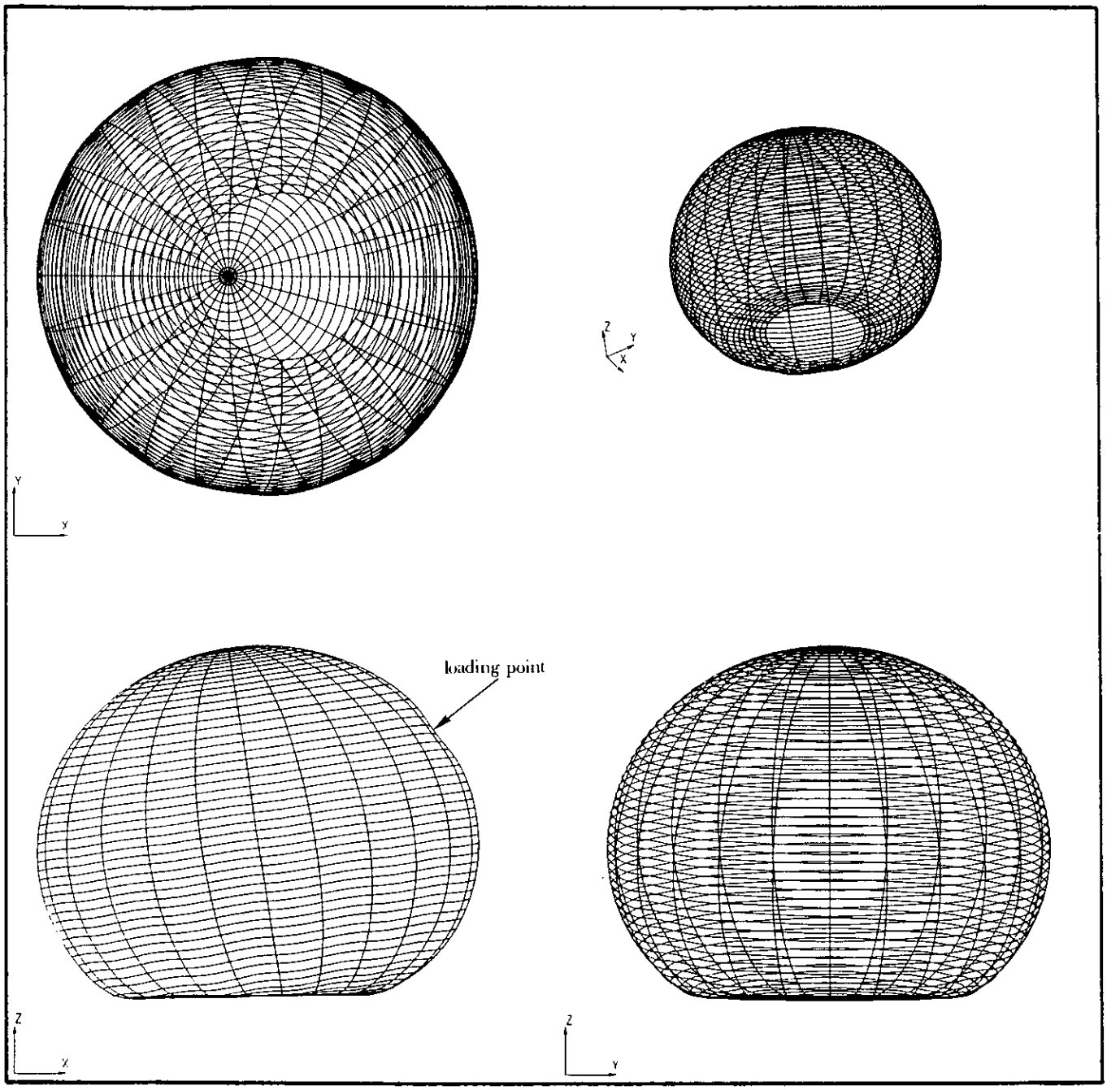

FIG. 3.31–*DEFORMED STRUCTURE UNDER DYNAMIC COLLAPSE BUCKLING FOR A NORMAL POINT LOAD ACTING* 60° *AWAY FROM APEX*
––COLLAPSE LOAD = 7.75 *kN––*
(*DISPLACEMENTS* ×1)

CHAPTER 4

MODAL TESTING OF THE ECHINODOME

4.1 SUMMARY

A comprehensive modal testing of the Echinodome was carried out adopting a monoreference technique. Coordinates used in the modal test were selected and an oblique degree of freedom was added to the prototype, to be used as the driving point, in order to excite all vibrational modes. A triaxial accelerometer was utilised in the measurement of response data. Four different excitation techniques were investigated and the best used in the modal test.

Data were collected and stored using the SMS modal analysis software which provided a wide range of curve fitting techniques in both frequency and time domains. A comparison between the various curve fitting techniques was carried out. Non–linearities of stiffness and damping were carefully considered.

A comparison between the test structure and the finite element modal models was carried out, in five different forms, to identify poorly modelled areas. Then updating of the finite element mesh and correction of experimental data were performed and a better modelling of the test structure was achieved.

4.2 INTRODUCTION

Modal testing is a vibration test carried out with the purpose of determining the modal properties of a structure which are : natural frequencies, damping and mode shapes (modal vectors).

A modal test may be composed of the following three stages,

i. data acquisition and signal processing;

ii. modal properties extraction; and,

iii. forming a spatial mathematical model.

RESPONSE CHARACTERISTICS	→	MODAL PROPERTIES	→	SPATIAL MATHEMATICAL MODEL
$....H_{jk}(\omega)....$		$....\omega_r,\zeta_r,\{\phi\}_r....$		$....k_r, m_r, c_r....$

Firstly, a known excitation is applied to a structure and the corresponding structural response is measured. Acquiring both input (excitation) and output (response) signals a relationship in the form of the FRF is obtained.

Secondly, curve fitting techniques are applied to the measured FRF to extract the modal properties of the structure under consideration.

Thirdly, spatial models are constructed, from the structural modal parameters, in the form of stiffness, mass and damping.

Results obtained from a modal test have three widely used applications.

1. **Model Verifications :** a theoretical analysis, using the finite element method or any other theoretical procedure, is carried out to obtain structural dynamic properties hence permitting a theory–experimental comparison. In some cases such an application ends by carrying out a comparison for the modal properties. Recently, new methods have been developed for correlating finite element and modal testing results [54-56] . These methods make it possible to identify inaccurately modelled regions thus enabling the updating of the finite element model.
2. **Modification Simulation :** once a verified theoretical model is obtained it can be used in determining the effect on the structural modal properties resulting from physical modifications (mass, stiffness, damping and substructures).
3. **Response/Force Predictions :** the availability of an experimental set of response characteristics (FRFs) enables the prediction of structural response to any combination of excitations and in the same manner force can be derived from response measurements.

In conclusion, to obtain a validated finite element model for the Echinodome to be used in the dynamic analysis a modal test must be performed on it.

4.3 STRUCTURE PREPARATION

Before a modal test is started the following three main elements must be considered,

i. distribution of measurement points;

ii. supporting conditions; and,

iii. driving point location and direction.

In the current investigation a monoreference modal testing technique was adopted which is based on measuring a group of FRFs between a set of degrees of freedom and a common reference degree of freedom.

After initial trials for the test structure supporting conditions response was measured at a number of spatially distributed stations on the prototype and excitation was applied to the structure's surface obliquely.

4.3.1 Measurement Points

A total of forty nine measurement stations were marked, one of which was the apex and the rest were located on twelve equally spaced meridians 30° apart M1 $\rightarrow$ M12 (see Fig. 2.5). On each meridian four points were positioned, separated by an angle $\phi = 30^{\circ}$, starting from the apex downwards ($\phi = 30^{\circ}, 60^{\circ}, 90^{\circ}, 120^{\circ}$) as shown in Fig. 4.1(a).

Using a triaxial accelerometer, response was measured at each position in three mutually perpendicular directions —radial, meridional and circumferential— (see Fig. 4.1(b)), thus giving a sum of 147 degrees of freedom (147 measurements).

4.3.2 Supporting Conditions

The test structure was tested in two different supporting conditions, free and grounded. For the free state the prototype was soft mounted to ground using a mat of rubber foam, as shown in Fig. 4.2(a). The structure was excited using a modally tuned impact hammer. Excitation was applied normal to the surface at several points while response was measured at a single reference point, in three mutually perpendicular directions, using a triaxial accelerometer.

After the acquisition of a number of FRFs it was noticed that two of the natural modes existed in the frequency range 12 $\rightarrow$ 21 Hz and for some measurements the FRF was highly contaminated with noise in that range, thus casting some doubt on the quality of modal parameters (ω_r, ζ_r, $\{\phi\}_r$) which would be extracted.

Consequently, attention was reversed to the grounded state. A cubical steel mass, with a linear dimension of 350 mm, was placed on a vibration isolator to seclude any ground vibrations. Several FRF measurements were performed on the mass block at a number of stations to determine the vibration level in the range $0 \rightarrow 1600$ Hz.

A tufnol plate of dimensions $350 \times 350 \times 25$ mm was fixed to the cubical steel mass using four bolts, on top of which the Echinodome with its tufnol base ($200 \times 200 \times 19$ mm) was secured by means of another set of four bolts. A thin layer of grease was applied between the large tufnol plate and the steel cube, and between each of the tufnol plates with the advantage of enhancing coupling between each of the surfaces (see Fig. 4.2(b)).

FRF measurements were carried out on the test structure using the impact hammer and the triaxial accelerometer, and on comparing the vibration levels with those of the steel block measured earlier it was established that the latter levels were too low thus arriving at the conclusion that the test structure was attached to a sufficiently rigid base which provided the necessary grounding conditions.

4.3.3 Driving Point

To excite all vibrational modes within a specific frequency range careful consideration must be given to the choice of the common reference degree of freedom because of the axisymmetry of the Echinodome.

From earlier numerical investigation of the mode shapes (vide Chapter 3) it was established that the first four modes were two repeated symmetric modes, one axisymmetric and one torsional. If excitation was applied normal to the surface only one of the symmetric modes would be excited as well as the axisymmetric mode. The driving point degree of freedom would be a vibrational node for both the second symmetric mode and the torsional mode and, as a result, they would not be excited. In order to excite all four modes the driving force must be applied at an angle to the plane containing the meridian on which the driving point lies (an asymmetric direction).

An oblique degree of freedom was introduced by attaching a steel adaptor to the test structure at the driving point. The adaptor weighed less than 4 gm and was glued firmly to the surface of the prototype. A hole was drilled and tapped along the adaptor's centreline to allow for a push rod (stinger) attachment. A similar idea was developed by Døssing [57] .

The excitation force was applied to the structure using a freely supported electro–magnetic shaker. The force was transmitted from the shaker to the structure through a 3 mm diameter stinger. FRF measurements were performed with stingers of three different lengths, 275 mm, 50 mm and 10 mm. The measured FRFs were compared together and it was noticed that in changing the length of the stinger from 275 mm to 50 mm the second peak was shifted from

112 Hz to 93 Hz while no significant change was observed when using the 10 mm long stinger. Consequently it was decided to apply the excitation to the structure utilising the shortest stinger (10 mm). Details of the orientation of the oblique degree of freedom relative to the test structure are shown in Fig. 4.3 and photographic presentation of the driving point is in Fig. 4.4.

When measuring the cross point FRFs the triaxial accelerometer was placed as close as possible to the driving point.

4.4 INSTRUMENTATION

Fig. 4.5 shows a block diagram of the instrumentation and data acquisition system employed in the current modal test. In the following subsections a brief description of the modal testing set–up is given while more detailed information for individual instruments can be found in the relevant instruction manuals [58] .

4.4.1 Excitation

Usage of two different exciters was possible in the form of non–attached and attached exciters represented by an impact hammer and vibration exciter (shaker) respectively. Choice of a vibration exciter was preferred for two reasons : firstly, it was possible to generate a wide range of various signal waveforms and secondly, the excitation signal could be band limited (not possible when employing an impact hammer for excitation) thus enabling the concentration of the excitation energy in the frequency band of interest, hence achieving a minimum dynamic range for the measurement which results in a better signal to noise ratio.

A B&K type 4809 vibration exciter was utilised to apply an excitation to the test structure via a push rod of 10 mm length and 3 mm diameter. The excitation signal was generated using an HP model 3562A dual channel dynamic signal analyser and was routed to the exciter after being fed to a B&K type 2706 power amplifier. The input force signal to the structure was measured with a KISTLER model 9001 force cell which was signal conditioned by means of a B&K type 2635 charge amplifier. The force cell weighed less than 4 gm and was fixed between the steel adaptor and one end of the stinger.

4.4.2 Response

The response signal was acquired for three global axes at each station on the test structure with the aid of a miniature triaxial quartz accelerometer PCB model 303A06. The response transducers had a total mass of 22 gm and an operating frequency range 10 Hz $\rightarrow$ 1000 Hz. A combined power supply and signal amplifier unit PCB model 480D06 was used to power the electronics of each response transducer and amplify its signal. Petro wax was utilised in mounting

the triaxial accelerometer on the surface of the prototype.

4.4.3 Accelerance Measurement

Both excitation and response signals were captured and digitised using the HP model 3562A dual channel dynamic signal analyser. Once the time records for each channel were filled with 2048 samples, fast Fourier transformations were performed to compute the FRFs according to the following formula :

$$H_1(\omega) = \frac{G_{FR}(\omega)}{G_{FF}(\omega)} \qquad \text{.....} \qquad (4.1)$$

where $G_{FR}(\omega)$ represents the cross spectrum between the excitation and the response signals; and,

$G_{FF}(\omega)$ represents the auto–spectrum of the force signal.

The information of the FRF was presented in 801 equally spaced spectral lines in the form of accelerance.

Several trials were carried out to select the most optimum frequency range of interest which was established to be 29.69 → 654.69 Hz with a frequency resolution Δf = 0.78125 Hz.

For each measured FRF the coherence function (Eqn (4.2)) was computed and displayed on the analyser's monitor.

$$\text{Coherence}(\omega) = \frac{|G_{FR}(\omega)|^2}{G_{FF}(\omega) \cdot G_{RR}(\omega)} \qquad \text{.....} \qquad (4.2)$$

where $G_{RR}(\omega)$ represents the auto–spectrum of the response signal.

The coherence magnitude varies between zero and unity and values of 0.9 and over indicate a measurement of high quality. Low coherence values do not necessarily point to poor quality measurements and can be attributed to any of the following reasons,

i. bias error which is due to a low frequency resolution at rapidly changing resonances and antiresonances;

ii. presence of noise in input and/or output signals;

iii. structural non–linearity; and,

iv. existence of secondary unwanted excitations arising due to incorrect attachment of the shaker.

4.4.4 Data Acquisition and Analysis

Once an FRF measurement was made the 801 data points were transferred from the analyser to an HP 9000 model 236 desk top computer, running the SMS MODAL 3.0 modal analysis software, via its HPIB (interface bus). Each individual FRF was then stored by the program in a data file for later analysis on a mass storage medium (disk) after recording information concerning the location of the excitation degree of freedom and the degree of freedom at which response was measured. The computer was connected to a plotter and a printer for documentation purposes.

4.5 EXCITATION TECHNIQUES

Employing a vibration exciter necessitated the usage of a signal generator. The HP 3562A analyser is capable of generating several waveforms which can be classified as follows :

1. **Steady state or harmonic → fixed sine**
2. **Periodic → periodic chirp**
3. **Random → pure random**
4. **Transient → burst random and burst chirp**

In the following subsections the advantages and disadvantages of the above waveforms are stated with emphasis on the signals generated by the analyser. Several other excitation techniques are discussed elsewhere [49,59-63] .

4.5.1 Steady State Excitation

Excitation is applied to the structure at a single frequency using a fixed sinusoidal wave and by either stepping or sweeping a frequency range of interest is encompassed. Such a technique produces a high signal to noise ratio because of the concentration of the excitation energy at each particular frequency.

The harmonic excitation technique can be used to identify non–linear systems. By exciting such systems with different excitation levels different FRFs are obtained describing the non–linearity characteristics.

The main disadvantage of the current excitation method lies in its slow speed especially for lightly damped structures.

The frequency spectrum of steady state signals must be scaled whether in terms of mean square (power — PWR), in units squared or in terms of root mean square (RMS), in units [64] .

4.5.2 Periodic Excitation

Periodic chirp, periodic random and pseudo random signals are examples of periodic waveforms used in the current excitation technique. Characteristics of the latter two signals are discussed in detail in Refs (59) and (60).

The analyser was capable of generating a periodic chirp signal which is a fast sine sweep over a specified frequency span characterised by an almost flat spectrum. The process of weighting the time signals needed to alleviate the problem of leakage was unnecessary as the signal was repeated exactly every time record (the periodic time of the signal was equal to the length of the time record).

The periodic chirp can be used to characterise non–linearities in a similar manner to that described in the previous subsection.

The periodic chirp waveform is a deterministic signal and its frequency spectrum should be scaled whether in terms of mean squared (PWR) in units, squared or in terms of root mean square (RMS), in units.

4.5.3 Random Excitation

The dynamic signal analyser had the facility of supplying continuous random noise across a selected frequency span. Because of the randomness of the magnitude and the phase of the spectral components it is not possible to characterise a non–linear system using the current excitation technique as the non–linear distortion reduces to zero on averaging a number of time records.

The main disadvantage of random excitation is that the time records for both excitation and response are not periodic and Hanning windows are utilised to reduce the effect of leakage errors. Multiplication in the time domain is equivalent to convolution in the frequency domain and as both excitation and response spectra are unequal, the Hanning weighting distorts the true FRF.

A smooth spectrum can be produced by using a high number of ensemble averages and to reduce the measurement time overlap averaging can be employed.

Random signals are scaled in terms of power spectral density (PSD) in units squared per Hz which can be achieved by normalising the mean square spectrum by the frequency resolution (Δf).

4.5.4 Transient Excitation

Burst chirp and burst random are classed as transient signals. A succession of bursts of signal are generated for a specific percentage of the time record.

If the response decays to zero before the end of the time record then no weighting is necessary. But for lightly damped structures this might not be the case and as a result an exponential window for both excitation and response time records would be used to force sufficient decay at the end of the time record. The previous weighting process does not introduce any leakage errors and a mathematical proof has been provided in Ref. (65).

Similar to periodic chirp, burst chirp excitation can describe non–linear systems while a burst random excitation would produce a least square estimate of the structure's linear response.

Transient signals should have spectra scaled in terms of energy spectral density (ESD) in units squared times seconds per Hz and is obtained by scaling the mean square spectrum by the time record length (T), to obtain the total energy, and by normalising the resulting spectrum by the frequency resolution (Δf).

4.5.5 Comparison Between Various Excitation Techniques

The triaxial accelerometer was mounted at the apex of the test structure and four accelerance measurements were performed for each of the radial, meridional and circumferential directions. A different excitation waveform was employed in each of the four measurements and can be listed as follows : periodic chirp, true random, burst chirp and burst random. After viewing the measured FRFs a decision was made to study the effect of various excitation techniques on the meridional accelerance only as it possessed the worst of the three coherences (radial, meridional and circumferential). Table 4.1 contains extracts of the individual measurement set–ups while Figs 4.6(a $\rightarrow$ d) contain the results of the various measurements.

SIGNAL TYPE	SOURCE LEVEL (mV)	WINDOW TYPE	AVERAGING		(BURST LENGTH)/T (%)
			NUMBER OF AVERAGES	OVERLAP (%)	
Periodic chirp	250 (RMS)	uniform	10	0	—
Random	250 (peak)	Hanning	20	50	—
Burst chirp	250 (RMS)	uniform	10	0	50
Burst random	250 (peak)	uniform	10	0	50

TABLE 4.1 — *MEASUREMENT SET–UPS FOR VARIOUS EXCITATION TECHNIQUES*

The excitation frequency spectra for all measurements were characterised by a low force level adjacent to the first two peaks which can be explained as follows.

In the vicinity of structural resonance the velocity of the shaker armature (drive coil and assembly table) is at a maximum and such a motion within a magnetic field produces a back e.m.f. of maximum magnitude at structural resonance which results in a marked reduction in the force level. Consequently, to measure the true force applied to the structure a force cell is required between the structure and the shaker armature which was the case for all current and future measurements.

In order to detect the existence of any non–linear characteristics the level of the periodic chirp excitation was increased from 250 mV RMS to 500 mV RMS.

Accelerance magnitudes at seven different peaks are listed together with their corresponding frequencies and coherence magnitudes in Table 4.2.

(i)

SIGNAL TYPE		FREQUENCY (Hz) PEAK NUMBER						
		1	2	3	4	5	6	7
Periodic chirp	(500 mV RMS)	60.94	82.81	245.31	327.34	508.59	511.72	577.34
Periodic chirp	(250 mV RMS)	61.72	85.94	246.09	338.28	509.38	512.50	575.78
Random	(250 mV peak)	61.72	85.94	246.09	338.28	509.38	513.28	575.78
Burst chirp	(250 mV RMS)	61.72	85.94	246.09	338.28	509.38	512.50	575.78
Burst random	(250 mV peak)	61.72	85.94	246.09	338.28	509.38	513.28	575.78

(ii)

SIGNAL TYPE		ACCELERANCE MAGNITUDE (dB) PEAK NUMBER						
		1	2	3	4	5	6	7
Periodic chirp	(500 mV RMS)	18.73	–12.38	–15.55	–19.36	–6.03	–3.49	–23.69
Periodic chirp	(250 mV RMS)	18.31	–3.23	–15.54	–16.77	–5.08	1.08	–8.15
Random	(250 mV peak)	15.23	–4.46	–14.92	–16.15	–6.92	–3.23	–9.38
Burst chirp	(250 mV RMS)	18.92	–3.23	–14.92	–16.15	–5.69	–1.38	–8.15
Burst random	(250 mV peak)	18.31	–3.23	–15.54	–16.15	–6.92	–2.62	–9.38

(iii)

SIGNAL TYPE		COHERENCE PEAK NUMBER						
		1	2	3	4	5	6	7
Periodic chirp	(500 mV RMS)	1.00	1.00	0.99	0.99	1.00	1.00	0.92
Periodic chirp	(250 mV RMS)	1.00	1.00	0.98	0.98	1.00	1.00	0.99
Random	(250 mV peak)	0.77	0.97	0.98	0.98	0.59	0.83	0.93
Burst chirp	(250 mV RMS)	1.00	1.00	0.97	0.98	1.00	1.00	0.99
Burst random	(250 mV peak)	1.00	0.95	0.98	0.94	0.97	1.00	1.00

TABLE 4.2 — *ACCELERANCE MEASUREMENT RESULTS FOR THE MERIDIONAL DOF AT APEX USING VARIOUS EXCITATION WAVEFORMS AND LEVELS*

It was observed from the results of the last four excitation techniques listed in Table 4.2 that except for the random technique all coherence values were greater than or equal to 0.95 which indicated good quality accelerance measurements. The reason for the low coherence encountered when using random excitation was due to leakage though an attempt was made to minimise it by Hanning weighting of the input and output time domain signals.

When comparing the peak positions on the frequency axis of the accelerance functions obtained by periodic chirp signals of different levels (see Table 4.2(i)) no marked difference was noticed for peaks 1, 3, 5 and 6, while peaks 2, 4 and 7 suffered a considerable shift. As will be explained later the fourth peak corresponded to a torsional mode which makes the apex a node in both meridional and circumferential directions. Consequently, it becomes very difficult to measure accurate response levels because the response signal would be highly contaminated with noise which leads to incorrect estimates of peak locations.

A choice was made to carry out the modal testing using a periodic chirp waveform excitation with a level of 500 mV RMS as it produced a high signal to noise ratio and at the same time the excitation force was considered too low to invoke structural non–linearity.

In recent years, simple methods have been developed to detect the non–linearity of either stiffness or damping of a system in a structural dynamics test, but such techniques were only applicable to SDOF systems. By limiting the excitation frequency range to encompass one mode at a time it was possible to identify if either types of non–linearity (stiffness and damping) existed. Such a process appeared to be unnecessary due to the low force level which induced a nominally linear elastic structural response thus making it possible to apply conventional modal analysis procedures, based on linear models, to extract the modal parameters.

4.6 CALIBRATION

Calibration tests, before and after the modal test, were carried out to ensure that the overall sensitivity of each accelerometer and the force transducer was conformable with that computed from the manufacturer's certificates.

A stainless steel, rigid steel mass of cylindrical shape and 4.198 kg mass was used in the current calibration test. An attempt was made to excite the mass along its centreline, while freely suspending it, with the shaker–stinger–force cell–adaptor combination but it was unsuccessful. This was because of the difficulty of joining the adaptor and the rigid mass due to the small area of contact.

As a result, a different calibration arrangement was used as depicted in Fig. 4.7. Excitation was applied with the aid of an impulse hammer on the force cell which was fixed on one end along the centreline of the rigid mass while the triaxial accelerometer was mounted on the other end along the same line. An accelerance measurement was carried out by acquiring the excitation and response signals through the force cell and the relevant accelerometer. The calibration constants fed to the analyser for both channels were unit volts and a frequency range $0 \rightarrow 800$ Hz was selected. The average overall sensitivity was deduced for each accelerometer–force cell combination from the corresponding accelerance function (see Fig. 4.8) according to the following formula :

$$\frac{\ddot{\bar{\delta}}}{\bar{F}} = S_o \frac{V_{\ddot{\bar{\delta}}}}{V_F} \qquad \text{(4.3)}$$

where $\ddot{\bar{\delta}}$ represents the average of the acceleration spectrum;

$\bar{F}$ represents the average of the force spectrum;

$V_{\ddot{\bar{\delta}}}$ represents the voltage output from the electronics of the accelerometer;

V_F represents the voltage output from the electronics of the force cell; and,

S_o represents the overall sensitivity of an accelerometer and force cell combination in kg^{-1} units.

Table 4.3 lists measured and computed (from manufacturer's calibration constants) overall sensitivities for each of the three accelerometers with the force cell. In the calculation of the overall sensitivity from the measured accelerance functions the total rigid mass was considered to be composed of the rigid mass (4.198 kg), triaxial accelerometer (22 gm) and force cell (4 gm).

ACCELERANCE NUMBER (DIRECTION)	OVERALL MEAN SENSITIVITY (ms^{-2}/N)		
	MEASURED		COMPUTED
	BEFORE MODAL TEST	AFTER MODAL TEST	
1 (meridional)	3.075	3.269	3.323
2 (normal)	2.959	3.069	3.173
3 (circumferential)	2.994	3.053	3.267

TABLE 4.3 — *COMPARISON BETWEEN MEASURED AND COMPUTED OVERALL SENSITIVITIES FOR TRIAXIAL ACCELEROMETER–FORCE CELL COMBINATION*

4.7 EXPERIMENTAL MODAL ANALYSIS

Experimental modal analysis is the stage in a modal test where structural modal properties are extracted from an FRF data base using curve fitting techniques. In order to achieve good results in experimental modal analysis it is necessary to understand the theory behind it. The mathematical development of the equations of motion for the general cases of viscous and hysteretic damping can be found in Appendix F.

4.7.1 Curve Fitting Techniques

From Appendix F, the receptance FRF can be represented for the general case of viscous damping by

$$\alpha_{jk}(\omega) = \sum_{r=1}^{N} \left[\frac{{}_rR_{jk}}{(i\omega - s_r)} + \frac{{}_rR^*_{jk}}{(i\omega - s_r^*)} \right] \qquad \text{.....} \qquad (4.4)$$

where $s_r = -\zeta_r\omega_r + i\omega_r\sqrt{1-\zeta_r^2}$ and represents the r^{th} pole location of the FRF on the frequency axis;

ζ_r represents the critical damping constant;

$_rR_{jk}$ represents the jk^{th} element of the residue matrix for the r^{th} mode; and,

j, k are subscripts denoting the response and excitation locations respectively.

While for the general case of hysteretic damping the receptance FRF can be written as

$$\alpha_{jk}(\omega) = \sum_{r=1}^{N} \left[\frac{{}_rR_{jk}}{(\omega_r^2 - \omega^2 + i\eta_r\omega_r^2)} \right] \quad \text{.....} \quad (4.5)$$

where η_r represents the structural damping loss factor.

A curve fitting process is required to extract the modal parameters (natural frequency, damping and residue) from a measured FRF and such a transformation is often thought of as a data reduction process. The data points of the measured FRFs could then be described by either of the above analytical functions (Eqn (4.4) or (4.5)) the coefficients of which are ω_r, ζ_r (or η_r) and $_rR_{jk}$.

At present, several curve fitting techniques are available in both frequency and time domains. Ref. (68) lists a summary of most of the currently used parameter estimation methods together with the assumption used by each technique and their capabilities as well as the evaluation criteria.

It is important to emphasise that the success of the curve fitting process is largely dependent on the type of model used to represent the dynamic characteristics of the structure under test.

4.7.1.1 Local curve fitters— MODAL 3.0 [69] , the modal analysis software used in the current research offered two types of curve fitters for analysing a whole set of measured FRFs. The first class is known as a local curve fitting. After measuring a set of FRFs one is chosen in which all of the modal peaks appear and is characterised by having the least contamination of electrical noise as well as possessing a good coherence function throughout the encompassed frequency range or at least around the resonance peaks. Then any of the implemented curve fitting techniques (SDOF methods : Coincident or Quadratic Fitting, Peak Value Fitting, Circle Fitting, Rational Fraction Polynomial Fitting — MDOF methods : Rational Fraction Polynomial Fitting, Pole/Zero Fitting, Exact or Least Squares Complex Exponents Fitting) is used to extract the modal parameters (ω_r, ζ_r, $_rR_{jk}$) of the chosen function. The natural frequency and damping are global dynamic characteristics of a structure and do not change from one station to another. As a result, the previously identified ω_r and ζ_r values are kept constant for all of the rest of the measured FRFs and only the residues ($_rR_{jk}$) are determined from each newly fitted function.

Local curve fitting was implemented in MODAL 3.0 in such a way that the frequency and damping tables may be updated from different FRFs which overcome the problem of the need for the appearance of all modes with high coherence values in the same measurement.

4.7.1.2 Global curve fitters— The second class of curve fitters available in MODAL 3.0 is known as a global curve fitting which differs from the local curve fitting in that the natural frequency and damping for each mode are estimated using all of the measured FRFs. Thus the pole (s_r) location on the frequency axis is determined in a least squares sense. The second step performed using the curve fitter is to extract the residues and hence mode shapes by processing each individual FRF.

The main benefit of such a technique is that the natural frequencies and dampings are identified accurately which results in better estimates of residues especially when nodal points are encountered. Details of the mathematical background behind the current technique will be described briefly in the following subsection.

4.7.2 Applications of Curve Fitting

MODAL 3.0 offered two of the often used curve fitting techniques in the experimental modal analysis field which were : the least squares complex exponential fitting and rational fraction polynominal fitting. The former method fits a summation of complex exponential functions to an impulse response function which meant that the measured FRF had to be inverse Fourier transformed to the time domain and because of the limited frequency range of the FRF on which the IDFT was to be performed, the wrap around error (time domain leakage) would have occurred which would lead to serious inaccuracies in the estimates of the modal parameters. Conversely, the rational fraction polynomial technique undertook a frequency domain MDOF modal analysis and consequently it was the one to be used in the current research.

The rational fraction polynomial form of FRF was first introduced in 1982 by Richardson and Formenti [70] . In this technique the usual partial fraction expression of Eqn (4.4) is replaced by a ratio of two polynomials in the following form :

$$H(\omega) = \left. \frac{\sum_{k=0}^{m} \left[a_k \, s^k \right]}{\sum_{k=0}^{2N} \left[b_k \, s^k \right]} \right|_{s=i\omega} \qquad \text{.....} \qquad (4.6)$$

where a_k, b_k represent the k^{th} coefficients of the numerator and denominator polynomials respectively.

The direct analysis of the previous formula is difficult because of the ill–conditioning which sometimes occurs in the solution equations and as a result Eqn (4.6) is reformulated in terms of orthogonal polynomials as follows :

$$h_i = H(\omega_i) = \frac{\sum_{k=1}^{m} \left[c_k \, \phi_{i,k} \right]}{\sum_{k=1}^{2N} \left[d_k \, \theta_{i,k} \right]} \quad ; i = 1, 2, 3, \ldots\ldots, L \qquad \ldots\ldots\ldots\ldots \qquad (4.7)$$

$$\sum_{i=1}^{L} \left[\phi^*_{i,k} \, \phi_{i,j} \right] = \begin{cases} 0.0 & ; \quad k \neq j \\ 0.5 & ; \quad k = j \end{cases} \qquad \ldots\ldots\ldots\ldots \qquad (4.8)$$

$$\sum_{i=1}^{L} \left[\theta^*_{i,k} \, |h_i|^2 \theta_{i,j} \right] = \begin{cases} 0.0 & ; \quad k \neq j \\ 0.5 & ; \quad k = j \end{cases} \qquad \ldots\ldots\ldots\ldots \qquad (4.9)$$

where c_k, d_k represent the k^{th} coefficients of the numerator and denominator orthogonal polynomials respectively; and,

h_i represents the i^{th} value of the FRF.

In addition to the orthogonal properties stated in Eqns (4.8) and (4.9), the preceding Eqn (4.7) takes advantage of the Hermitian symmetry of the FRF about the origin of the frequency axis and that the real part of the FRF is even while the imaginary part is odd. The transformation of the FRF expression from Eqn (4.6) to (4.7) removes the ill–conditioning of the solution equations and reduces the number of equations to be solved to approximately half of the initial representation.

The global version of rational fraction polynomial [71] modal analysis method split the modal extraction task into two steps. The first step was to identify the natural frequencies and the corresponding damping values using the whole set of measured FRF, while the second step was to analyse each individual measurement to extract the modal residues. Richardson [71] proved that the global rational fraction polynomial algorithm performs favourably for measurements containing heavy modal coupling and random noise.

4.7.2.1 Determination of the number of modes— When viewing all of the measured accelerance functions it was noticed that the Echinodome prototype exhibited some motion in seven clear regions on the frequency axis and as a result the frequency ranges of interest were chosen to be as listed in Table 4.4.

RANGE NUMBER	LOWER AND UPPER FREQUENCY BOUNDS	NUMBER OF CONTAINED PEAKS
1	50.00 → 71.88	1
2	75.00 → 125.00	1
3	200.00 → 380.47	2
4	494.53 → 529.69	2
5	566.41 → 586.72	1

TABLE 4.4 — *FREQUENCY RANGES OF INTEREST FOR THE ECHINODOME PROTOTYPE*

When using the global rational fraction polynomial curve fitting technique two ways were possible to compensate for the out of band modes. The first [71] was to specify extra numerator polynomial terms while the second [72] was by overspecifying the number of modes. In general the first approach is preferred as it eliminates the requirement of sorting computational modes, which is a necessity for the latter approach.

The introduction of an oblique degree of freedom through which excitation was applied (details of which are given in an earlier section) ensured that all vibrational modes were excited and as a result the existence of double modes with identical natural frequencies and damping values was expected due to the axisymmetry of the test structure. Though such modes were expected to uncouple because of the geometrical imperfections present in the prototype in the form of non–uniform shell thickness and the seam.

Maia and Ewins [73] described an approach to overcome the problem of identifying the correct number of modes within a frequency range and a similar technique was adopted in the current investigation to analyse the measured accelerance functions of the test structure.

For the first frequency range a single measurement was chosen and a global curve fitting was performed to extract the natural frequencies and critical damping values of the specified number of modes (N). The previous step was repeated for each of the remaining measurements using the same number of modes and the same frequency range.

Initially it was assumed that a double mode existed within the frequency range of interest and then a computer program called INTEL, which will be described in the following paragraphs, was used to identify the correct number of modes. The out of band modes were compensated for using two different approaches, the first was by using two additional modes while the second was by utilising 16 extra numerator polynomial terms and then the output for each case was examined separately using the INTEL program.

The flow chart of the INTEL program is shown in Fig. 4.9. The program takes in the number of identified modes (N) for each measurement (which is kept constant for all of the remaining measurements) together with the identified natural frequencies and damping values. The bounds of the frequency range of interest are given as well.

After the input data is submitted the program removes the computational modes from any future analysis. The computational modes were selected on the following bases,

i. if the natural frequency (ω_r) of the considered mode lay outside the frequency range of interest; or,

ii. if the critical damping value (ζ_r) of the considered mode was less than or equal to zero, or if it was greater than 5 percent.

Next the program enters a loop to count the number of times the following conditions are satisfied for each of the remaining measurements :

1. $(1 - \text{F.T.}) \times \omega_{r_o} \leq \omega_r \leq (1 + \text{F.T.}) \times \omega_{r_o}$

2. $(1 - \text{D.T.}) \times \zeta_{r_o} \leq \zeta_r \leq (1 + \text{D.T.}) \times \zeta_{r_o}$

where $r_o = 1, 2, 3, \ldots\ldots, 147 \times N$ and $r_o \neq r$;

F.T. and D.T. represent a frequency and a damping tolerance respectively, specified by the operator.

The preceding conditions represent a check of the existence of the considered mode in any of the remaining measurements and consequently if the number of times the above conditions are satisfied for an individual FRF is greater than one then the program counts it only once.

Once the loop is ended the two maximum number of repetitions (NMAX1 and NMAX2) are determined (they could be equal) for two different modes. A comparison between NMAX1 and NMAX2 is carried out to establish the number of existing modes. The comparison was based on the following rules :

1. If NMAX1 ≥ 147 × 0.3 [§]
   and NMAX2 ≥ 147 × 0.3 [§]
   and (NMAX1 − NMAX2) ≤ 147 × 0.15 [§]
   ⇒ **There are two modes.**

2. If NMAX1 ≥ 147 × 0.3
   and NMAX2 ≥ 147 × 0.3
   and (NMAX1 − NMAX2) > 147 × 0.15
   ⇒ **There is one mode.**

3. If NMAX1 ≥ 147 × 0.3
   and NMAX2 < 147 × 0.3
   ⇒ **There is one mode.**

4. If NMAX1 < 147 × 0.3
   and NMAX2 < 147 × 0.3
   ⇒ **There are zero modes.**

Then the number of modes is output together with the mean and coefficient of variation of both the natural frequencies and damping values. Several frequency tolerances (F.T.) were specified for the modes identified using the global rational fraction polynomial technique of MODAL 3.0 (the damping tolerance was kept constant, D.T. = 0.15) and the results are listed in Table 4.5 for the first, second and fourth frequency range of interest.

§ Various limits introduced in the INTEL program were similar to those adopted by Maia and Ewins [73] although it is necessary to emphasise that the frequency and damping tolerances were different because of the difference in the degree of modal coupling between the Echinodome prototype and the circular disc used in Ref. (73).

FREQUENCY RANGE NUMBER	FREQUENCY TOLERANCE (%)	COMPENSATION FOR THE OUT OF BAND MODES											
		TWO ADDITIONAL MODES						16 EXTRA NUMERATOR POLYNOMIAL TERMS					
		NUMBER OF MODES	NUMBER OF REPETITIONS	FREQUENCY		DAMPING		NUMBER OF MODES	NUMBER OF REPETITIONS	FREQUENCY		DAMPING	
				MEAN (Hz)	C.O.V. (%)	MEAN (%)	C.O.V. (%)			MEAN (Hz)	C.O.V. (%)	MEAN (%)	C.O.V. (%)
1	0.25	2	48 46	60.56 61.41	0.13 0.14	1.82 1.30	8.21 7.41	1	46	60.68	0.13	1.41	7.64
	0.50	2	65 61	60.61 61.43	0.23 0.23	1.83 1.31	8.62 7.92	2	58 63	60.68 61.65	0.21 0.27	1.42 1.45	8.04 7.71
	0.75	2	76 78	60.67 60.71	0.36 0.36	1.60 1.31	18.43 41.00	2	64 70	60.73 61.63	0.30 0.34	1.42 1.50	8.05 9.18
	1.00	1	103	60.73	1.42	1.32	40.45	1	110	60.83	1.31	1.44	13.85
2	0.25	0	—	—	—	—	—	0	—	—	—	—	—
	0.50	0	—	—	—	—	—	0	—	—	—	—	—
	0.75	0	—	—	—	—	—	0	—	—	—	—	—
	1.00	0	—	—	—	—	—	1	47	91.41	3.56	1.91	9.05
4	0.25	0	—	—	—	—	—	1	74	510.49	0.07	0.06	8.18
	0.50	0	—	—	—	—	—	1	82	510.60	0.36	0.06	10.80
	0.75	0	—	—	—	—	—	2	65 87	510.45 513.17	0.41 0.50	0.07 0.06	10.72 13.98
	1.00	0	—	—	—	—	—	1	88	510.40	0.56	0.06	10.69

TABLE 4.5 — *RESULTS FROM THE INTEL PROGRAM USING VARIOUS FREQUENCY TOLERANCE FACTORS*

It can be seen from the previous table that in general a 0.25 percent frequency tolerance was considered very tight for the INTEL program to identify the existence of more than one mode, if any. As a result the frequency tolerance was increased and the effect on the number of identified modes was noted.

For the first frequency range, by increasing the frequency tolerance two clear modes were identified for both cases of residual energy compensation (two additional modes and 16 extra numerator polynomial terms) until the frequency tolerance contained both modes and then the INTEL program output the characteristics of a single mode, yet it was evident that the first peak was composed of two almost identical (in frequency and damping) vibrational modes. The program suffered some difficulty in identifying the correct number of modes forming the first peak because of the heavy modal coupling as well as the considerably large frequency resolution around such a peak.

When observing the results for the second frequency range, in most of the cases the program failed to identify any modes because the number of repetitions was less than the limit specified in INTEL, although viewing the measured accelerance functions there was a clear mode within the considered frequency range. The failure of the mode identification by the program was attributed to the reason that the second peak varied its position on the frequency axis between 85 $\rightarrow$ 105 Hz throughout all of the measurements and thus it was difficult for such a mode to fall inside the specified tolerance.

The application of INTEL on the curve fitting results of the fourth frequency range was not as effective as for the first range for several reasons,

i. the modal coupling was of a higher degree than the first range;

ii. the critical damping value was very small; and,

iii. the low accelerance magnitudes of modes considered.

In summary, it can be concluded that there were two modes in the first frequency range, a remark which can be substantiated by the evidence available in Table 4.5. Therefore, changing either the compensation technique or the frequency tolerance values had little influence on the number of identified modes.

In addition, the use of the INTEL program has proven to be effective in detecting whether a specified peak changes its position along the frequency axis.

4.7.2.2 Natural frequency and damping estimates— The above conclusions assisted in specifying the correct number of modes within each frequency range. The global rational fraction polynomial curve fitter of MODAL 3.0 was applied to all of the measured accelerance functions for each frequency range to determine the least square estimates for both the natural frequency and critical damping value of each mode. Compensation for the residual energy of the out of band modes was carried out using the maximum number of extra numerator polynomial terms. The global curve fitter in MODAL 3.0 could analyse N modes with $2(10 - N)$ extra numerator polynomial terms provided that N is not greater than ten.

The specifications of the input for MODAL 3.0 are listed in Table 4.6 while the frequency and damping estimates can be found in Table 4.7.

FREQUENCY RANGE NUMBER	CURSOR POSITIONS (Hz)	MODE RANGE	NUMBER OF EXTRA NUMERATOR POLYNOMIAL TERMS
1	50.00 → 71.88	1 → 2	16
2	75.00 → 125.00	3	18
3	200.00 → 380.47	4 → 5	16
4	494.53 → 529.69	6 → 7	16
5	566.41 → 586.72	8	18

TABLE 4.6 — *SPECIFICATIONS OF INPUT DATA FOR MODAL 3.0*

MODE NUMBER	FREQUENCY (Hz)	CRITICAL DAMPING (%)
1	60.67	1.448
2	61.64	1.467
3	95.06	1.495
4	243.69	1.787
5	333.12	3.196
6	510.37	0.060
7	513.06	0.065
8	576.17	0.064

TABLE 4.7 — *FREQUENCY AND DAMPING LEAST SQUARES ESTIMATES*

It is encouraging to note from the above table that the first and second modes were detected correctly and the damping estimates were approximately equal (it will be demonstrated later that the motion of both modes was very similar) thus confirming the earlier derived conclusion concerning the number of modes in the first frequency range.

4.7.2.3 Modal constants identification— The modal constants (residues) were calculatable following the determination of the global estimates of the natural frequencies and damping values.

Three different procedures using the global rational fraction polynomial curve fitter were adopted in an attempt to determine the most accurate mode shape estimates for later analysis. All three procedures used the same frequency and damping estimates listed in Table 4.7.

The first procedure was based on curve fitting all of the measured accelerance functions for one frequency range using the maximum extra polynomial numerator terms to compensate for the out of band energy (similar values to those in Table 4.6 were used). The process was repeated for each of the frequency ranges and at the end the modal constants for all measurements and for all modes were determined. The procedure was named LFIT.

The second procedure was slightly different in that the curve fitting process was carried out on a single measurement for the entire frequency domain without compensating for the out of band modes as none should have existed. The previous step was performed for all of the measurements and the whole process was called GFIT.

The third and last procedure was similar to the above procedure, GFIT, with the exception that four extra numerator polynomial terms were used in curve fitting for the modal constants. The procedure was termed GFIT4.

The complex modal constants extracted using the above mentioned procedures are listed in Table 4.8. As observed, attention was concentrated on one of the cross point accelerance functions as it contained all of the vibrational mode shapes.

MEASUREMENT STATION NAME AND DIRECTION	MODE NUMBER	LFIT		GFIT		GFIT4	
		MAGNITUDE ($kg^{-1}s$)	PHASE (Degs ^{o})	MAGNITUDE ($kg^{-1}s$)	PHASE (Degs ^{o})	MAGNITUDE ($kg^{-1}s$)	PHASE (Degs ^{o})
	1	89.2	341.3	92.2	347.4	87.8	345.5
	2	39.9	50.5	36.0	65.5	35.3	56.8
	3	9.9	37.2	13.3	33.9	11.3	17.0
5B	4	222.7	196.8	213.2	193.3	224.0	195.5
Meridional	5	44.8	27.7	75.3	39.3	40.6	26.1
	6	4.5	49.7	5.7	41.1	5.0	52.0
	7	4.9	234.7	3.3	239.8	4.7	229.6
	8	11.9	220.1	9.9	227.3	11.0	219.2

TABLE 4.8 — *COMPARISON BETWEEN VARIOUS CURVE FITTING PROCEDURES FOR MODAL CONSTANTS*

It can be noted from the previous table that each curve fitting procedure resulted in a different set of modal constants and a decision concerning which was the most correlated to the measured data was established with the aid of graphic representation.

4.7.2.4 Regenerating cross point accelerance functions— Using the above estimates of modal parameters (ω_r, ζ_r and ${}_rR_{jk}$) theoretical FRFs were generated and superimposed on experimental measurements in order to assess the quality of various curve fitting procedures. Fig. 4.10 contains a comparison of LFIT, GFIT and the experimental measurements of the cross point accelerance functions. It is obvious that both curve fitting procedures result in theoretically regenerated accelerance functions that do not conform with the experimental measurements.

A comparison between GFIT, GFIT4 and experimental data is presented in Fig. 4.11 from which the effect of introducing an additional set of four extra polynomial numerator terms can be seen. In theory, compensation for the out of band modes was unnecessary because the excitation spectrum was band limited in the frequency range 26.69 → 654.69 Hz, but the variation of the third mode (second peak) along the frequency axis presented a problem. In regions away from the third mode it was possible to minimise the mismatch of theoretical and experimental data using the four extra polynomial terms yet no possible cure was available for any local disagreement.

4.7.2.5 Mode shapes extraction— Once the modal constants were extracted a sorting process was performed to calculate the mode shapes and the results were transformed to a global set of axes. The MODAL 3.0 estimates of mode shapes had to be mass normalised [74] for later analysis, a job which required the modal constants of the direct point accelerance function. The application of the driving force on the test structure through an oblique degree of freedom made it difficult to measure the latter FRF but a derivation was possible through coordinate transformation using the cross point accelerance functions measured at that station. When mass normalising the mode shapes MODAL 3.0 assumes that the structure under test is lightly damped.

After the sorting process was carried out the phase angles of the modal displacements were plotted for each mode shape as shown in Fig. 4.12 to assess the degree of complexity of the modes. The radial lines represented the relative magnitudes of the modal displacements. Although the phase difference for some eigenvector elements of modes 1 and 2 were of an angle closer to 90° than to 0° or 180° their magnitudes were relatively small and unlikely to affect the overall behaviour of the mode shapes. Consequently, they were assumed to be real modes, an assumption which was deservedly extended to modes 4 and 5. From Fig. 4.12 it was observed that modes 3, 6, 7 and 8 were highly complex and any whitewashing (taking the magnitude of the eigenvector elements and attaching a + or – sign to it, depending on the closeness of the phase difference to either 0° or 180°) would significantly change the experimental mode shapes.

4.7.2.6 Orthogonality of experimental modal vectors— As it was concluded in the above paragraph that some of the experimental mode shapes were highly complex a whitewash exercise was performed on the modes in order to check their orthogonality property (characterising real modes) which can be stated as follows :

$$\{\phi\}_j \cdot \{\phi\}_k = \begin{cases} \dfrac{1}{m_r} & ; \quad j = k = r \\ 0 & ; \quad j \neq k \end{cases} \qquad \text{..... (4.10)}$$

where m_r represents the modal mass of the r^{th} mode shape.

The orthogonality check results of the experimental mode shapes are depicted in Fig. 4.13 for the various curve fitting procedures (the plots were prepared using UNIMAP [75] , a part of the comprehensive graphics software UNIRAS). The diagonal elements of the 3–D grid maps represented the product of the same mode shape vectors (j=k) and the large peaks along the diagonal indicated that modes 1, 2, 4 and 5 confirmed the assumption of real modes. On the other hand it would be wrong to apply the previous assumption on the highly complex modes 3, 6, 7 and 8.

When comparing the grid maps of Fig. 4.13 it was deduced that some of the mode shapes resulting from GFIT4 followed the orthogonality property for real modes to a higher extent than their correspondents from GFIT. Though LFIT produced a number of real modes similar in quantity and quality to those of GFIT4, a decision was taken to consider results of GFIT4 only, as they yielded theoretically regenerated FRFs with least variance to experimental measurements.

4.7.2.7 Identification of real and complex mode shapes— Theoretically, complex mode shapes exist for structures characterised by a distribution of damping which is not proportional to either the structural stiffness or mass. Complex modal vectors can as well be the result of experimental errors [76] as described below.

In the current study higher modes 6, 7 and 8 had a weak amplitude when compared with the initial modes of vibration and the mass loading from the triaxial accelerometer could indeed result in inaccurate estimates of natural frequencies and damping values which in turn would produce complex mode shapes. In regions where the frequency resolution was too low, as was the case for the last three modes, the damping estimates will be incorrect thus the yielding of complex mode shapes.

The main characteristic of complex modes is that they possess non–stationary nodal points, as a consequence of that the modal deflection of the various degrees of freedom of the test structure do not reach their maximum simultaneously. The experimental mode shapes are plotted in Figs 4.14(a → h) after whitewashing the elements of the modal vectors and their types were identified with the aid of animated displays on the computer monitor.

4.7.2.8 The spurious mode shape— The third mode shape can be described as being complex with a symmetric motion similar to that of the first mode (in the driving direction — see Figs 4.14(a) and 4.14(c)) with an almost equal damping value. When curve fitting various measured accelerance functions it was generally observed that some local discrepancies occurred

between the experimental measurements and the theoretically regenerated FRFs indicating inaccuracies in the modal parameter estimates, an error which existed because the resonance peak varied its position along the frequency axis.

The previous remarks suggest that the spurious mode was incurred on the test structure from the driving point set–up. The variation of the peak position was because the fixation of the adaptor to the prototype broke off more than once and each time it was rebonded a different stiffness was achieved, causing variation in the boundary conditions and hence resulting in a different natural frequency and damping value.

To overcome such a problem, a curve fitting process was needed to fit for different frequency and damping values for each individual measurement and in this way accurate modal parameters for the remaining modes would be achieved while results for the non–stationary mode would have to be ignored. Another method to remove the effect of such a mode from the modal parameters of other modes is by using either extra numerator polynomial terms (a technique which was adopted in the current analysis) or additional modes, more than two for the current case (which was not possible because it meant the specification of a number of modes greater than that allowed by MODAL 3.0) as the use of two modes resulted in large discrepancies between the theoretically regenerated accelerance functions and the measurements.

4.7.2.9 Regenerating cross point and transfer FRFs— In order to assess the quality of the GFIT4 curve fitting procedure the three cross point accelerance functions and three transfer accelerance functions for a station on the lowest parallel circle were theoretically regenerated, using the corresponding modal parameters, and compared with the experimental measurements. Results are presented in Figs 4.15(a $\rightarrow$ c) and 4.16(a $\rightarrow$ c) which comprise a bode graphic representation of the considered FRF with a zoom on the heavy coupled mode regions (modes 1, 2 and modes 6, 7). In addition, a Nyquist plot of the mobility function around each peak is disclosed.

Studying the above figures it was clear that in general the theoretically regenerated FRFs agreed well with their corresponding measurements thus indicating good estimates of modal parameters except in regions close to the second peak that suffered from a non–stationary position on the frequency axis for which reasoning was given earlier.

When zooming on heavy coupled modes it can be noted that the global rational fraction polynomial curve fitting technique functioned well in identifying the modal characteristics of repeated or closely spaced modes although the correct number of modes was determined using a separate program (INTEL).

4.7.2.10 Checks on measured FRFs— The initial part of any of the measured accelerance functions, plotted on a Log frequency scale, was asymptotic to a stiffness line (positive slope) as well as for the upper end of the frequency range which is a characteristic for grounded structures [49] .

Using the viscous damping model, the Nyquist plot of a mobility function of a resonance region is expected to follow a circular arc [49] . The above mentioned accelerance functions were numerically integrated (divided by $i\omega$; $\omega = 2\pi \times (29.69 \rightarrow 654.69)$) to yield mobility functions and each was split into six regions containing a modal peak. The Nyquist plot for each frequency range is depicted in Figs. 4.15(a → c) and 4.16(a → c) where it was noticed that, with the exception of nodal points for some of the modes and for heavy coupled modes, the mobility functions traced out at least a part of of a circular arc. From the Nyquist plot of the theoretically regenerated mobility functions it was observed that as the magnitude of the modal constants (represented by the diameter of the circular arc) decreased the phase estimates became inaccurate, which could account for the complexity of the small mode shape elements.

In general, it can be concluded that the global rational fraction polynomial curve fitting method has proven to work excellently when nodal points and noisy data were encountered.

4.7.2.11 Derivation of the direct point accelerance function— Applying linear coordinate transformation to the three cross point accelerance functions the direct point accelerance function was obtained. Fig. 4.17 shows the driving FRF in both Bode and Co–quad formats. The two following checks [49] were indicating a set of good quality measurements (concerning the driving stations only) ,

i. an antiresonance existed between each pair of resonances; and,

ii. all imaginary peaks corresponding to modal peaks occurred in the same directions (all peaks were negative) meaning they were in all phase.

4.7.2.12 Synthesising FRFs— Rewriting Eqn (4.4),

$$\alpha_{jk}(\omega) = \sum_{r=1}^{N} \left[\frac{{}_rR_{jk}}{(i\omega - s_r)} + \frac{{}_rR^*_{jk}}{(i\omega - s^*_r)} \right] \quad \text{.....} \quad (4.4)$$

Considering a real normal mode approximation and assuming unit modal mass scaling

$$\Rightarrow {}_rR_{jk} = \frac{{}_r\phi_k \, {}_r\phi_j}{1} \qquad \text{(4.11)}$$

It can be deduced that if $\{\phi\}_r$ (where r = 1, 2, 3, ... , N) were determined it is possible to derive the modal parameters for any of the unmeasured FRFs, e.g. α_{mk} can be synthesised since ${}_r\phi_m$, ${}_r\phi_k$ and s_r have been estimated where α_{mk} represents an unmeasured receptance function.

Accordingly, the accelerance functions of three different stations, lying on the same parallel circle, namely 4B, 5B and 6B were synthesised. For each set of FRFs (Normal, Meridional and Circumferential) its local radial (normal) direction was taken as the reference. The nine measured accelerance functions were :

$A_{4BN/4BN}$, $A_{4BM/4BN}$, $A_{4BC/4BN}$, $A_{5BN/5BN}$, $A_{5BM/5BN}$, $A_{5BC/5BN}$, $A_{6BN/6BN}$, $A_{6BM/6BN}$ and $A_{6BC/6BN}$.

Thus if the test structure was perfectly axisymmetric only one of the symmetric modes and its higher correspondent would be excited as well as the axisymmetric mode and the last combined mode. In addition, the following conditions would have been satisfied :

$$A_{4BN/4BN} = A_{5BN/5BN} = A_{6BN/6BN}$$
$$A_{4BM/4BN} = A_{5BM/5BN} = A_{6BM/6BN}$$
$$A_{4BC/4BN} = A_{5BC/5BN} = A_{6BC/6BN}$$

Fig. 4.18 shows that the preceding equalities were in general fulfilled except for the higher modes. The presence of the torsional mode and the discrepancies for higher modes was due to the geometrical imperfections of the test structure as well as inaccuracies inherent in the modal parameter estimates of the higher modes.

In summary, all previous checks made indicated good measured data and reliable extracted modal parameters for only the first four vibrational modes (excluding the spurious mode). Some doubt was cast on the remaining fitted data for the rest of the modes due to the heavy coupling encountered combined with weak amplitudes and large frequency resolution.

4.8 COMPARISON BETWEEN EXPERIMENTAL AND THEORETICAL MODAL PROPERTIES

The main objective of the current modal test was to verify dynamically the theoretical model (finite element mesh) described in the previous chapter. Earlier modal tests ended with the comparison of both experimental and theoretical in the form of tables for natural frequency estimates and graphic representations for the mode shapes. However recently, new methods [54-56]

have been evolving with the purpose of identifying the origins of discrepancies between both test structure and finite element modal models following which attempts can be made to correct for existing errors in either one.

The techniques are described in the following subsections and were applied to compare experimental results with both an initial and updated finite element mesh. All results for both theoretical models are presented side by side whether in table or graphic forms in order to manifest the effect of updating.

4.8.1 The Number of Modes to Be Considered

Because of the orthogonal properties of the vibrational mode shapes of a structure any dynamic response can be expressed as a linear combination of the response due to individual modes. As a result, the degree of importance of a mode depends on how much it participates in the overall structural response.

The effective mass concept has been used effectively on other structures [77] and was used herein to determine the number of modes to take into account in the current investigation. It is defined as follows :

$$\mu_r^x = m_r \left[\frac{\{\psi\}_r^T [M] \{I\}_x}{\{\psi\}_r^T [M] \{\psi\}_r} \right]^2 \qquad \text{(4.12)}$$

where μ_r^x represents the effective modal mass for the r^{th} mode in the X direction (similar expressions can be derived for μ_r^y and μ_r^z) ; and,

$\{I\}_x$ is a vector containing unit values for each row of the mass matrix, that is associated with the X direction and the remaining elements are zeros.

Basically, the effective mass can be interpreted as that part of the total mass responding to a dynamic load in each mode and if the number of modes is equal to the total number of degrees of freedom then the sum of the effective masses of each mode in a specific direction will be identical to that of the rigid body mass. The effective masses were calculated for the initial and updated theoretical models and the results as percentages of the rigid body mass of the test structure (2.334 kg) are listed in Table 4.9.

MODE NUMBER	INITIAL MODEL EFFECTIVE MASSES				UPDATED MODEL EFFECTIVE MASSES			
	X (%)	Y (%)	Z (%)	SUM (%)	X (%)	Y (%)	Z (%)	SUM (%)
1	16.32	33.81	0.00	50.13	1.99	50.90	0.00	52.89
2	33.81	16.32	0.00	50.13	50.90	1.99	0.00	52.89
3	0.00	0.00	99.79	99.79	0.00	0.00	98.37	98.37
4	0.00	0.00	0.00	0.00	0.00	0.00	0.00	0.00
5	34.11	0.00	0.00	34.11	35.04	1.01	0.00	36.05
6	0.00	34.11	0.00	34.11	1.01	35.04	0.00	36.05
7	0.00	0.00	0.00	0.00	0.00	0.00	0.00	0.00
8	0.00	0.00	0.00	0.00	0.00	0.00	0.00	0.00
Summation for 8 modes	84.23	84.23	99.79	268.27	88.94	88.94	98.37	276.25
:	:	:	:	:	:	:	:	:
:	:	:	:	:	:	:	:	:
147	0.00	0.00	0.00	0.00	0.00	0.00	0.00	0.00
Summation for 147 modes	86.25	86.25	99.87	272.37	89.55	89.55	98.37	277.47

TABLE 4.9 — *EFFECTIVE MODAL MASSES FOR INITIAL AND UPDATED THEORETICAL MODELS*

No rotational directions were considered in the above table as the 4371 degrees of freedom were condensed on to 147 translational master degrees of freedom using the Guyan reduction technique (see Appendix D) in order to match their experimental counterparts.

It can be noted from the preceding table that more than 80 percent of the total mass was accounted for in the **X** and **Y** directions using the first six modes and beyond 99 percent for the **Z** direction when using the third mode only. The results of the updated model followed a trend similar to that of the initial model results but with even larger effective modal mass values for the leading mode shapes.

It is important to emphasise that if rotational degrees of freedom were introduced among the master degrees of freedom the torsional mode would have had a relatively high effective mass in the Θ_z direction (rotation about the axis of symmetry – Z—axis –).

From the previous conclusions it was found that the first eight modes were more than sufficient to consider in any model verification analysis.

The notion of effective mass was not applied to experimental results for the following reasons :

1. The mass of the shaker, stinger, force cell, adaptor and triaxial accelerometer would influence the results.
2. The higher experimental modes were complex thus complicating the calculation if not invalidating the whole concept.
3. It is clear from Eqn (4.12) that estimating the effective modal mass parameter necessitated the use of a theoretical mass matrix which might contain undetected large approximations thus producing poor estimates.
4. If a dynamically verified finite element model is achieved the above calculation would be a repetition if it has already been performed for the finite element mesh.

4.8.2 Identification of Correlated Experimental and Theoretical Mode Shapes

Before carrying out any experiment–theory comparison on modal parameters it is necessary to identify those modal vectors which correlate with each other. One of the available techniques is to calculate a statistical parameter known as the modal assurance criterion (MAC) [78] for m experimental modes and n theoretical modes. The MAC value for a pair of modes is defined as follows :

$$\mathrm{MAC}(\{{}_x\psi\}_j, \{{}_t\psi\}_k) = \frac{|\{{}_x\psi\}_j^T \cdot \{{}_t\psi\}_k^*|^2}{\{{}_x\psi\}_j^T \cdot \{{}_x\psi\}_j^* \cdot \{{}_t\psi\}_k^T \cdot \{{}_t\psi\}_k^*} \quad \text{..... (4.13)}$$

where $\{{}_x\psi\}_j$ represents the j^{th} experimental mode shape;

$\{{}_t\psi\}_k$ represents the k^{th} theoretical mode shape;

j, k are subscripts denoting the mode numbers;

x, t are subscripts indicating an experimental and theoretical mode; and,

* indicates a complex conjugate.

The result is a matrix of order m×n with values varying between zero and unity for perfectly uncorrelated and perfectly correlated modes respectively. It is clear that although the output of Eqn (4.13) is a scalar quantity complex mode shapes can be used.

A unity MAC value does not necessarily indicate two correct modes as both modes can contain similar systemic errors and yet be consistently correlated. High MAC values can be encountered as well for two different modes when the number of degrees of freedom is too low to define a higher mode, such an effect is known as "**Spatial Aliasing**".

Table 4.10 includes the results of the MAC calculation for the test structure and theoretical models while Fig. 4.19 is a graphic representation of the MAC matrices in the form of 3–D grid maps.

(i)

TEST STRUCTURE MODE NUMBER	INITIAL THEORETICAL MODEL MODE NUMBER							
	1	2	3	4	5	6	7	8
1	0.332	0.538	0.001	0.001	0.003	0.004	0.003	0.000
2	0.520	0.445	0.000	0.000	0.008	0.003	0.000	0.000
3	0.216	0.002	0.003	0.002	0.003	0.024	0.015	0.000
4	0.000	0.000	0.978	0.002	0.000	0.000	0.000	0.000
5	0.000	0.000	0.000	0.985	0.004	0.005	0.000	0.000
6	0.723	0.041	0.001	0.000	0.046	0.067	0.000	0.000
7	0.015	0.609	0.000	0.021	0.032	0.088	0.007	0.001
8	0.000	0.000	0.965	0.003	0.000	0.001	0.000	0.000

TABLE 4.10 — *MODAL ASSURANCE CRITERION BETWEEN EXPERIMENTAL AND THEORETICAL MODAL VECTORS (CONTD)*

(ii)

TEST STRUCTURE MODE NUMBER	UPDATED THEORETICAL MODEL MODE NUMBER							
	1	2	3	4	5	6	7	8
1	0.954	0.009	0.000	0.001	0.001	0.001	0.001	0.000
2	0.003	0.970	0.000	0.000	0.004	0.001	0.000	0.000
3	0.128	0.090	0.003	0.002	0.002	0.008	0.012	0.000
4	0.001	0.000	0.982	0.002	0.000	0.000	0.000	0.000
5	0.000	0.000	0.000	0.986	0.003	0.006	0.000	0.000
6	0.206	0.555	0.001	0.000	0.084	0.057	0.000	0.000
7	0.406	0.214	0.000	0.020	0.023	0.126	0.006	0.001
8	0.000	0.000	0.965	0.003	0.000	0.001	0.000	0.000

TABLE 4.10 — *MODAL ASSURANCE CRITERION BETWEEN EXPERIMENTAL AND THEORETICAL MODAL VECTORS*

Real modes (whitewashed modal vectors) were used to represent the experimental mode shapes in the preceding calculation although Eqn (4.13) permitted the inclusion of their complex version. The reason was that the experimental real modes were to be used in any future analysis and it was necessary to determine their general characteristics. Appendix G contains tables of MAC values obtained using complex experimental mode shapes.

The high MAC values in Table 4.10 indicated that the mode pairs $\{_x\phi\}_4$, $\{_t\phi\}_3$ and $\{_x\phi\}_5$, $\{_t\phi\}_4$ were correlated while the effect of spatial aliasing was the cause of a 96.5 percent correlation coefficient between $\{_x\phi\}_8$ and $\{_t\phi\}_3$. It was clear as well that some correlation existed between $\{_x\phi\}_1$, $\{_t\phi\}_2$ and $\{_x\phi\}_2$, $\{_t\phi\}_1$.

When considering the pictorial representation (in the form of animated mode shapes) of the experimental mode shape estimates modes 6 and 7 appeared to have similar motion to that of theoretical eigenvectors 5 and 6 respectively.

The following table contains a list of experimental and theoretical natural frequency estimates for the first six correlated mode pairs.

CORRELATED MODE PAIR NUMBER	EXPERIMENTAL FREQUENCIES (Hz)	INITIAL MESH		UPDATED MESH	
		FREQUENCY (Hz)	|DIFFERENCE| (%)	FREQUENCY (Hz)	|DIFFERENCE| (%)
1	60.67	73.78	21.61	57.77	4.78
2	61.64	73.78	19.70	57.77	6.28
3	243.69	275.64	13.11	223.20	8.40
4	333.12	606.47	82.06	336.37	0.01
5	510.37	1115.42	118.55	878.52	72.13
6	513.06	1115.42	117.41	878.52	71.23

TABLE 4.11 — *COMPARISON BETWEEN EXPERIMENTAL AND THEORETICAL NATURAL FREQUENCY ESTIMATES*

A comparison between the first four correlated mode pairs magnitudes was performed by plotting each experimental modal vector element versus its theoretical correspondent as depicted in Fig. 4.20(a). Both sets were mass normalised. The points for the first and second correlated mode pairs showed very poor tendencies to be on a straight line. Plots for correlated mode pair number (CMPN) 3 and 4 almost lay on straight lines with slopes 1.2 and 0.9 respectively (the slope of the best fitted line through the points) indicating that although each mode pairs were highly correlated a difference in the scaling existed.

4.8.3 Identification of Coordinates with Large Discrepancies

In the following analysis only the first four correlated mode pairs will be used due to the inaccuracies encountered in higher modes in addition to their weak influence on any dynamic structural response.

The identification of coordinates which harbour large discrepancies between experimental and theoretical mode shapes has been carried out with the aid of newly developed statistical parameters [55] and matrix methods [54,56,79] . The adopted techniques have been evolving recently aiming to explain low MAC values as well as identifying the poorly modelled regions of a structure when using the finite element method.

4.8.3.1 Coordinate modal assurance criterion (COMAC)— The coordinate MAC is complementary to the modal assurance criterion for mode shapes. It attempts to locate parts of the structure which cause low MAC coefficients.

In the current study the COMAC was calculated for each degree of freedom using the following equation :

$$\text{COMAC(i)} = \frac{\left(\sum_{L=1}^{L_{max}} \{{}_x\psi_i\}_L \cdot \{{}_t\psi_i\}_L\right)^2}{\left(\sum_{L=1}^{L_{max}} \{{}_x\psi_i\}_L^2\right)\left(\sum_{L=1}^{L_{max}} \{{}_t\psi_i\}_L^2\right)} \quad \text{..... (4.14)}$$

where **i** is a subscript indicating the i^{th} degree of freedom;

L represents the correlated mode pair number; and,

$\{{}_x\psi_i\}$, $\{{}_t\psi_i\}$ represent the i^{th} eigenvector element of the experimental and theoretical modal vectors respectively.

Lieven *et al.* [55] when suggesting the COMAC value, used a slightly different expression,

$$\text{COMAC(i)} = \frac{\left(\sum_{L=1}^{L_{max}} |\{{}_x\psi_i\}_L \cdot \{{}_t\psi_i\}_L|\right)^2}{\left(\sum_{L=1}^{L_{max}} \{{}_x\psi_i\}_L^2\right)\left(\sum_{L=1}^{L_{max}} \{{}_t\psi_i\}_L^2\right)} \quad \text{..... (4.15)}$$

The modulus sign in the preceding expression was inside the summation thus limiting the interest to that of the relative magnitude at a specified coordinate over all the correlated mode pairs. By comparison the more comprehensive format of Eqn (4.14) takes magnitude and phase into consideration.

It is important to mention that in order to correctly estimate the COMAC, all correlated mode pairs had either to lie in phase or out of phase.

4.8.3.2 Modulus difference matrix (MDM)— The elements of the MDM are computed for two sets of correlated eigenvector pairs using the following formula :

$$\{\Delta\psi_i\}_L = |\{{}_x\psi_i\}_L - \{{}_t\psi_i\}_L| \quad ; L = 1, 2, 3, \ldots\ldots, L_{max} \quad \text{..... (4.16)}$$

where $\{\Delta\psi_i\}_L$ represents the difference for the i^{th} element of the L^{th} CMPN.

Again Lieven *et al.* [55] used a different expression listed below,

$$\{\Delta\psi_i\}_L = \left|\left|\{_x\psi_i\}_L\right| - \left|\{_t\psi_i\}_L\right|\right| \quad ; L = 1, 2, 3, \ldots\ldots, L_{max} \quad \ldots\ldots \quad (4.17)$$

In Eqn (4.17) the modulus of the eigenvector elements is taken before the difference is calculated while Eqn (4.16) accounted for both magnitude and phase information.

In a later subsection it will be demonstrated how the MAC, COMAC and MDM can work together to locate the position of errors, whether for test structure or finite element modal model.

4.8.3.3 Error matrix method (EMM)— The EMM is a technique developed with the aim of identifying local errors for either the stiffness or mass matrices. It makes no assumption concerning the accuracy of either matrices whether theoretical or experimental, instead it uses a set of modal parameters as a reference basis.

Several approximations are involved when calculating the error matrices. In most cases the experimental degrees of freedom are much less than those of the finite element mesh (in the current case a ratio greater than 1 : 29). In general, it is possible to follow two routes in order to match both sets of freedoms, the first of which is to expand the experimental degrees of freedom to be compatible with those of the theoretical model giving the benefit of regaining the rotational degrees of freedom results without measuring their corresponding FRFs. The other route, which was adopted for the current study, is to condense both the stiffness and mass matrices on master degrees of freedom which are the experimental degrees of freedom with the consequence of not considering rotations.

When viewing the following formulae for error matrices it will be noticed that only a few modes are considered in the calculation — another approximation which is encountered due to the difficulty in measuring all vibrational mode shapes.

An additional approximation is inherent in the formulation of the analytical stiffness and mass matrices.

The theory behind the EMM can be stated as follows :

$$[\Delta K] = [K_x] - [K_t] \quad \ldots\ldots \quad (4.18)$$

where $[\Delta K]$ represents the stiffness error matrix;

$[K_t]$ represents the theoretical stiffness matrix; and,

$[K_x]$ represents the experimental stiffness matrix.

As it is not possible to measure the stiffness matrix the above equation was approximated [54] ignoring higher order terms as follows :

$$[\Delta K] \approx [K_t]([\Phi_t][\Omega_t^2]^{-1}[\Phi_t]^T - [\Phi_x][\Omega_x^2]^{-1}[\Phi_x]^T)[K_t] \quad \text{.....} \quad (4.19)$$

where $[\Phi_t]$, $[\Phi_x]$ represent the theoretical and experimental mass normalised vibrational mode shape matrices respectively, having an incomplete set of modal vectors and an incomplete set of coordinates; and,

$[\Omega_t^2]$, $[\Omega_x^2]$ represent the corresponding theoretical and experimental estimates respectively of the square of the natural frequencies in rad^2/s^2.

Eqn (4.19) is based on the assumption that the discrepancies between the theoretical and experimental stiffness matrices is small ($[\Delta K] << $). A similar expression was derived for the mass error matrix :

$$[\Delta M] \approx [M_t]([\Phi_t][\Phi_t]^T - [\Phi_x][\Phi_x]^T)[M_t] \quad \text{.....} \quad (4.20)$$

where $[\Delta M]$ represents the mass error matrix; and,

$[M_t]$ represents the theoretical mass matrix.

Because of the limited number of measured modes a new method was developed [56] to localise the errors between the experimental and theoretical models using the following equation :

$$[\Delta K]([\Phi_x][\Phi_x]^T) = [M_t]([\Phi_x][\Omega_x^2][\Phi_x]^T) - [K_t]([\Phi_x][\Phi_x]^T) \quad \text{.....} \quad (4.21)$$

and its symmetric version could be written as follows :

$$[\Delta K_m] = ([\Phi_x][\Phi_x]^T)[\Delta K] + [\Delta K]([\Phi_x][\Phi_x]^T) \quad \text{.....} \quad (4.22)$$

where $[\Delta K_m]$ represents the modified stiffness error matrix.

The preceding equation was applied to models with a single measured mode and excellent results were obtained [80].

4.8.4 Application of Error Locating Techniques

A Fortran 77 program (called COMP) was prepared to calculate the COMAC, MDM, $[\Delta K]$, $[\Delta M]$ and $[\Delta K_m]$ for a given number of correlated mode pairs using Eqns (4.14), (4.16), (4.19), (4.20) and (4.22) respectively. It required the input of the theoretical condensed mass and stiffness matrices $[M_t]$ and $[K_t]$ as well as the theoretical and experimental modal parameters including mass normalised modal vectors (theoretical information was supplied using PAFEC).

4.8.4.1 Raw experimental data and initial finite element model— Initially, theoretical data provided to the program was that of the finite element mesh described in the previous chapter (with perfect fixity at the base) and the raw experimental data. COMAC results are listed in the following table.

STATION NUMBER	POSITION ON TEST STRUCTURE	INITIAL THEORETICAL MODEL WITH RAW EXPERIMENTAL DATA			UPDATED THEORETICAL MODEL WITH CORRECTED EXPERIMENTAL DATA		
		X	Y	Z	X	Y	Z
1	apex	0.496	0.324	0.981	1.000	0.968	0.981
2		0.477	0.705	0.977	0.992	0.957	0.967
3		0.491	0.555	0.930	0.987	0.998	0.992
4		0.546	0.443	0.913	0.990	0.993	0.988
5		0.585	0.399	0.911	0.993	0.983	0.980
6		0.580	0.489	0.937	0.998	0.992	0.979
7	seam	0.477	0.490	0.965	0.996	0.974	0.973
8		0.256	0.541	0.487	0.997	0.994	0.987
9		0.468	0.517	0.925	0.993	0.997	0.991
10		0.525	0.369	0.905	0.994	0.975	0.984
11		0.620	0.371	0.902	0.995	0.974	0.973
12		0.613	0.427	0.923	0.997	0.975	0.968
13	seam	0.521	0.565	0.911	0.991	0.999	0.986
14	driving point	0.395	0.625	0.770	0.978	0.980	0.945
15		0.443	0.564	0.823	0.967	0.976	0.970
16		0.597	0.419	0.808	0.975	0.968	0.977
17		0.639	0.316	0.688	0.975	0.962	0.974
18		0.513	0.390	0.551	0.940	0.957	0.916
19	seam	0.334	0.495	0.629	0.926	0.944	0.924
20		0.109	0.491	0.607	0.806	0.926	0.869
21		0.252	0.431	0.816	0.834	0.916	0.959
22		0.677	0.416	0.790	0.992	0.965	0.977
23		0.753	0.343	0.766	0.995	0.958	0.957
24		0.736	0.521	0.810	0.998	0.978	0.954
25	seam	0.610	0.699	0.828	0.998	0.997	0.966
26		0.461	0.813	0.752	0.998	0.992	0.995
27		0.606	0.765	0.759	0.981	0.990	0.994
28		0.779	0.577	0.681	0.992	0.978	0.983
29		0.837	0.307	0.715	0.979	0.955	0.985
30		0.803	0.606	0.837	0.981	0.985	0.978
31	seam	0.588	0.738	0.857	0.940	0.983	0.985
32		0.429	0.825	0.734	0.976	0.994	0.994
33		0.638	0.749	0.759	0.995	0.988	0.996
34		0.589	0.376	0.741	0.870	0.884	0.993
35		0.860	0.304	0.698	0.996	0.925	0.968
36		0.827	0.622	0.842	0.988	0.964	0.967
37	seam	0.645	0.798	0.892	0.979	0.993	0.970
38		0.497	0.921	0.806	0.984	0.996	0.996
39		0.857	0.877	0.792	0.867	0.991	0.985
40		0.887	0.761	0.731	0.986	0.977	0.971
41		0.921	0.322	0.758	0.991	0.931	0.966
42		0.877	0.728	0.891	0.989	0.983	0.953
43	seam	0.719	0.898	0.854	0.955	0.994	0.993
44		0.405	0.935	0.743	0.957	0.998	0.995
45		0.793	0.908	0.795	0.995	0.997	0.996
46		0.922	0.619	0.754	0.991	0.894	0.992
47		0.937	0.332	0.752	0.999	0.861	0.984
48		0.982	0.790	0.825	0.977	0.986	0.989
49	seam	0.805	0.931	0.874	0.988	0.998	0.984

TABLE 4.12 — *COMPARISON OF THE COMAC VALUES FOR INITIAL AND UPDATED FINITE ELEMENT MODELS*

Three dimensional grid maps were plotted as in Figs 4.21 → 4.25 to represent the modulus difference and error matrices.

The MAC values for CMPN 1 and 2 were relatively low (see Table 4.10) and when observing the COMAC results in Table 4.12 it was noted that low values were randomly scattered, giving no clear indication. Very low values existed at some stations as can be observed from the previous table.

Figs 4.21(a → c) indicated that in both the **X** and **Z** directions for the first correlated mode pair at the 8th measurement station large differences between experimental and theoretical models occurred. Relatively high peaks were also observed in the vicinity of the 21st and 35th stations for all degrees of freedom in the **X**, **Y** and **Z** directions for CMPN 1 and 2.

When plotting a stiffness error matrix as in Figs 4.22(a → c) it is important to mention that while the diagonal elements quantified the amount of error between the two models at a given station, in a given direction, the off diagonal elements were influenced by more than one station. As a result, the diagonal elements of the stiffness error matrices using individual correlated mode pairs for the **X**, **Y** and **Z** directions were plotted as shown in Figs 4.23(a → c). A similar policy was followed for the modified stiffness error matrix and results are depicted in Figs 4.24(a → c) and 4.25(a → c).

The preceding observations relating to the error locations were reiterated in all figures concerned with the stiffness error matrices.

4.8.4.2 The route to error location— Careful inspection of both sets of listings of the modal vector estimates indicated that some error existed in the raw experimental data at the 8th measurement station for CMPN 1 → 4 in the **X** and **Z** directions. The error was attributed to the weakening of the adaptor fixation to the test structure at the driving point. Depending on the type of mode, its direction of motion and the relative position of the considered degree of freedom with respect to the axis of symmetry, the experimental data was adjusted.

The previous correction did not improve the difference between the experimental and theoretical natural frequency estimates and as a result further corrections or updating was necessary and consequently attention was directed to the finite element model.

In general, the difficulties in obtaining similar or identical modal parameters for the test structure and finite element model could be due to any of the following reasons,

i. inaccurate representation of the material properties;

ii. inaccurate representation of the geometrical properties; and,

iii. inaccurate properties of the boundary conditions.

Accordingly, a material control test was carried out in order to eliminate any doubt with regards to the material properties and the average results were

$E = 8800$ MPa

$\nu = 0.36$

$\rho = 1100$ kg/m^3

Following this, attempts were made to decrease the shell element thickness at selected parts of the finite element model but almost no effect was observed on the natural frequency predictions. This was because as the thickness decreased the mass and structural stiffness decreased with nearly the same rates thus resulting in no change in the natural frequency estimates.

The last available route was to review the boundary conditions. Springs with compatible degrees of freedom were attached to the nodes of the last parallel circle. Keeping the spring stiffnesses equal, their magnitudes were varied several times and each time a new set of theoretical modal parameters was computed. The MAC and COMAC were used as indicators to establish an optimum stiffness value for the base fitting which was found to be 3×10^6N/m.

4.8.4.3 Corrected experimental data and updated finite element model— Results for both finite element models were presented side by side in order to demonstrate the effect of updating. The MAC calculation results listed in Table 4.10 assisted in identifying the correlated mode pairs. Subsequently, a consistent comparison between experimental and theoretical modal parameters was carried out and results are represented in Tables 4.10, 4.11 and Figs 4.20(b), 4.21 → 4.25.

From Table 4.10 and Fig. 4.19 it is clearly shown that the correlation of the first two modes has greatly improved and in Fig. 4.20(b) the points are lying on almost straight lines with slopes 0.98 and 0.91. In addition, the difference between experimental and theoretical natural frequency estimates has been greatly narrowed.

The COMAC values for the correlated mode pairs were found to be superior to their earlier estimates and with the exception of a scarce number of freedoms the COMAC was in excess of 90 percent. It was noted that the degrees of freedom in the X direction in the vicinity of the 20th and 34th stations for CMPN 1 and 2 possessed minimum COMAC, an indication of some disagreement between the corrected experimental and the updated finite element modal models.

When viewing Figs 4.21(a → c), the above sequel was repeated for the degrees of freedom in the **X, Y** and **Z** directions. Peak stiffness errors were observed in regions near to the latter stations in Figs 4.22 → 4.25.

The mass error matrices for both finite element models (initial and updated) led to no conclusive direction and consequently, its results were not considered in the current study.

In conclusion, although the updating performed on the finite element model and correction of experimental modal vector estimates has greatly improved the correlation coefficients (MAC and COMAC) still some randomly scattered errors existed. The non–symmetric distribution of the errors indicated that either geometrical imperfections or measurement errors could account for such discrepancies. It is interesting to note that neither low COMAC nor large error peaks were observed at the driving point nor for stations lying on the seam. Thus it is possible to conclude that neither the driving point set–up nor the existing seam did grossly change the dynamic characteristics of the test structure.

4.9 CONCLUSIONS

The main aim of the modal test was to acquire an accurate finite element model which correctly represents the dynamic characteristics of the Echinodome prototype. Such a demand was fulfilled up to a certain extent. Greater improvements were possible by observing the following points :

1. The inclusion of more vibrational modes as well as increasing the number of measurement stations and hence the total number of experimental degrees of freedom.
2. Due to the heavy coupling of the test structure vibrational modes, experimental modal parameters can be accurately extracted by exciting one mode at a time.
3. Complex mode shapes, if occurring, could be used without whitewashing in order to retain the damping characteristics which could be included in new correlation techniques [80] .
4. Attempting to expand the experimental mode shapes rather than condensing theoretical model is a process which benefits from including rotational degrees of freedom in any correlation thus enhancing the theoretical model.
5. Introducing updating iteration techniques eventually leads to a correct theoretical model.

It is important to emphasise that the verified finite element model is suitable for dynamic analysis but not necessarily for static, as the theoretical model obtained was correlated consistently to the test structure at the natural frequencies only. While a static loading would require a finite element mesh which correctly represented the test structure at 0 Hz frequency.

To summarise, a thorough modal test can be used to validate a theoretical model representing a real structure for dynamic analysis, e.g. structural response prediction to a given dynamic force.

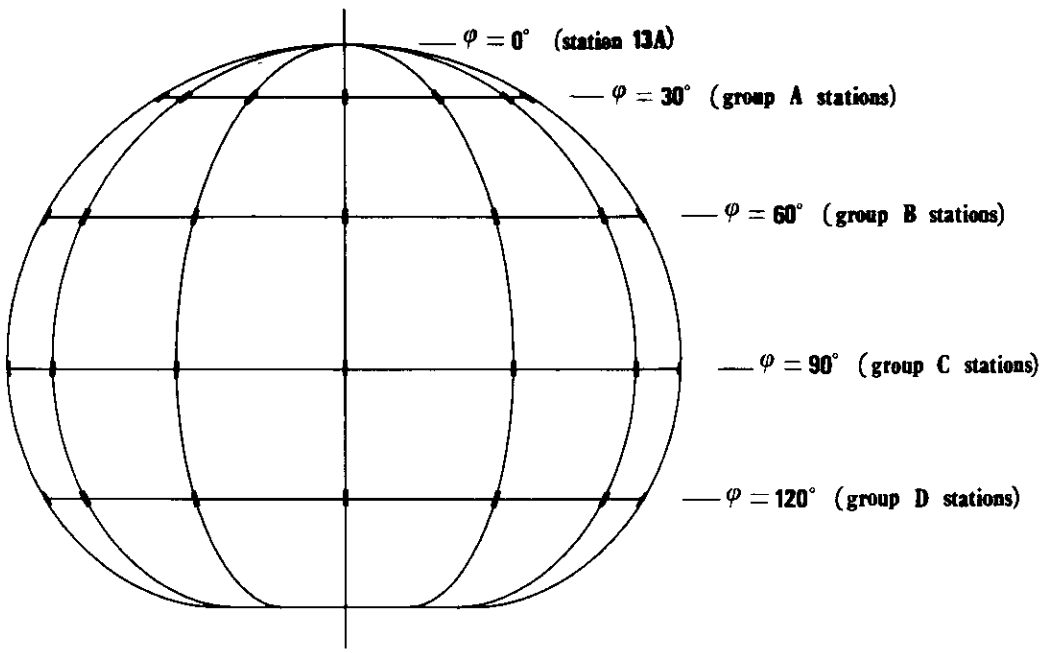

FIG. 4.1(a)–SPATIAL DISTRIBUTION OF MEASUREMENT STATIONS

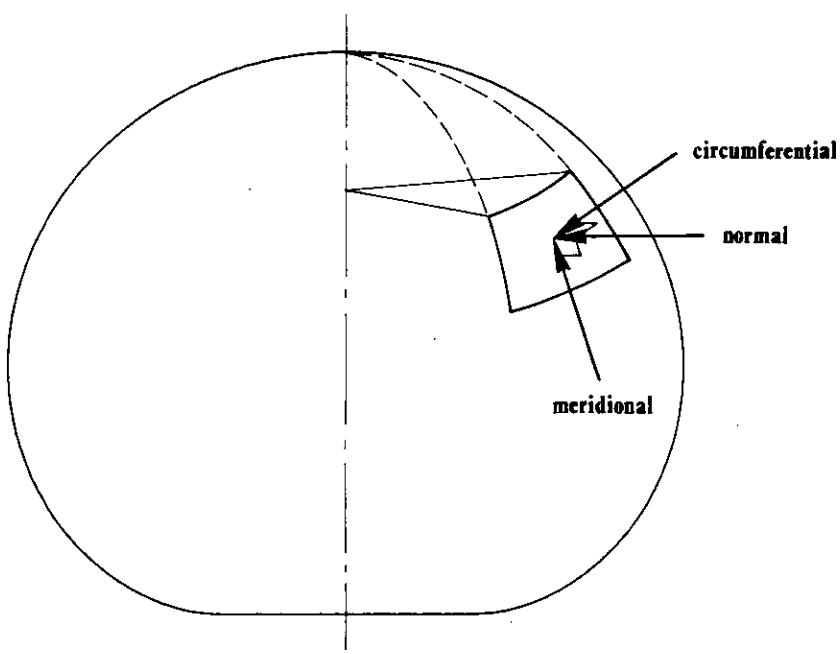

FIG. 4.1(b)–EXPERIMENTAL DEGREES OF FREEDOM AT EACH MEASUREMENT STATION

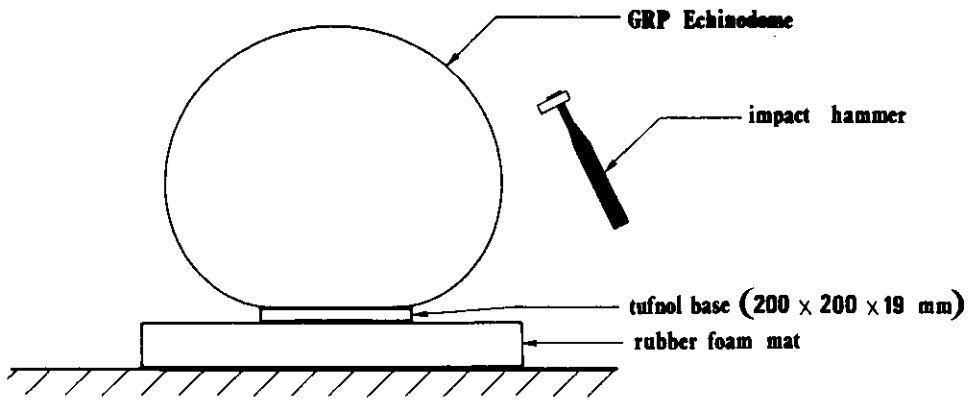

FIG. 4.2(a)–ACCELERANCE MEASUREMENT OF THE ECHINODOME UNDER FREE SUPPORTING CONDITIONS

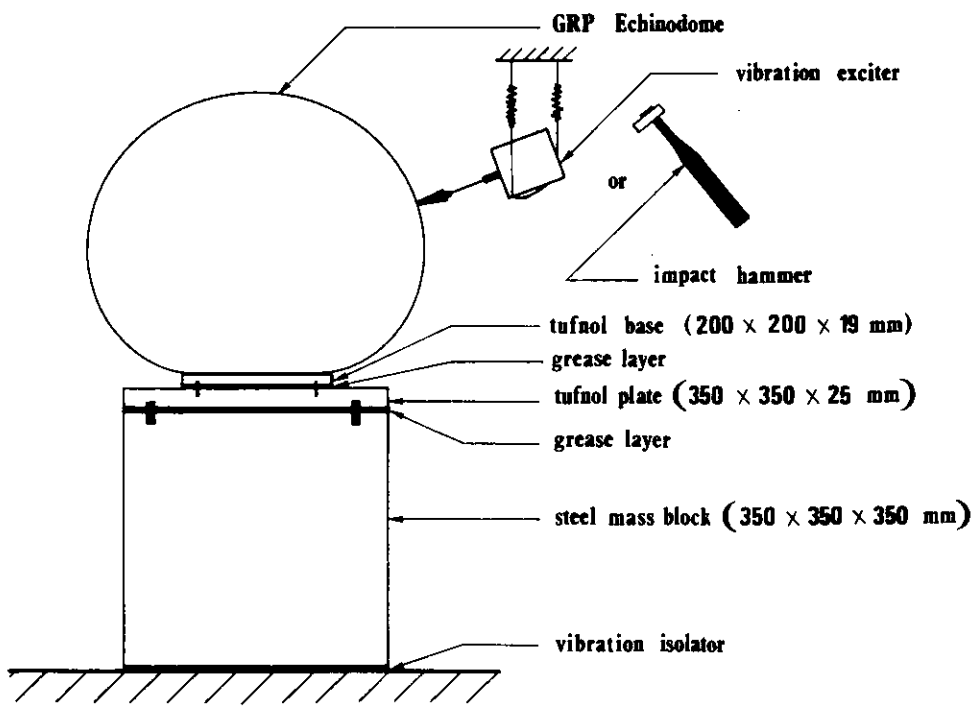

FIG. 4.2(b)–ACCELERANCE MEASUREMENT OF THE ECHINODOME UNDER GROUNDED SUPPORTING CONDITIONS

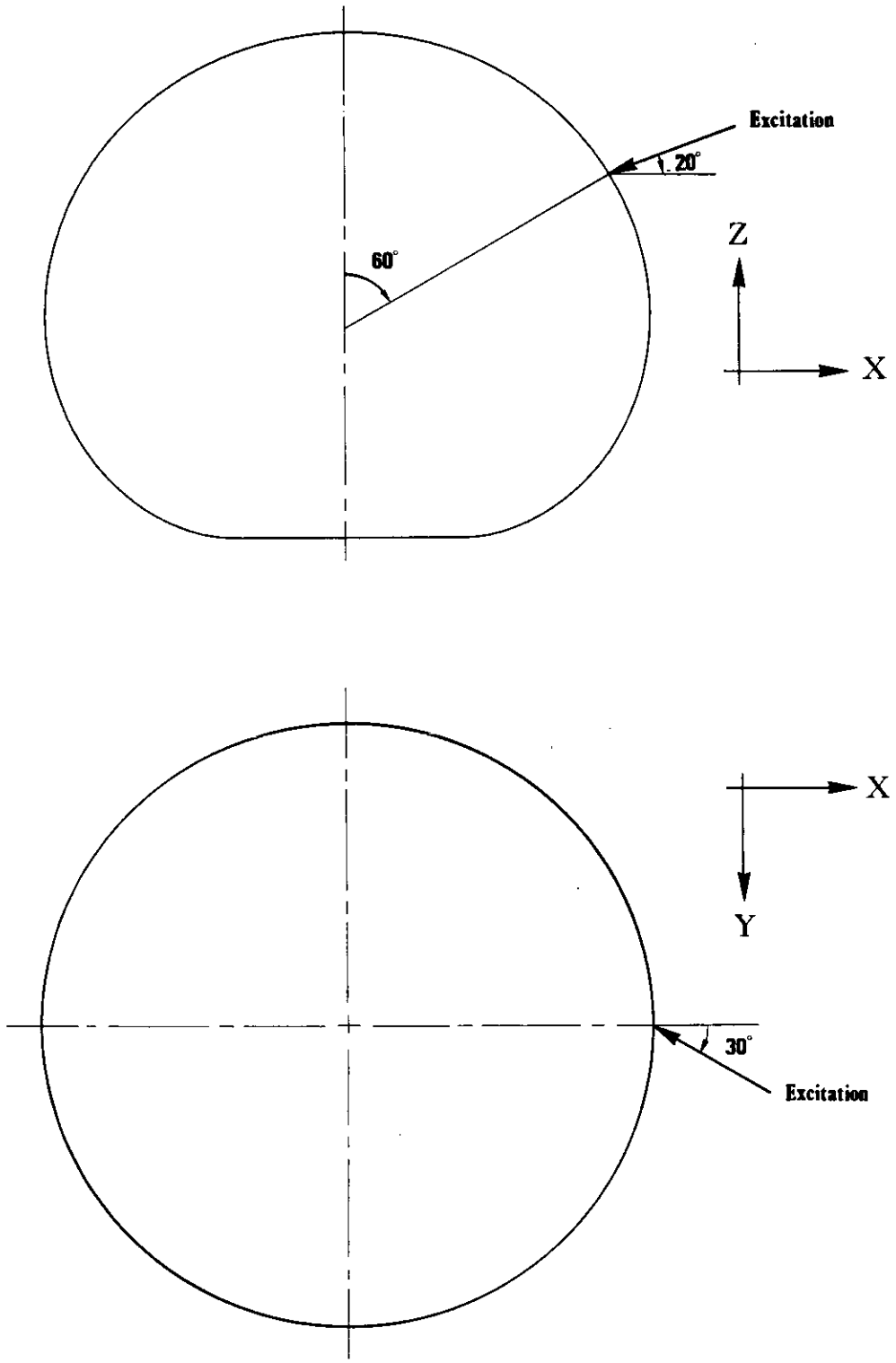

FIG. 4.3–DETAILS OF THE OBLIQUE DEGREE OF FREEDOM

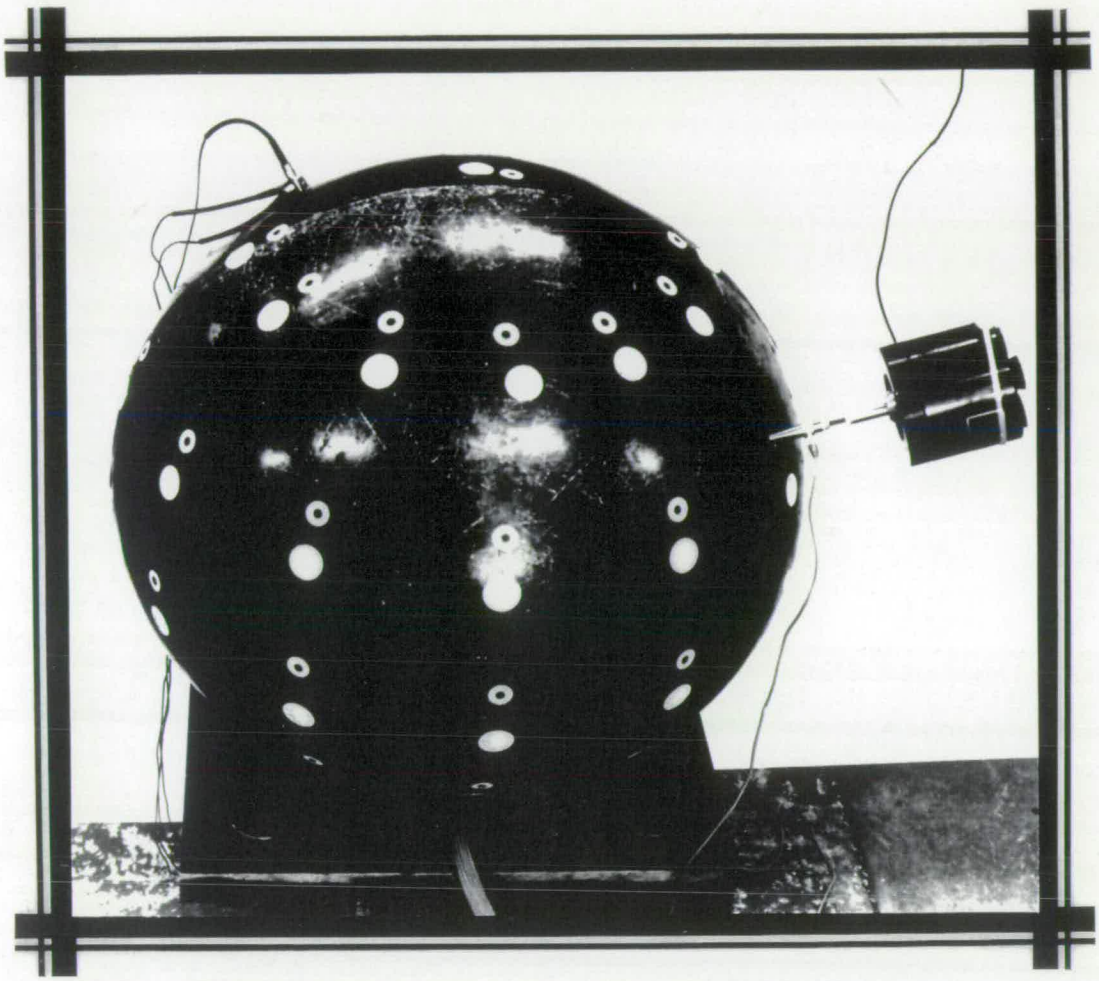

FIG. 4.4–EXCITER ATTACHMENT TO THE TEST STRUCTURE

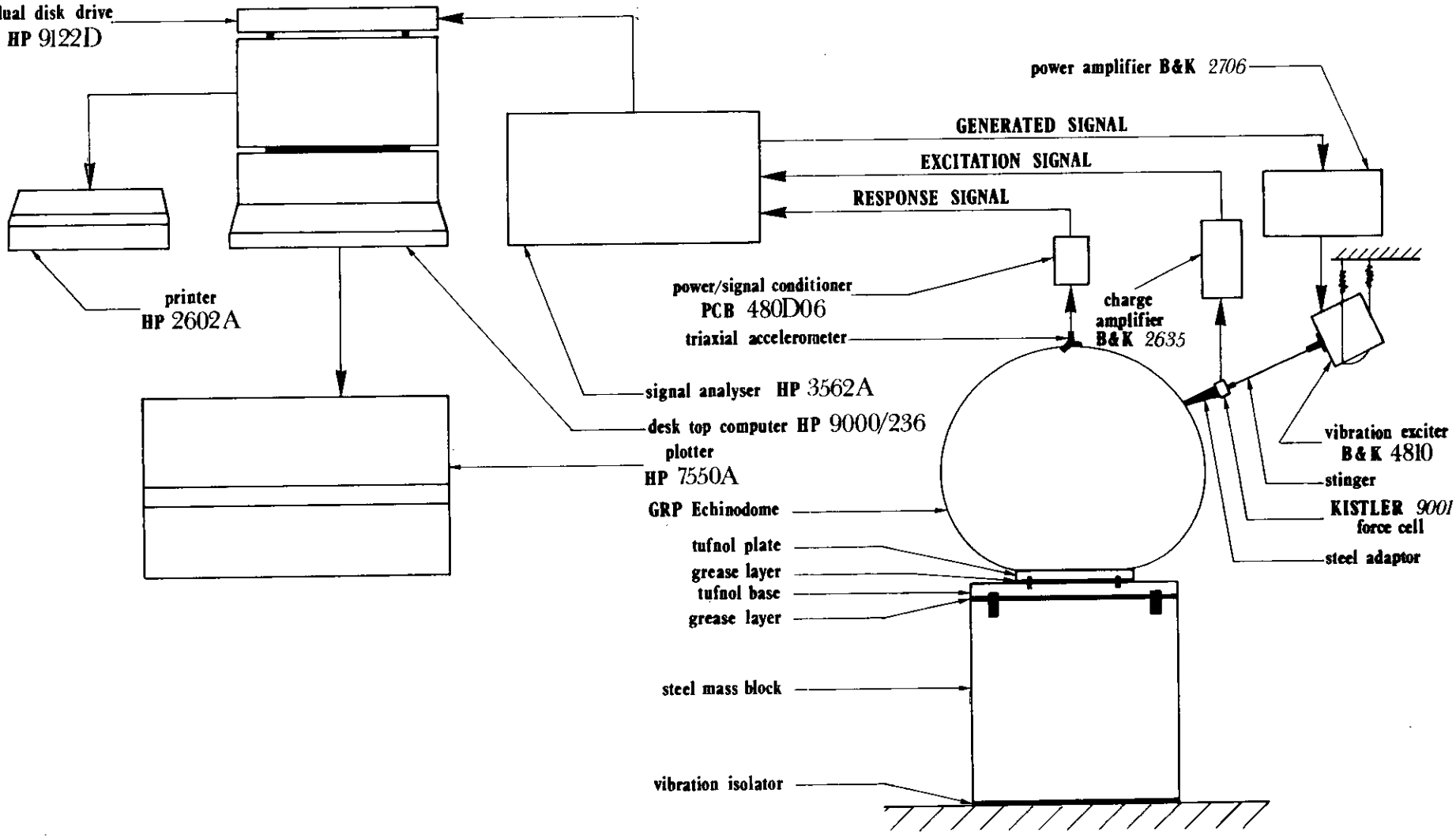

FIG. 4.5–INSTRUMENTATION USED IN THE MODAL TEST

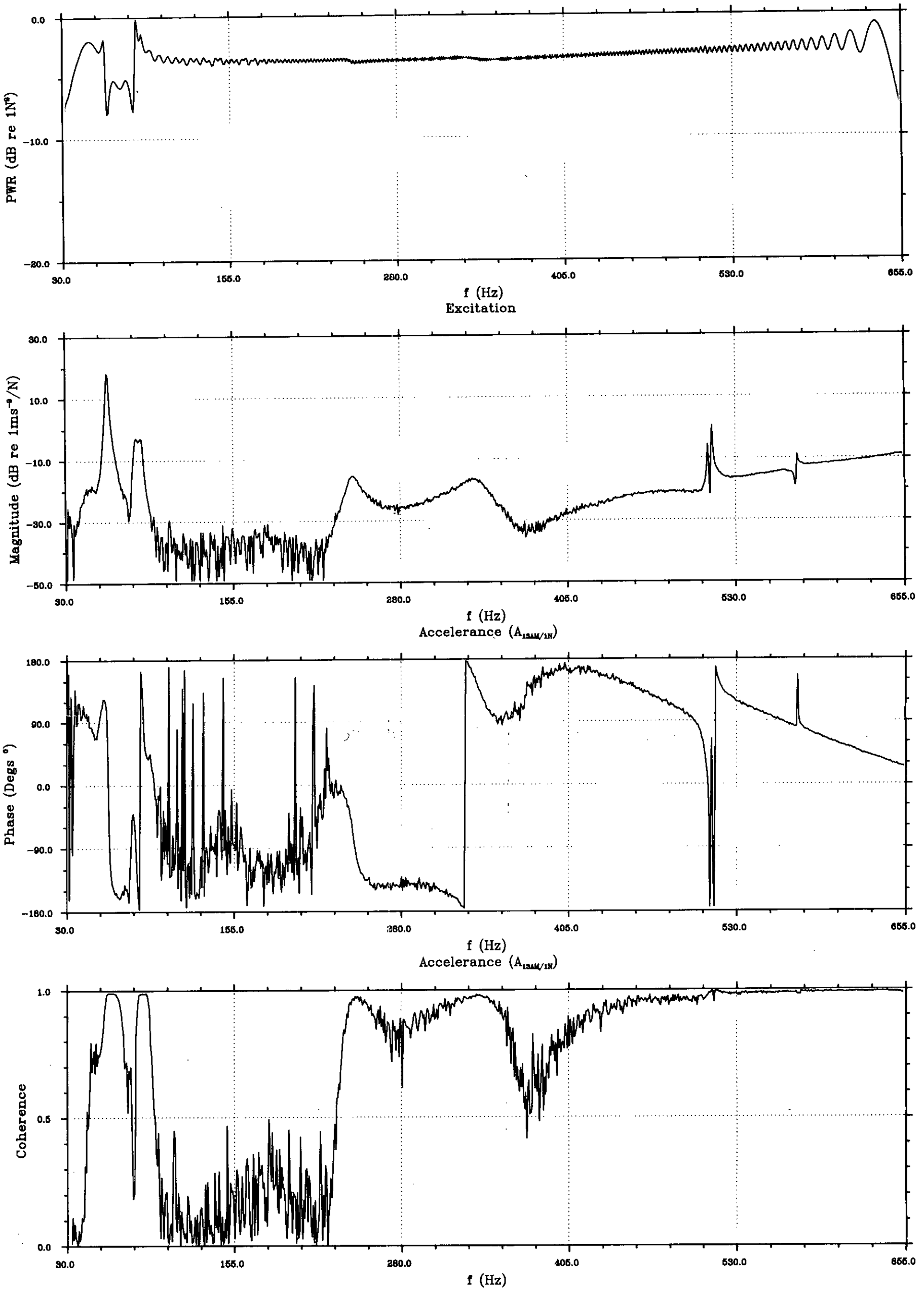

FIG. 4.6(a)–MEASUREMENT RESULTS USING PERIODIC CHIRP EXCITATION

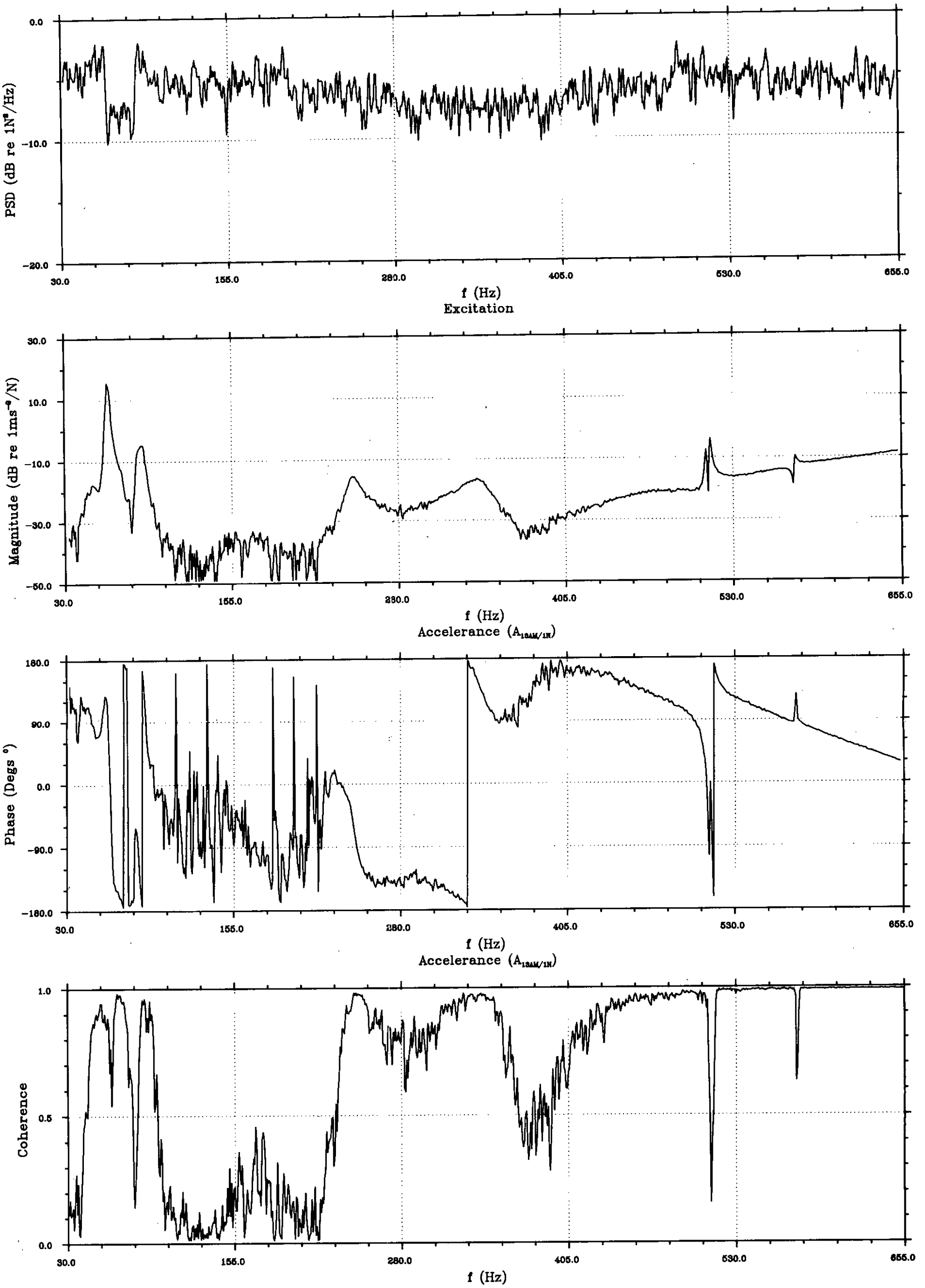

FIG. 4.6(b)–MEASUREMENT RESULTS USING RANDOM EXCITATION

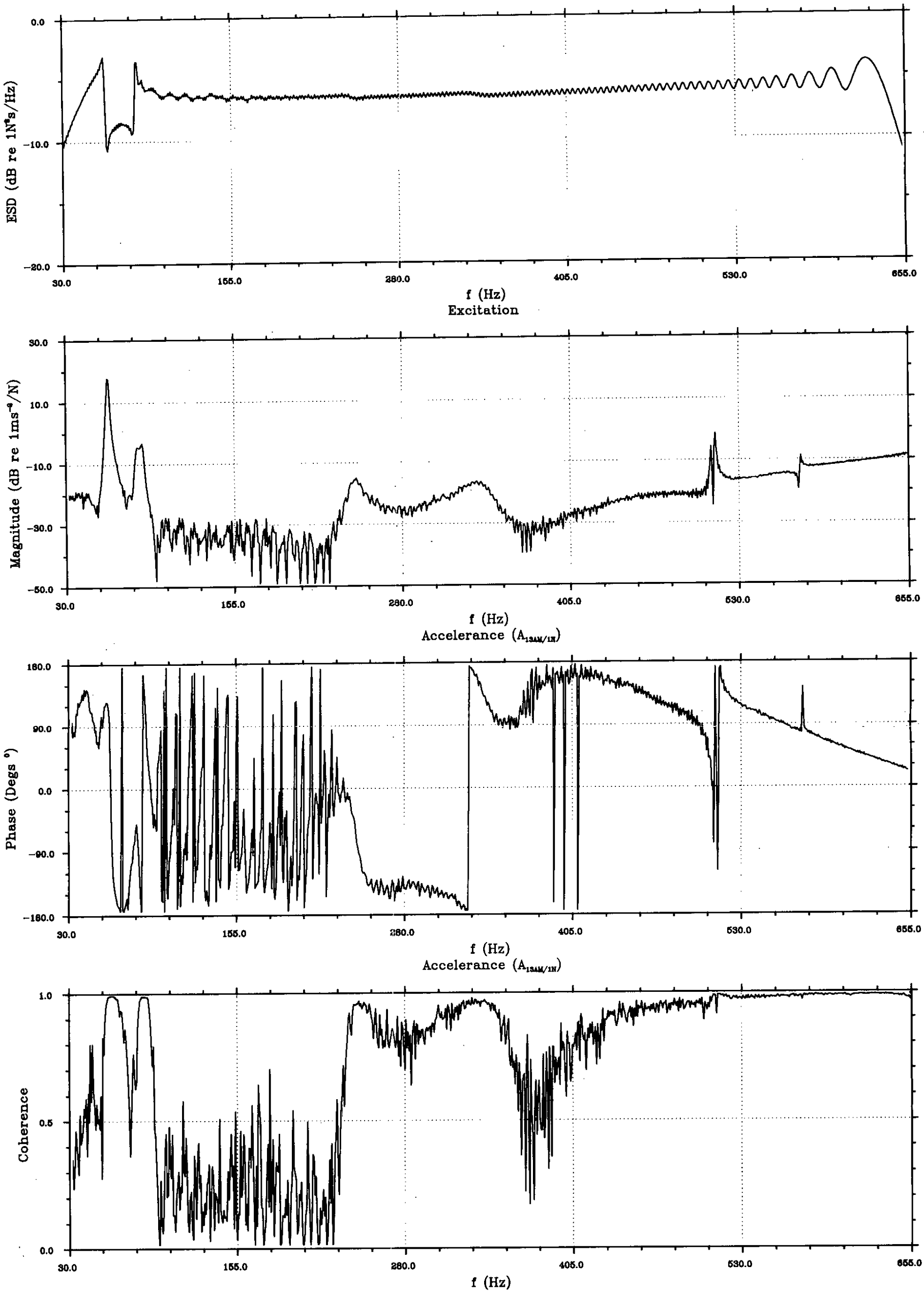

FIG. 4.6(c)–MEASUREMENT RESULTS USING BURST CHIRP EXCITATION

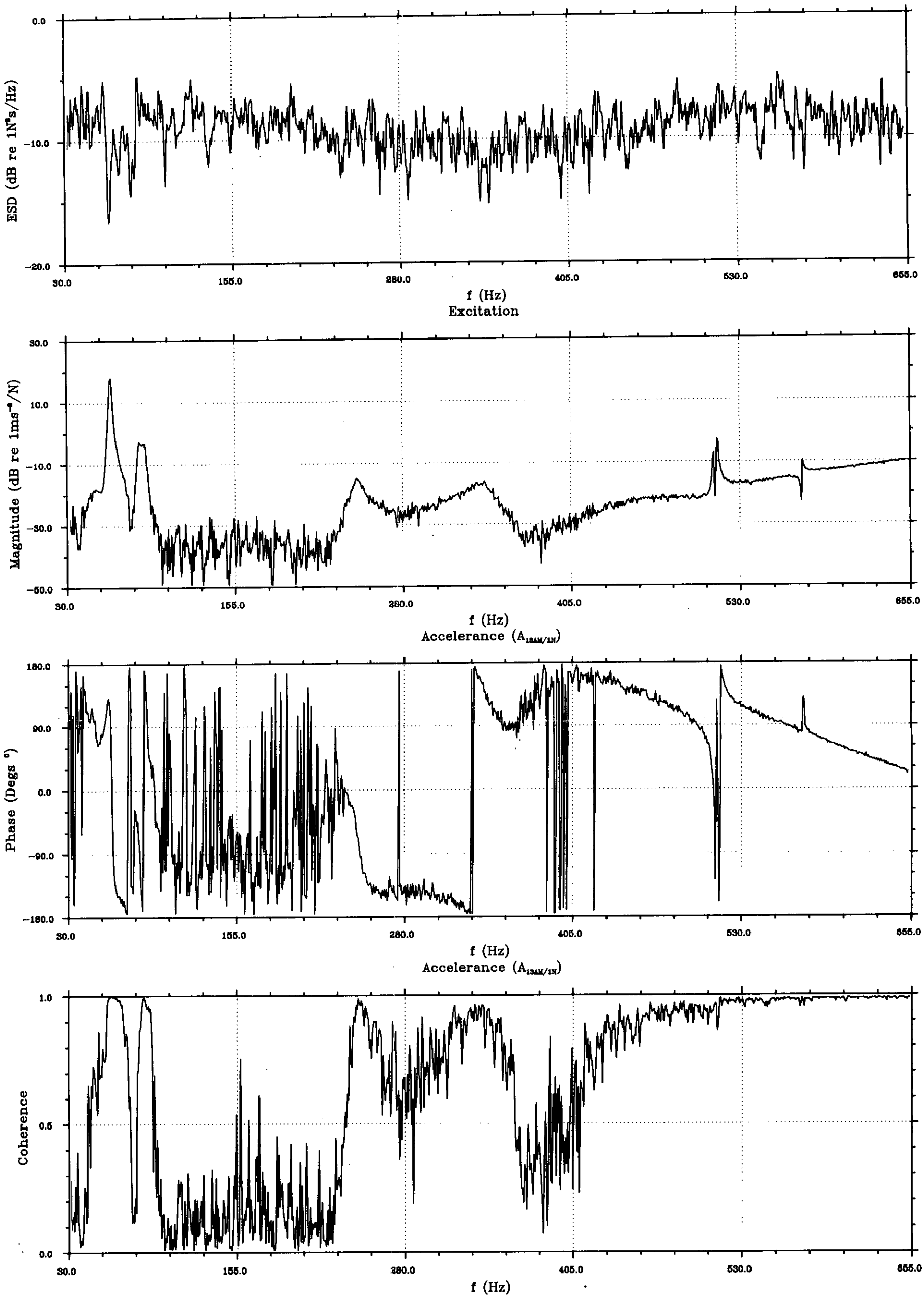

FIG. 4.6(d)–MEASUREMENT RESULTS USING BURST RANDOM EXCITATION

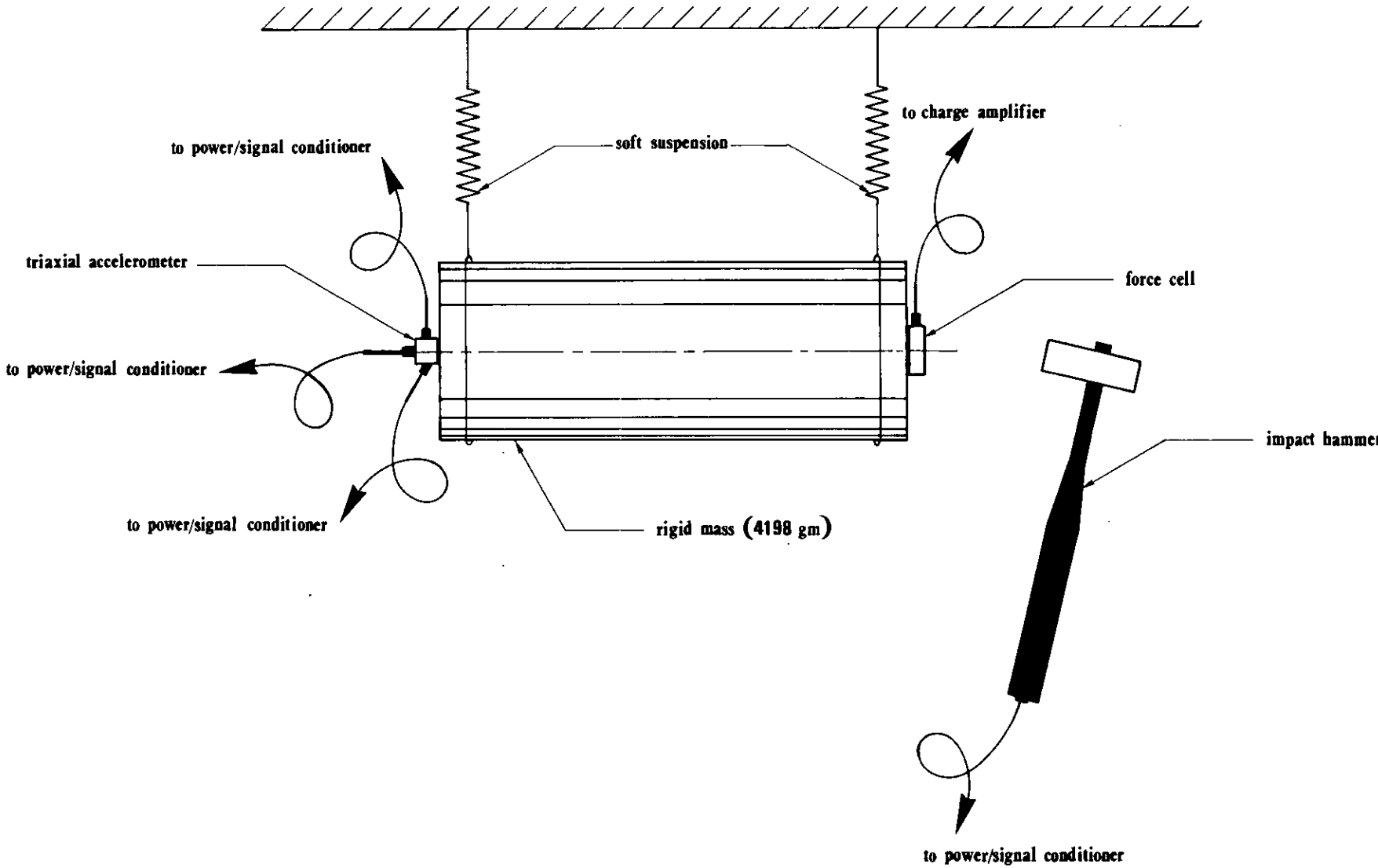

FIG. 4.7–CALIBRATION SET–UP

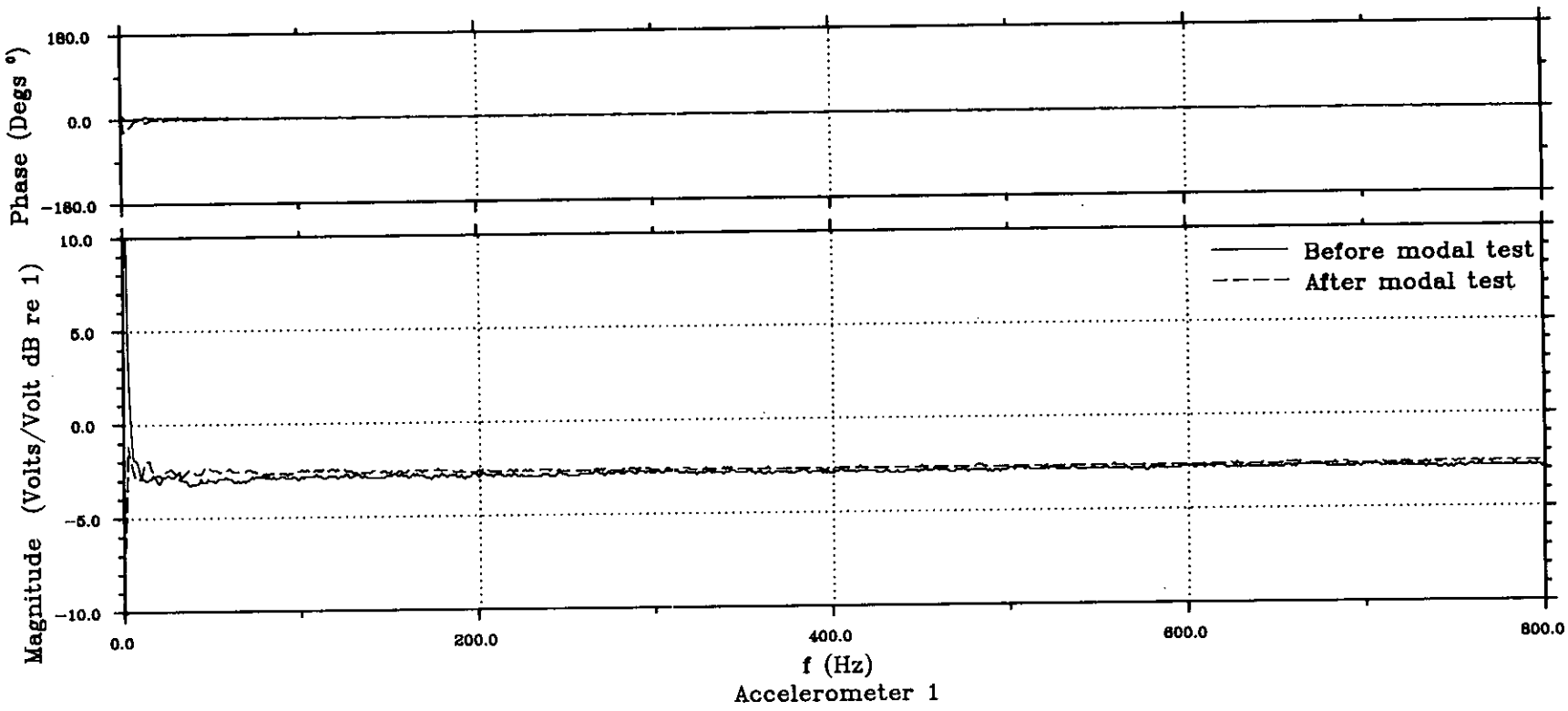

Accelerometer 1

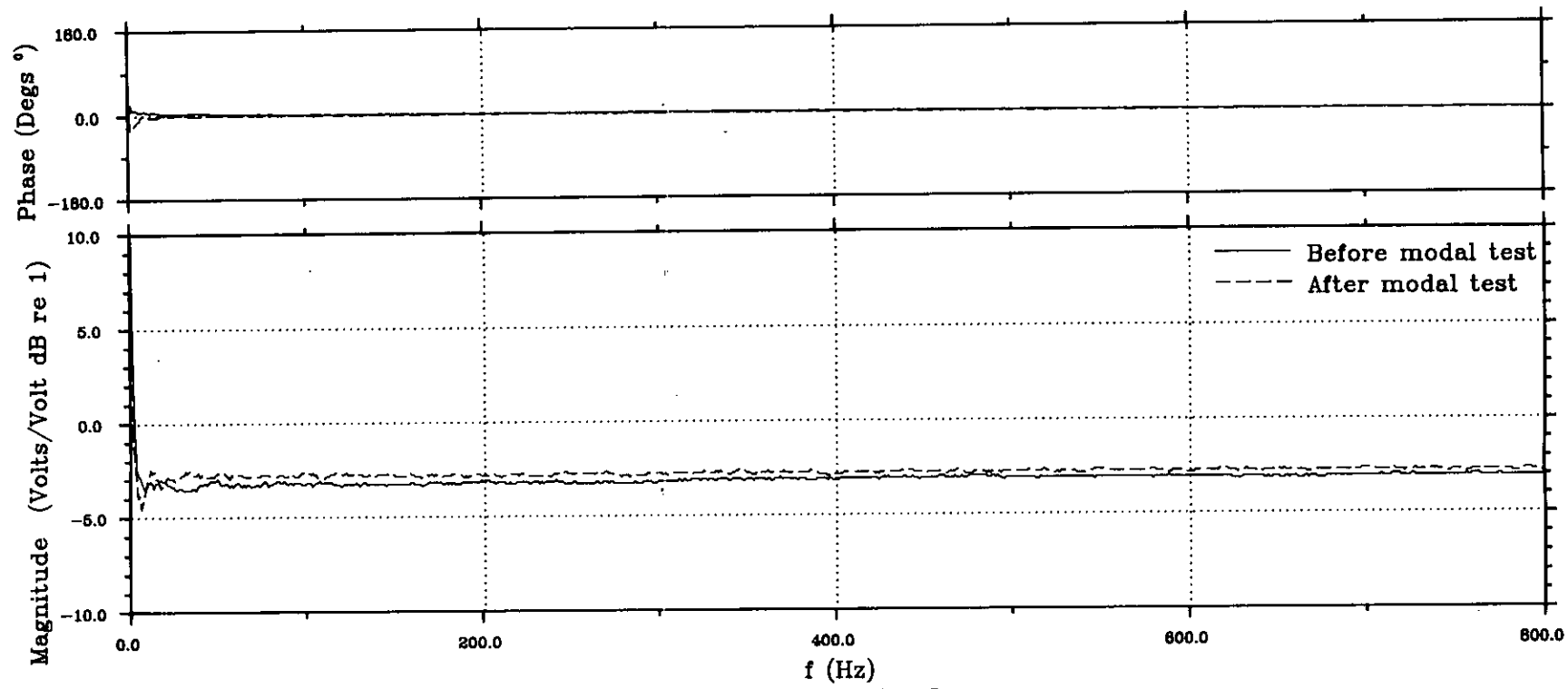

Accelerometer 2

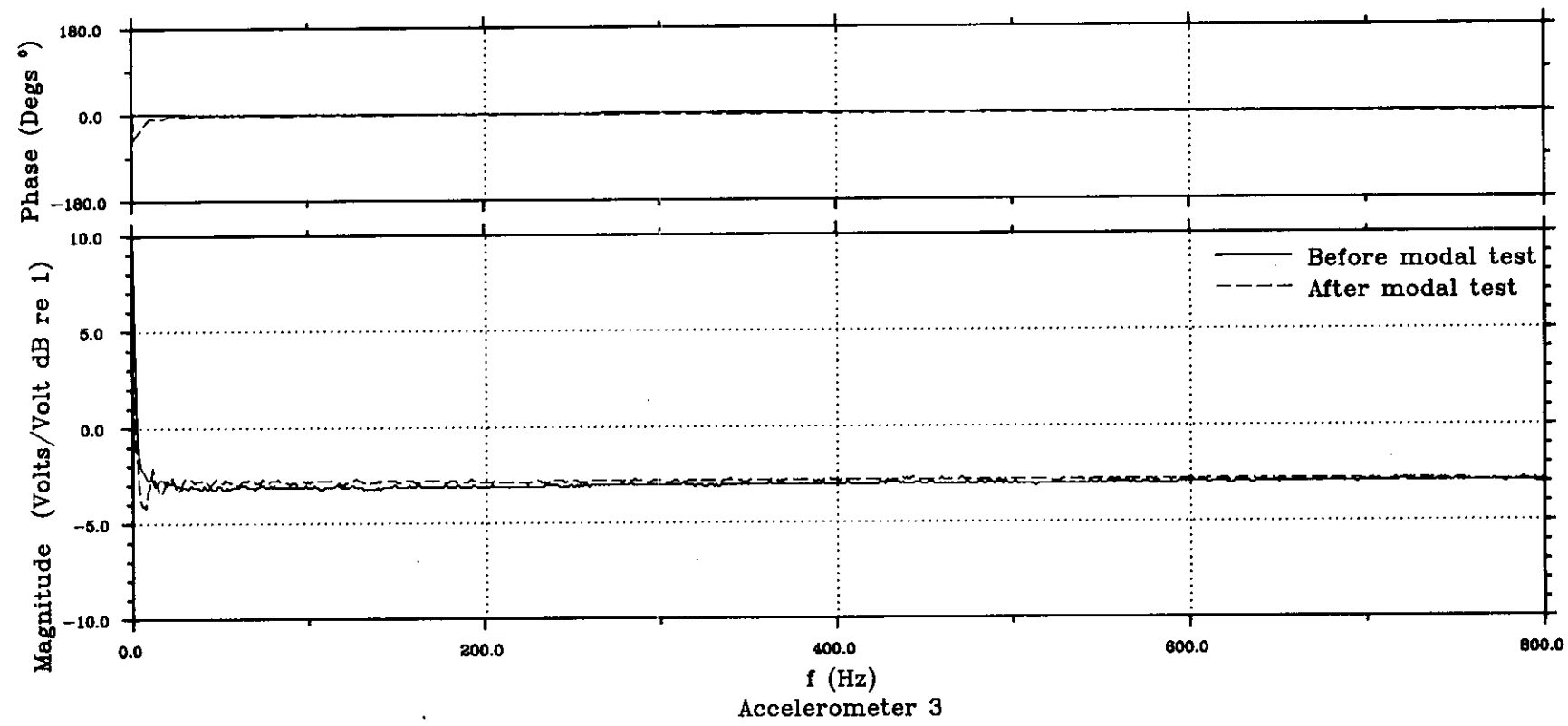

Accelerometer 3

FIG. 4.8–TYPICAL ACCELERANCE FUNCTIONS OF MINIATURE TRIAXIAL ACCELEROMETER

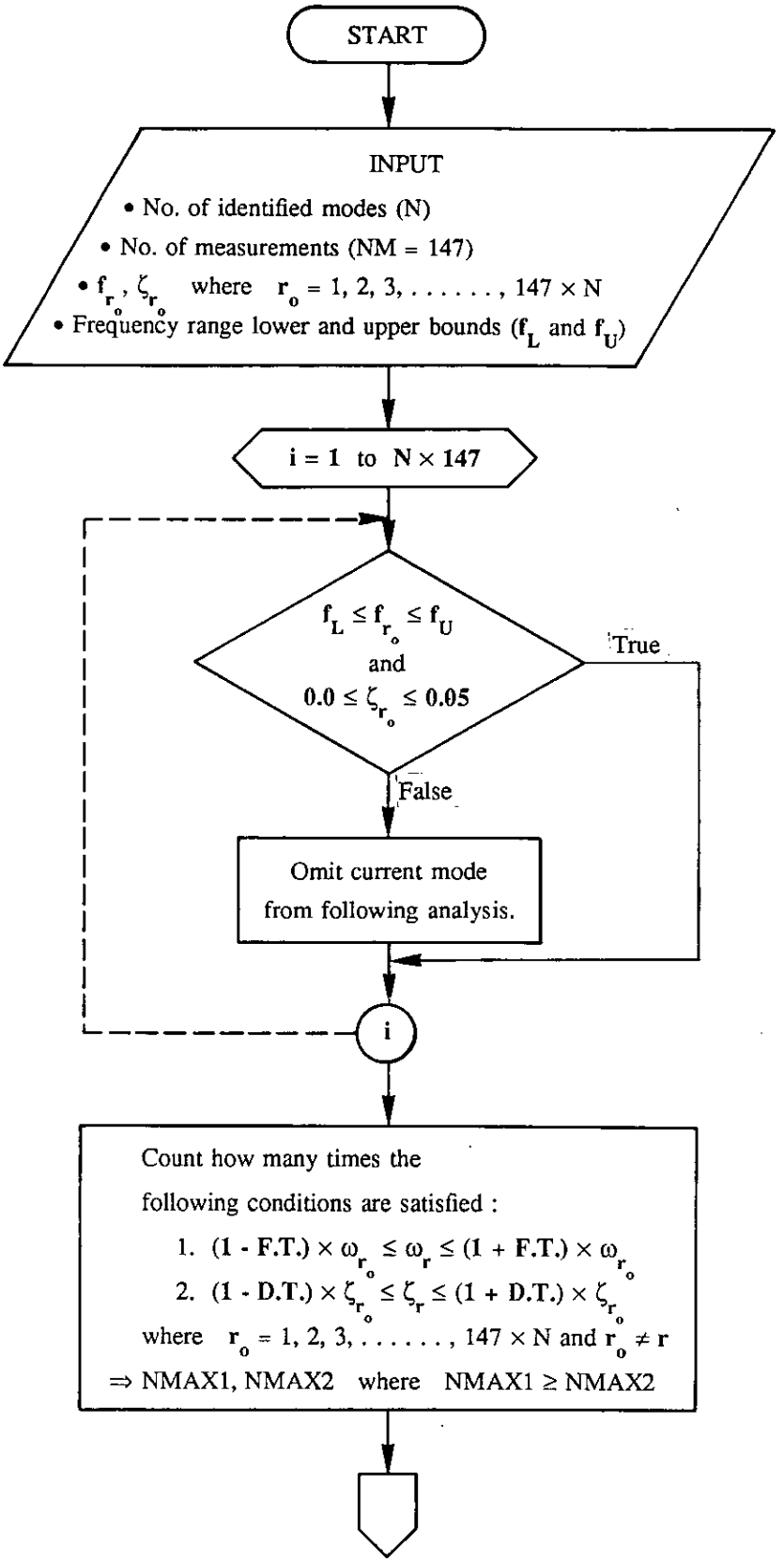

FIG. 4.9–FLOW CHART OF THE INTEL MAIN PROGRAM (CONTD)

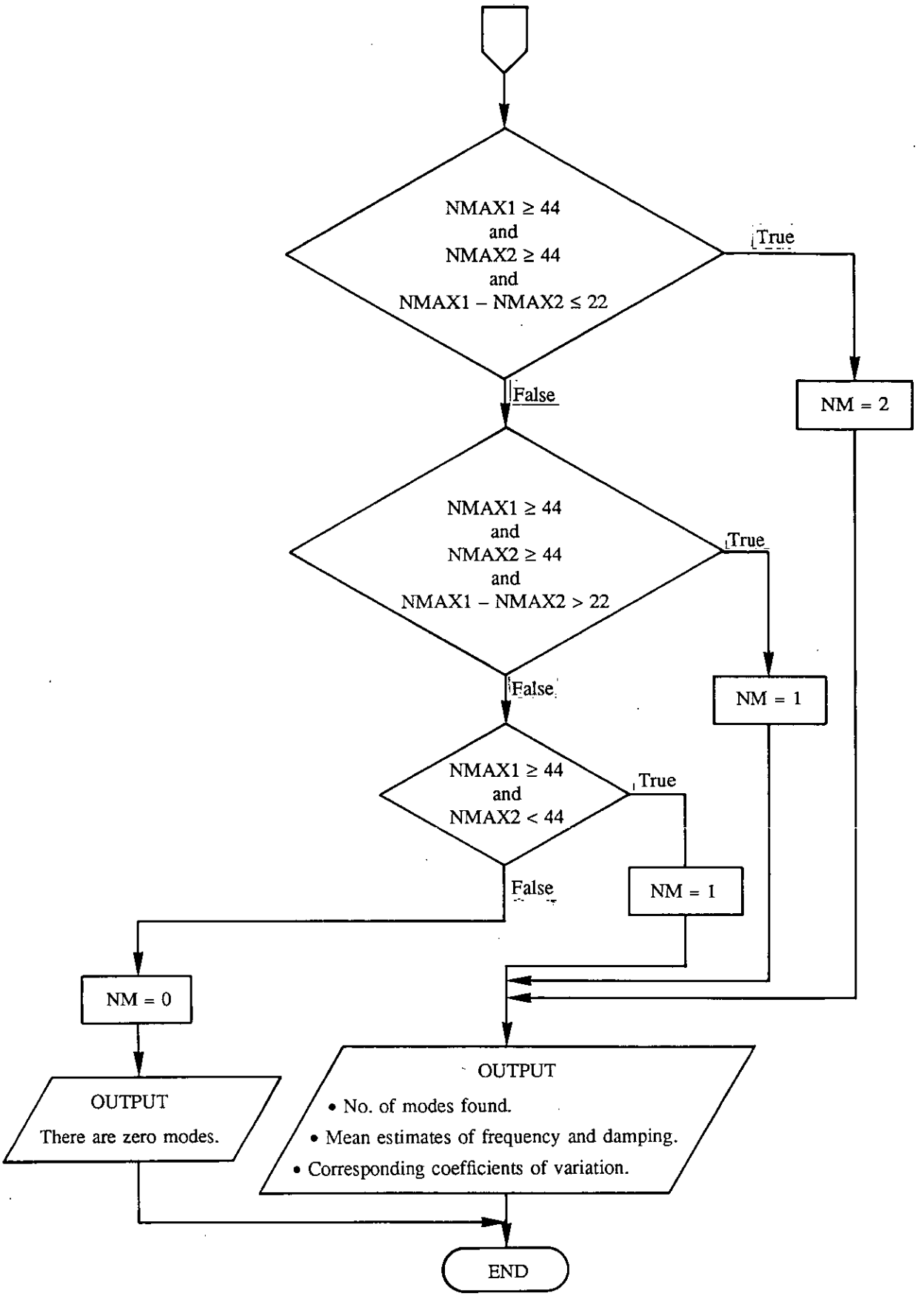

FIG. 4.9–FLOW CHART OF THE INTEL MAIN PROGRAM

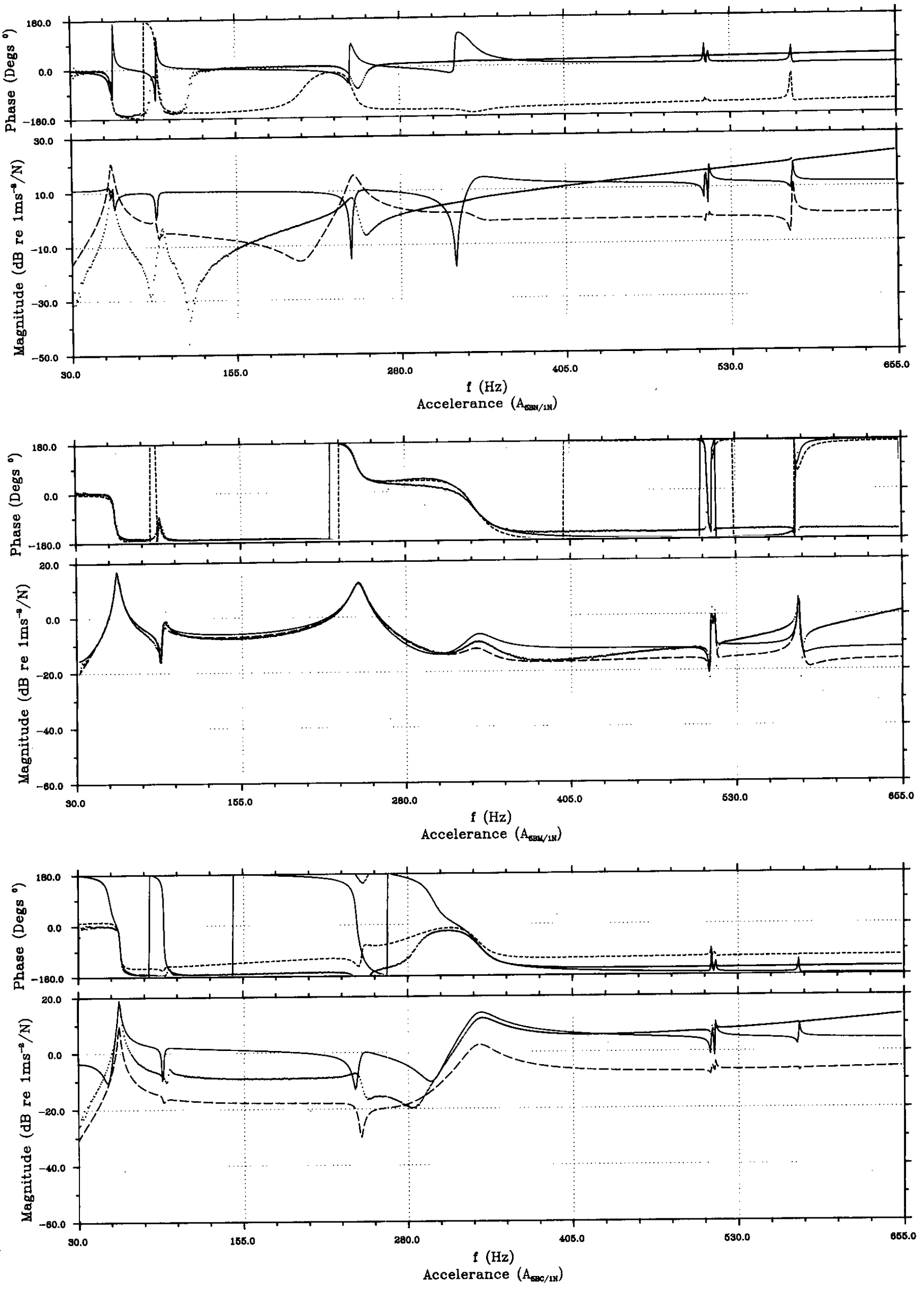

FIG. 4.10–COMPARISON BETWEEN VARIOUS GLOBAL CURVE FITTING PROCEDURES

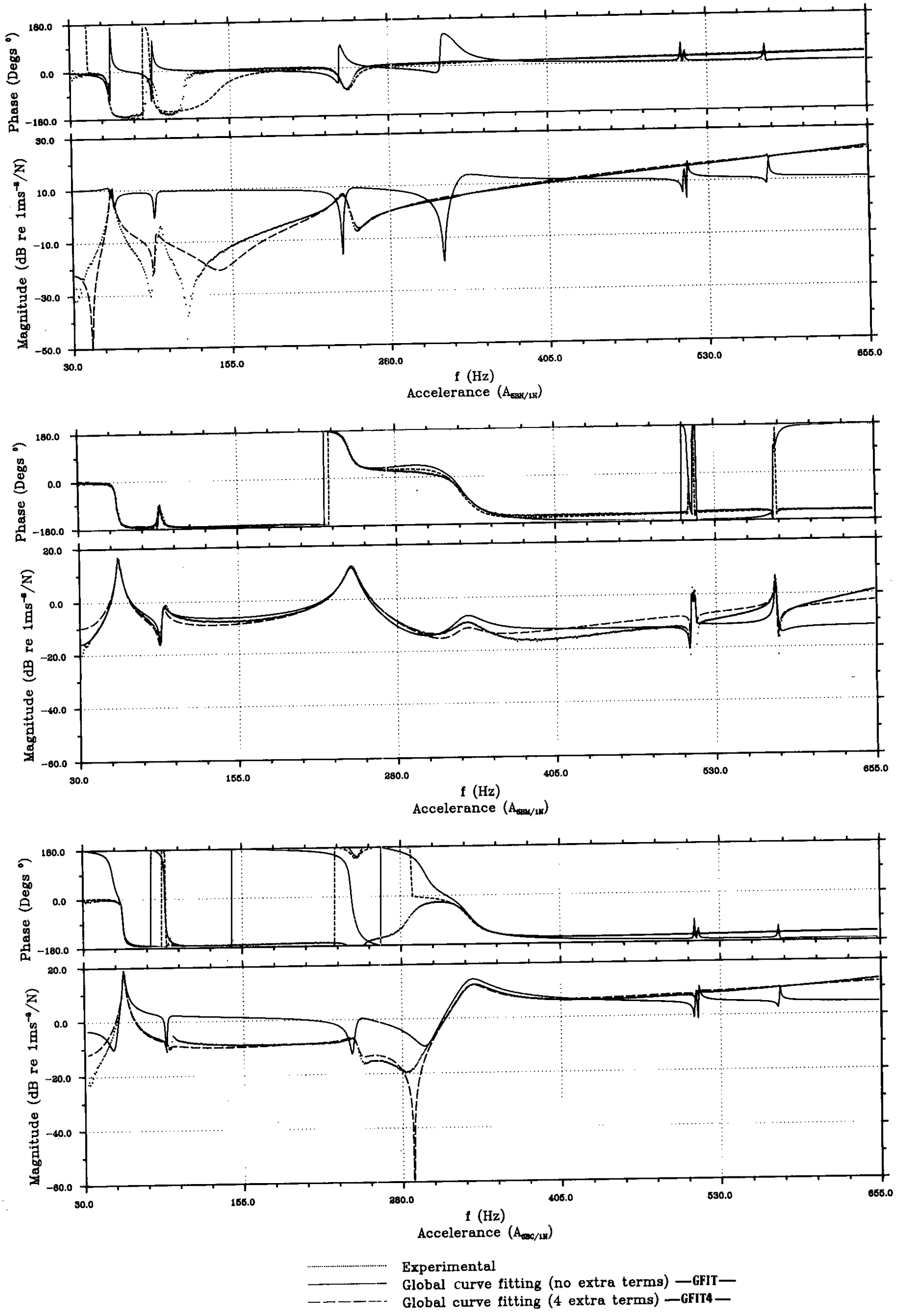

FIG. 4.11–EFFECT OF EXTRA NUMERATOR POLYNOMIAL TERMS ON GLOBAL CURVE FITTING

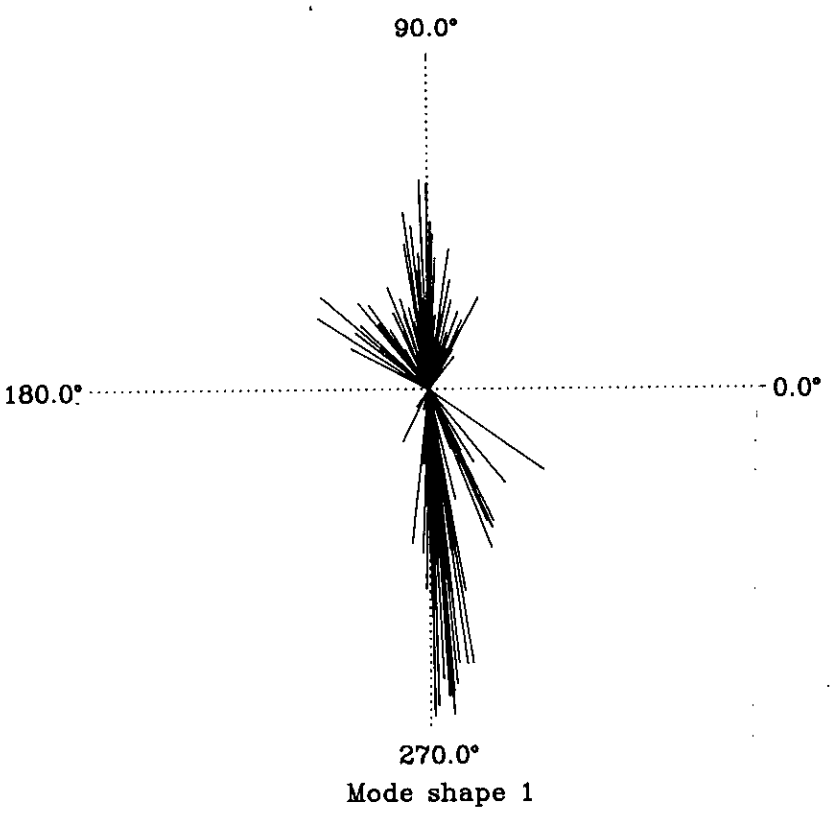

Mode shape 1

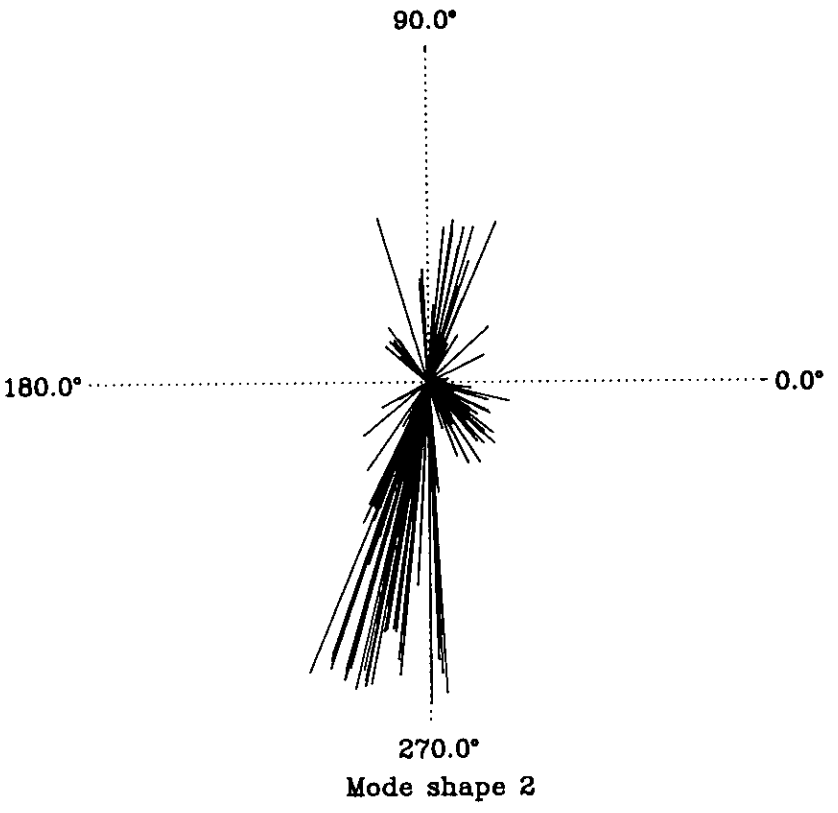

Mode shape 2

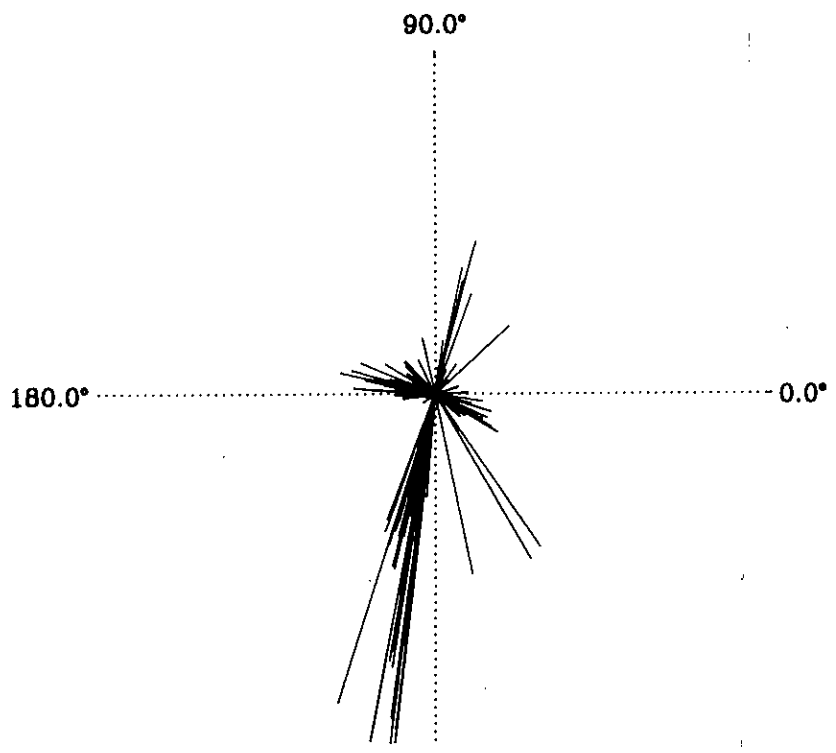

Mode shape 3

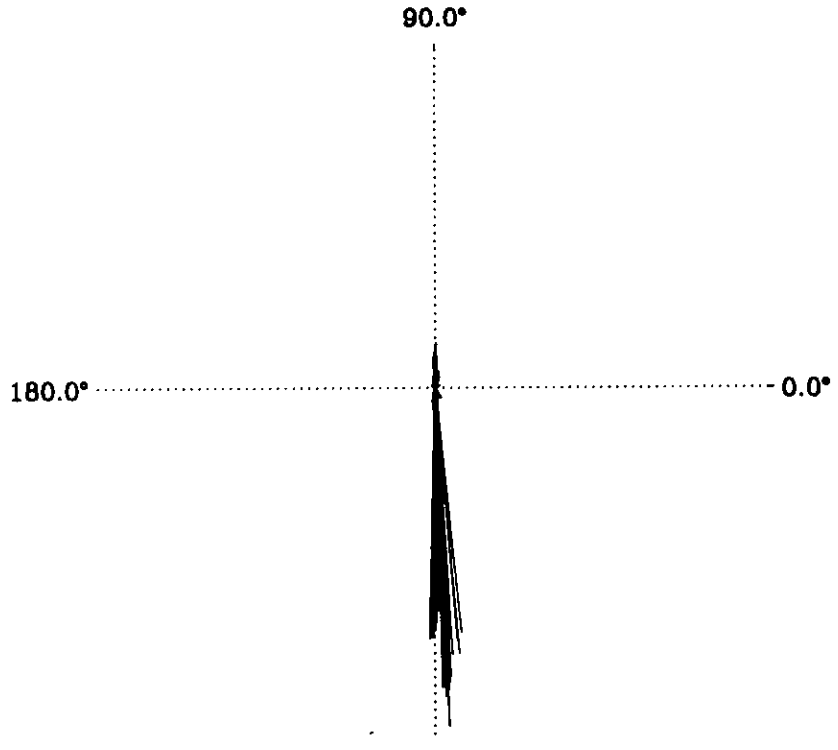

Mode shape 4

FIG. 4.12–PHASE ANGLE FOR EXPERIMENTAL MODE SHAPES (CONTD)

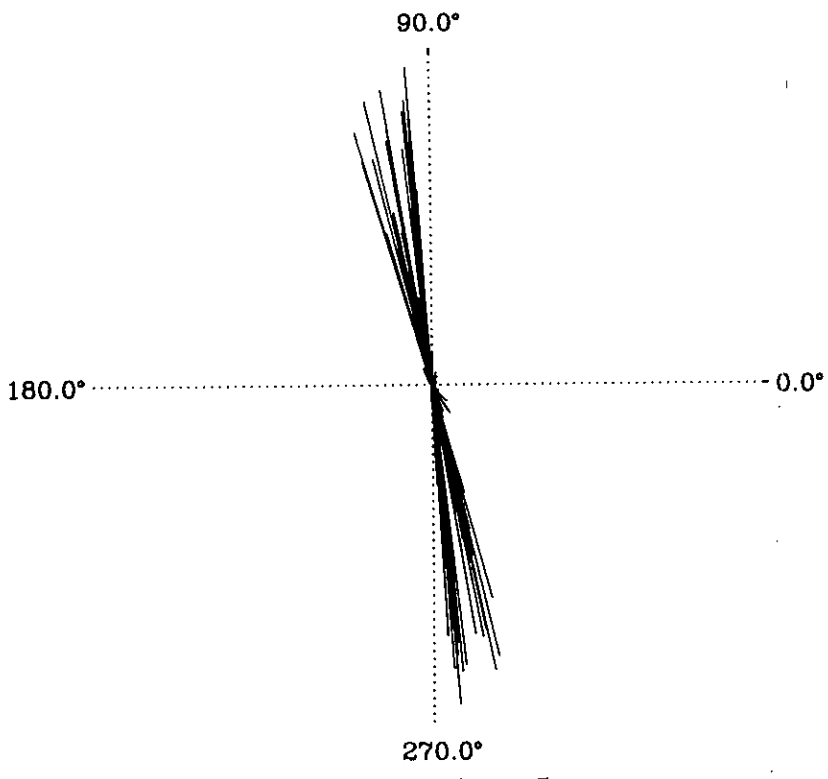

Mode shape 5

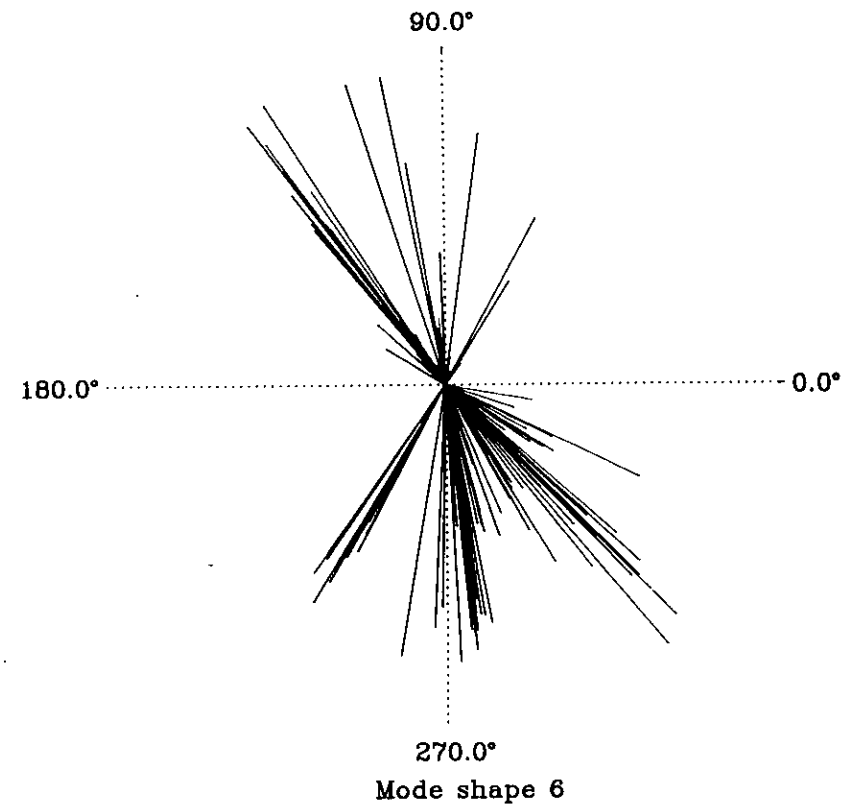

Mode shape 6

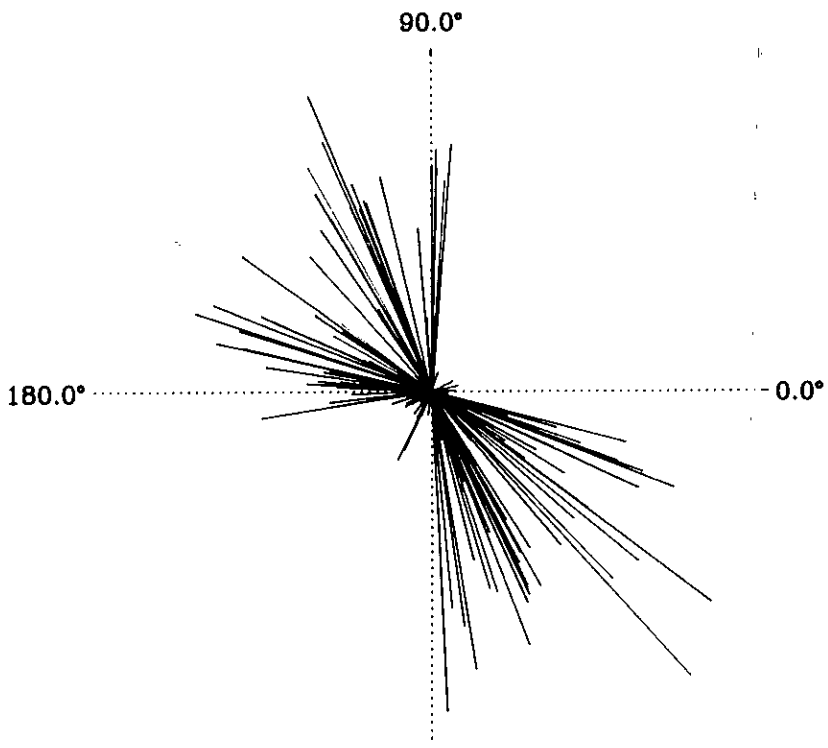

Mode shape 7

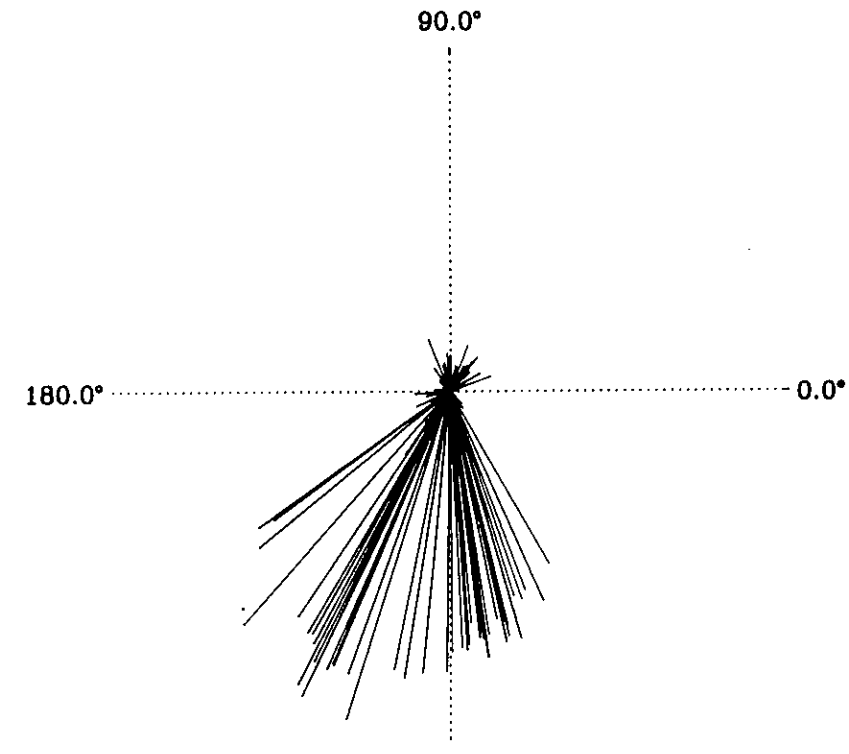

Mode shape 8

FIG. 4.12–PHASE ANGLE FOR EXPERIMENTAL MODE SHAPES

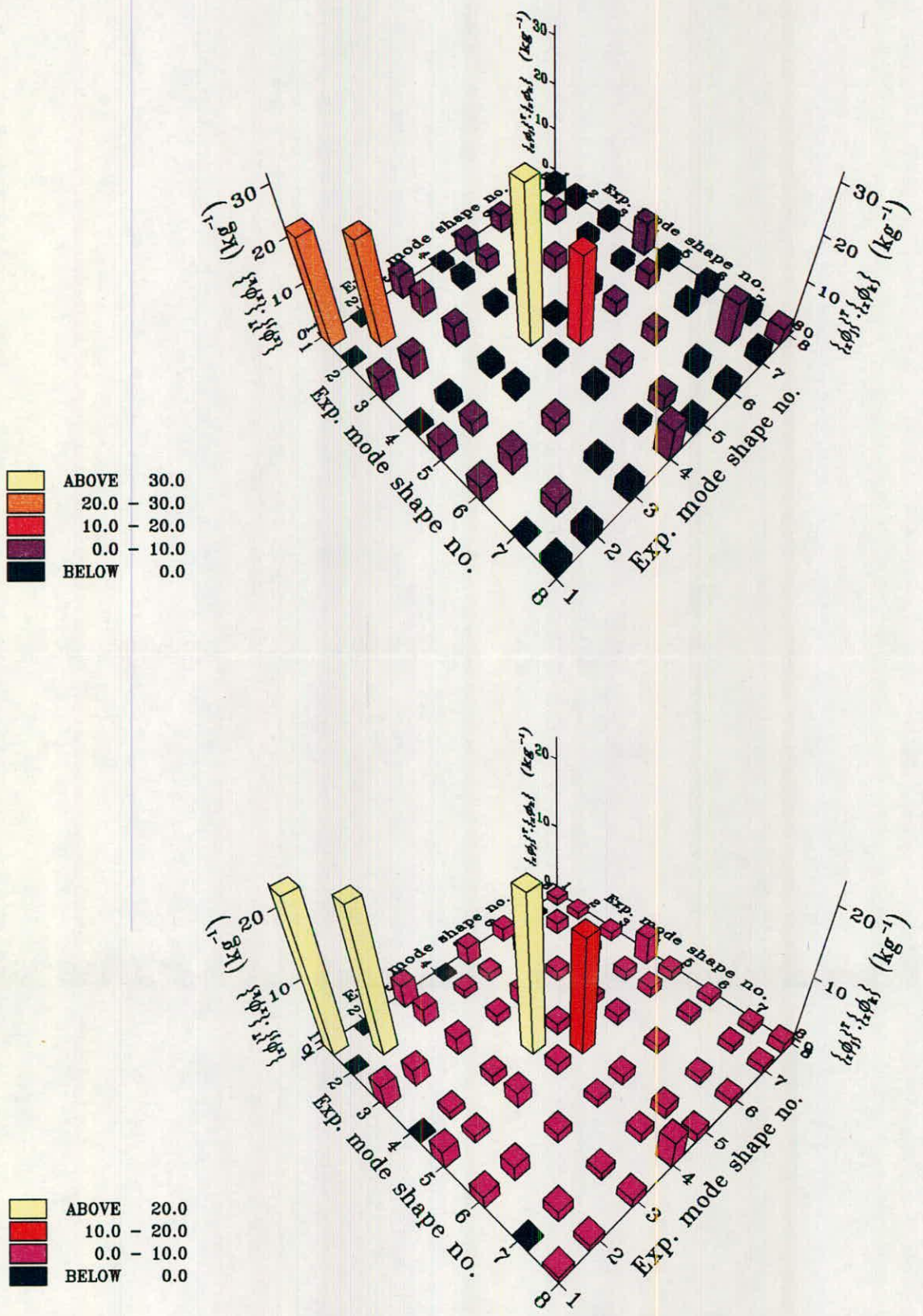

-LFIT-

-GFIT-

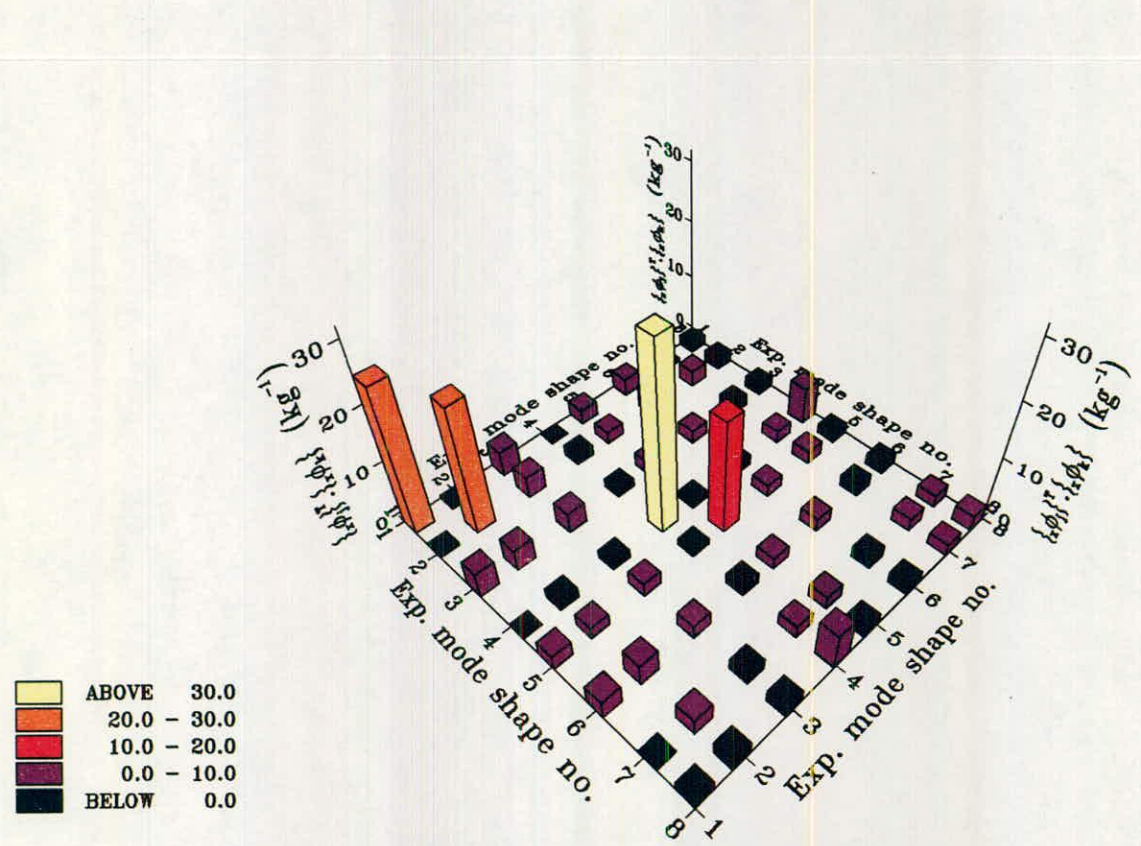

-GFIT4-

FIG. 4.13–ORTHOGONALITY CHECK FOR VARIOUS MODAL VECTOR ESTIMATES

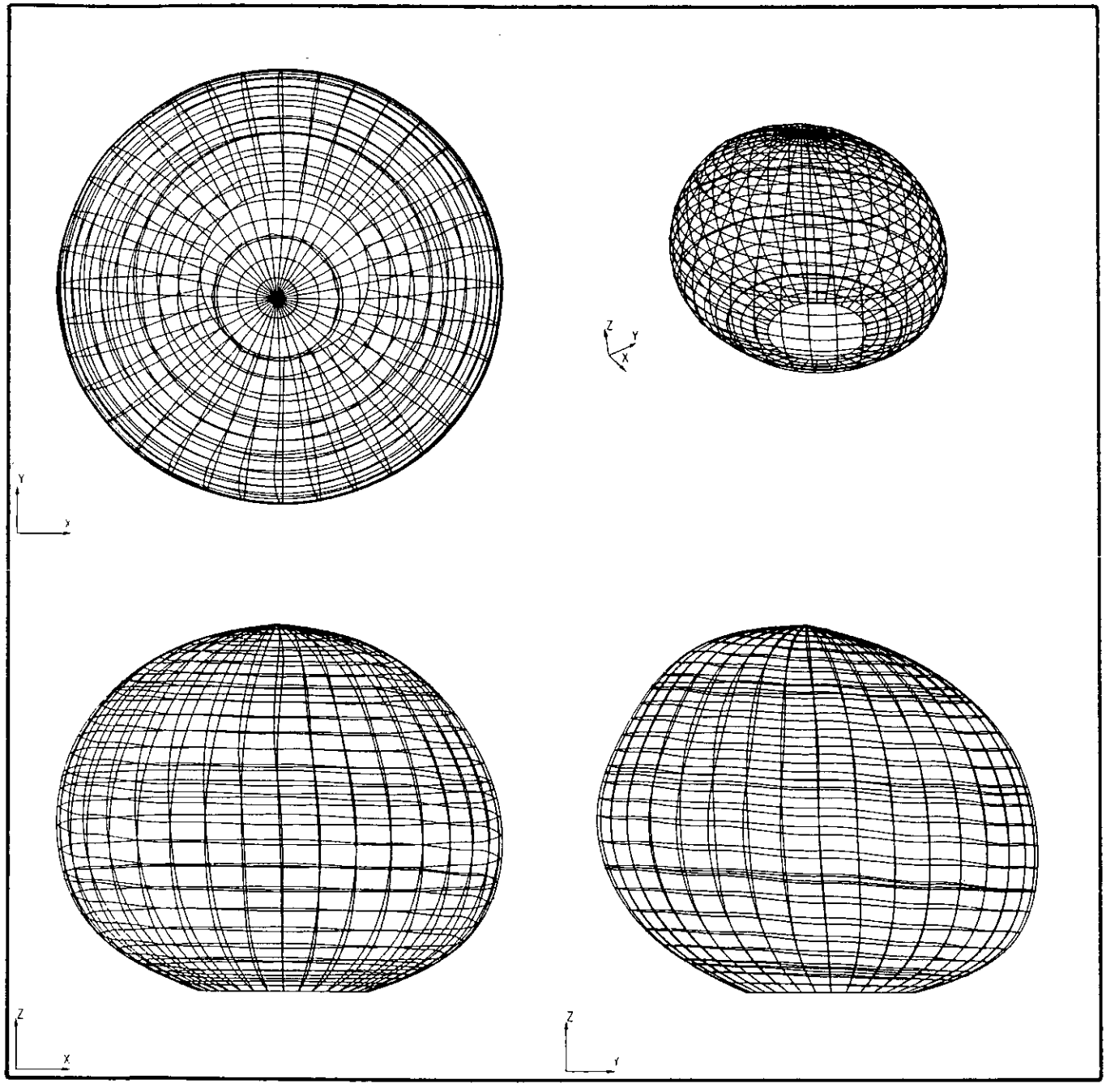

FIG. 4.14(a)–*VIBRATING MODE SHAPE* 1
––*FREQUENCY*=60.67 *Hz*––
––*DAMPING* (ζ)=1.448 %––
FIRST SYMMETRIC MODE

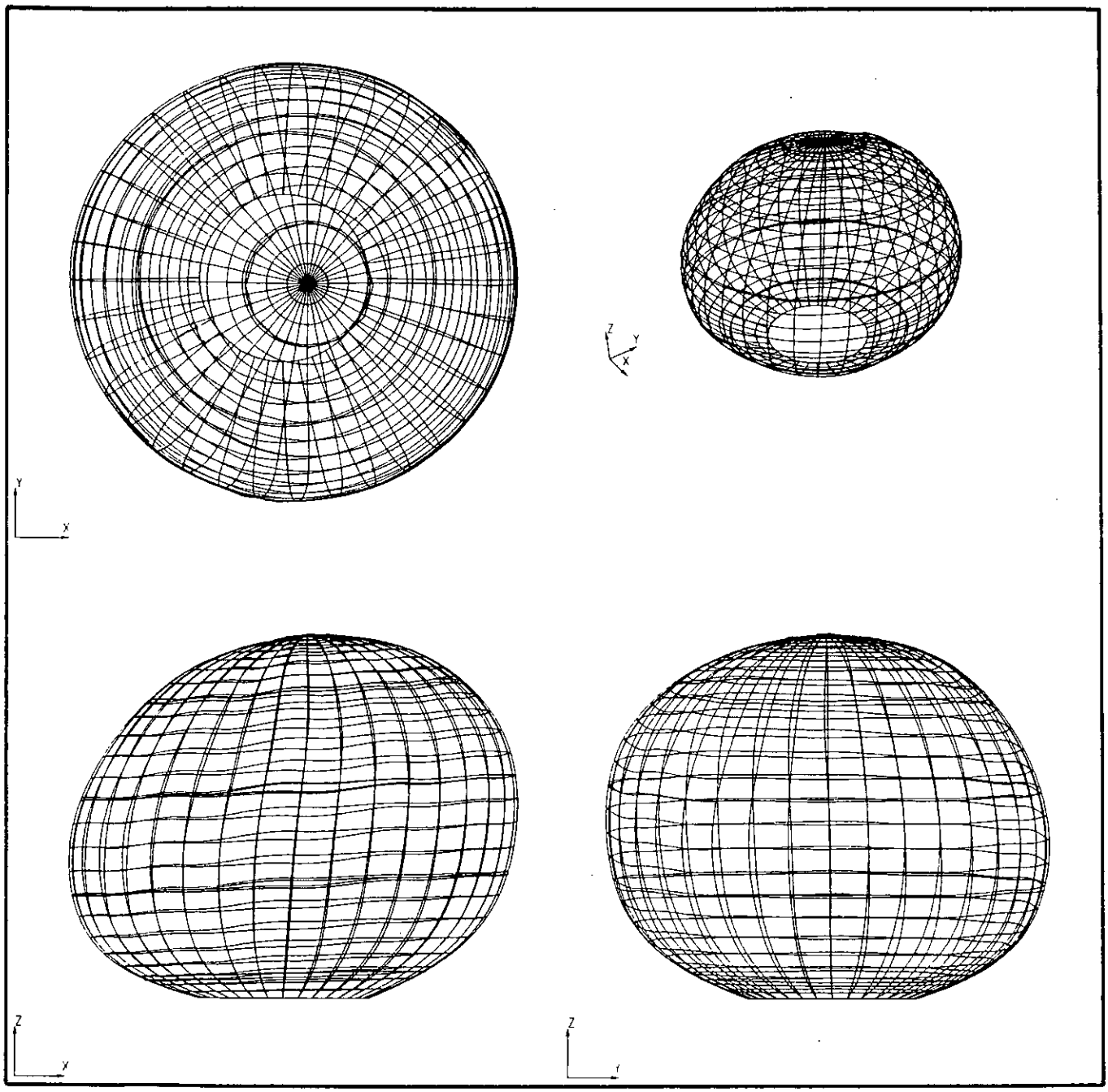

FIG. 4.14(b)–*VIBRATING MODE SHAPE 2*
––FREQUENCY=61.64 *Hz––*
––DAMPING (ζ)=1.467 %––
SECOND SYMMETRIC MODE

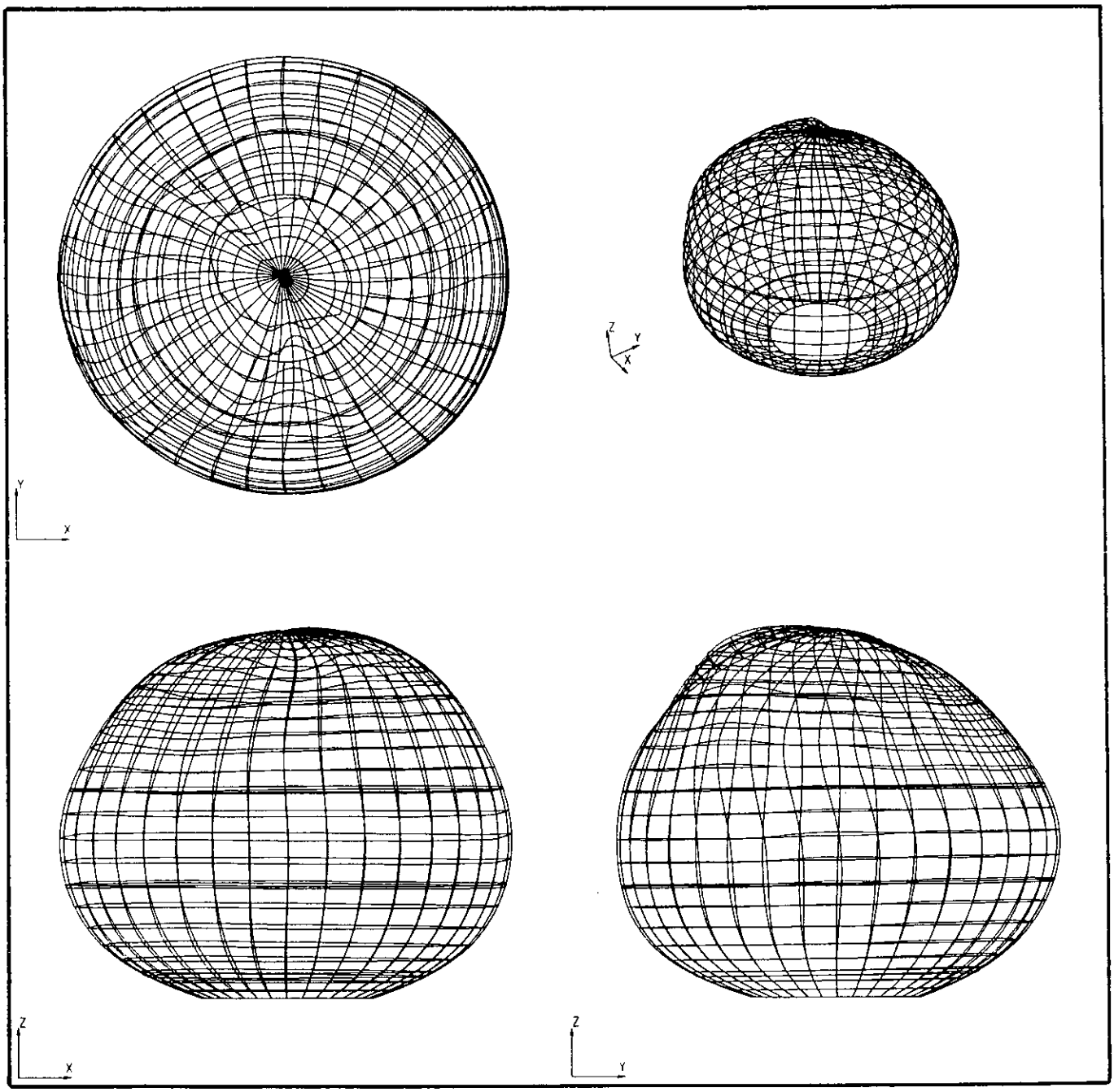

FIG. 4.14(c)–*VIBRATING MODE SHAPE* 3
––FREQUENCY=95.06 *Hz––*
––DAMPING (ζ)=1.495 %––
SPURIOUS SYMMETRIC MODE

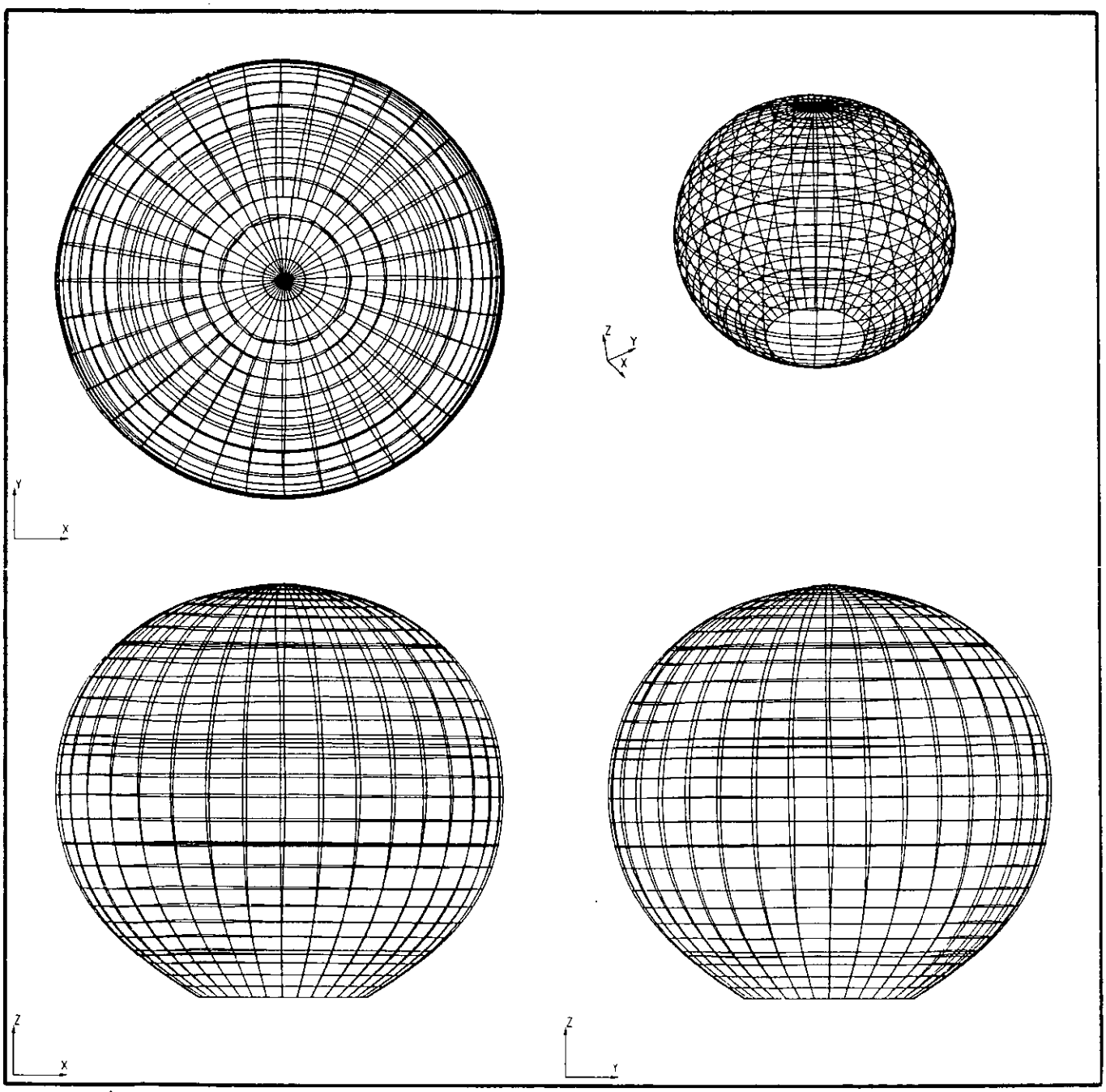

FIG. 4.14(d)–*VIBRATING MODE SHAPE* 4
––*FREQUENCY*=243.69 *Hz*––
––*DAMPING* (ζ)=1.787 %––
FIRST AXISYMMETRIC MODE

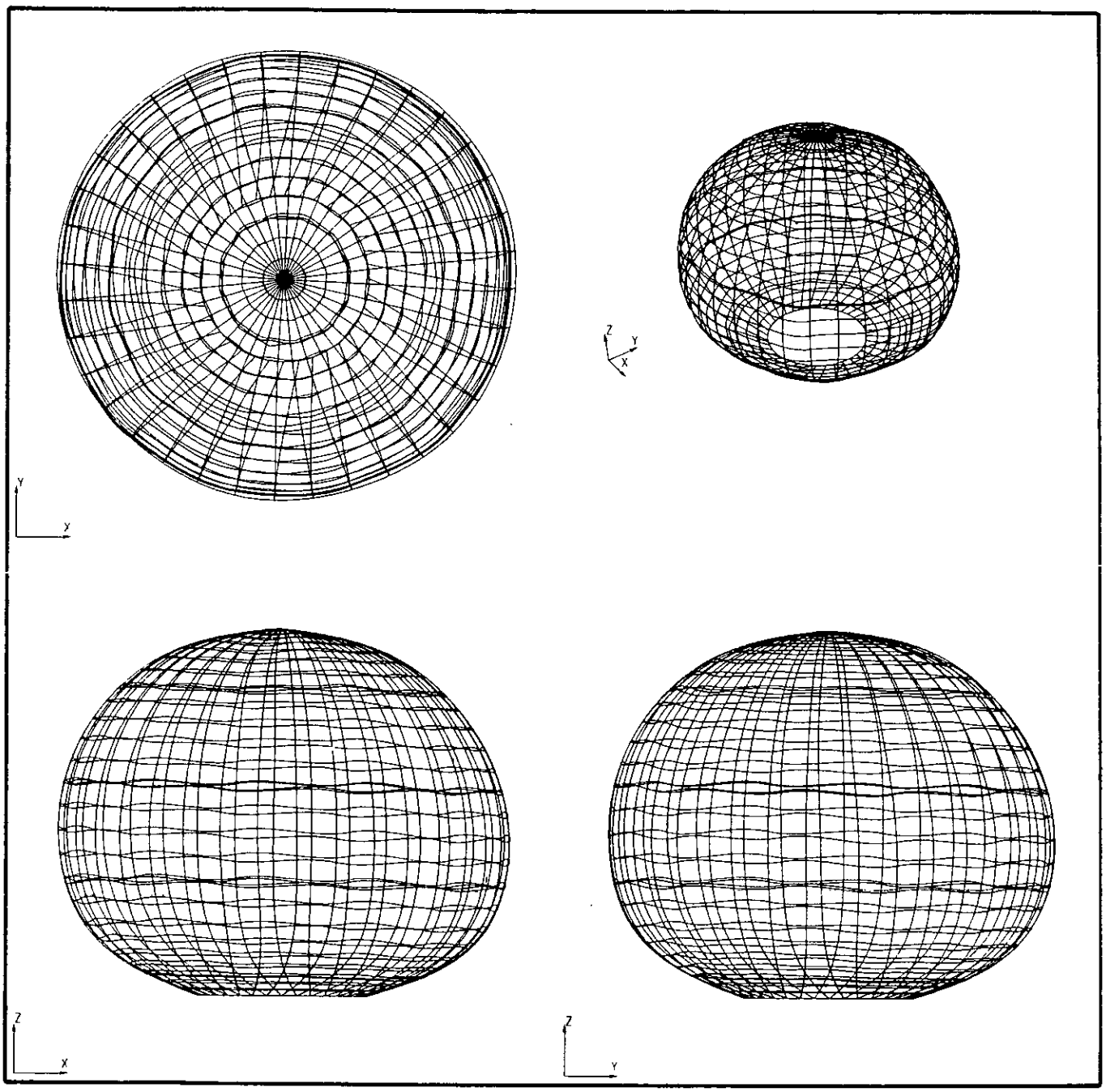

FIG. 4.14(e)–*VIBRATING MODE SHAPE* 5
––FREQUENCY=333.12 *Hz––*
––DAMPING (ζ)=3.196 %––
FIRST TORSIONAL MODE

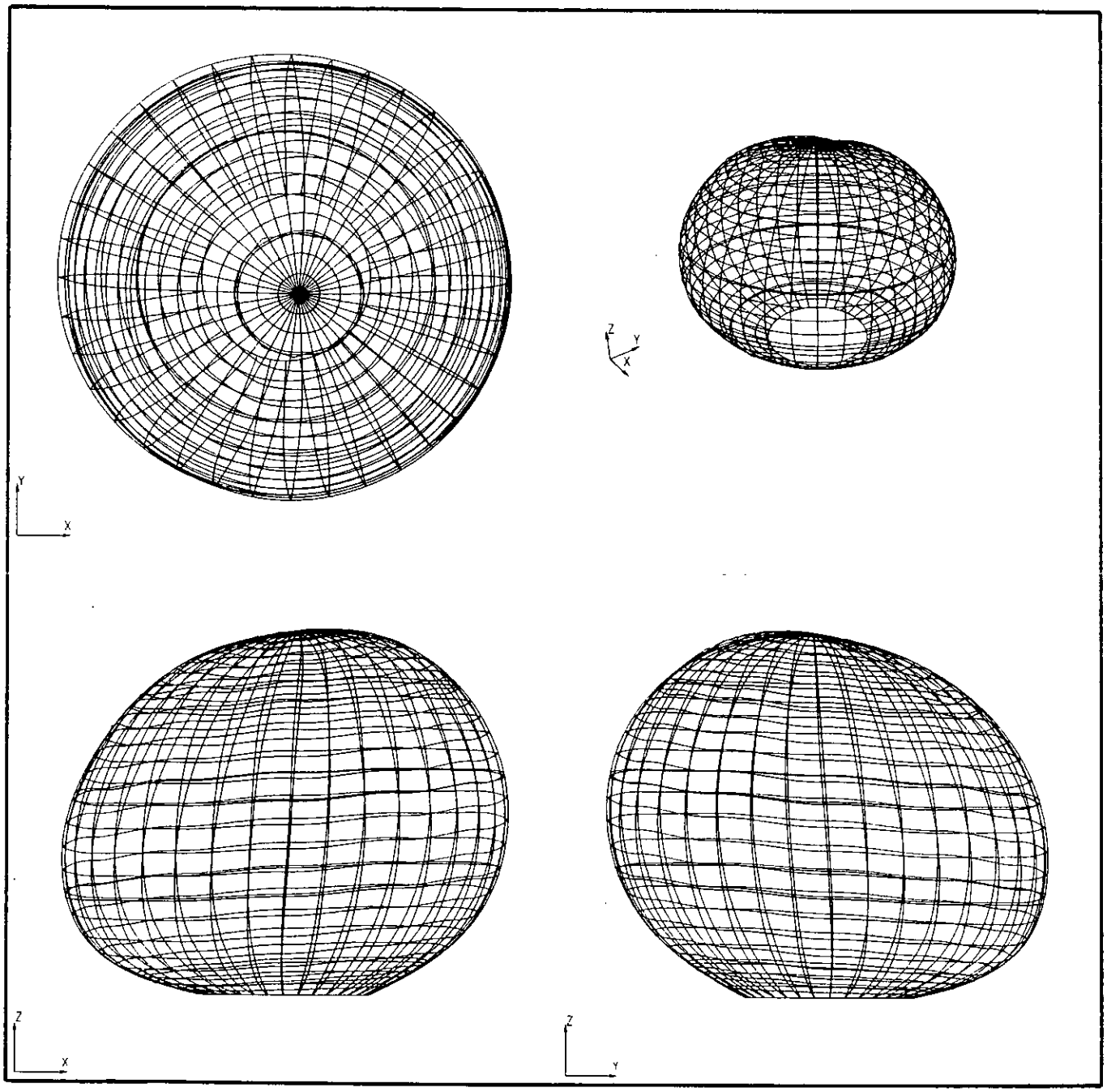

FIG. 4.14(*f*)*—VIBRATING MODE SHAPE* 6
——FREQUENCY=510.37 *Hz——*
——DAMPING (ζ)=0.060 %*——*
THIRD SYMMETRIC MODE

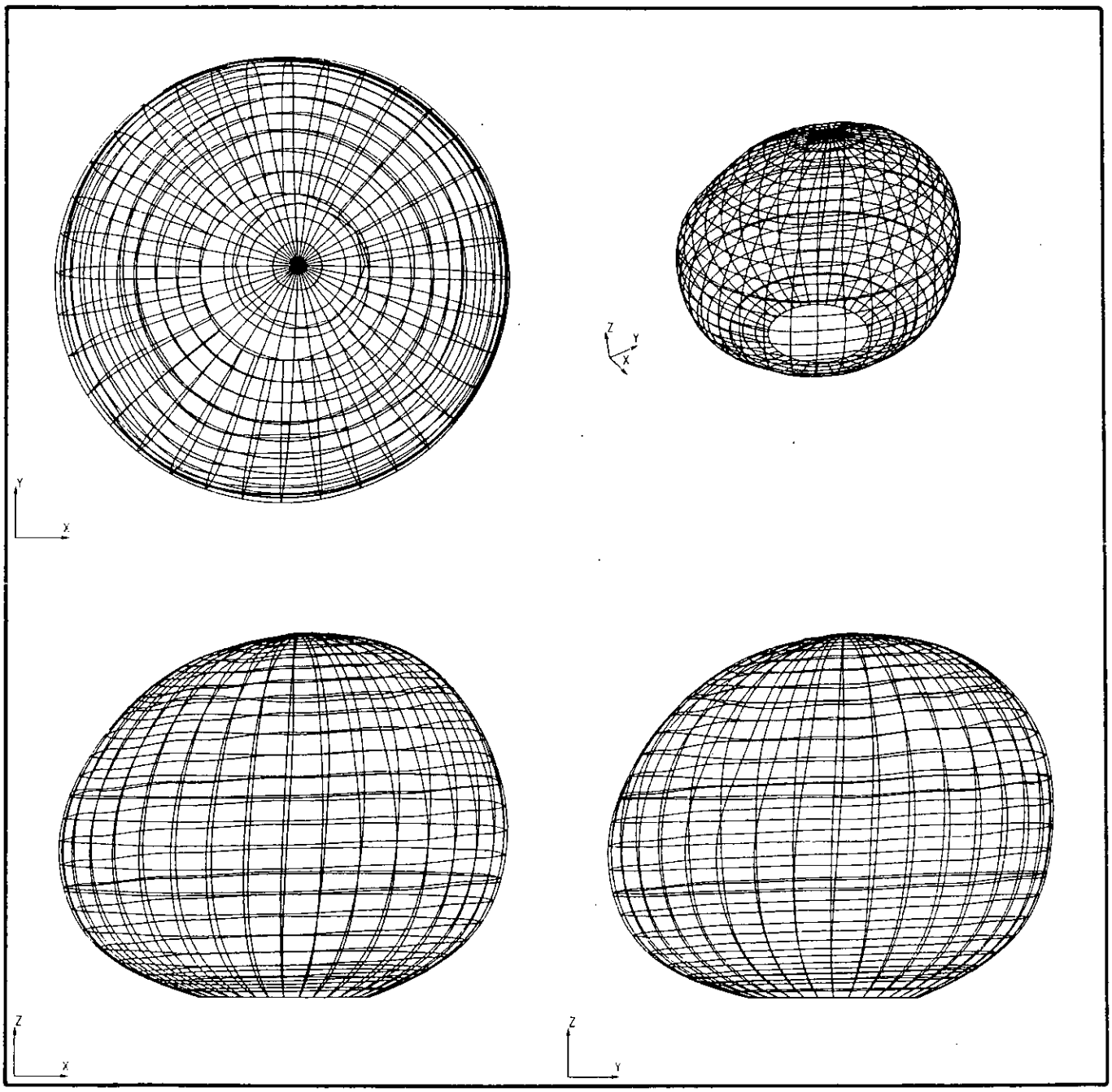

FIG. 4.14(*g*)–*VIBRATING MODE SHAPE 7*
––FREQUENCY=513.06 *Hz––*
––DAMPING (ζ)=0.065 %––
FOURTH SYMMETRIC MODE

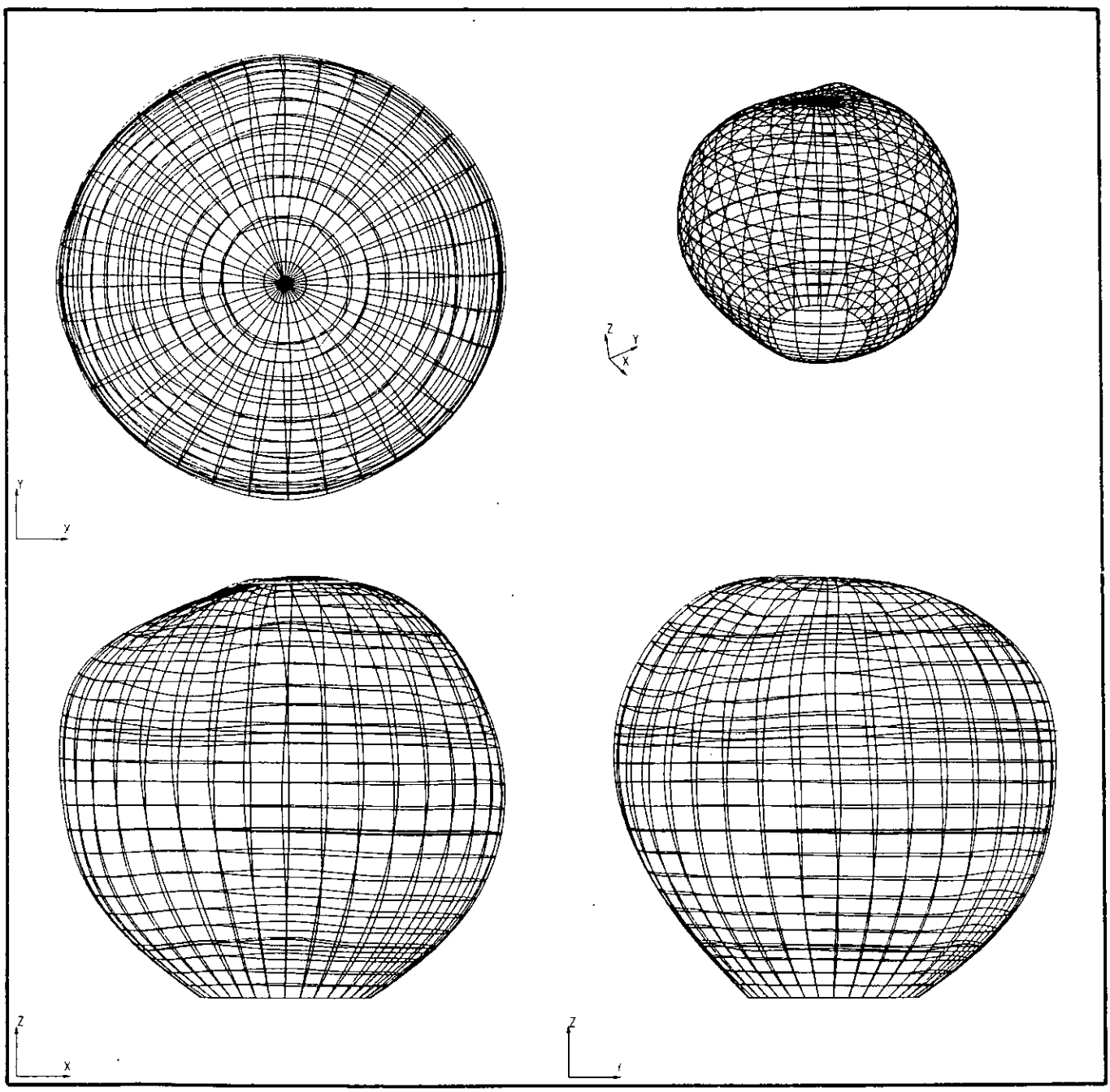

FIG. 4.14(*h*)*–VIBRATING MODE SHAPE* 8
––FREQUENCY=576.17 *Hz––*
––DAMPING (ζ)=0.064 %*––*
COMBINED AXISYMMETRIC–TORSIONAL MODE

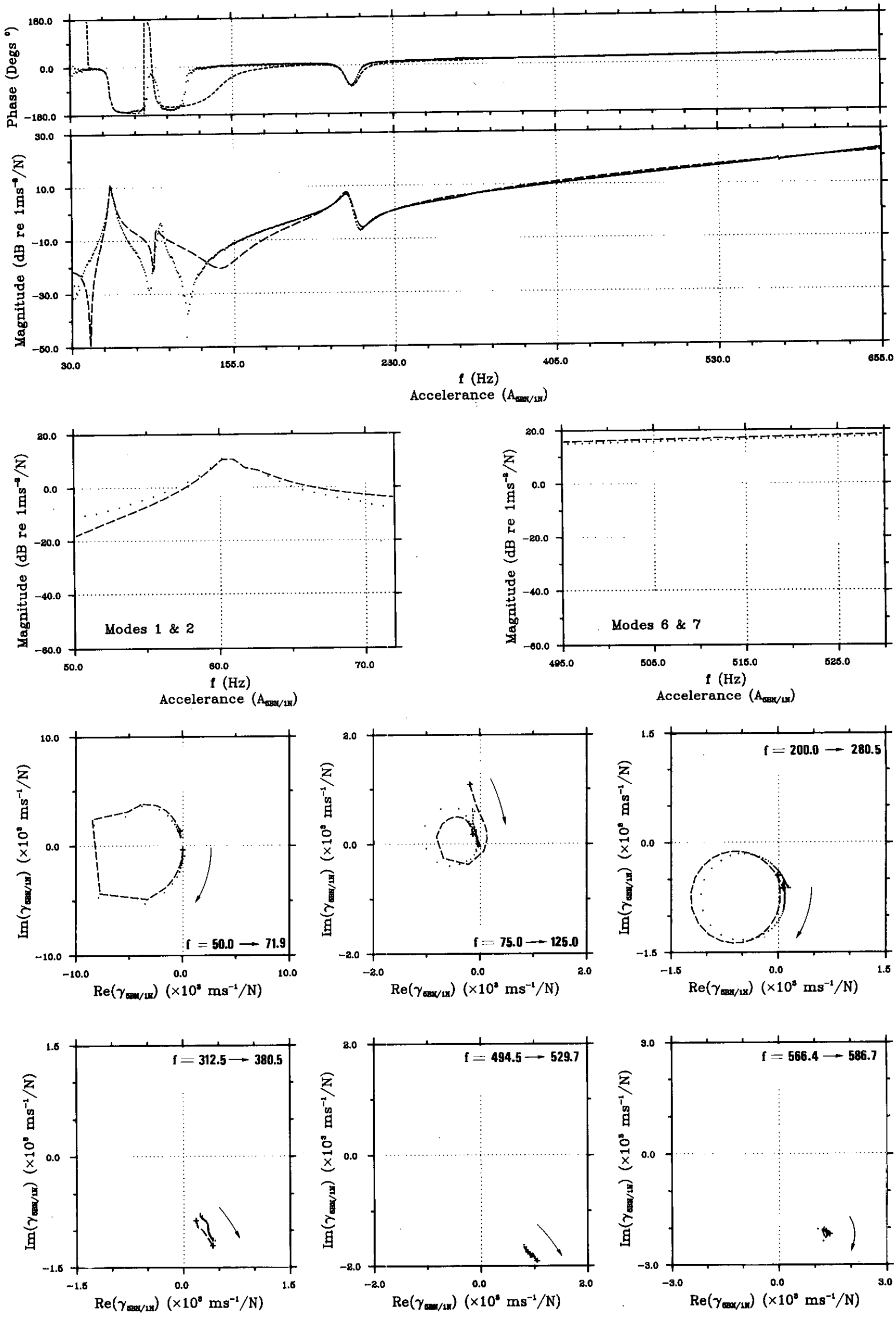

FIG. 4.15(a)–THEORETICALLY REGENERATED CROSS POINT FREQUENCY RESPONSE FUNCTION --NORMAL DIRECTION--

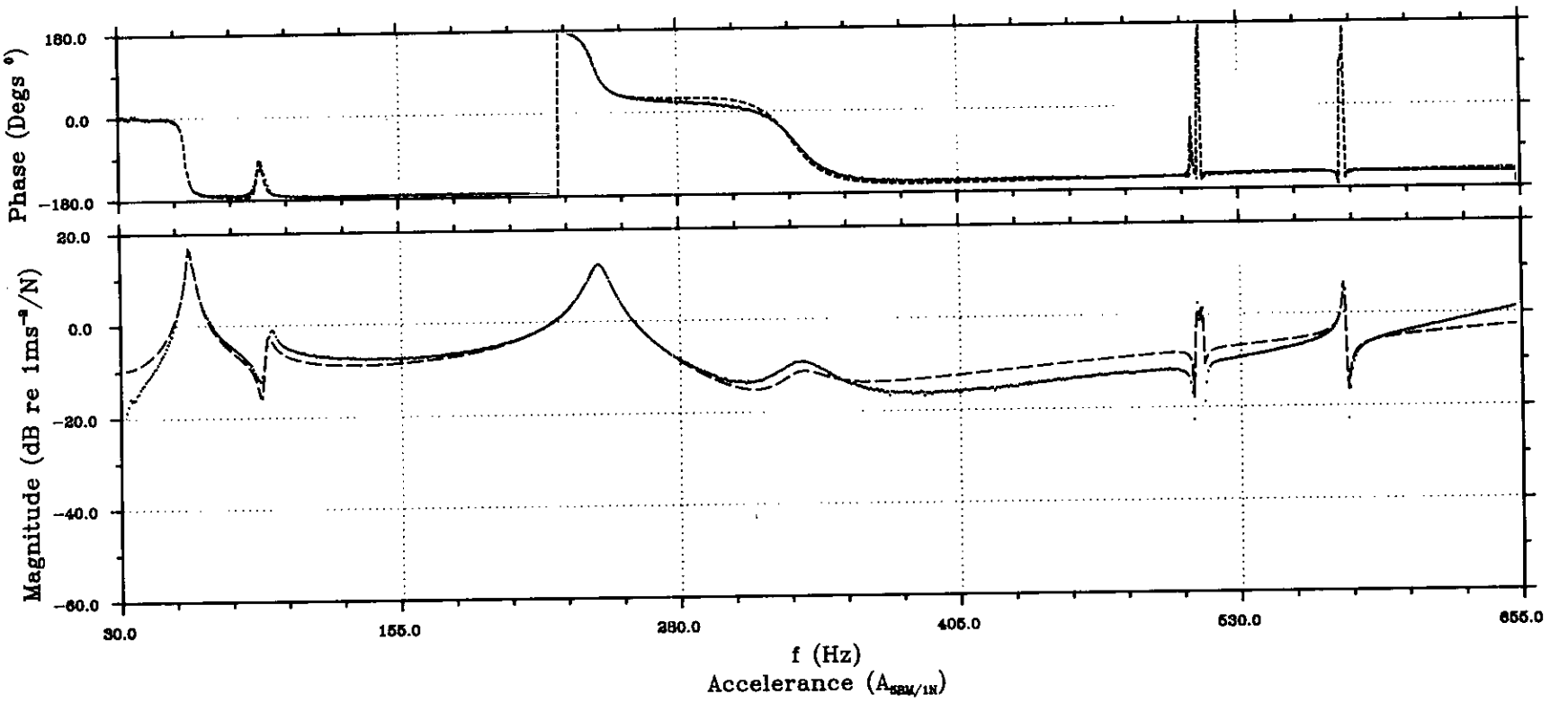

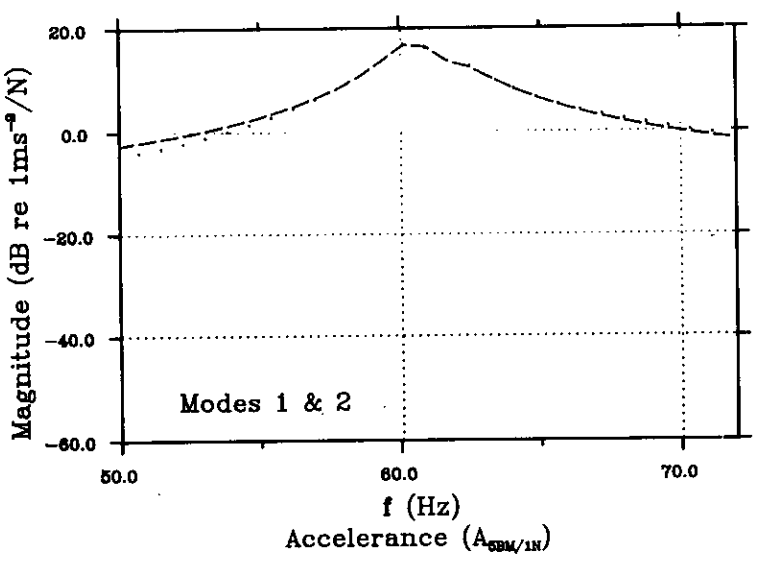

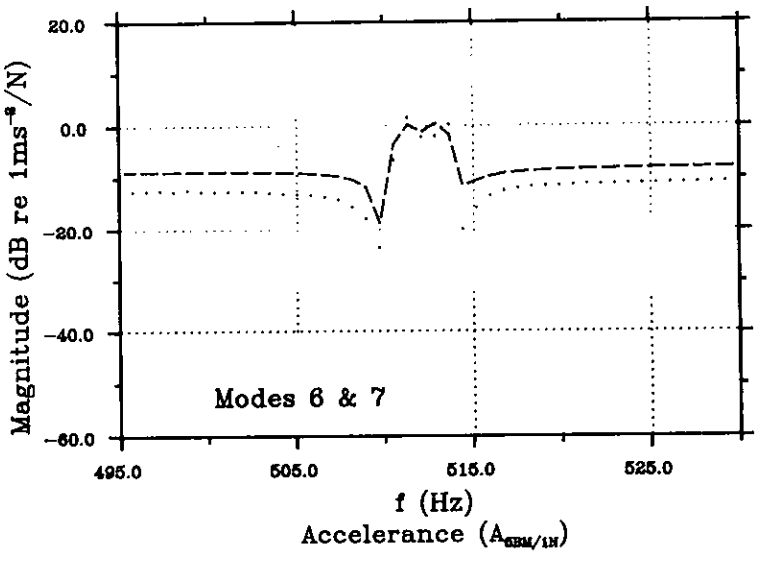

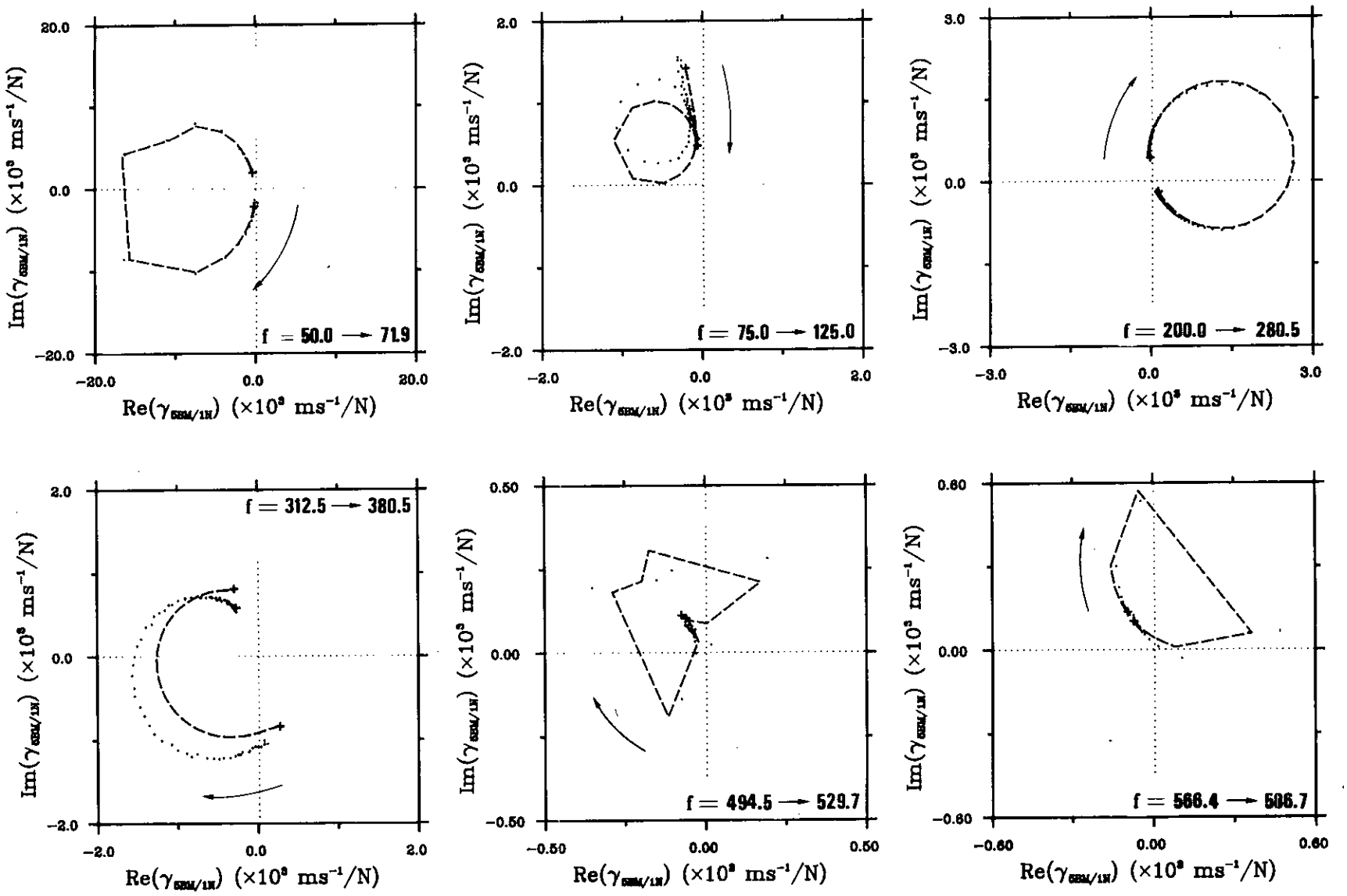

FIG. 4.15(b)–THEORETICALLY REGENERATED CROSS POINT FREQUENCY RESPONSE FUNCTION ––MERIDIONAL DIRECTION––

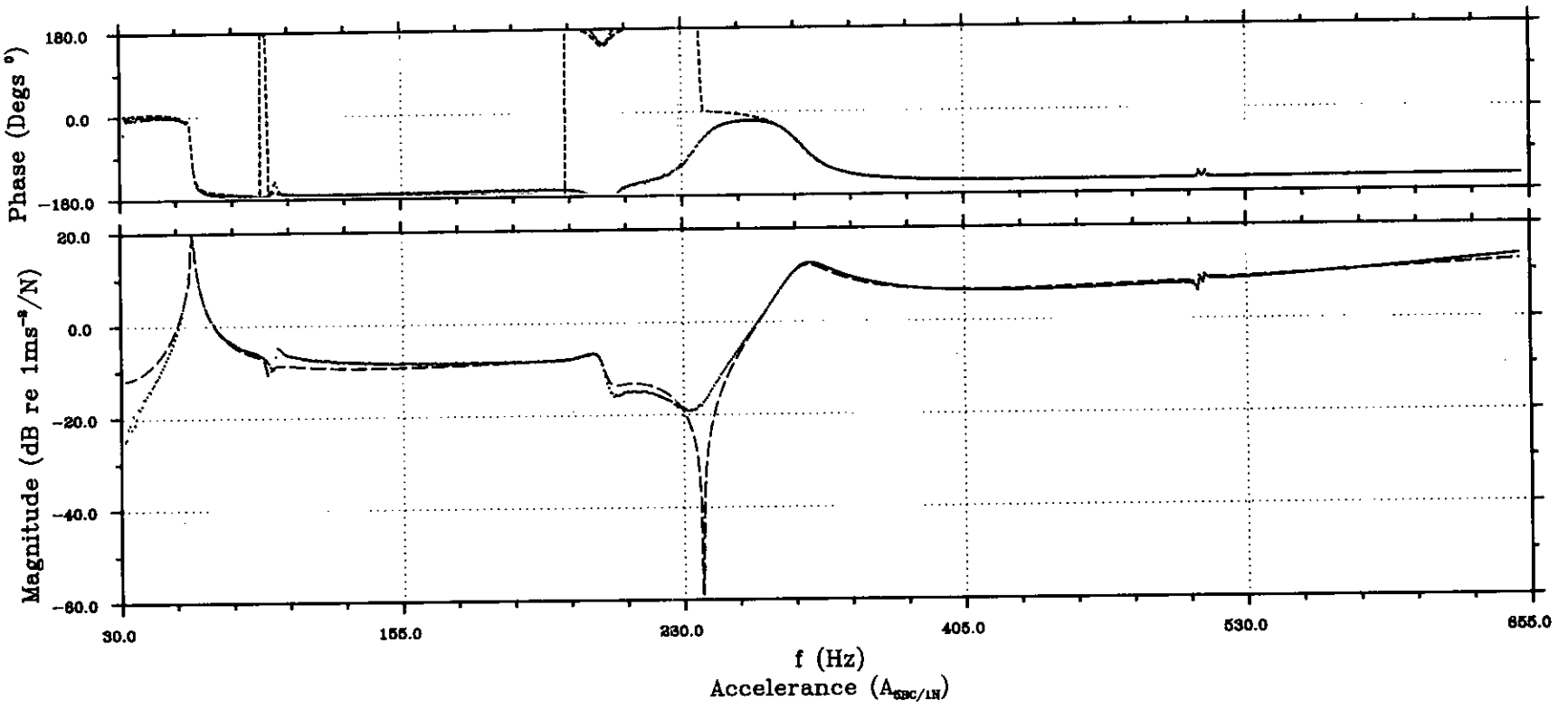

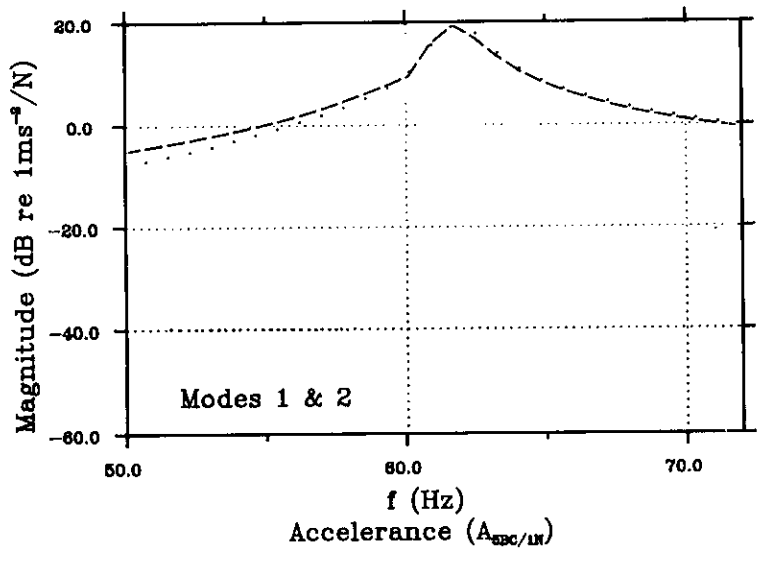

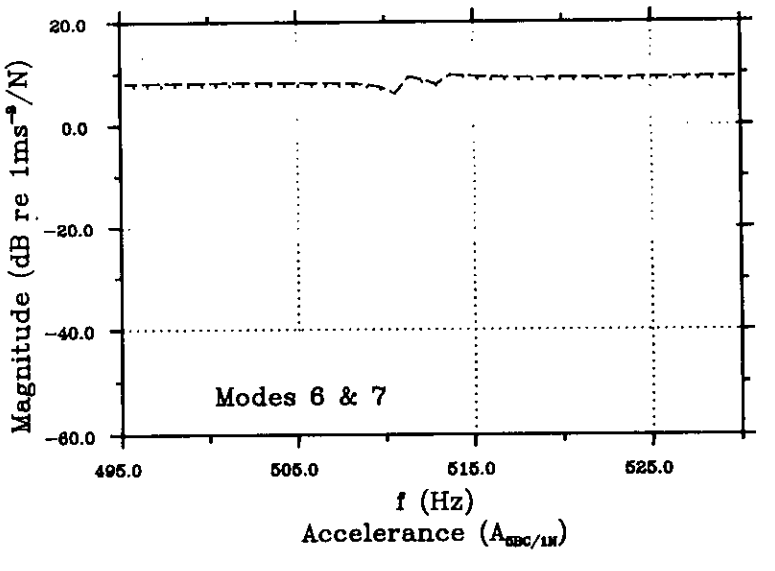

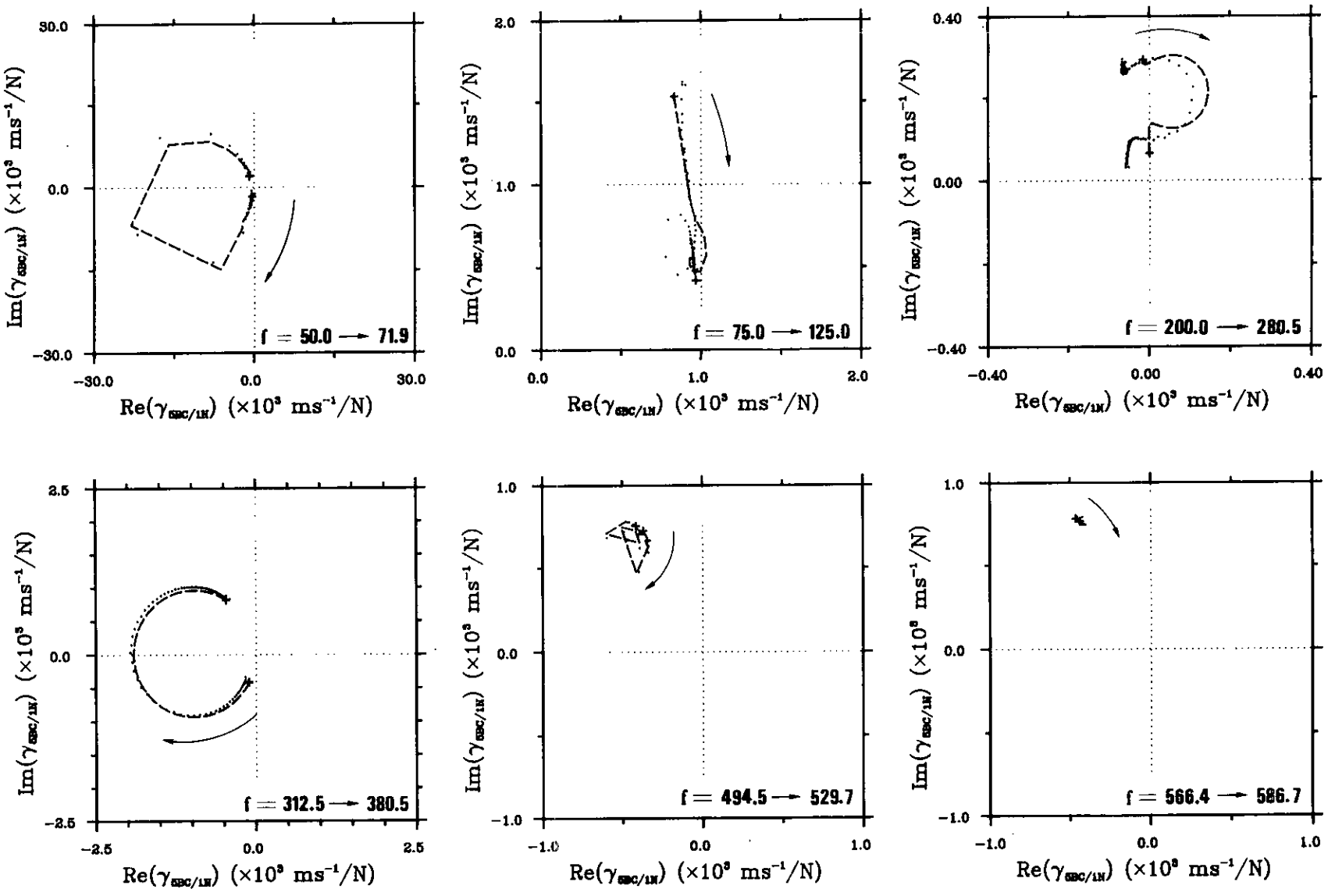

Experimental

Global curve fitting (4 extra numerator terms)

FIG. 4.15(c)–THEORETICALLY REGENERATED CROSS POINT FREQUENCY RESPONSE FUNCTION --CIRCUMFERENTIAL DIRECTION--

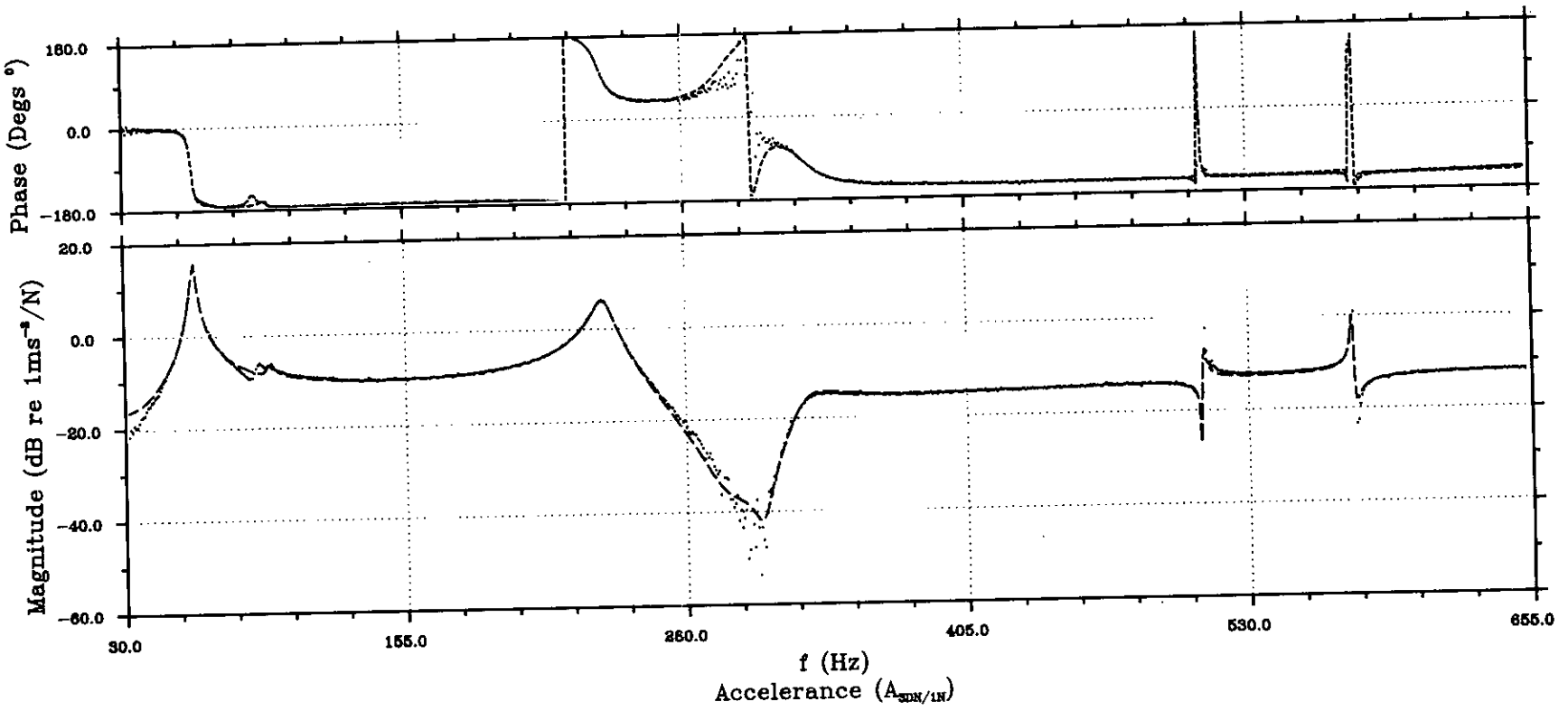

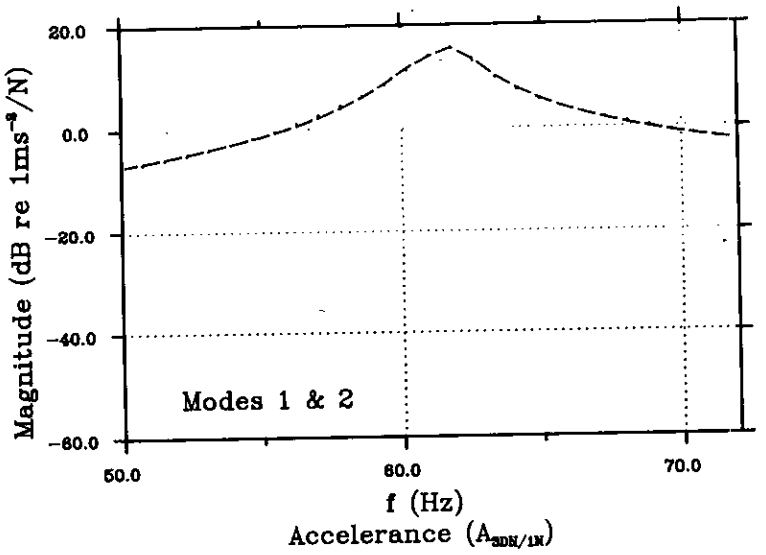

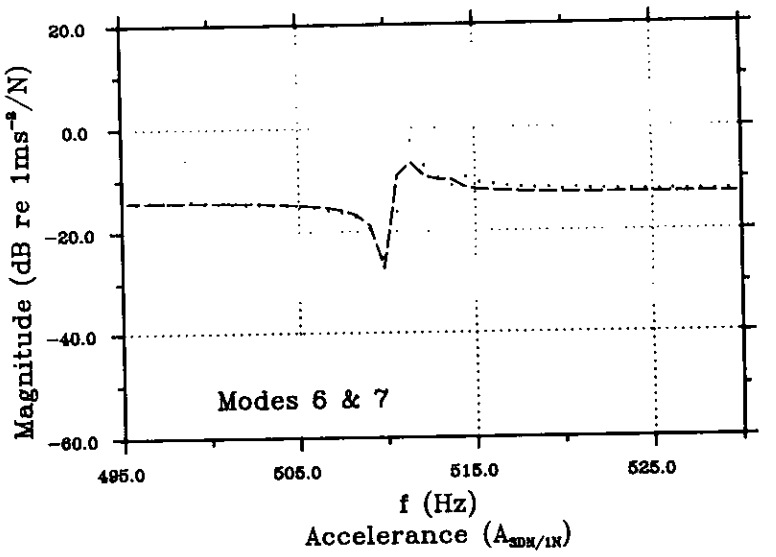

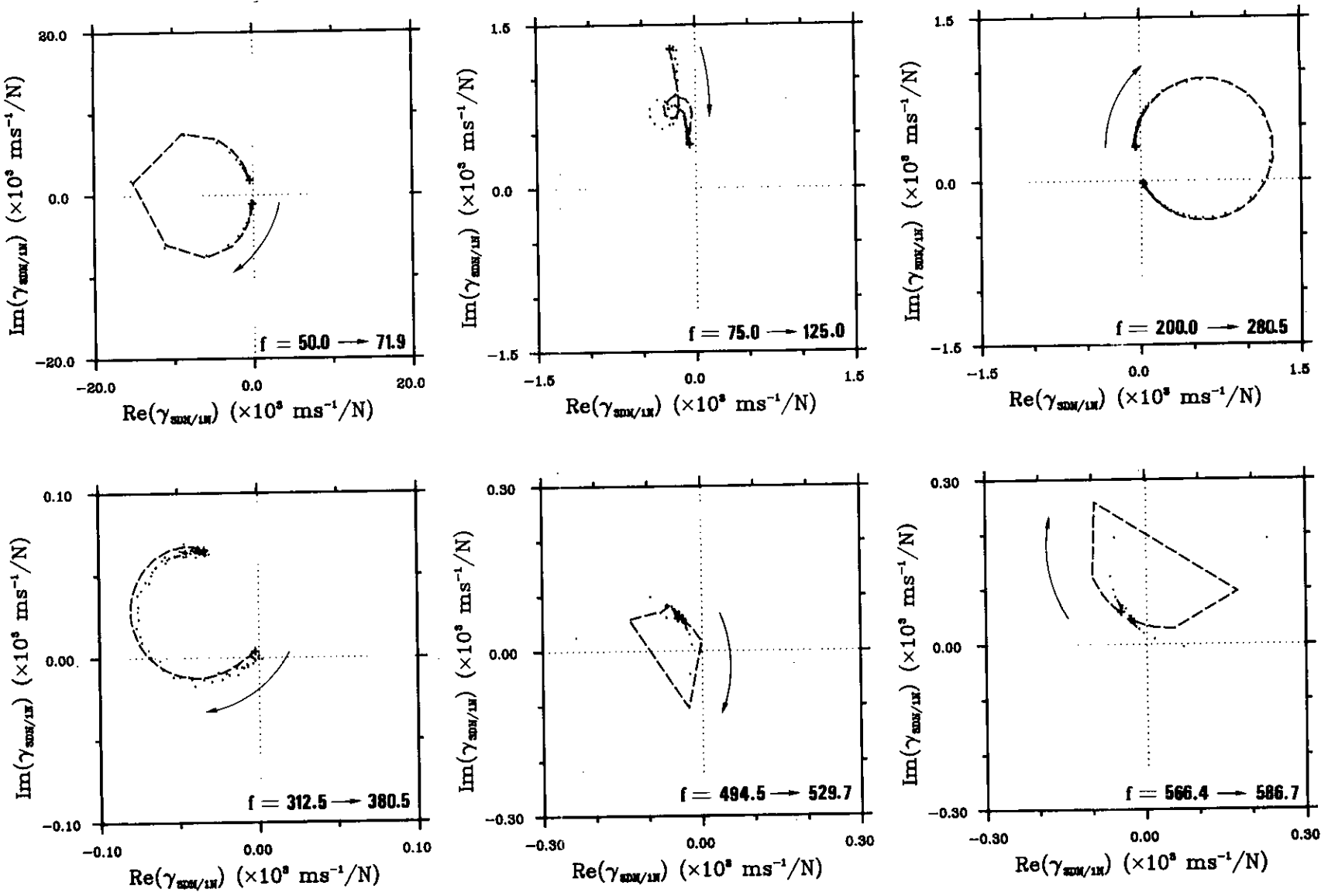

Experimental

Global curve fitting (4 extra numerator terms)

FIG. 4.16(a)–THEORETICALLY REGENERATED TRANSFER FREQUENCY RESPONSE FUNCTION ––NORMAL DIRECTION––

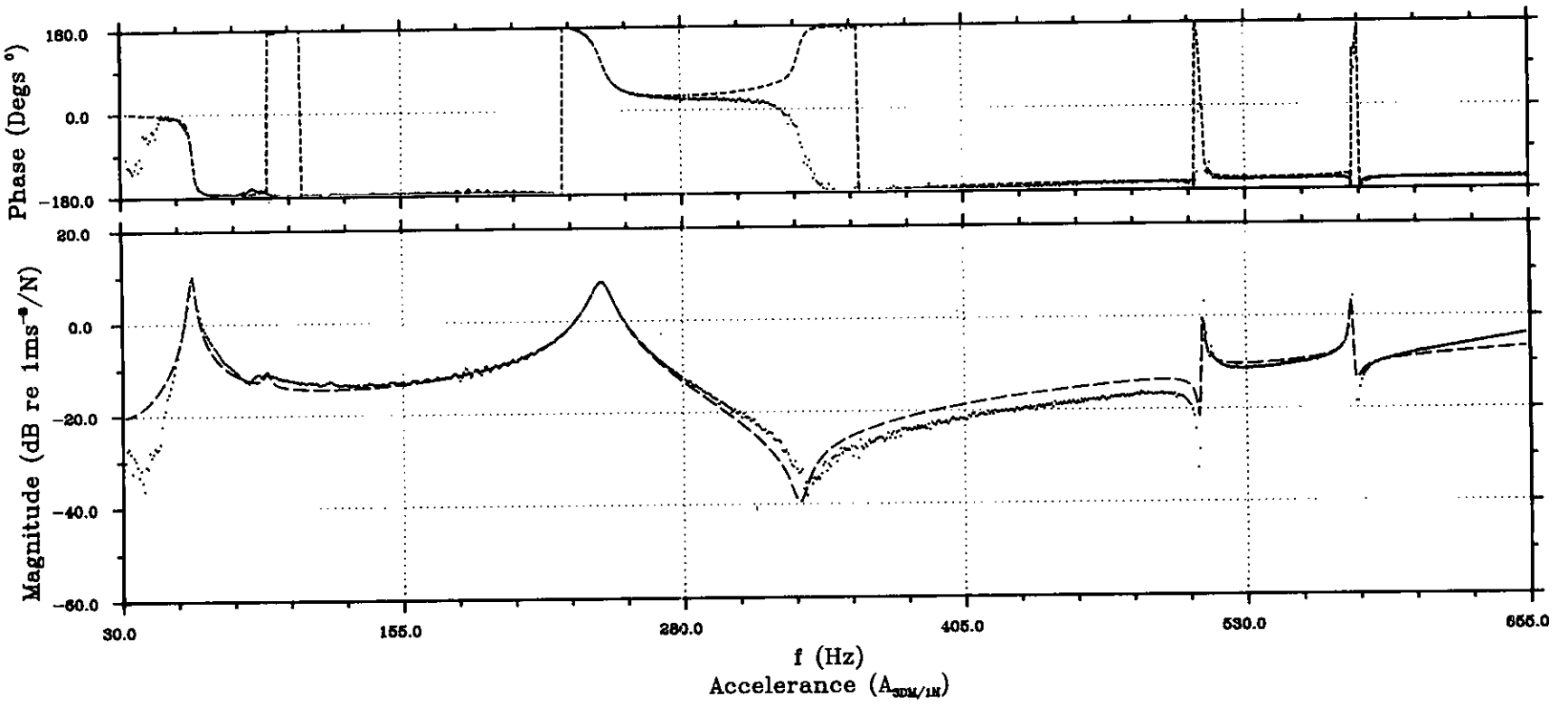

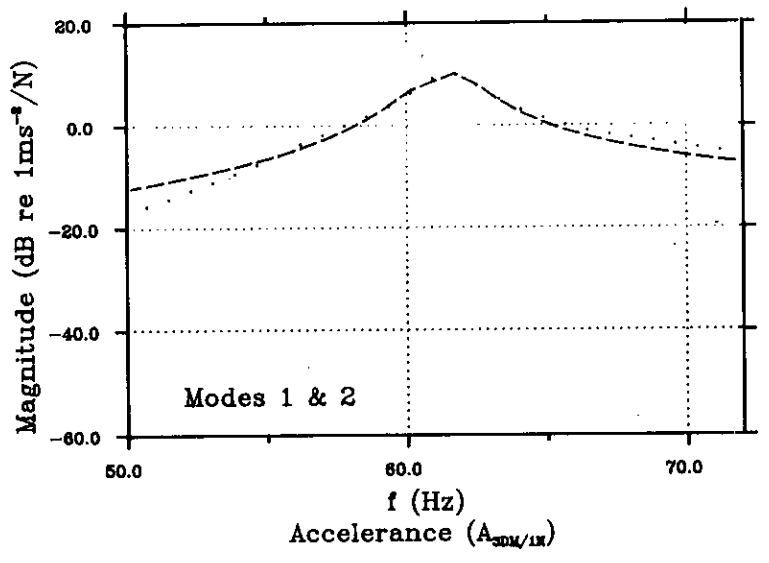

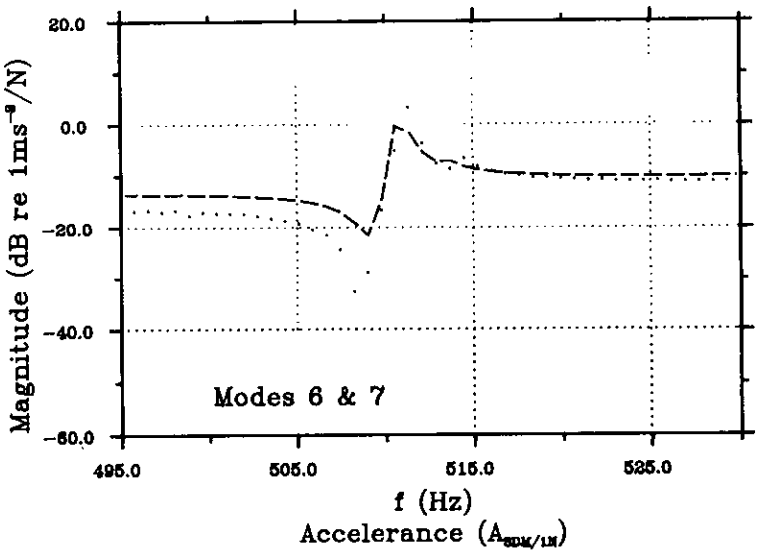

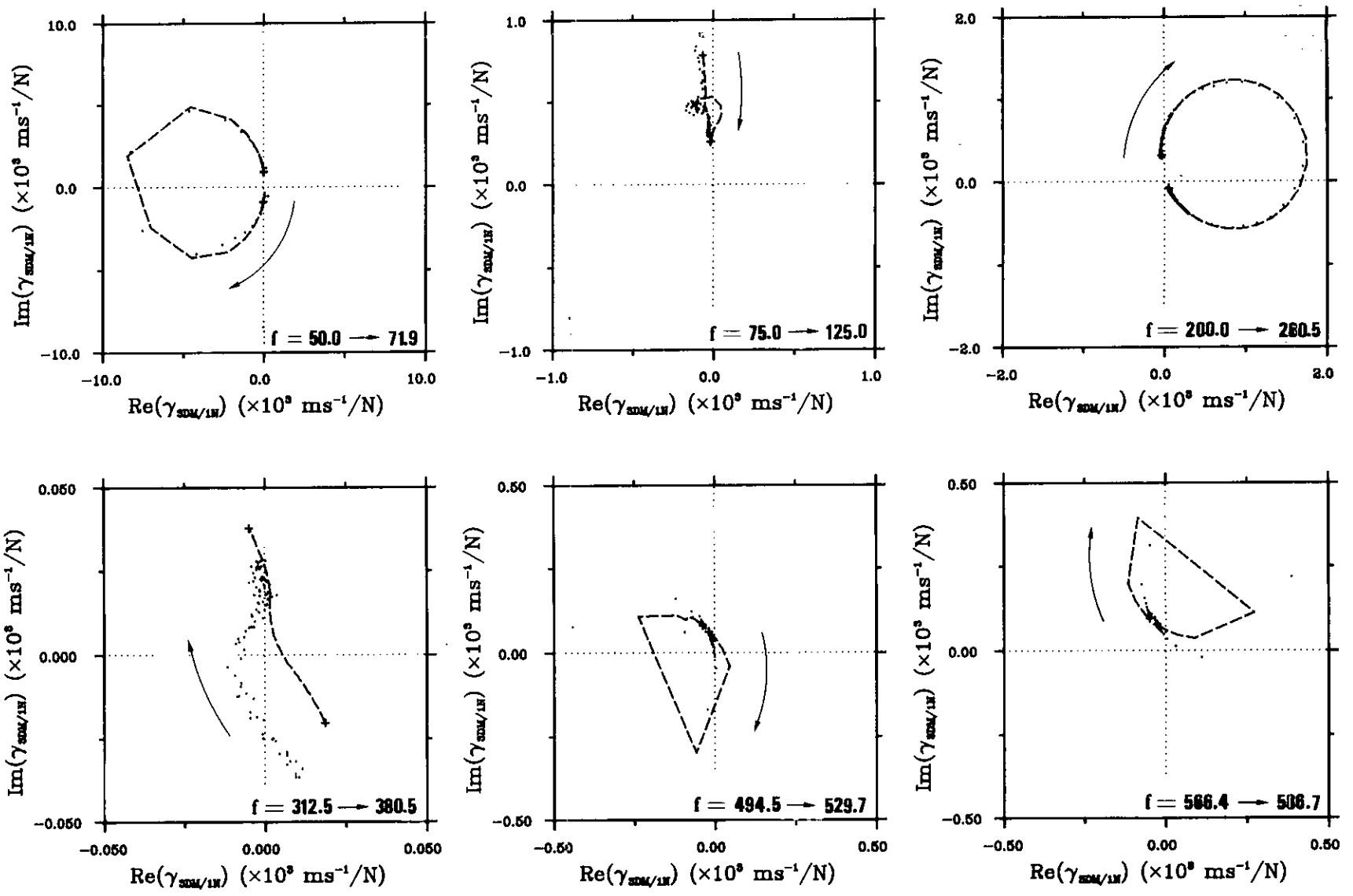

FIG. 4.16(b)–THEORETICALLY REGENERATED TRANSFER FREQUENCY RESPONSE FUNCTION --MERIDIONAL DIRECTION--

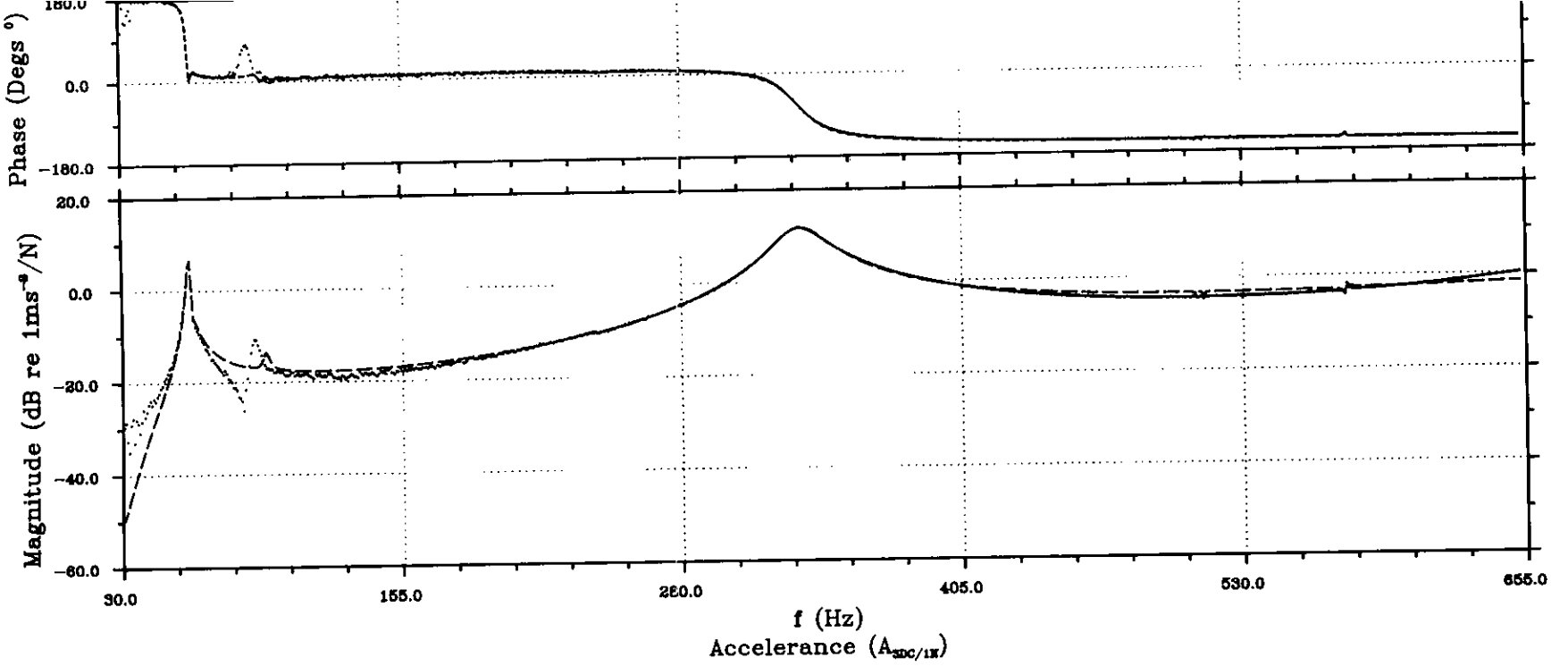

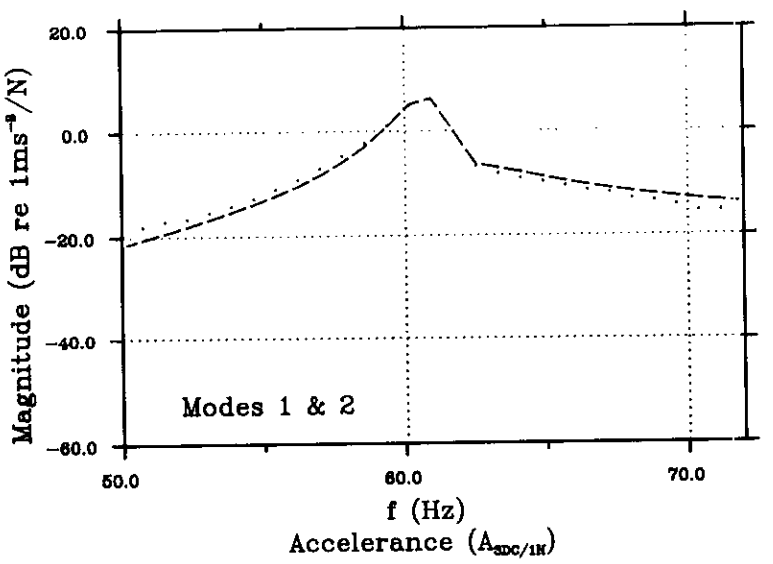

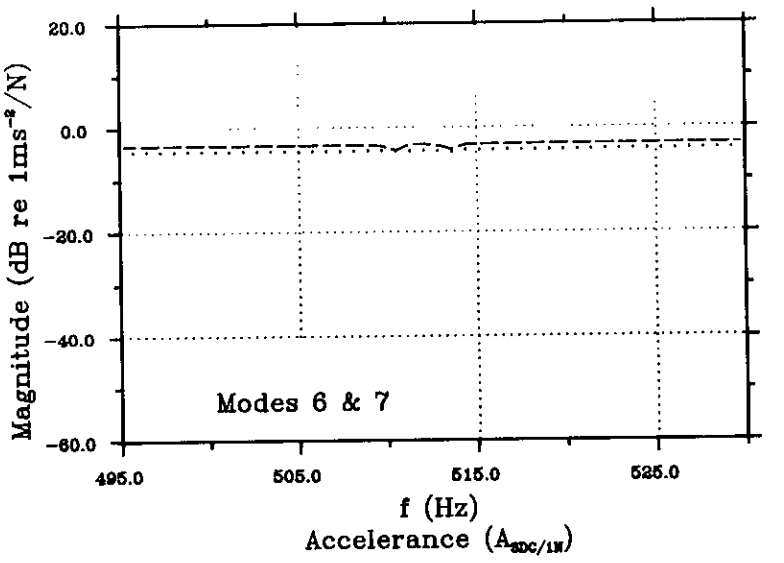

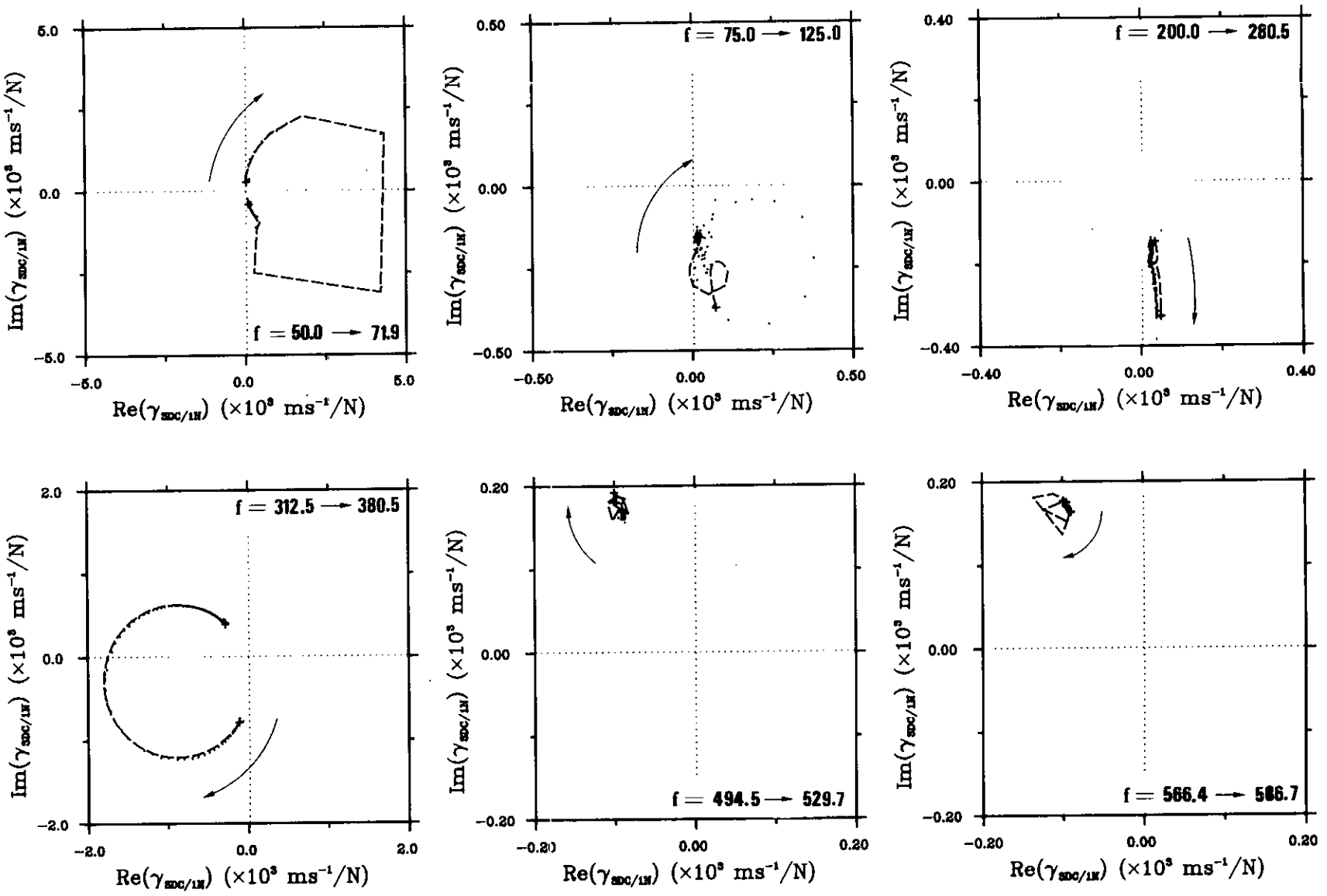

Experimental

Global curve fitting (4 extra numerator terms)

FIG. 4.16(c)–THEORETICALLY REGENERATED TRANSFER FREQUENCY RESPONSE FUNCTION --CIRCUMFERENTIAL DIRECTION--

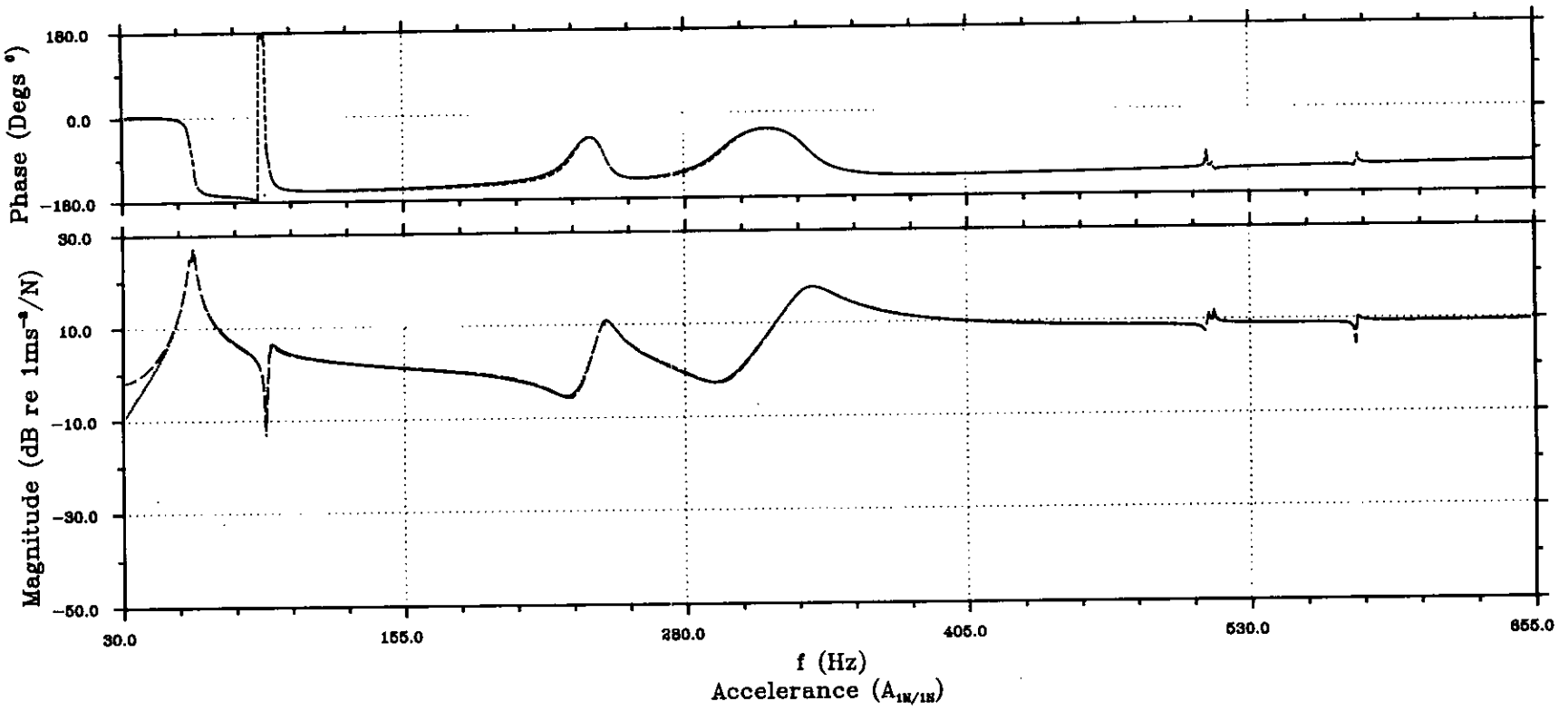

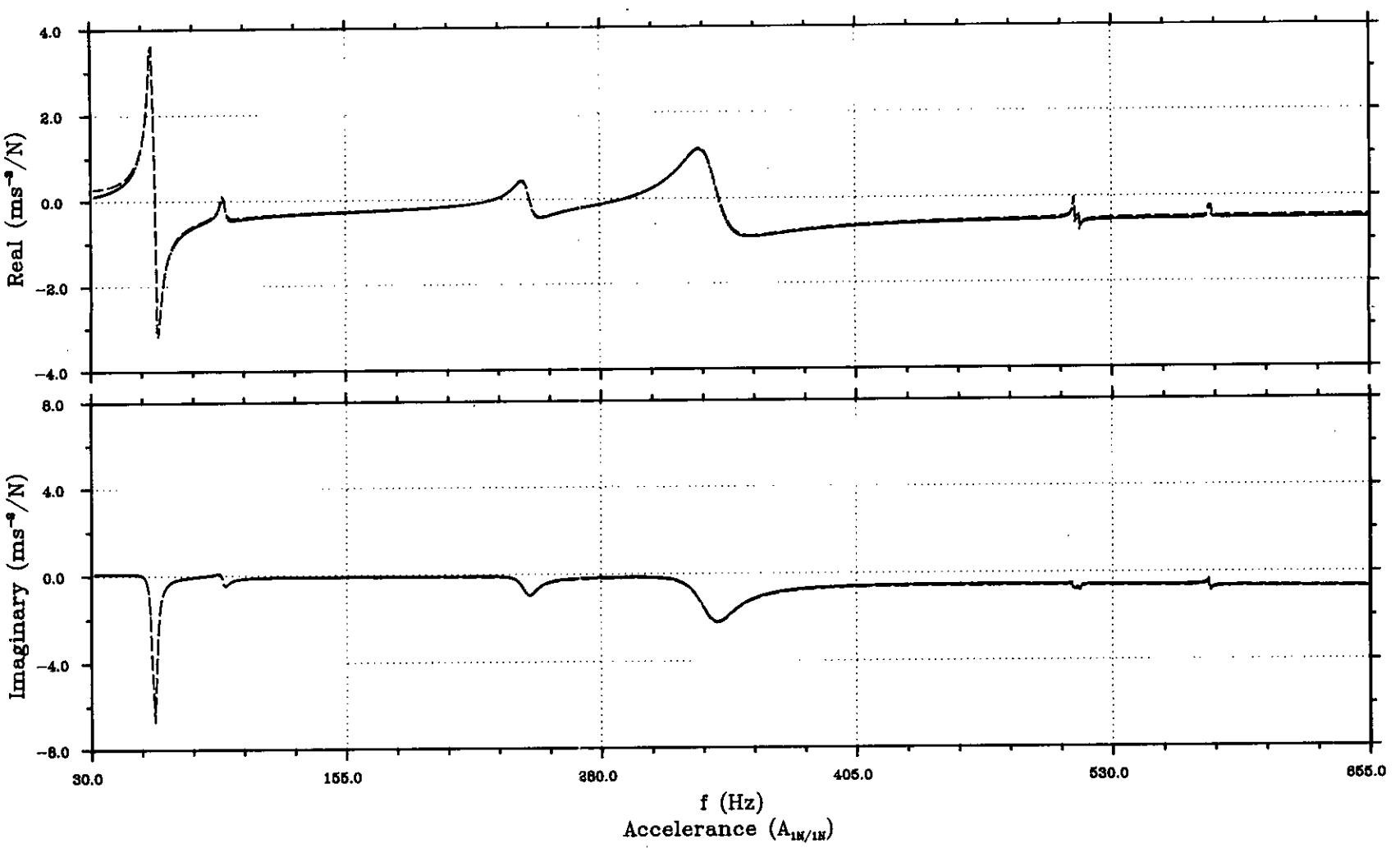

Synthesised

Global curve fitting (4 extra numerator polynomial terms)

FIG. 4.17–DRIVING POINT FREQUENCY RESPONSE FUNCTION : SYNTHESISED AND THEORETICALLY REGENERATED

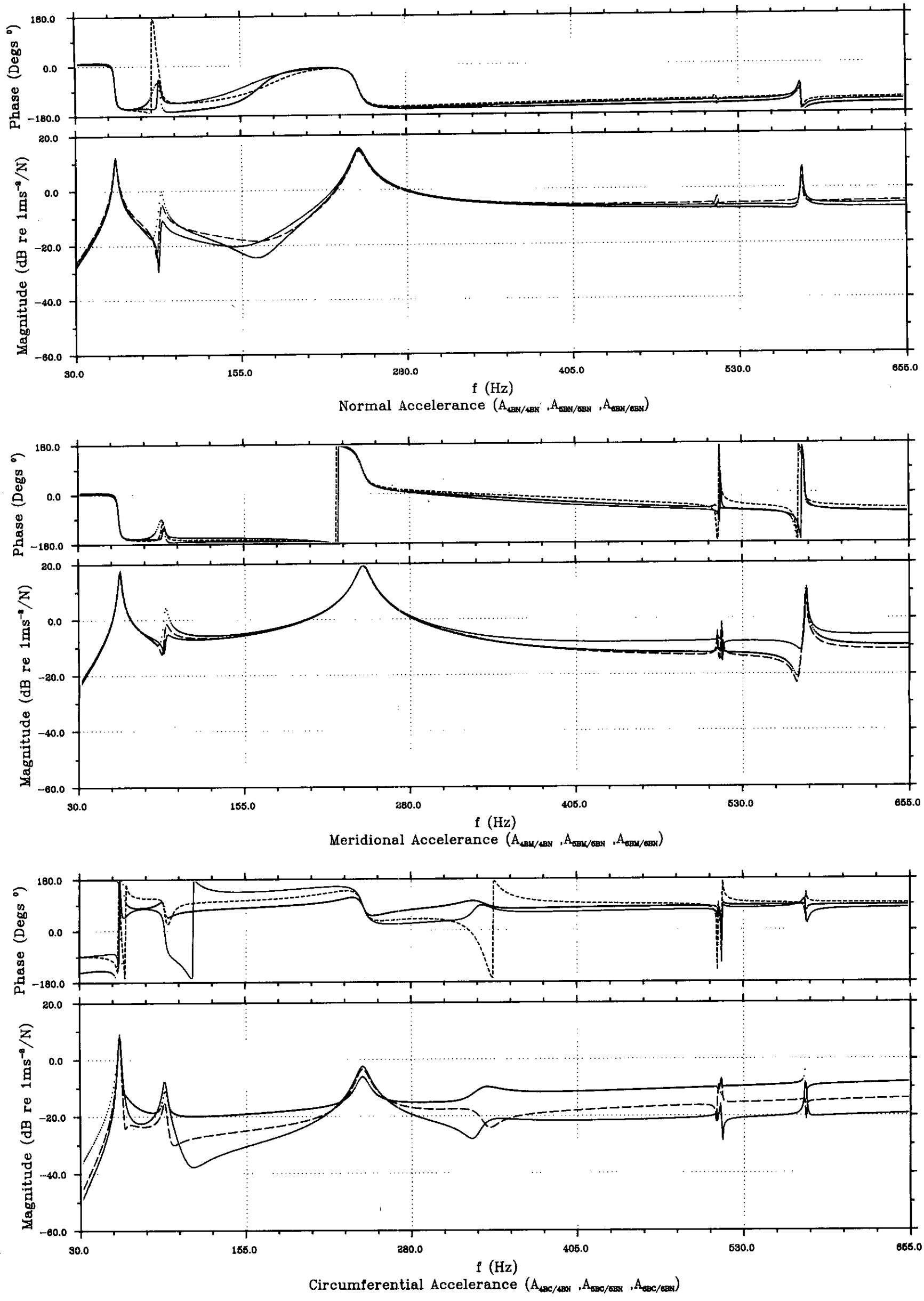

FIG. 4.18–SYNTHESISED FREQUENCY RESPONSE FUNCTIONS

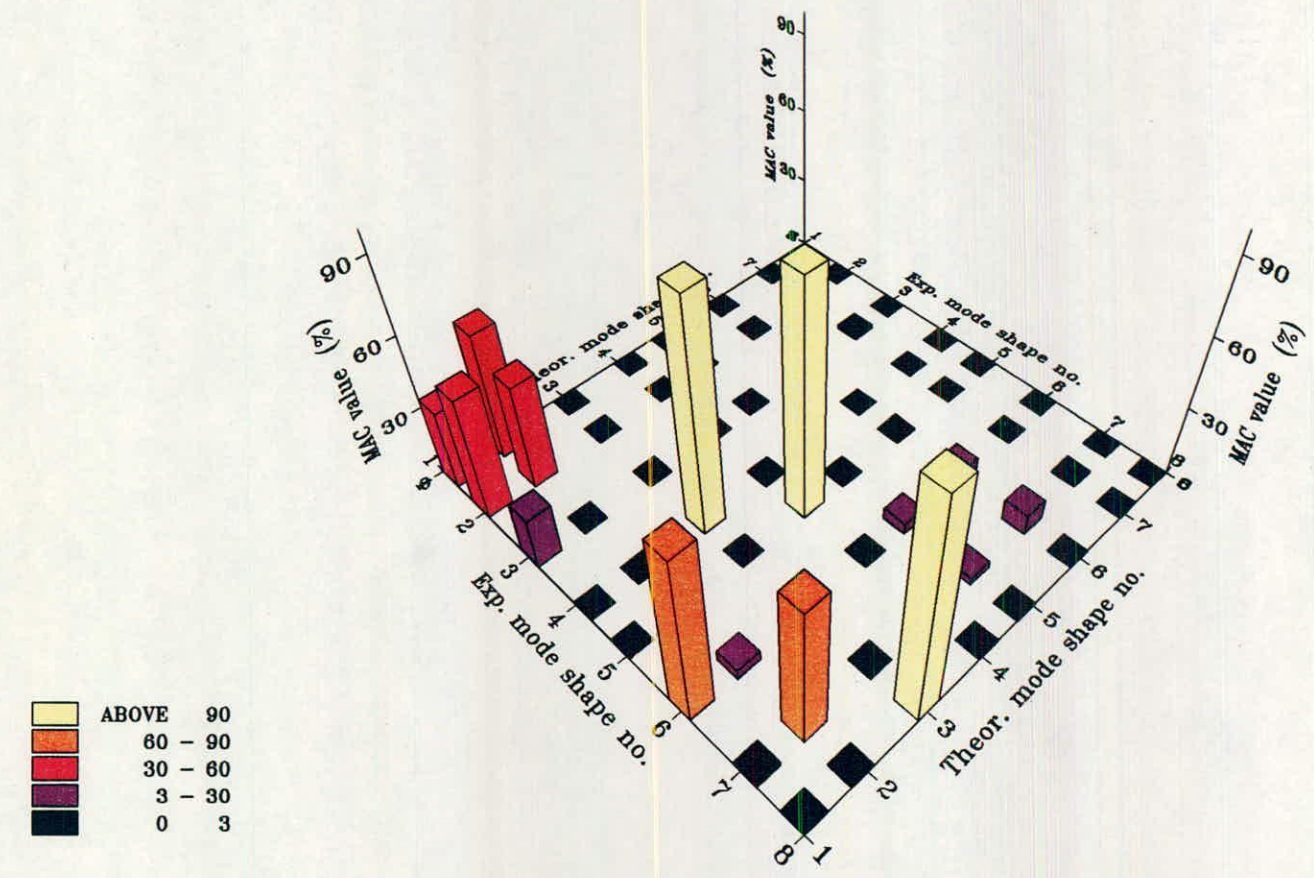

-INITIAL MODEL-

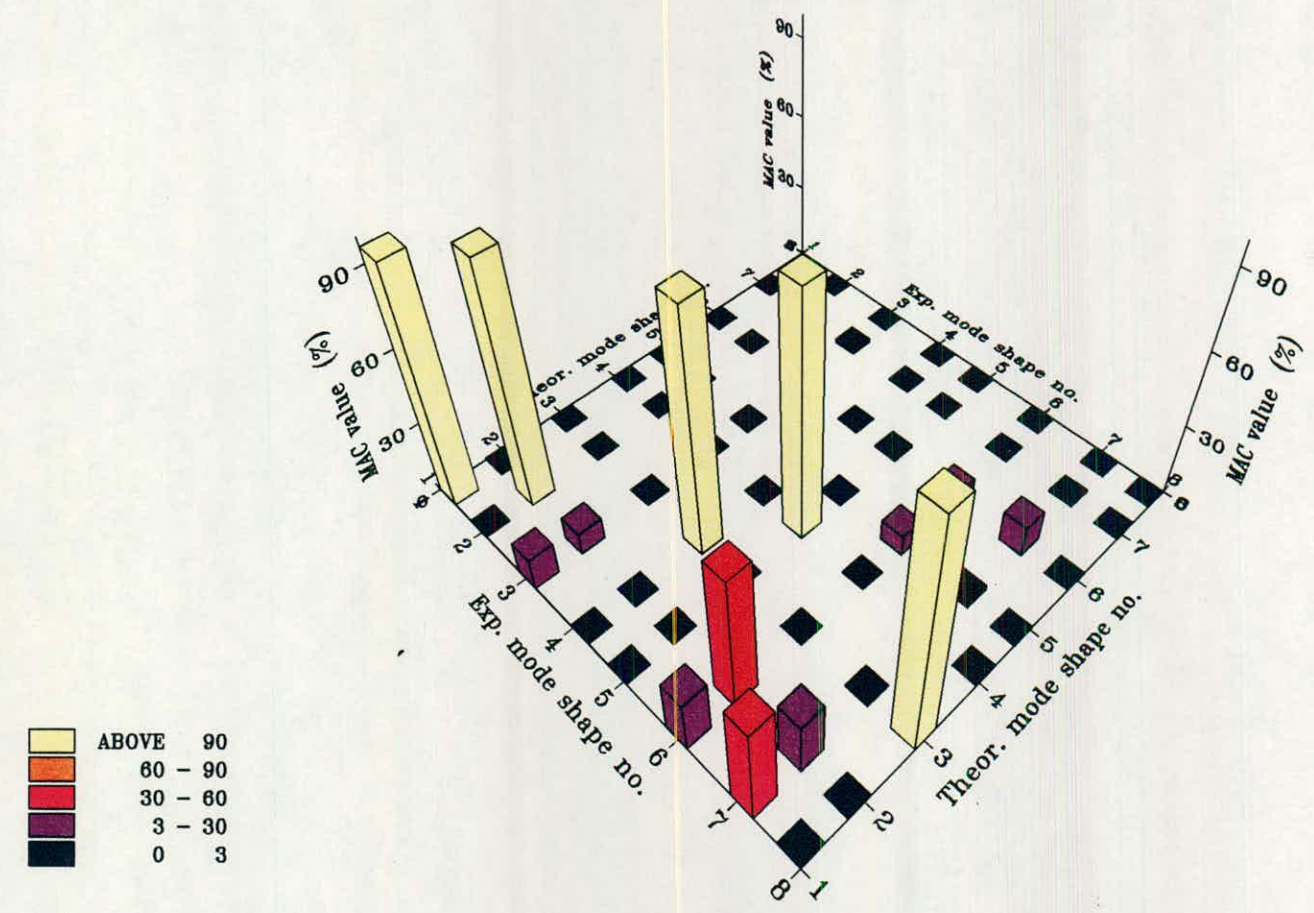

-UPDATED MODEL-

FIG. 4.19–MODAL ASSURANCE CRITERION FOR EXPERIMENTAL AND THEORETICAL MODE SHAPES

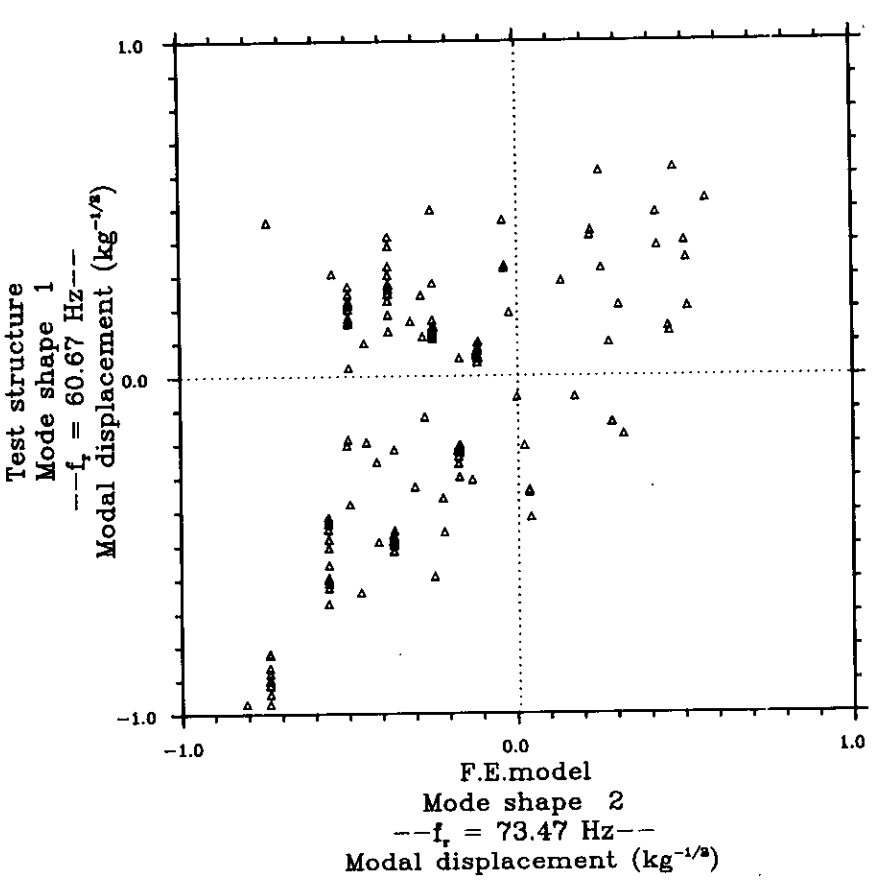

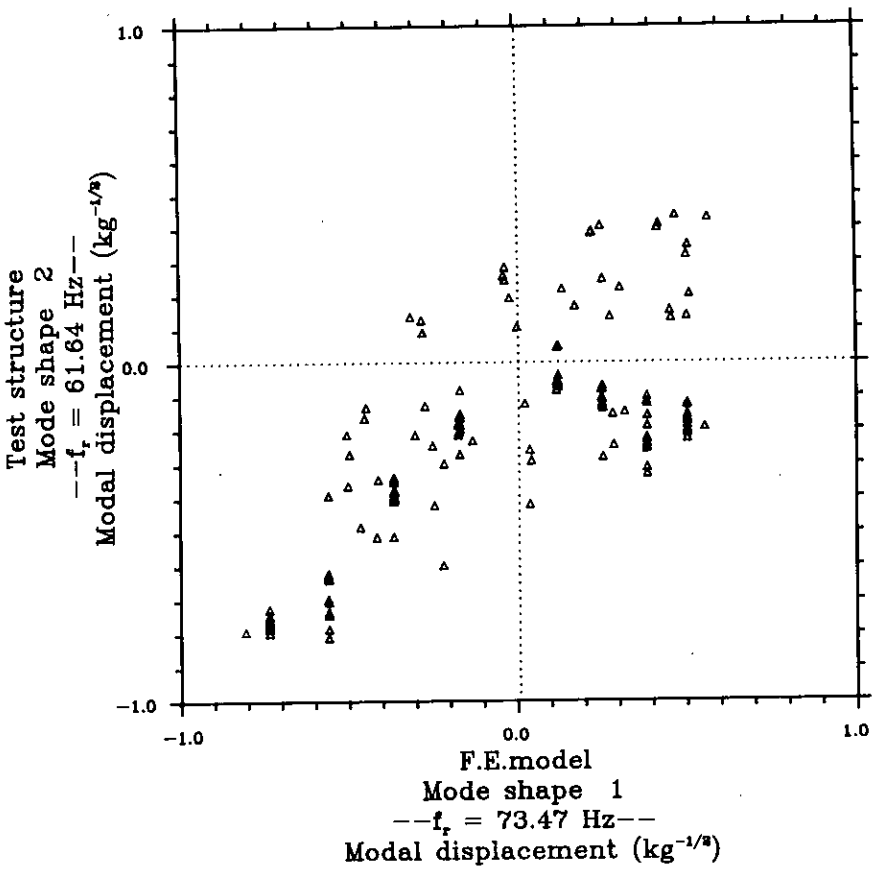

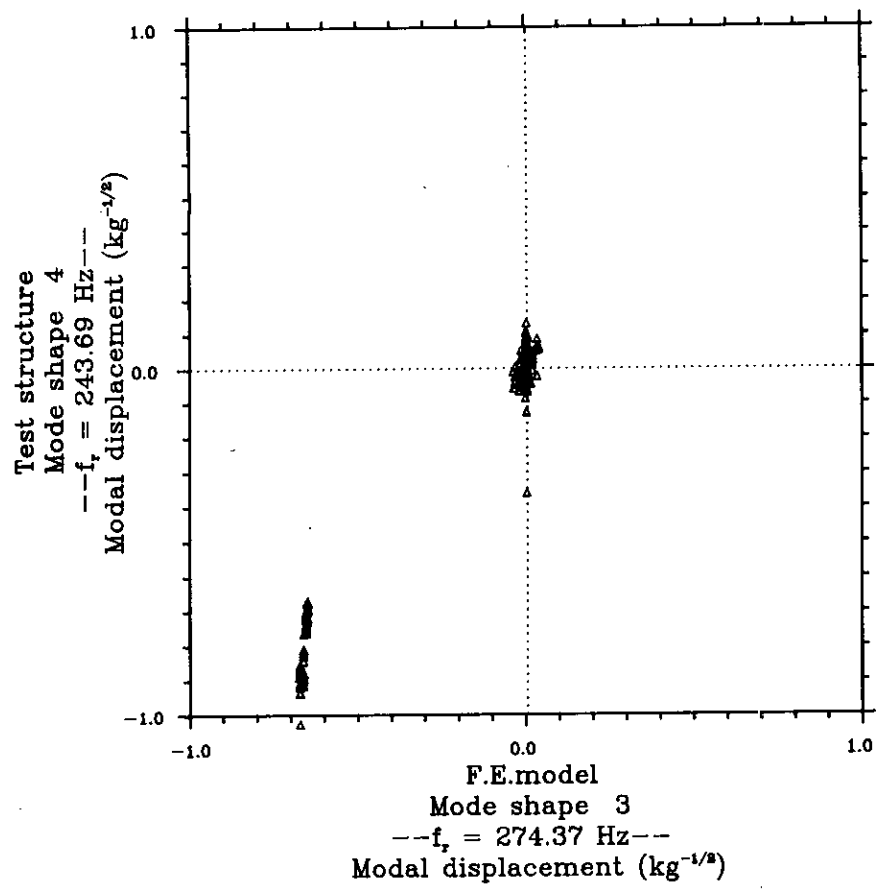

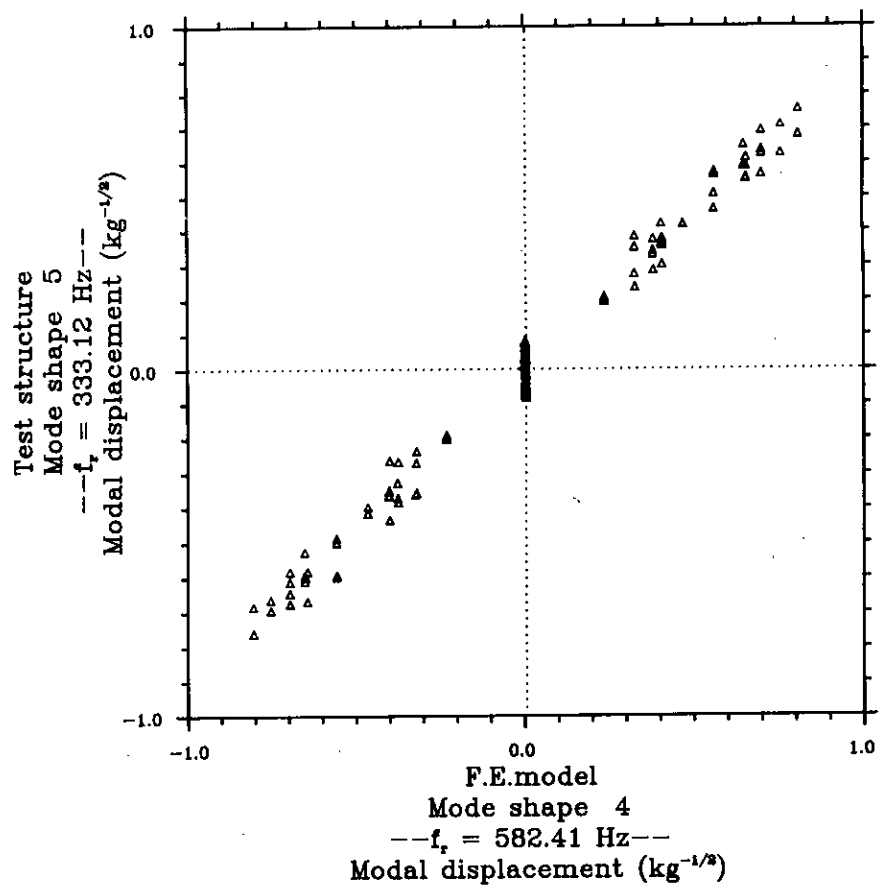

FIG. 4.20(a)–COMPARISON BETWEEN EXPERIMENTAL AND THEORETICAL MODE SHAPES --INITIAL MESH--

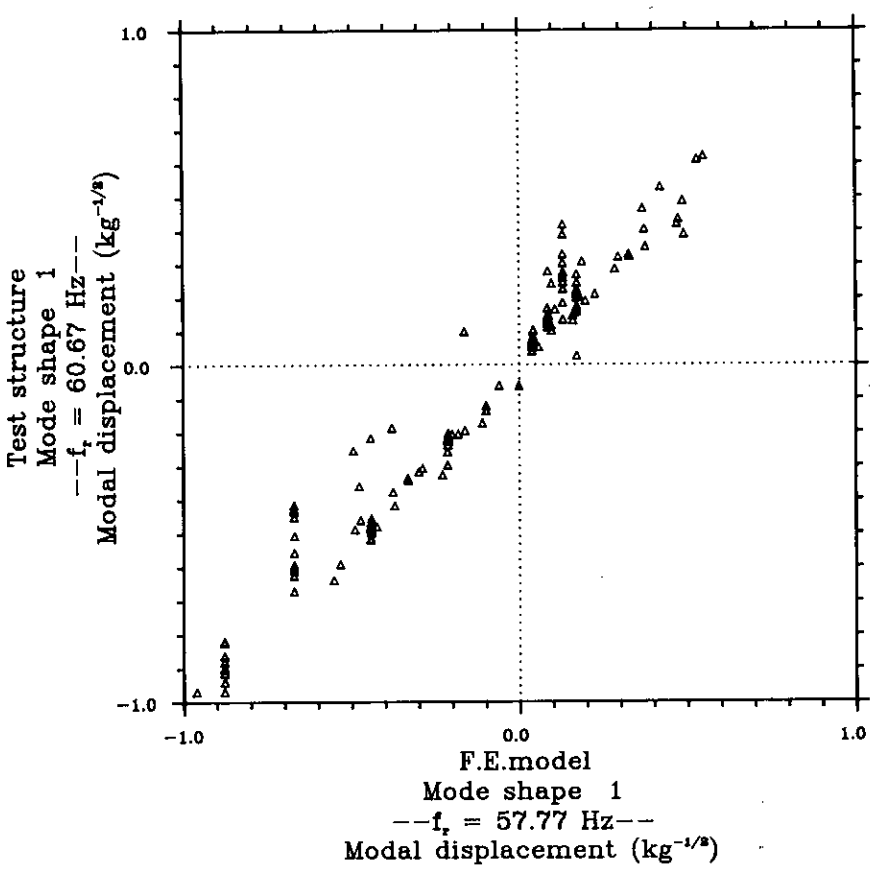

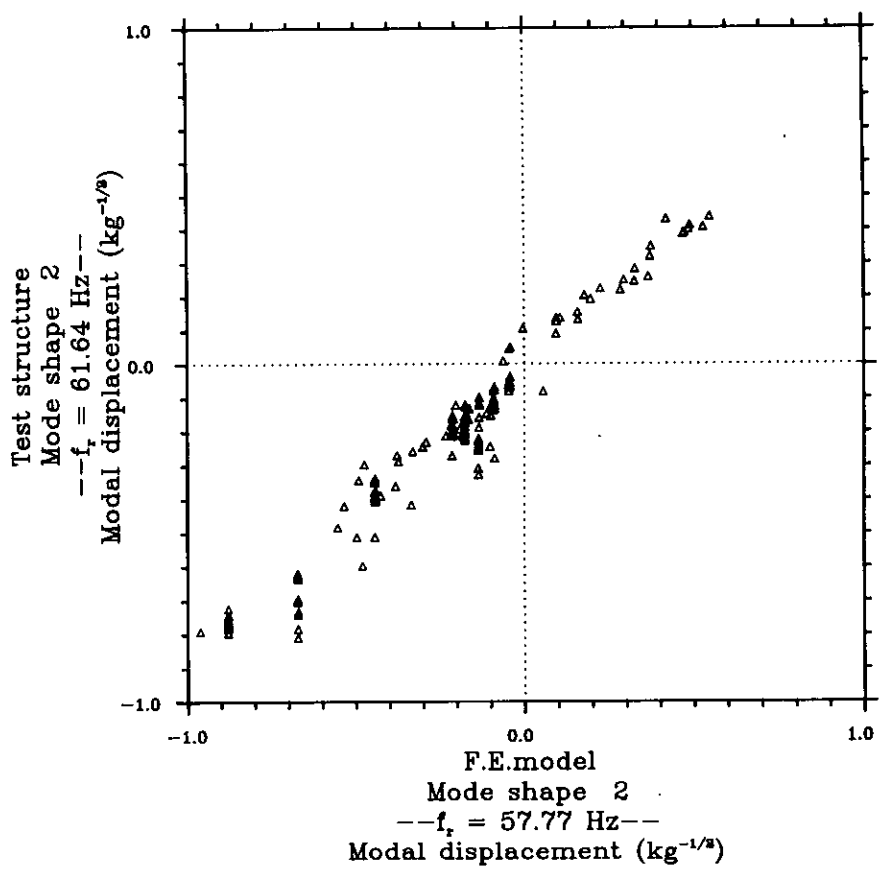

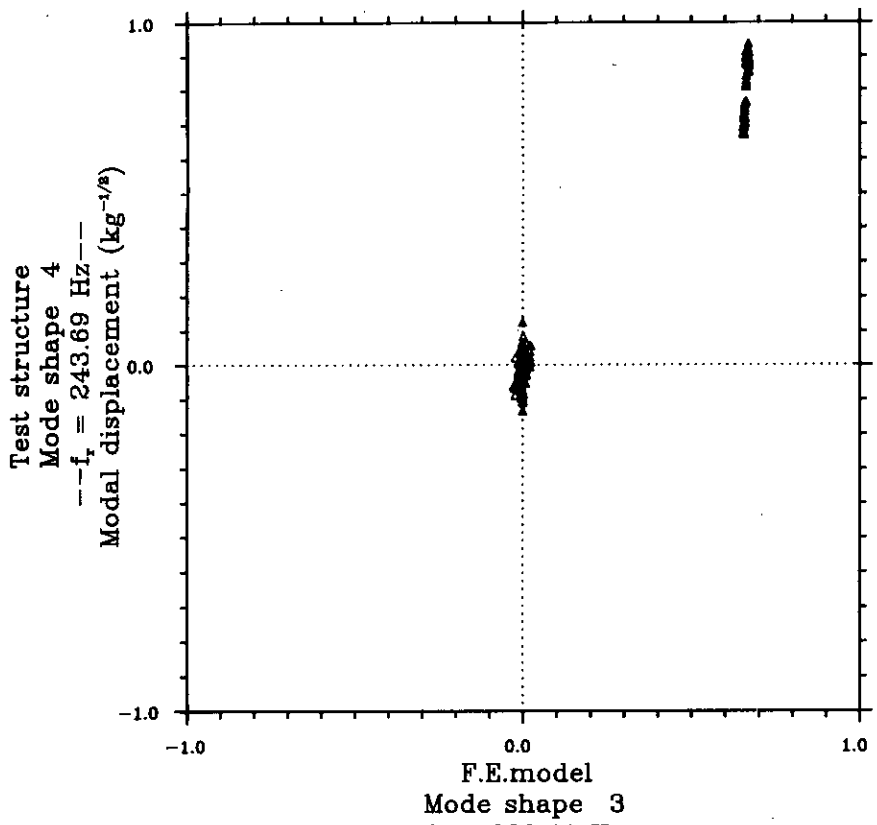

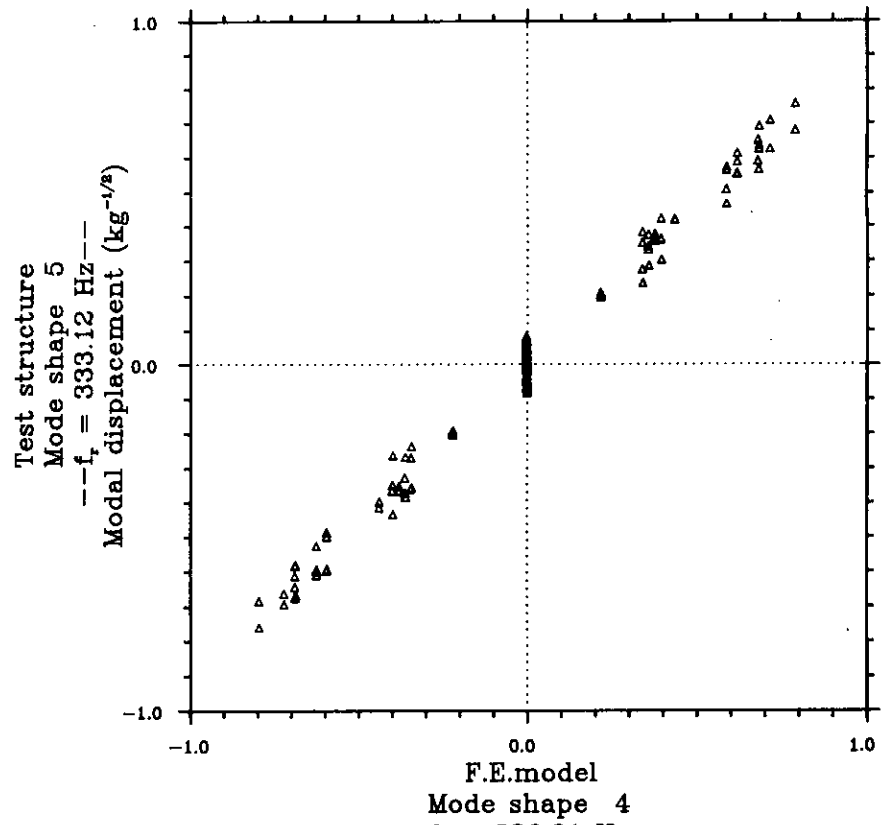

FIG. 4.20(b)–COMPARISON BETWEEN EXPERIMENTAL AND THEORETICAL MODE SHAPES --UPDATED MESH--

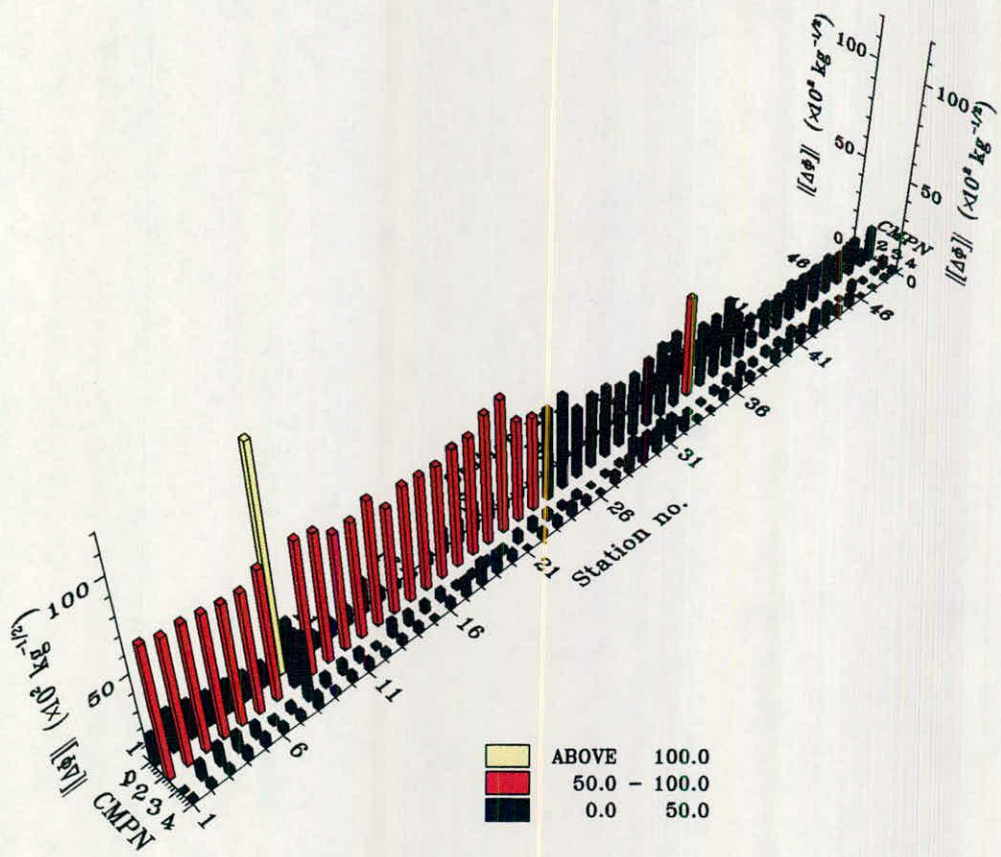

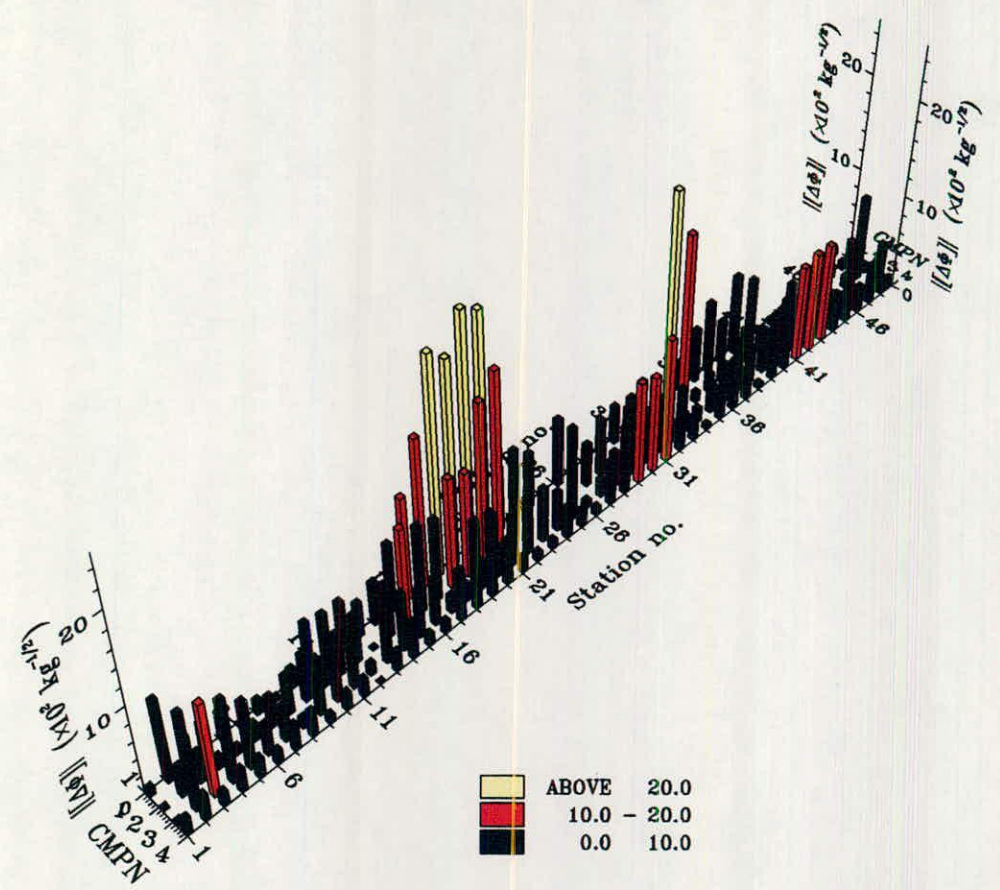

FIG. 4.21(a)–MODULUS DIFFERENCE MATRIX FOR EXPERIMENTAL AND THEORETICAL MODE SHAPES –X DIRECTION–

-INITIAL MODEL-

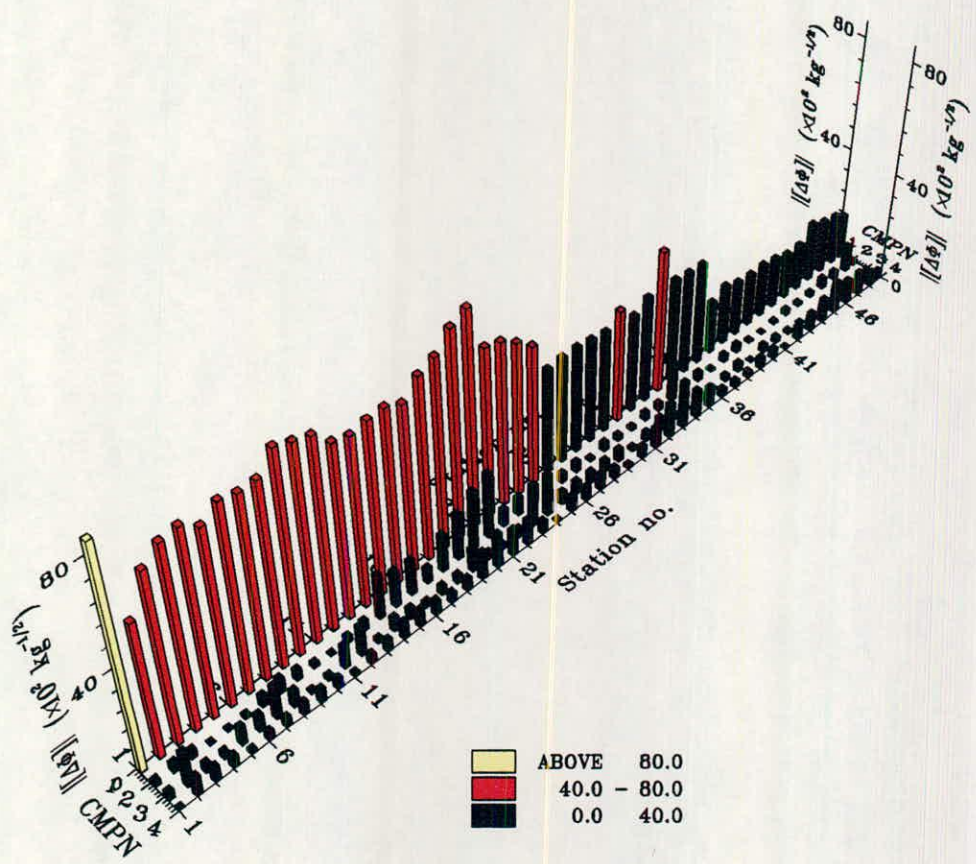

-UPDATED MODEL-

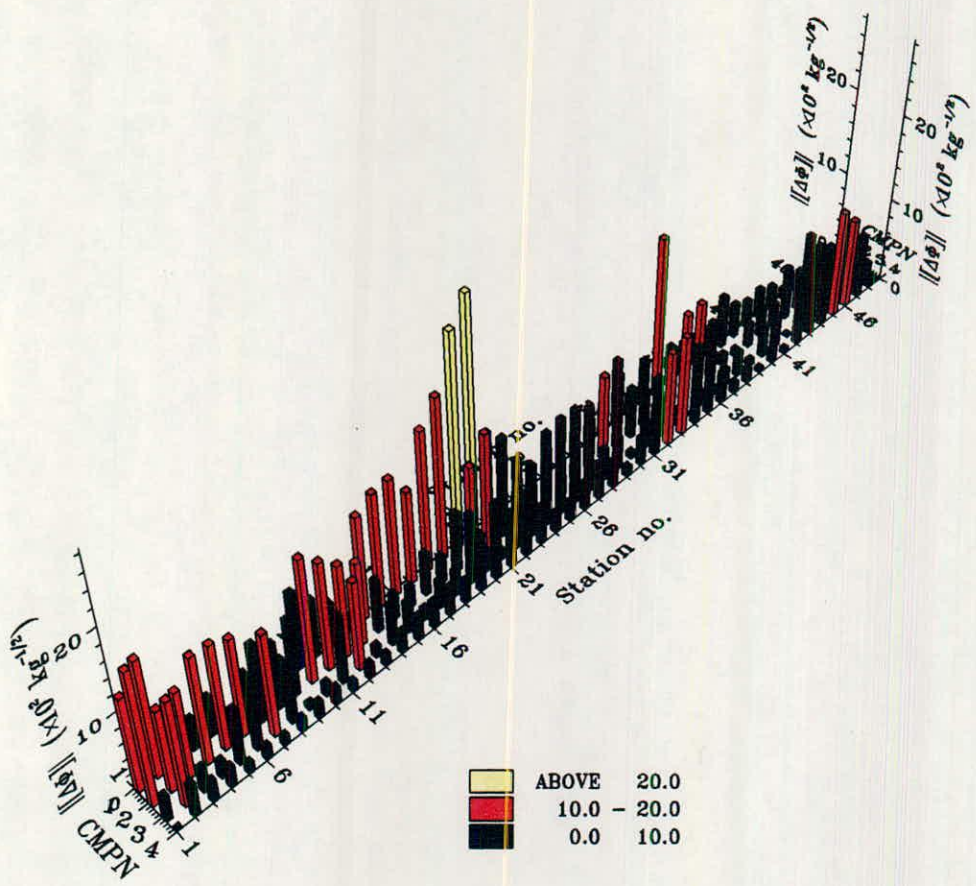

FIG. 4.21(b)–MODULUS DIFFERENCE MATRIX FOR EXPERIMENTAL AND THEORETICAL MODE SHAPES –Y DIRECTION–

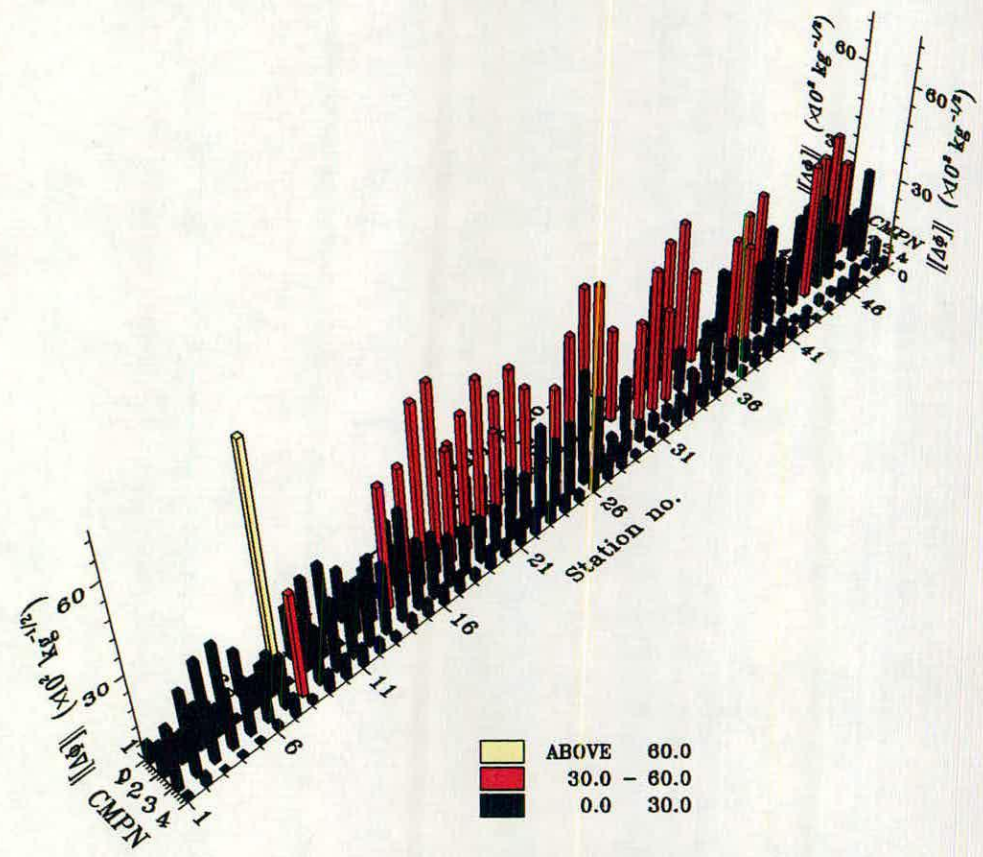

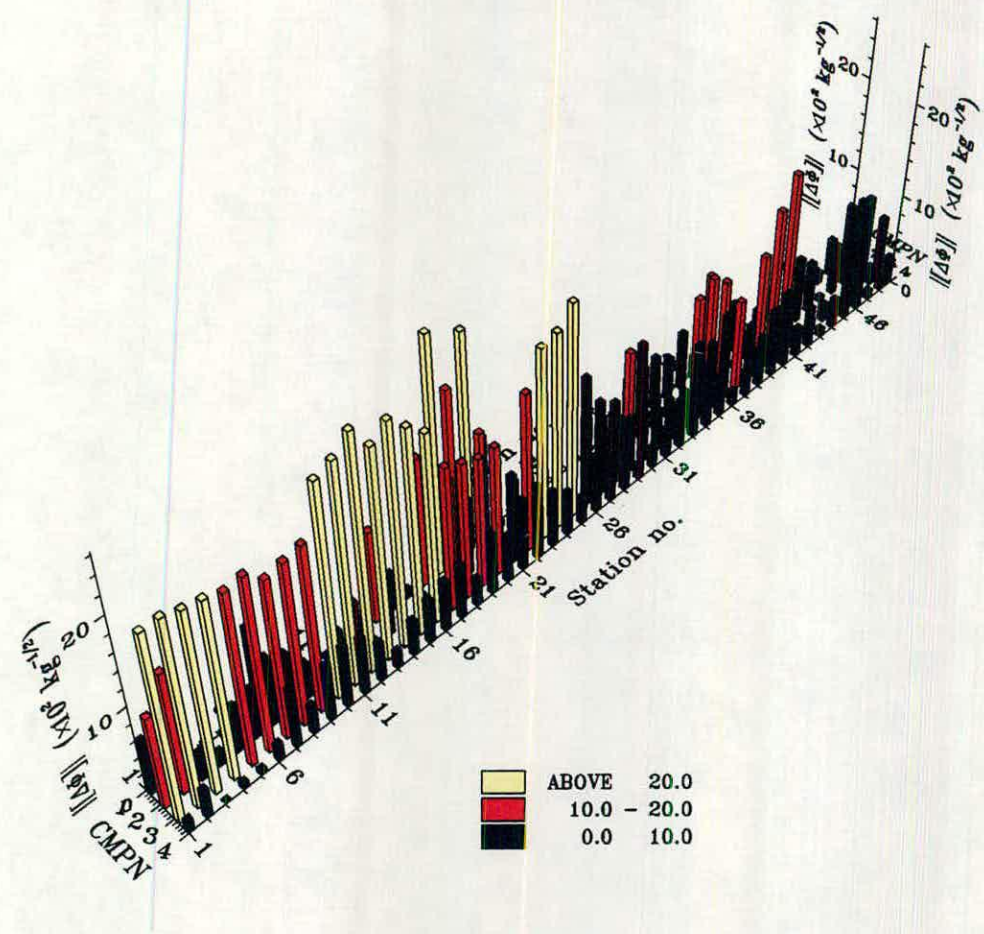

FIG. 4.21(c)–MODULUS DIFFERENCE MATRIX FOR EXPERIMENTAL AND THEORETICAL MODE SHAPES –Z DIRECTION–

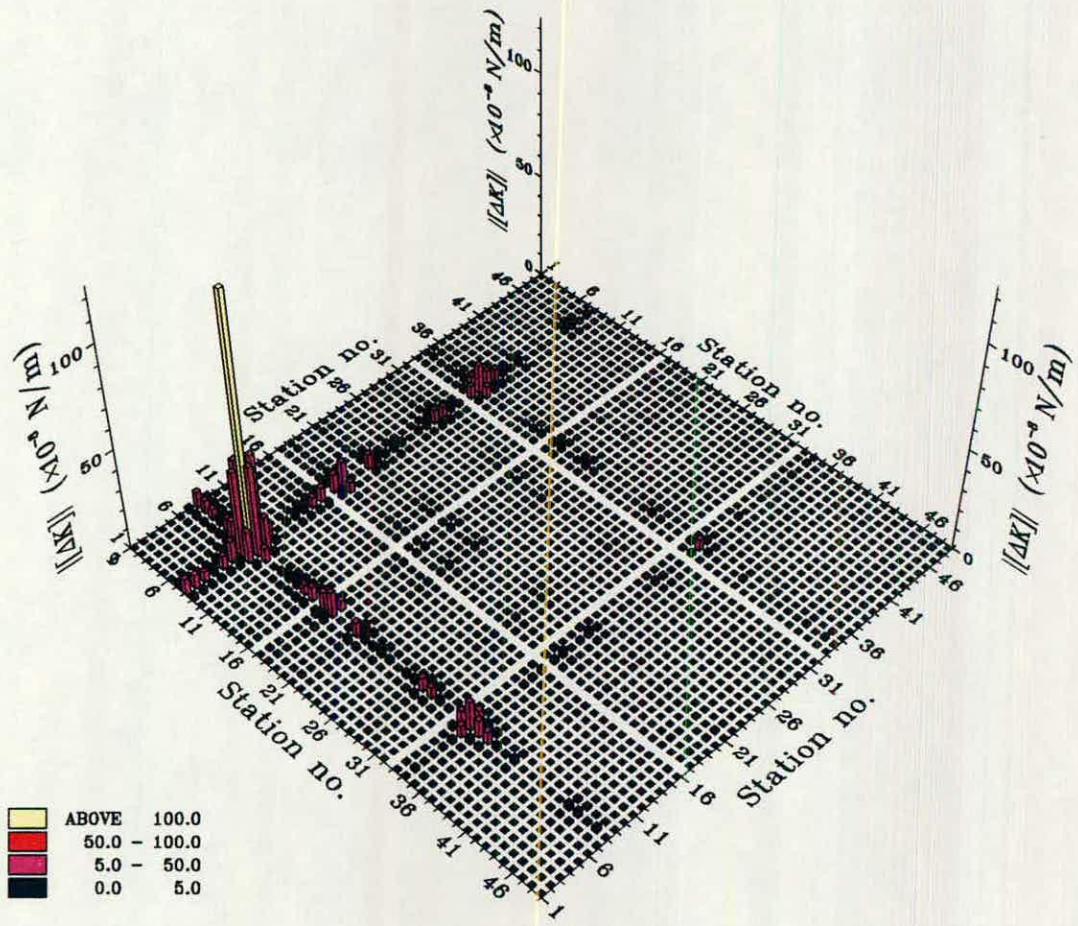

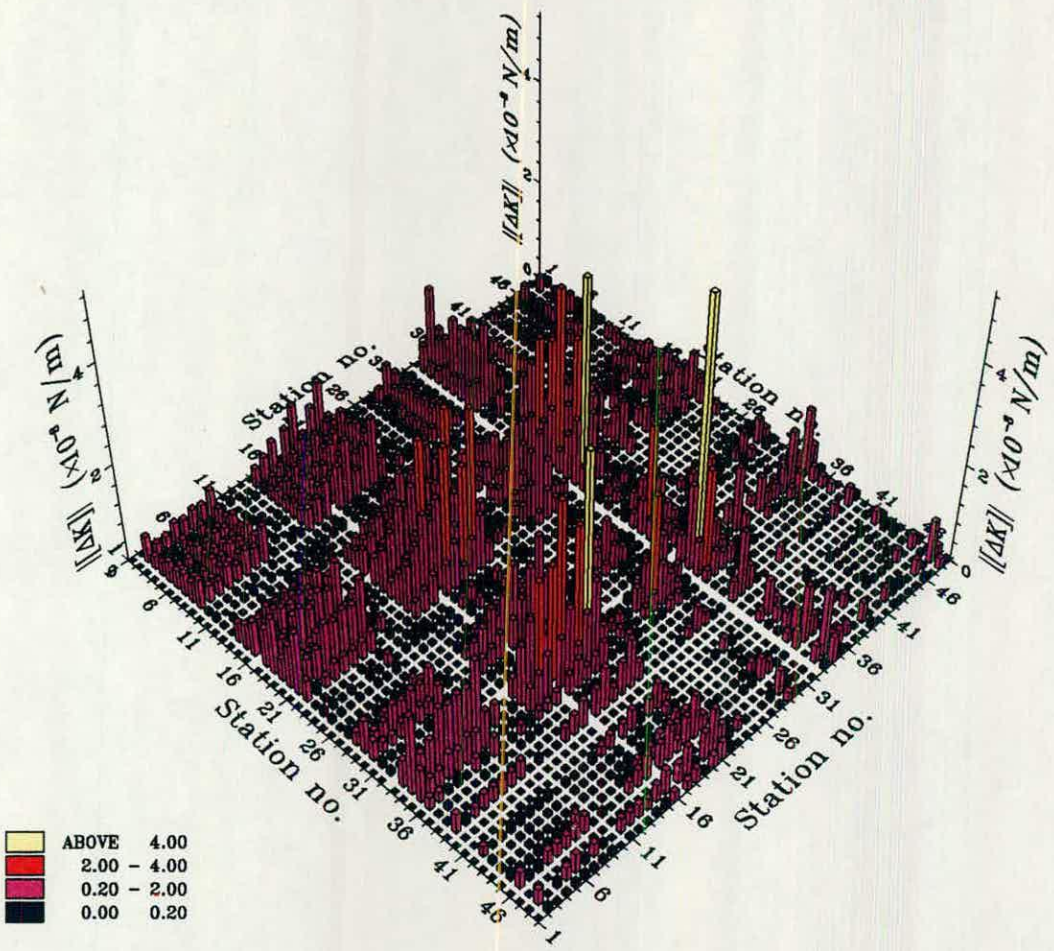

FIG. 4.22(a)–STIFFNESS ERROR MATRIX FOR EXPERIMENTAL AND THEORETICAL MODE SHAPES –X DIRECTION–

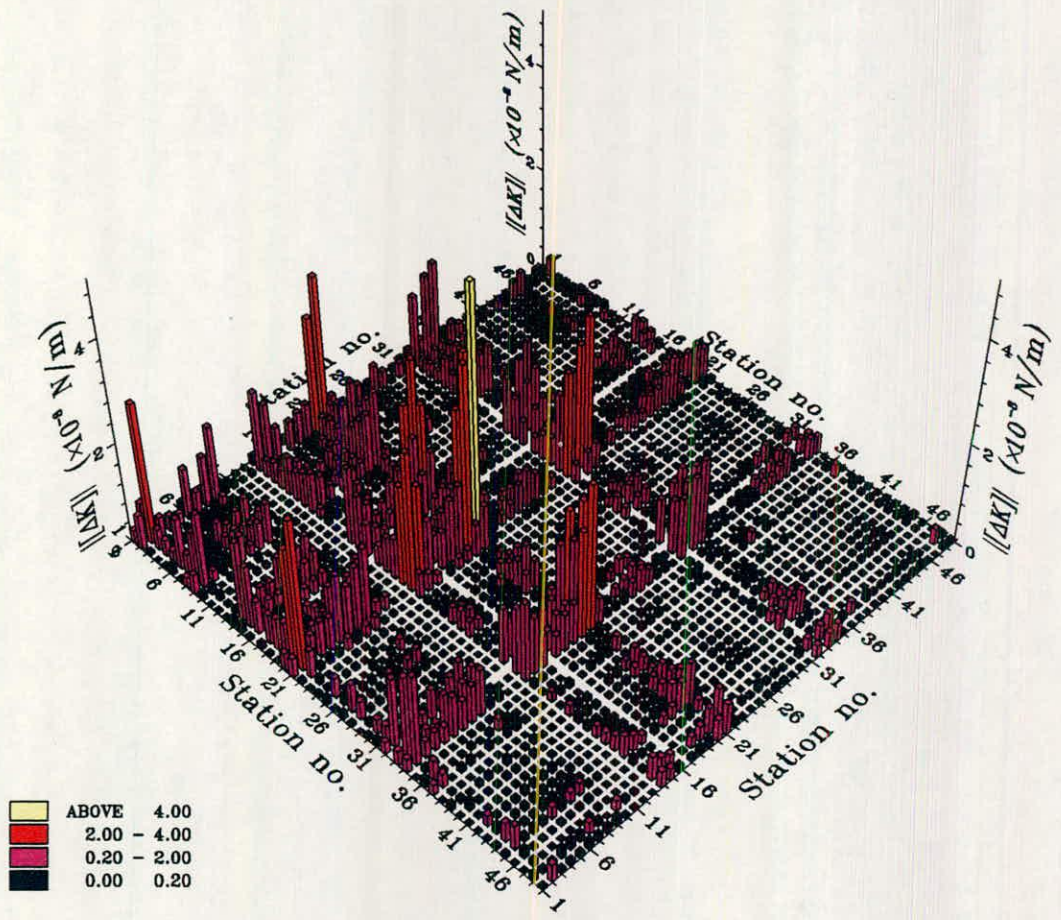

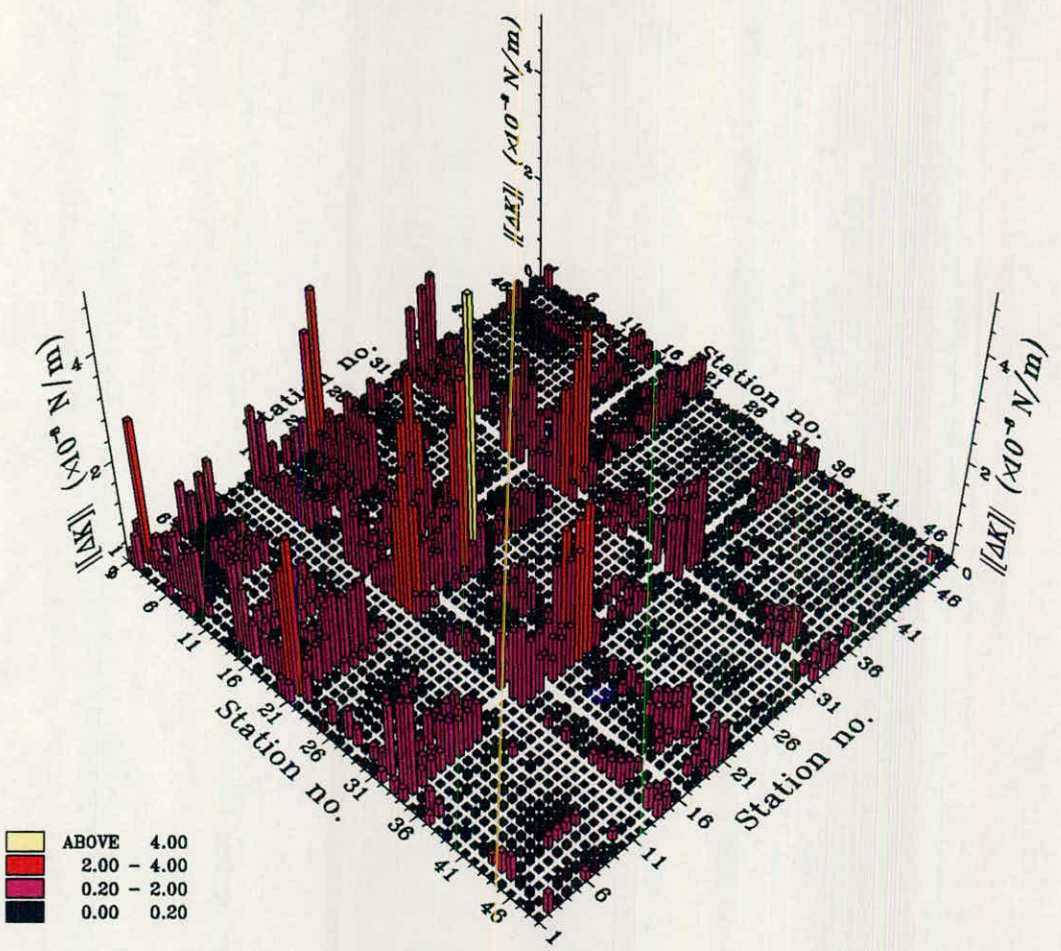

FIG. 4.22(b)–STIFFNESS ERROR MATRIX FOR EXPERIMENTAL AND THEORETICAL MODE SHAPES –Y DIRECTION–

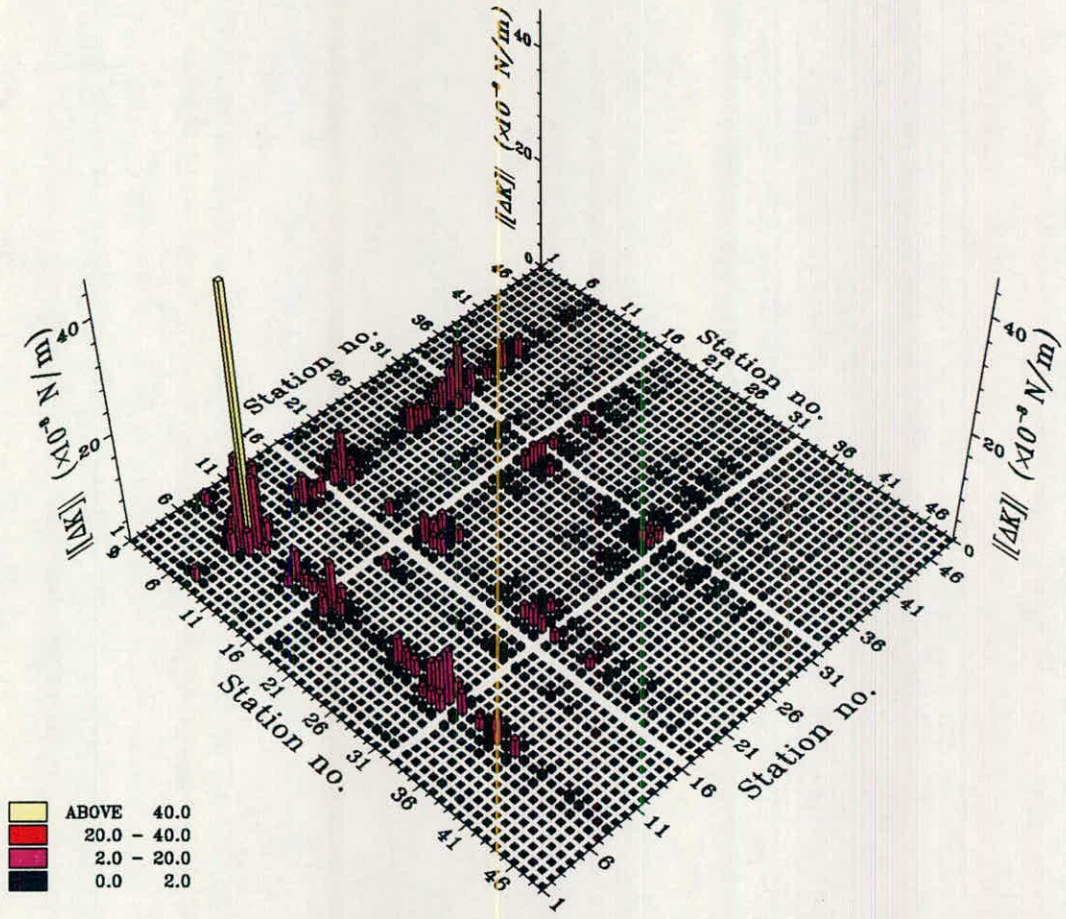

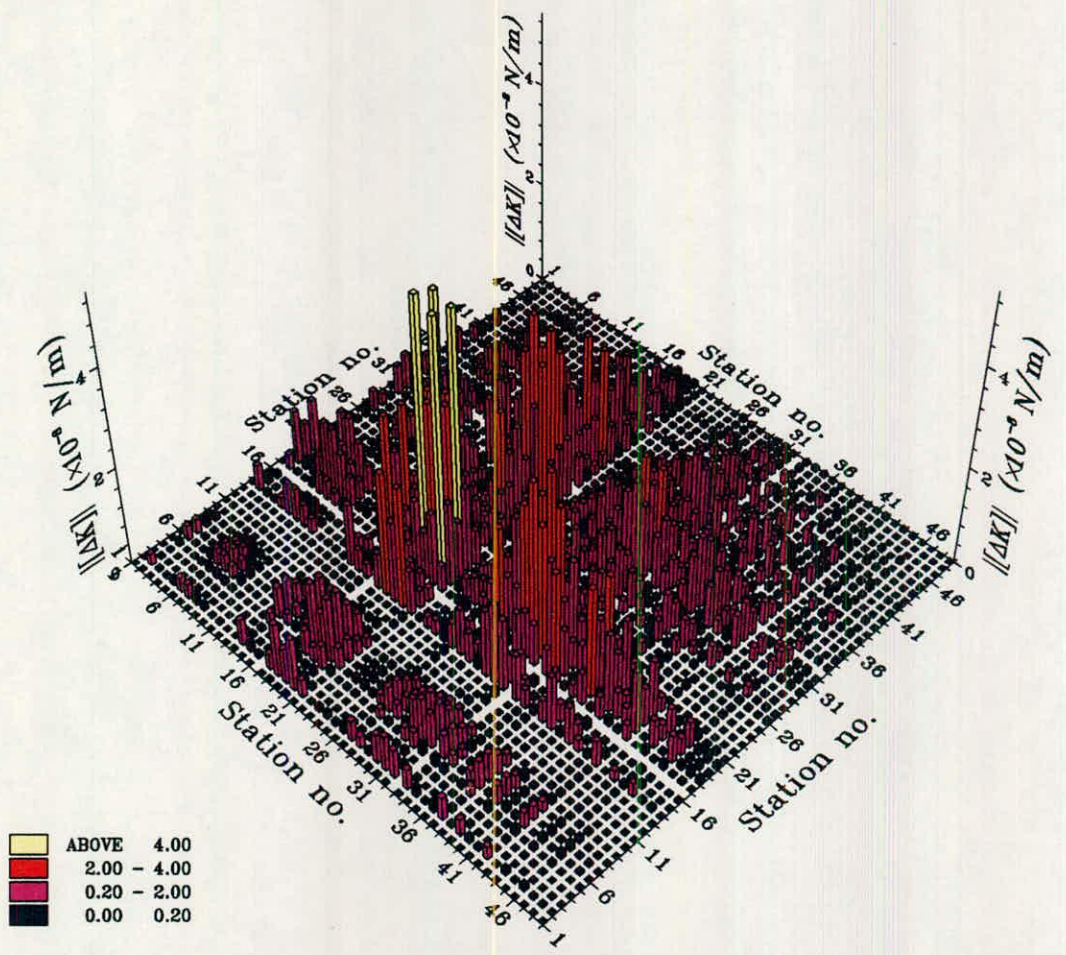

FIG. 4.22(c)–STIFFNESS ERROR MATRIX FOR EXPERIMENTAL AND THEORETICAL MODE SHAPES –Z DIRECTION–

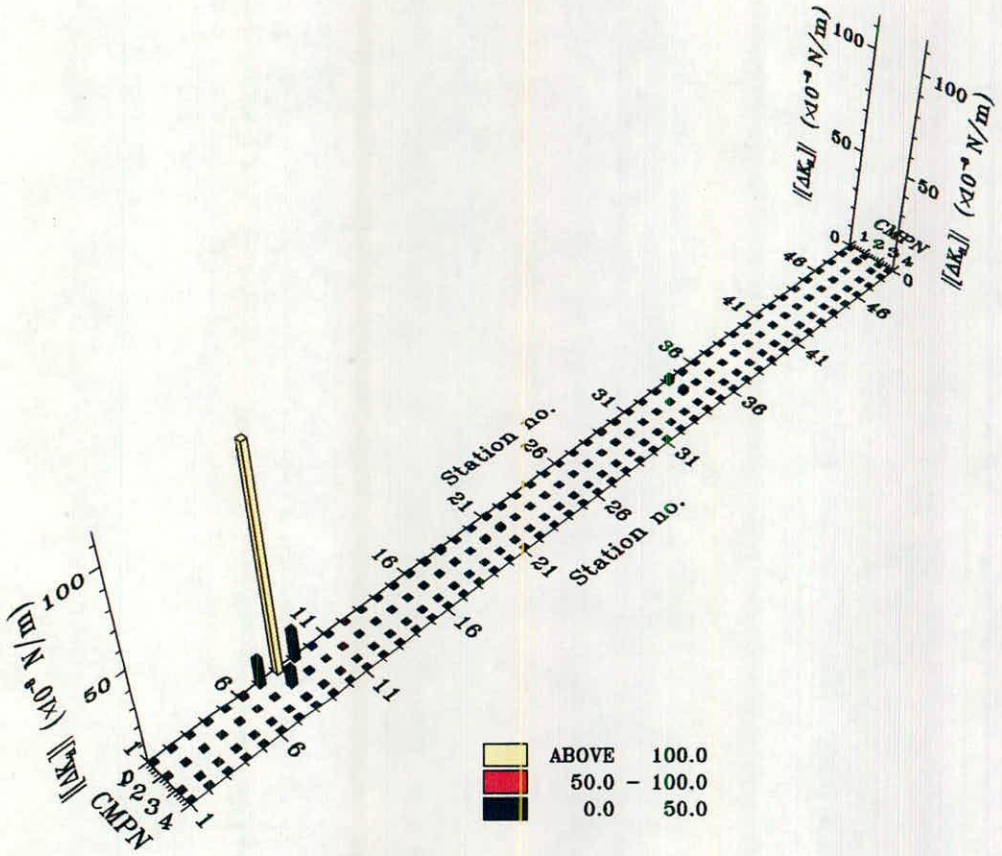

FIG. 4.23(a)–DIAGONAL TERMS OF THE STIFFNESS ERROR MATRIX –X DIRECTION–

-INITIAL MODEL-

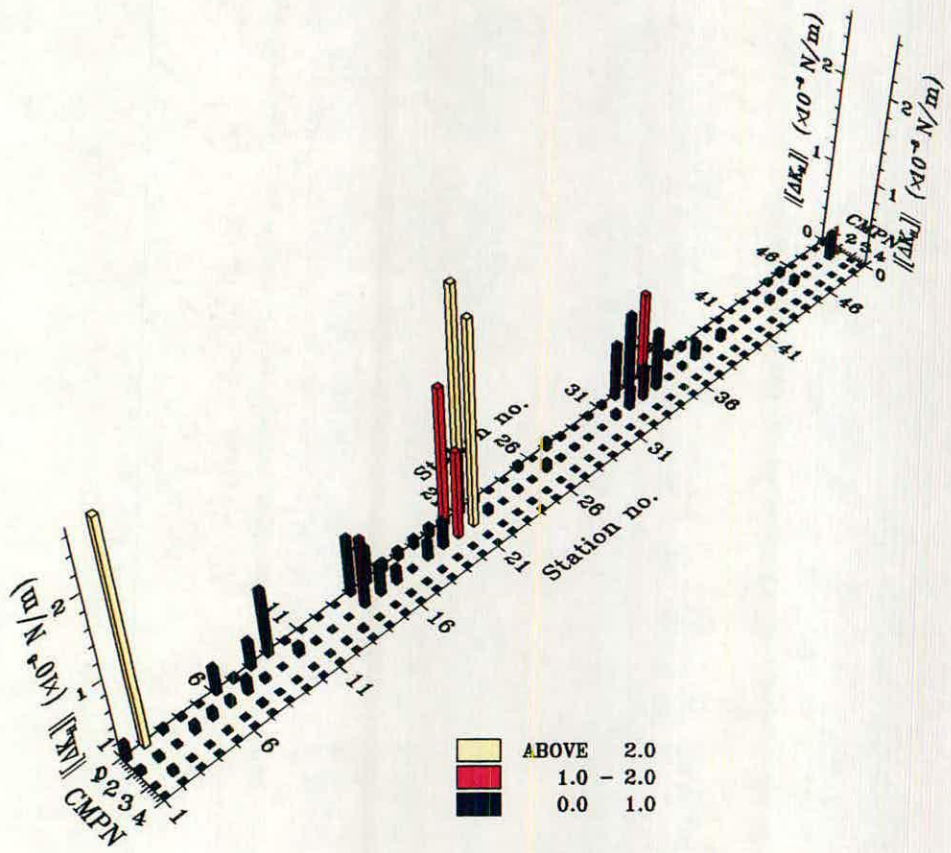

-UPDATED MODEL-

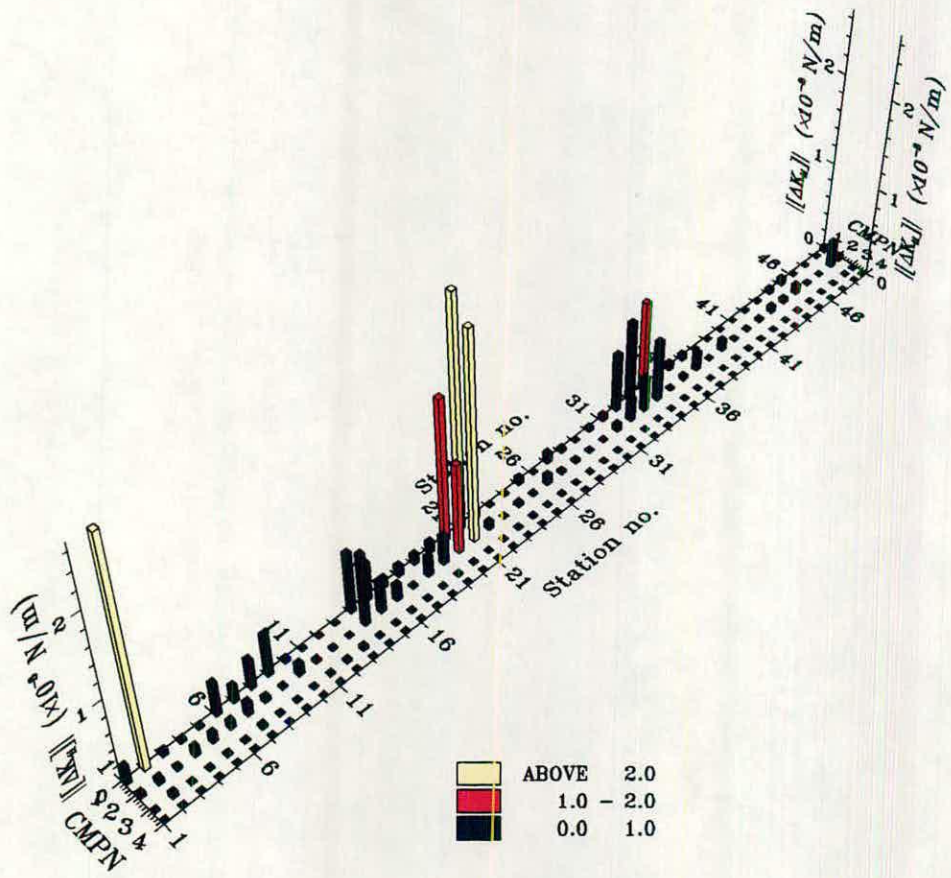

FIG. 4.23(b)–DIAGONAL TERMS OF THE STIFFNESS ERROR MATRIX –Y DIRECTION–

-INITIAL MODEL-

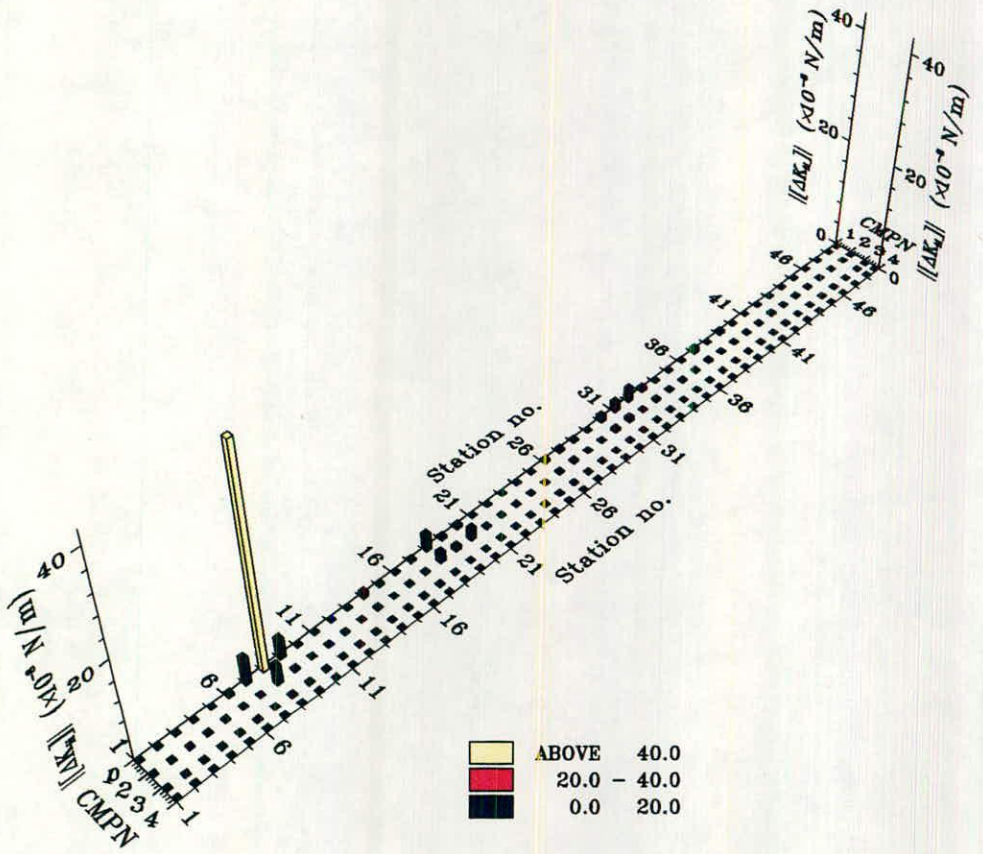

-UPDATED MODEL-

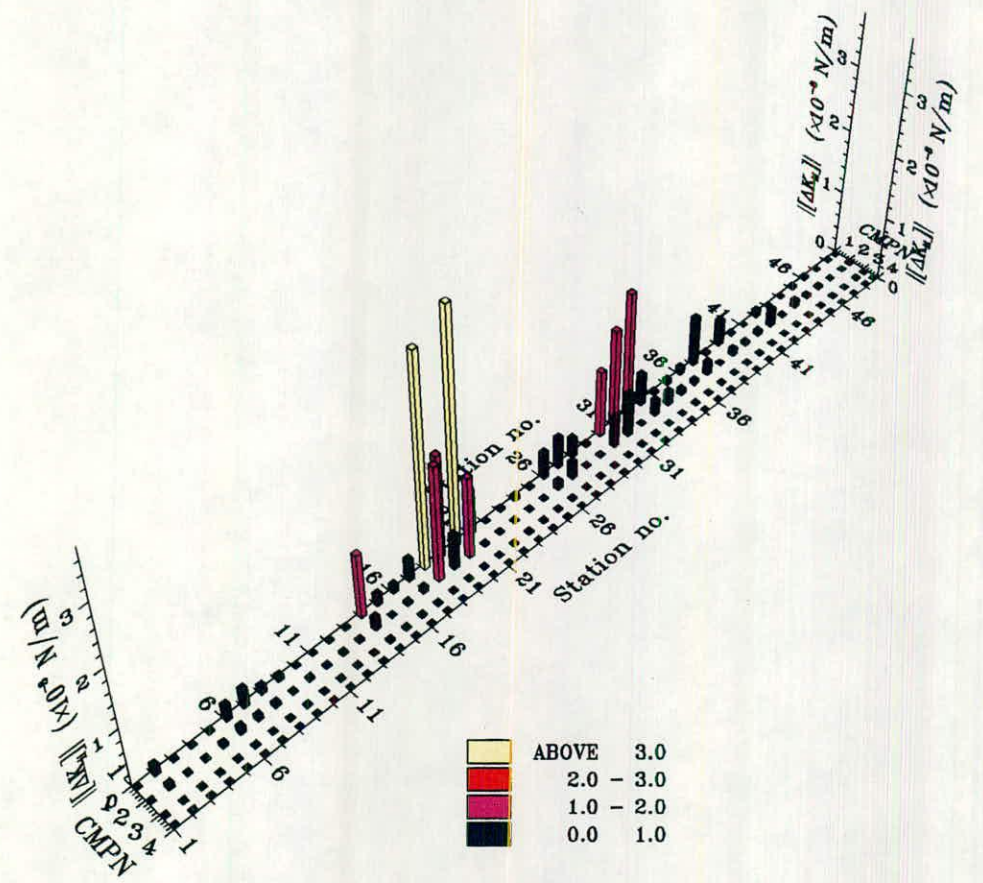

FIG. 4.23(c)–DIAGONAL TERMS OF THE STIFFNESS ERROR MATRIX –Z DIRECTION–

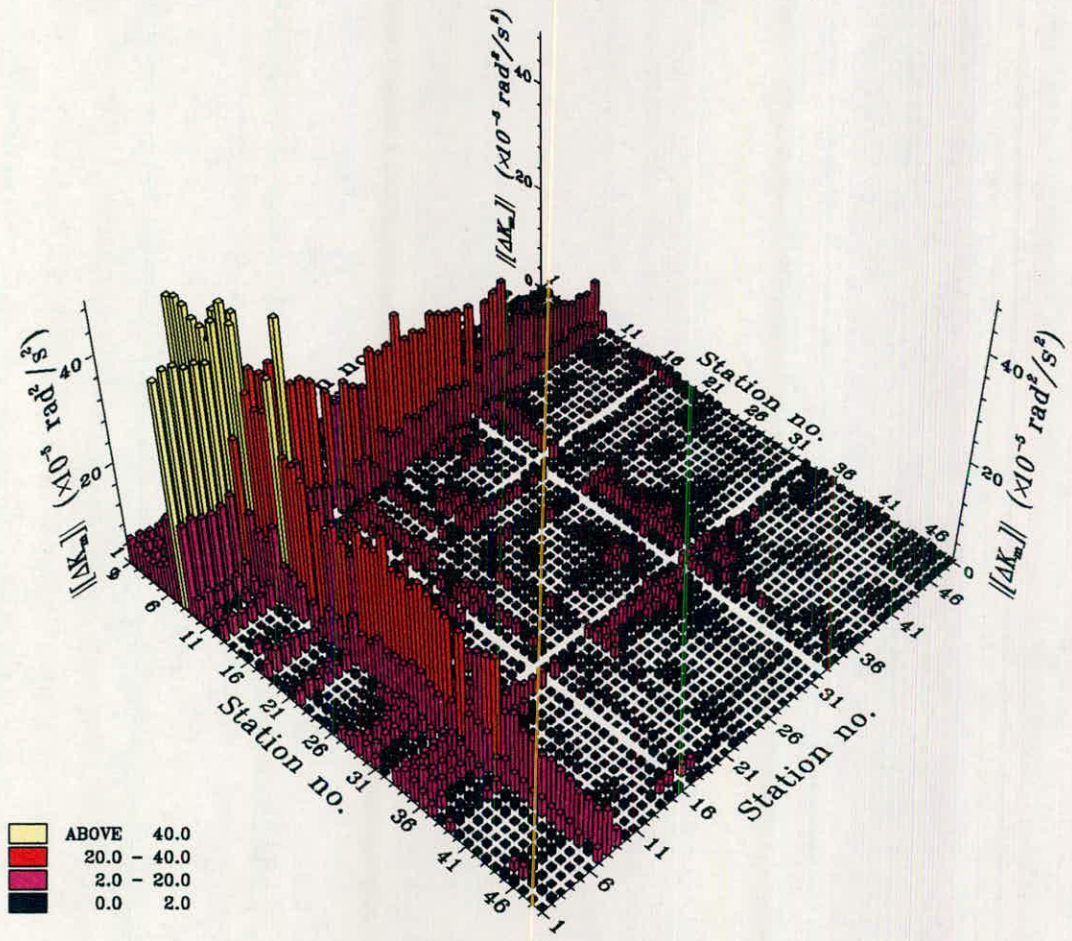

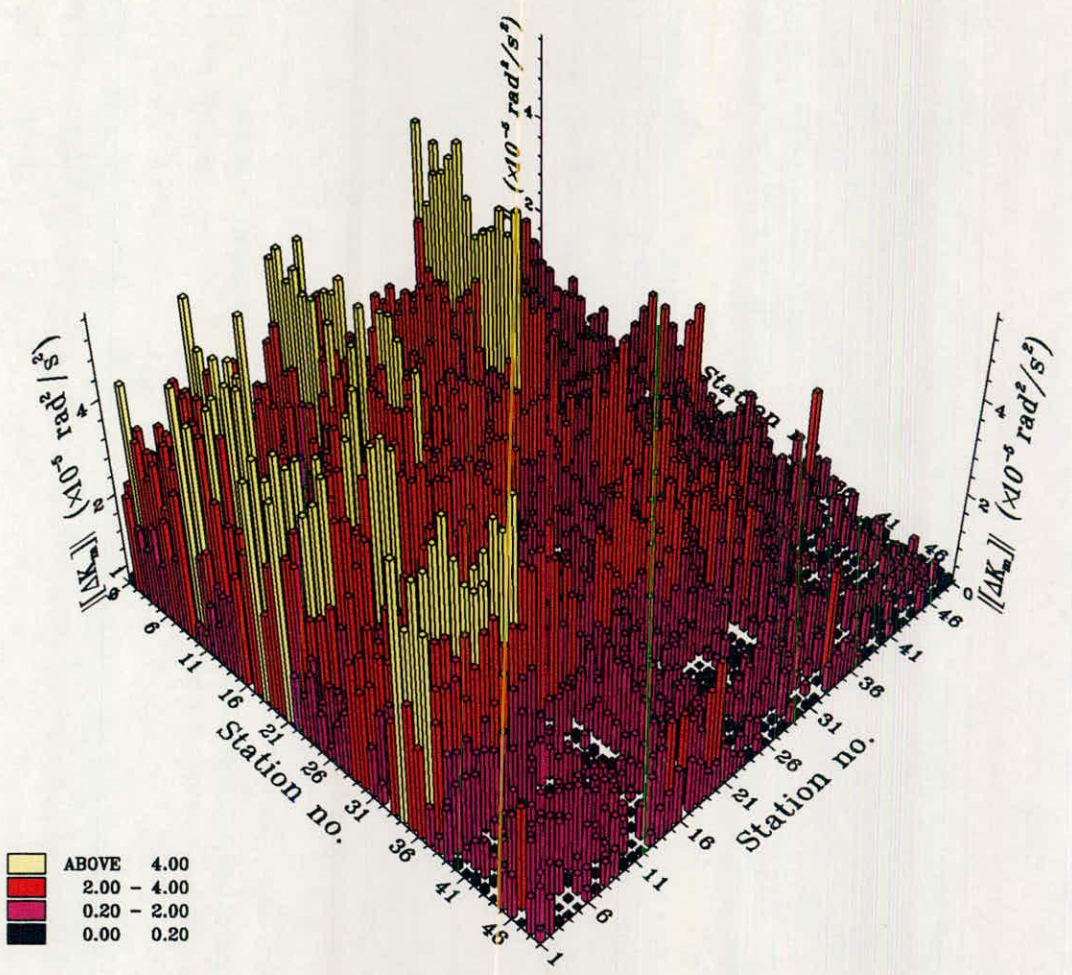

FIG. 4.24(a)–MODIFIED STIFFNESS ERROR MATRIX FOR EXPERIMENTAL AND THEORETICAL MODE SHAPES –X DIRECTION–

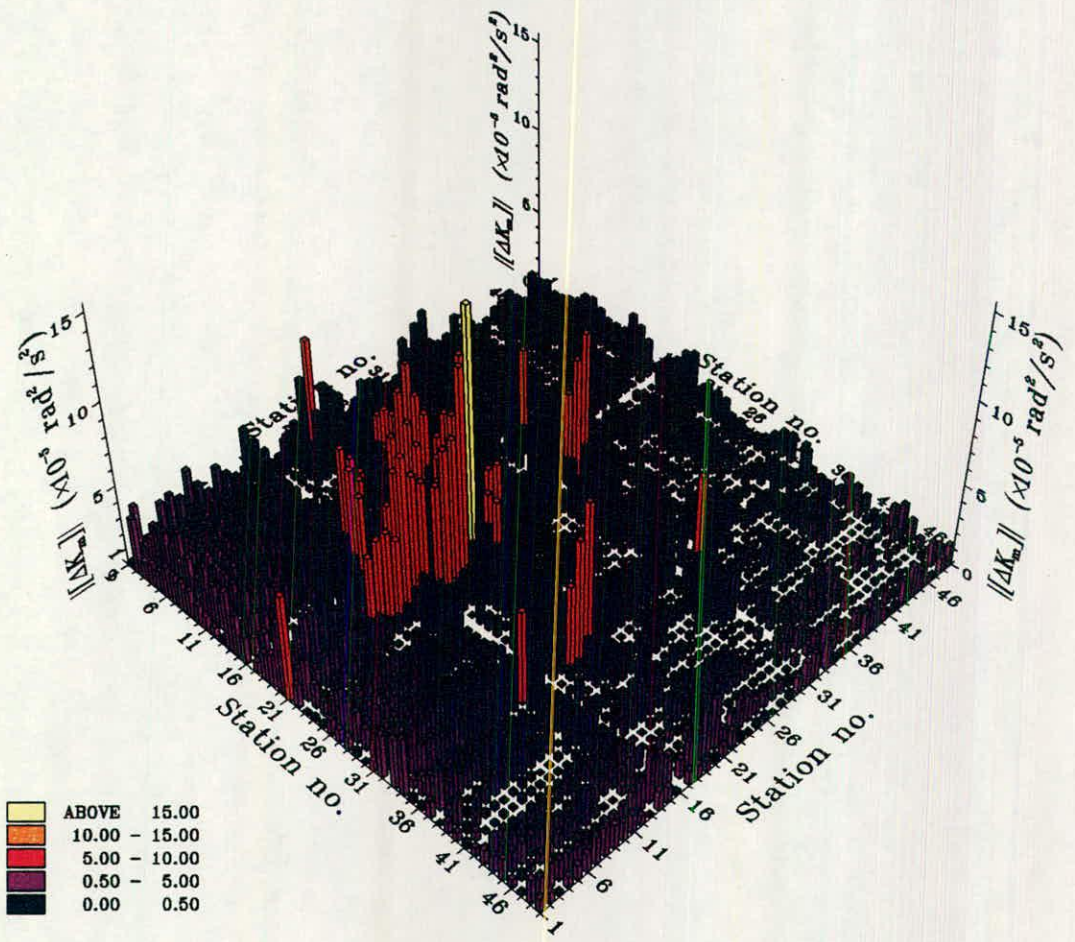

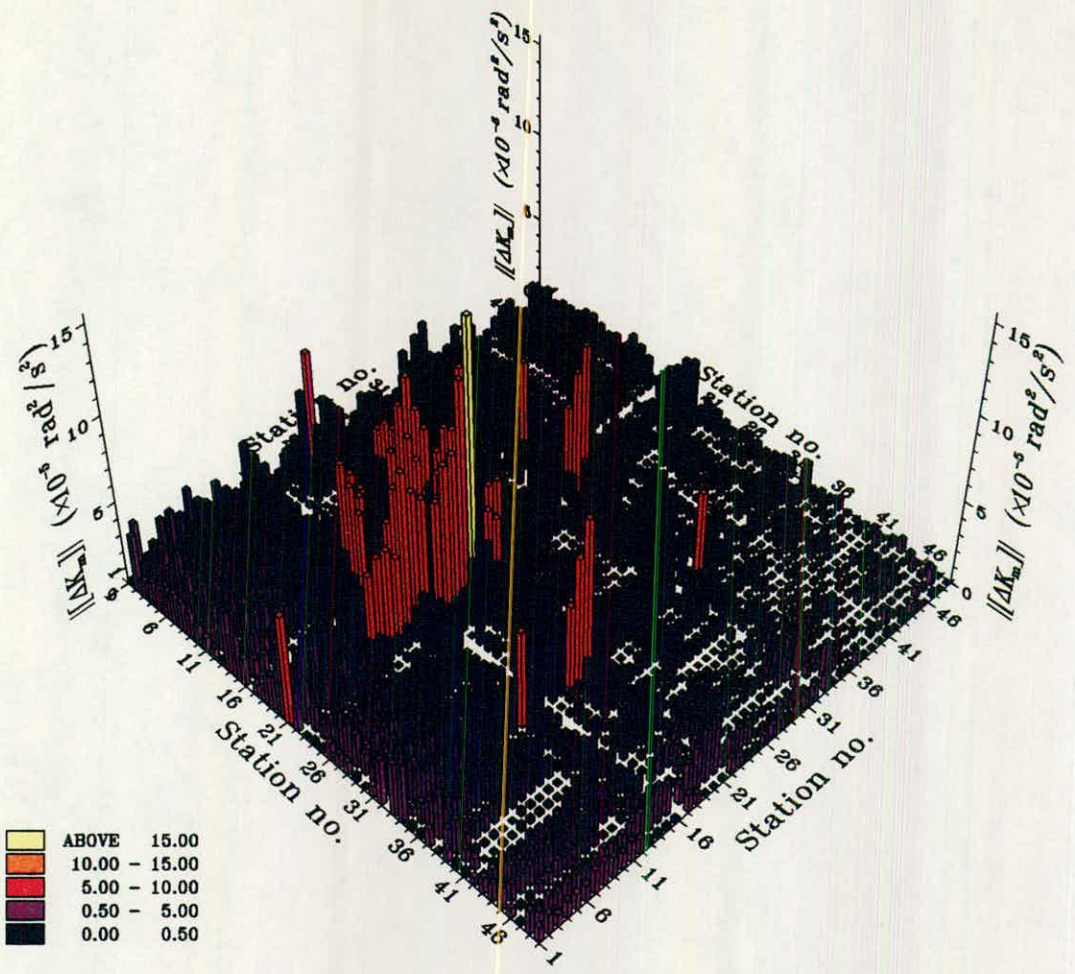

FIG. 4.24(b)–MODIFIED STIFFNESS ERROR MATRIX FOR EXPERIMENTAL AND THEORETICAL MODE SHAPES –Y DIRECTION–

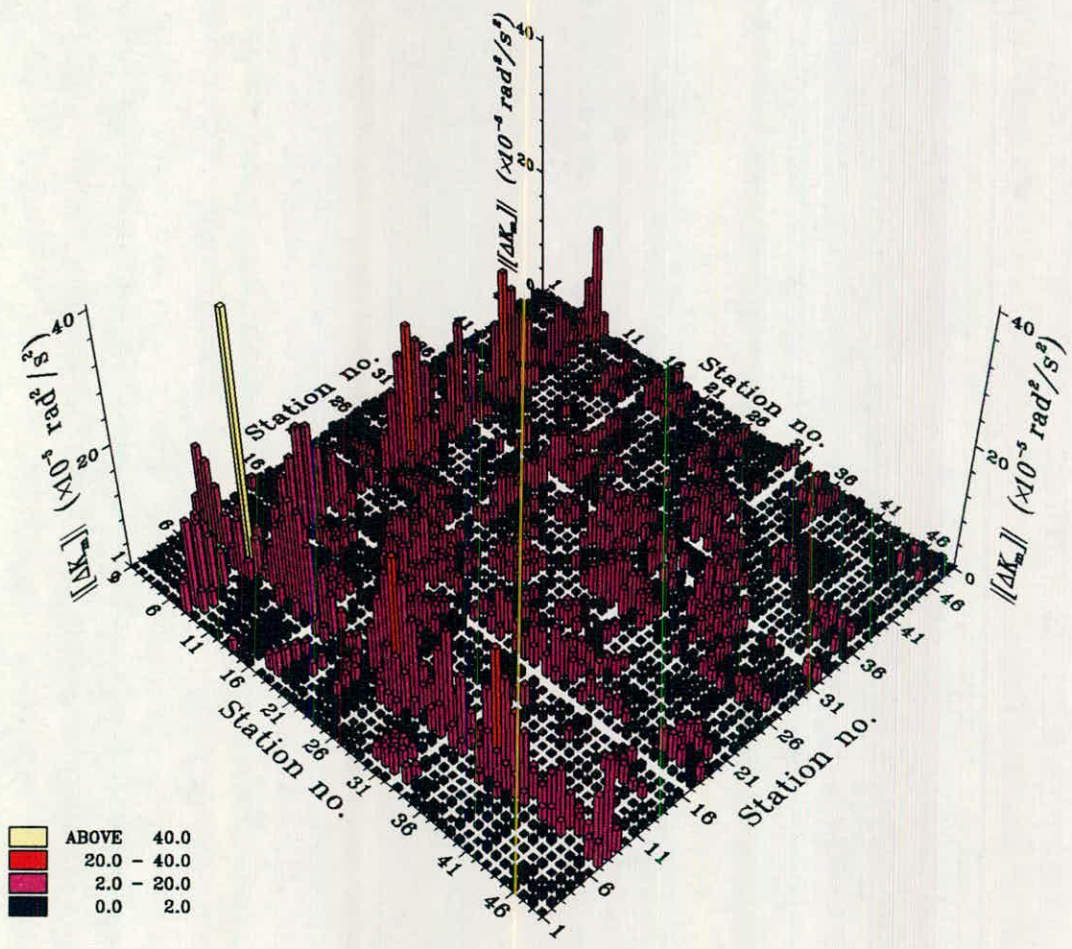

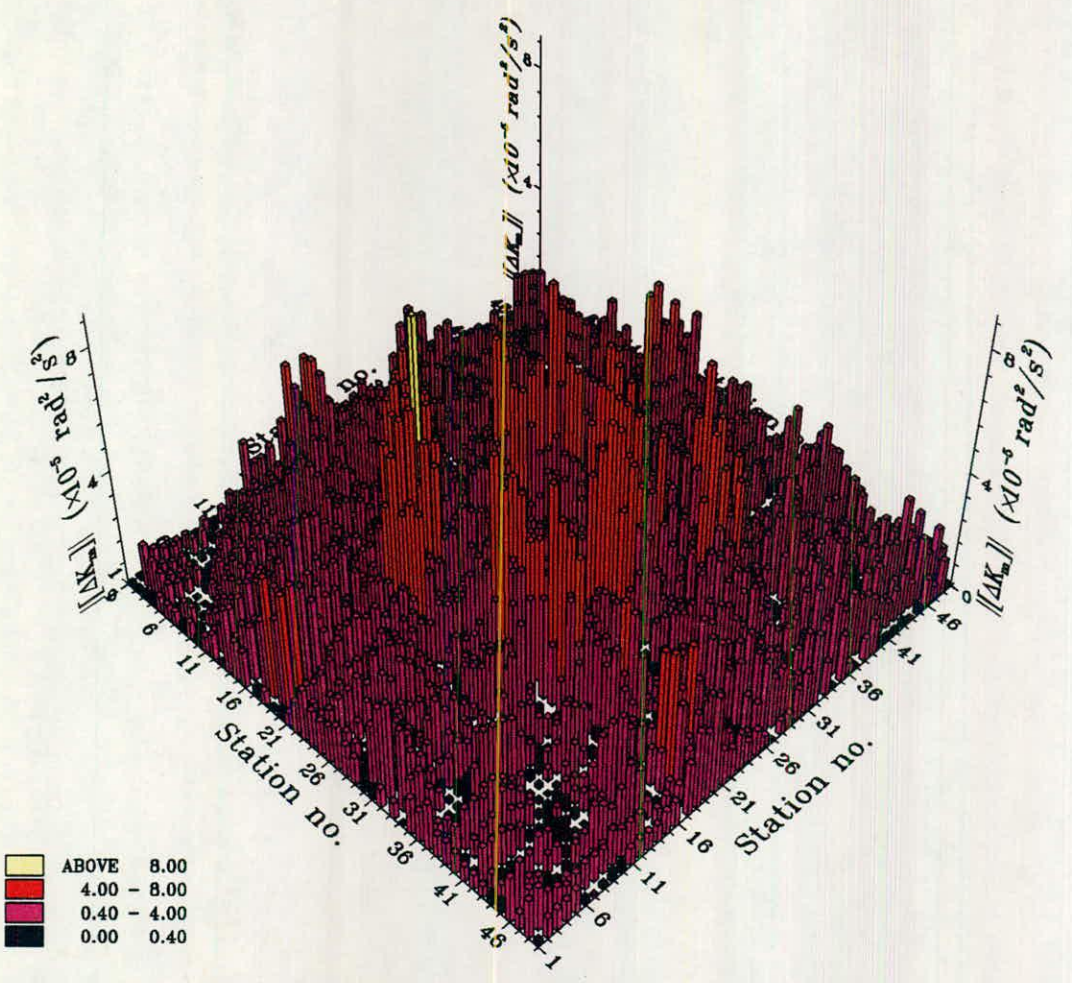

FIG. 4.24(c)–MODIFIED STIFFNESS ERROR MATRIX FOR EXPERIMENTAL AND THEORETICAL MODE SHAPES –Z DIRECTION–

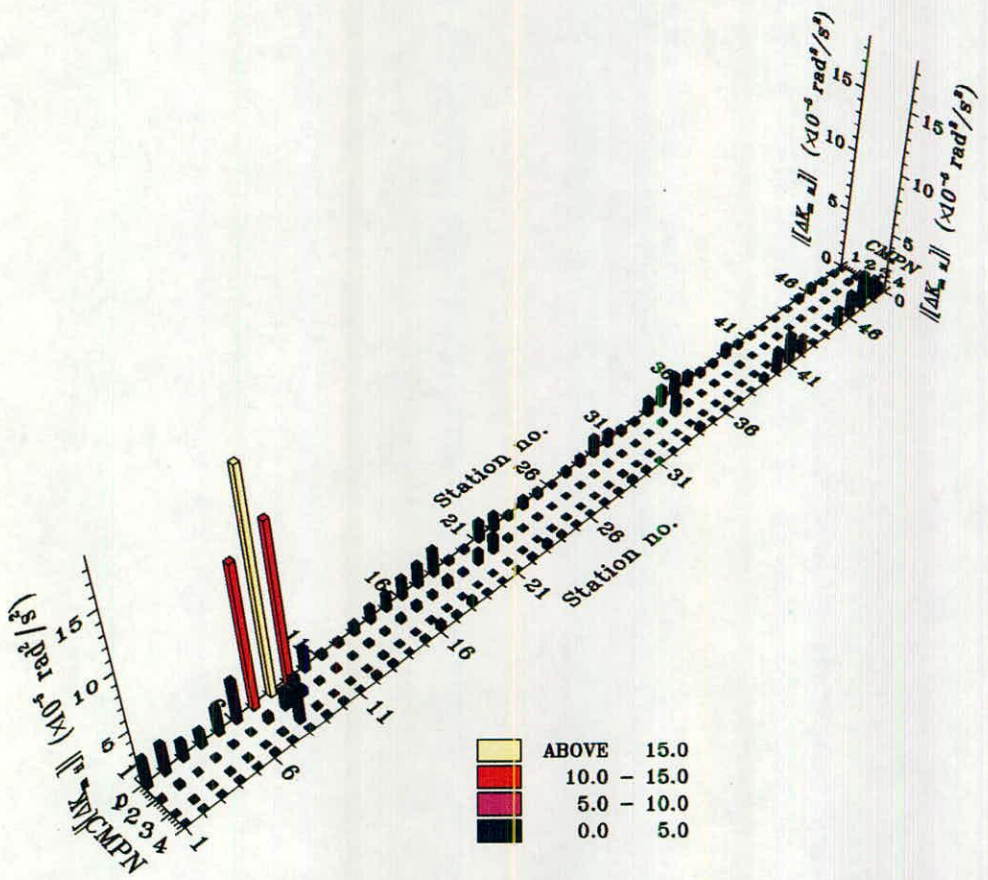

FIG. 4.25(a)–DIAGONAL TERMS OF THE MODIFIED STIFFNESS ERROR MATRIX –X DIRECTION–

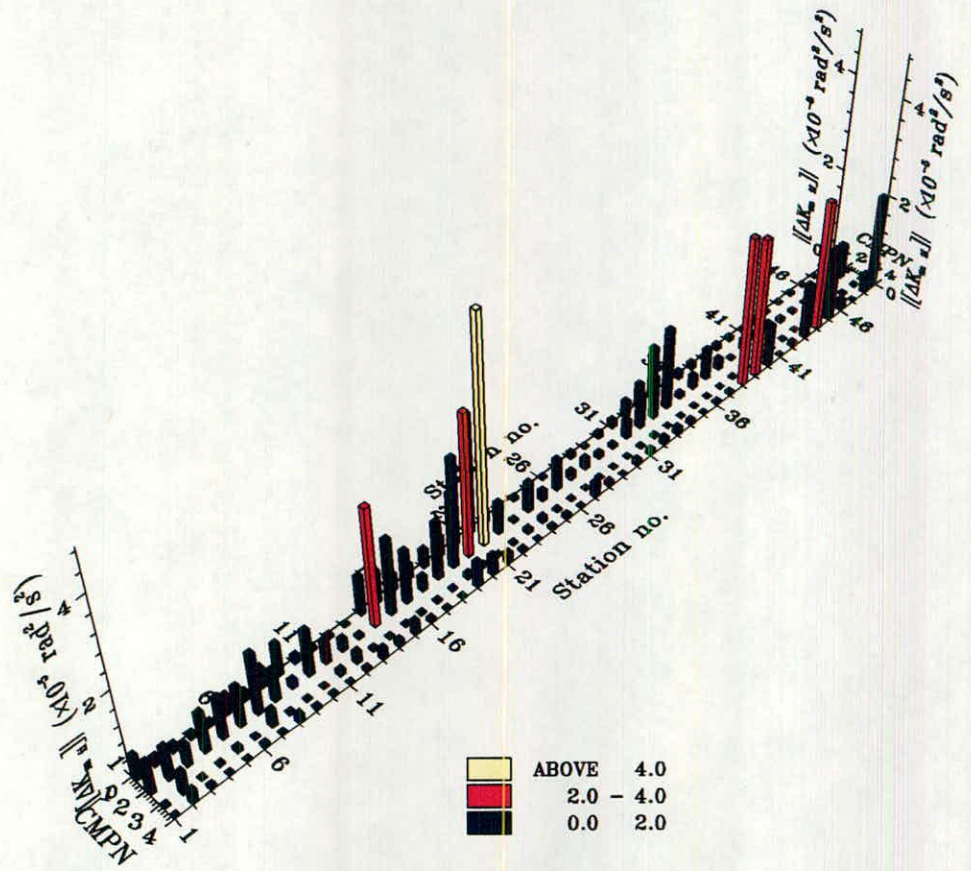

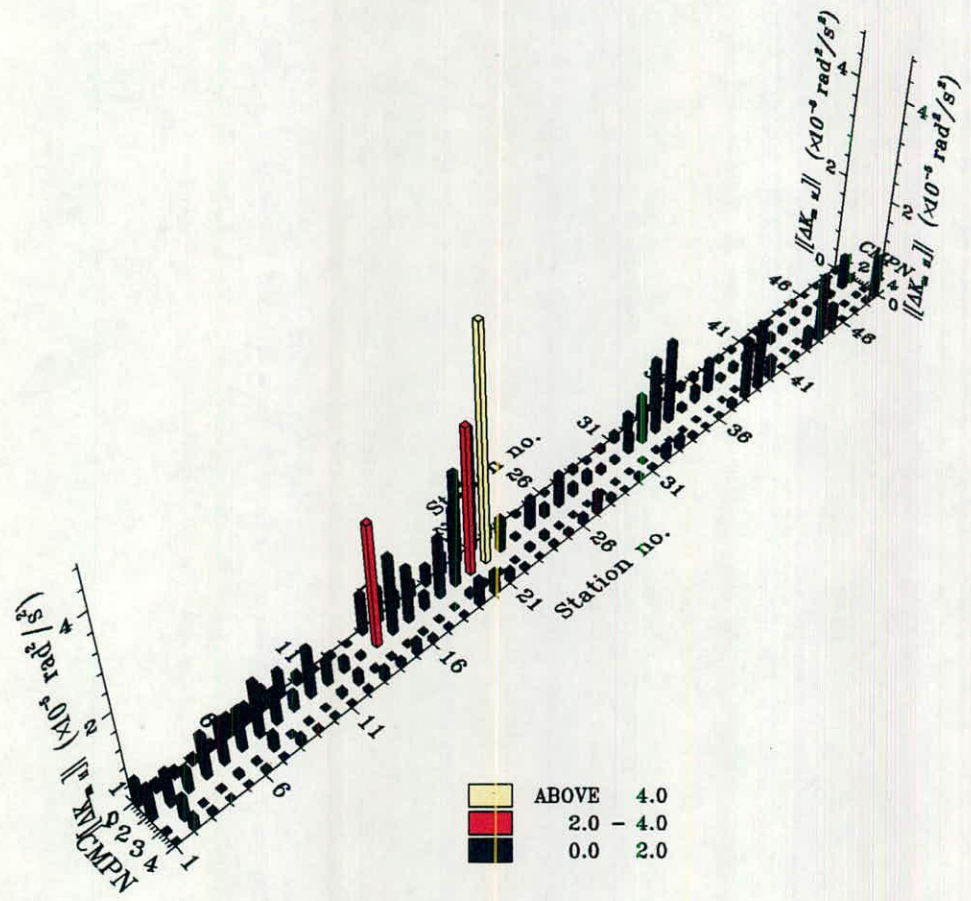

FIG. 4.25(b)–DIAGONAL TERMS OF THE MODIFIED STIFFNESS ERROR MATRIX –Y DIRECTION–

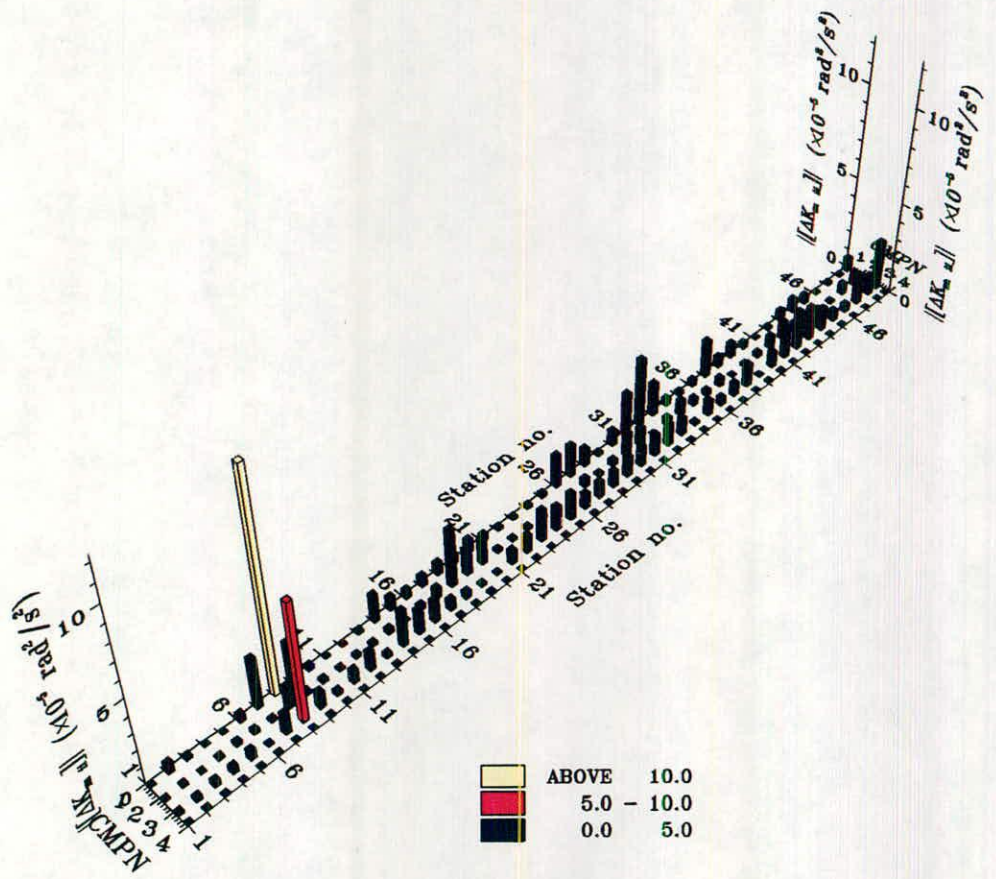

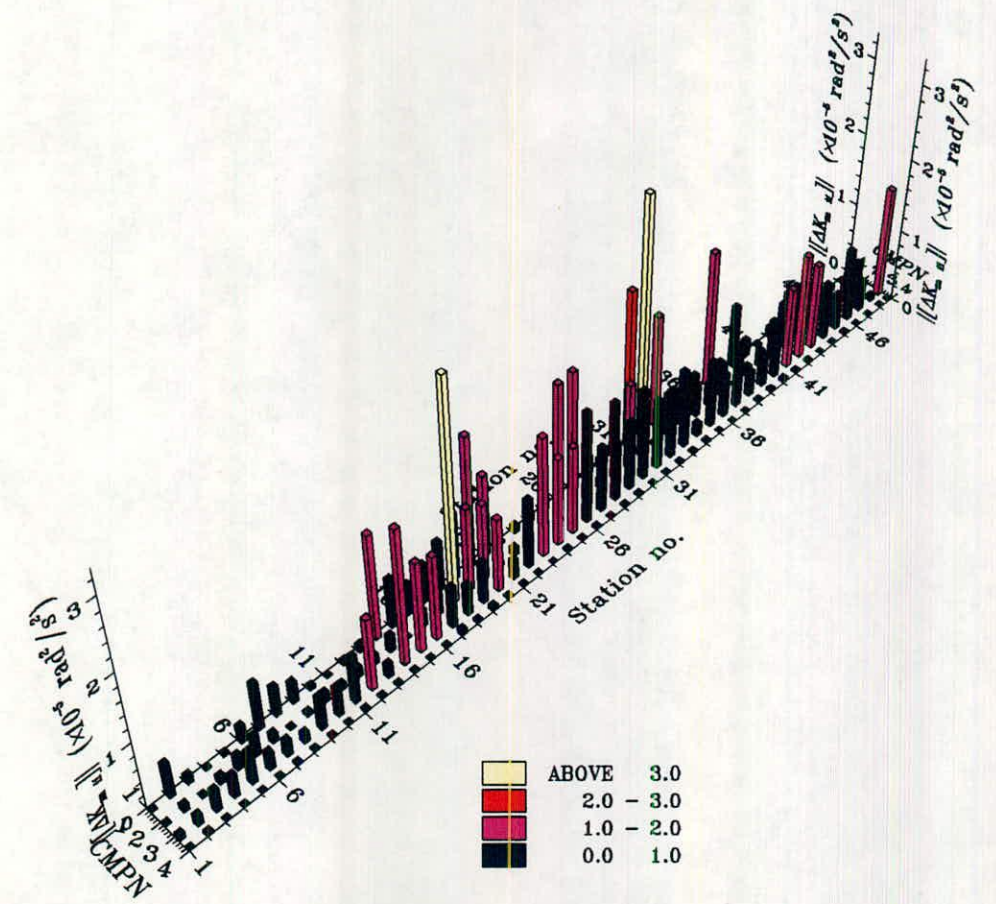

FIG. 4.25(c)–DIAGONAL TERMS OF THE MODIFIED STIFFNESS ERROR MATRIX –Z DIRECTION–

CHAPTER 5

ECHINODOME RESPONSE TO AN UNDERWATER EXPLOSIVE LOADING

5.1 SUMMARY

The explosion phenomenon is described starting from the detonation process and ending with the venting of the gas bubble. The effects of nearby free or rigid surfaces are also discussed.

A free field experiment was carried out to determine the general characteristics of the pressure pulse generated by a detonator underwater. Then the Echinodome was subjected to a shock wave from the same detonator while it was in a floating submerged state. Structural response was measured with the aid of strain gauges.

A theoretical analysis was undertaken using the finite element method to model the prototype and boundary element technique to simulate an infinite region of water surrounding the structure. Subsequently, experimental and theoretical principal stresses–time histories were compared.

5.2 INTRODUCTION

When a spill of a refrigerant liquid becomes superheated to an extent that permits homogeneous nucleation to take place, an overpressure is produced and such a phenomenon is known as rapid phase transition (RPT).

Liquefied natural gas (LNG) is generally stored under high pressure, or at very low temperatures, or a combination of lower levels of both and if leakage took place from an underwater container the cold liquid would be superheated after contacting the surrounding medium (water) resulting in an RPT which resembles an explosion and consequently, shock waves would be transmitted to nearby structures. Therefore it is necessary to consider RPT loadings on underwater reservoirs such as Echinodomes, containing highly volatile liquids at very low temperatures.

The doubly asymptotic approximation (DAA) is a numerical approach implemented in PAFEC–DOLPHIN to analyse shock problems. Good agreement was obtained earlier [81] between the theoretical DAA and exact solutions for a submerged spherical shell impinged upon by a plane step pressure wave. An underwater explosion test was carried out using the Echinodome prototype

as the target and measured strains were compared with their predicted correspondents in order to assess the performance of DAA.

5.3 SEQUENCE OF THE UNDERWATER EXPLOSION PHENOMENON [82]

An explosion is a rapid release of energy in a considerably short time. Explosive materials undergo chemical reactions releasing gaseous materials at very high temperatures. Underwater the explosive gases are compressed by the surrounding medium (water) eventually taking the shape of a sphere. In the following subsections the behaviour of the gas sphere (often known as the bubble) is described and the effect of rigid and free surfaces is mentioned. More details can be found elsewhere [82].

5.3.1 Detonation Process

Detonation is the initial phase of the explosion phenomenon in which the chemical reaction takes place rapidly so that it can keep up with the resulting physical change and it is accompanied by the evolution of large amounts of heat. A detonation wave develops, behind the shock front of the initiated explosive, separating the unstable substance (explosive material in its initial form) from the stable product of the reaction. The detonation wave propagating speed is a characteristic of each explosive material and is several times that of the shock wave.

5.3.2 Shock Wave

At the boundary between the explosion gases and the surrounding water compression waves are generated, developing very steep fronts as they progress. Such waves are known as shock waves and they travel at an average velocity of 1400 $\rightarrow$ 1500 m/s when they are considerably away from the charge.

In practice, the rise time of a steep fronted shock wave is usually less than the resolving time of the experimental measurements and therefore, the time histories of the pressure pulse is generally characterised by having a discontinuous rise followed by an exponential decay.

For spherical shaped charges the pressure level drops off with a rate higher than the first power of the inverse of the stand off distance from the source of the explosion. The decay rate of the pressure pulse is slower as the shock wave spreads away from the charge.

Pulse shapes measured off the side of cylindrical charges are similar to those of spherical charges in that the discontinuous rise is followed by an exponential decay. However, the pressure–time curves differ in shape and peak level if measurements are made along the axis of symmetry, often possessing two pressure peaks.

A large amount of energy is dissipated to heat in the vicinity of the charge with the propagation of the shock wave outwards. This is caused as a result of the steep pressure and velocity gradients occurring at the shock front.

5.3.3 Gas Sphere and Secondary Pulses

A gas sphere (bubble) is formed as a result of an underwater explosion. Initially, the gases are under maximum compression and thus occupy a minimum volume. With the emission of the shock wave the bubble expands and the pressure drops. The water behind the shock front flows outwards, remaining in such a condition as long as the inside pressure of the bubble is larger than the sum of the atmospheric and hydrostatic pressures ($p_a + p_w$).

At later times the outward flow of water drops until the gas pressure is slightly below the equilibrium value ($p_a + p_w$). The gas sphere at this stage is characterised by having a maximum diameter, the outward motion stops and contraction of gases starts. The inward motion continues until the bubble reaches its minimum radius. Several cycles of expansion and contraction are repeated ending by the collapse of the bubble.

The shock wave pressure is determined by the degree of compressibility of gases inside the bubble and therefore, at maximum contraction of the gas sphere (minimum bubble radius) the pressure value is at a peak.

After the emission of the shock wave the first occurring peak pressure is known as the first "**Bubble Pulse**" or "**Secondary Pulse**". The first bubble period is equal to the time elapsed from the initiation of the explosion to the occurrence of the first bubble pulse.

The maximum pressure of the first secondary pulse is much less than the shock wave peak pressure and later pulses are of even much less strength due to the energy losses in successive contractions. However, it cannot be concluded that the bubble pulses are of no (or less) significance than the shock wave. This is because the areas under both pressure–time curves are comparable since the time duration of the secondary pulse is much longer than that of the initial pulse (see Fig. 5.1).

As the bubble is experiencing expansion and contraction it rises towards the surface because of the buoyancy effect. The maximum upwards migration taking place when the volume occupied by the gas sphere is at its minimum. Gas spheres are attracted to rigid surfaces while free boundaries have the opposite effect.

Therefore, the effectiveness of secondary pulses produced by the bubble to cause damage depends not only on the charge size and stand off distance but also on the depth at which the charge is fired and the proximity of free and rigid boundaries relative to the charge position.

5.3.4 Surface Effects

In real life, a water media is finite due to the existence of top and bottom surfaces. The effect of such surfaces on the propagation of pressure waves varies.

When a pressure wave strikes an infinitely rigid boundary the net component of particle velocity normal to the surface becomes zero. This condition is satisfied by the reflection of the incident wave back into the water medium with a positive pressure value (a compression shock wave).

A free surface (boundary between water and air media) possesses very low resistance to compressibility and as a result no compression can develop along such a boundary. There is no opposition to the motion of the surface and consequently, the necessary condition for equilibrium is that there will be no pressure change at the free surface, a requirement fulfilled by the generation of a reflected wave with negative pressure (a tension shock wave).

Due to the reflected negative pressure waves incurred at free surfaces there will exist regions in the water medium where the resultant pressure is negative. Water is generally weak in tension and therefore, if circumstances occur in which considerable negative pressures are encountered, the water mass is pulled apart from itself and holes are formed in order to prevent an increase in tension. Such a phenomenon is known as "**Cavitation**".

The effects of reflection from boundaries are easily determined for the shock wave pulse and if encountered for bubble pulses they complicate its shape, hence errors can set in during the analysis stage.

5.4 ECHINODOME BEHAVIOUR UNDER A BLAST LOADING

An experimental investigation as well as a numerical analysis were carried out in order to determine the Echinodome dynamic response to underwater explosive loading.

Experimentally, the test structure was submerged in a water tank and tethered to a known position with the aid of four tension legs. The Echinodome was said to be in a floating submerged state.

The following subsections contain a description of the experimental work involved and details of the theoretical simulation using the finite element–boundary element methods.

5.4.1 Experimental Approach

The experimental investigation was divided into two parts. The first part comprised a set of free field experiments which were carried out in order to determine the pressure pulse characteristics (peak pressure, decay rate, impulse and energy) for a cylindrical charge of a specific mass at a given position. While in the second part the cylindrical charge was detonated at a predetermined stand off distance from the Echinodome prototype.

5.4.1.1 Charge design— The extent of damage caused by an underwater explosion depends on the dimensions and characteristic (periodic) times of the structure upon which the generated pressure wave acts. The time duration of the pressure pulse relative to the structural periodic times is one of the parameters controlling the dynamic response to such transient loadings. The longer the duration of the pulse the more likely the response will be similar to that invoked by a static pressure. Thus, the initial peak of the shock wave would be the influential factor. From Cole [82]

$$p_m \propto \left[\frac{W^{1/3}}{R}\right]^{\alpha} \qquad \text{(5.1)}$$

$$\Rightarrow \text{structural response} \propto p_m \qquad \text{(5.2)}$$

$$\propto \left[\frac{W^{1/3}}{R}\right]^{\alpha} \qquad \text{(5.3)}$$

where p_m represents the peak pressure of the shock waves;

W represents the mass of the explosive charge;

R represents the stand off distance; and,

α represents a constant.

In the other limiting case, a pressure wave with a duration much less than the structure's natural period, damage would be proportional to the impulse of the wave.

$$\Rightarrow \text{structural damage} \propto I \qquad \text{(5.4)}$$

$$\simeq \propto \frac{W^{2/3}}{R} \qquad \text{.....} \qquad (5.5)$$

where I represents the impulse of the shock wave.

In between the above two extremes structural damage may then depend on a fraction of the impulse of the emitted wave. Cole [82] mentioned that if cavitation occurred in water near the structure the resultant deformation would roughly be proportional to the square root of the incident shock wave energy.

$$\Rightarrow \text{structural deformation} \propto E_f^{1/2} \qquad \text{.....} \qquad (5.6)$$

$$\simeq \propto \frac{W^{1/2}}{R} \qquad \text{.....} \qquad (5.7)$$

where E_f represents the energy of the shock wave per unit area (or energy flux density).

The variation of the peak pressure (p_m), impulse (I) and energy (E_f) with the charge mass (W) and stand off distance (R) are empirical laws and therefore, the above relationships cannot be taken literally. However, their use may be beneficial in determining the charge size that would or would not cause structural damage.

A similar idea [83] was adopted in estimating an explosion charge mass placed 5 m away from the target that would not invoke any geometric non–linearity of the Echinodome prototype and at the same time produce measurable strains.

The estimated charge mass was found to be equal to 1 gm and a standard electric detonator 79 was selected for the purpose of the current experimental study. The charge was of cylindrical shape.

5.4.1.2 Free field set–up— For a given charge size and type the pulse characteristics of the shock wave, in the form of peak pressure, decay rate or time duration, impulse and energy, vary with the increase or decrease of the stand off distance. Consequently, a set of free field experiments were carried out in order to estimate such properties as well as to determine the pulse shape at the point where the shock wave would impinge the Echinodome prototype in a later experimental set–up.

The changes in the pressure field surrounding detonator 79 when initiating it were measured utilising seven tube like tourmaline pressure gauges. Pressures of up to several hundreds of MPa could be measured. Calibration was performed at site. The sensitivity of each gauge was determined by applying a standard pressure pulse of 6.88 MPa (1000 psi) and measuring the corresponding voltage change using a digital oscilloscope.

A frame made of steel was erected on which the pressure gauges were fixed as shown in Fig. 5.2. The frame was then lowered in a water tank of dimensions 12.190×6.100 m in a 3.470 m of water depth. The tank walls and base were made of reinforced concrete with thick steel plates lining it. The position of pressure gauge 7 was identical to that of the nearest point of the test structure to the explosive charge. Pressure gauges 2 and 3 were used in order to determine the characteristics of the reflected shock waves from the bottom of the tank (rigid boundary) and the water surface (free boundary) respectively.

The transducer signals were conditioned using MELEC model M124 charge amplifiers and recorded with a THORN EMI model SE7000 magnetic tape recorder (FM type).

5.4.1.3 Target set–up— When the test structure was to be subjected to an underwater explosion a different experimental set–up was prepared. A set of four cables was used to position the prototype at a depth of 1.525 m of water from its apex (the design pressure head of the test structure). Each cable was made of six strands and a single core. The four cables acted as tension legs supporting an underwater structure because of the buoyant forces acting upwards on the empty shell structure.

Part of the steel frame used in the free field experiment was again employed with some of the attached pressure gauges to gain more confidence in the measured pressure pulses as well as to position the detonator at the same water depth as the maximum diameter of the Echinodome prototype.

Structural response was measured using electrical resistance foil strain gauge rosettes with each gauge having a resistance of $350 \pm 1\Omega$, 3 mm gauge length and an average gauge factor equal to 2.15. The rosettes were bonded on the outer surface of the shell at five different positions in the same meridional plane with angles $\phi = 30^{\circ}$, 60°, 90°, 120° and 150° away from the apex as depicted in Fig. 5.3. For each rosette one gauge was aligned with the meridional profile, another along the corresponding parallel circle and the third in between them at an inclination of 45° . Voltage excitation of the strain gauges, filtering and conditioning of the strain signals were carried out using special signal conditioning amplifier units.

The detonator was set at a position approximately 5 m away from the prototype. The strain gauge rosettes, the explosive charge and the three pressure gauges were in the same vertical plane as shown in Fig. 5.4.

A newly developed miniature tourmaline pressure gauge PCB model 105M114 was attached to the test structure at its maximum diameter ($\phi = 90^{o}$), 30 mm from the strain gauge rosette lying on the same parallel circle and was nominated P.G. 8. The gauge has a maximum range of 6.88 MPa. Wax which was employed in the waterproofing process acted as a bonding agent between the transducer and the prototype. (The pressure gauge was on loan for an evaluation of its performance). Energisation and signal conditioning was performed using PCB model 480DO6 power supply–signal amplifier unit.

The PCB model 303A06 triaxial accelerometer described earlier was mounted on the Echinodome prototype at its apex to measure the dynamic response there but unfortunately the recorded signals were erroneous because the excitation frequency was much higher than the accelerometer's mounted resonant frequency.

All time domain signals were recorded in analogue form using RACAL model STORE 14DS and THORN EMI model SE7000 FM magnetic recorders for response (strain and acceleration) and excitation (pressure) histories respectively.

5.4.1.4 Data acquisition and analysis instrumentation— Analogue pressure and strain signals were digitised by means of a KONTRON model 700 transient recorder which possessed a maximum sampling rate of 10 MHz. Digital data was then stored on floppy discs for later analysis.

Post processing of the digital signals was carried out using the signal processing software DADISP [84] , mounted on an IBM PS/2 model 55SX desk top computer. DADISP enabled averaging of signals, d.c. shift removal, calibration, filtering, discrete Fourier transformation and many more mathematical applications.

A block diagram showing the instrumentation employed in the current experimental investigation for the data acquisition and analysis stages is presented in Fig. 5.5.

5.4.1.5 Digital signal processing— Digital signals stored on floppy disks were recalled using the DADISP program for data correction and processing. The current analysis stage comprised the following five main steps :

1. **Common triggering :** before performing any averaging process on any ensemble of time domain signals it was important to adjust the trigger points to have the same time of occurrence.

2. **Ensemble averaging :** time domain signals were averaged in order to reduce inherent random errors in the form of noise.
3. **Offset removal :** d.c. offsets were determined by averaging all sample points prior to trigger, then such transitions were subtracted from the corresponding ensemble averaged signals.
4. **Digital filtering :** low pass filters were designed to be applied to pressure and strain signals with the purpose of attenuating the high frequency components.
5. **Calibration :** all digital signals were scaled by the corresponding calibration constants to transform their amplitudes from voltage units to pressure or strain units.

The above operations were applied for each data set of a given transducer in an identical order.

5.4.1.6 Digital filtering— Only the initial part of each pressure signal comprising the shock wave pulse was considered in the filtering process because of the enormous number of computations involved if the secondary pulses were to be included.

Discrete time pressure signals, each formed of 2048 samples equally spaced by 100ns, were transformed to the frequency domain in order to determine the maximum excitation frequency above which any data were considered to be highly contaminated with electrical noise. The ESD of the pressure pulse for pressure gauge 1, depicted in Fig. 5.6, indicated that the frequency components above 100 kHz were buried in the noise floor. Consequently, the cut off frequency, (f_c), to be used in designing a low pass digital filter was equated to 100 kHz, (a low pass filter passes all low frequency components and stops high frequency components).

Before analysing the strain signals, with $N = 4096$ and $\Delta t = 40\ \mu s$, it was necessary to establish that the structural dynamic response had decayed to at least the noise floor level [61] of the pretriggering level or else exponential weighting would be required. This was achieved by using a Hilbert transform to display the magnitude of a strain signal in the time domain with a logarithmic vertical axis as is show in Fig. 5.7 . The magnitude function resulting from a Hilbert transform represents the positive envelope of the signal under consideration.

A Fortran 77 program was prepared to calculate the envelope function of the strain records employing DFT and IDFT techniques. The equations involved in the derivation are listed below and more details concerning the mathematical formulation leading to the Hilbert transform can be found elsewhere [85, 86] .

$$z(t) = x(t) + \boxed{i\,\bar{x}(t)} \qquad (5.8)$$

$$z(t) = |z(t)|\, e^{i\phi(t)} \qquad \text{(5.9)}$$

where $z(t)$ represents an analytical signal, its magnitude $|z(t)|$ is known as the envelope signal;

$\tilde{x}(t)$ represents the Hilbert transform of $x(t)$; and,

$\phi(t)$ represents an instantaneous phase signal.

$$Z(\omega) = \begin{cases} 2X(\omega) & ; \quad \omega > 0 \\ 0 & ; \quad \omega < 0 \end{cases} \qquad \text{(5.10)}$$

where $Z(\omega)$ and $X(\omega)$ represent the Fourier transform of $z(t)$ and $x(t)$ respectively.

It was observed from Fig. 5.7 that the response level at the end of the time record was below that of the noise floor. Therefore, a procedure similar to that adopted for the pressure signals has been applied to the strain records to determine the cut off frequency, f_c, of the digital filter which was established to be 6 kHz.

The design of the low pass linear phase finite impulse response (FIR) digital filter was carried out using the window method [87, 88] . The window technique starts by assuming the desired frequency response of the filter,

$$H_d(\theta) = \begin{cases} 1 & ; \quad |\theta| \le \theta_c \\ 0 & ; \quad \text{otherwise} \end{cases} \qquad \text{(5.11)}$$

where $\theta = 2\pi \left[\dfrac{\omega}{\omega_s}\right]$;

$\theta_c = 2\pi \left[\dfrac{\omega_c}{\omega_s}\right]$;

ω_s represents the sampling frequency in rads/s; and,

ω_c represents the cut off frequency in rads/s.

The corresponding impulse response can be obtained by evaluating the following series :

$$h_d(k) = \frac{2}{\theta_c}\sin(k\theta_c) \quad ; k = 0, 1, 2, \ldots\ldots, \infty \qquad \text{(5.12)}$$

In specifying the number of filter coefficients N the length of the filter becomes finite and hence its impulse response is approximated as follows :

$$h_d(k) \approx h_a(k) = \frac{2}{\theta_c}\sin(k\theta_c) \qquad ; k = 0, 1, 2, \ldots\ldots, N-1 \quad \ldots\ldots\ldots\ldots \quad (5.13)$$

Truncation of terms involved in the above series is equivalent to multiplying the infinite $h_d(k)$ by a rectangular window which results in oscillations or ripples in both the passband and stopband of the filter's frequency response. These oscillations are known as the "**GIBBS**" phenomenon. It is known that lengthening the filter, by increasing the number of its coefficients, results in faster ripples but no reduction in their amplitudes. To alleviate the ringing effect a window with tapered edges (decaying to zero gradually) should be used instead of uniform weighting.

In the current study, the length of the digital filters depended on the number of samples forming a digital signal. For pressure and strain records the length was 2049 and 4097 respectively. Once the cut off frequency and length of the low pass digital filter were determined it was possible to construct it using DADISP as follows :

1. The truncated form of the filter's impulse response is generated at discrete times.
2. The above function is multiplied by a given window (rectangular, Hanning, Hamming, Kaiser, etc. . . . .) to obtain the approximate impulse response, $h_a(k)$, of the desired FIR low pass linear phase filter.

Then, digital filtering was performed by multiplying the filter's frequency response by the DFT of the signal under consideration. Then an IDFT was carried out to acquire the filtered discrete time signal.

A comparison between different FIR low pass filters can be seen in Fig. 5.8. In the current analysis, the Kaiser window was utilised in the filtering process of both the pressure and strain signals because of the good characteristics its frequency response possessed, less rippling in the passband and stopband as well as lower side lobes. Figs 5.9 and 5.10 show the effect of digital filtering on a sample of a pressure and a strain record respectively.

5.4.1.7 Analysis of pressure records— When viewing the pressure peaks of individual measurements for a given gauge some variation was observed. Such scatter of the data suggested dissimilarity in the detonators used resulting from either different densities of materials composing the explosive charge, different length to diameter ratios or both.

The average filtered pressure records can be seen in Fig. 5.11 for the various gauges. It is worth mentioning that the pressure pulses of gauges 2 and 3 were measured in the same vertical plane below and above the cylindrical charge, the axis of which was in a horizontal plane and pointing towards the target position, while the shots were being fired (see Fig. 5.2 and 5.4).

Observing Fig. 5.11 it was noticed that all pulse shapes possessed more than one peak with the first having the maximum value of pressure and the rest on a decreasing level. However, pulses of pressure gauges 2 and 3 had their second peak absorbed by the first.

In general, as the pressure gauge was positioned further from the explosive charge, the duration of the shock wave pulse was longer.

The miniature tourmaline pressure gauge on trial appeared to perform satisfactorily in measuring the peak of the pulse impinging the test structure but failed to trace the rest of the pulse. This can be explained by splitting the pressure surrounding the structure into the following components :

1. Incident pressure (p_I) is that which would occur in the absence of the target.
2. Reflected pressure (p_R) is that which would occur if the target represented a perfectly rigid boundary.
3. Radiated pressure (p_r) is the remaining component of the pressure field and is dependent on the surface motions of the submerged structure.

The scattered pressure (p_s) is defined by the following formula :

$$p_s = p_R + p_r \quad \text{.....} \quad (5.14)$$

Initially, when the shock wave struck the Echinodome prototype, the miniature tourmaline pressure gauge was measuring the incident pressure p_i , but at later times the scattered pressure from the structure decreased the pressure magnitudes. This explanation was confirmed by observing the relevant pressure pulse for pressure gauge 8; a correct measuring of the peak pressure, p_m, for the shock wave followed by an uncharacteristic rapid decay.

In many cases of structural damage, the effectiveness of shock wave pulse depends on either of the following three parameters :

1. p_m
2. Impulse per unit area given by

$$I = \int_0^t [p(t) - p_w]dt \quad \text{.....} \quad (5.15)$$

where $p(t)$ represents the total pressure as a function of time; and,

p_w represents the hydrostatic pressure.

3. Energy flux density given by

$$E_f = \frac{1}{\rho c}\int_0^t [p(t) - p_w]^2 dt \quad \text{.....} \quad (5.16)$$

where c represents the shock wave speed underwater; and,

ρ represents the mass density of the surrounding water medium.

Therefore, it becomes important to study the characteristics of a shock pulse for a given charge type.

The filtered pressure pulses depicted in Fig. 5.11 indicate that the pressure values did not reach zero ($p(t) = p_w$) by the end of each record and for Eqns (5.15) and (5.16) to converge to a limiting value a very long time record was necessary which was considered time consuming. In most cases, integration is performed over a time span including the initial pressure pulse with its main features until the pressure values are very small when compared with the initial peak (p_m) which is considered to be a reasonable approximation.

Cole in his book [82] suggested that the characteristics of shock wave results for a particular explosive can be represented using power laws as follows :

$$p_m = k\left[\frac{W^{1/3}}{R}\right]^{\alpha} \quad \text{.....} \quad (5.17)$$

$$I = l W^{1/3} \left[\frac{W^{1/3}}{R} \right]^{\beta} \quad \text{.....} \quad (5.18)$$

$$E_f = m W^{1/3} \left[\frac{W^{1/3}}{R} \right]^{\gamma} \quad \text{.....} \quad (5.19)$$

The above laws can be regarded as fair approximations depending on the range of $(W^{1/3}/R)$. Using the experimentally measured pressure records a linear regression analysis was carried out to determine the constants k, l, m and α, β, γ for detonator 79 excluding experimental observations of pressure gauges 2, 3 and 8. (see Fig. 5.12). The resulting characteristic formulae were found to be as follows :

$$p_m = 73.20 \left[\frac{W^{1/3}}{R} \right]^{1.36} \quad \text{.....} \quad (5.20)$$

$$I = 6124.18 \times W^{1/3} \left[\frac{W^{1/3}}{R} \right]^{0.92} \quad \text{.....} \quad (5.21)$$

$$E_f = 189236.45 \times W^{1/3} \left[\frac{W^{1/3}}{R} \right]^{2.41} \quad \text{.....} \quad (5.22)$$

where p_m is in units of MPa ;

W is in units of kg ;

R is in units of m ;

I is in units of $Nm^{-2}s$; and,

E_f is in units of Nm^{-1} .

Shock wave pulse properties (p_m, I and E_f) were determined utilising the above equations (named theor. 1) as well as empirical formulae [89] (named theor. 2) derived from experimental measurements of bigger charges at various stand off distances. Table 5.1 contains a comparison between the preceding predictions and the current average experimental observations.

PRESSURE GAUGE NUMBER	PEAK PRESSURE (MPa)			IMPULSE ($Nm^{-2}s$)			ENERGY FLUX DENSITY (Nm^{-1})		
	TEST	THEOR.1	THEOR.2	TEST	THEOR.1	THEOR.2	TEST	THEOR.1	THEOR.2
1	2.66	2.78	3.07	70.72	67.70	69.41	67.34	61.83	52.71
4	1.19	1.15	1.59	34.92	37.78	38.29	14.87	13.03	14.84
5	0.68	0.67	1.06	25.47	26.02	26.64	1.08	5.04	6.85
6	0.46	0.46	0.80	20.17	20.15	20.62	3.43	2.58	3.97
7	0.31	0.34	0.64	17.35	16.56	16.94	1.87	1.54	2.61

TABLE 5.1 — *COMPARISON BETWEEN AVERAGE EXPERIMENTAL OBSERVATIONS AND PREDICTIONS OF SHOCK WAVE PULSE CHARACTERISTICS ALONG THE AXIS OF DETONATOR 79*

The above table indicated that Eqns (5.20) → (5.22) were suitable for small charges while other empirical formulae [89] were best suited for larger charges.

In conclusion, empirical formulae are useful in predicting peak pressures of shock waves which enable experimentalists to optimise the dynamic range of the instrumentation used. Additionally, when designing the size of an explosive charge, to be fired in front of a structure, predictions of pressure pulse characteristics assist in avoiding structural damage which after all may be necessary.

5.4.1.8 Analysis of strain records— After the averaging and filtering of strain records the results for each rosette were processed to produce the principal stresses (σ_1, σ_2) and equivalent stresses (σ_e) which can be seen in Figs 5.13(a, b) and 5.14 respectively.

The experimental principal angle distribution versus time (not shown) was uneven which meant that at a specific point on the shell's surface, the principal stresses are likely to vary their direction unsystematically between $0^\circ \rightarrow 180^\circ$ and not be constant at any time.

From the above stress figures it was noticed that the maximum stresses were experienced by the nearest point on the shell's surface to the explosive charge. The figures indicated that the stresses at $\phi = 30^\circ$, $\phi = 60^\circ$ were greater than at $\phi = 120^\circ$, $\phi = 150^\circ$ and could be attributed to the higher rate of curvature change in the bottom part of the shell's meridional profile, which made the structure appear more stiff in that region. Beneath $\phi = 90^\circ$ the stresses were on the increase on approaching the base of the shell, thus conforming with an earlier conclusion (vide Chapter 2) that the lower region of an Echinodome shell was a critical zone for design.

In all cases, the maximum, minimum and equivalent stresses were much less ($\approx$ 5 percent) than the maximum strength of the test structure material (55.4 MPa). It can be concluded that the pressure pulse, generated using 1 gm of explosive charge (detonator 79) and located approximately 5.0 m away from the test structure, was too low to invoke the structure's geometrical non–linearity to a degree which could cause serious inaccuracies if ignored in the theoretical analysis. In general, in Figs 13(a and b), the principal stresses tended to be on one side of the abscissa because they were the most positive and negative stresses respectively.

For all stress records the magnitudes appeared initially to be decaying but at later times another peak with a relatively high level evolved. This was caused by the bubble secondary pulse as will be shown in the following subsection.

On examining the strain records of gauges bonded on the steel links (part of the tension leg) the magnitudes were found to be very low and highly contaminated with electrical noise. This was because of the considerably large cross sections of the link elements.

5.4.1.9 Secondary pulses— As was shown earlier in Fig. 5.1 for a 1 gm explosive charge (detonator 79) a secondary pulse occurred 27 ms after the initial peak. This corresponded to the second peak recorded in the strain–time histories. The time difference between both peaks could be determined from either the pressure records as in Fig. 5.1 or using the magnitude functions for a strain record as in Fig. 5.7 .

Typical bubble periods were established to be approximately equal to 27 ms and 45 ms for 1 gm and 4 gm explosive charges respectively. Table 5.2 contains a comparison between characteristics of both the shock wave and bubble pulses.

PRESSURE GAUGE NUMBER	CHARGE SIZE (gm)	PEAK PRESSURE (MPa)		IMPULSE ($Nm^{-2}s$)		ENERGY FLUX DENSITY (Nm^{-1})	
		SHOCK WAVE PULSE	BUBBLE PULSE	SHOCK WAVE PULSE	BUBBLE PULSE	SHOCK WAVE PULSE	BUBBLE PULSE
1	1	2.80	0.73	70.39	189.80	68.27	39.88
	4	5.08	0.99	149.15	———	265.36	111.52
2	1	1.78	0.54	45.43	164.98	32.00	29.80
	4	3.72	0.70	100.71	242.49	139.68	79.47

TABLE 5.2 — *COMPARISON BETWEEN SHOCK WAVE AND BUBBLE PULSE CHARACTERISTICS*

From the above table it can be observed that although the peak pressure of the secondary pulse was much less than that of the shock wave, the area under the pressure–time curve (impulse per unit area) was more than double. A clear indication of the importance of considering the effects of the bubble pulse in structural damage.

5.4.1.10 Surface effects— It was concluded earlier that the miniature tourmaline pressure gauge performed commendably in measuring peak pressures and hence it was used in determining the effects of free and rigid boundaries on the shock wave. It was established from the pressure records of P.G.8 and other pressure gauges that at both surfaces, free and rigid, the shock wave was reflected fully with negative and positive magnitudes respectively.

By knowing the dimensions of the tank together with the pressure gauge positions and by determining the time delay of reflected signals the average shock wave speed (c) was estimated to be equal to 1418 m/s.

5.4.2 Theoretical Approach

The PAFEC–DOLPHIN acoustics subsystem was used to study the fluid–structure interaction phenomenon between the floating submerged test structure and the surrounding medium (water). The software is capable of modelling finite, infinite, compressible and incompressible fluid regions but does not take account of fluid flow viscosity and cavitation effects.

5.4.2.1 Problem idealisation— In the current investigation the Echinodome prototype was assumed to be surrounded by an infinite fluid region. Because of symmetry only half the structure and the infinite medium were necessary to model. Idealisation of the test structure was carried out using conventional semi–loof shell elements (as was described in Chapter 2). Each meridional segment subtended a circumferential angle of 30^{o} and was discretised into 20 elements (one triangular and 19 quadrilateral) along the profile. While the fluid region was simulated employing a single boundary element made up of triangular and quadrilateral patches, forming a closed surface coinciding with the wet surface of the structure. This meant that the flat base of the prototype had to be included in the analysis.

In practice, the base was composed of two materials, a circular nominally 2.75 mm thick GRP base having a diameter of 170 mm and a square 19 mm thick tufnol plate with 200 mm linear dimensions. However, due to the enormous memory requirements of the boundary element technique a single set of six triangular semi–loof shell elements was used to model half a 19 mm thick circular base with a 170 mm diameter. An additional six triangular patch elements were coupled with the previous structural elements to form a complete surface together with the plane of symmetry. The existing extra material (tufnol) making up the rest of the square base was modelled by increasing the density of the base material in the numerical analysis (see Table 5.3).

MATERIAL PROPERTIES	GRP	TUFNOL	BASE MATERIAL USED IN THEORETICAL ANALYSIS
E (MPa)	8800	13200	13200
ν	0.36	0.284	0.284
ρ (kg/m^3)	1100	1360	3350

TABLE 5.3 — *COMPARISON BETWEEN ACTUAL MATERIAL PROPERTIES AND THOSE ASSUMED IN THE THEORETICAL ANALYSIS FOR THE STRUCTURAL BASE*

It can be observed from the above table that the **E** and ν used in the current theoretical analysis were those characterising the tufnol material. The density, on the other hand, was deduced from a preliminary eigenvalue analysis described as follows.

Another finite element mesh modelling the whole structure was prepared with an accurate representation of the structural base, and the natural frequencies for the first eight modes were determined assuming the structure was in vacuo. Various densities were considered for the initial

approximate mesh and the corresponding eigenvalues for the structure in air were compared with those of the latter accurate mesh until both sets of results were virtually identical. The higher modes (post the first eight modes) were not considered in the preliminary analysis because their contribution to the dynamic response was considered small, based on an equivalent mass analysis (vide Chapter 4) and in any case variations between both sets of natural frequencies were bound to occur for higher modes due to the inherent approximations.

It is important to emphasise that the above approximation was necessary in order to avoid the use of the 3–D family elements (15 and 20 noded isoparametric wedge and brick elements respectively) in the modelling of the structural base which would have made an exceedingly large demand on the existing computer resources [§].

The finite element library of the PAFEC software comprised no cable elements to simulate the tension legs and therefore, linear spring elements were employed to model the supporting members having only axial stiffness. The disadvantage of using such elements was that their tensile properties were equal to their compressive counterparts which resulted in an inaccurate representation of the supporting conditions.

The size of the detonator and the stand off distance from the target were selected in the experimental tests so that minimal structural geometric non–linearity was invoked and this was because the only available software did not take into account either geometric or material non–linearities for dynamic load cases. Thus, any discrepancies occurring between experimental and theoretical results would be due to the following causes,

i. inaccurate modelling of the structural base;

ii. inaccurate representation of the true supporting conditions in the theoretical model; and,

iii. too few finite elements and boundary patches idealising the interaction between the structural and fluid regions.

A separate finite element analysis was carried out to determine the effect of the imposed hydrostatic pressure head, during the explosive experimental tests, on the Echinodome shape under the above supporting conditions but very small deformations were found to be experienced by the structure. Consequently, it was concluded that the degree of geometric non–linearity ensued by the static load would not affect its dynamic response to the explosive loading.

§ The requirements of the current job were 40 MB virtual memory, 14 MB physical memory and 45 MB disk space, consuming a total of 23 hours of CPU time on a VAX 6410 with a processing power of 7 mips.

The selected master degrees of freedom had an identical spatial distribution to those described in Chapter 3 and included as well all of the base's unrestrained translational degrees of freedom giving a total of 139 masters.

5.4.2.2 Analysis techniques— In the current analysis a boundary element formed of a total of 126 patches, covering the wet surface of the structural mesh, was used to model the surrounding infinite fluid medium. The patches were interconnected at 409 fluid nodes which were coincident with the structural nodes on the wet surface, each having a single pressure degree of freedom normal to the surface with its positive direction pointing from the infinite region to the finite region (out of the fluid into the structure). Unlike finite element techniques where assembled element matrices are stored in banded form because of their sparseness, the fluid matrices in the boundary element method are stored in full and this explains the current demand for considerably large computing resources.

The PAFEC–DOLPHIN software possessed three approximation techniques for the solution of the boundary element integrals involved in the analysis of an underwater structure excited by incident spherical pressure waves. The suitability of an approximation for a specific analysis was dependent on the compressibility of the surrounding medium and the domain in which the shock wave presure magnitudes were provided (time or frequency domains). The approximation methods were namely :

1. Virtual mass approximation (VMA)
2. DAA1
3. DAA2c

In the VMA the surrounding fluid is assumed to be incompressible and since the only effect of the fluid would be to increase the inertia of the submerged structure a fluid mass matrix is formulated and then added to the structural mass matrix. When undertaking such an analysis the fluid freedoms are eliminated and hence the problem size is greatly reduced and the analysis is made more efficient. The VMA is valid for long acoustic wavelengths ($\lambda_a = c/f$) when compared with the structural wavelength (λ_s), i.e. late stages of response or low frequency analysis ($\lambda_a >> \lambda_s$).

The DAA are differential equations for a simplified analysis of transient motions of a submerged structure. These approximations approach exactness in the limit of low and high motions ($\lambda_a >> \lambda_s$ and $\lambda_a << \lambda_s$) and effect a smooth transition in the intermediate frequency range. Hence, such approximations are applicable to complete response calculations. In addition, the general theory of the DAA takes the compressibility of the surrounding infinite medium into

account.

In PAFEC–DOLPHIN two formulations of the DAA existed. The DAA1 was suitable for transient shock analyses only, while the higher order approximation DAA2c was valid for both transient and sinusoidal response analysis. Although the DAA2c initially appears to be more computationally efficient for applying to a steady state vibration analysis, because of the frequency independency of the fluid matrices, it is generally accompanied by inherent inaccuracies at structural resonances and antiresonances. Moreover, because of the excited high frequencies, the long measured strain records and the small time step involved, the previous advantage was obliterated. Therefore, based on the above discussion and earlier made conclusions [81,90-92] the DAA1 was adopted in the current simulation due to the relatively short shock pulse duration (t_d = 200 μs) and a Δt of 1 μs was selected for the numerical integration of the structural and fluid equations.

5.4.2.3 Explosion sources— It was noted that the dynamic response of the Echinodome prototype would be influenced to a certain extent by the existence of both the rigid boundaries (side walls and base) of the tank and the free water surface. As described earlier (Section 5.3.4), a shock wave is reflected with positive pressure magnitudes if striking an infinitely rigid boundary, while a negative pressure wave would be reflected from a free surface. Therefore, the rigid boundaries and the free surface were modelled using multiple point sources. Because of the short response–time history to be taken into account in the current analysis (5 ms) only reflections from the side walls parallel to the plane of symmetry, the bottom of the tank and the water surface were considered and due to symmetry a total of four explosion point sources were declared to PAFEC–DOLPHIN (one original point source, and relative to it two positive and one negative image point sources — modelling the shock wave of the original explosion source, its reflection from the rigid boundaries of the base and one side wall, and the reflection from the free surface respectively).

In PAFEC–DOLPHIN the pressure magnitude of an incident wave varied with the inverse of the stand off distance from its source ($p_i \propto (1/R)$) but Eqn (5.20) indicated that the peak pressure of the shock wave pulse for detonator 79 was proportional to a higher power than unity ($p_m \propto (1/R)^{1.36}$). Consequently, it was necessary to compensate for such a difference in the pressure tables provided for the software. This was carried out by scaling the pressure magnitudes using a constant derived from Eqn (5.20) on the basis of the length of propagated distance.

Although in performing the above step the pressure field surrounding the structure was modelled more accurately, it was not possible to compensate for the variation in the decay rate of the shock pulse. As the shock wave spreads out from the source the duration of its pulse increases and hence part of the energy (or impulse) utilised in exciting the prototype during the

experimental tests was not represented in the theoretical analysis. The difficulty in simulating such an effect was due to the low pressure magnitudes involved and with the added complication that shock pulses emitted by cylindrical charges possessed multiple decay rates, it was not possible to derive an empirical formula. In addition, experimentally no pressure gauges were dedicated to measure the reflected shock wave pulses at a point where it would have struck the target or even measure the original pressure pulse at a distance equal to that which the reflected wave would have travelled.

5.4.3 Comparison Between Experimental and Theoretical Results

On viewing the experimental principal stresses in Figs 5.13(a and b), it was noted that an initial peak response occurred in the first 10 ms. Then at a much later time $t \approx 28$ ms another peak response was observed which was attributed to the energy released by the bubble pulse in a secondary stage of contraction. In adopting the DAA for the solution of the fluid–structure interaction the damping effect of the surrounding medium on the structure would be overestimated. Hence any late time response calculations would be overdamped and incorrect response magnitudes would be yielded. Because of this and due to local restrictions on the maximum CPU time permitted for a single job the time history for the acoustic analysis was limited to 5ms, (in PAFEC no restarts were possible during a transient response analysis).

A comparison between the predicted and measured dynamic response of the Echinodome prototype to the symmetric explosive load was carried out for the maximum, minimum and equivalent stresses (σ_1, σ_2 and σ_e). Graphic representation of the comparison is shown in Figs 5.15(a, b) and 5.16 for five positions ($\phi = 30^\circ$, 60°, 90°, 120° and 150°) on the nearest meridian to the explosive charge (meridian M1).

It can be noted that for the upper three locations ($\phi = 30^\circ$, 60° and 90°) the DAA was unsuccessful in predicting the correct magnitudes of the peak responses and their time of occurrence. As the response time progressed the theoretical stresses tended to zero which was an indication of the overestimation of the surrounding fluid damping effect by the DAA.

On the other hand, the peak stresses were greatly exaggerated in the early stages of response for the lower two positions on the shell ($\phi = 120^\circ$ and 150°). A higher frequency mode appeared to be superimposed to the dynamic stresses. This could be attributed to the fact that several time steps were necessary for the pressure wave to cross each element of the flat base which resulted in the increase of the total force applied to the structure in a discontinuous manner and hence artificially exciting a higher vibrational mode. Due to the high density characterising the material at that part of the structure the mode appeared to be more pronounced on approaching the base. The consequence was that, unlike experimental measurements, the acoustic analysis failed to

predict that the nearest point to the explosive source was to experience the maximum (most positive and most negative) stresses and instead considered the base to be the most critical part of the structure.

It was worrying as well to note that, along the same meridian, the peak stresses at corner nodes were approximately double those at midside nodes for the same semi–loof shell element (see Table 5.4). Similar behaviour evident in other parts of the structure suggested an inaccurate approach adopted for the transformation of the equivalent nodal forces from the incident pressure pulse.

ELEMENT NUMBER	NODE POSITION ON ELEMENT	NODE POSITION ON STRUCTURE		σ_1		σ_2	
		θ (Degs ^{o})	ϕ (Degs ^{o})	MAGNITUDE (MPa)	OCCURRENCE TIME (μs)	MAGNITUDE (MPa)	OCCURRENCE TIME (μs)
25	corner	0	28	1.19	32	-2.28	10
	midside	0	30	0.62	32	-1.28	10
	corner	0	32	0.85	32	-2.12	10
49	corner	0	58	0.57	22	-1.56	8
	midside	0	60	0.31	22	-0.78	8
	corner	0	62	0.60	22	-1.52	8
67	corner	0	85	0.99	20	-2.15	9
	midside	0	90	0.55	20	-0.83	9
	corner	0	95	0.87	20	-2.12	9
85	corner	0	114	1.08	37	-3.30	8
	midside	0	120	0.65	37	-1.45	8
	corner	0	126	1.63	37	-3.52	8
103	corner	0	147	2.51	15	-3.49	7
	midside	0	150	1.65	15	-2.13	7
	corner	0	153	2.57	15	-4.29	7

TABLE 5.4 — *COMPARISON BETWEEN PEAK STRESSES FROM AN ACOUSTIC ANALYSIS AT CORNER AND MIDSIDE NODES ON THE OUTER SURFACE OF SEMI–LOOF SHELL ELEMENTS*

In spite of the above observations which could be used to condemn the DAA technique and its current implementation it is encouraging to note that for most of the considered locations on the theoretical model the stresses were of identical type (compressive) during the early stages of the response. In addition, the discrepancies were not extremely large.

It can be concluded from the above results that the reasons for the disagreement between both predicted and measured dynamic responses (maximum and minimum principal stresses) were as follows,

i. inaccurate modelling of the structural base;

ii. inexact description of the pressure field surrounding the theoretical model; and,

iii. inaccurate incident pressure transformation to equivalent nodal forces.

5.5 CONCLUSIONS

The main aim of the earlier described explosion tests was to assess qualitatively the ability of the available PAFEC–DOLPHIN version to predict the dynamic structural response to blast pressure waves. The structure was simulated using conventional semi–loof shell elements and the surrounding infinite medium was modelled with a single boundary element. A DAA formulation was employed in the solution of the fluid–structure equations. The boundary element approach based on the use of the DAA appeared to be attractive as it allowed a large percentage of computational resources to be devoted for structural modelling, unlike fluid finite elements which would consume a larger percentage and would require the application of proper boundary conditions at an appropriate distance from the structure. Supported by experimental strain measurements and predicted responses the following conclusions were reached :

1. The theoretical results could be greatly improved by discretising the finite element model into a finer mesh and by remeshing the structural base to represent more accurately the prototype base.

2. Although the DAA can be considered an accurate scheme for the prediction of early time response it overestimates the fluid resistance to the structural oscillations and would not be useful in the prediction of intermediate and late time oscillatory type response (e.g. free vibration analysis) or in the application to dynamic stability problems because of its overstabilising effect.

3. The current PAFEC–DOLPHIN software should be reformed to do the following ,

- adopt a more accurate approach for the transformation of incident pressure to equivalent nodal forces;
- enable the input of blast overpressures as point sources if a VMA was to be adopted in an acoustic analysis;
- facilitate the output of incident pressure (p_i), reflected pressure (p_R), radiated pressure (p_r), scattered pressure (p_s) and total pressure (p_t) and forces at any specified instance for any point on the structure or in the fluid; and,
- provide cable elements for the simulation of tension leg members, i.e. uniaxial elements with no compressive strength.

4. If the above improved software was to be employed in the modelling of new experimental tests using the same prototype it would be advisable to observe the following recommendations during the experimental work ,
   - use of a spherical shaped explosive charge with well defined characteristics (p_m, decay rate, I and E_f);
   - site where the experiments are to be carried out should have no proximate boundaries (minimum time delay between incident and reflected shock waves must be greater than 250 ms);
   - explosive source should be located at an appropriate distance from the structure to avoid exciting it with strong shock waves or pressure pulses containing large amounts of energy which might invoke the structural geometrical non–linearity; and,
   - it would be useful to mount several miniature tourmaline pressure gauges on the prototype's surface in addition to response measuring gauges, e.g. accelerometers and strain gauges.

It is clear from the above conclusions than an acoustic analysis would be relevant for linear shock analysis problems only. In the design stages of a full size underwater Echinodome vessel, with the purpose of storing a hazardous liquid, structural stability against strong shock waves would have to be investigated. An acoustic fluid model would be incorrect as it would yield a reflected pressure of only twice the incident pressure.

Therefore, it would be necessary to employ a numerical technique in which the non–linear terms of both the structure and fluid models are retained [93] and the coupling boundary conditions at the fluid–structure interface are required to accommodate the possibility of the cavitation phenomenon occurring. Initially, a static buckling analysis would be performed and if a limit point (i.e. a zero stiffness point) existed in the load–deflection curve then the dynamic stability of the

underwater structure when subjected to shock waves would have to be investigated thoroughly.

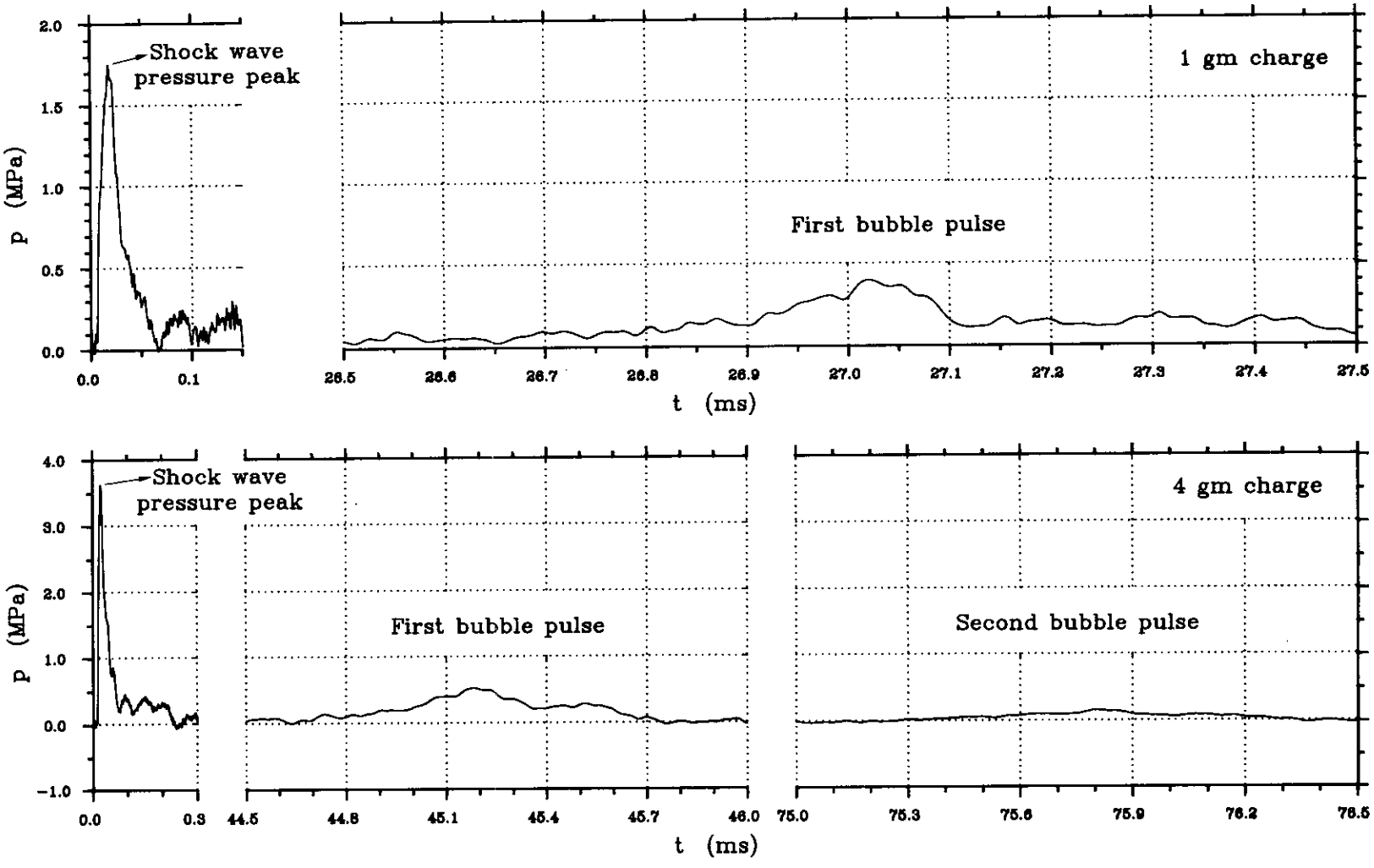

FIG. 5.1–OFF SIDE PRESSURE TIME HISTORY 1.535m AWAY FROM CYLINDRICAL CHARGES OF VARIOUS MASS (DETONATOR NO.79)

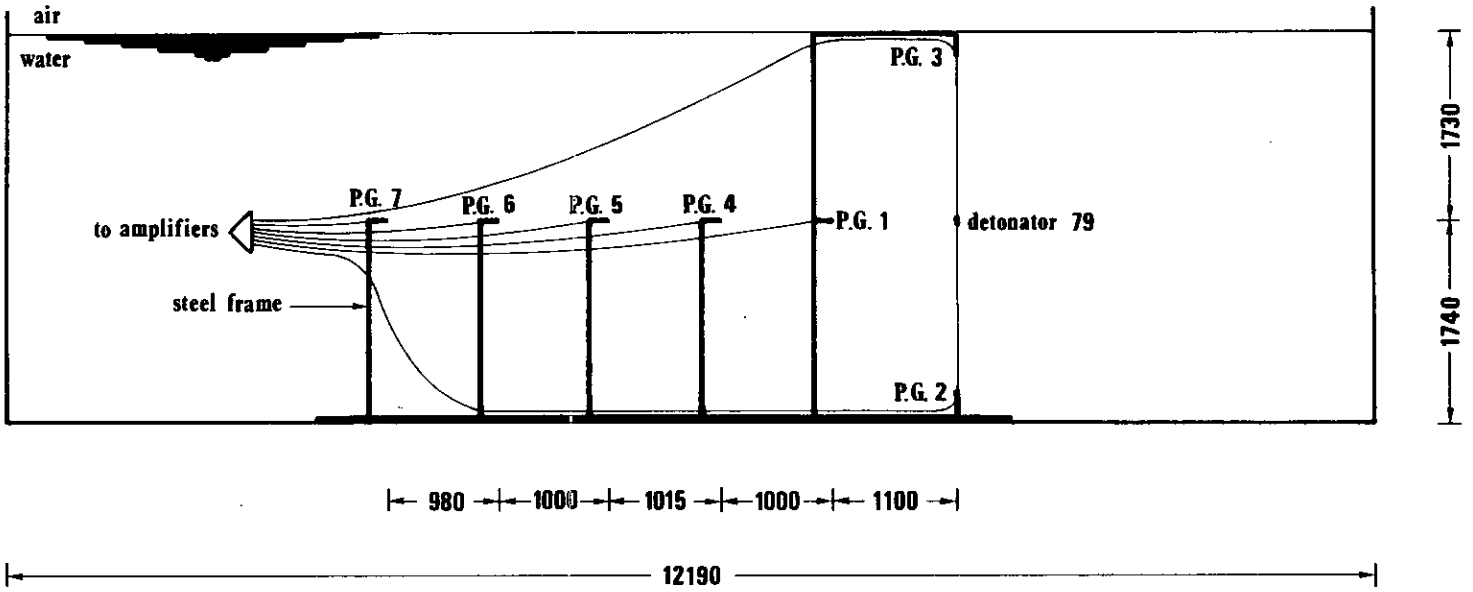

(dimensions in mm)

FIG. 5.2–ARRANGEMENT OF PRESSURE GAUGES FOR UNDERWATER FREE FIELD EXPLOSION TESTS

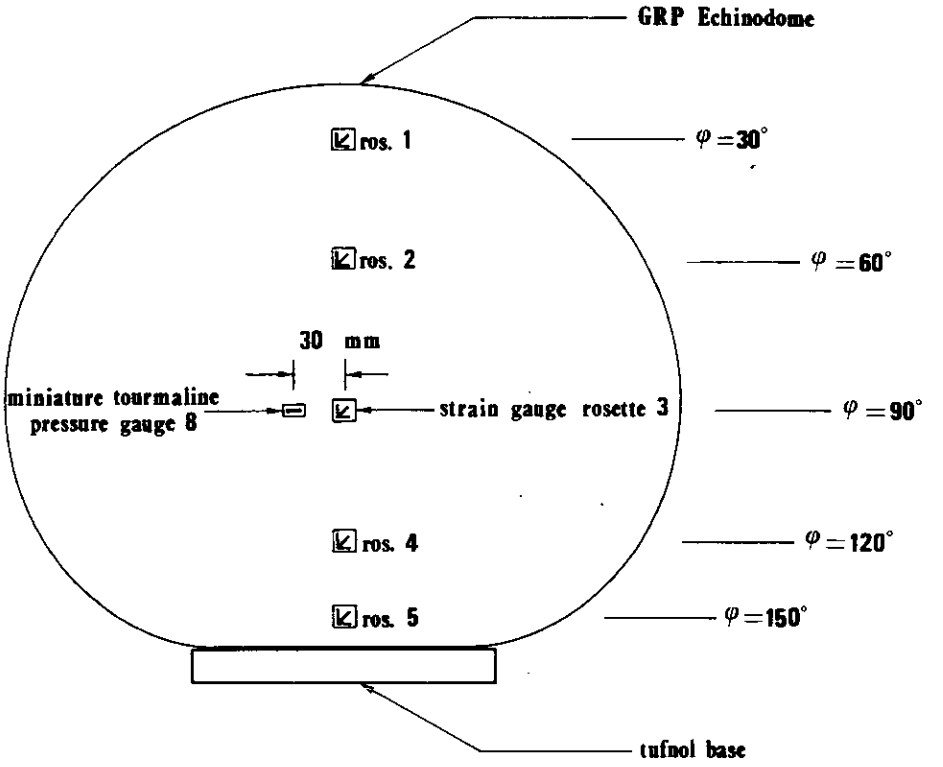

FIG. 5.3–DISPOSITION OF MINIATURE TOURMALINE PRESSURE GAUGE AND STRAIN GAUGE ROSETTES ON SHELL SURFACE

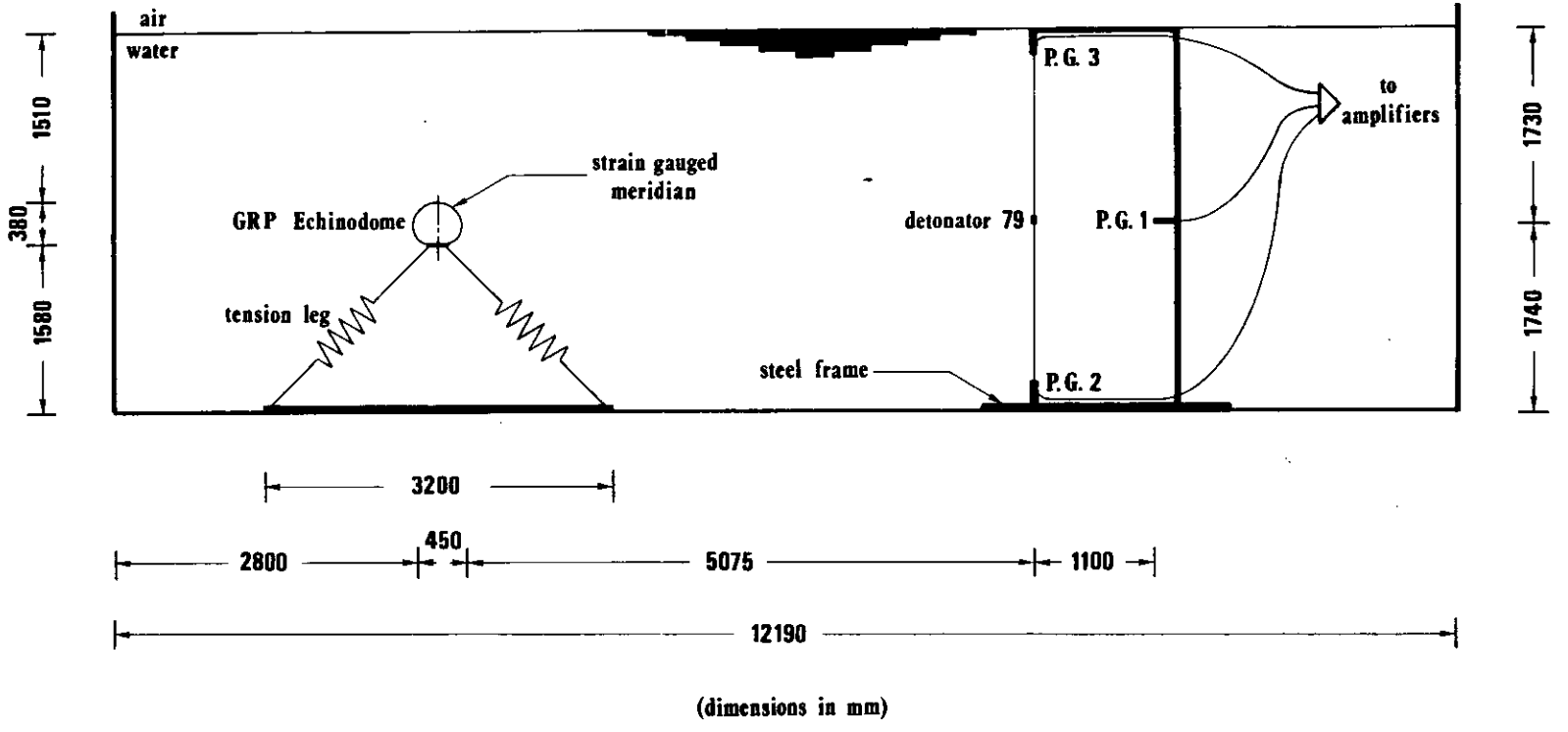

FIG. 5.4–PROTOTYPE LOCATION IN WATER TANK FOR UNDERWATER EXPLOSION TESTS

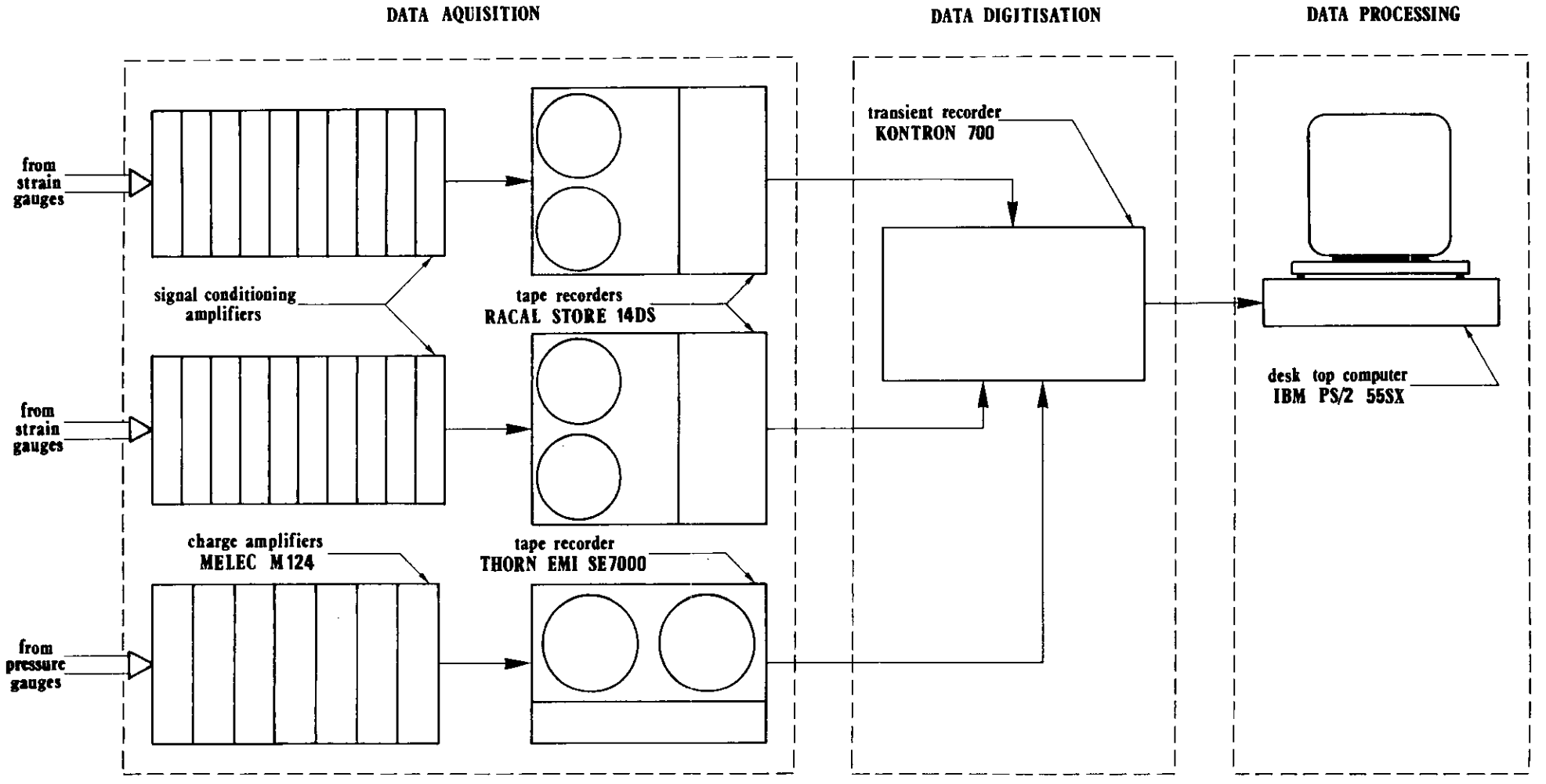

FIG. 5.5–DATA AQUISITION AND ANALYSIS INSTRUMENTATION USED IN UNDERWATER EXPLOSION TESTS

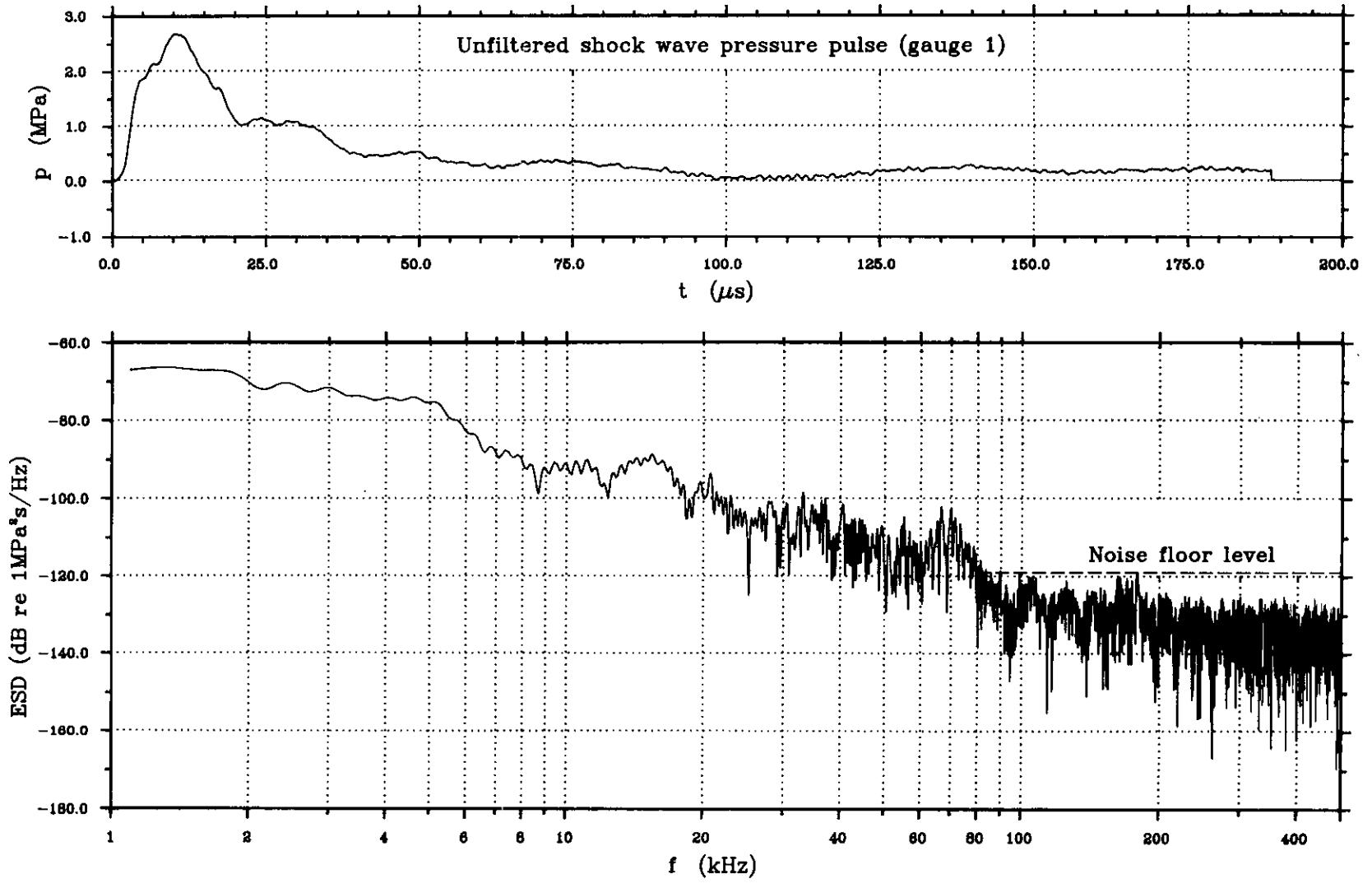

FIG. 5.6–ENERGY SPECTRAL DENSITY OF SHOCK WAVE PRESSURE PULSE MEASURED BY GAUGE 1

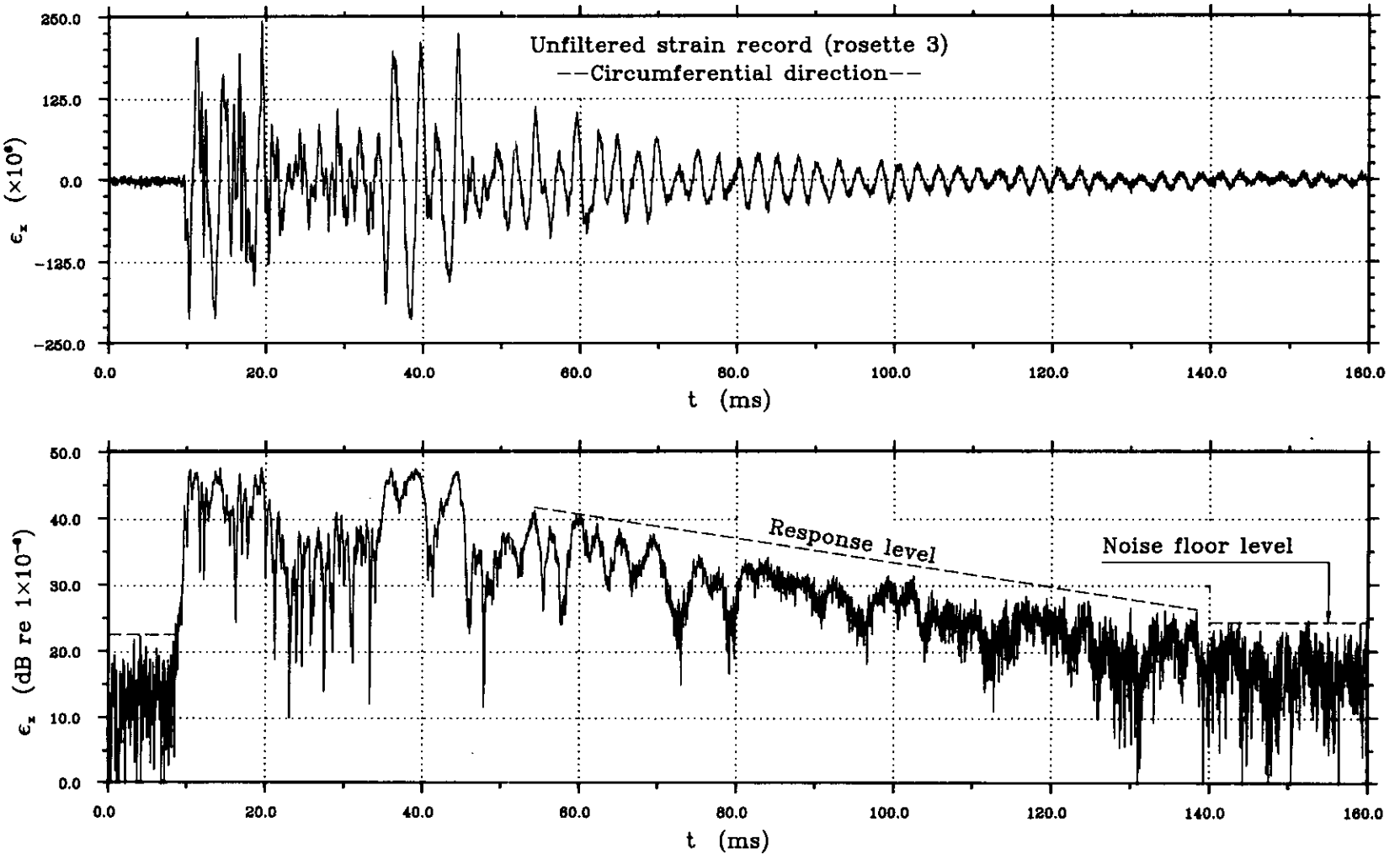

FIG. 5.7–MAGNITUDE FUNCTION OF A TYPICAL STRAIN RECORD (ROSETTE 3) --CIRCUMFERENTIAL DIRECTION--

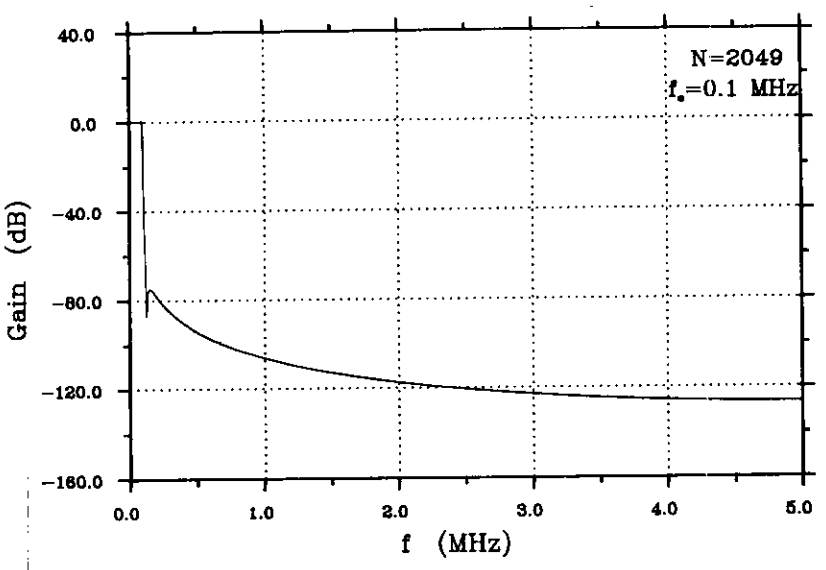

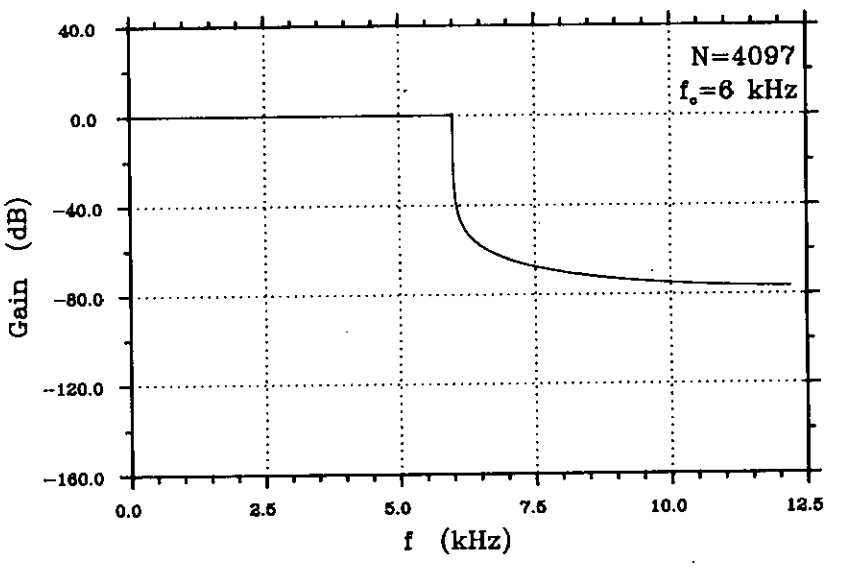

Lowpass FIR filters designed with a rectangular window

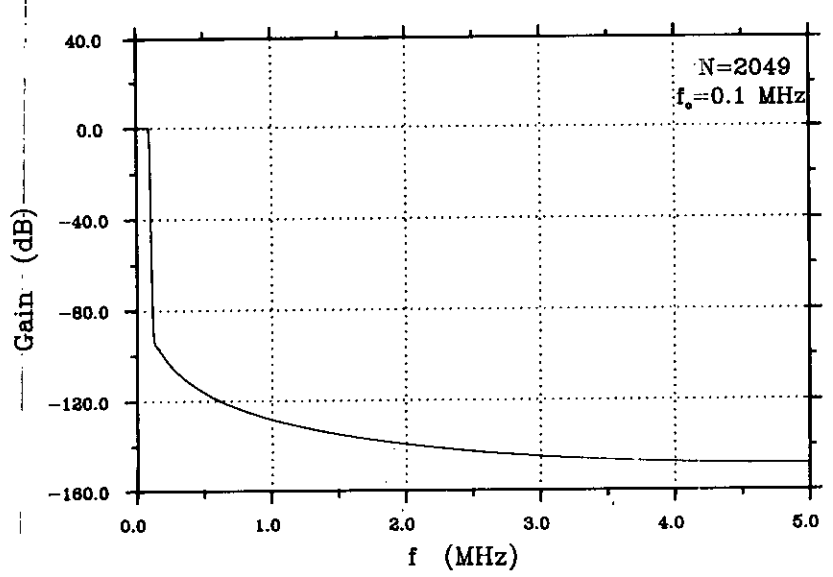

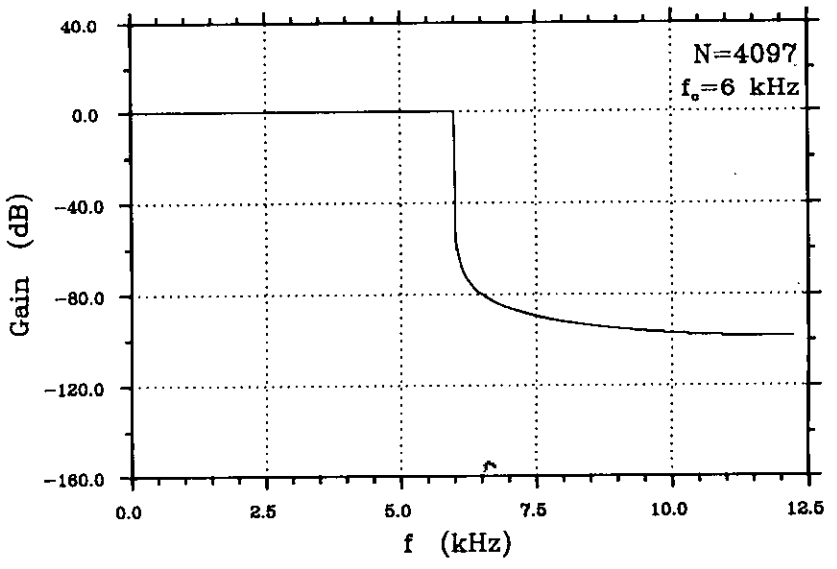

Lowpass FIR filters designed with Hamming window

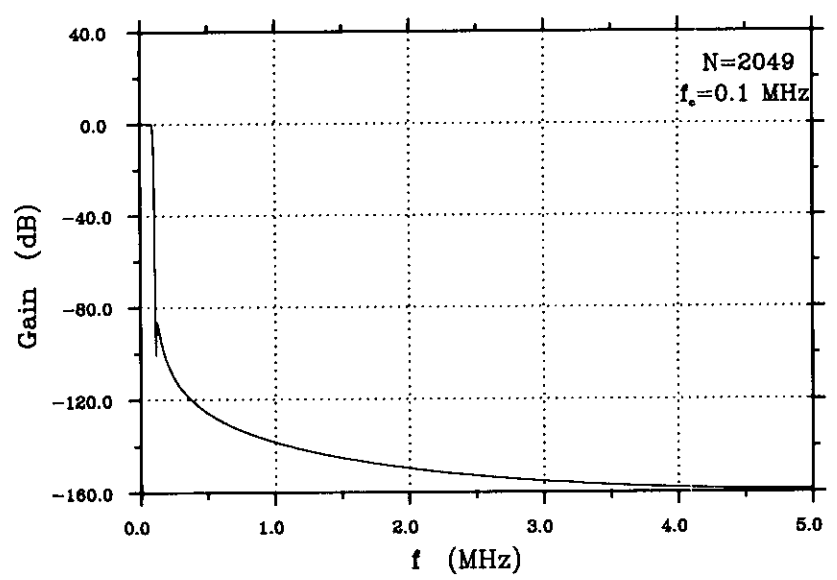

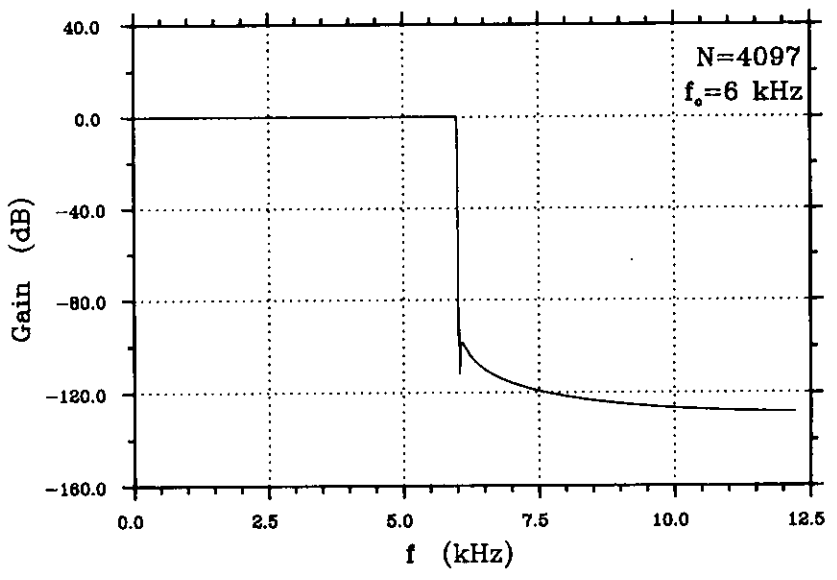

Lowpass FIR filters designed with Kaiser window

FIG. 5.8–FREQUENCY RESPONSES OF VARIOUS LOW PASS FIR DIGITAL FILTERS

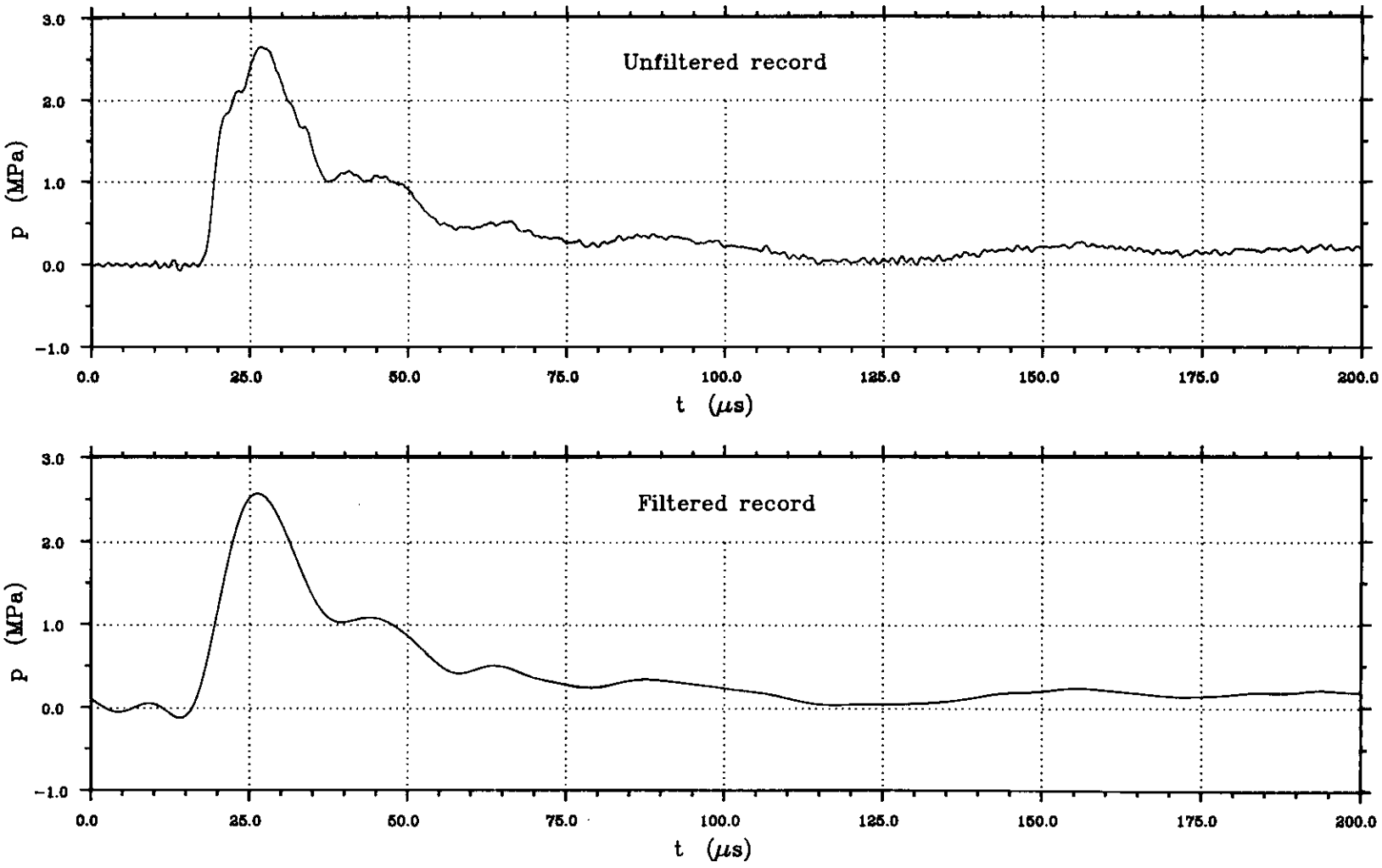

FIG. 5.9–EFFECT OF FILTERING ON A TYPICAL PRESSURE RECORD (GAUGE 1)

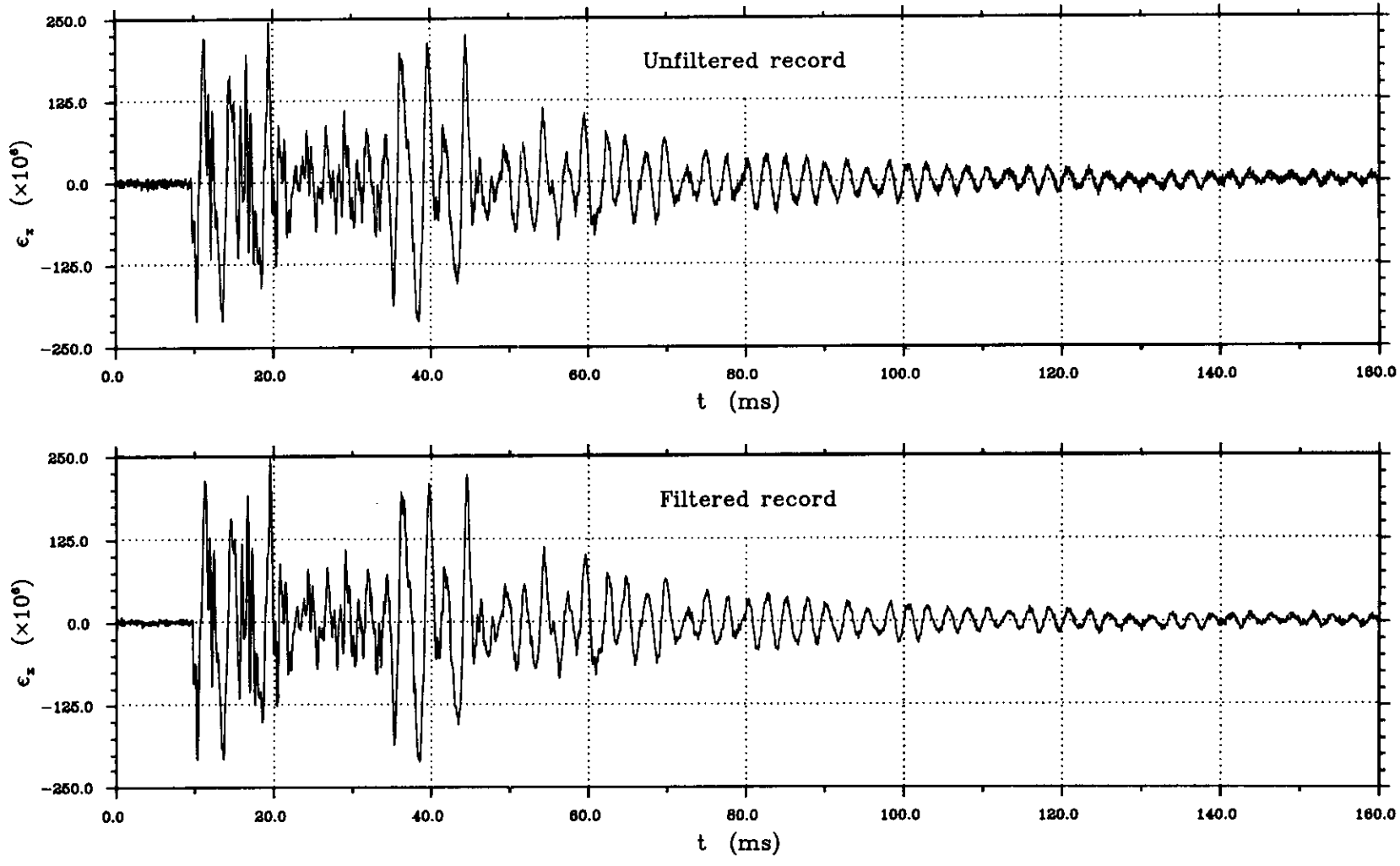

FIG. 5.10–EFFECT OF FILTERING ON A TYPICAL STRAIN RECORD (ROSETTE 3) --CIRCUMFERENTIAL DIRECTION--

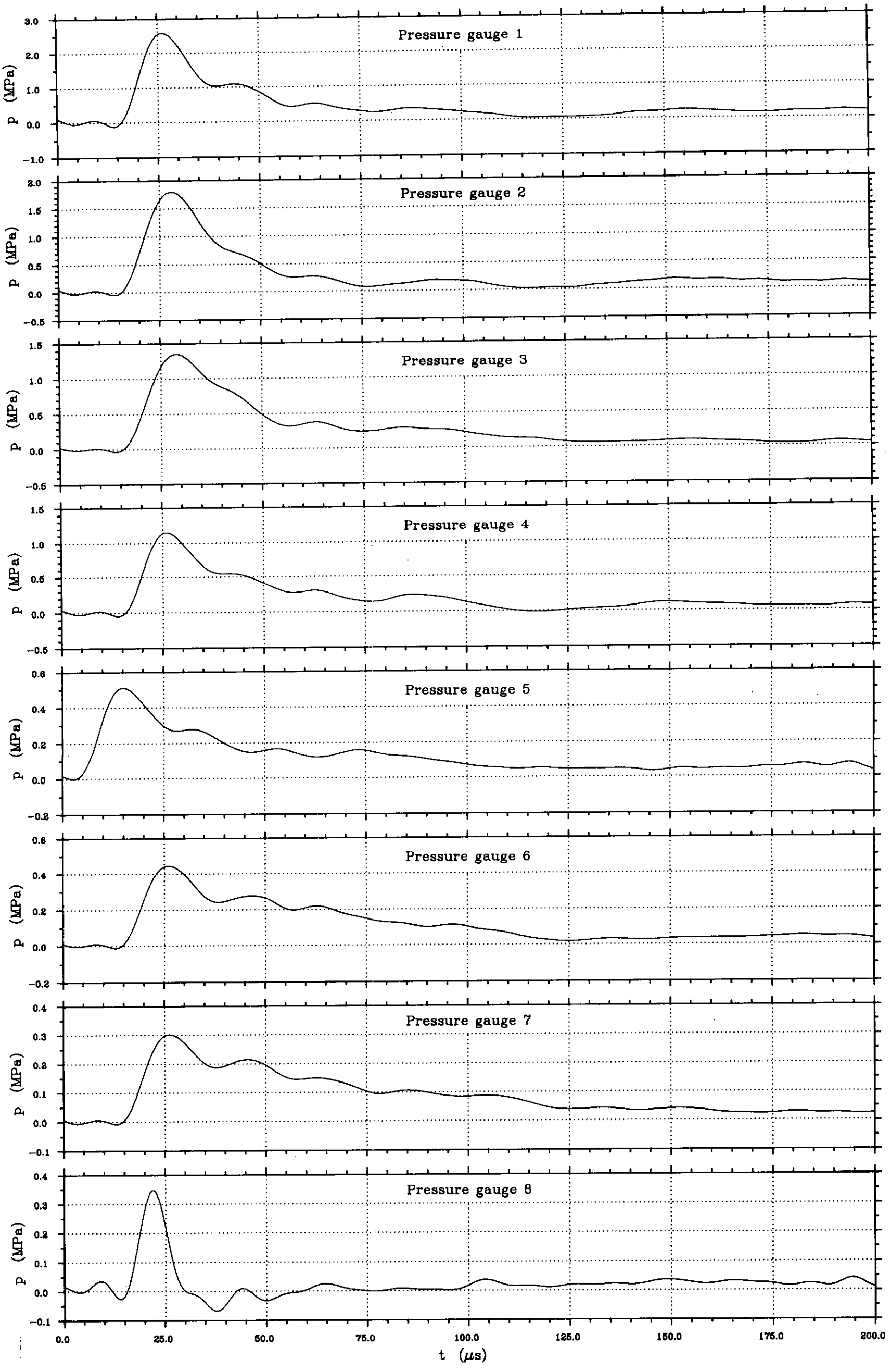

FIG. 5.11–AVERAGE FILTERED SHOCK WAVE PRESSURE PULSE MEASURED AT DIFFERENT DISTANCES

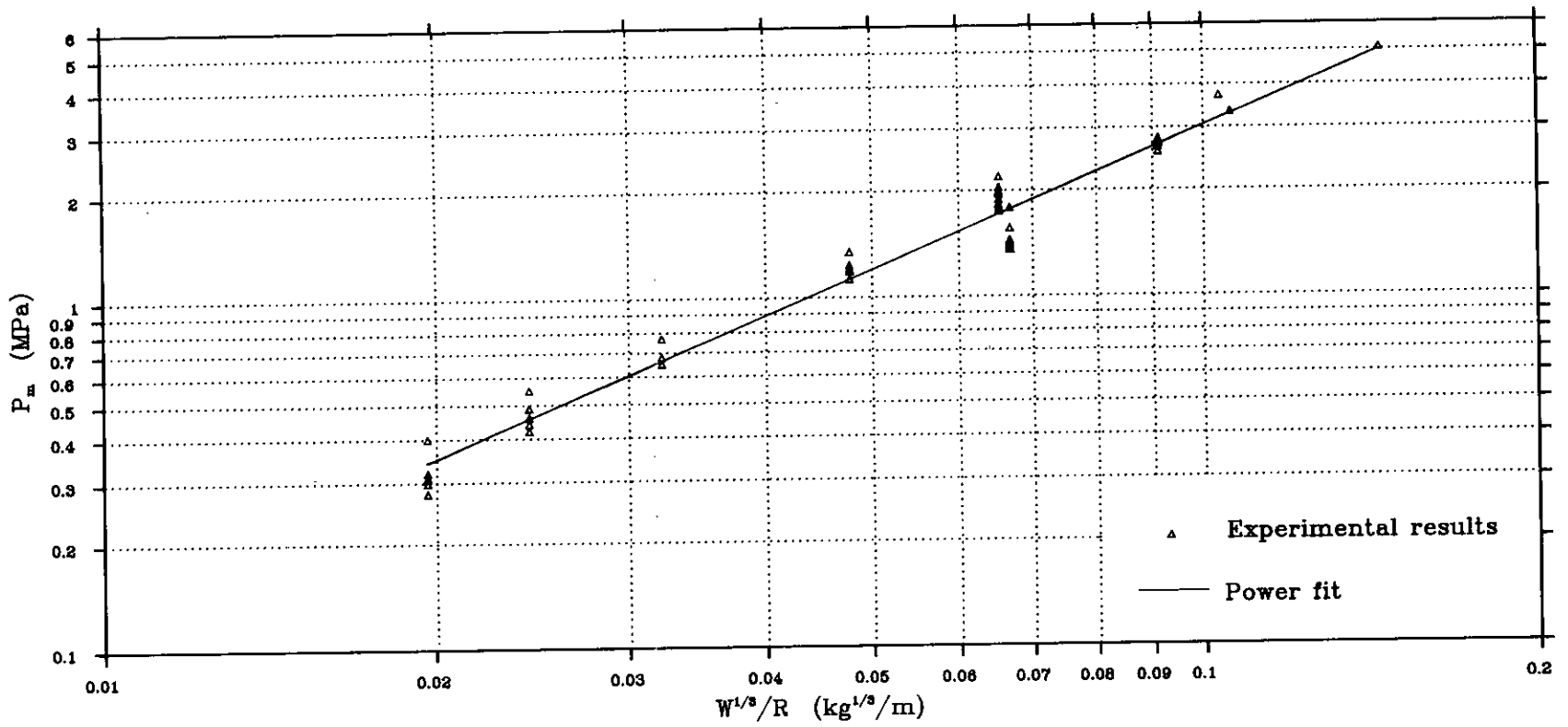

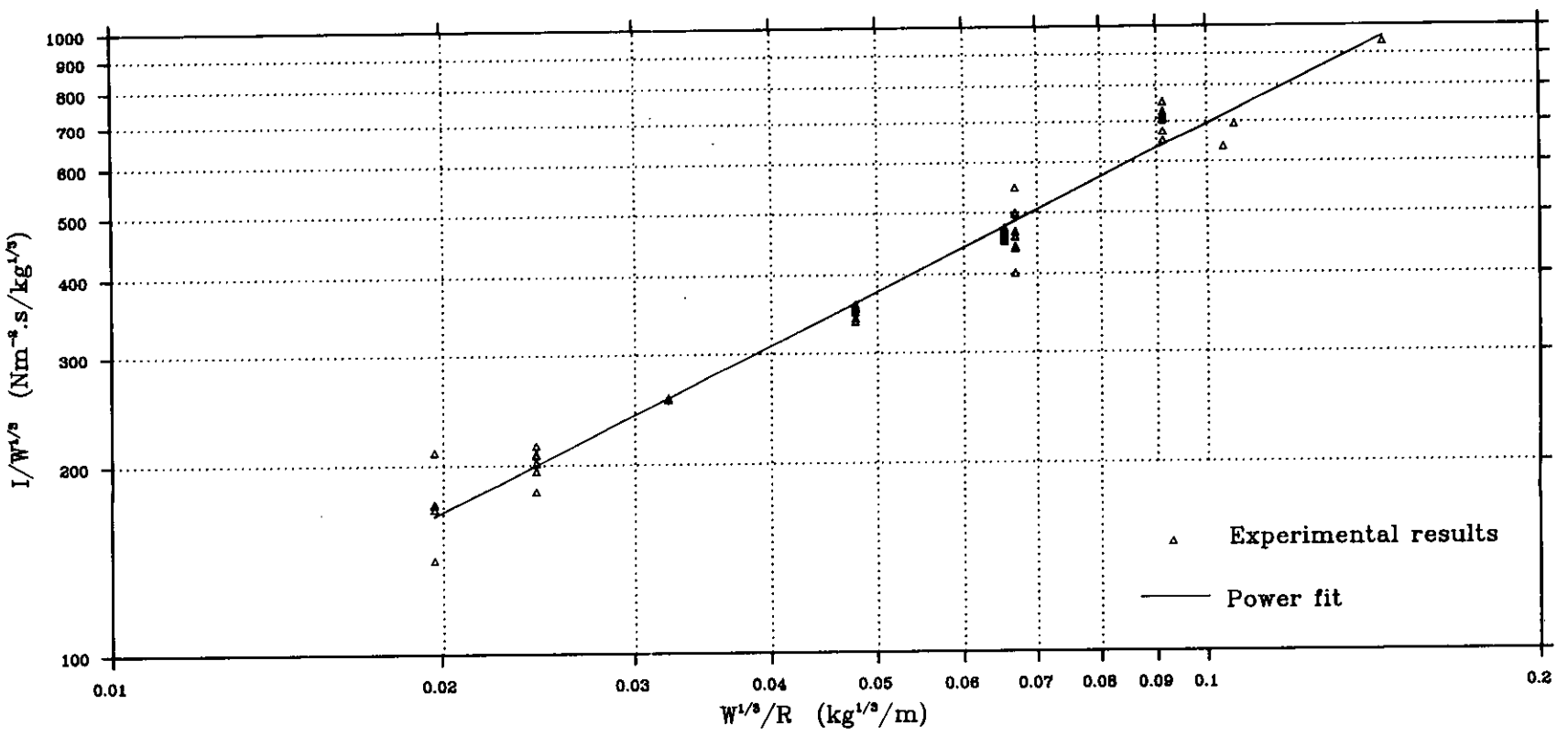

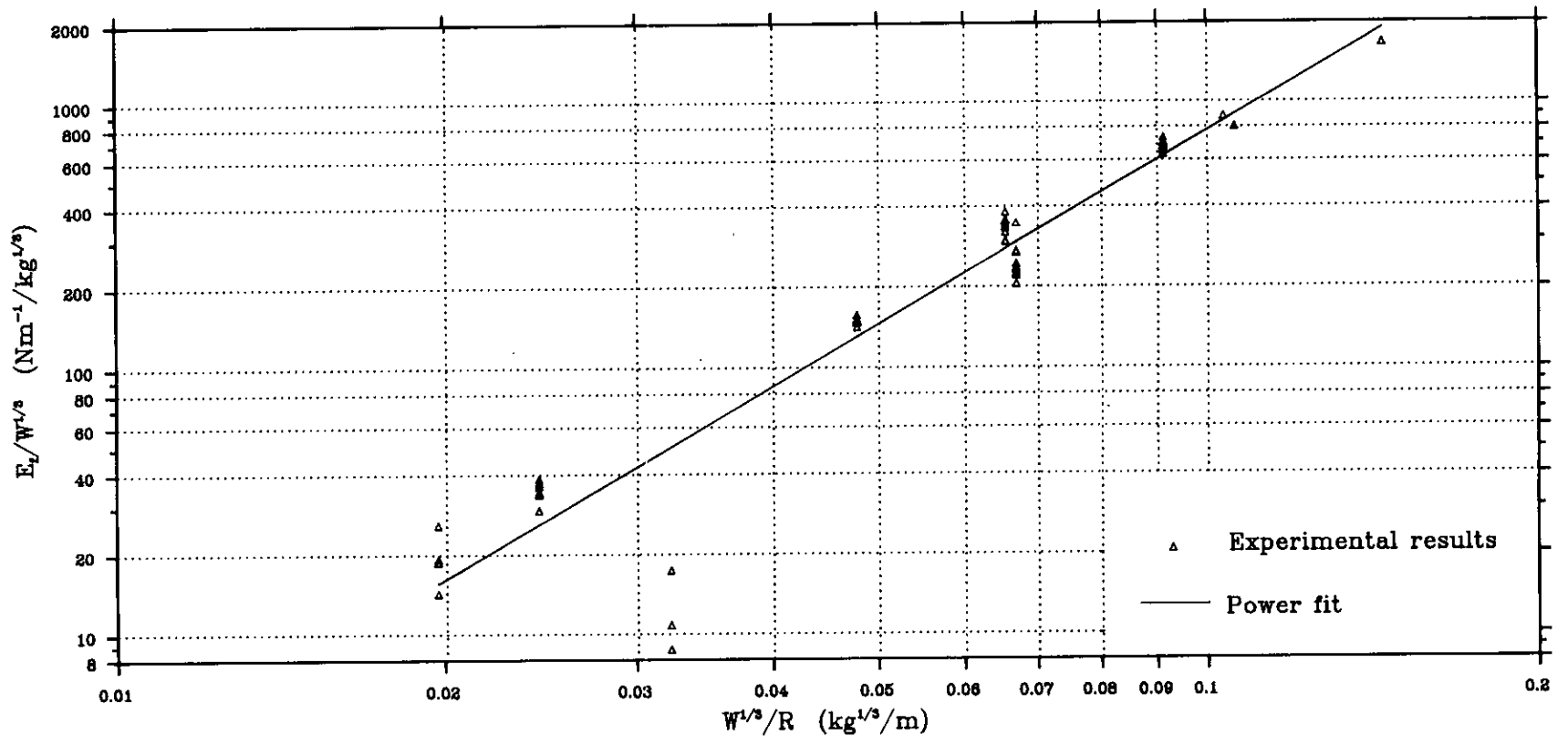

FIG. 5.12–FITTED MODELS OF SHOCK WAVE PRESSURE PULSE CHARACTERISTICS FOR DETONATOR 79

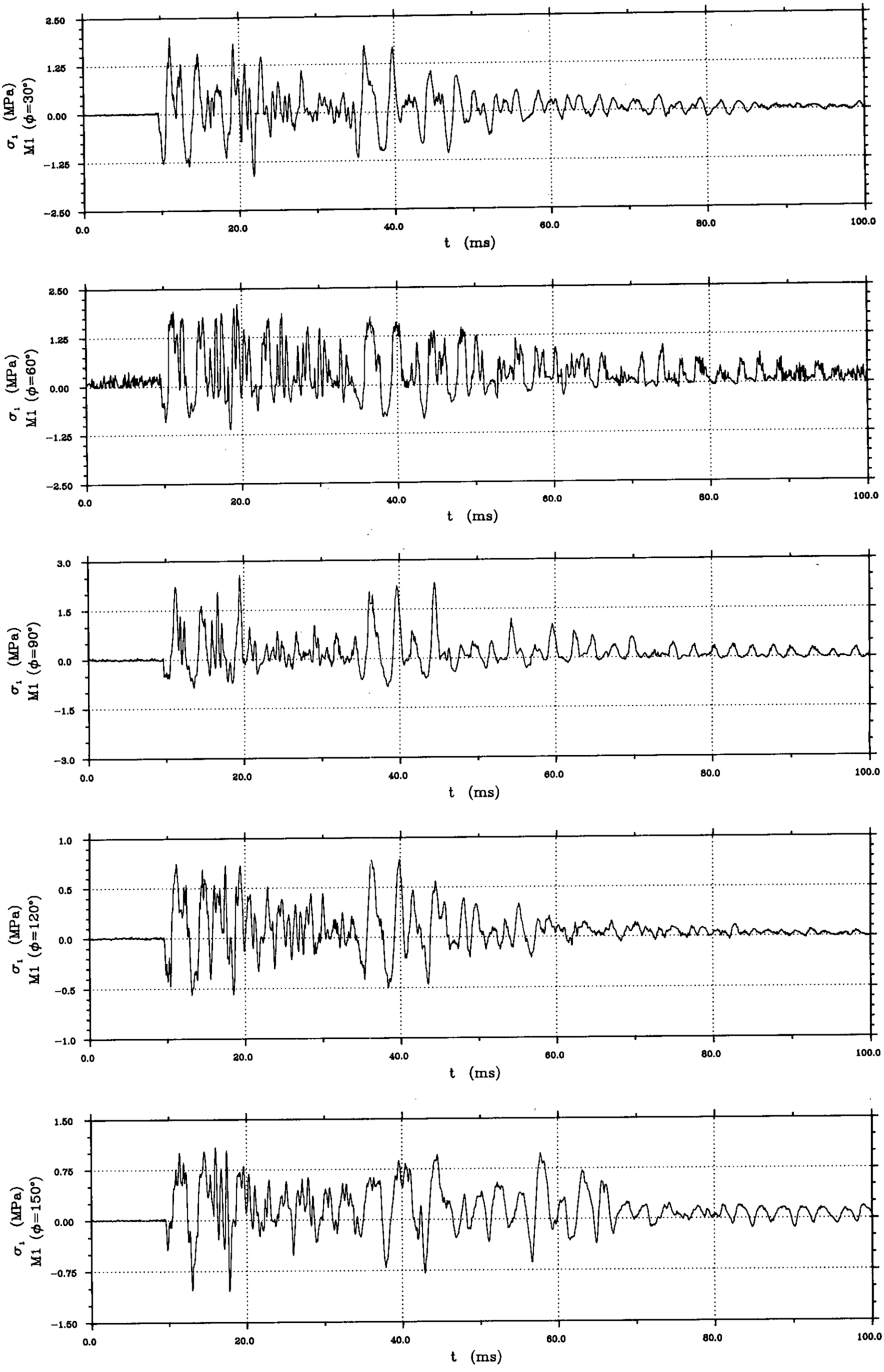

FIG. 5.13(a)–EXPERIMENTAL MAXIMUM PRINCIPAL STRESSES DUE TO A SYMMETRIC EXPLOSIVE LOADING

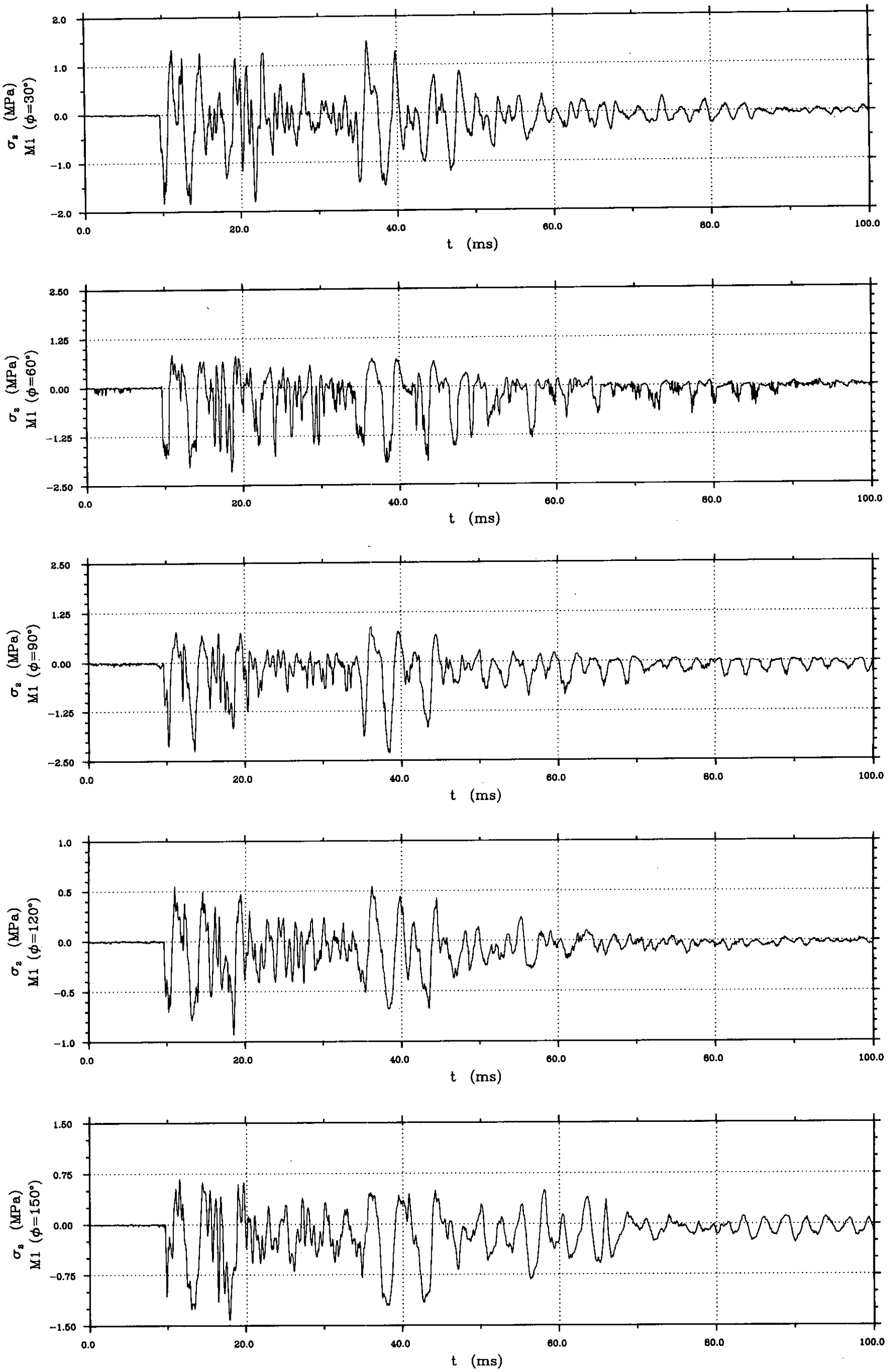

FIG. 5.13(b)–EXPERIMENTAL MINIMUM PRINCIPAL STRESSES DUE TO A SYMMETRIC EXPLOSIVE LOADING

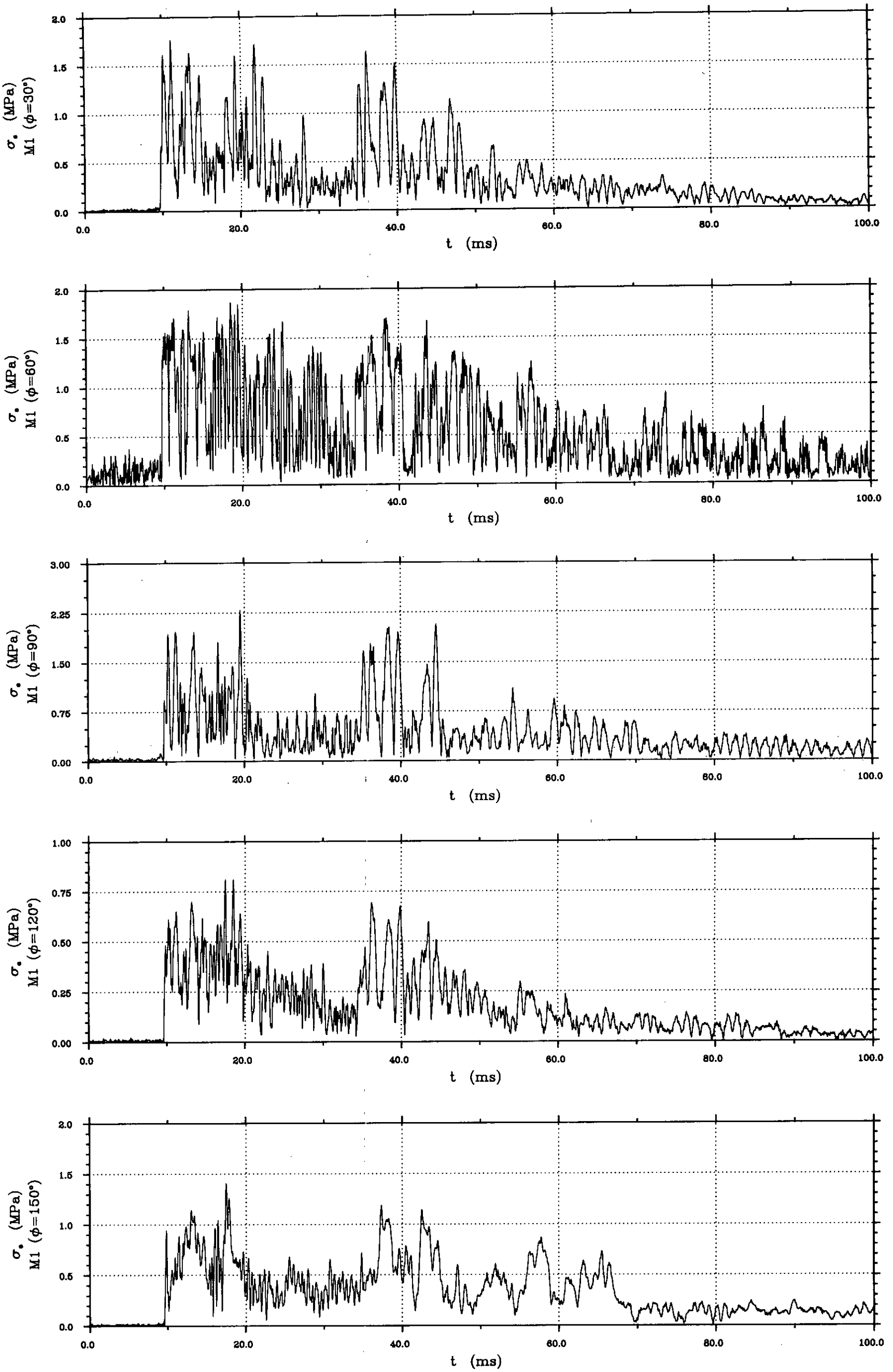

FIG. 5.14–EXPERIMENTAL EQUIVALENT STRESSES DUE TO A SYMMETRIC EXPLOSIVE LOADING

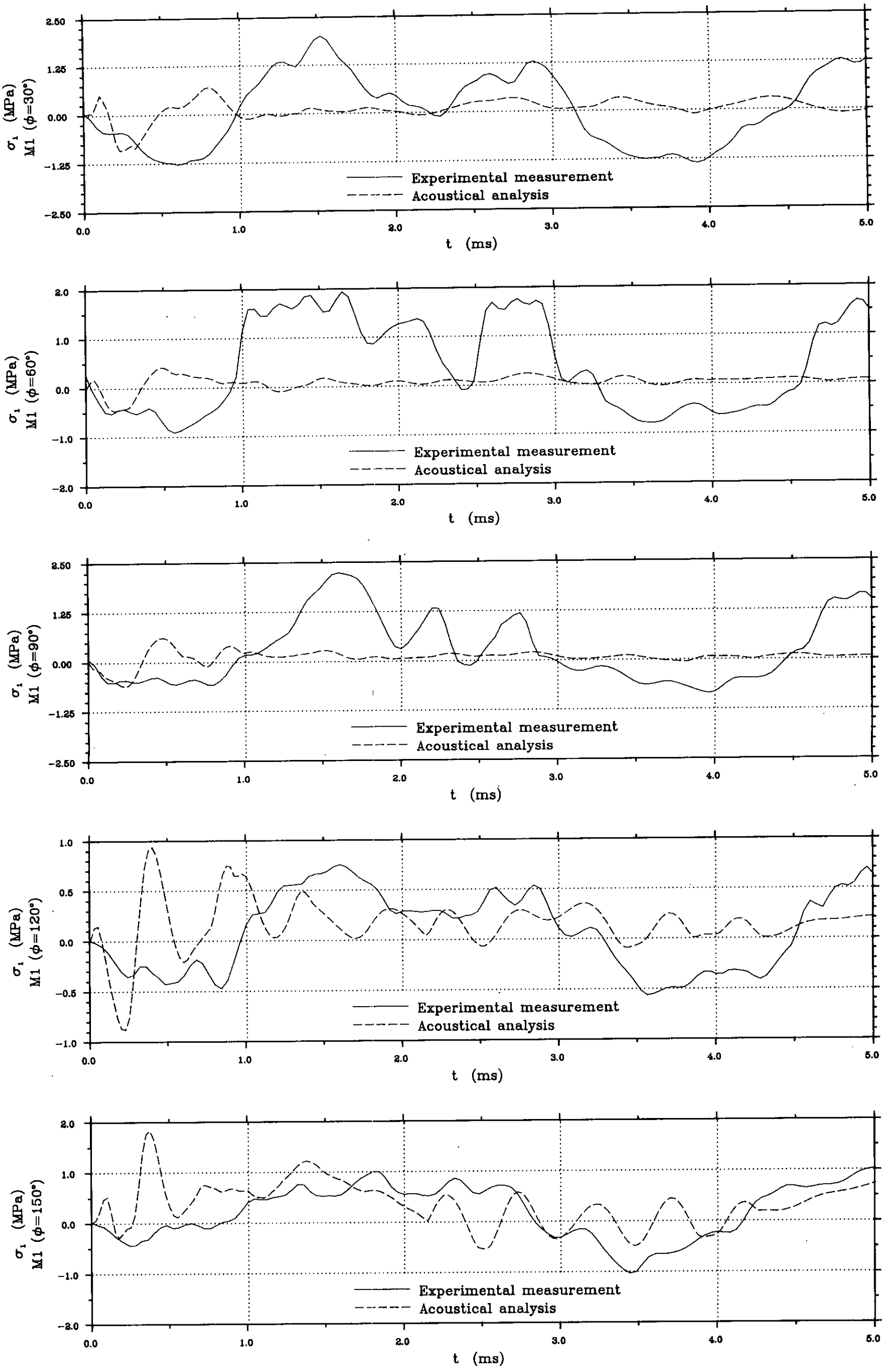

FIG. 5.15(a)–COMPARISON BETWEEN EXPERIMENTAL AND THEORETICAL MAXIMUM PRINCIPAL STRESSES DUE TO A SYMMETRIC EXPLOSIVE LOADING

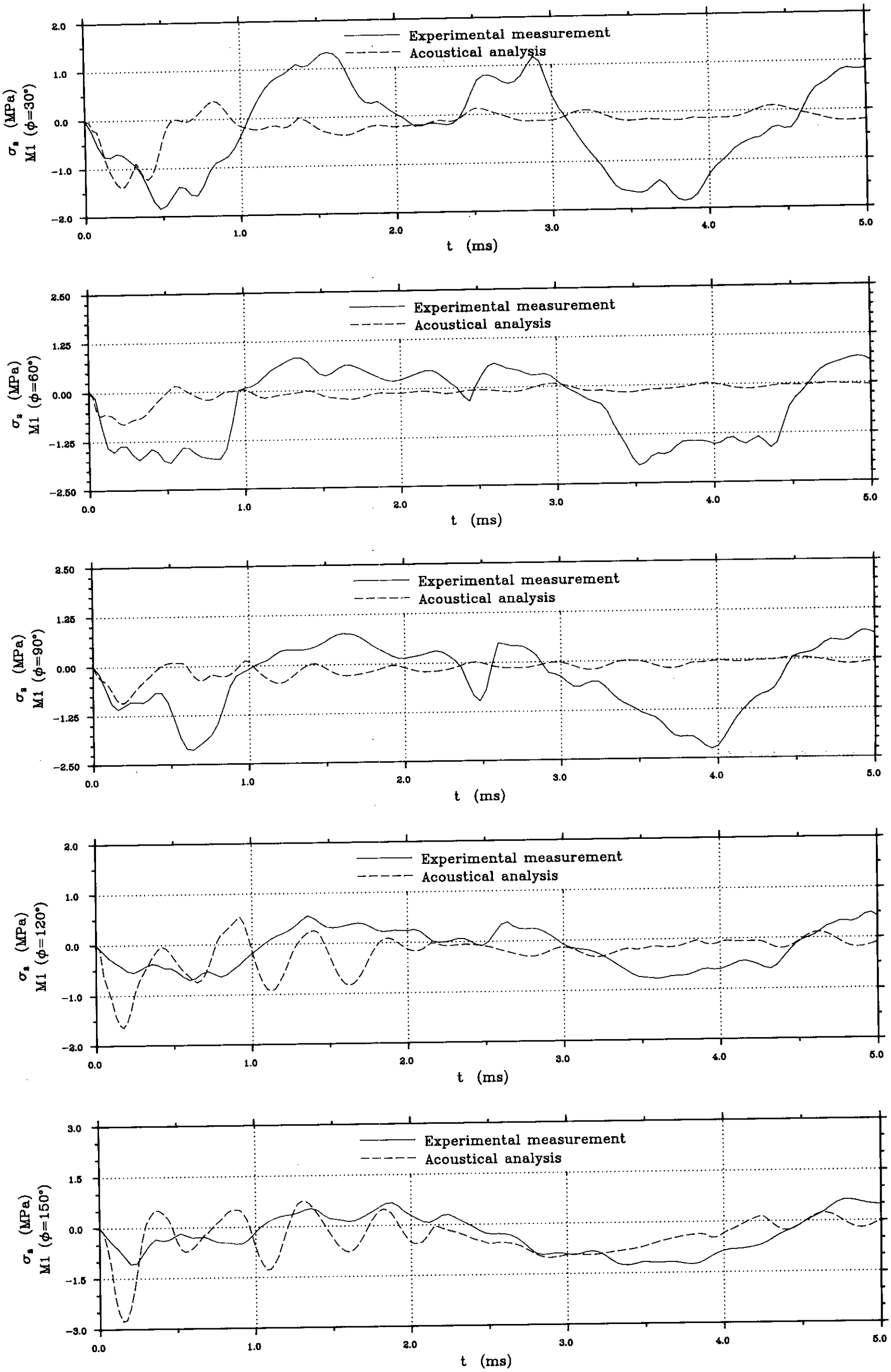

FIG. 5.15(b)–COMPARISON BETWEEN EXPERIMENTAL AND THEORETICAL MINIMUM PRINCIPAL STRESSES DUE TO A SYMMETRIC EXPLOSIVE LOADING

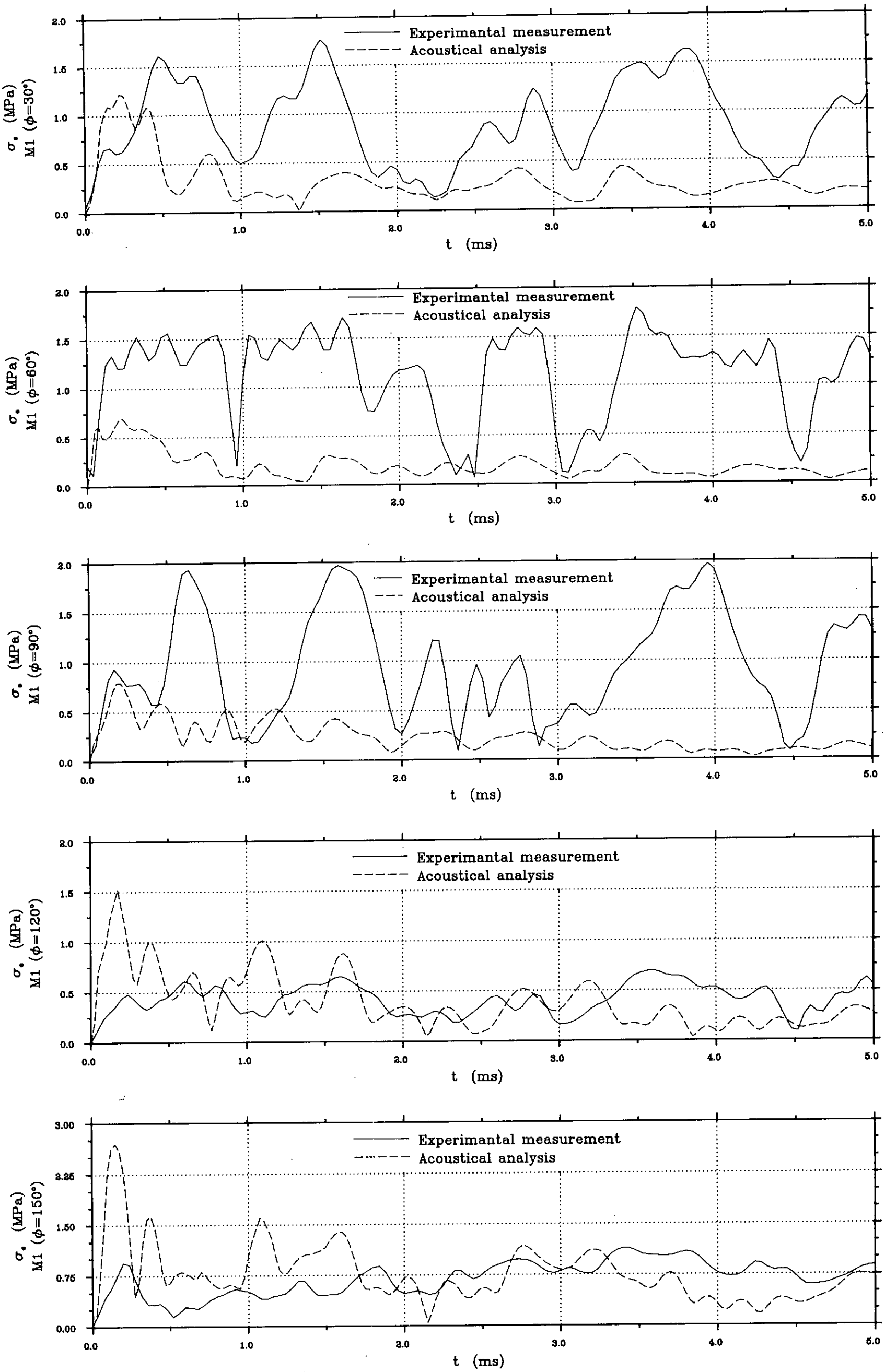

FIG. 5.16–COMPARISON BETWEEN EXPERIMENTAL AND THEORETICAL EQUIVALENT STRESSES DUE TO A SYMMETRIC EXPLOSIVE LOADING

CHAPTER 6

DESIGN AND CONSTRUCTION OF A STATE OF THE ART ECHINODOME FOR UNDERWATER STORAGE OF LNG

6.1 SUMMARY

A proposal is made for an offshore LNG peak shaving facility using Echinodomes for storage. The design loads for an underwater floating submerged tank are reviewed with emphasis on dynamic loads (impact and explosion). Then a summary is given for the loading conditions against which it is necessary to design the underwater storage vessel, during its various life stages : construction, launching, towing out, commissioning, operation and decommissioning.

The assessment of response of a reinforced concrete Echinodome, with an inner steel tank containing LNG, to accidentally dropped slender and bulky objects employing empirical formulae is discussed.

An outline for construction works is described along with the general principles and practice of prestressing the Echinodome structure to overcome any developed tension cracks in the reinforced concrete outer shell.

6.2 INTRODUCTION

In earlier chapters, the research work was concentrated on assessing the use of the finite element method as a numerical procedure to predict the Echinodome response to static and dynamic loadings. The current chapter makes use of the previously reached conclusions in the design procedure of a full size Echinodome emphasising its function as an underwater storage vessel for a hazardous material; liquefied natural gas (LNG).

LNG is a cryogen used in space programs, energy and chemical industries as a pollution–free fuel. It is stored under atmospheric pressure at very low temperatures (–162°C) or under a higher pressure and temperature not higher than its critical temperature (–82.5°C), the temperature above which the gas cannot be liquefied by compression alone. Hence, LNG must be stored in a perfectly insulated container.

Underwater LNG storage vessels may experience impact loadings as a result of accidentally dropped objects which can cause local structural damage. Another extreme load case can occur when the stored cold liquid leaks into the surrounding media (in the current case water) forming a spill which is superheated originating an RPT. As a consequence an overpressure is created which is transmitted to nearby structures through a shock wave.

Therefore, an underwater Echinodome storing a cryogenic liquid (considered to be hazardous) is required to be safe against a wide variety of load cases including deterministic and probabilistic loads. It is imperative that such vessels are designed to resist structural failure when subjected to severe loadings, static or dynamic, during their operational life.

The main aim of the current chapter is to establish a design and construction procedure for the Echinodome structure and assess its performance as an underwater LNG storage tank.

6.3 AN OFFSHORE LNG PEAK SHAVING FACILITY

An LNG peak shaving facility is a plant where means exist for processing and liquefaction of natural gas. The facility responsibilities include,

i. pretreatment and purification of feed gas;

ii. liquefaction;

iii. storage;

iv. distribution : pump out and vaporisation;

v. control and instrumentation; and,

vi. fire protection and safety.

Economy of an LNG processing plant and its operating costs depends greatly on the proper integration of the pretreatment, purification and liquefaction facilities with the type of storage of the gas. Natural gas can be stored in the liquid state fully pressurised at a temperature not higher than its critical temperature (–82.5°C), non–pressurised at a very low temperature (–162°C) or a combination of both cases. The most economical method of storage is dependent on parameters such as the size of the stored LNG and the filling rate.

In 1984, Royles *et al.* [9] proposed an offshore system for LNG processing and underwater storage. A similar concept is adopted in the current investigation with some modifications introduced to the storage tank configuration and more details concerning plant processing. The system is described in the following paragraphs.

An LNG peak shaving plant is to operate offshore with feed gas pretreatment, purification and liquefaction taking place on board a production platform sited on top of a natural gas field. Pretreatment and purification of the inlet gas is an important process for the removal of any substances that may solidify during the liquefaction stage, hence avoiding fouling and plugging problems. An integrated pretreatment, purification and liquefaction process would be most advantageous to implement rather than other single use systems for simplistic and economical reasons.

The purification process would have to be reliable in removing carbon dioxide, water and mercaptans from LNG and should be capable of handling wide variations and concentrations of contaminants with minimal effect on the liquefaction capacity. The combined system could involve the use of a mixture of refrigerants in a single loop to obtain lower temperatures. The mixture would be condensed under moderate pressure at ambient temperature.

LNG would then be stored under $2 \rightarrow 3$ bars at $-162^{\circ}C$ in a single or a chain of insulated Echinodomes, situated proximate to the production platform. The pump out system comprised of a pump and motor drive is to be mounted inside the storage tank in order to take advantage of the cryogenic fluid for motor cooling. Extra pumps would be installed as spare capacity for the distribution system.

The storage vessel would be supported in a floating submerged state with the aid of tension cables in order to avoid adverse weather conditions encountered at the air/sea interface and at the same time minimise the effect of ground motions on the structure.

The apex of an underwater Echinodome is a critical part of the structure and would be prone to accidentally dropped objects. Therefore, liquid filling and withdrawal lines would be located in the circular base. Insulated flexible hoses would be employed in the transfer of LNG from the storage vessel to tankers for transportation to onshore satellite plants where LNG would be stored. The liquid would then be pumped to sufficient pressure before vaporisation in order to enter the distribution system.

The control and instrumentation of the offshore plant would be located on the production platform where controls would be automatically operated.

6.4 DESIGN PROCEDURE

The current section is concerned with the design procedure for the underwater storage system of the above described LNG peak shaving facility.

6.4.1 Site Considerations

It is important to consider the characteristics of the chosen site when designing an underwater Echinodome for mainly four reasons.

Firstly, the water depth during favourable weather conditions at the selected site is required to enable the designer to generate the meridional coordinates of the Echinodome and hence determine its dimensions.

Secondly, a thorough geotechnical investigation is to be carried out to determine the soil characteristics at the sea bed. The provided information is paramount in the design of the foundations to which the floating submerged Echinodome is to be attached.

Thirdly, a seismic evaluation of the location is necessary in order to predict the effect of ground acceleration on the integrity of the structure and connection outlets to pipework.

Lastly, severe environmental conditions of the locality must be considered in assessing the types of environmental loadings (waves, currents, sea ice and icebergs) that might affect the strength and stability of the Echinodome.

6.4.2 Material Selection

The Echinodome under consideration is to possess two walls separated by an insulating material, all acting as a full containment system. Typical wall and base cross sections can be seen in Fig. 6.1.

6.4.2.1 Exterior shell wall— When considering the safety of the surroundings the aim should be the prevention of a catastrophe in case of a structural failure [94] . In today's technology concrete is recognised as the best available construction material for protecting structures against explosions and striking objects. Therefore, reinforced concrete would be selected as the construction material for the outer shell.

The outer skin is to be covered with a fender layer made of lightweight concrete having a very low strength. The idea has been suggested before and tested on small scale dome type models [95] . The thickness of the fender must be enough to ensure the absorption of energy imparted to the structure through an impacting object by crushing and penetration of the lightweight concrete directly beneath it. At the same time the structural concrete must not be activated to impact respond in order to minimise the contact force. Lightweight concrete would be chosen rather than other fender materials (e.g high density polystyrene) because of its ability to hold its shape in deep water under relatively high hydrostatic pressure.

6.4.2.2 Interior shell wall— The inner tank would be constructed from 9 percent nickel (9% Ni) steel characterised by high toughness at very low temperatures and hence improve the safety of the inside tank containing the LNG. Welded joint strength tests and fracture toughness tests carried out earlier [96] confirmed that 9% Ni steel plates were adequately applicable for the construction of LNG tanks.

6.4.2.3 Insulation material— Insulating the Echinodome would be achieved using two different systems, one between the tank walls and another for the base.

The basic insulation system for the annular space between the inner and outer shell would be composed of loose granular perlite, which is an inorganic, non–flammable, lightweight material produced from special volcanic rock. In order to minimise moisture and air voids in the insulation, the perlite would be finely ground and expanded within in–situ portable furnaces and then placed in the gap between the steel inner and concrete outer shells [97] .

The powdered form of perlite is subject to settlement and consolidation and therefore a resilient blanket would be wrapped around the steel tank. The flexible layer would prevent the build–up of pressure on the outside surface of the inner tank, a situation which might arise when the vessel walls expanded and contracted due to thermal and/or hydrostatic load variations.

A wall liner is to be installed on the inner surface of the outer shell which would act as a liquid and vapour product boundary, thus preventing any LNG leakage into the surrounding media (in the current case water) in the event of a spill into the annular space. Under such conditions perlite loses its effectiveness as an insulating material and hence a secondary insulation system would be introduced in the form of polyurethane foam (PUF). The material is sprayed on the wall liner to prevent it from direct contact with the spilled LNG and in that way the rate of vapour evolution would be kept to a minimum. The PUF insulating material would then be sanded and coated with a layer of glass reinforced epoxy.

Foamed glass blocks would be utilised in insulating the Echinodome base. The blocks would be stacked normally in layers on a bituminous bedding membrane covering the inner surface of the reinforced concrete base. The load bearing insulating system would be organised with filled and staggered vertical joints and interleaved with bituminous layers [98] . The above insulating material is of limited strength and brittle nature and hence, care must be taken not to overload the foamed glass slabs from the hydrostatic pressure of the liquid contained in the steel tank. Such a requirement could be fulfilled for large tanks by installing a ring beam of perlite concrete (cast in place or precast oven dried sealed blocks) under the bottom edge of the inner tank.

A secondary 9% Ni steel plate would be installed below the base of the inner steel tank separated from it by a reinforced concrete layer. The plate would be introduced to contain any spill from the inner reservoir and would normally be at product temperature. In addition, a bottom liner would be provided under the foamed glass layer to enclose the load bearing insulating system. The bottom insulation would be connected to the annular gaps via a pipeline. If a leakage was to occur the connecting pipe could be shut off and the base insulation purged. In the case of continuous leakage it would be possible to detect LNG in that space using thermocouples, attached to both the liner and the steel plate, which would measure temperature variations.

6.4.3 Structural Dimensions

The meridional profile of the outer shell would be generated by the Echinodome shape prediction program with the structural dimensions depending on the selected design stress and wall thickness. The coordinates of the inner jacket profile would be determined from the outer shell meridian, by specifying an adequate gap for the insulation system between the two walls and floors.

Llambias in his thesis [4] determined the centreline of both meridional profiles and stiffened the structure in the critical zones by gradually increasing the thickness of both walls in the bottom tenth. The previous step was necessary in order to achieve a higher factor of safety against structural instability.

The same structural dimensions are employed in the current investigation after performing some modifications to the Echinodome outer shell and insulation system.

General characteristics of the storage system are listed below and the Echinodome wall and base composition are depicted in Fig. 6.1.

CONCRETE SHELL

• Height from inner surface of base	(m)	=	34.80	
• Maximum diameter	(m)	=	52.55	
• Base diameter	(m)	=	30.00	
• Enclosed volume	(m^3)	=	51968	
• Fender thickness and material	(mm)	=	250	of lightweight concrete
• Wall thickness and material	(mm)	=	250	minimum and
			500	maximum of grade 80 concrete
• Base thickness and material	(mm)	=	2000	of grade 80 concrete

STEEL SHELL

• Height from inner surface of base	(m)	=	31.97	
• Maximum diameter	(m)	=	48.34	
• Base diameter	(m)	=	30.00	
• Enclosed volume	(m^3)	=	42861	
• Wall thickness and material	(mm)	=	50	minimum and
			80	maximum of 9% Ni steel
• Base thickness and material	(mm)	=	88	of 9% Ni steel

INSULATION SYSTEM

• Wall insulation thickness	(mm)	=	1500
• Resilient layer thickness	(mm)	=	100
• Load bearing insulation thickness	(mm)	=	750
• High load bearing ring beam depth	(mm)	=	500
• Polyurethane foam layer thickness	(mm)	=	60

In the critical zone around the base the insulating material (powdered perlite) thickness would be less than at other parts due to the narrower gap between the two walls.

6.4.4 Design Loads Assessment

In order to assess the design loads of an underwater Echinodome vessel storing LNG it is necessary to establish the degree of safety required. The requirements dictated by the safety measures involved in achieving a state of the art design of the Echinodome are mentioned in the following subsection.

6.4.4.1 Safety requirements— The probability of accidental events occurring in an LNG bulk storage installation is usually small but such facilities are characterised by an inherent high risk level. Risk can be defined as the product of the probability of occurrence and the potential amount of damage. Therefore, limiting risk by attempting to decrease the probability of occurrence of hazardous incident does not suffice. The main objective should rather be limiting the extent of damage during upset conditions, hence preventing a catastrophe from occurring and achieving a higher quality of safety.

Safety systems can be classified as either active or passive. A computer controlled safety system and structural safety are examples of such systems respectively. Active safety systems require a high standard of quality and high redundancy level and, when employing computers, are

subject to computer bugs. On the other hand, measures in the structural field to limit damage are more reliable because of their deterministic nature and hence are considered more attractive than other safety systems, especially in developing countries where human error (the main source of accidents) is more probable.

Safety at an underwater LNG bulk storage facility could be enhanced by employing burstproof Echinodome vessels. Normally, the criteria for designing a tank to contain a cryogenic flammable substance are specified by the customer but if a state of the art configuration (as is considered for the current case) is necessary to limit potential damage in the event of any upset condition (e.g. zipper type tearing of the inner steel tank, an overpressure wave from nearby explosions or impact by striking objects) then the following requirements must be satisfied,

i. safe, efficient and economic operation under normal conditions;

ii. safe containment of product spills under upset conditions — the primary tank storing the product liquid is to be protected by a secondary tank which should be,

- vapour and liquid tight,
- highly resistant to perforation and punching, and,
- burstproof; and,

iii. high availability and repairability after being subjected to severe loadings.

In general, the storage configuration must be safe under all prescribed design loads, e.g. loads experienced by the structure during construction, testing, initial floating, towing out, installation, operation and severe dynamic loads. High quality of safety is possible but the questions remain — how safe is safe and how expensive is safety?

It is beneficial in the current investigation to gain experience from already existing vessels [99,100] to ensure that the above–described underwater Echinodome storage vessel (see Fig. 6.1) is within the current state of art concerning design, construction and operation.

Reinforced concrete is considered as the most attractive choice for the protective outer tank. If in a prestress state the concrete would be under compression and thus could take up the space enclosing function as well, while the prestressing tendons and the reinforcement bars would be carrying the tensile forces. Zipper type tearing and bursting employing this type of design are resisted by the discontinuous absorption of tensile forces and consequently the concrete vessel relieves any sudden overpressure through material softening, a behaviour known as "**Structural Blowdown**" [100].

In the event of a single prestressing tendon failure (the probability of this occurring is very low) the tensile stresses are redistributed in the adjacent tendons resulting in the increase of the steel stress state and it is very unlikely that a catastrophe would result from such an effect.

When designing the Echinodome vessel it is not advantageous to use prestressing to counteract upset conditions as such action would cause the structure to behave according to the theory of elasticity. But if material softening of concrete is the acting mechanism (through the formation of cracks) then the concrete outer tank could behave as an overload relief system.

It can be concluded from the above discussion that an adequately reinforced and prestressed concrete outer shell can limit the amount of damage in a hazardous situation by acting as an effective, efficient and economic passive safety system which would make the use of an expensive active safety system redundant.

6.4.4.2 Upset loading conditions— Transient dynamic loadings may be exerted on an underwater Echinodome as a result of any of the following incidents,

i. sudden failure of the inner tank;

ii. a nearby explosion initiating a shock wave which impinges the outer shell; and,

iii. striking and dropped objects impacting the outer concrete shell.

In the event of zipper type failure of the inner steel vessel the liquid product would suddenly be released causing a hydrodynamic load on the outer tank, the duration of which lies in the range $0.15 \rightarrow 0.48$ s [99] . Both experimental and analytical work [99] indicated that if the annular space was filled with perlite the hydrodynamic pressure would approximately be 2.5 times the LNG hydrostatic pressure. Since LNG has a much lighter density 424 kg/m^3 than that of sea water (1025 kg/m^3) the end effect would be a non–critical situation. The reason is that the total inner hydrodynamic pressure would be counteracted by a portion of the outer hydrostatic pressure depending on how far the Echinodome was from the sea surface level.

If an LNG spill was to occur from a pipeline or storage vessel underwater the spilled liquid would be superheated by the hotter, less volatile surrounding media (water). The hydrocarbon then vapourises transforming into a more stable state. Under such circumstances the course of events can change rapidly to produce an explosion like phenomena (RPT) which in turn generates shock waves. Depending on the rate and amount of spilled LNG a small scale incident can propagate and escalate the RPT phenomena through premixed and fragmented LNG and sea water. Consequently, proximate structures may suffer severe transient overpressures.

Impact loads may be exerted on underwater Echinodomes as a result of objects dropped from above the sea surface, e.g. a pump or a ship anchor. Following a nearby explosion concrete fragments and debris may strike the storage vessel at relatively high speeds which may cause local structural damage in the form of spalling, scabbing or perforation [101] (see Fig. 6.2).

6.4.4.3 Summary of design loads— Table 6.1 contains a list of the loading conditions for which an underwater Echinodome should be designed. The types of loads described vary with respect to structural geometry : axisymmetric, symmetric and asymmetric.

DESIGN LOADING CONDITIONS

- **CONSTRUCTION LOADS**
  - Temporary omission of wall panels
  - Temporary erected structures
- **DEAD LOADS**
  - Structural self–weight
  - Permanent attachments and ancillaries, (e.g. pipes, valves, pumps and stairways)
- **PRESTRESSING FORCES**
- **IMPOSED LOADS**
  - Internal hydrostatic pressure of water during testing
  - Internal hydrostatic pressure of LNG during operation
  - Internal gas pressure and vacuum
  - External hydrostatic pressure of water
- **ENVIRONMENTAL LOADS**
  - Wind loading during construction, launching and tow out
  - Wave loading during operation
  - Current loading
    - Wave height increase
    - Current drag forces
  - Sea ice and icebergs
- **THERMAL LOADS**
  - Temperature gradients during commissioning (initial cooling)
  - Temperature gradients during operation (filling and emptying)
  - Temperature gradients during accidents (LNG leakage)
  - Temperature gradients during decommissioning (warming)
- **SUPPORT LOADS**
  - Base reaction during construction, floating, towing out and operation
  - Structural behaviour under unsymmetric supporting conditions
- **ACCIDENTAL LOADS**
  - Impact forces induced by striking or dropped objects
  - Blast overpressures caused by a proximate explosion
  - Sudden failure of a single or multiple tension leg members

TABLE 6.1 — *DESIGN LOADING CONDITIONS FOR AN OFFSHORE FLOATING SUBMERGED ECHINODOME STORING LNG*

Except for impact and explosive loadings most of the above load cases were assessed and their effect on a slightly different storage configuration was examined by Llambias [4] . Therefore only transient loadings will be considered herein.

Four important parameters determine the effect of impact on the Echinodome vessel which are,

i. the mass of the striking or dropped object;

ii. the terminal velocity at which the object impacts the structure;

iii. the shape and dimensions of the impacting object; and,

iv. the structural stiffness of both bodies at the point of contact.

When studying the effect of impact on the Echinodome structure it is necessary to derive values for each of the above variables in order to assess the magnitude of the contact force between both bodies. If the contact stiffness is low the impact load is classified as soft impact characterised by long duration and low contact force. While a hard impact load can be experienced by the structure having a much shorter duration and a higher force magnitude, if the contact stiffness is high.

When considering explosive loadings, structural response is dependent on the following controlling parameters :

i. the stand off distance from where the explosion occurs;

ii. the duration and decay rate of the pressure pulse;

iii. the peak pressure pulse; and,

iv. the structural stiffness.

Other dynamic loadings which are less critical but require consideration are the sudden failure of a tension leg member and sudden release of product jets. The risk of resonance from liquid motions or production pumps need to be assessed as well.

In general, an underwater Echinodome LNG storage tank should be designed to sustain prescribed impact and explosive loadings without the spilling or leakage of the contained liquid.

Examples :

- Impact by slender deformable objects (soft impact) [102] .
- Impact by slender and bulky non–deformable objects (hard impact) [102] .
- Blast wave having a pressure pulse varying linearly from maximum (at $t = 0$) to zero [103] .

6.4.5 Structural Analysis

To date, the most powerful numerical procedure available for analysing the Echinodome under various loadings is the finite element method. It can predict structural response to almost all types of loads under normal and upset conditions. Consequently, it would be employed in the design of a storage tank having a configuration similar to that described above (see Fig. 6.1). Recommendations for a finite element simulation of the underwater Echinodome vessel are mentioned in the following subsections regarding element types, material models and types of loads necessary to include in the analysis and check against for structural failure.

6.4.5.1 Element types— Three dimensional shell elements, allowing for strains in the plane normal to the shell surface, would be used to idealise the outer concrete tank. The fender layer and the structural concrete would be represented using two different sets of elements each possessing its own material properties. Thin shell elements qualified for attaching to the surface of the above shell elements would be required to model the liner, the inner steel tank and the secondary steel base. Additionally 3–D compatible solid elements would be assigned for the insulation layer in the annular space between both tanks and the load bearing insulation system.

Depending on the reinforcement and prestressing layout, 3–D bar elements along the side nodes or in the body, parallel to the curvilinear axes, of the three dimensional shell elements would be employed in modelling reinforcement bars and prestressing tendons. In the case of a bond slip analysis 3–D link elements or springs would be attached to the finite element mesh between the concrete shell elements and the bar elements. If shear reinforcement in the form of stirrups was to be introduced in the outer concrete shell in order to enhance its perforation resistance against soft and hard impact, then it would be essential to define such reinforcement explicitly in the theoretical model. A finite element mesh discretisation scheme for a 90^{o} segment of the apex zone is depicted in Fig. 6.3. Lastly, cable elements would be utilised to simulate the tension leg supporting system.

6.4.5.2 Material models— Concrete behaviour varies according to its stress state. When reaching a limiting stress value it fractures either by crushing if in a state of compression or by cracking if in a state of tension. A concrete constitutive model would be assigned to the concrete 3–D shell elements to represent such behaviour.

If concrete is in a compression state the constitutive model would have to allow for material softening following the crushing failure mode. Only after reaching an ultimate strain the strength of elements in such a state would cease and the stresses would be redistributed in the neighbouring elements. While, if under tension, assumptions for the numerical model would have to be made

regarding initiation, closure and reopening of cracks. A crack is formed as a result of exceeding a limiting tensile strength or strain, in a plane normal to the maximum principal stress. Thereafter, the surrounding concrete material could be represented by an orthogonal model with the local material axes coinciding with principal stress directions. Cracked concrete could not carry tensile stresses normal to the crack plane, on the other hand stresses parallel to the crack could be supported according to the constitutive laws of the material model. For small cracks shear could be resisted by the interlock of aggregate along the parallel crack faces. The previous shear stresses could be assumed to vary linearly with strains caused by the parallel differential movement of both opposite crack faces. The interlock phenomena would cease to exist for large cracks. Cracked sections of concrete could support compressive stresses orthogonal to the crack plane.

The insulation material in the annular space between both shells was considered to be in powdered form and could be assumed to possess no resistance to either compressive or tensile stresses. The description of such a material in the finite element method would present a problem when evaluating the structural stiffness and hence it could be provided with some compressive strength if in a confined state with its value depending on the original material properties in such a condition. The foamed glass material of the load bearing insulation system would be represented with a similar constitutive model.

Contrary to concrete, steel is considered to be a strain hardening material and consequently an elasto–plastic strain hardening numerical model would have to be used to represent the various steel components (reinforcing bars, prestressing tendons, liner, inner tank and secondary base) of the storage tank.

The bond between concrete and steel is due to the combination of chemical adhesion, bearing action and friction. Initially, the concrete fine particles are adhered to the surface of the reinforcement bars and prestressing tendons, but when slippage starts the adhesion drops to zero. Slip is initiated as a result of concrete failure at the steel surface and complete bond failure is dependent on the friction level at the failure surface. Friction is destroyed for large slippage. The bearing action is caused by the deformation of steel members in contact with the concrete material. In general, it is vital to consider the bond–slip relationship for bonded structures subject to incremental and ultimate loads. Therefore a bond–slip model should be provided for the 3–D link elements in the finite element analysis by assuming a non–linear relationship between the bonding stress and the amount of slip.

6.4.5.3 Types of loads and solution methods— The types of loads that would be used in the preliminary analysis of the Echinodome under normal operating conditions and severe weather conditions are static pressures, initial stresses or strains and concentrated loads. The structural stability of both the inner and outer shell would be checked taking both geometrical and material non–linearities into consideration. Since hydrostatic pressure is a non–conservative type load then an appropriate geometrical non–linear formulation should be used by referring all relevant variables to the deformed configuration of the structure. A high factor of safety would be required against the lesser of the non–linear collapse and non–linear bifurcation buckling pressure heads.

A thermal shock analysis would be carried out to simulate incidents of LNG leakage in the annular space or in the base area. The structure is required to be vapour and liquid tight under such circumstances and therefore no cracks would be permitted in the outer concrete shell.

If impact loads resulting from dropped objects are to be analysed using the finite element method then provisions should be made in the formulations for large deformations, slide lines and rezoning. Slide lines would be necessary between the striking object and the target and would be required between portions of the target to permit the formation of a plug ahead of the impacting body. If large deformations are encountered and the finite element mesh becomes excessively distorted, rezoning could be used to permit the division of the structure into changing sets of elements during the course of the calculation. It is necessary to establish dynamic stability of the structure under such impulsive loads with a considerable factor of safety.

The response to explosive type loadings, having a prescribed pulse occurring at a specified distance from the Echinodome, should be determined. It is important that the numerical procedure employed in such an analysis would allow for both geometrical and material non–linearities. The structural stability of the Echinodome should be examined for the case of a shock wave propagating through a fluid medium then striking the structure and a reasonable factor of safety would be required. The DAA could not be employed in the analysis of such problems and therefore more experimental work is needed to validate newly developed numerical techniques.

For the latter two dynamic loadings (impact and explosion) the applied constitutive laws should include the strain rate dependency of the material properties and structural damping could be ignored as its effect, if considered, would be to attenuate the structural response.

When analysing an underwater Echinodome vessel the structure would behave according to the theory of elasticity if under operating loads. If it were subjected to severe loads under upset conditions then permanent deformations could be permitted on the condition that the outer shell was capable of safely containing any internal spilled product.

6.4.5.4 Empirical damage assessment induced by dropped objects— The types of objects that might impact an underwater Echinodome can be classified as follows [102] ,

i. slender deformable objects impacting end–on or broadside, e.g. pipe;

ii. slender non–deformable objects impacting end–on or broadside, e.g. drain caisson; and,

iii. bulky objects, e.g. pump.

A falling slender object can either strike the structure end–on or with its broadside. The case for end–on impact is considered here to have a more serious effect on the protective concrete shell than broadside impact because the impact force would be concentrated on a smaller area and its terminal velocity at collision would be higher.

If after the impact event the slender object suffered large deformations then some of the energy to be imparted to the target would be lost. The duration of the transient phenomenon would be longer and therefore the maximum peak force would drop. Conversely, a non–deformable object would experience very little deformation and hence the pulse shape of the impact force would be characterised by a shorter duration and a sharper peak. Consequently, impact by deformable and solid non–deformable objects can be described as soft and hard impact respectively.

From the above discussion it can be concluded that the most critical impact load cases are those of a slender non–deformable objects falling end–on and collision by a bulky object. For the former case a sufficient amount of experimental data exist to enable the understanding of the impact phenomenon under such conditions.

When a non–deformable object strikes a structure, having no fender, with a very low velocity the object rebounds in a non–predictable fashion, away from the target without inducing any local damage. With the increase of the impacting velocity of the object damage can be inflicted upon the structure in any of the following defined forms (see Fig. 6.2) :

1. **Penetration** — is the measure of indentation on the struck face.
2. **Spalling** — is the cratering damage with target material ejection from the struck face.
3. **Scabbing** — is the fracturing and detachment of target material from the remote face.
4. **Shear plug** — is formed as a result of inclined cracks through the target thickness.
5. **Perforation** — is the complete penetration of the projectile through the target.

On the other hand, forms of impact damage caused by dropped bulky objects can be any of the following,

i. punching shear;

ii. local bending; or,

iii. dynamic collapse buckling.

In their report, Brown and Perry [104] recommended the use of certain empirical formulae to predict the extent of damage to offshore structures caused by dropped objects (5 → 25 m/s). In a separate study, Dinic [95] proposed with qualifications another set of empirical relationships (0 → 10 m/s) based on his own experimental results. The former and latter relationships could predict penetration, scabbing, shear plug formation and perforation but could not be applied to structures with fender layers. Such formulae take no account of the hydrostatic pressure imposed on the structure, any existing prestressing forces, the membrane action of curved shells which is likely to increase the target's punching shear resistance or the effect of any disposed shear links.

Considering the above described Echinodome and assuming an object of 10.4 t mass falling freely, its terminal velocity in water would be 19.3 m/s [102] . If the structure had no fender layer the striking object would cause severe damage to a 250 mm thick concrete shell in the form of scabbing and shear plug movement. Depending on the concrete compressive strength and bending reinforcement level the object might even perforate the concrete shell. In either the case of scabbing or perforation it is obvious that a 250 mm wall thickness would not be sufficient to protect the storage system against such severe loadings and hence the choice of a 250 mm fender layer of lightweight concrete. The protective covering is intended to act as an energy dissipating system (energy absorber) by accommodating gross deformations, between the striking object and the structure, which is required to neutralise the incoming kinetic energy.

Therefore, to predict structural damage of such configurations induced by impacting bodies it is necessary to perform experimental tests on scaled models to enable the derivation of relevant empirical formulae. This approach is considered as the most attractive because the experimental results would be beneficial in validating numerical procedures such as the finite element and finite difference methods.

6.5 CONSTRUCTION AND PRESTRESSING PROCEDURES

Design engineers and constructors can influence their portion of the development effectively by adopting a sound design, construction planning and construction management. The latter two aspects are often encompassed by the single term "**Constructibility**" which involves the employment of work simplifications and standardisation to overcome the inherent difficulties of

complex and sophisticated fabrication processes.

As described earlier the Echinodome goes through a series of very distinct stages starting with fabrication, to testing, to towing, to installation, to operation and ending with decommissioning. In construction planning, fabrication is a major stage and can be subdivided into several actual steps to allow the selection of the most efficient method for each step. Such a procedure should be accompanied with sketches, preferably isometric drawings, to portray the key element of each individual step. Once the constructor is satisfied that all steps have been set forth, then structural analysis should be carried out for each step to ensure that a safe structural design has been achieved. This is because some parts of the storage vessel can be subjected to higher stresses during the construction stage than under operational conditions.

In general, the various construction steps of an underwater Echinodome, with the purpose of storing LNG, could be itemised as follows :

1. Preparation of a dry basin where the Echinodome construction and initial floatation could take place. The structure would be fabricated on a platform which would allow easy access and movement of facilities and equipment to the inside of the structure through its base.

2. Concrete base construction would start with the arrangement of the reinforcement cage, the dispensation of the meridional prestressing tendons and any extra prestressing members necessary to strengthen the structural base against the buoyancy forces. Spacers would be used to provide a margin for the concrete cover. Reinforcing bars would have additional lengths to permit the embedment of enough longitude in the concrete structural wall. The prestressing tendons would be of endless form and therefore would be placed only partly in the concrete base. Space required for penetrations and appurtenances would be accommodated by employing a weak material which would occupy the predetermined locations of such openings during concrete pouring. Such a weak material would be detached after the concrete hardened.

3. The steel liner attached to the inner surface of the outer shell would be erected and studs welded on its outer surface to tie it permanently to the concrete tank. A temporary supporting system would be provided for the liner during its construction and the concrete placement of the outer shell wall. The inner reinforcement layer, the prestressing members and the outer reinforcement layer would be laid according to the design layouts on the outer side of the liner. The prestressing tendons would run all over the structure in the form of endless loops, while the reinforcing bars would be disconnected at three mutually perpendicular planes passing through the structural wall

and base as depicted in Figs 6.4(a → c). Two vertical orthogonal planes passing through the apex would intersect a third horizontal plane at the maximum diameter. If required, shear links (stirrups) would be installed at specified structural zones (which were prone to impact loads) to increase the punching shear resistance of the structural concrete wall. Before the pouring of the high strength concrete layer and the lightweight concrete fender, seams would be located along the three predetermined planes to allow the fabrication of the outer concrete shell in eight separate parts joined only by the prestressing tendons.

4. A preshaped PVC fabric form would be attached to the concrete base and inflated, using water, to a pressure level sufficient to create a specified gap distance along the seams. The structural parts would be linked by placing concrete in the space joints to form a monolithic Echinodome shell. After curing of the seam concrete the flexible membrane would be deflated and taken away. Following this, the concrete vessel would be water tested for any existing leaks especially around the construction joints.

5. The concrete base would be covered with a steel liner on top of which thermocouples would be fitted. A high bearing ring beam made of lightweight concrete blocks with embedded steel bars would be constructed around the base edge of the inner steel tank. Pipes connecting the tank base and annular space would be fitted, and the necessary space for the tank appurtenances including manholes would be preserved. The various layers forming the load bearing insulation system would be placed according to the layout shown in Fig. 6.1. Then the steel base of the inner tank would be erected on top of a thin concrete layer.

6. The steel liner located on the inner side of the outer tank would be sprayed with PUF acting as a secondary insulating system after attaching a number of thermocouples. The surface would then be sanded and coated with a layer of glass reinforced epoxy.

7. Crane units would be moved to the inside of the concrete shell through the structural base. Such units would assist in the movement and disposition of the heavy steel plates forming the inner tank. As the tank is being constructed in circular rings hot powdered perlite would be placed in the annular space. Thermocouples would be mounted on the inner shell tank for operational purposes. An automated welding procedure would be employed in the fabrication of the inner tank and should take place in a dehumidified environment to ensure the quality of the work and increase its efficiency. Integrity of the weld would be checked for surface flaws and liquid/gas tightness.

8. Pressure relief systems would be provided for both the inner and outer tank for the purpose of preventing any overpressure incidents during normal or upset conditions. In addition, vacuum vents should be installed in order to avoid excess vacuum developing in either of the tanks.

9. A carefully selected list of fittings and appurtenances would be provided for the Echinodome vessel including pump wells inside the tank. A special railing system holding a hoist would be installed for pump manoeuvring. All nozzles and penetrations into the tank would take place through the base and access to most of the tank equipment, piping and valves would be achieved by an internal stair tower. The penetrations through the structural base would perform at least the following functions,
   - perlite refill nozzles;
   - nitrogen purge connections for the tank pumps;
   - instrument connections;
   - liquid filling and withdrawal lines; and,
   - passage for spares.

10. The inner tank would then be cleaned by broom sweeping it thoroughly of all loose residue followed by a degreased filtered gas drying.

6.6 FLOATING, TOWING, INSTALLATION AND OPERATION

After the completion of the construction, prestressing, testing and cleaning stages of the Echinodome the construction basin would be flooded with water by opening the closure system. On floating, tugs would tow the vessel from a series of locally stiffened points on the structure to the required location. The general procedure and relevant precautions concerning the initial floating and towing out stages have been discussed elsewhere [4] and should be adopted accordingly.

On arrival at the installation site the vessel would be lowered to the sea bed by admitting water to the inner tank. In the next step the storage tank would be attached to a preplaced concrete base or a set of anchoring piles using several mooring lines in the form of catenary or wire rope. By emptying the tank it would float again because of the buoyancy forces and the structure would be held in its position by the tension leg members.

The vessel would then be connected to the production platform where degreasing filtered gas would be circulated inside the inner tank to dry it. Finally, the Echinodome vessel would be ready for operation and after securing the tank in its position LNG would be pumped to the inner steel shell.

Thermocouples mounted on various parts of the structure would be utilised in monitoring the temperature of the cyrogenic liquid and the detection of any LNG spills from the primary tank. Several of the submerged pumps would be used for loading purposes and the rest would be employed in the circulation of the product to prevent its stratification in the tank and to keep the loading lines cold. The inner shell would normally have a maximum allowable filling limit of 98 percent of its enclosed geometrical volume. This is to ensure that the pressure relief valves would always remain in the vapour space and would receive only vapour when blowing off and therefore they should be placed on the highest location within the vapour space.

LNG would be exported to onshore satellite plants via shuttle tankers for later distribution. A catenary anchor leg moored (CALM) buoy would be positioned at an adequate distance from the production platform and the storage system. Transference of LNG from the storage tank to the carrier would be accomplished through the CALM buoy employing a floating flexible hose.

In the event of repairs being carried out on the buoy bearings, the floating loading hose or any other related problems the LNG would be pumped for storage into adjacent Echinodome vessels without halting production and hence a higher overall production uptime would be achieved. The same would be applied during tanker changes on the single buoy mooring (SBM) or in the case of severe weather conditions preventing the LNG carrier from approaching the buoy. The overall proposed operating scheme is depicted in Fig. 6.5.

6.7 CONCLUDING REMARKS

In attempting to assess the structural response of a state of the art Echinodome operating underwater for storage of LNG, to general loadings, the following remarks were drawn regarding a double wall vessel :

1. The secondary tank (outer concrete shell) should limit the extent of damage in the event of any upset loading conditions rather than minimise risk and this could be achieved by designing it to withstand the following loadings safely,
   - impact by bulky and slender non–deformable objects;
   - transient overpressure shock waves resulting from nearby explosions; and,
   - the sudden failure of the inner tank containing LNG.
2. The proposed configuration of the Echinodome vessel would satisfy the state of the art qualifications which are,
   - safe, efficient and economic operation under normal conditions;

- safe containment of product spills under upset conditions; and,
- high availability and repairability after being subjected to severe loadings.

3. More experimental work is required to assist in the prediction of failure modes by impact and explosive loadings. The experimental results would be beneficial in both the derivation of empirical formulae and the validation of existing or new numerical procedures.

4. The structural wall thickness of the outer shell would first be determined from the previous empirical relationships and would be provided for the shape prediction program which then would generate the coordinates of the meridional profile. If the resulting enclosed volume was less than required the structural thickness could be increased, while if it was larger then the material strength input to the program could be decreased and a higher factor of safety would be acquired.

In summary, it can be concluded that the Echinodome storage vessel is possible to design, construct, prestress and install employing existing procedures, without the need of any complicated unpredictable methods.

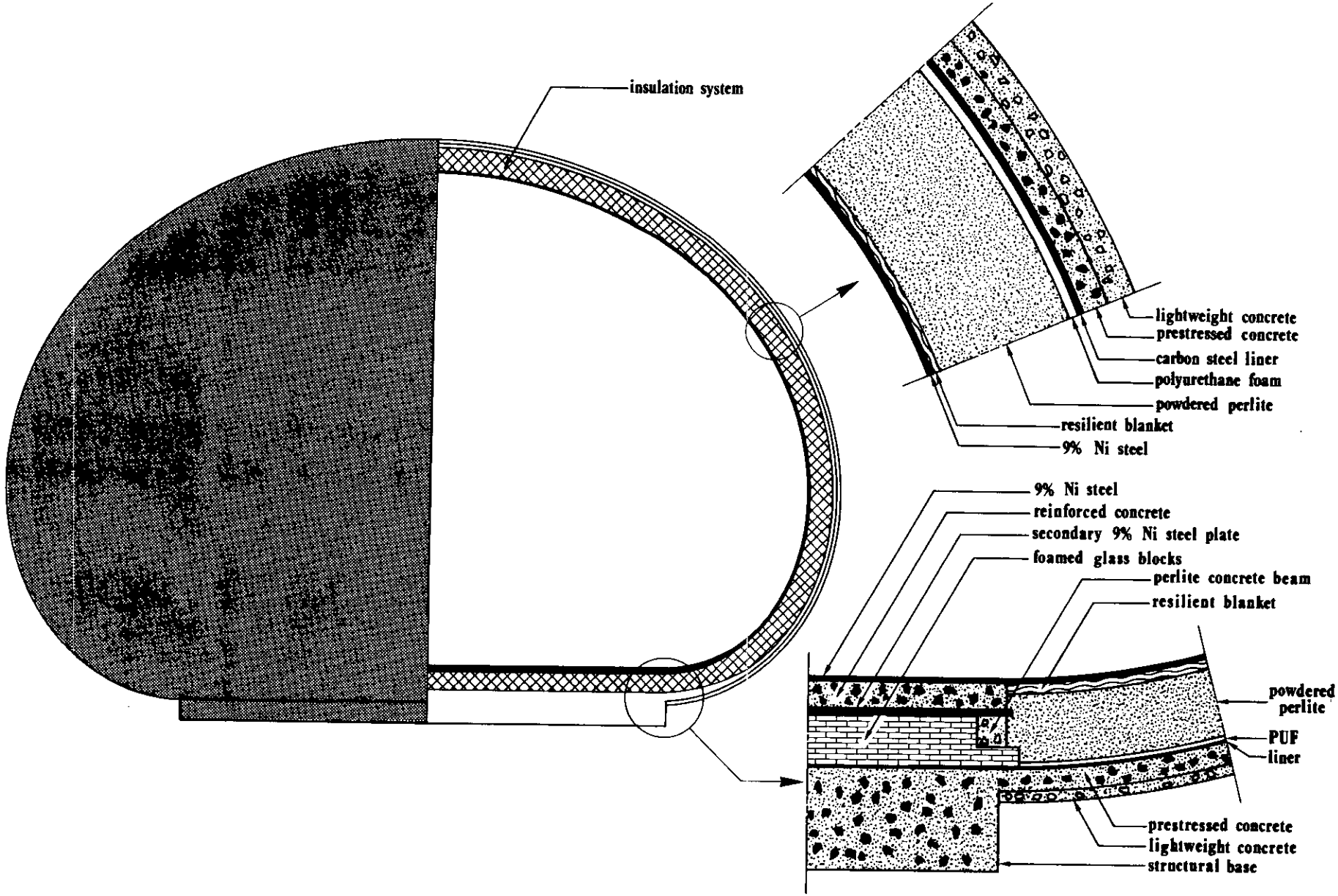

FIG. 6.1–DOUBLE WALL ECHINODOME STORAGE TANK

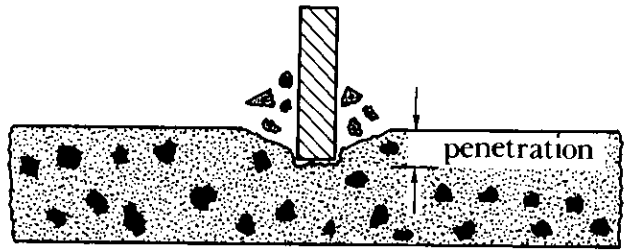

spalling

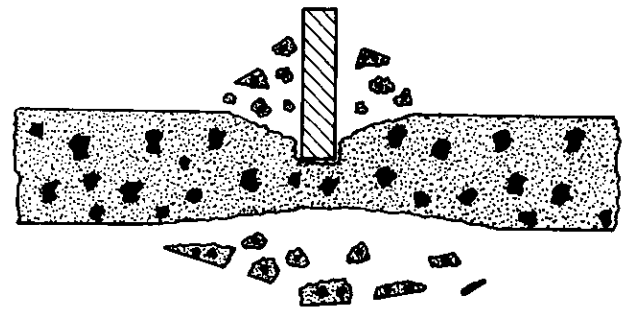

scabbing

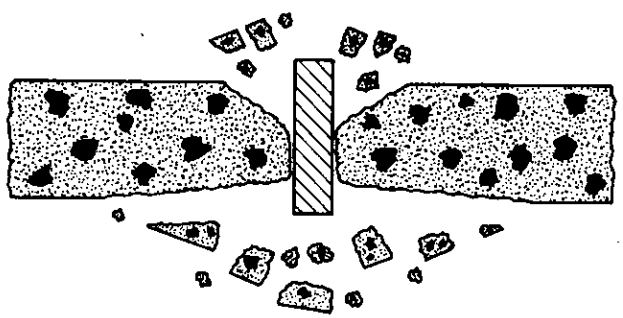

perforation

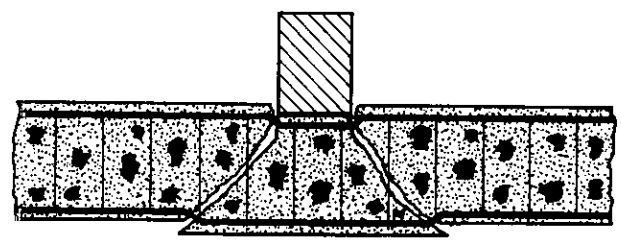

shear plug formation

FIG. 6.2–VARIOUS FORMS OF IMPACT DAMAGE

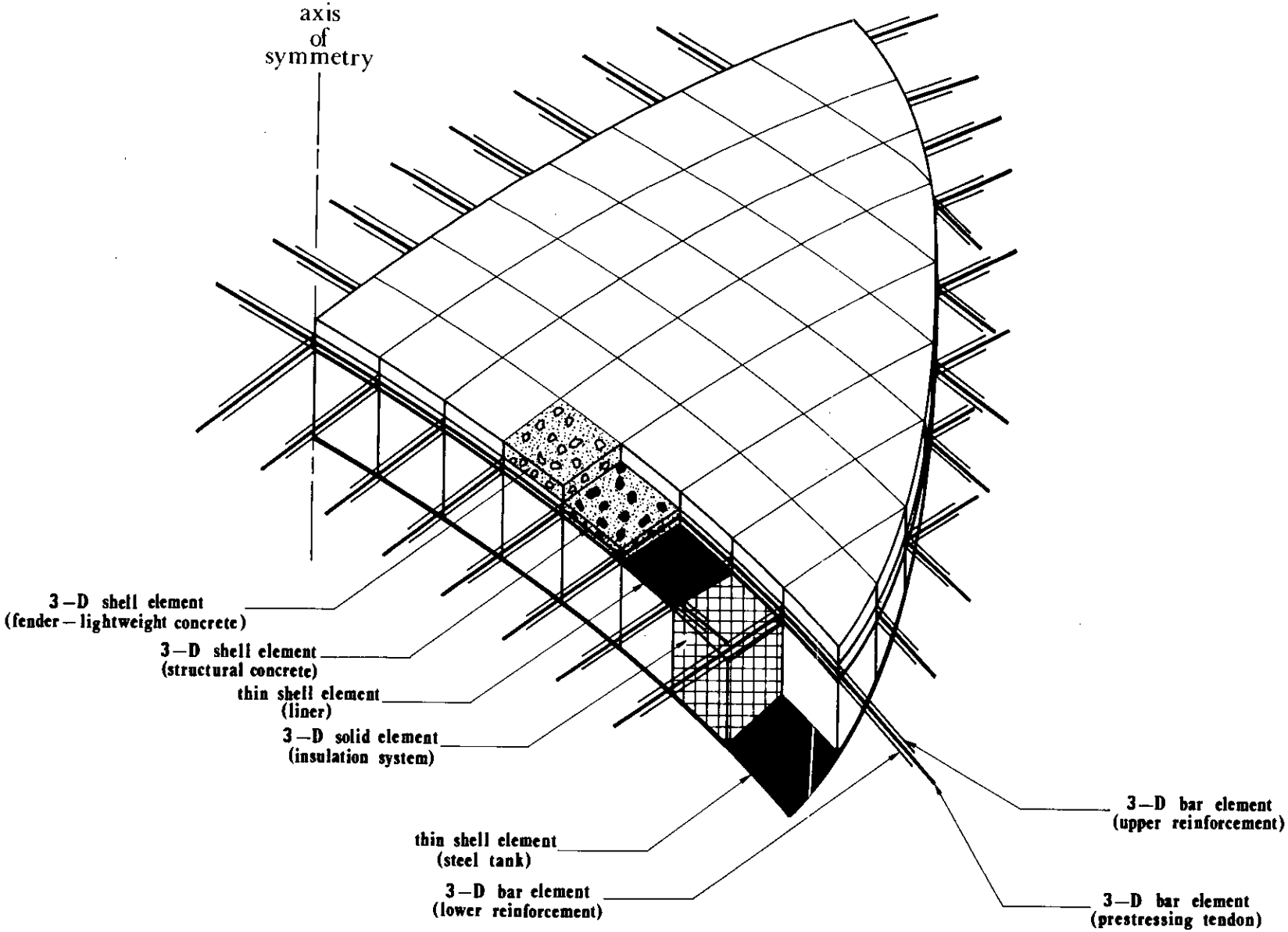

FIG. 6.3–FINITE ELEMENT IDEALISATION OF SHELL WALL (APEX ZONE)

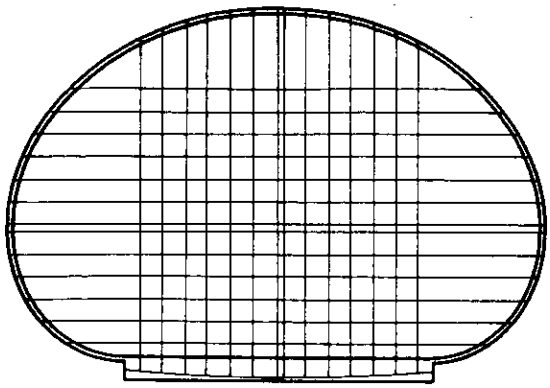

a—Prestressing layout

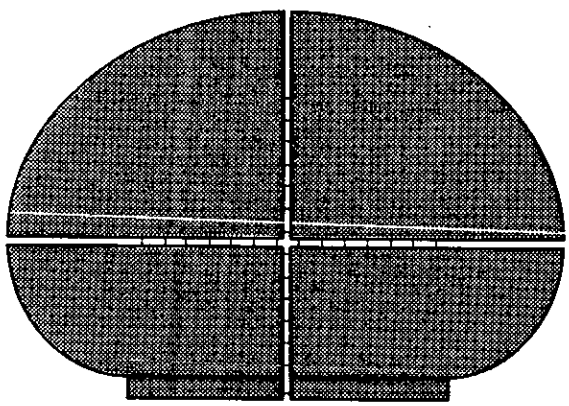

b—Inflated Echinodome

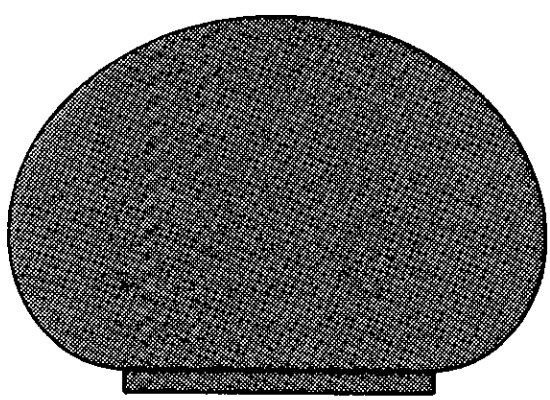

c—Monolithic prestressed Echinodome vessel

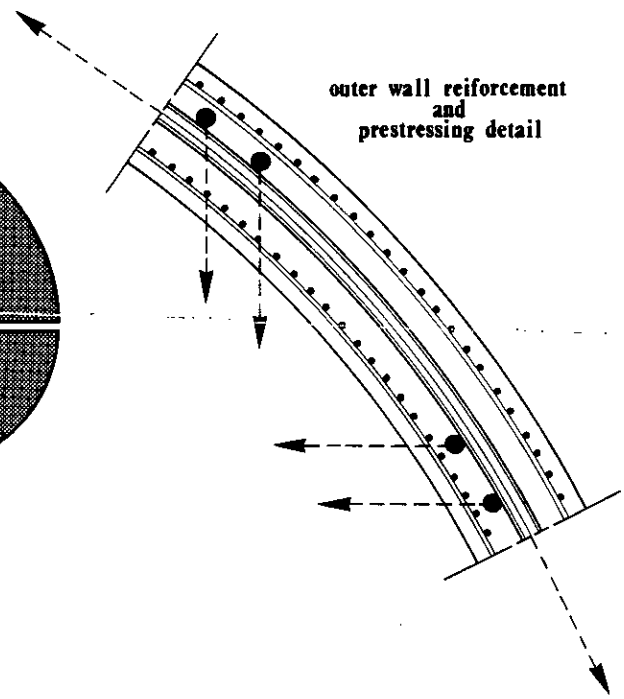

FIG. 6.4—PRESTRESS DETAILING AND PROCEDURE OF OUTER SHELL WALL

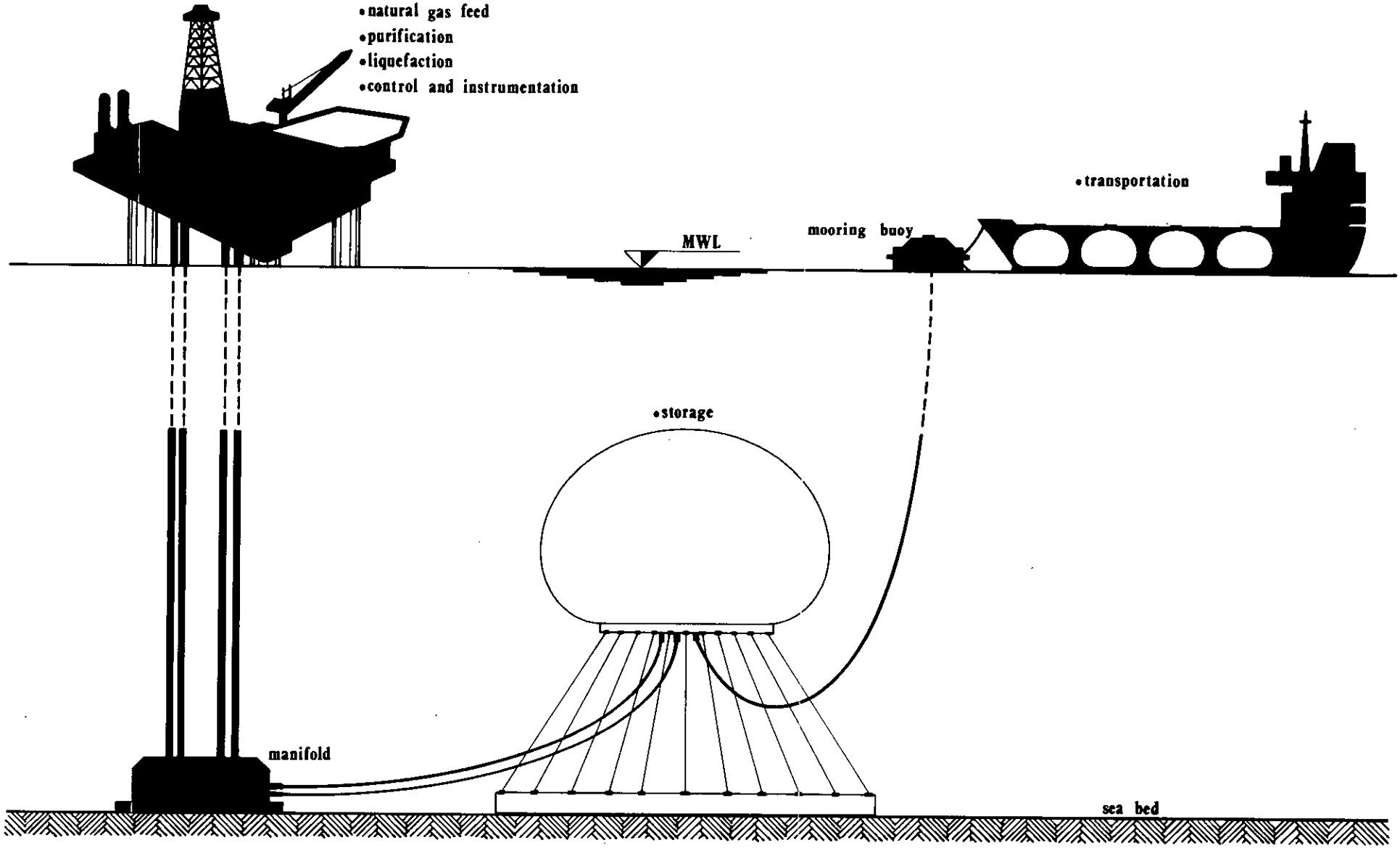

FIG. 6.5–PROPOSED OPERATING SCHEME FOR AN OFFSHORE LNG PEAK SHAVING FACILITY

CHAPTER 7

CONCLUSIONS AND RECOMMENDATIONS FOR FUTURE WORK

7.1 CONCLUSIONS

The research work of this thesis dealt with the effects of dynamic loads (impact and explosion) on the shell of uniform strength. Experimental tests were performed on a GRP model and theoretical simulation was achieved by employing the finite element method and in some cases accompanied with the boundary element technique. The main aim was to assess qualitatively the applicability of the previous numerical methods to the static, dynamic and non–linear analysis of the Echinodome. Both experimental and theoretical work carried out in the scope of this research led to the following conclusions with regard to full size Echinodome shell structures, with the purpose of storing LNG :

1. The last 10 percent of the meridional profile would have to be stiffened either by gradually thickening the shell wall, using extra reinforcement bars or a combination of both. This would increase the structure's resistance against buckling by preventing the development of high bending stresses near the base area.
2. Around towing or hose attachment points extra reinforcement is needed to resist any local bending stresses which might initiate a local buckling failure mode.
3. The maximum structural response to transient loadings is affected by the pulse shape, peak magnitude and pulse duration. The effect of pulse shape is lost for very short pulse durations and as the rise time of the pulse increases with respect to the structure's periodic time, the structural response tends towards static response (DLF $\rightarrow$ 1.0).
4. Step loading with infinite duration and zero ramping time is considered to be the most severe dynamic loading function to be applied to the Echinodome and hence it should be employed as the load–time history in a dynamic buckling analysis.
5. Before performing a dynamic collapse buckling analysis for an impact load case it is necessary to determine the load–deflection relationship under a similar form of loading applied statically. If a limit point existed then dynamic collapse due to geometrically

non–linear effects is likely to occur at a much lower magnitude than that of the static value.

6. If dynamic tests are to be carried out on an Echinodome prototype then modal testing would be useful in validating the finite element model. Newly developed correlation techniques would assist in identifying poorly modelled regions thus enabling the correction of the theoretical model. It is important to emphasise that modal testing is suitable for verifying a finite element model to be used in dynamic analyses only.

7. It would be incorrect to employ an acoustic fluid model in the theoretical investigation of strong blast pressure wave effects on a floating submerged Echinodome vessel as it would yield a reflected pressure from the structure of only twice that of the incident. It is important to preserve the non–linear terms of both the structure and fluid models, as well as accommodate the possibility of the cavitation phenomenon occurring at the fluid–structure interface. Initially, a static non–linear buckling analysis would be performed and from the load–deflection curve an appropriate decision would be taken concerning the determination of the dynamic collapse buckling pressure load.

8. A double wall Echinodome vessel, inner steel and outer reinforced or prestressed concrete covered by a fender layer, would satisfy the state of the art qualifications. This would be achieved by designing the secondary tank to limit the extent of damage in the event of any of the following upset load conditions,

   - impact by bulky and slender non–deformable objects;
   - transient overpressure shock waves resulting from nearby explosions; and,
   - the sudden zip failure of the inner tank containing LNG.

7.2 RECOMMENDATIONS FOR FUTURE WORK

The current investigation comprises a relevant part of the Echinodome behaviour under dynamic loadings and unveiled the cover for other interesting areas.

1. Without a doubt static and dynamic stability is one such area. The Souza method, which is based on observing the structure's natural frequency under different loading increments, could be employed in the determination of the critical buckling load. Then a comparison could be carried out with the Southwell predictions and numerical bifurcation and collapse estimates. The merit in using the Souza technique is that it relies on measuring a global characteristic of the structure, unlike the Southwell approach which predicts different critical loads at different parts of the structure, depending on local imperfections.

2. The ability of shock analysis programs to predict structural response to underwater explosions needs a thorough review by applying numerical techniques other than the DAA or the VMA.

3. The effect of liquid sloshing and earthquakes, acting as lateral loads, on the global and local sliding of the inner tank for a double wall configuration requires investigation.

4. Impact resistance would have to be a design criteria of Echinodome vessels containing hazardous liquids in order to limit the extent of damage during upset conditions. Therefore, experimental tests are necessary on large Echinodomes to determine the effects of the following parameters on the structure's impact resistance,

   - fender layer;
   - membrane action of curved surfaces;
   - prestressing;
   - extra bending reinforcement;
   - extra shear reinforcement in the form of stirrups;
   - mass, shape and the terminal velocity of the striking object; and,
   - prestressing from the hydrostatic pressure.

   The results of the above tests would then be used in deriving empirical formulae relevant for the prediction of wall thickness, safe against spalling, scabbing, perforation and shear plug formation. A finite element model which simulates the material behaviour during crushing, cracking and high strain rates would be employed in the theoretical investigation. Hence, the quality of the finite element formulations could be assessed by comparing the numerical predictions with the experimental measurements.

5. With the advent of parallel processing on computers a great deal of computing time could be saved when generating the Echinodome design curves for the selection of a particular shape. Experimentally derived relationships, regarding the prediction of an adequately safe wall thickness which could resist the various impact failure modes, need to be incorporated in the shape prediction program. In addition, it would be beneficial to modify the program to generate the coordinates of the meridional profile for more than one skin, with a specified gap separating each profile. Depending on the available finite element program and the type of finite element (shell or 3–D element) to be employed in the theoretical analysis, a subprogram should be included to generate the coordinates of a discretised mesh. Triangular shell elements or 3–D wedge elements should be avoided where possible, especially around the apex zone.

An intelligent computer aided design system could even be developed adopting knowledge based system techniques to combine all of the above functions which would in turn generate input data files for an existing finite element analysis program.

The finite element method of analysis is being enhanced every day by the rapid development of computers and the improvement of the solution algorithms which enable the handling of large finite element systems. It has dominated the scene of structural analysis due to its versatility in modelling complex structures, its ability to predict structural response at any point on the model to almost any load case and the possibility of incorporating constitutive models other than linear for describing the material properties under various loading conditions. Regardless of the previous statements, a theoretical analysis technique cannot be declared viable without the support of experimental evidence on scaled models or full size structures. Therefore, whenever possible during this type of research theoretical analysis was accompanied by experimental tests for comparative purposes.

REFERENCES

1. ANON., "A New Shape on the Agriculture Horizon", *Engineering Outlook*, vol. 27, no. 2, College of Engineering, University of Illinois at Urbana–Champaign, (1985).

2. ROYLES, R., SOFOLUWE, A. B., BAIG, M. M., and CURRIE, A. J., "Behaviour of Underwater Enclosures of Optimum Design", *Strain*, vol. 16, no. 1, pp. 12–20, (1980).

3. SOFOLUWE, A. B., "Studies of a Structural Form for Underwater Structures", Ph.D. Thesis, Dept Civil Engineering & Building Science, University of Edinburgh, (1980).

4. LLAMBIAS, J. M., "Response of an Underwater Structure of Optimum Shape to General Loading", Ph.D. Thesis, Dept Civil Engineering & Building Science, University of Edinburgh, (1985).

5. NOVOZHILOV, V. V., *The Theory of Thin Shells*, pp. 124–130, P. Noordhoff, Groningen, The Netherlands, (1959).

6. FLÜGGE, W., *Stresses in Shells*, pp. 39–45, Springer–Verlag, Berlin, Germany, (1959).

7. TIMOSHENKO, S. P. and WOINOWSKY-KRIEGER, S., *Theory of Plates and Shells, 2nd Edition*, pp. 442–445, McGraw–Hill, New York, (1970).

8. PEDERSEN, P. T. and JENSEN, J. J., "Correlation Between Experimental Buckling Loads and Theoretical Predictions for Spherical Cargo Tanks for LNG", in *Proceedings of the Steel Plated Structures Conference*, pp. 638–657, Crosby Lockwood, London, (1976).

9. ROYLES, R. and LLAMBIAS, J. M., "Storage Aspects of Liquid Gases Underwater and the Structural Implications", in *Proceedings of the International Symposium on Storage and Transport of LPG and LNG*, vol. 2, pp. 55–72, Koninklijke Vlaamse Ingenieursvereniging, Technologisch Instituut (Kommissie Metaalbouw), Antwerpen, Belgium, (1984).

10. ROYLES, R., LLAMBIAS, J. M., and EL-DEEB, K. M., "Response of Echinodomes to Asymmetric Loading", in *Proceedings of the International Conference on the Design and Construction of Non–Conventional Structures*, ed. B. H. V. TOPPING, vol. 1, pp. 167–183, Civil-Comp Press, Edinburgh, (1987).

11. ROYLES, R. and LLAMBIAS, J. M., "Buckling Aspects of the Behaviour of an Underwater Pressure Vessel", in *Proceedings of the Applied Solid Mechanics — 1*, ed. A. S. TOOTH and J. SPENCER, pp. 287–303, Elsevier Applied Science, London, (1985).

12. ROYLES, R. and LLAMBIAS, J. M., "Buckling Behaviour of an Underwater Storage Vessel", *Experimental Mechanics*, vol. 25, no. 4, pp. 421–428, (1985).

13. ROYLES, R. and JEFFREY, D. C., "A Microcomputer–Controlled Scanning System for Transducers", *Experimental Techniques*, vol. 7, no. 4, pp. 26–28, (1983).

14. HENDRY, A. W., *Elements of Experimental Stress Analysis, SI Edition*, Pergamon Press, Oxford, (1977).

15. CHAPRA, S. C. and CANALE, R. P., *Numerical Methods for Engineers*, McGraw–Hill, Singapore, (1985).

16. ZIENKIEWICZ, O. C., *The Finite Element Method, 3rd Edition*, McGraw–Hill, London, (1977).

17. BATHE, K. J., *Finite Element Procedures in Engineering Analysis*, Prentice–Hall, Englewood Cliffs, NJ, U.S.A., (1982).

18. ANON., *LUSAS User Manual Version 9*, FEA Ltd, London, (1989).

19. ANON., *LUSAS Theory Manual Version 9*, FEA Ltd, London, (1989).

20. ANON., *PAFEC Data Preparation User Manual Level 7.1*, PAFEC Ltd, Nottingham, (1989).

21. ANON., *PAFEC Theory Manual*, PAFEC Ltd, Nottingham, (1984).

22. IRONS, B. M., "The Semiloof Shell Element", in *Finite Elements for Thin Shells and Curved Members*, ed. D. G. ASHWELL and R. H. GALLAGHER, pp. 197–222, John Wiley & Sons, London, (1976).

23. ABU KASSIM, A. M., "The Theorems of Structural and Geometric Variation for Linear and Nonlinear Finite Element Analysis", Ph.D. Thesis, Dept Civil Engineering & Building Science, University of Edinburgh, (1986).

24. OWEN, D. R. J. and HINTON, E., *Finite Elements in Plasticity*, Pineridge Press, Swansea, Wales, (1980).

25. ANON., *DOGS User Manual Level 3.2*, PAFEC Ltd, Nottingham, (1986).

26. ANON., *SWANS User Manual Level 3.2A*, PAFEC Ltd, Nottingham, (1986).

27. BUSHNELL, D., *Computerized Buckling Analysis of Shells*, Martinus Nijhoff, Dordrecht, The Netherlands, (1985).

28. SOUZA, M. A., "Vibration Characteristics of Buckled Structures", Ph.D. Thesis, Dept Civil & Municipal Engineering, University College London, University of London, (1982).

29. HORTON, W. H., NASSAR, E. M., and SINGHAL, M. K., "Determination of the Critical Loads of Shells by Nondestructive Methods", *Experimental Mechanics*, vol. 17, no. 4, pp. 154–160, (1977).

30. SOUZA, M. A., FOK, W. C., and WALKER, A. C., "Review of Experimental Techniques for Thin–Walled Structures Liable to Buckling Part — I Neutral and Unstable Buckling", *Experimental Techniques*, vol. 7, no. 9, pp. 21–25, (1983).

31. ROORDA, J., "Some Thoughts on the Southwell Plot", *Journal of the Engineering Mechanics Division, A.S.C.E.*, vol. 93, no. EM6, pp. 37–48, (1967).

32. SPENCER, H. H. and WALKER, A. C., "Critique of the Southwell Plots with Proposals for Alternative Methods", *Experimental Mechanics*, vol. 15, no. 3, pp. 303–310, (1975).

33. ANON., *MINITAB Reference Manual Release 6.1*, MINITAB, Inc., State College, PA, U.S.A., (1988).

34. RYAN, B. F., JOINER, B. L., and RYAN, T. A., *MINITAB Handbook, 2nd Edition*, PWS–Kent, Boston, U.S.A., (1985).

35. BERGAN, P. G. and SØREIDE, T. H., "Solution Of Large Displacement and Instability Problems Using the Current Stiffness Parameter", in *Proceedings of the International Conference on Finite Elements in Nonlinear Solid and Structural Mechanics*, ed. P. G. BERGAN *et al.*, vol. 2, pp. 647–669, TAPIR, Trondheim, Norway, (1978).

36. BERGAN, P. G., HOORRIGMOE, G., KRÅKELAND, B., and SØREIDE, T. H., "Solution Techniques for Nonlinear Finite Element Problems", *International Journal for Numerical Methods in Engineering*, vol. 12, no. 11, pp. 1677–1696, (1978).

37. GUYAN, R. J., "Reduction of Stiffness and Mass Matrices", *A.I.A.A. Journal*, vol. 3, no. 2, p. 380, (1965).

38. ZUKAS, J. A., NICHOLAS, T., SWIFT, H. F., GRESZCZUK, L. B., and CURRAN, D. R., *Impact Dynamics*, John Wiley & Sons, Inc., New York, (1982).

39. JONES, N., "Dynamic Elastic and Inelastic Buckling of Shells", in *Developments in Thin–Walled Structures — 2*, ed. J. RHODES and A. C. WALKER, pp. 49–91, Elsevier Applied Science, London, (1984).

40. JACOBSEN, L. S. and AYRE, R. S., *Engineering Vibrations*, McGraw–Hill, New York, (1958).

41. BUZDUGAN, G., MIHAILESCU, E., and RADEŞ, M., *Vibration Measurement*, Martinus Nijhoff, Dordrecht, The Netherlands, (1986).

42. RANDALL, R. B., *Frequency Analysis, 3rd Edition*, Brüel & Kjær, Nærum, Denmark, (1987).

43. NEWLAND, D. E., *An Introduction to Random Vibrations and Spectral Analysis, 2nd Edition*, Longman, New York, (1984).

44. NICKELL, R. E., "On the Stability of Approximation Operators in Problems of Structural Dynamics", *International Journal of Solids and Structures*, vol. 7, no. 3, pp. 301–319, (1971).

45. KRIEG, R. D. and KEY, S. W., "Transient Shell Response by Numerical Time Integration", *International Journal for Numerical Methods in Engineering*, vol. 7, no. 3, pp. 273–286, (1973).

46. HILBER, H. M., HUGHES, T. J. R., and TAYLOR, R. L., "Improved Numerical Dissipation for Time Integration Algorithms in Structural Dynamics", *Earthquake Engineering and Structural Dynamics*, vol. 5, no. 3, pp. 283–292, (1977).

47. WOOD, W. L., "On the Zienkiewicz Four–Time–Level Scheme for the Numerical Integration of Vibration Levels", *International Journal for Numerical Methods in Engineering*, vol. 11, no. 10, pp. 1519–1528, (1977).

48. WEEKS, G., "Temporal Operators for Nonlinear Structural Dynamics Problems", *Journal of the Engineering Mechanics Division, A.S.C.E.*, vol. 98, no. EM5, pp. 1087–1104, (1972).

49. EWINS, D. J., *Modal Testing : Theory and Practice*, Research Studies Press, Letchworth, Herts, England, (1984).

50. SVALBONAS, V. and KALNINS, A., "Dynamic Buckling of Shells : Evaluation of Various Methods", *Nuclear Engineering and Design*, vol. 44, pp. 331–356, (1977).

51. BATHE, K. J. and OZDEMIR, H., "Elasto–Plastic Large Deformation Static and Dynamic Analysis", *Computers and Structures*, vol. 6, no. 2, pp. 81–92, (1976).

52. SONG, B. and JONES, N., "Dynamic Elastic Buckling of Complete Spherical Shells with Initial Imperfections", *Journal of Structural Mechanics*, vol. 11, no. 3, pp. 327–350, (1983).

53. AKKAS, N., "Bifurcation and Snap–Through Phenomena in Asymmetric Dynamic Analysis of Shallow Spherical Shells", *Computers and Structures*, vol. 6, no. 3, pp. 241–251, (1976).

54. SIDHU, J. and EWINS, D. J., "Correlation of Finite Element and Modal Test Studies of a Practical Structure", in *Proceedings of the 2nd International Modal Analysis Conference*, ed. P. B. JUHL and D. J. DEMICHELE, vol. 2, pp. 756–762, Society of Experimental Mechanics, Bethel, CT, U.S.A., (1984).

55. LIEVEN, N. A. J. and EWINS, D. J., "Spatial Correlation of Mode Shapes, the Coordinate Modal Assurance Criterion (COMAC)", in *Proceedings of the 6th International Modal Analysis Conference*, vol. 1, Society of Experimental Mechanics, Bethel, CT, U.S.A., (1988).

56. EWINS, D. J., HE, J., and LIEVEN, N. A. J., "A Review of the Error Matrix Method (EMM) for Structural Dynamic Model Comparison", in *Proceedings of the European Space Agency International Conference*, Abstracts esa sp—289, pp. 1–8, Paris, (1988).

57. DØSSING, O., "Improvement to Monoreference Modal Data by Adding an Oblique Degree of Freedom for the Reference", *Brüel & Kjær Technical Review*, no. 3, pp. 23–42, (1986).

58. ANON., *Model 3562A Dynamic Signal Analyzer Operating Manual*, Hewlett-Packard Co., Everett, WA, U.S.A., (1985).

59. RAMSEY, K. A., "Effective Measurements for Structural Dynamics Testing — Part II", *Sound and Vibration*, vol. 10, no. 4, pp. 18–31, (1976).

60. HERLUFSEN, H., "Dual FFT Analysis — Part I", *Brüel & Kjær Technical Review*, no. 1, pp. 3–56, (1984).

61. SOHANEY, R. C. and NIETERS, J. M., "Proper Use of Weighting Functions for Impact Testing", *Brüel & Kjær Technical Review*, no. 4, pp. 21–31, (1984).

62. CORELLI, D. and BROWN, D. L., "Impact Testing Considerations", in *Proceedings of the 2nd International Modal Analysis Conference*, ed. P. B. JUHL and D. J. DEMICHELE, vol. 2, pp. 735–742, Society of Experimental Mechanics, Bethel, CT, U.S.A., (1984).

63. OLSEN, N., "Excitation Functions for Structural Frequency Response Measurements", in *Proceedings of the 2nd International Modal Analysis Conference*, ed. P. B. JUHL and D. J. DEMICHELE, vol. 2, pp. 894–902, Society of Experimental Mechanics, Bethel, CT, U.S.A., (1984).

64. GADE, S. and HERLUFSEN, H., "Signals and Units", *Brüel & Kjær Technical Review*, no. 3, pp. 29–38, (1987).

65. TABER, R. C., VOLD, H., BROWN, D. L., and ROCKLIN, G. T., "Exponential Window for Burst Random Excitation", in *Proceedings of the 3rd International Modal Analysis Conference*, ed. D. J. DEMICHELE, vol. 2, pp. 989–995, Society of Experimental Mechanics, Bethel, CT, U.S.A., (1985).

66. EWINS, D. J., "Whys and Wherefores of Modal Testing", *Journal of the Society of Environmental Engineers*, vol. 18, no. 3, pp. 3–15, (1979).

67. EWINS, D. J., *Advanced Structural Dynamics Using Integrated Finite Element and Test Methods (course notes)*, Dept Mechanical Engineering, Imperial College of Science and Technology, University of London, (1989).

68. SNOEYS, R., SAS, P., and AUWERAER, V. D., "Trends in Experimental Modal Analysis", *Mechanical Systems and Signal Processing*, vol. 1, no. 1, pp. 5–27, (1987).

69. ANON., *MODAL 3.0 Operating Manual Version 5.0*, Structural Measurement Systems, Inc., California, (1987).

70. RICHARDSON, M. H. and FORMENTI, D. L., "Parameter Estimation from Frequency Response Measurements Using Rational Fraction Polynomials", in *Proceedings of the 1st International Modal Analysis Conference*, ed. P. B. JUHL and D. J. DEMICHELE, pp. 167–181, Society of Experimental Mechanics, Bethel, CT, U.S.A., (1982).

71. RICHARDSON, M. H., "Global Frequency and Damping Estimates from Frequency Response Measurements ", in *Proceedings of the 4th International Modal Analysis Conference*, ed. D. J. DEMICHELE, vol. 1, pp. 465–470, Society of Experimental Mechanics, Bethel, CT, U.S.A., (1986).

72. BRINKMAN, B. A., "Generating Modal Parameters that Compensate for Residual Energy", in *Proceedings of the 4th International Modal Analysis Conference*, ed. D. J. DEMICHELE, vol. 1, pp. 119–122, Society of Experimental Mechanics, Bethel, CT, U.S.A., (1986).

73. MAIA, N. M. M. and EWINS, D. J., "Modal Analysis of Double Modes : A First Approach to "Intelligent" Curve–Fitting", in *Proceedings of the 5th International Modal Analysis Conference*, ed. D. J. DEMICHELE, vol. 2, pp. 1302–1308, Society of Experimental Mechanics, Bethel, CT, U.S.A., (1987).

74. BRINKMAN, B. A. and MACIOCE, D. J., "Understanding Modal Parameter Terminology and Mode Shape Scaling", in *Proceedings of the 3rd International Modal Analysis Conference*, ed. D. J. DEMICHELE, vol. 2, pp. 840–844, Society of Experimental Mechanics, Bethel, CT, U.S.A., (1985).

75. ANON., *UNIMAP Manual Version 2.4*, European Software Contractors A/S, Lyngby, Denmark, (1985).

76. HOPTON, G. W. and DEBLAUWE, F., "Relationships between Analysis Errors and Complex Mode Shapes", in *Proceedings of the 5th International Modal Analysis Conference*, ed. D. J. DEMICHELE, vol. 1, pp. 381–388, Society of Experimental Mechanics, Bethel, CT, U.S.A., (1987).

77. CHEN, J. C. and TRUBERT, M., "Galileo Modal Test and Pre-Test Analysis", in *Proceedings of the 2nd International Modal Analysis Conference*, ed. P. B. JUHL and D. J. DEMICHELE, vol. 2, pp. 796–802, Society of Experimental Mechanics, Bethel, CT, U.S.A., (1984).

78. ALLEMANG, R. J. and BROWN, D. L., "A Correlation for Modal Vector Analysis", in *Proceedings of the 2nd International Modal Analysis Conference*, ed. P. B. JUHL and D. J. DEMICHELE, vol. 1, pp. 110–116, Society of Experimental Mechanics, Bethel, CT, U.S.A., (1984).

79. DOBSON, B. J., "Modification of Finite Element Models Using Experimental Modal Analysis", in *Proceedings of the 2nd International Modal Analysis Conference*, ed. P. B. JUHL and D. J. DEMICHELE, vol. 2, pp. 593–601, Society of Experimental Mechanics, Bethel, CT, U.S.A., (1984).

80. HE, J., "Identification of Structural Dynamic Characteristics", Ph.D. Thesis, Dept Mechanical Engineering, Imperial College of Science and Technology, University of London, (1987).

81. MACEY, P. C., "Acoustic and Structure Interaction Problems Using Finite and Boundary Elements", Ph.D. Thesis, University of Nottingham, (1987).

82. COLE, R. H., *Underwater Explosions*, Princeton University Press, New Jersey, (1948).

83. A.R.E., *Private Communications*, M.o.D., Dunfermline, Scotland, (1988).

84. ANON., *DADISP Worksheet Manual Version 1.05*, DSP Development Co., Cambridge, MA, U.S.A., (1987).

85. BENDAT, J. S., *The Hilbert Transform and Applications to Correlation Measurements*, Brüel & Kjær, Nærum, Denmark, (1985).

86. THRANE, N., "The Hilbert Transform", *Brüel & Kjær Technical Review*, no. 3, pp. 3–15, (1984).

87. ROBERTS, R. A. and MULLIS, C. T., *Digital Signal Processing*, Addison–Wesley, Reading, MA, U.S.A., (1987).

88. PROAKIS, J. G. and MANOLAKIS, D. G., *Introduction to Digital Signal Processing*, Macmillan, New York, (1988).

89. ANON., *Extracts of Explosive Charge Nomographs*, A. R. E., Dunfermline, Scotland.

90. HUANG, H., "A Qualitative Appraisal of the Doubly Asymptotic Approximation for Transient Analysis of Submerged Structures Excited by Weak Shock Waves", *NRL Memorandum Report 3135*, Naval Research Laboratory, Washington, DC, (1975).

91. GEERS, T. L., "Doubly Asymptotic Approximations for Transient Motions of Submerged Structures", *Journal of the Acoustical Society of America*, vol. 64, no. 5, pp. 1500–1508, (1978).

92. GEERS, T. L. and FELIPPA, C. A., "Doubly Asymptotic Approximations for Vibration Analysis of Submerged Structures", *Journal of the Acoustical Society of America*, vol. 73, no. 4, pp. 1152–1159, (1983).

93. AKKAS, N. and JACKSON, J. E., "Structural Instability in Fluid–Structure Systems Under Hydrodynamic Shock Conditions", *Journal of Sound and Vibration*, vol. 97, no. 2, pp. 247–259, (1984).

94. BOMHARD, H., "Concrete Structures as a Preventative Answer to Environmental Catastrophes", *FIP Notes*, no. 3, pp. 15–19, (1988).

95. DINIC, G., "Hard Impact of Reinforced Concrete Domes, Circular Slabs and Fender Materials", Ph.D. Thesis, Dept Civil Engineering, Imperial College of Science and Technology, University of London, (1985).

96. SUZUKI, S., NAKANO, Y., HIROSE, K., OKUMURA, T., NISHIKAWA, H., and SATO, M., "Production of 9% Ni Steel Plates for Liquefied Natural Gas Tanks", *Kawasaki Steel Technical Report*, no. 6, pp. 31–44, (1982).

97. ANON., "Cryogenic Storage", *Bulletin No. 8600*, Chicago Bridge & Iron Company, (1977).

98. *Guide to Good Practice — Preliminary Recommendations for the Design of Prestressed Concrete Containment Structures for the Storage of Refrigerated Liquefied Gases (RLG)*, FIP/3/6, Federation Internationale de la Precontrainte, (1982).

99. MORRISON, D. M., "Prestressed Concrete/Steel Tanks for Liquefied Natural Gas Storage in the Arabian Gulf", in *Proceedings of GASTECH 86 LNG/LPG Conference*, pp. 409–414, GASTECH Ltd, Herts, England, (1987).

100. BOMHARD, H., "Concrete Pressure Vessels–The Preventative Answer to the Mexico City LPG Disaster", in *Proceedings of GASTECH 86 LNG/LPG Conference*, pp. 415–421, GASTECH Ltd, Herts, England, (1987).

101. PERRY, S. H., "Identification and Repair of Marine Concrete Damaged by Hard Impact", in *Proceedings of the International Conference on Concrete in the Marine Environment*, pp. 57–68, The Concrete Society, London, (1986).

102. WIMPEY LABORATORIES, "Review of Object Types and Velocities, and of Available Empirical Formulae", in *The Assessment of Impact Damage Caused by Dropped Objects on Concrete Offshore Structures, Part A*, pp. 7–78, HMSO, London, (1989).

103. Committee for Cryogenic Storage in Concrete Tanks, "Storage Tanks for Refrigerated Liquefied Gases with an Outer Concrete Container", *Final Report*, Central Environmental Control Agency Rijnmond, Schiedam, The Netherlands, (1985).

104. BROWN, I. C. and PERRY, S. H., "Development on a New Assessment Method", in *The Assessment of Impact Damage Caused by Dropped Objects on Concrete Offshore Structures, Part B*, pp. 79–151, HMSO, London, (1989).

APPENDIX A

SOLUTION PROCEDURE FOR A GEOMETRICALLY NON-LINEAR ANALYSIS

The non–linear system can be written as a set of algebraic equations as follows [23] :

$$\{R(\delta)\} = [K(\delta)]\{\delta\} - \{P\} = \{0\} \quad \text{.....} \quad \text{(A.1)}$$

where $\{R(\delta)\}$ represents the vector of residual loads; and,

$\{0\}$ represents a null vector.

and when using the Newton–Raphson technique to solve Eqn (A.1) it may be rewritten as follows :

$$\{dR\} = [K_T]\{d\delta\} \quad \text{.....} \quad \text{(A.2)}$$

$$[K_T] = [K_o] + [K_L] + [K_\sigma] \quad \text{.....} \quad \text{(A.3)}$$

where $[K_T]$ represents the total tangential stiffness matrix;

$[K_o]$ represents the small displacements stiffness matrix;

$[K_L]$ represents the large displacements stiffness matrix; and,

$[K_\sigma]$ represents the initial stresses or geometric stiffness matrix.

After using a Taylor series expansion and rearranging terms Eqn (A.2) is replaced by the following (for more details see Ref. (23)):

$$[K_T^r]\{\Delta\delta_i^r\} = -\{R_i^r\} \quad \text{.....} \quad \text{(A.4)}$$

$$\{\delta_i^r\} = \{\delta_i^{r-1}\} + \{\Delta\delta_i^r\} \quad \text{.....} \quad \text{(A.5)}$$

where **r** is a superscript indicating the r^{th} iteration; and,

i is a subscript indicating the i^{th} increment.

The optimum solution procedure [24] employing a modified Newton–Raphson approach can be summarised as follows :

1. The total load is divided into several increments with the size of each dependent on the amount of deformation the structure undergoes when subjected to the load increment.
2. For the first iteration of each load step a linear solution is carried to estimate $\{\delta_i^o\}$.
3. The tangential stiffness matrix $[\mathbf{K}_{T\,i}^1]$ corresponding to $\{\delta_i^o\}$ is determined.
4. The residual load vector $\{\mathbf{R}_i^1\}$ is computed using Eqn (A.1).
5. The correction to the displacements is calculated using the following equation :

$$\{\Delta\delta_i^1\} = -[\mathbf{K}_{T\,i}^1]^{-1}\{\mathbf{R}_i^1\} \quad \text{.....} \quad \text{(A.6)}$$

6. An improved approximation to the displacements $\{\delta_i^1\}$ is obtained using Eqn (A.5).

Steps 3, 4, 5 and 6 are repeated, each time updating the tangential stiffness matrix, until some convergence criterion is satisfied indicating that $\{\mathbf{R}_i^r\}$ is sufficiently small, then the solution procedure shifts to start from step 2 for the following load increment.

In LUSAS another modified Newton–Raphson solution procedure was possible by keeping the initial tangential stiffness matrix constant throughout the subsequent equilibrium iterations. The former approach was adopted in the current research.

APPENDIX B

DERIVATION OF THE MODIFIED SOUTHWELL PLOT EQUATIONS

From Eqn (2.5)

$$\Rightarrow \frac{\delta}{P} = \frac{\delta}{P_{cr}} + \frac{\delta_o}{P_{cr}} \quad \text{.....} \quad \text{(B.1)}$$

Let $s \equiv$ the transducer's scale reading; and,

$s_o \equiv$ the true (but unknown) transducer reading at $s = 0$.

$$\Rightarrow \delta = s - s_o \quad \text{.....} \quad \text{(B.2)}$$

Substituting in Eqn (B.1)

$$\Rightarrow \frac{(s - s_o)}{P} = \frac{(s - s_o)}{P_{cr}} + \frac{\delta_o}{P_{cr}} \quad \text{.....} \quad \text{(B.3)}$$

Multiplying both sides by $\frac{s}{(s - s_o)}$

$$\Rightarrow \frac{s}{P} = \frac{1}{P_{cr}} \left[s + \frac{s\delta_o}{(s - s_o)} \right] \quad \text{.....} \quad \text{(B.4)}$$

The previous equation contains three unknown constants P_{cr}, δ_o and s_o. Introducing the pivot point (P^*, s^*) into Eqn (B.4)

$$\Rightarrow \frac{s^*}{P^*} = \frac{1}{P_{cr}} \left[s^* + \frac{s^*\delta_o}{(s^* - s_o)} \right] \quad \text{.....} \quad \text{(B.5)}$$

$$\Rightarrow \delta_o = \left[P_{cr}\frac{s^*}{P^*} - s^*\right]\frac{s^* - s_o}{s^*} \quad \text{.....} \quad \text{(B.6)}$$

Using Eqn (B.4)

$$\Rightarrow \delta_o = \left[P_{cr}\frac{s}{P} - s\right]\frac{s - s_o}{s} \quad \text{.....} \quad \text{(B.7)}$$

$$\Rightarrow \left[P_{cr}\frac{s}{P} - s\right]\frac{s - s_o}{s} = \left[P_{cr}\frac{s^*}{P^*} - s^*\right]\frac{s^* - s_o}{s^*} \quad \text{.....} \quad \text{(B.8)}$$

$$\Rightarrow P_{cr}\frac{s}{P} - s - P_{cr}\frac{s_o}{P} + s_o = P_{cr}\frac{s^*}{P^*} - s^* - P_{cr}\frac{s_o}{P^*} + s_o \quad \text{.....} \quad \text{(B.9)}$$

$$\Rightarrow P_{cr}\left[\frac{(s - s_o)}{P} - \frac{(s^* - s_o)}{P^*}\right] = (s - s^*) \quad \text{.....} \quad \text{(B.10)}$$

$$\Rightarrow P_{cr}\left[\frac{(P^*s - Ps^*) + s_o(P - P^*)}{PP^*}\right] = (s - s^*) \quad \text{.....} \quad \text{(B.11)}$$

Multiplying both sides by $\dfrac{P^*P}{(P - P^*)}$

$$\Rightarrow \left[\frac{P^*P}{P - P^*}(s - s^*)\right] = P_{cr}\left[\frac{P^*s - Ps^*}{P - P^*}\right] + P_{cr}s_o \quad \text{.....} \quad \text{(B.12)}$$

APPENDIX C

THE SUBSPACE ITERATION METHOD

The technique is presented mathematically as follows :

1. Subspace iteration

$$[K][\overline{X}_{k+1}] = [M][X_k] = [Y_k] \quad \text{.....} \quad \text{(C.1)}$$

$$[K_{k+1}] = [\overline{X}_{k+1}]^T[Y_k] \quad \text{.....} \quad \text{(C.2)}$$

$$[\overline{Y}_{k+1}] = [M][\overline{X}_{k+1}] \quad \text{.....} \quad \text{(C.3)}$$

$$[M_{k+1}] = [\overline{X}_{k+1}]^T[\overline{Y}_{k+1}] \quad \text{.....} \quad \text{(C.4)}$$

$$[K_{k+1}][Q_{k+1}] = [M_{k+1}][Q_{k+1}][\Omega^2_{k+1}] \quad \text{.....} \quad \text{(C.5)}$$

$$[Y_{k+1}] = [\overline{Y}_{k+1}][Q_{k+1}] \quad \text{.....} \quad \text{(C.6)}$$

2. Convergence check

$$\frac{|\Omega_i^{2\,(l+1)} - \Omega_i^{2\,(l)}|}{\Omega_i^{2\,(l+1)}} \leq \text{tolerance} \quad ; i = 1, 2, 3, \ldots\ldots, p \quad \text{.....} \quad \text{(C.7)}$$

and as $l \rightarrow \infty$

$$\Omega_{k+1}{}^2 \rightarrow \Omega^2 \text{ and } [X_{k+1}] \rightarrow [\Phi]$$

3. Sturm sequence check

$$[\overline{K}] = [K] - [\mu][M] \qquad \text{(C.8)}$$

$$[\overline{K}] = [L][D][L]^T \qquad \text{(C.9)}$$

4. Error estimates

$$\frac{\|[K]\{\phi\}_i^{(l+1)} - \Omega_i^{2\,(l+1)}[M]\{\phi\}_i^{(l+1)}\|_2}{\|[K]\{\phi\}_i^{(l+1)}\|_2} \qquad \text{(C.10)}$$

where k is a subscript denoting the iteration number;

l is a superscript denoting the last iteration number; and,

$\| \|_2$ indicates an Euclidean vector norm.

From the previous presentation it is observed that a set of q iteration vectors must be established to start the solution procedure and this is achieved by assuming the first column in $[M][X_1]$ ($[Y]_1$) to be the diagonal of [M] and the other columns are unit vectors $\{e_i\}$ § with entries +1 corresponding to the degrees of freedom that have the smallest k_{ii}/m_{ii} ratios, where k_{ii} and m_{ii} are diagonal elements in [K] and [M] respectively.

The number of q iteration vectors was recommended by Bathe [17] to be a minimum of either of (2p, p+8), where p is the required number of eigenvalues and eigenvectors to be computed.

The matrix $[\overline{K}]$ is to be factorised into $[L][D][L]^T$, where [L] is a lower triangular matrix and [D] is a diagonal matrix. The number of negative elements in [D] will be equal to the number of eigenvalues smaller than the applied shift [μ] and as a result a conservative estimate for the region in which the exact eigenvalues lie may be given by :

§ $\{e_i\}$ is a unit vector which contains zero elements throughout except for one element having a value of +1.

$$0.99\Omega_i^{2\,(l+1)} < \Omega_i^2 < 1.01\Omega_i^{2\,(l+1)} \quad \text{.....} \quad \text{(C.11)}$$

$$\Rightarrow [\mu]_i = 0.01\ \Omega_i^{2\,(l+1)} \quad \text{.....} \quad \text{(C.12)}$$

APPENDIX D

THE GUYAN REDUCTION TECHNIQUE

The displacement vector is partitioned into master and slave degrees of freedom as follows :

$$\{\delta\} = \begin{Bmatrix}\{\delta_m\}\\ \{\delta_s\}\end{Bmatrix} = \begin{bmatrix}[I]\\ [T]\end{bmatrix}\{\delta_m\} = [T^*]\{\delta_m\} \quad \text{..... (D.1)}$$

where $\{\delta_m\}$ represents the displacement vector for the master degrees of freedom; and,

$\{\delta_s\}$ represents the displacement vector for the slave degrees of freedom.

Partitioning the structural equations $\{P\} = [K]\{\delta\}$

$$\Rightarrow \begin{Bmatrix}\{P_m\}\\ \{P_s\}\end{Bmatrix} = \begin{bmatrix}[K_{mm}] & [K_{ms}]\\ [K_{sm}] & [K_{ss}]\end{bmatrix}\begin{Bmatrix}\{\delta_m\}\\ \{\delta_s\}\end{Bmatrix} \quad \text{..... (D.2)}$$

Substituting $\{P_s\} = \{0\}$ into Eqn (D.2)

$$\Rightarrow [K_{mm}]\{\delta_m\} + [K_{ms}]\{\delta_s\} = \{P_m\} \quad \text{..... (D.3)}$$

$$\Rightarrow [K_{sm}]\{\delta_m\} + [K_{ss}]\{\delta_s\} = \{0\} \quad \text{..... (D.4)}$$

$$\Rightarrow \{\delta_s\} = -[K_{ss}]^{-1}[K_{sm}]\{\delta_m\} \quad \text{..... (D.5)}$$

Substituting Eqn (D.5) into Eqn (D.3)

$$\Rightarrow \{P_m\} = \left([K_{mm}] - [K_{ms}][K_{ss}]^{-1}[K_{sm}]\right)\{\delta_m\} \quad \text{..... (D.6)}$$

$$\Rightarrow [K_m] = [K_{mm}] - [K_{ms}][K_{ss}]^{-1}[K_{sm}] \quad \text{.....} \quad \text{(D.7)}$$

From Eqns (D.1) and (D.5)

$$\Rightarrow \{\delta\} = \begin{bmatrix} [I] \\ -[K_{ss}]^{-1}[K_{sm}] \end{bmatrix} \{\delta_m\} \quad \text{.....} \quad \text{(D.8)}$$

$$\Rightarrow [T^*] = \begin{bmatrix} [I] \\ -[K_{ss}]^{-1}[K_{sm}] \end{bmatrix} \quad \text{.....} \quad \text{(D.9)}$$

The structural energies are written as follows :

$$\text{S.E.} = \frac{1}{2}\{\delta\}^T[K]\{\delta\} \quad \text{(strain energy)} \quad \text{.....} \quad \text{(D.10)}$$

$$\text{K.E.} = \frac{1}{2}\{\dot{\delta}\}^T[M]\{\dot{\delta}\} \quad \text{(kinetic energy)} \quad \text{.....} \quad \text{(D.11)}$$

Partitioning the mass matrix [M]

$$\Rightarrow [M] = \begin{bmatrix} [M_{mm}] & [M_{ms}] \\ [M_{sm}] & [M_{ss}] \end{bmatrix} \quad \text{.....} \quad \text{(D.12)}$$

Using the principles of coordinate transformation [16] ,

$$\text{S.E.} = \frac{1}{2}\{\delta_m\}^T[T^*]^T[K][T^*]\{\delta_m\} \quad \text{.....} \quad \text{(D.13)}$$

$$\text{K.E.} = \frac{1}{2}\{\dot{\delta}_m\}^T[T^*]^T[M][T^*]\{\dot{\delta}_m\} \quad \text{.....} \quad \text{(D.14)}$$

$$\Rightarrow [K_m] = [T^*]^T [K][T^*] \quad \text{.....} \quad \textbf{(D.15)}$$

$$\Rightarrow [M_m] = [T^*]^T [M][T^*] \quad \text{.....} \quad \textbf{(D.16)}$$

Substituting Eqn (D.9) into Eqn (D.16),

$$[M_m] = [M_{mm}] - [K_{ms}][K_{ss}]^{-1}[M_{sm}] - [M_{ms}][K_{ss}]^{-1}[K_{sm}] + [K_{ms}][K_{ss}]^{-1}[M_{ss}][K_{ss}]^{-1}[K_{sm}] \quad \text{.....} \quad \textbf{(D.17)}$$

APPENDIX E

STABILITY CONDITIONS FOR VARIOUS NUMERICAL INTEGRATION SCHEMES NEGLECTING DAMPING

1. Stability conditions for a three–point integration scheme [16] (zero damping) :

$$\beta \geq \frac{1}{4}(1/2 + \gamma)^2 \quad \text{.....} \quad \text{(E.1)}$$

$$\gamma \geq 1/2 \quad \text{.....} \quad \text{(E.2)}$$

$$1/2 - \gamma + \beta \geq 0 \quad \text{.....} \quad \text{(E.3)}$$

2. Stability conditions for a four–point integration scheme [16,47] (zero damping) :

$$3/2 < \gamma \leq \beta/3 + 1/2 \quad \text{.....} \quad \text{(E.4)}$$

$$3/4 + 9\beta/2 - 5\gamma < \alpha \leq -9\gamma^2 + 3\beta\gamma + 13\gamma - 6 \quad \text{.....} \quad \text{(E.5)}$$

3. Application of stability conditions to various temporal operators :

   i. **Central difference ($\beta = 0, \gamma = 1/2$)**

   When applying the stability conditions of Eqns (E.1 → E.3) the first relationship fails.

   ii. **Newmark ($\beta = 1/4, \gamma = 1/2$)**

   The three stability conditions of Eqns (E.1 → E.3) are satisfied.

   iii. **Houbolt ($\alpha = 27, \beta = 9, \gamma = 3$)**

   The stability conditions of Eqns (E.4 and E.5) are satisfied.

iv. **Wilson–θ ($\alpha = 2028/125$, $\beta = 457/75$, $\gamma = 12/5$)**

The stability conditions of Eqns (E.4 and E.5) are satisfied.

v. **Galerkin higher order ($\alpha = 702/35$, $\beta = 36/5$, $\gamma = 13/5$)**

When applying the stability conditions of Eqns (E.4 and E.5) the second relationship fails.

vi. **Hilber–Hughes–Taylor ($\alpha = 22777/2000$, $\beta = 917/200$, $\gamma = 2$)**

The stability conditions of Eqns (E.4 and E.5) are satisfied.

APPENDIX F

MATHEMATICAL BACKGROUND OF EXPERIMENTAL MODAL ANALYSIS

In the following appendix a mathematical development of the equations of motion for the general cases of viscous and hysteretic damping will be presented. Special cases of negligible damping and proportional damping as well as other cases will not be described but can be found elsewhere [49,66].

1. Viscous damping

Rewriting Eqn (3.1)

$$[M]\{\ddot{\delta}\} + [C]\{\dot{\delta}\} + [K]\{\delta\} = \{P\} \quad \text{.....} \quad \text{(F.1)}$$

and in the case of no excitation the previous equation does not reduce to a standard eigenproblem and as a result it is necessary to define the following :

$$\{y\} = \begin{Bmatrix} \delta \\ \dot{\delta} \end{Bmatrix} \quad \text{.....} \quad \text{(F.2)}$$

Eqn (F.2) can be used with Eqn (F.1) to form a standard eigenvalue problem as follows :

$$\begin{bmatrix} C & M \\ M & 0 \end{bmatrix} \begin{Bmatrix} \dot{\delta} \\ \ddot{\delta} \end{Bmatrix} + \begin{bmatrix} K & 0 \\ 0 & -M \end{bmatrix} \begin{Bmatrix} \delta \\ \dot{\delta} \end{Bmatrix} = \begin{Bmatrix} P \\ 0 \end{Bmatrix} \quad \text{.....} \quad \text{(F.3)}$$

$$[A]\{\dot{y}\} + [B]\{y\} = \{f\} \quad \text{.....} \quad \text{(F.4)}$$

In the case of no excitation,

$$[A]\{\dot{y}\} + [B]\{y\} = \{0\} \quad \text{.....} \quad \text{(F.5)}$$

The solution of the preceding equation can be assumed to be of the following form :

$$\{y\} = \{\psi\}e^{st} \quad \text{.....} \quad \text{(F.6)}$$

Substituting Eqn (F.6) in Eqn (F.5) yields

$$s[A]\{\psi\} + [B]\{\psi\} = \{0\} \quad \text{.....} \quad \text{(F.7)}$$

which is a standard eigenproblem and leads to a set of 2N eigenvalues and eigenvectors,

$$[S] = \begin{bmatrix} s_1 & & & 0 \\ & s_2 & & \\ & & s_3 & \\ & & & \ddots \\ 0 & & & s_{2N} \end{bmatrix}$$

$$[\Psi] = [\ \{\psi\}_1\ \{\psi\}_2\ \{\psi\}_3 \cdots \{\psi\}_{2N}\ ]$$

Because the damping distribution is not proportional to either the stiffness or mass distributions the resulting eigenvalues [S] and eigenvectors [Ψ] are complex and for a resonant system both occur in conjugate pairs,

$$[S] = \begin{bmatrix} s_1 & & & & & & & 0 \\ & s_2 & & & & & & \\ & & s_3 & & & & & \\ & & & \ddots & & & & \\ & & & & s_N & & & \\ & & & & & s_1^* & & \\ & & & & & & s_2^* & \\ & & & & & & & s_3^* \\ 0 & & & & & & & & \ddots \\ & & & & & & & & & s_N^* \end{bmatrix}$$

$$[\Psi] = [\ \{\psi\}_1\ \{\psi\}_2\ \{\psi\}_3 \cdots \{\psi\}_N\ \{\psi\}_1^*\ \{\psi\}_2^*\ \{\psi\}_3^* \cdots \{\psi\}_N^*\ ]$$

where * indicates a complex conjugate.

The eigenvectors are characterised by being orthogonal with respect to both [A] and [B]

$$\Rightarrow [\Psi]^T[A][\Psi] = \begin{bmatrix} \ddots & & 0 \\ & a_r & \\ 0 & & \ddots \end{bmatrix} \quad \text{.....} \quad \text{(F.8)}$$

$$\Rightarrow [\Psi]^T[B][\Psi] = \begin{bmatrix} \ddots & & 0 \\ & b_r & \\ 0 & & \ddots \end{bmatrix} \quad \text{.....} \quad \text{(F.9)}$$

Premultiplying Eqn (F.7) by $\{\psi\}_r^T$

$$\Rightarrow s_r\{\psi\}_r^T[A]\{\psi\}_r + \{\psi\}_r^T[B]\{\psi\}_r = \{0\} \quad \text{.....} \quad \text{(F.10)}$$

$$\Rightarrow s_r a_r + b_r = 0 \quad \text{.....} \quad \text{(F.11)}$$

$$\Rightarrow s_r = -\frac{b_r}{a_r} \quad \text{.....} \quad \text{(F.12)}$$

Returning to the forced vibration case and directing interest towards the frequency domain,

$$\{f\} = \{F\}e^{i\omega t} \quad \text{.....} \quad \text{(F.13)}$$

Then seeking a solution of Eqn (F.4) in the following form :

$$\{y\} = \begin{Bmatrix}\delta \\ \dot{\delta}\end{Bmatrix} = \begin{Bmatrix}Q \\ i\omega Q\end{Bmatrix} e^{i\omega t} = \{Y\}e^{i\omega t} \quad \text{.....} \quad \text{(F.14)}$$

Eqn (F.4) can be rewritten as follows :

$$i\omega[A]\{Y\} + [B]\{Y\} = \{F\} \quad \text{.....} \quad \text{(F.15)}$$

and since the eigenvectors of $[\Psi]$ are linearly independent in a space of dimension 2N

$$\Rightarrow \{Y\} = \sum_{r=1}^{2N}(\gamma_r\{\psi\}_r) \quad \text{.....} \quad \text{(F.16)}$$

indicating that the solution of Eqn (F.15) can be written as a linear combination of the 2N eigenvectors in the eigenproblem of Eqn (F.7). Substituting Eqn (F.16) into Eqn (F.15) and premultiplying by $\{\psi\}_p^T$

$$\Rightarrow i\omega\{\psi\}_p^T[A]\sum_{r=1}^{2N}(\gamma_r\{\psi\}_r) + \{\psi\}_p^T[B]\sum_{r=1}^{2N}(\gamma_r\{\psi\}_r) = \{\psi\}_p^T\{F\} \quad \text{.....} \quad \text{(F.17)}$$

$$\Rightarrow i\omega a_p\gamma_p + b_p\gamma_p = \{\psi\}_p^T\{F\} \quad \text{.....} \quad \text{(F.18)}$$

$$\Rightarrow \gamma_p = \frac{\{\psi\}_p^T\{F\}}{i\omega a_p + b_p} \quad \text{.....} \quad \text{(F.19)}$$

Hence substituting Eqn (F.19) into Eqn (F.16) yields

$$\{Y\} = \sum_{r=1}^{2N}\left[\frac{\{\psi\}_r^T\{F\}\{\psi\}_r}{i\omega a_r + b_r}\right] \quad \text{.....} \quad \text{(F.20)}$$

and from Eqn (F.12)

$$\Rightarrow \{Y\} = \sum_{r=1}^{2N} \left[\frac{\{\psi\}_r^T \{F\} \{\psi\}_r}{a_r(i\omega - s_r)} \right] \quad \text{.....} \quad \text{(F.21)}$$

Multiplying both sides by $e^{i\omega t}$

$$\Rightarrow \begin{Bmatrix} \delta \\ \dot{\delta} \end{Bmatrix} = \sum_{r=1}^{2N} \left[\frac{\{\psi\}_r^T \begin{Bmatrix} P \\ 0 \end{Bmatrix} \{\psi\}_r}{a_r(i\omega - s_r)} \right] \quad \text{.....} \quad \text{(F.22)}$$

Considering response at point j due to a single harmonic excitation force at point k the corresponding receptance can be written as follows :

$$\alpha_{jk}(\omega) = \sum_{r=1}^{2N} \left[\frac{{}_r\psi_k \, {}_r\psi_j}{a_r(i\omega - s_r)} \right] \quad \text{.....} \quad \text{(F.23)}$$

$$\alpha_{jk}(\omega) = \sum_{r=1}^{N} \left[\frac{{}_r\psi_k \, {}_r\psi_j}{a_r(i\omega + \zeta_r\omega_r - i\omega_r\sqrt{1-\zeta_r^2})} + \frac{{}_r\psi_k^* \, {}_r\psi_j^*}{a_r^*(i\omega + \zeta_r\omega_r + i\omega_r\sqrt{1-\zeta_r^2})} \right] \quad \text{...} \quad \text{(F.24)}$$

where $s_r = -\zeta_r\omega_r + i\omega_r\sqrt{1-\zeta_r^2}$; and,

ζ_r represents the critical damping constant.

Eqn (F.24) is frequently written as,

$$\alpha_{jk}(\omega) = \sum_{r=1}^{N} \left[\frac{{}_rR_{jk}}{(i\omega - s_r)} + \frac{{}_rR_{jk}^*}{(i\omega - s_r^*)} \right] \quad \text{.....} \quad \text{(F.25)}$$

where s_r represents the r^{th} pole location of the FRF on the frequency axis; and,

$_rR_{jk}$ represents the jk^{th} element of the residue matrix for the r^{th} mode.

It was demonstrated before [67] that each eigenvector exhibited the following property :

$$\{\psi_{i+N}\}_r = s_r\{\psi_i\}_r \quad ; i = 1, 2, 3, \ldots\ldots, N \qquad \text{(F.26)}$$

Thus using the orthogonality Eqns (F.8) and (F.9), and considering the first N components of each eigenvector

$$\Rightarrow \frac{\{\psi\}_r^T[C]\{\psi\}_r^*}{\{\psi\}_r^T[M]\{\psi\}_r^*} = \frac{c_r}{m_r} = 2\omega_r\zeta_r \qquad \text{(F.27)}$$

$$\Rightarrow \frac{\{\psi\}_r^T[K]\{\psi\}_r^*}{\{\psi\}_r^T[M]\{\psi\}_r^*} = \frac{k_r}{m_r} = \omega_r^2 \qquad \text{(F.28)}$$

where k_r, m_r and c_r represent the modal stiffness, mass and damping respectively.

For the case of light damping the real part of the eigenvector terms dominate

$$\Rightarrow \text{Real}(\{\psi\}_r) \gg \text{Imaginary}(\{\psi\}_r)$$

$$\Rightarrow [\Psi]^T[M][\Psi] \approx \begin{bmatrix} \ddots & & 0 \\ & m_r & \\ 0 & & \ddots \end{bmatrix} \qquad \text{(F.29)}$$

$$\Rightarrow [\Psi]^T[C][\Psi] \approx \begin{bmatrix} \ddots & & 0 \\ & c_r & \\ 0 & & \ddots \end{bmatrix} \qquad \text{(F.30)}$$

$$\Rightarrow [\Psi]^T[K][\Psi] \approx \begin{bmatrix} \ddots & & 0 \\ & k_r & \\ 0 & & \ddots \end{bmatrix} \quad \text{.....} \quad \text{(F.31)}$$

where $[\Psi]$ represents the vibrating mode shape matrix containing N vectors and each vector is formed of N components ($\{\psi\}_r$; i = 1, 2, ... , N and r denotes the mode shape number).

$$\Rightarrow \{\phi\}_r = \{\psi\}_r / \sqrt{m_r} \quad \text{.....} \quad \text{(F.32)}$$

where $\{\phi\}_r$ represents the r^{th} mass normalised mode shape vector.

2. Structural (hysteretic) damping

To derive an expression for the FRF in terms of hysteretic damping the equation of motion is rewritten as follows :

$$[M]\{\ddot{\delta}\} + i[H]\{\delta\} + [K]\{\delta\} = \{P\} \quad \text{.....} \quad \text{(F.33)}$$

Assuming zero excitation and seeking a solution of the form $\{\delta\} = \{Y\}e^{i\omega t}$

$$\Rightarrow (-\omega^2[M] + i[H] + [K])\{Y\} = \{0\} \quad \text{.....} \quad \text{(F.34)}$$

The preceding equation is a standard eigenproblem and its solution yields N complex eigenvalues and N complex eigenvectors of the following form :

$$[S^2] = \begin{bmatrix} s_1^2 & & & & 0 \\ & s_2^2 & & & \\ & & s_3^2 & & \\ & & & \ddots & \\ 0 & & & & s_N^2 \end{bmatrix}$$

$$[\Psi] = [\ \{\psi\}_1\ \{\psi\}_2\ \{\psi\}_3 \cdots \{\psi\}_N\ ]$$

where $s_r^2 = \omega_r^2(1 + i\eta_r)$; and,

η_r represents the structural damping loss factor of the r^{th} mode.

The eigenvectors possess the following orthogonal property :

$$[\Psi]^T[M][\Psi] = \begin{bmatrix} \ddots & & & 0 \\ & & & \\ & & m_r & \\ & & & \ddots \\ 0 & & & \ddots \end{bmatrix} \quad \text{..... (F.35)}$$

$$[\Psi]^T(i[H] + [K])[\Psi] = \begin{bmatrix} \ddots & & & 0 \\ & & & \\ & & k_r & \\ & & & \ddots \\ 0 & & & \ddots \end{bmatrix} \quad \text{..... (F.36)}$$

$$\Rightarrow s_r^2 = k_r / m_r \quad \text{..... (F.37)}$$

$$\Rightarrow \{\phi\}_r = \{\psi\}_r / m_r \quad \text{..... (F.38)}$$

As [Ψ] forms a set of linear independent vectors the solution of the equation of motion for forced vibration can be achieved by adopting a procedure similar to that described in Eqns (F.13 → F.22) and thus

$$\alpha_{jk}(\omega) = \sum_{r=1}^{N} \left[\frac{{}_r\Psi_k \, {}_r\Psi_j}{m_r\left(\omega_r^2 - \omega^2 + i\eta_r\omega_r^2\right)} \right] = \sum_{r=1}^{N} \left[\frac{{}_r\phi_k \, {}_r\phi_j}{\left(\omega_r^2 - \omega^2 + i\eta_r\omega_r^2\right)} \right] \quad \text{.....} \quad \text{(F.39)}$$

$$\alpha_{jk}(\omega) = \sum_{r=1}^{N} \left[\frac{{}_rR_{jk}}{\left(\omega_r^2 - \omega^2 + i\eta_r\omega_r^2\right)} \right] \quad \text{.....} \quad \text{(F.40)}$$

APPENDIX G

MODAL ASSURANCE CRITERION CALCULATION

USING COMPLEX EXPERIMENTAL MODE SHAPES

(i)

TEST STRUCTURE MODE NUMBER	INITIAL THEORETICAL MODEL MODE NUMBER							
	1	2	3	4	5	6	7	8
1	0.346	0.491	0.002	0.001	0.002	0.005	0.003	0.001
2	0.440	0.496	0.000	0.000	0.009	0.001	0.002	0.000
3	0.314	0.010	0.001	0.005	0.001	0.022	0.010	0.001
4	0.000	0.000	0.977	0.002	0.000	0.000	0.000	0.000
5	0.000	0.000	0.000	0.980	0.004	0.004	0.000	0.000
6	0.580	0.040	0.007	0.001	0.042	0.071	0.001	0.001
7	0.023	0.544	0.000	0.027	0.025	0.050	0.002	0.001
8	0.002	0.000	0.824	0.003	0.004	0.005	0.000	0.000

TABLE G.1 — *MODAL ASSURANCE CRITERION BETWEEN COMPLEX EXPERIMENTAL AND REAL THEORETICAL MODAL VECTORS (CONTD)*

(ii)

TEST STRUCTURE MODE NUMBER	UPDATED THEORETICAL MODEL MODE NUMBER							
	1	2	3	4	5	6	7	8
1	0.832	0.006	0.002	0.001	0.001	0.003	0.003	0.000
2	0.023	0.912	0.000	0.000	0.004	0.000	0.001	0.000
3	0.215	0.108	0.001	0.005	0.000	0.009	0.008	0.001
4	0.000	0.000	0.976	0.002	0.000	0.000	0.000	0.000
5	0.000	0.000	0.000	0.981	0.003	0.006	0.000	0.000
6	0.155	0.462	0.007	0.001	0.076	0.056	0.001	0.001
7	0.377	0.187	0.000	0.027	0.020	0.073	0.002	0.001
8	0.001	0.002	0.824	0.003	0.005	0.003	0.000	0.000

TABLE G.1 — *MODAL ASSURANCE CRITERION BETWEEN COMPLEX EXPERIMENTAL AND REAL THEORETICAL MODAL VECTORS*

When comparing the results listed in the above table with those in Table 4.10 it appeared that both follow a similar trend.

APPENDIX H

PUBLISHED PAPERS

1. "Response of Echinodomes to Asymmetric Loading", Co-authors R. ROYLES and J. M. LLAMBIAS, *Proceedings of the International Conference on Non*–Conventional Structures, ed. B. H. V. TOPPING, vol. 1, pp. 167–183, Civil–Comp Press, Edinburgh, (1987).

2. "Deformation Measurements on an Underwater Structure Relating to Buckling", Co-authors R. ROYLES and J. M. LLAMBIAS, *Proceedings of the International Conference on Stress Determination and Strain Measurement in Aeronautics*, pp. 11.1–11.16, Royal Aeronautical Society, London, (1988).

RESPONSE OF ECHINODOMES TO ASYMMETRIC LOADING

R. Royles, BSc(Eng), PhD, CEng, MICE, MIStructE, FBSSM,
Department of Civil Engineering and Building Science, University of Edinburgh
J. M. Llambias, BSc(Eng), PhD,
Dynamics Division, National Nuclear Corporation Limited, Knutsford, England
and K. M. El-Deeb, BSc(Eng),
Department of Civil Engineering and Building Science, University of Edinburgh, Scotland

The Echindome is a flat bottomed shell of revolution based on the shape of the common Sea Urchin. It has application in underwater storage or habitation for both industrial or leisure purposes.

The structure could operate either founded on the sea bed or tethered to it in a floating submerged attitude. One of the most complex loading forms which such structures would have to sustain is that due to concentrated effects.

The paper considers experimentally the behaviour of a small scale prototype under the action of a general regime of point loads. Computer methods of simulation are presented for the structure under these conditions and comparisons are made between predicted and experimental measurements of deformation and stresses. Implications for design are discussed.

LIST OF SYMBOLS

D	Maximum diameter
E	Young's modulus
H	Height of shell
N_ϕ, N_θ	Meridional and circumferential stress resultants
P	Point load
r_1, r_2	Meridional and circumferential radii
t	Shell wall thickness
z	Pressure head on a general shell element
z_θ	Pressure head at shell apex
γ	Density of water
ϕ	Angle in meridiodal plane defining position of shell element
ν	Poisson's ratio
ρ	Mass density of shell wall materials
σ_d	Design stress
$\sigma_\phi, \sigma_\theta$	Meridional and circumferential stresses
σ_1, σ_2	Principal stresses
θ	Azimuth angle

INTRODUCTION

General Requirements:

Historically man has sought support for the development of civilisation from the seas and oceans. This trend is intensifying as the twenty first century approaches and land based resources become more scarce. The wealth within the sea, and on and under its bed is being explored vigourously. This has led to a need for a means of storing some of the raw materials found, and their bi-products, for long or short periods near to the point of discovery.

The siting of storage facilities on land convenient for distribution is governed by the availability of suitable space and the safety aspects surrounding the material to be stored. An alternative in some instances could be to locate such facilities offshore.

Whether the requirement for storage facilities is in association with offshore exploration and production operations or the logistics of distribution the question arises as to where they should be placed - on the surface or underwater?

There is little doubt that conditions at the air/sea interface are more exacting than those prevailing underwater. Consequently it is in the latter type of environment that containers could be placed with greatest benefit.

Structures founded directly on the sea bed are more likely to suffer from ground transmitted vibrations than those positionsed in a floating submerged but tethered mode. Furthermore the recovery and relocation of the latter category of structure would be more feasible than with the

ixed leg and entirely gravity type structures. nother advantage of a floating submerged tructure would be its relatively small isturbance to the aesthetics of the surface main although strict precautions would have to taken to divert errant shipping away from it.

plications for underwater storage vessels are merous and include oil, liquid gases, sewage, xic wastes, and water. Many of these materials e of a hazardous nature and have to be treated th care wherever they are kept.

derwater oil tanks could be utilised close to oduction platforms and would be valuable in tuations where the nearest commercially suitable ndfall was beyond the economic reach of a pipe- ne. During adverse weather conditions tanker ips could be prevented from mooring to take on pplies of oil and some storage capacity would be cessary to permit the production process to ntinue through such periods.

milar arguments to those above are applicable to quid natural gas (L.N.G.) and liquid petroleum s (L.P.G.). Further, the risks attached to oring large quantities of L.N.G., in paricular, land could be dimished by transferring such cilities to underwater, but inshore, locations ere the consequential effects of leaks would be duced.

en storms occur treatment plant for liquid stes collected through drainage systems often come overloaded. Excess untreated material has be passed direct to the nearest water course, ke or the sea. Some alleviation of such llution problems could be achieved by means of mporary storage facilities. In the vicinity of ke shores and the sea coast underwater ntainers could be employed for this purpose. e stored material would be passed back to the eatment plant after the peak flow period.

quite a number of parts of the world surface orage of potable water is very difficult, either e to lack of suitable land space or the problem surface evaporation. For coastal regions derwater storage vessels could be of great sistance in this matter and could be very fective in the support of desalination cilities.

ructural Shape:

optimum form for a structure to fulfil the kind functions described above could be defined as e in which the design loads were resisted in the st efficient way. For a fixed geometry ructure there would be a single configuration r a particular design load condition. It has en shown that in an underwater situation at a rticular water depth a structure with a escribed constant material thickness and uniform ressing throughout would assume the shape of the inodome or globule of liquid on a flat surface ef.1]. This an axisymmetric shell of revolution e shape of which is dependent on the pressure d at the apex and the constant product of shell l thickness and stress, see Fig.1. These design nciples, based on membrane theory, have been ed previously for land based surface storage ssels containg L.P.G. and water [Refs.2,3]. dies have been undertaken also for the derwater storage of L.N.G. and oil [Refs.4-7].

Designs of this nature, especially for an underwater environment, must be checked under a wide variety of loading conditions. Among the more complex load types are concentrated effects. These could be of a static or dynamic nature, the former arising from service connections and the latter from impact and explosion. A prerequisite to the understanding of concentrated dynamic effects is a study of structural behaviour under static point loads. Some preliminary work has indicated that simple membrane analysis could provide a reasonable basis for design against axistmmetric point loads [Refs. 8,9].

The present paper investigates the effects of general point loading on the Echindome both experimentally and numerically, and the implications for design and construction are discussed.

EXPERIMENTAL ARRANGEMENTS

Test Shell:

The test shell was designed for an apex pressure head, z_o = 1.525m of water, with a uniform design stress, σ_d = 0.46MPa, and a mean shell wall thickness, t = 3.8mm. The actual wall thickness was measured over the whole shell with the aid of an ultrasonic thickness tester and the variation in t over the average meridian was established [Ref.10].

The shell material was glass reinforced plastic having an epoxy matrix and 0.26 glass fraction, the fibres being in the form of layers of randomly arranged chopped strand mat. The shell was constructed in two halves from the same mould and joined along a meridional seam using a slow curing araldite. The complete shell was bonded with araldite on to a flat tufnol base. The leading dimensions of the shell are given in Fig.1 and the material characteristics were determined from control specimens taken out of the bottom of the shell, see Table 1.

Table 1

Shell Wall Material Properties

Young's modulus,	E	8800 MPa
Poisson's ratio,	ν	0.36
Mass density,	ρ	1100 kg/m
Ultimate tensile strength		55.4 MPa

Instrumentation

Electric resistance strain gauges of the foil type in rectangular rosette form were bonded to the outer surface of the shell at the intersection of three meridians with four parallel circles. The meridians were spaced at 120 in azimuth and the parallel circles were distributed over the height, H, of the shell as shown in Fig.2. Each gauge has a resistance of 350°±0.1Ω, gauge length = 3mm, and gauge factor = 2.15. At the intersection of the lowest parallel circle with two of the meridians, rectangular rosettes were bonded to the inner surface of the shell to monitor bending effects near the base. The electrical leads from these internal strain gauges were brought out through the centre of the base of the shell.

Rectilinear potentiometric displacement transducers were disposed normal to the shell surface along five meridians at 45° . Their locations down the meridian relative to the axis of symmetry were at the apex, 45°, 90°, and 135 , see Fig.3. The full scale resistance of each transducer was 2kΩ and the full scale output was 5V d.c. for a mechanical stroke of 100mm with a linearity of 0.25% and a resolution of ± 1 micron using a microcomputer controlled data logging system, Fig.4, [Ref.11]

Static loading was carried out using a lever which applied load through a stiff strut normal to the shell surface. The angular position of the axis of symmetry of the shell was variable between 0° (vertical) and 90°. An impression of the general loading arrangement can be gained from Fig.5.

Test Procedure:

In order not to overstrain the test structure, but produce measurable deformations increment, of 50N in applied point load were employed betwen 0 and 300N and for each step, on the load increasing part of the cycle, readings from all displacement transducers and strain gauges were obtained using the logging system. The process was repeated five times and between each loading cycle a period of five minutes was allowed for creep recovery during which time the strain gauge energisation was isolated to minimise heating problems. A constant loading rate was maintained consistent with that adopted in the material control tests; a typical load increasing run took 2 minutes to complete. The mean results for the five runs were determined for several angular positions of the shell.

SIMULATION OF SINGLE POINT LOADING

There are three types of concentrated loading on shells namely axisymmetric, symmetric and asymmetric. In terms of a single point load the first two types would be normal to the surface and the last non-normal, as shown in Fig.6.

Since the curvature of the Echinodome changes down the meridian, as illustrated in Fig.1, the shape lends itself more readily to numerical analysis than to an exact mathematical solution of equilibrium equations.

Half of the shell was simulated for the axisymmetric and symmetric load cases, Fig.6a, using semiloof shell elements and a finite element method (F.E.M.) of analysis was performed using the LUSAS computer package [Ref.12]. The total number of elements was 168 in two groups made up of 162 type QSL8 (an eight noded semiloof quadilateral shell element) in circumferential bands covering all but the apex cap of the shell which comprised 6 type TSL6 (a six noded semiloof triangular shell element).

Loads similar to those used experimentally were considered and both linear static and geometric non-linear analyses were carried out.

DISCUSSION

The general behaviour of the shell under symmetric loading is considered firstly as it was typified by the response to a normal point load at the maximum diameter of the shell i.e. at $\phi = 90^{\circ}$ from the vertical axis of symmetry. Behaviour in relation to point loads at other values of ϕ less than 90° were similar and the case of $\phi = 0^{\circ}$ (axisymmetric apex point load) has been reported in detail elsewhere [Ref. 8,9].

The displaced shape of the shell is depicted in Fig.7 for the plane containing the meridian through the load point at azimuth angle $\theta = 0^{\circ}$, and its complement at $\theta = 180^{\circ}$. The zone of greatest deformation was under the point load followed by the region around the base. In general over the surface experimental values were in quite good agreement with the theoretical results except in the close vicinity of the point load where there was evidence of local dimpling and actual deformation was much greater than predicted. Overall the actual deflections might be expected to be greater than predicted since the bonding of the shell to its base could not provide the perfect rigidity which was assumed at that boundary.

The localised deformation was not permanent as illustrated in Fig.8 for the point load position. Here it can be seen that there was very little difference between linear and geometric non-linear static analyses. However, the theoretical results were significantly less than the experimental ones and this could be attributed to the assumption of uniform thickness around a parallel circle in the computer simulation and no account being taken of the meridional seam joining the two halves of the shell. Also local thinning near to the seam was not taken into account. None the less the experimental results were linear elastic over the range considered with the predicted values following a similar but stiffer pattern. The actual normal displacements were nowhere in excess of 1mm which was small in comparison with the shell dimensions.

The theoretical predictions of displacement might be improved by using a finer mesh locally around the load point together with a more detailed description of the thickness over that area. The actual mesh employed in this work consisted of elements with a meridonal arc length of the order of 20mm and each element subtending 30°in azimuth.

The stresses deduced from the strain measurements were compared with theoretical predictions and found to be in good agreement over the shell as a whole, although strains were not measured at the load point, This is demonstrated in Figs. 9 and 10 for the meridian at azimuth angle $\theta = 30^{\circ}$ from the loaded meridian and its complement $\theta = 210^{\circ}$ (symmetrical with $\theta = 150^{\circ}$) the normal point load being at the maximum diameter i.e. at $\phi = 90^{\circ}$. In these plots distance is measured along the meridian from the apex with the load side negative and the base at the extremities.

g. 9a and b show the variation of the rcumferential and meridional stresses, σ_θ and σ_ϕ spectively for the inner and outer shell rfaces. It can be seen from them that bending edominated in the base region covering the west 15% of the meridian on each side of the ex for both orthogonal directions. This was nsistent with the overturning effect on the body a whole consequent upon the inward normal load the maximum diameter. Additionally the resses in the vicinity of the load point, vering approximately 30% of the length of the ridian, were influenced by bending but the mbrane effect was dominant. Over the rest of e double meridian section the stresses, σ_θ and σ_ϕ re of a membrane nature and approximately zero this case. The zone affected by the point load s approximately circular in area as might be pected in the elastic state.

e associated principal stresses, σ_1 and σ_2, for e meridians $\theta = 30^\circ$ and $\theta = 210^\circ$ relative to e loaded one are shown in Fig. 10a and b. It s clear from the data on principal angles that σ_1 d σ_2 were in close alignment with σ_θ and σ_ϕ spectively over most of this double meridian. was true even in the bas region remote from e loaded area. There σ_1 and σ_2 were almost ual to σ_θ and σ_ϕ indicating little shear in at region. However, in the base region nearest the loaded area $\sigma_1 > \sigma_\theta$ and $\sigma_2 < \sigma_\phi$ indicating e effect of significant shear. In the loaded gion there was a tendency for $\sigma_1 > \sigma_\theta$ and $> \sigma_\phi$ which could be attributed directly to cal shearing effects. The stresses in this gion fluctuated markedly which was due most obably to the influence of localised bending.

e applied loading resulted in stresses being set which nowhere exceeded a quarter of the timate strength of the material, the greatest resses occurring in the base region near the ad. For the loadings applied the overall sponse was elastic.

e prediction of stresses was not enhanced by the e of a geometric non-linear static analysis as posed to a linear static one, as can be seen om the almost direct coincidence of the plots in gs 9 and 10. These figures illustrate that away om the point load and the base region the rcumferential, meridional and principal stresses re approximately equal and uniform in value.

e stress behaviour described above was relevant the whole shell surface and was appropriate to l single point load cases - axisymmetric [Refs.8 d 9] and symmetric. The pattern became more centuated the closer a meridional section proached the loaded one.

INFERENCES FOR DESIGN AND CONSTRUCTION

For underwater service an Echinodome is proportioned initially according to the mean operating head of water at the shell apex using membrane analysis and uniform wall thickness with a design stress within the strength capabilities of the chosen construction material.

Axisymmetric loadings produce bending and shearing effects in the base region and some thickening of the shell wall is required in the bottom 10% of the meridian [Ref.7].

The present investigation confirms that the least disturbing positions for the application of concentrated loads are at the apex and the flat base. This indicates that access for services and maintenance etc should be in those locations. Point loadings applied in other positions would necessitate localised strengthening of the shell.

The axisymmetric geometry of a shell of revolution of this type with a uniform thickness over most of the profile lends itself to a construction process involving repitition. The formwork for cementitious materials, see Fig.11, or the jigging for metal construction [Ref.3], could be rotated through 360° about the vertical axis. If fabric or rubber materials were employed there would be economies available in the repetitive nature of cutting patterns and seaming. When using rigid materials such as concrete or steel the apex region would be constructed last in the form of a cap. Reinforcement in concrete would be orientated mainly in the circumferential and meridional directions.

The base for such a structure has not been considered in this investigation but clearly in the construction process it would be built first.

CONCLUSIONS

1. Membrane action predominated in the shell away from the base and applied load regions.

2. Simulation procedure gave results in good agreement with measurements except near load point and base.

3. Basic reinforcement pattern in concrete Echinodomes should follow circumferential and meridional directions.

ACKNOWLEDGEMENTS

The authors wish to express their thanks to Professor A.W. Hendry, Head, Department of Civil Engineering and Building Science, University of Edinburgh, for his encouragement of this work and for the kind support of his secretarial and technical staff. The financial support of the Vans Dunlop Scholarship is appreciated greatly.

REFERENCES

1. Royles, R., Sofoluwe, A.B., Currie, A.J.,and Baig, M.M., Behaviour of underwater enclosures of optimum design, Strain 16, 1980, 12-20.

2. Daric, G., Aperçu général sur la construction des reservoirs de stockages dans l'industrie du petrole, Construction, 1960, 117-129.

3. Rotterdam Municipal Water Authority, Private Communication, 1980.

4. Royles, R., and Sofoluwe, A.B., An optimum form for underwater storage vessels, I.A.S.S.S. (Committee of Pipes and Tanks), Symposium on Recent developments in the field of liquefied gas tanks, Delft, June 1980.

5. Royles, R. and Sofoluwe, A.B., Form for an underwater storage vessel, Nigerian Journal of Science and Technology, 3, Issue 2, 1985.

6. Royles, R., and Llambias, J.M., Storage aspects of liquid gases underwater and the structural implications, Proceedings of International Symposium on Storage and transportation of LPG and LNG, Brugge, 2, 1984, 55-72.

7. Llambias, J.M., Response of an underwater structure of optimum shape to general loading, Ph.D. Thesis, University of Edinburgh, 1985.

8. Llambias, J.M. and Royles, R., Response of an underwater structure of optimum form to concentrated loading, Proceedings of International Conference on Experimental Mechanics, Beijing, Editors Li R.Q.,& Shi, G.Y., Science Press Academica Sinica, Beijing, 1985, 687-697.

9. Royles, R., and Llambias, J.M., Point loading effects on the Echinodome, International Journal Computers and Structures, Pergamon Press, Oxford, to be published 1988

10. Royles, R., and Llambias, J.M., Buckling aspects of the behaviour of an underwater pressure vessel, Applied Solid Mechanics - 1 Editors A.S. Tooth and J. Spence, Elsevier Applied Science Publishers, London, 1985, 287-303.

11. Royles, R., and Jeffrey, D.C., A microcomputer controlled scanning system for transducers, Experimental Techniques, 7, 4, 1983, 26-28.

12. Anon, L.U.S.A.S.- finite element analysis system, User's Manual 86.07, F.E.A.Ltd., Kingston upon Thames, London, 1986.

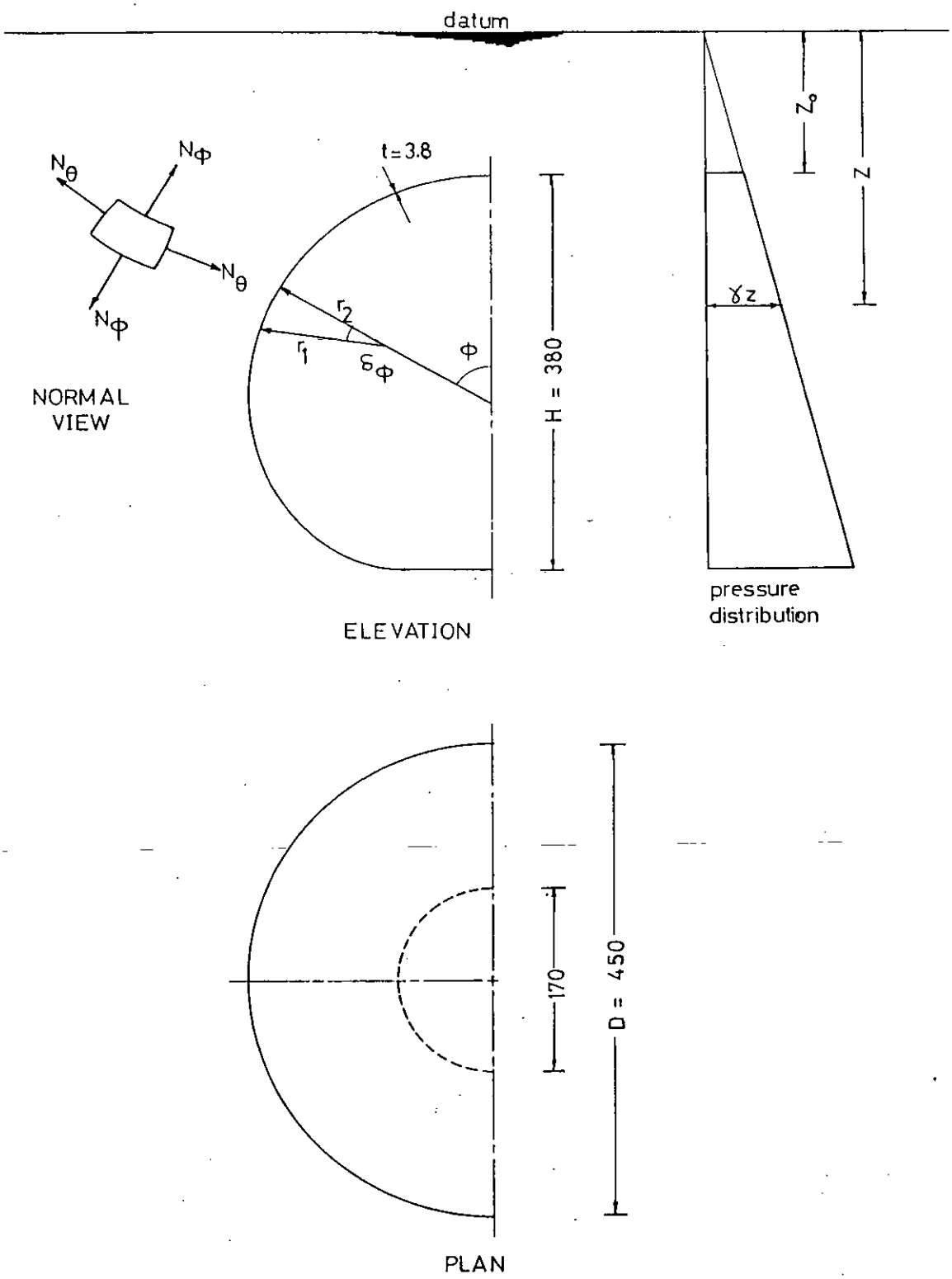

Fig.1 Shell shape and dimensions

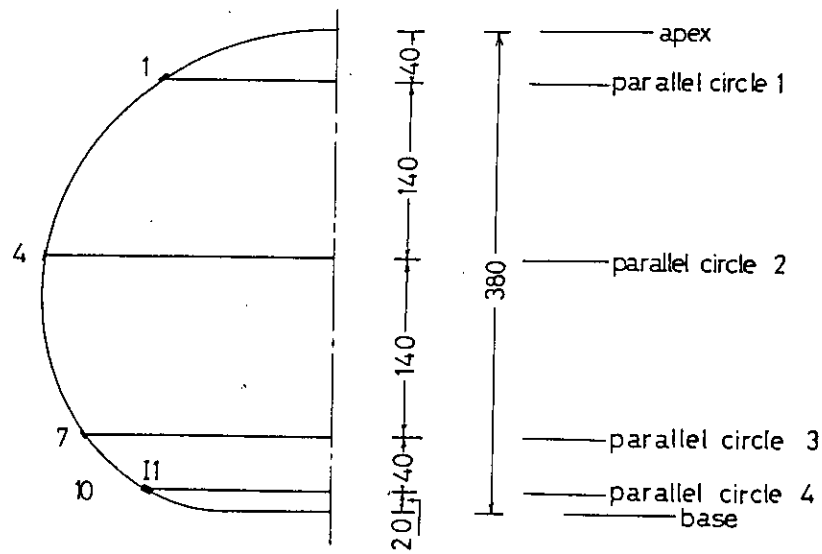

ELEVATION

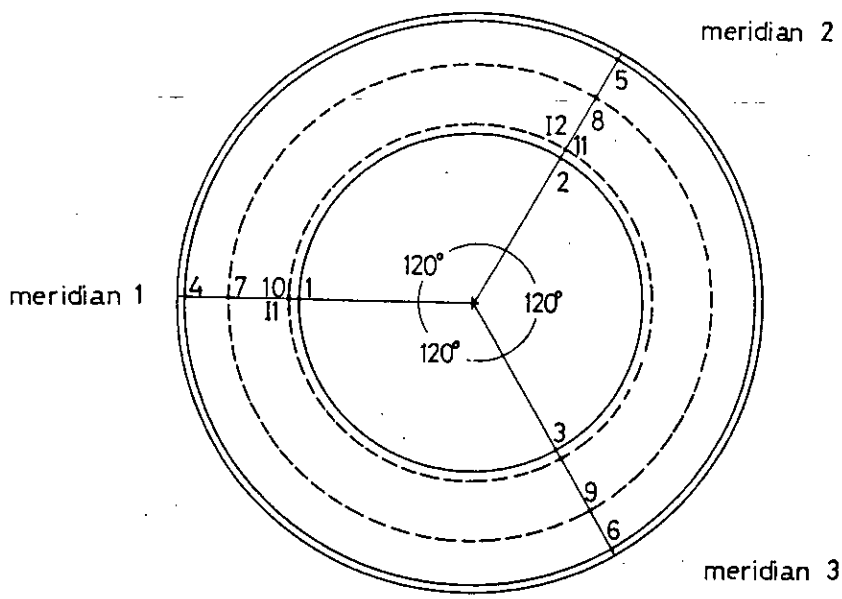

PLAN

Fig.2 Location of strain gauges

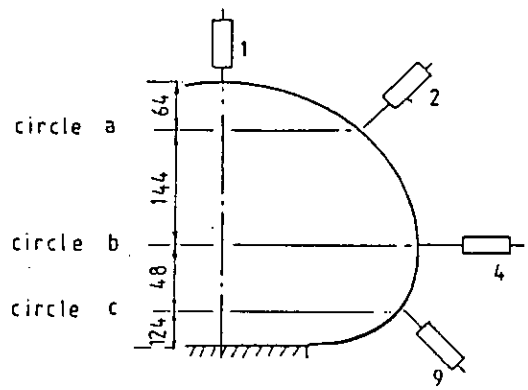

ELEVATION

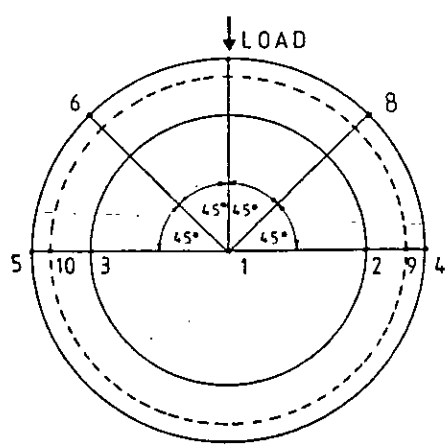

PLAN

Fig.3 Location of displacement gauges

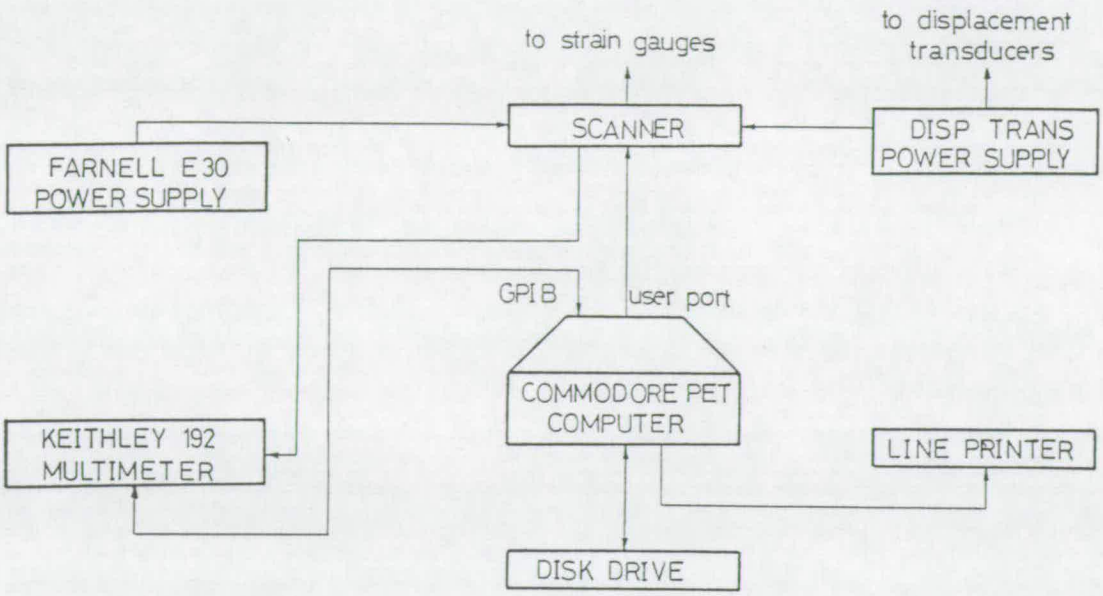

Fig.4 Instrumentation

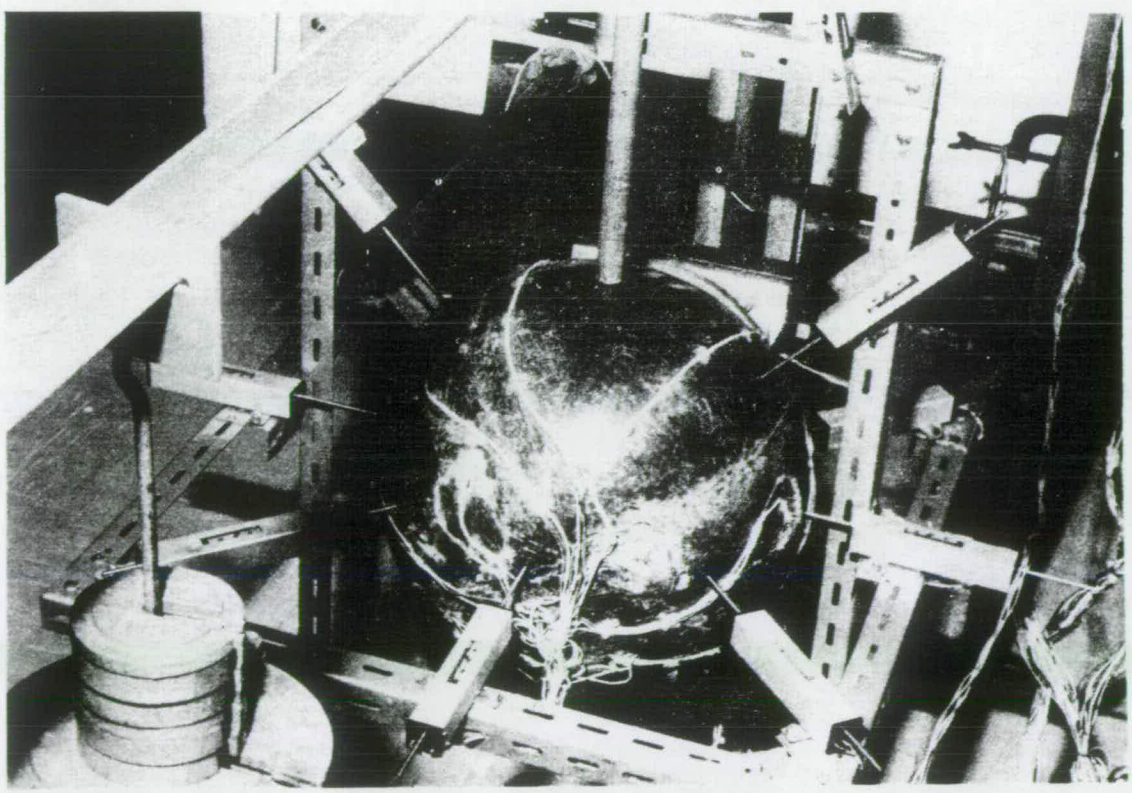

Fig.5 Loading arrangement

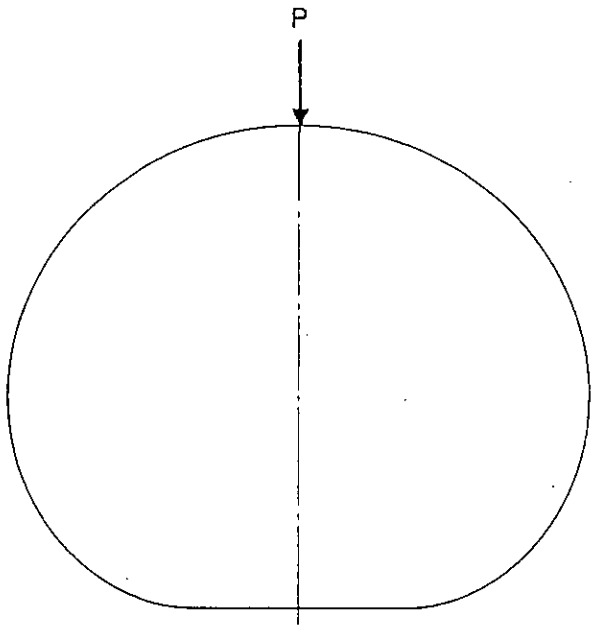

axisymmetric

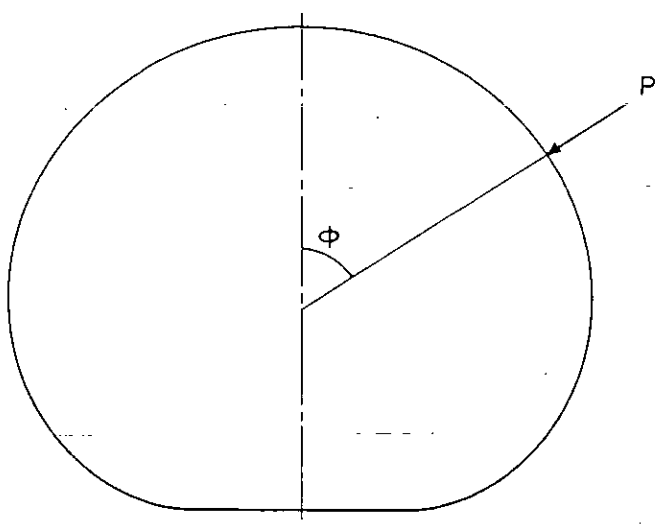

symmetric

(a) normal loading

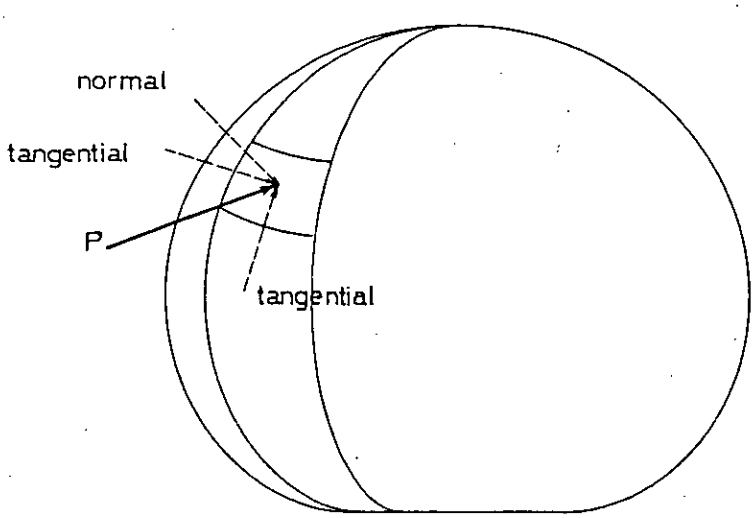

asymmetric

(b) non-normal loading

Fig.6 Single point loading cases

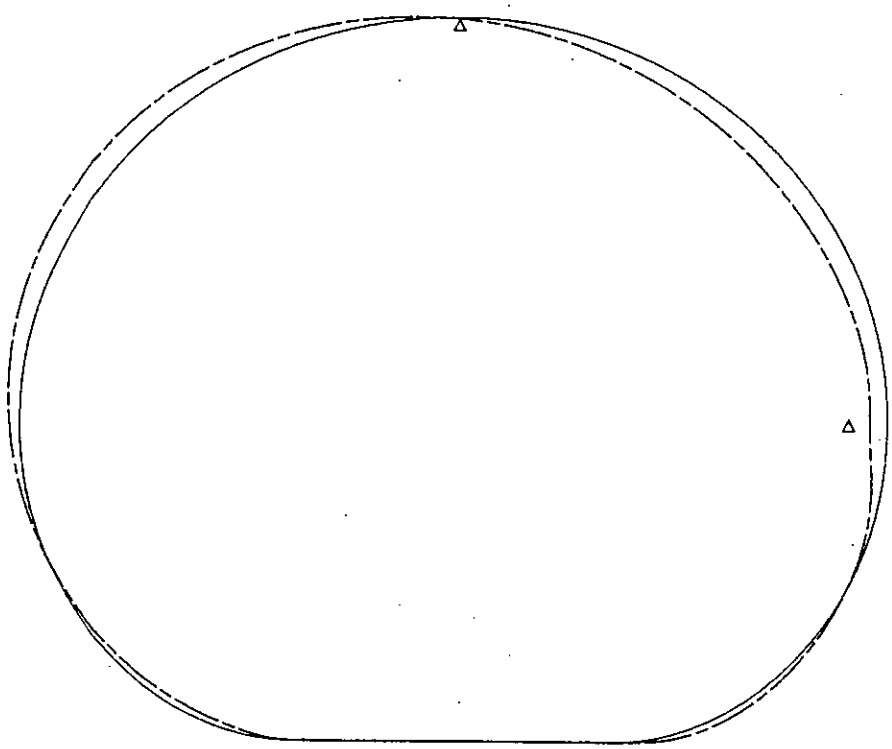

——————— Original Profile
- - - - - - - - - - - Deformed Profile (Linear Analysis)
——— — ——— Deformed Profile (Geometrically Nonlinear Analysis)
△ Experimental Results

Fig.7 Displacement shape of shell along double meridional plane, $\theta = 0^{\circ}$ and $\theta = 180^{\circ}$ relative to load plane, load at $\phi = 90^{\circ}$

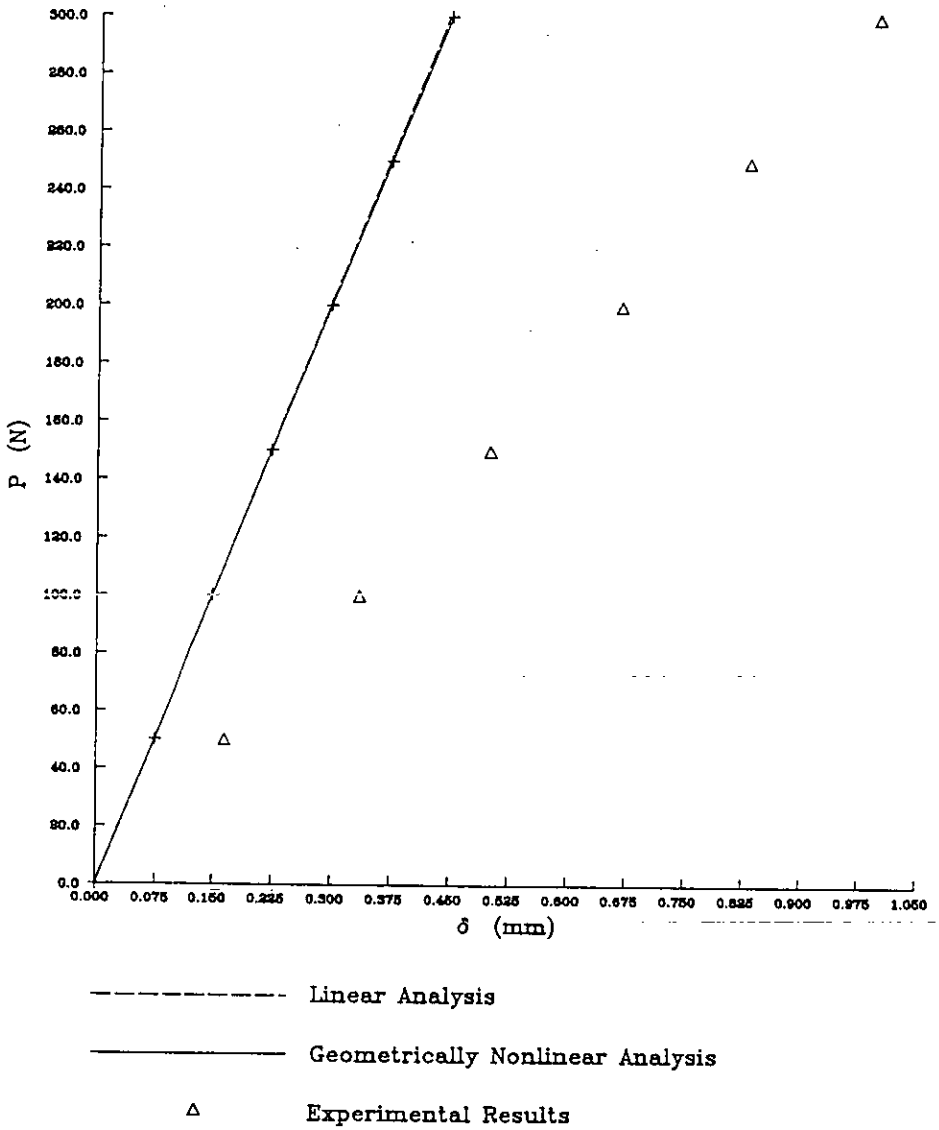

Fig.8 Normal displacement at load point, $\phi = 90^{\circ}$

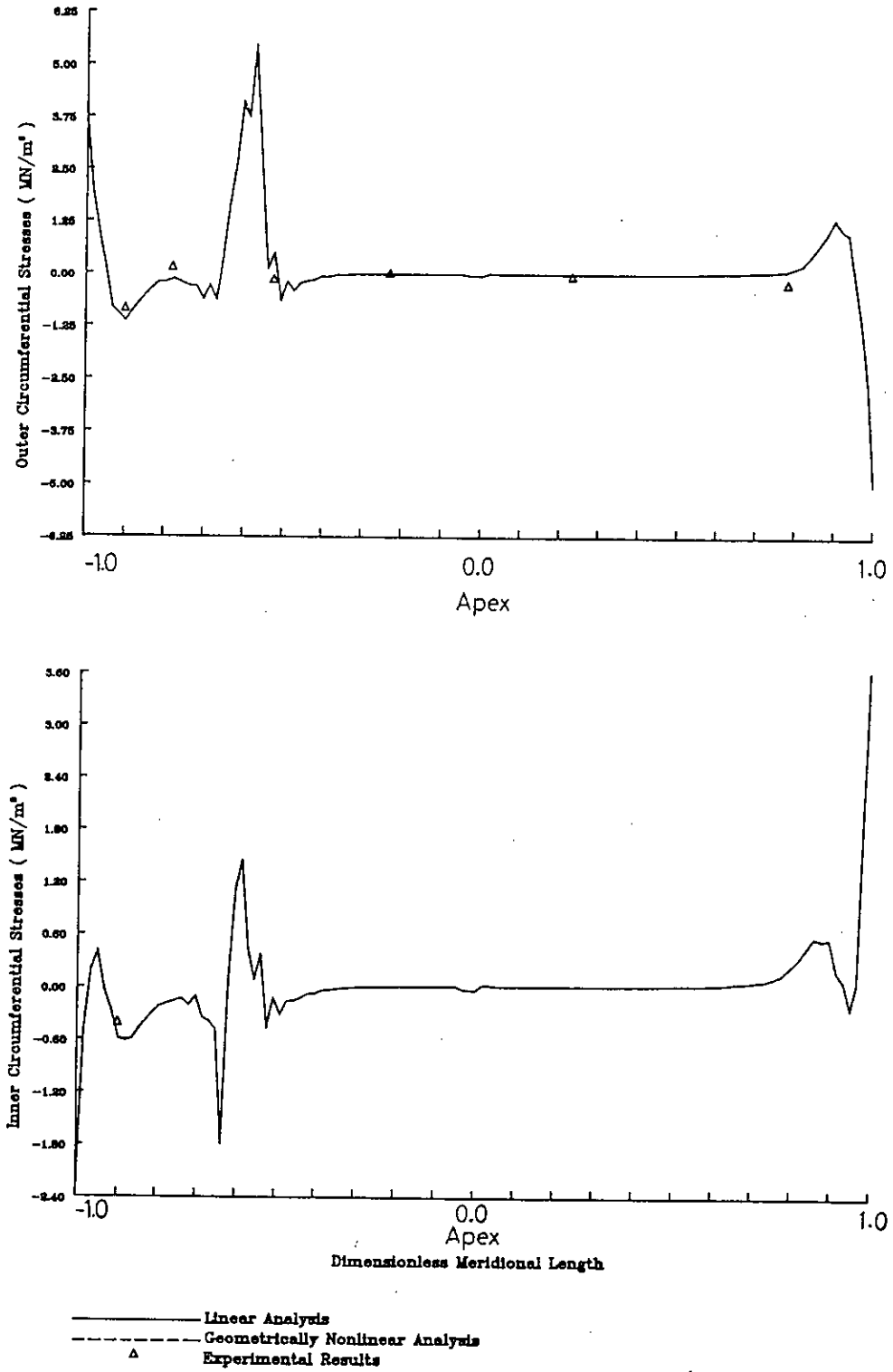

Fig.9a Circumferential stresses along double meridian, $\theta = 30^{\circ}$ and $\theta = 210^{\circ}$ relative to load plane, load at $\phi = 90^{\circ}$

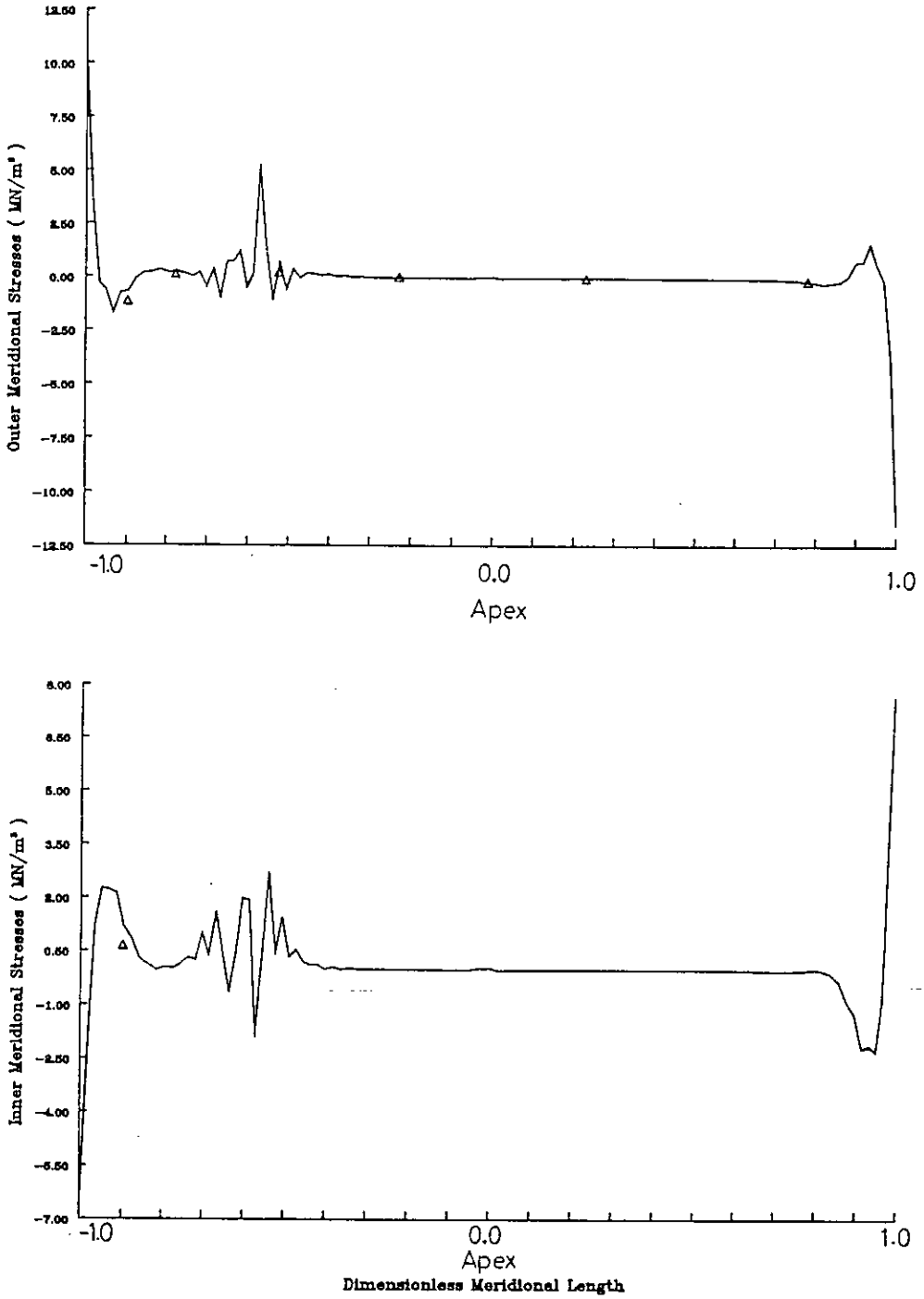

Fig.9b Meridional stresses along double meridian, $\theta = 30^{o}$ and $\theta = 210^{o}$ relative to load plane, load at $\phi = 90^{o}$

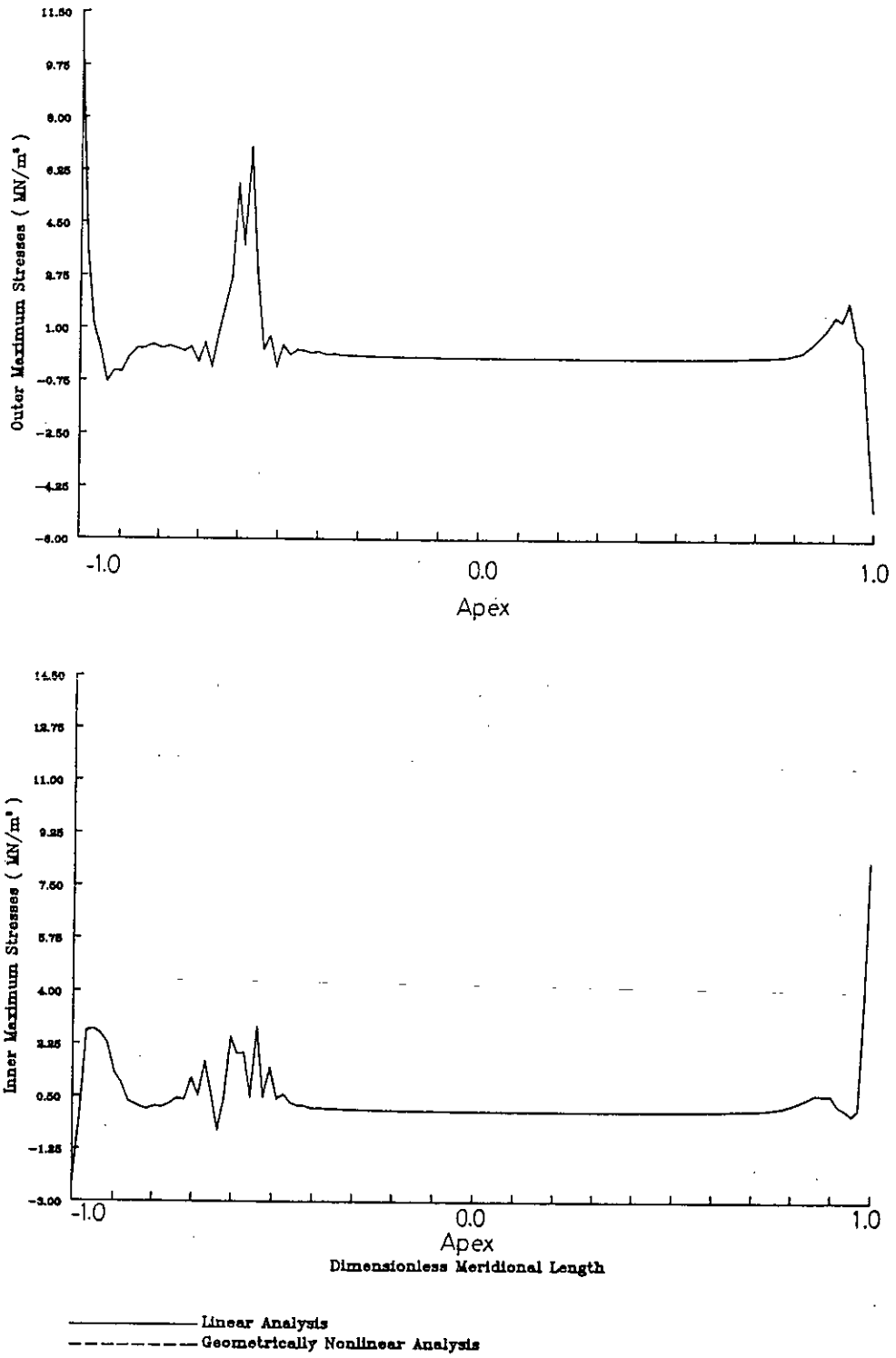

Fig. 10a Maximum principal stress along double meridian, $\theta = 30^{\circ}$ and $\theta = 210^{\circ}$ relative to load plane, load at $\phi = 90^{\circ}$

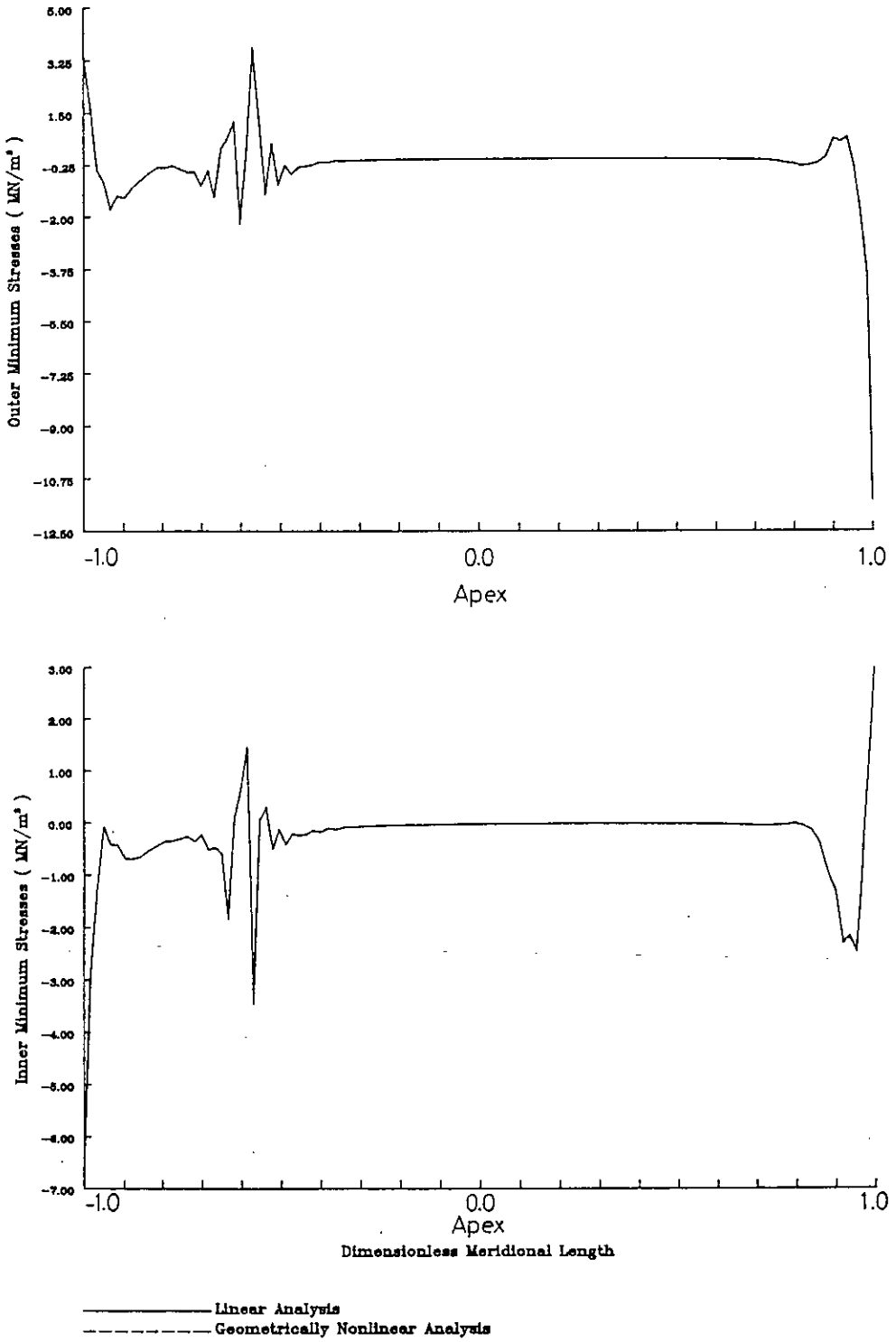

Fig.10b Minimum principal stress along double meridian, $\theta = 30^{o}$ and $\theta = 210^{o}$ relative to load plane, load at $\phi = 90^{o}$

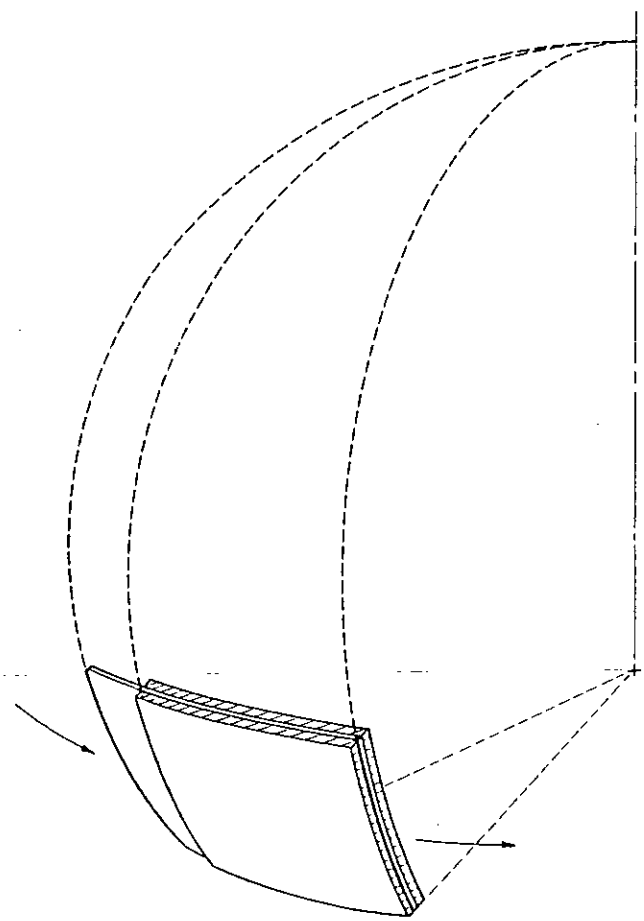

Fig.11 Construction technique for a concrete Echinodome.

DEFORMATION MEASUREMENTS ON AN UNDERWATER STRUCTURE RELATING TO BUCKLING

by

R.Royles, B.Sc.(Eng), Ph.D.,C.Eng., M.I.C.E., M.I.Struct.E., F.B.S.S.M.,
Department of Civil Engineering and Building Science,
University of Edinburgh.

K.M.El-Deeb, B.Sc.(Eng),
Department of Civil Engineering and Building Science,
University of Edinburgh.

J.M.Llambias, B.Sc.(Eng), Ph.D.,
Dynamics Division, National Nuclear Corporation Limited, Knutsford.

ABSTRACT

A structure is described which is suitable for underwater storage of liquids or as a one atmosphere accommodation/operations chamber. The structure is an axisymmetric thin shell of revolution of optimum form in relation to the design hydrostatic head. The buckling tendencies of this type of thin membrane structure under external load were examined and details are given of the reaction of the shell to axisymmetric pressure and concentrated loadings as well as to symmetric point loads.

The responses were based on electric resistance strain gauge measurements and displacement monitoring at various points on the inner and outer surfaces of the shell during incremental loading. Southwell type plots are employed to interpret the experimental data in terms of critical buckling loads. These non-destructive type experimental predictions are compared with theoretical values established using the finite element method with both axisymmetric shell of revolution elements and semi-loof thin shell elements. Good comparisons between experimental and numerical predictions are demonstrated. The shapes of the Southwell plots in relation to the localities of the measurements is discussed along with the validity of the approach.

The general nature of the buckling modes under the various loading forms is assessed. Zones sensitive to buckling are identified and the implications for the design of such structures are outlined.

Keywords: Echinodome, buckling, design, displacement and strain measurements.

INTRODUCTION

In relation to the amount of space available on land for industrial and urban development as well as leisure activities the surface and sub-surface zones at sea are vast. The latter zones offer plenty of scope to support land based societies. A manifestation of this is in the creation of habitats and storage facilities for the exploration and development of offshore resources such as gas and oil.

The conditions offshore for surface structures can be quite hostile and a much calmer state prevails underwater although means of access are generally more difficult to establish. A lot can be said in favour of placing a habitat/operations chamber or a storage vessel in the relatively tranquil submerged environment. In particular, the deployment of the structure in a tethered floating submerged manner reduces the need for expensive foundations, and enables it to cope more easily with seabed disturbances such as seismic activity and settlement.

One type of structure suitable for underwater operations is the axisymmetric thin shell of revolution and the loadings to be considered are many and varied ranging from axisymmetric to completely asymmetric and consisting of an assortment of dynamic and quasi-static/static effects. A common problem faced by this sort of structure is buckling and strict design precautions have to be taken to guard against it.

The present paper is concerned with the buckling behaviour of the Echinodome or drop shaped shell which has been proposed for underwater use (Ref.1-4). The structure is considered under both axisymmetric pressure and concentrated loadings. The structure is examined analytically/numerically using finite element simulations and experimentally using a small prototype. Comparisons are made between experimental and numerical predictions of critical buckling loads, use being made of the Southwell (Ref.5) approach with the experimental data. Buckling mode shapes are determined and experimental and predicted forms are compared. The implications for the design of such structures are discussed.

NOTATION

D	Maximum diameter of shell
E	Young's modulus of elasticity
H	Height of shell
N_ϕ, N_θ	Meridional and circumferential stress resultants
P	Point load
P_{cr}	Critical buckling load
r_1, r_2	Meridional and circumferential radii of curvature
t	Shell wall thickness
w	Normal displacement

z	Pressure head
z_o	Pressure head at apex of shell
z_{od}	Design pressure head at apex of shell
z_{cr}	Critical buckling pressure at apex of shell
ϕ,θ	Meridional and azimuth angles
γ	Density of water
ν	Poisson's ratio
ρ	Mass density of shell wall material
σ_d	Design stress

SHELL STRUCTURE

The Echinodome is an axisymmetric thin shell of revolution which is an optimum form for one set of design conditions relating to the mean hydraulic head, z_o , at the apex and the product of the design stress, σ_d , and the shell wall thickness, t, where $\sigma_d.t$ is constant. Consequently under these conditions uniform stressing prevails throughout a shell wall of constant thickness ie the stress resultants N_ϕ, N_θ in the meridional and circumferential directions, Fig.1, are equal at all points. The design approach is based on membrane theory (Ref.6).

For axisymmetric pressure heads at the apex other than the design value the stressing in the shell becomes non-uniform, and above the design level the question arises of buckling, especially near the base.

It has been demonstrated that membrane analysis could be used in the treatment of axisymmetric point loads on the Echinodome (Ref.7) but for more general concentrated loading, Fig.2, a numerical assessment of the shell behaviour has to be made. This is true particularly in relation to buckling both for axisymmetric and non-axisymmetric loadings.

ANALYTICAL APPROACH

Exact analytical solutions of the equilibrium equations for the shell structure are not easy to achieve under most forms of loading and numerical methods must be adopted.

For axisymmetric pressure loading the shell was simulated by means of complete circular ring elements, Fig.3a, having two nodes each with four degrees of freedom (3 translational and 1 rotational). Both linear and non-linear buckling analyses were carried out by means of the MISTRY program (Ref.8).

Concentrated loadings on the shell were investigated by discretising the structure with semi-loof elements into an apical ring of triangular elements followed by bands of quadrilateral elements, Fig.2b. Linear bifurcation and non-linear collapse buckling analyses were performed using

the LUSAS program (Ref. 9).

Some typical predicted deformed shapes are shown in Figs 4 and 5 and predicted buckling loads are listed in Table 1.

All the computer simulations related to the prototype test structure described in the next section and took into account variations in shell wall thickness.

EXPERIMENTAL APPROACH

The test structure was made using glass reinforced plastics (GRP) with a glass fraction of 0.26 in an epoxy resin matrix and had the following design parameter values,

$z_\varphi = z_{od} = 1.525m; \sigma_d = 0.46\ MN/m^2;\quad t = 3.8mm$

and material properties,

Young's modulus, $E = 8800MN/m^2$;
Poisson's ratio, $\nu = 0.36$;
Ultimate tensile strength = $55.4\ MN/m^2$;
Mass density, $\rho = 1100\ kg/m^3$

The shell had a maximum diameter of 450mm and maximum height = 380mm, see Fig.1. Variations in shell wall thickness were determined ultrasonically (Ref.10,11).

Axisymmetric Pressure Tests

Electric resistance strain gauges in the form of rectangular foil type rosettes were bonded to the external and internal shell surfaces at the intersections of three symmetrical meridians and four parallel circles, as indicated in Fig.6 (I1, I2 are internal rosettes near the base with their leads passing through the centre of the base). The gauge characteristics were as follows,

resistance = 350 ± 0.1 ohms; gauge length = 3mm; gauge factor = 2.15.

An external half bridge arrangement was used with a dummy shell for temperature compensation in the same environment. The gauges and leads were waterproofed with bees' wax. The three gauges at a point were orientated clockwise with the first pointing along the meridian towards the apex.

Details of the pressure chamber (water filled), the instrumentation and test procedure have been given previously (Ref.10,11). The pressure head at the apex was raised incrementally at a uniform rate (approximately 6.25mm/s, consistent with the material control tests, and strain gauges scanned at each increment of pressure up to a total head of 3.5m. By this stage response was non-linear but the structure was not damaged permanently. Five pressure increasing runs were carried out and due allowance for creep recovery was made between each run. A typical pressure-strain curve is shown in Fig.7a for one of the gauges.

Concentrated Loadings

In a normal atmospheric air environment the shell was mounted on a base which could be rotated about a horizontal axis and clamped to permit the axis of symmetry of the shell to be varied between 0° and 90°. Point loading normal to the external shell surface was applied through a vertical stiff strut using a dead load lever system.

Displacement transducers of the rectilinear potentiometric type having a full scale resistance of 2000 ohms and a mechanical stroke of 100mm were arranged as in Fig.8 and a more general view of the set-up is given in Fig.9. The resolution of this transducer system was ± 1 micron with a linearity of 0.25%. The scanning of the transducers was controlled by a microcomputer in the same way as for the axisymmetric pressure tests described above.

For each angular position of the shell incremental load was applied at a uniform rate (consistent with the material control tests) and the mean results from ten test runs were established. The shell was loaded into the non-linear response range but well below failure, and adequate time was allowed for creep recovery between loading runs.

A typical load-displacement response is shown in Fig.10a.

Buckling Assessment

The plots of pressure-strain and load-displacement for the shell were very much of the rectangular hyperbola form typified by Figs.7a and 10a. This shape of curve makes it possible to employ a Southwell approach to predict the actual buckling load of the shell with its imperfections (Ref.5,10,11,14).

Strain per unit pressure versus strain relations were deduced for each strain gauge in the axisymmetric pressure tests and displacement per unit load versus displacement relations were obtained for each measurement point in the concentrated load tests. These relations were the best straight lines determined using linear regression techniques (Ref.15,16). The results of such processes applied to the data points in Figs.7a and 10a are shown in Figs.7b and 10b respectively. In each case the inverse of the slope of the straight line yielded the buckling load.

DISCUSSION

Under axisymmetric pressure loading the predictions of the actual buckling load using Southwell plots of the type shown in Fig.7b varied depending on the position of the strain gauge on the shell. All the gauges near the base (ie on parallel circle 4, see Fig. 6), six on each of the outer and inner surfaces, gave values for the critical pressure head, $z_o = z_{cr}$, within a 6% wide scatter band about a mean of 44.3m. On the higher parallel circles the meridional strain gauges indicated a very similar critical buckling pressure and suggested that some global buckling was taking place with an overall mean value of $z_{cr} = 41.7$m.

Six of the twelve non-meridional gauges on parallel circles 2 and 3 near the maximum diameter of the shell demonstrated the existence of a lower mean critical buckling pressure of $z_{cr} = 27.4$m within a 20% scatter band. The other six gauges in this group, mainly with a circumferential orientation either produced erratic results from small measured strains or yielded a negative slope to the Southwell plot indicating local stiffening

of the structure. These results were ignored in relation to the buckling behaviour.

Consequently the general performance under axisymmetric pressure loading was for a dominant axisymmetric buckling mode to develop with greatest deformation near the base where an annular bulge tended to form. However, considering only meridional gauges near the apex a slightly lower mean value of z_{cr} = 36.3m was established suggesting a tendency for some axisymmetric dimpling to occur in this region. Evidence of a lower non-axisymmetric buckling mode was found in the region of the shell's maximum diameter.

Computer predictions of this behaviour can be seen to be in quite good agreement with these overall results, Table 1.

Under concentrated loading the predictions of actual buckling loads using Southwell plots of the type shown in Fig. 10b varied also depending on the position of the displacement transducer. For symmetric point loading the greatest measurable signals were produced from transducers at or near the load point and results from such transducers, it was felt,- were the more reliable for the purpose of predicting actual buckling load. The deformation pattern was for dimpling to develop at the load point and a sway to occur in the direction of the load. The data given in Fig.10a for loading on the 60° normal to the shell axis are typical of the responses obtained. The comparisons of experimental and numerical predictions of buckling load show the latter to be about twice the former, Table 1, in the case of bifurcation buckling which, as might be expected, is the lower of the numerical predictions.

For axisymmetric point loading at the apex the largest measurable signals for normal displacements were obtained at the load point. Again it was felt that such results were the most reliable. Overall behaviour was axisymmetric and took the form of dimpling at the apex with significant displacement near the base but only slight displacement in the region of the maximum diameter. This is exemplified by the computer predictions shown in Figs 4 and 5 for bifurcation and non-linear collapse buckling respectively (Ref.17). The difference in these two shapes lies in the reversal of curvature near the apex in the case of bifurcation buckling. The ratio between numerical and experimental predictions of buckling load is also of the order of 2:1, see Table 1. These discrepancies might be attributable in some part to the difficulty in simulating the actual shell containing a meridional seam or discontinuity with semi-loof type elements. The problem is being investigated.

DESIGN IMPLICATIONS

In order to insure against premature failure due to buckling some gradual thickening of the shell wall near the base is required in the case of both axisymmetric pressure and point loadings, and also in the case of concentrated normal loadings. The actual base itself could be extended slightly beyond the tangent point so that any development of a bulge would be restricted before it became too serious. Precautions would have to be taken in this region to deflect any dragged objects which might strike or become wedged in any re-entrant angle at the base.

Local buckling at other points on the shell due to the attachement of

nozzles or towing points could be resisted by a thickening of the shell wall in these regions.

CONCLUSIONS

1. Using axisymmetric ring elements good predictions of buckling behaviour under hydrostatic loading were achieved.

2. The Southwell plot approach to non-destructive buckling tests produced consistent results.

ACKNOWLEDGEMENTS

The authors wish to thank Professor A. W. Hendry, Head, Department of Civil Engineering and Building Science, University of Edinburgh for his support and encouragement. Thanks are expressed also to the secretarial and technical staff of the above department for their kind assistance. The financial support of the Vans Dunlop Scholarship fund is appreciated greatly.

TABLE 1
Buckling Loads

METHOD OF PREDICTION	AXISYMMETRIC PRESSURE HEAD m		AXISYMMETRIC Concentrated Load kN	SYMMETRIC Concentrated Load at 60° kN
	Axisymmetric Mode	Non-axisymmetric Mode		
Experimental	41.7	27.4	3.7	1.2
Theoretical bifurcation	-	31.5	6.8	2.4
snap through (non-linear collapse)	43.2	-	11.9	9.3

REFERENCES

1. R.Royles, A.B.Sofoluwe, M.M.Baig, and A.J.Currie, "Behaviour of underwater enclosures of optimum design",Strain,16,(1980),12-20.
2. R.Royles and A.B.Sofoluwe, "An optimum form for underwater storage vessels", I.A.S.S.S. (Committee of Pipes and Tanks) Symposium on 'Recent developments in the field of liquefied gas tanks', Delft, (June 1980).
3. R. Royles and A.B. Sofoluwe, "Form for an underwater storage vessel", Nigerian Journal of Science and Technology, 3, Issue 2, (1985).

4. R. Royles and J. M. Llambias, "Storage aspects of liquid gases underwater and the structural implications", Proceedings of International Symposium on 'Storage and transportation of LNG and LPG', Brugge, 2, (1984), 55-72.
5. R.V.Southwell, "On the analysis of experimental observations in problems of elastic stability", Proceedings of Royal Society, 135A (1932), 601-616.
6. S.P. Timoshenko and S. Woinowsky-Krieger, "Theory of plates and shells", McGraw Hill, New York, 2nd Edition, (1960), 442-445.
7. R. Royles and J. M. Llambias, "Point loading effects on the Echinodome", International Journal of Computers and Structures, Pergamon Press, 29, 3, (1988), 527-530.
8. J. Mistry, "Application of a finite element method to axisymmetric shells", Report, University of Liverpool, Department of Mechanical Engineering (1973).
9. Anon, "LUSAS - finite element analysis system", User Manual 87 -08, F.E.A. Ltd., Kingston upon Thames, London, (1987).
10. R. Royles and J.M. Llambias, "Buckling behaviour of an underwater storage vessel", Experimental Mechanics, 25, 4, (1985), 421-428.
11. R. Royles and J.M. Llambias, "Buckling aspects of the behaviour of an underwater pressure vessel", Applied Solid Mechanics -1, Editors: A .S. Tooth and J. Spence, Elsevier Applied Science Publishers, London, (1985), 287-303.
12. J. M. Llambias and R. Royles, "Response of an underwater structure of optimum form to concentrated loading", Proceedings of International Conference on Experimental Mechanics, Beijing, Editors: Li R. Q. and Shi G. Y., Science Press, Academica Sinica, Beijing, (1985), 687-697.
13. R. Royles, J. M. Llambias, and K. M. El-Deeb, "Response of echinodomes to asymmetric loading", Proceedings of International Conference on 'The design and construction of non-conventional structures', 8-10 December 1987, London, Civil-Comp Press, Edinburgh (1987), 167-183.
14. W. H. Horton and F. L. Cundari, "On the applicability of the Southwell plot to the interpretation of test data from instability studies of shell bodies", Proceedings AIAA/ASME 8th 'Structures, structural dynamics and materials' Conference, California (1967), 651-660.
15. N. K. Mooljee, "Curvefit on EMAS 2900", Edinburgh Regional Computing Centre, User Note 11, Edinburgh, (1983)
16. Anon, "Minitab reference manual", Minitab Release 85, Minitab Inc., University Park, PA 16802, (1985).
17. D. Bushnell, "Computerized buckling analysis of shells", Martinus Nijhoff, Dordrecht The Netherlands, (1985), 7-10.

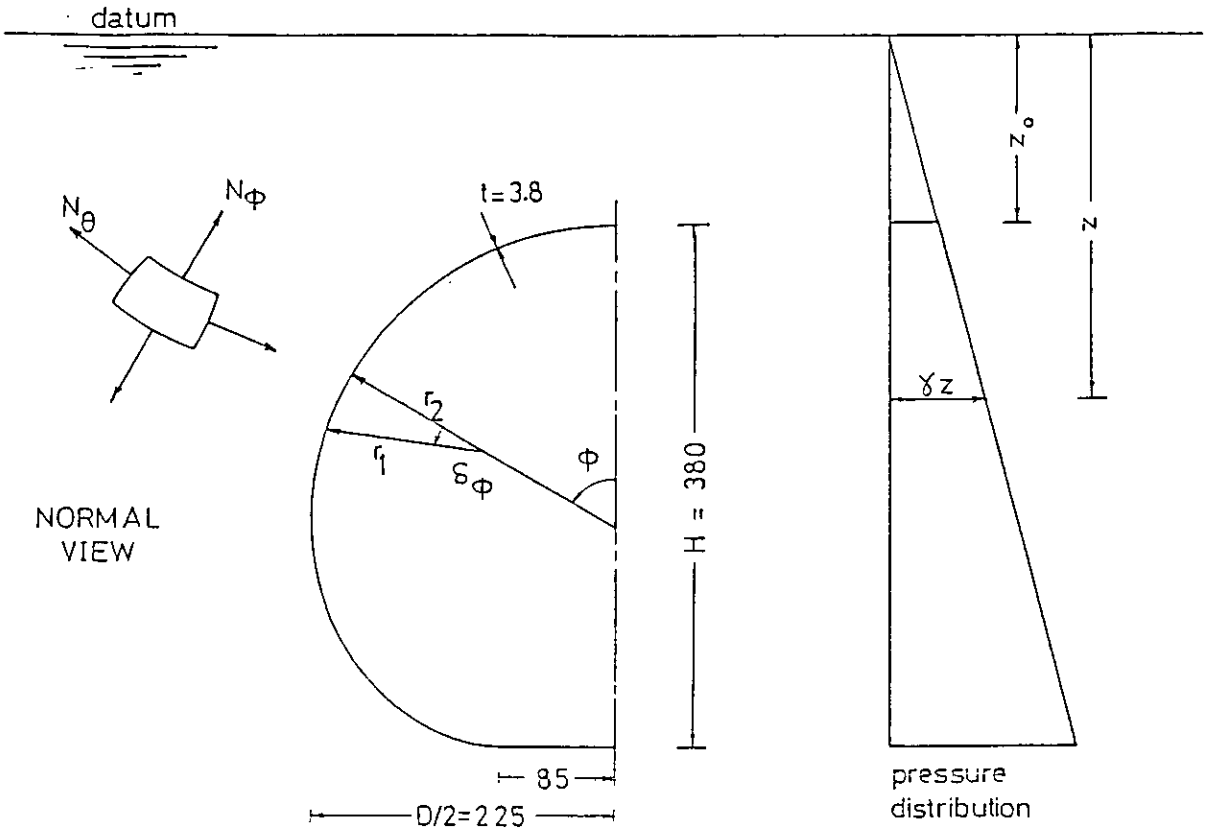

Fig. 1 Shell under axisymmetric pressure loading

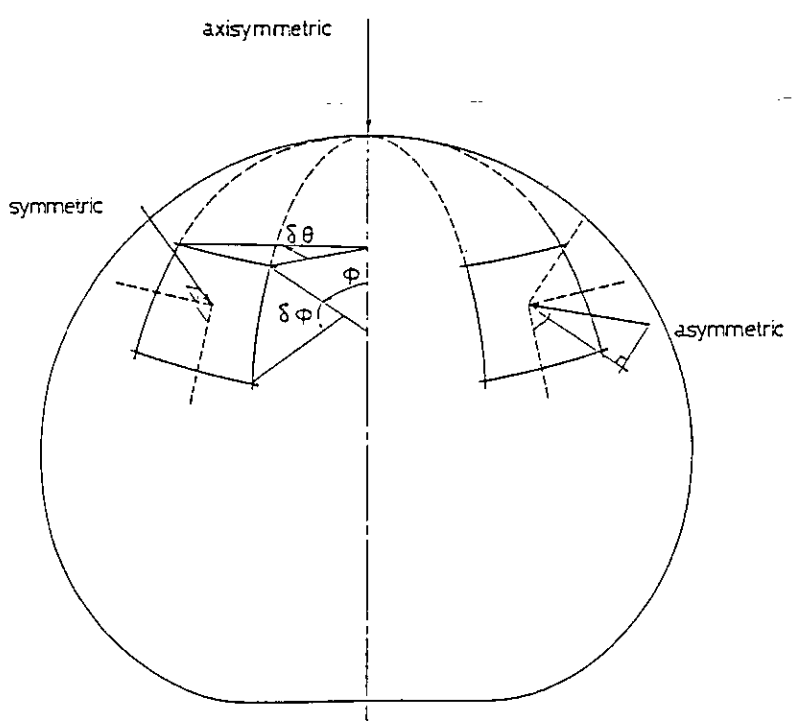

Fig. 2 Shell under concentrated loadings

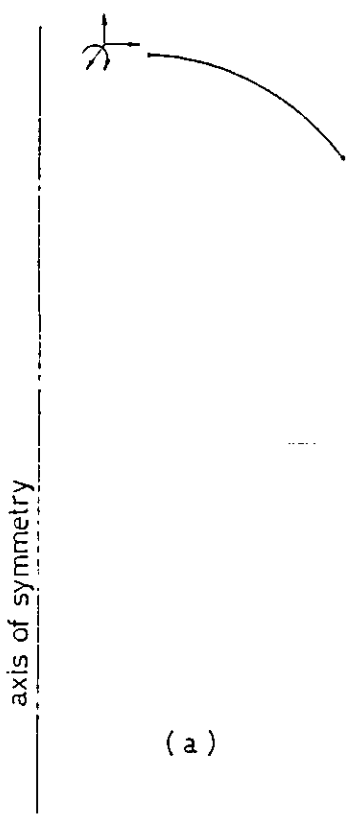

Fig. 3(a) Mistry ring element

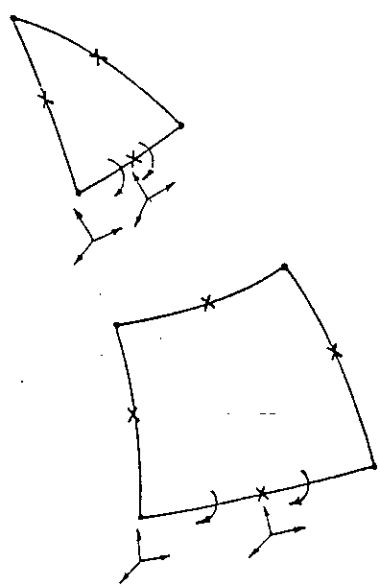

Fig. 3(b) Semi-loof shell elements

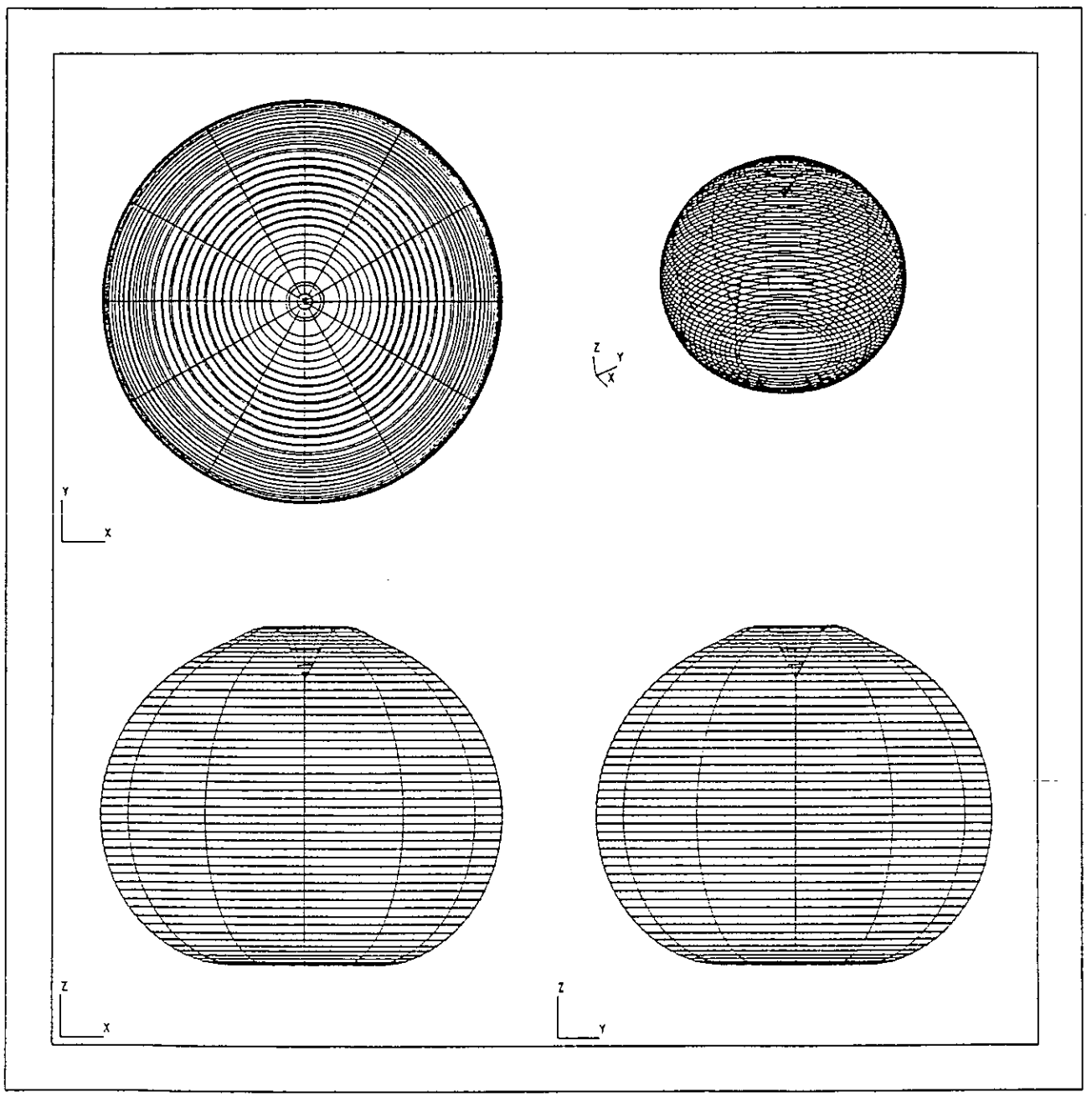

Fig. 4 Bifurcation buckling mode shape

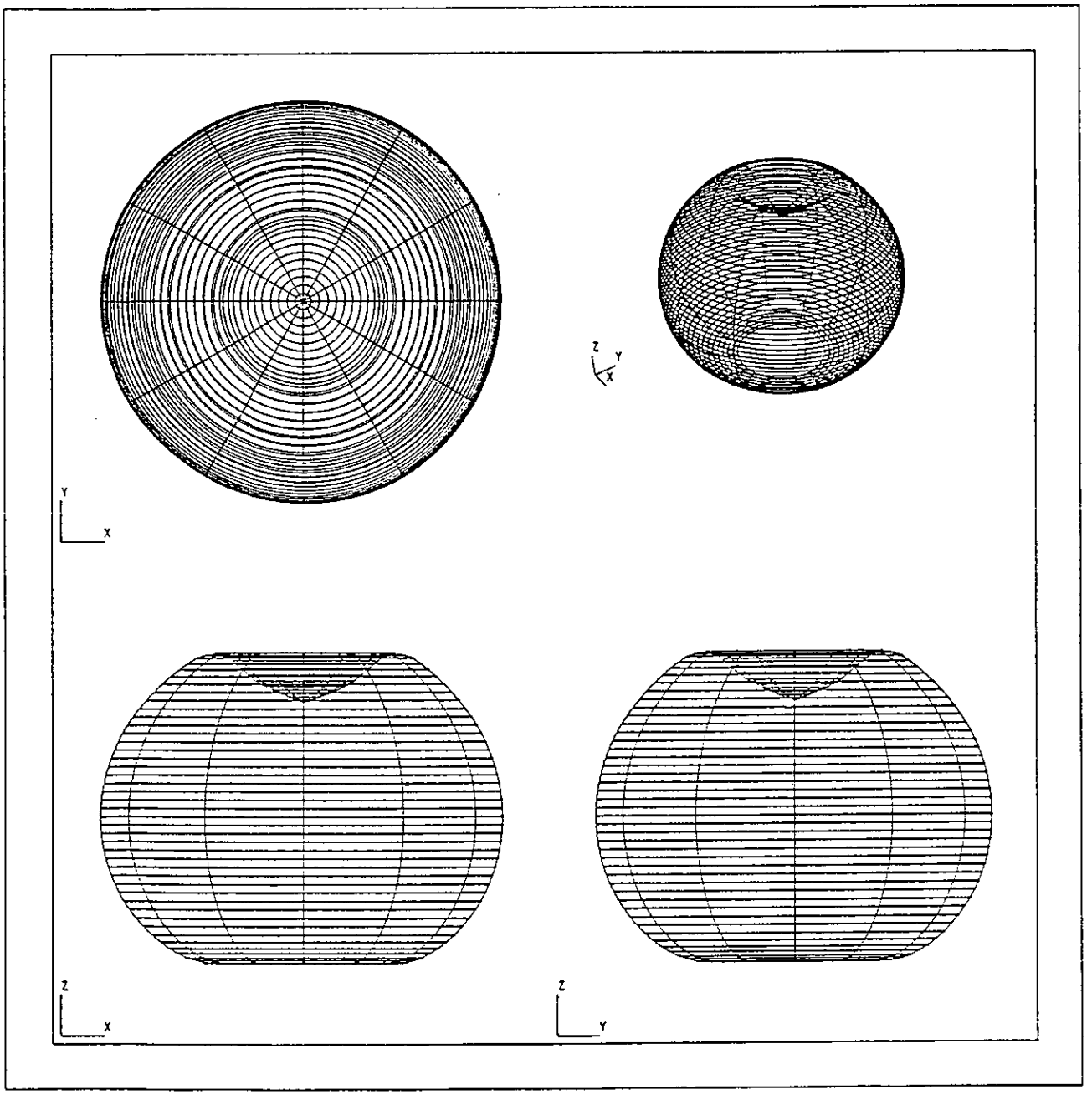

Fig. 5 Displaced shape at collapse load (snap through)

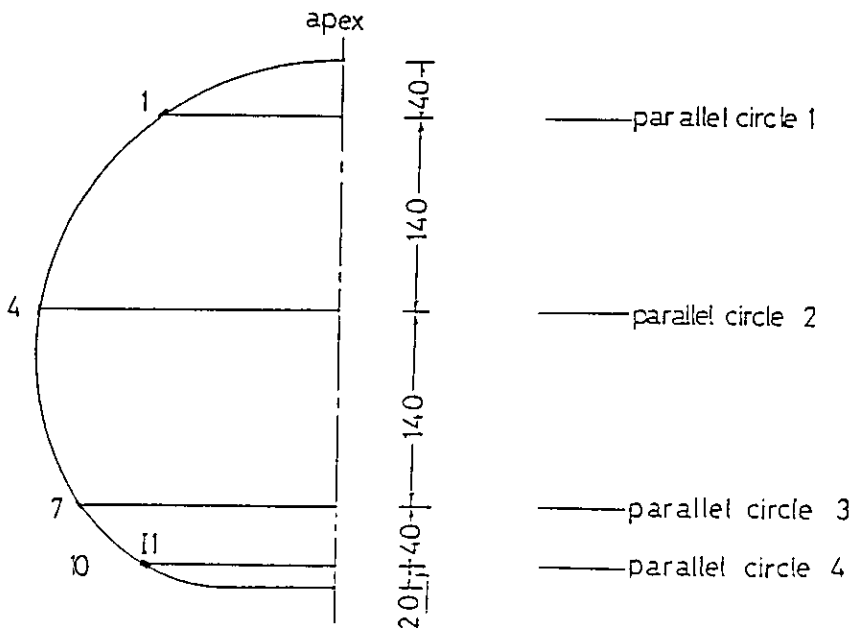

HALF SECTIONAL ELEVATION

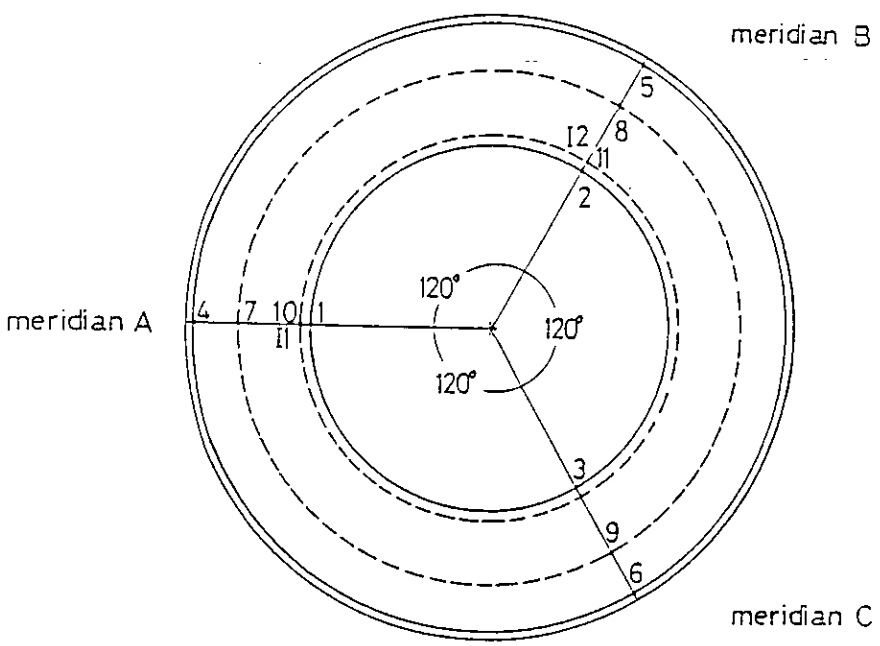

PLAN

Fig. 6 Disposition of strain gauges

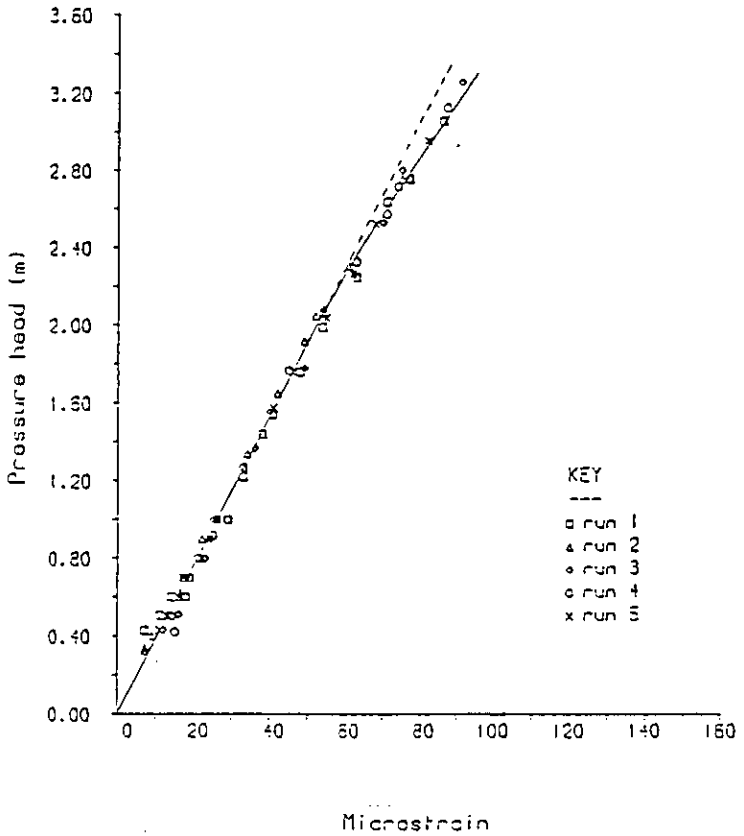

Fig. 7(a) Pressure-strain data (strain gauge 3, Ref. 11)

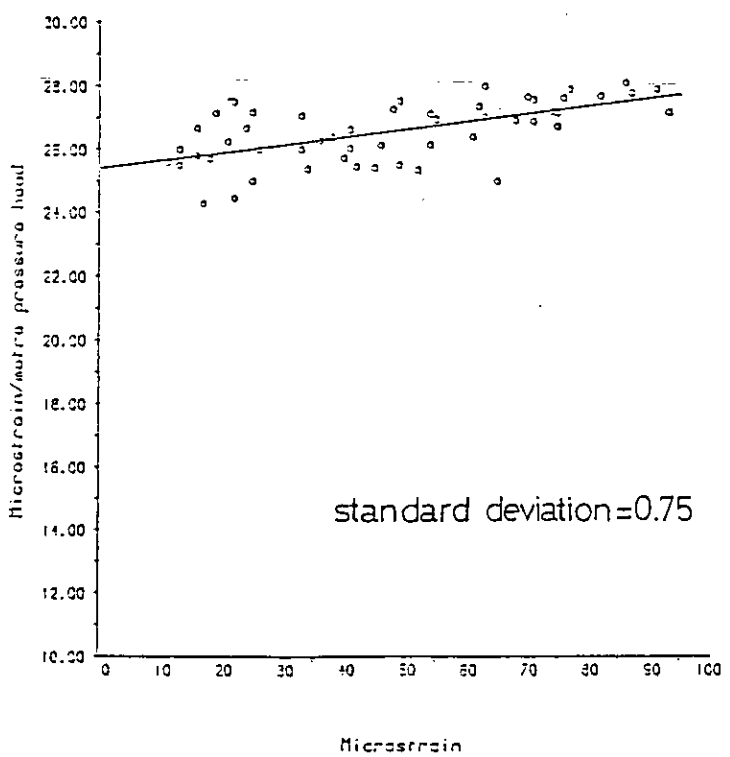

Fig. 7(b) Southwell plot of strain data (z_{cr} = 40.0m)

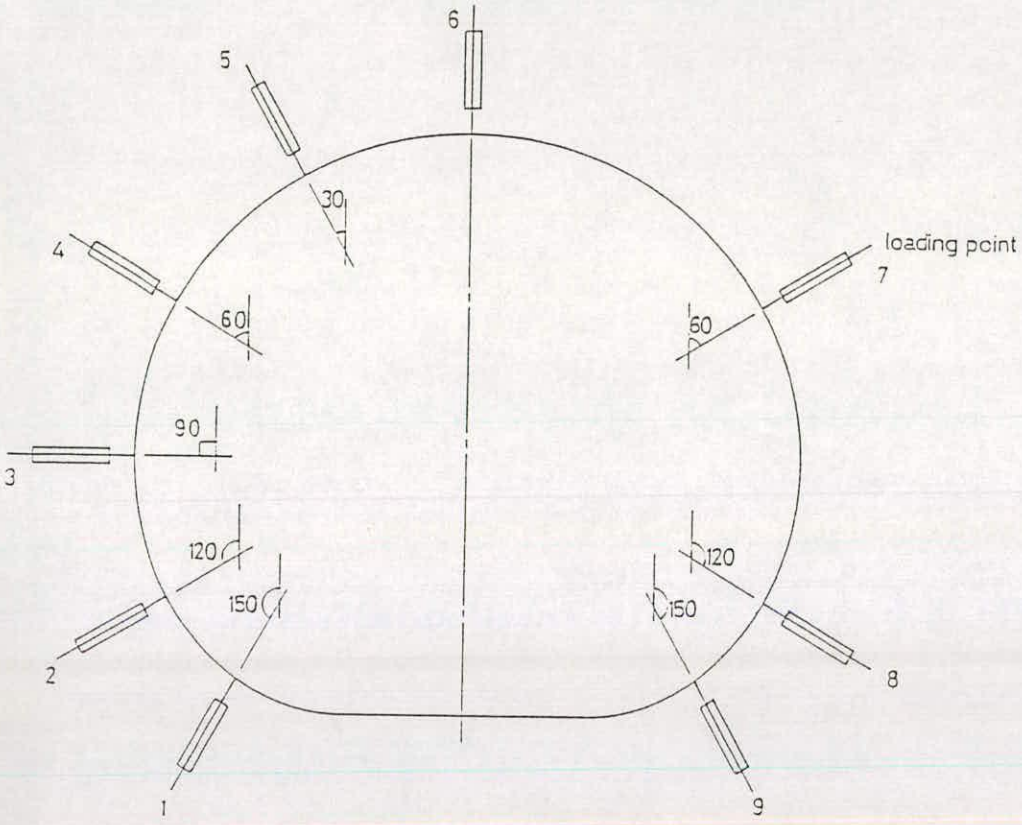

Fig. 8 Disposition of displacement transducers

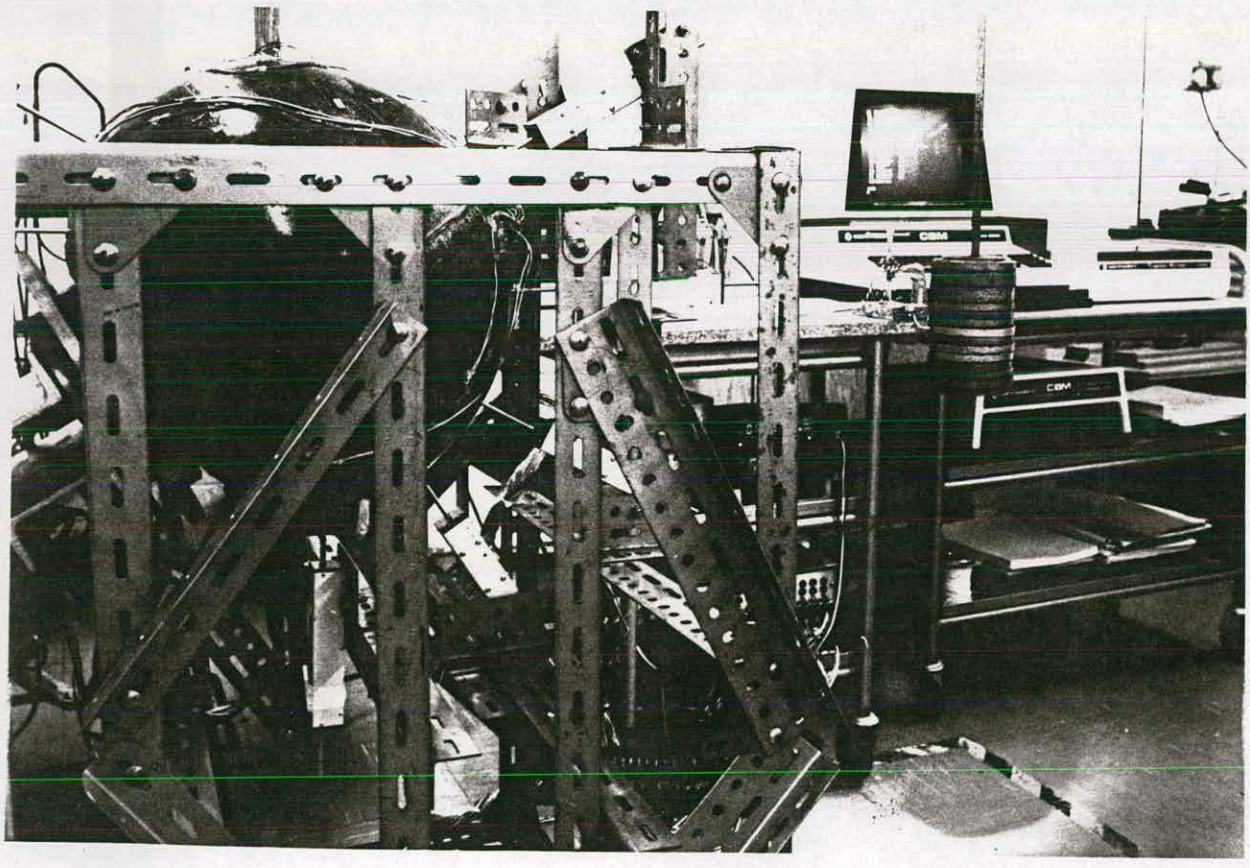

Fig. 9 Arrangement of shell under point loading

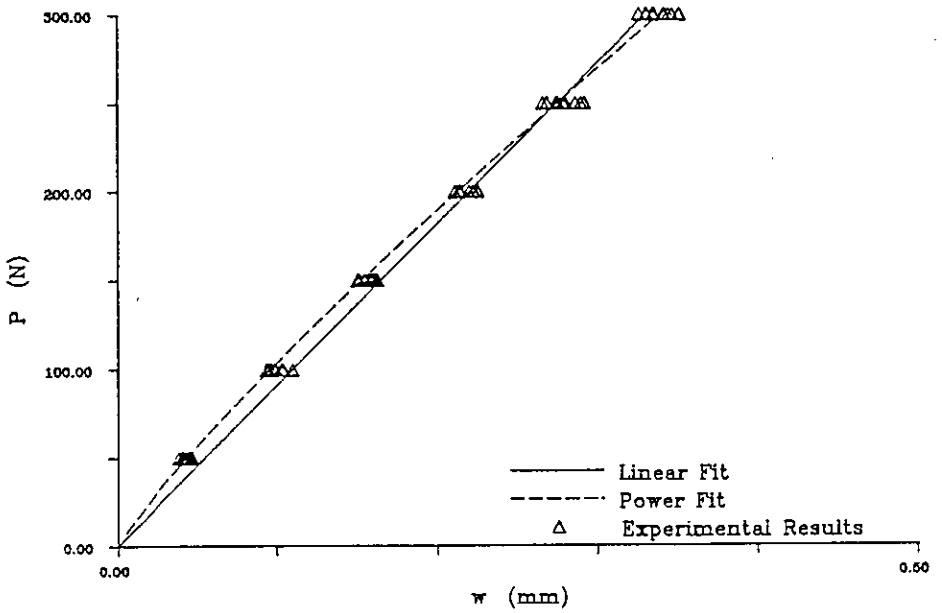

Fig. 10(a) Load-displacement data (transducer 9)

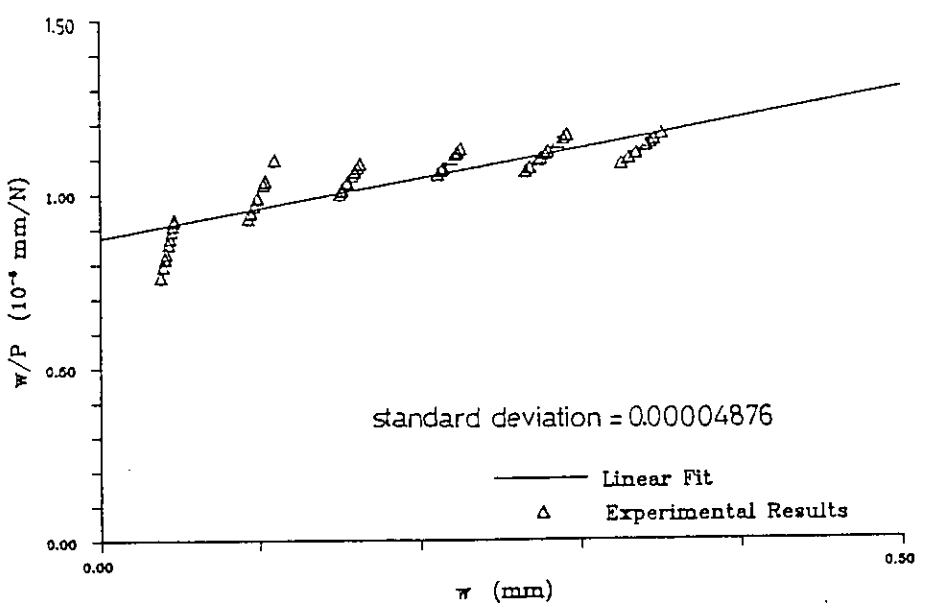

Fig. 10(b) Southwell plot of displacement data (P_{cr} = 1.2kN)